Outer Continental Shelf Environmental Assessment Program

Final Reports of Principal Investigators

Volume 74 **October 1991**

U.S. DEPARTMENT OF COMMERCE
National Oceanic and Atmospheric Administration
National Ocean Service
Office of Ocean Resources Conservation and Assessment
Arctic Environmental Assessment Center

U.S. DEPARTMENT OF THE INTERIOR
Minerals Management Service
Alaska OCS Region
OCS Study, MMS 91-0085

This is the final volume of the *OCSEAP Final Reports of Principal Investigators* to be published. These reports have been published and distributed by NOAA in order to disseminate the research findings of this program to a wide audience. Although several final reports remain to be published, budgetary limitations have resulted in the closing of the Arctic Environmental Assessment Center and the cessation of all publication efforts. Inquiries regarding OCSEAP publications can be made to:

U.S. Minerals Management Service
Attention: Library
949 E. 36th Street
Anchorage, AK 99508-4302

(907) 271-6621

OUTER CONTINENTAL SHELF ENVIRONMENTAL ASSESSMENT PROGRAM

Final Reports of Principal Investigators

Volume 74

October 1991

U.S. DEPARTMENT OF COMMERCE
National Oceanic and Atmospheric Administration
National Ocean Service
Office of Ocean Resources Conservation and Assessment
Arctic Environmental Assessment Center

U.S. DEPARTMENT OF THE INTERIOR
Minerals Management Service
Alaska OCS Region
OCS Study, MMS 91-0085

Anchorage, Alaska

The facts, conclusions, and issues appearing in these reports are based on research results of the Outer Continental Shelf Environmental Assessment Program (OCSEAP), which is managed by the National Oceanic and Atmospheric Administration, U.S. Department of Commerce, and funded (wholly or in part) by the Minerals Management Service, U.S. Department of the Interior, through an Interagency Agreement.

Mention of a commercial company or product does not constitute endorsement by the National Oceanic and Atmospheric Administration. Use for publicity or advertising purposes of information from this publication concerning proprietary products or the tests of such products is not authorized.

The content of these reports has not been altered from that submitted by the Principal Investigators. In some instances, grammatical, spelling, and punctuation errors have been corrected to improve readability; some figures and tables have been enhanced to improve clarity in reproduction.

Outer Continental Shelf Environmental Assessment Program

Final Reports of Principal Investigators

VOLUME 74 OCTOBER 1991

CONTENTS

SYNTHESIS OF SEISMICITY STUDIES FOR WESTERN ALASKA

by

N. N. Biswas, J. Pujol, G. Tytgat, and K. Dean

Geophysical Institute
University of Alaska Fairbanks
Fairbanks, Alaska 99701

Final Report
Outer Continental Shelf Environmental Assessment Program
Research Unit 486

1983

ACKNOWLEDGMENTS

We thank L. Thorsteinson and J. Kravitz of the Office of Marine Pollution Assessment (OMPA), NOAA, and R. Combellick, Alaska Department of Geology and Geophysical Surveys (formerly of OMPA), for their continuous support and encouragement during the study period. We express appreciation to T. Sokolowski and other members of the Alaska Tsunami Warning Center of NOAA for their cooperation in operating the seismographic network. With great sadness, we note the loss of life of R. Abel and severe injuries received by K. McClure of the Geophysical Institute, in a helicopter accident during the last phase of the network operation. Without their dedication and support, this study would not have been possible.

This research was supported by NOAA Contract No. NA81-RAC00112 and by the State of Alaska funds appropriated to the Geophysical Institute through the University of Alaska.

SUMMARY: OBJECTIVES, CONCLUSIONS, AND IMPLICATIONS FOR OIL AND GAS DEVELOPMENT

The objective of this study was to synthesize the available geophysical and geological information relevant to evaluation of the extent of seismic hazards posed by earthquakes located in and around Norton and Kotzebue Sounds. The locations of earthquakes determined by employing the local seismographic network show offshore and onshore seismic activity. In some cases, the observed earthquake distribution patterns closely follow the mapped traces of geologic features, principally faults.

From the analysis of the available earthquake data, it appears that normal faulting is the principal mode of strain energy release in the area. This implies that, unlike the dominance of subduction tectonics in central and southcentral Alaska (Bhattacharya and Biswas 1979), areas in western Alaska are primarily under tensional stress. This interpretation appears to be substantiated by the presence of widespread late Cenozoic basaltic volcanism (Hudson 1977) and mapped normal faults in the offshore (Eittreim et al. 1979; Fisher et al. 1981) and onshore (Hudson and Plafker 1978; Grantz et al. 1979; Turner and Swanson 1981) areas of Seward Peninsula.

Two important seismic parameters, namely recurrence time for moderate to strong earthquakes and the characteristics of wave energy attenuation, remain unresolved. However, determination of the latter can be accomplished from further analysis of the available analog data. This has been shown by Biswas and Aki (1983) for central and southcentral Alaska. It is anticipated that the results of a similar study for western Alaska will have an immense benefit for an orderly development of hydrocarbon potentials, not only for areas around Seward Peninsula, but also for the neighboring areas in the Bering and Chukchi Seas. Nevertheless, for the exploration and exploitation of economically viable hydrocarbon deposits around Seward Peninsula, prudent utilization of the available technology should provide safeguards against seismic hazards in the offshore and onshore areas.

TABLE OF CONTENTS

LIST OF FIGURES

LIST OF FIGURES (continued)

LIST OF TABLES

INTRODUCTION

General Nature and Scope of Study

In this study an attempt has been made to compile the available data related to the seismicity of western Alaska, in order to address hazards posed by current tectonic activity in the area. The data compiled were analyzed for the regional stress field in the study area. Although the study was by no means exhaustive, some of the objectives outlined below have been achieved.

Scientific Objectives

The specific objectives of this study are the following:

(1) To determine the spatial and temporal characteristics of the seismicity of western Alaska, and its relationship to mapped tectonic features.

(2) To determine the predominant failure mechanisms associated with the earthquakes located along or near the known geological features or trends.

(3) To synthesize the results of studies under (1) and (2) in order to integrate the seismotectonic settings of the study area with the overall tectonic framework of Alaska.

Relevance to Problems of Petroleum Development

Geophysical and geological explorations for hydrocarbon concentrations in the offshore areas around Seward Peninsula are in progress. Consequently, the evaluation of the level of seismicity for these areas has been a logical undertaking to assist in the planning and design of future construction projects.

CURRENT STATE OF KNOWLEDGE

Earthquakes located during about a five-year period by a local network were found to distribute widely throughout the entire study area, including

Norton and Kotzebue Sounds. Most significantly, there are a number of instances where earthquake clusters tend to lie along, or parallel to, mapped faults of linear structural trends. The seismicity is mainly crustal in nature.

The strongest earthquake recorded during the study period was of magnitude 5.2. It was located in the Kotzebue area, where the earthquake was felt quite widely. Examination of past and present magnitudes of earthquakes located in and around Seward Peninsula shows that the strongest earthquake expected to occur in the area is in the magnitude range of 6 to 7.

STUDY AREA, METHODS, RATIONALE OF DATA COLLECTION, AND PROCESSING OF DATA

The outline of the study area is shown in Figure 1. The locations of the epicenters of earthquakes shown in this figure were compiled by Meyers (1976) from the Alaskan earthquake catalog of the U.S. Geological Survey. The data represent the time period from 1867 through 1974.

The data of Figure 1 illustrate that dense clustering of earthquakes occurs along the southern coastal belts and in the central interior. Earthquake activity west of 153°W, as shown in this figure, becomes progressively diffused. However, under OCSEAP sponsorship a related project dealing with the compilation of the Alaskan earthquake catalog was undertaken by the investigators of the Geophysical Institute. The purpose of this project was to update Meyers' (1976) catalog. A plot of all earthquakes of magnitude (M) greater than 4.0 sorted for western Alaska from the updated catalog is shown by hollow squares in Figure 2; they are listed in Table 1. In this figure, the locations of the epicenters of earthquakes of M greater than 5.5 are shown by solid circles.

In Table 1, the symbols NO, ERH, ERZ, RMS, GAP and DMIN refer, respectively, to the number of station readings used to locate each earthquake, standard error in epicentral location, standard error in focal depth, root mean square of travel time residuals, largest azimuthal difference between two neighboring stations with respect to the epicenter, and the distance of the epicenter from the nearest station.

It may be noted in Figure 2 that the strongest earthquakes located in offshore and onshore areas have been one of magnitude (M) 7.3 in 1958, and one of magnitude 6.9 in 1928. At the same location as the latter event, 3 months later an earthquake of magnitude 6.2 occurred. The other two events of magnitude greater than 6.0 in the Chukchi Sea during the same year were separated by 2 days. Since these four earthquakes occurred in 1928, we may anticipate significant uncertainties in their locations and perhaps in their magnitude values.

The other strong earthquake (1958, M = 7.3) mentioned above was located in the Koyukuk River basin near the village of Huslia. This earthquake will be referred to as the Huslia earthquake. It was felt widely in central and southcentral Alaska and caused extensive ground breakage in the epicentral area (Davis 1960).

On the basis of numerous fissures observed in the lake ice, Davis (1960) delineated an ENE-WSW zone of ground breakage over an area about 100 km long and 40 km wide. He also measured maximum vertical displacement of about 1.5 m near the epicentral area along a small northwesterly oriented fault. From the field data, Davis interpreted the observed ground displacements along fissures and their orientations as more related to the topography than to the primary movement associated with the Huslia earthquake.

The main shock of the Huslia earthquake was followed by an aftershock sequence. Utsu (1962) studied this sequence and obtained a b-value of 0.93. The strongest aftershock, magnitude 6.7, was located just ESE of the main shock (Fig. 2). From the location of the epicenter of this aftershock with respect to that of the main shock, it appears that the rupture propagated in

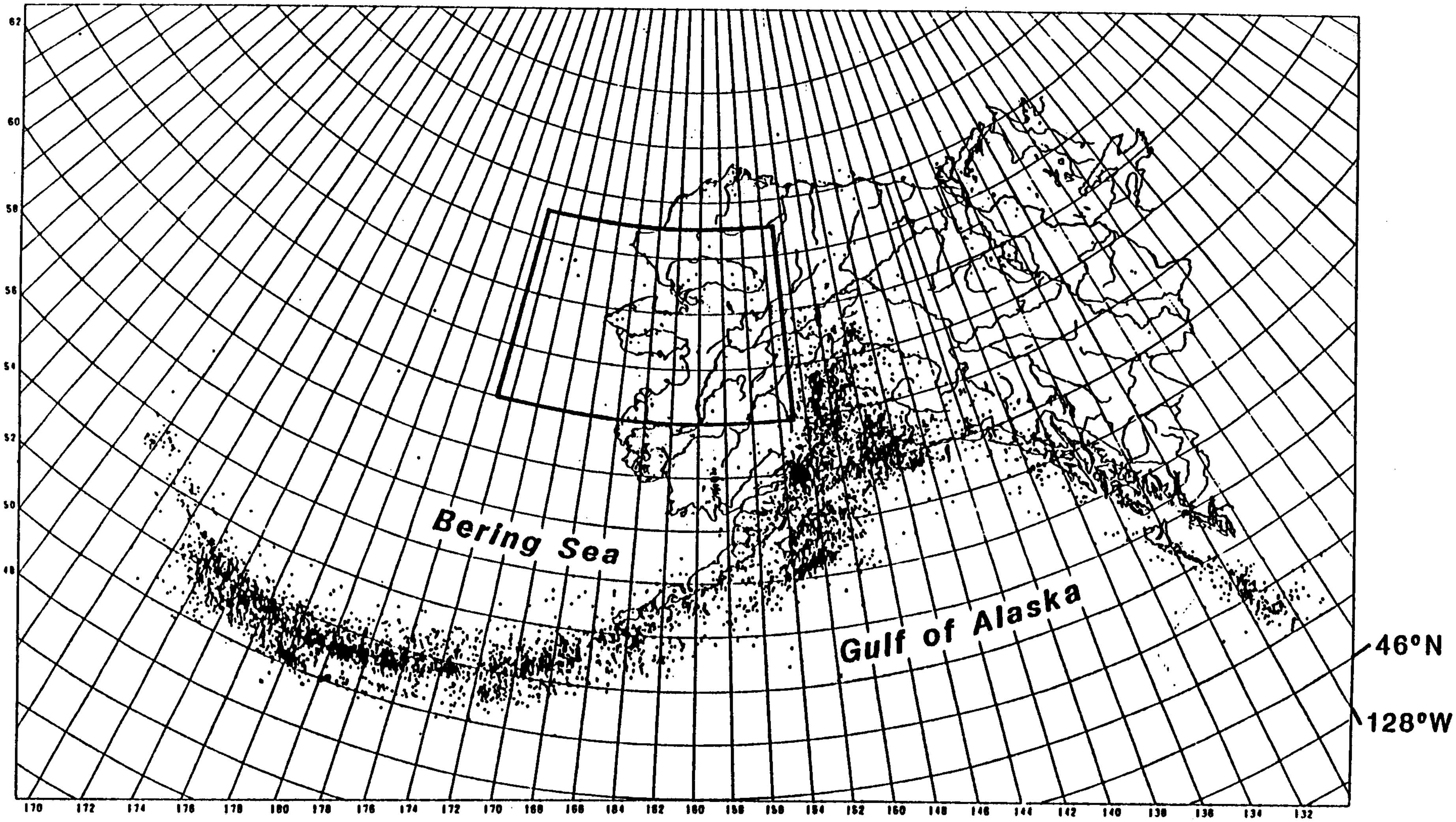

Figure 1.--Plot of epicenters of Alaskan earthquakes (Meyers 1976). Box indicates area of the present study.

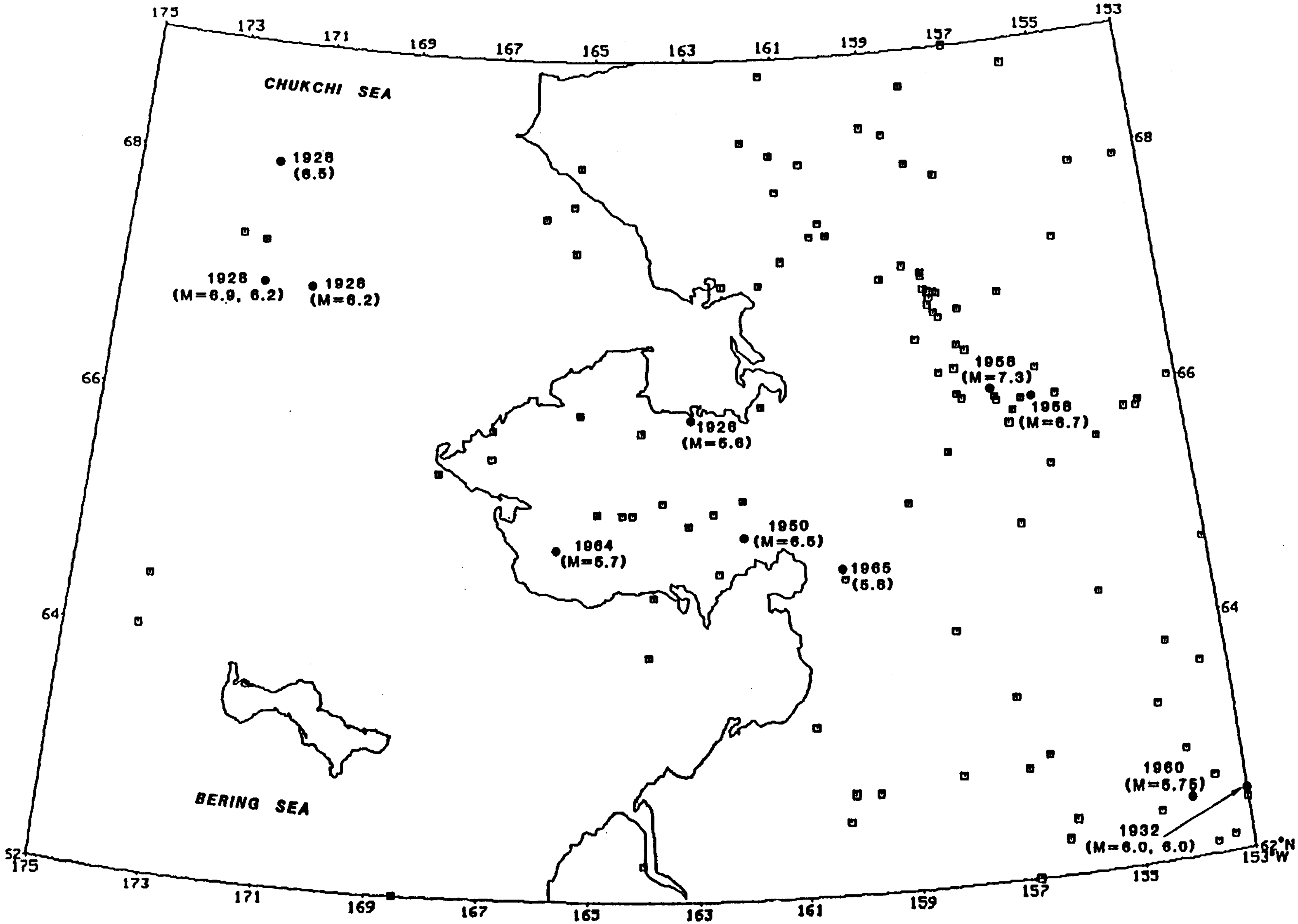

Figure 2.--Plot of epicenters of earthquakes within the area shown by solid lines in Figure 1 for magnitude (M) greater than 4.0 sorted from the Alaska Earthquake Catalog of the Geophysical Institute. Locations of events of M > 5.5 are shown by solid circles.

Table 1.--Western Alaska location details of earthquakes sorted for magnitude (M) greater than 4.0 from the Alaskan Earthquake Catalog of the Geophysical Institute. These earthquakes were located from data gathered by teleseismic and a few regional seismographic stations.

Src Yr MoDyHrMi Sec	Lat H	Long H	Depth	Ml	Src	Mc	Src	Mb	Src	MsASrc	MapICodes	FLR	CED	No	ERH	ERZ	RMS	GAP	DMIN
GUT19260714222225.00	66.000N	163.000W						5.60	PAS			676							
GUT19280221194904.00	67.000N	172.000W						6.90	PAS			670							
GUT19280224141023.00	67.000N	171.000W						6.25	PAS			672							
GUT19280226011910.00	68.000N	172.000W						6.50	PAS			672							
GUT19280501185441.00	67.000N	172.000W						6.25	PAS			670							
GUT19320325235451.00	62.500N	153.000W						6.00	PAS			1							
GUT19320608075239.00	62.500N	153.000W						6.00	PAS			1							
CGS19500826043927.00	65.000N	162.000W						6.50	PAS			676							
CGS19580407153039.50	66.100N	156.800W						7.30	PAS			676							
BCI19580408001415.00	66.000N	155.500W						5.50	MOS			676							
CGS19580413090724.00	66.000N	156.000W						6.75	PAS			676							
MOS19580706160310.00	64.300N	155.200W						5.07	MAT			1							
SYK19600716211938.80	65.890N	167.030W						4.50	PAL			676							
SYK19600716220254.40	65.650N	167.040W						4.40	PAL			676							
MOS19601221143957.00	62.500N	154.000W	00.0					5.75	PAS			1							
SYK19620304114020.10	67.340N	172.070W						4.70	PAL			670							
MOS19620716125435.00	62.000N	168.500W						5.25	MOS			3							
CGS19630708174930.90	65.800N	153.900W	33.0					4.80				676		024					
CGS19631228232026.60	62.900N	154.000W	33.0					4.20				001		009					
ISC19640322041141.00	64.100N	158.000W	33.0					4.00	ISC			1							
CGS19640611031156.60	65.500N	168.100W	33.0					4.90				673		021					
CGS19641123131501.70	63.500N	157.000W	33.0					4.30				001		006					
CGS19641213003209.40	65.200N	164.900W	33.0					4.90				676		015					
CGS19641213003324.70	64.900N	165.700W	15.0					5.40			6	676	D	046					
CGS19650221020943.50	63.600N	153.500W	33.0					4.10				001		007					
CGS19650416232218.60	64.700N	160.100W	05.0					5.80			6	001	D	071					
CGS19650707183001.20	64.500N	163.800W	33.0					4.30				676		007					
CGS19650802084529.70	62.000N	156.900W	33.0					4.60				001		005					
CGS19650815225315.80	68.100N	165.300W	66.0					4.40				676		010					
CGS19650910175717.00	63.300N	154.400W	33.0					4.30				001		005					
CGS19650913043436.50	65.300N	163.600W	33.0					4.10				676		009					
CGS19651016014405.50	65.200N	164.200W	33.0					4.40				676	F	012					
USC19651027151345.50	64.700N	162.500W	77.0					4.30	USC			676							
EPB19660224053714.00	66.080N	157.500W		4.50															
CGS19660420162440.60	65.200N	164.400W	33.0					4.10				676		012					
USE19660826101934.80	67.100N	161.500W						5.20			5	676	F	050					
CGS19670708070057.20	62.300N	156.300W	33.0					4.00			4	001	F	013					
CGS19670708091816.70	62.300N	156.300W	33.0					4.00			4	001	F	013					
NAK19671004034634.50	67.100N	158.000W	5.0	4.50	GIA									3			0.1		
LAD19671021060010.00	69.000N	157.000W						4.10	LAD			676							
GIA19671107013507.0	65.900N	156.400W	5.0	4.90	GIA									3					
GIA19680213101025.7	65.300N	162.000W	5.0	4.70	GIA									6			0.60		
GIA19680526164033.5	67.400N	165.400W	5.0	6.30	GIA									6			1.00		
CGS19680526164055.00	66.087N	161.548W	33.0					4.20				676	N	010					
GIA19680818220727.3	65.600N	154.800W	5.0	4.10	GIA									5			1.60		
NAK19680925225904.90	66.000N	156.700W	5.0	4.30	GIA									5			1.4		
NAK19690116180207.00	68.300N	161.800W	5.0	4.20	GIA									4			0.7		
NAK19690308095533.30	66.500N	157.400W	00.0	4.70	GIA									6			1.0		
NAK19690309053609.00	67.100N	158.900W	0.0	4.50	GIA									5			0.8		
USE19690409064903.90	67.100N	162.300W	06.0					4.20			5	676	F	016					
GIA19690524004301.6	65.800N	156.500W	75.0	4.10	GIA									7			0.10		
CGS19690530183736.70	65.415N	155.770W	20.0					4.10				676		014					
NAK19690719014826.20	68.800N	155.700W	15.0	5.10	GIA									5			0.3		
NAK19690801185102.90	68.300N	158.600W	00.0	4.50	GIA									6			0.1		
GIA19690813133657.5	65.600N	157.800W	50.0	4.00	GIA									4			0.70		
GIA19691019100828.4	65.100N	163.100W	25.0	4.80	GIA									3					
GIA19691218133735.5	64.000N	163.900W	50.0	4.50	GIA									8			3.90		

Table 1.--(continued)

Src Yr MoDyHrMi Sec	Lat H	Long H	Depth	Ml Src	Mc Src	Mb Src	MsASrc	MapICodes	FLR	CED	No	ERH	ERZ	RMS	GAP	DMIN
EPB19700212061130.00	67.670N	166.060W	18.0	4.40							5	24.3		1.8		
GIA19700406052742.2	65.200N	162.600W		4.90GIA							11			0.60		
NAK19700704234711.20	67.200N	158.400W	15.0	4.50GIA							6			0.2		
GIA19700828205927.2	62.900N	156.900W	50.0	4.20GIA							5			0.40		
GIA19701207214330.9	62.900N	158.100W	00.0	4.00GIA							11			5.60		
NAK19701218051940.80	66.900N	156.400W	50.0	4.10GIA							8			1.0		
NAK19710209233112.10	67.900N	153.500W	15.0	4.20GIA							6			1.5		
NAK19710405145306.50	66.800N	157.300W	00.0	5.30GIA							7			0.2		
EPB19710406205809.00	66.240N	155.840W	18.0	4.20							3	14.0		0.7		
EPB19710415204827.00	68.180N	161.150W	18.0	4.00							4	16.7		1.0		
EPB19710416013904.00	67.880N	161.060W	18.0	4.20							4	45.7		2.6		
NAK19710420011753.30	66.300N	157.500W	40.0	4.00GIA												
NAK19710422194539.60	68.100N	160.500W	40.0	4.50GIA												
GIA19710425034224.2	63.800N	154.100W	50.0	4.20GIA							8			3.70		
GIA19710429152955.1	62.300N	164.000W	00.0	5.00GIA							6			0.90		
GIA19710819222047.6	62.600N	160.200W	00.0	5.20GIA							7			2.20		
GIA19710906004711.3	65.200N	158.700W	00.0	4.20GIA							7			0.40		
ISC19711005014041.57	67.375N	172.575W	33.0			5.20			670		133	9.5				223.1
NAK19711124041253.90	67.300N	155.100W	62.0	4.50GIA												
NAK19711209173150.10	67.900N	154.500W		4.30GIA							5			1.3		
GIA19711224175940.3	63.000N	156.500W		4.00GIA							5			1.70		
NAK19720202112835.00	67.130N	158.010W	00.0	4.30GIA							14			0.4		
NAK19720306191726.00	66.960N	157.760W	50.0	4.00GIA							17			0.8		
NAK19720419071611.20	66.970N	157.890W	00.0	4.20GIA							16			0.6		
NAK19720421054122.90	66.860N	157.920W	75.0	4.00GIA							14			0.7		
NAK19720512065256.80	66.950N	157.700W	40.0	4.50GIA							20			1.0		
ISC19720618120908.03	62.426N	153.011W	27.0			4.70			1		71	6.4	6.2			222.9
NAK19720803051055.60	66.450N	157.230W	00.0	4.10GIA							11			1.7		
NAK19721003031845.60	66.790N	157.810W	75.0	5.10GIA							19			0.9		
ISC19721004054108.73	62.813N	159.638W	33.0			4.00			1		24	10.5				222.9
GIA19721022194055.1	62.820N	160.080W		4.80GIA							14			2.30		
ERL19721115154056.00	67.491N	159.994W	33.0			4.80			676	N	010					
ERL19721204084321.20	67.495N	160.333W	10.0			4.30			676		013					
NAK19730205173556.00	66.990N	157.980W	00.0	4.50GIA							15			0.8		
NAK19730322020507.50	68.860N	161.290W	00.0	4.20GIA							7			0.4		
NAK19730326074632.90	67.300N	161.000W	44.0	4.30GIA							10			0.7		
ISC19730411051218.09	64.614N	160.043W	15.0			4.20			1		72	8.0				111.5
NAK19730612121010.10	68.370N	159.090W	00.0	4.10GIA							9			1.6		
GIA19730623235238.2	65.840N	153.840W	50.0	4.10GIA							7			0.30		
NAK19730801110523.30	68.690N	158.080W		4.60GIA							10			0.3		
NAK19730811171348.90	66.580N	158.250W	50.0	4.30GIA							5			0.9		
NAK19730911090212.80	66.280N	157.820W	00.0	4.00GIA							15			4.4		
ISC19731005092211.87	66.027N	156.736W	68.0			4.10			676		30	25.8				111.5
NAK19731005094034.90	66.750N	157.710W	75.0	5.00GIA							18			1.0		
NAK19731006020451.50	66.960N	157.900W	00.0	4.90GIA							12			0.5		
NAK19731120024117.60	67.780N	165.440W		4.50GIA							8			1.9		
NAK19731211092330.10	66.910N	157.870W	00.0	5.10GIA							15			0.6		
GIA19740219210232.3	65.990N	156.200W	40.0	4.30GIA							18			1.70		
ISC19740414154314.57	64.458N	173.509W	46.0			4.50			671		51	22.7	14.0			557.4
ISC19740415022937.12	64.032N	173.594W	33.0			4.30			671		22	23.6				557.4
GIA19740526005733.56	64.944N	156.507W	39.5	4.95GIA							4			1.10	336	405.1
ISC19740811125749.15	66.030N	165.263W	33.0			4.00			676		16	22.3				557.5
LAR19740928033947.82	62.452N	156.122W	50.1		4.00LAR						4	25.0	25.0	0.03	314	322.
NAK19741021013137.16	68.041N	158.146W	34.0	4.75GIA							4			0.8	293	293.4
LAR19741021221325.32	62.141N	153.331W	69.4		4.30LAR						9	23.6	25.0	1.15	320	270.
GIA19741109154522.15	62.422N	154.594W	05.7	4.19GIA							8	27.5	24.7	0.40	276	222.3
ISC19750208113959.95	67.600N	160.137W				5.00			676		17	53.9				

Table 1.--(continued)

Src	Yr MoDyHrMi Sec	Lat H	Long H	Depth	Ml	Src	Mc	Src	Mb	Src	MsASrc	MapICodes	FLR	CED	No	ERH	ERZ	RMS	GAP	DMIN
NAK	19750406062231.73	66.043N	157.408W	22.4	4.05	GIA									6	34.3	123.3	0.2	200	168.7
LAR	19751127001422.25	62.105N	153.646W	85.0			4.10	LAR							8	12.7	23.7	0.70	317	199.
NAK	19760104155111.94	66.013N	153.167W	5.0	4.23	GIA									3				188	24.0
GIA	19760122081319.75	63.386N	160.749W	45.6	4.13	GIA									4			1.08	245	228.9
GS	19760127052717.60	64.618N	153.062W	33.0	4.20	PMR			3.9				001		15					
GIA	19760313231042.74	67.924N	157.516W	50.5	4.87	GIA									5	10.8	4.9	0.18	287	266.2
LAR	19760406133940.43	62.642N	153.542W	64.0			4.10	LAR							5	17.2	19.7	0.16	298	277.
GIA	19760407225259.79	65.807N	154.137W	17.1	4.50	GIA									7	22.2	9.0	0.54	240	35.9

the ESE direction. This direction roughly agrees with that of the small fault observed by Davis (1960), but it differs from the rectilinear zone (ESE-WSW) of ground breakage as noted by Davis. The most probable orientation of the rupture formed by the Huslia earthquake is discussed further in a later section.

The two earthquakes (magnitude > 5.5) located in 1964 and 1965 were felt strongly by the coastal communities of Norton Sound (Fig. 2). The characteristics of these earthquakes are given in a later section.

In view of the earthquakes shown in Figure 2, it appeared logical to investigate the nature of seismicity in western Alaska more closely. In order to achieve this objective, initially a seven-station local seismographic network was installed during the fourth quarter of 1976. These stations supplemented a single station on Granite Mountain (GMA) which was operated by the Alaska Tsunami Warning Center (ATWC) on the eastern side of Seward Peninsula. This station was closed in mid-1978.

The local earthquakes detected with the above network, besides having significant scatter, revealed a few clusters of epicenters along mapped geologic features. Biswas et al. (1980) have given the details of this phase of the study. However, to increase the precision in the locations of earthquakes, network density was increased in mid-1980 by installing another nine short-period vertical component stations. The layout of the network is shown in Figure 3; the stations shown by the hollow square and circles were installed in 1976, and those by solid circles in 1980.

Each station of the network consisted of a short-period vertical component seismometer (Geotech S13), set to a nominal one-second natural period with 0.5 of critical damping. However, the station located at Kotzebue (KTA) had three components (vertical, north-south, east-west) and was equipped with different model seismometers (Geotech S500) than the other stations. This model of seismometer is small enough (0.057 m diameter and 0.165 m

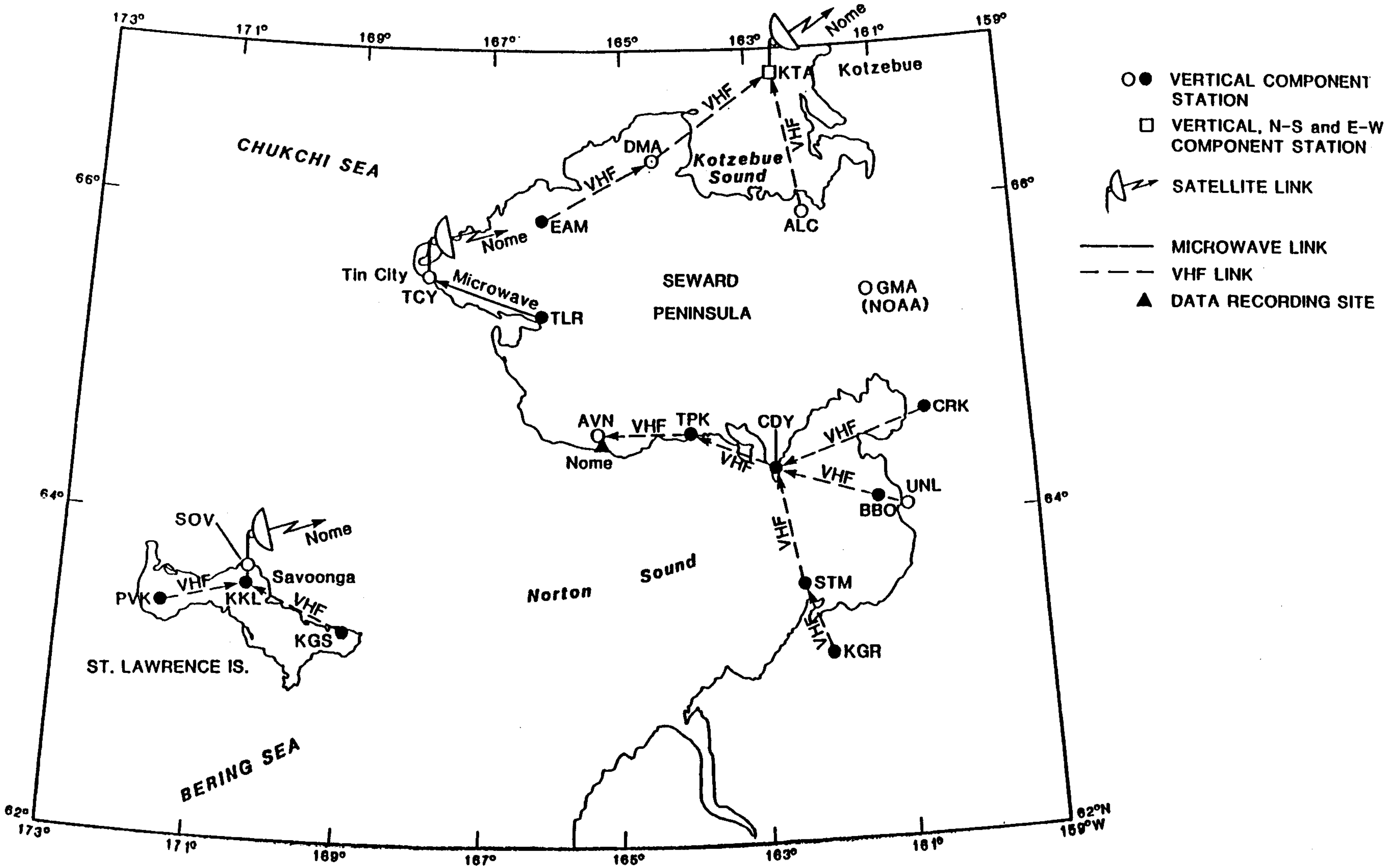

Figure 3.--Layout of the local seismographic network operated from 1976 through mid-1982. Hollow square and circles represent stations installed in the fourth quarter of 1976. Solid circles represent the stations added to the network in mid-1980. Station UNL was replaced by BBO in mid-1980.

length) to facilitate installation, and has the added benefit of being insensitive to ground tilt. This was particularly important because a layer of permafrost was encountered at shallow depth (1-2 ft) at this station site.

The signals from the seismometers were preamplified by Monitron Model 2000 or 2001 amplifiers. The electronic systems of all stations, except for the one at Kotzebue (KTA), were powered by a set of Carbonaire Model ST-22 batteries, capable of delivering 1100 Amp-hr of service. The electronic package at KTA was powered by locally available 110V lines. The data from the stations were telemetered to the central recording site at Northwest Community College at Nome by frequency-modulated audio subcarriers via a combination of VHF (transmitter: Monitron T15F; receiver: Monitron R15F) and microwave leased circuits.

The microseismic background was found to vary considerably from one station site to the next. However, the operational gain of each station was set to attain maximum signal-to-noise ratio. Consequently, all stations of the network could not be operated at identical gain settings. The system response of the network is shown in Figure 4 in which it may be noted that the lowest and highest gain settings were about 80K and 1M at 5Hz, respectively.

The recording site consisted of an uninterruptible power supply system (TOPAZ), a discriminator bank (EMTEL), synchronized digital clock (True-Time), and 16-mm film recorder (Geotech). The film record was changed daily and shipped to Fairbanks weekly.

In addition to recording the data of the network at Nome, the data from the local Nome seismographic station AVN (Fig. 3) were telemetered to the Geophysical Institute by microwave circuit. This long circuit was leased by the Alaska Tsunami Warning Center, Palmer. Though the station was operated by us, the data were shared by both the organizations. Station location details are given in Table 2.

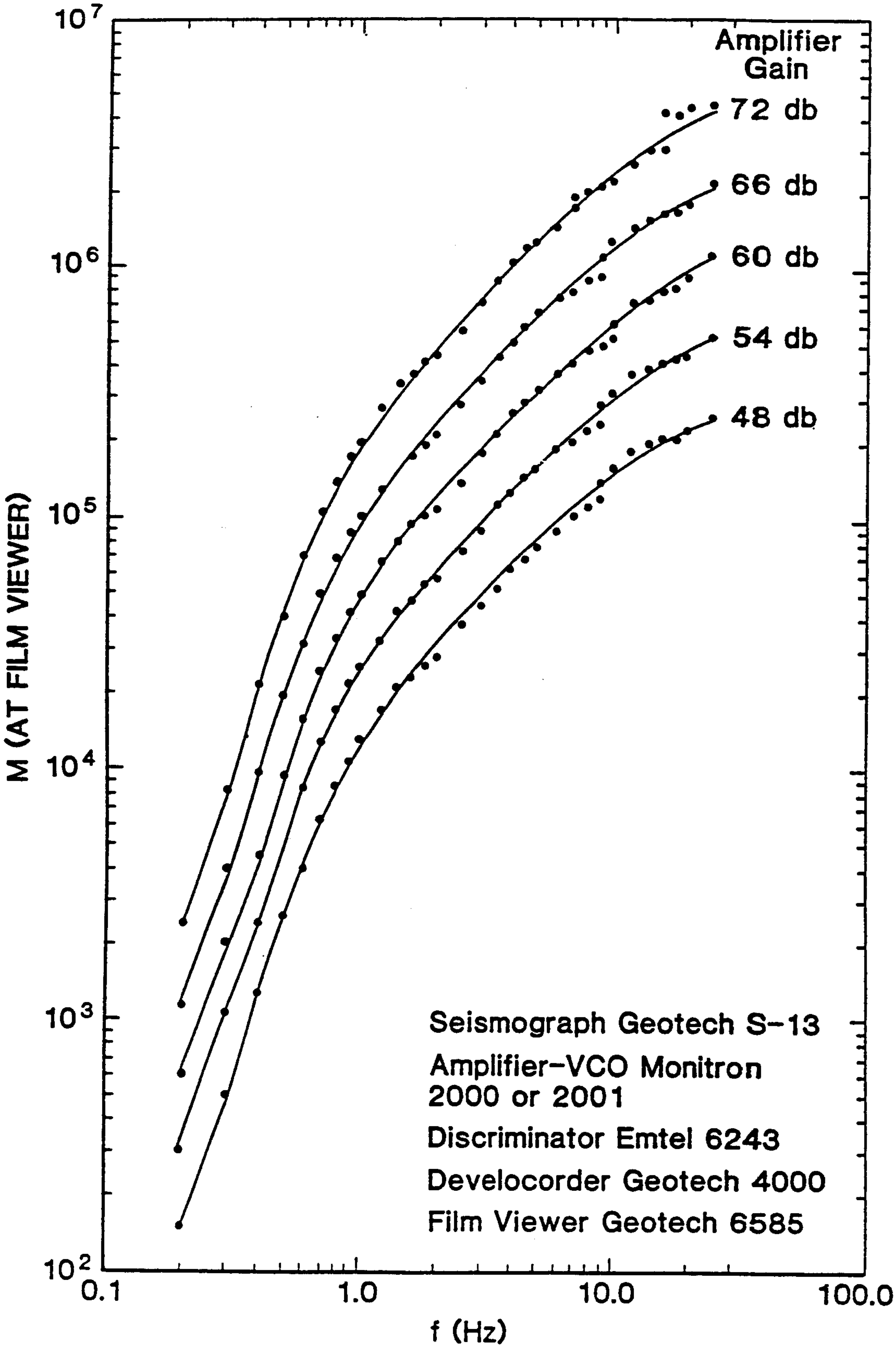

Figure 4.--Operational gain setting for the stations in Figure 3.

Table 2.--Location details of the local seismograph stations in western Alaska used for the present study.

Station Name	Code	Lat. (N) Degree	Long. (W) Degree	Elevation M	Satellite Time Delay (sec)	Site Geologic Formations
Alder Creek	ALC	62.62	141.01	582		Permafrosted Metamorphic (Pre-Cambrian)
Anvil Mt.	AVN	64.56	165.37	323		Metamorphic (Lower-Middle Paleozoic)
Besboro Is.	BBO	64.12	161.30	244		Volcanic (Cretaceous)
Cape Darby	CDY	64.34	162.79	335		Volcanic (Cretaceous)
Christmas Creek	CRK	64.67	160.53	680		Sedimentary (Cretaceous)
Devil Mt.	DMA	66.30	164.52	238	0.54	Volcanic (Quaternary)
Ear Mt.	EAM	65.92	166.24	701	0.54	Igneous (Upper Cretaceous)
Granite Mt. (NOAA, Closed mid 1978)	GMA	65.43	161.23	858		Volcanic (Tertiary)
Kogog River	KGR	63.16	162.05	320		Volcanic (Quaternary)
Kanguksam Mt.	KGS	63.30	168.99	488	0.54	Volcanic (Quaternary)
Kookooligit Mt.	KKL	63.59	170.37	655	0.54	Volcanic (Quaternary)
Kotzebue	KTA	66.84	162.59	24	0.54	Permafrosted Sedimentary (Quaternary)
Poovook Mt.	PVK	66.44	171.55	411	0.54	Volcanic (Cretaceous)
Savoonga	SOV	63.65	170.45	198	0.54	Volcanic (Quaternary)
Stuart Is.	STM	63.59	162.43	140		Volcanic (Quaternary)
Tin City	TCY	65.56	167.95	72	0.54	Igneous (Upper Cretaceous)
Teller	TLR	65.32	166.21	122	0.54	Metamorphic (Pre-Cambrian)
Topkok Pt.	TPK	64.55	163.99	122		Volcanic (Pre-Cambrian)
Unalakleet (Replaced by BBO in mid 1980)	UNL	63.89	160.67	122		Volcanic (Cretaceous)

At the Geophysical Institute, the telemetered data from AVN were recorded on heat sensitive paper by Helicorder (Geotech RV-301B). This recording mode facilitated the identification of local earthquakes and approximate origin time for rapid scaling of the daily film records recorded at the central recording site (Nome). The following data were scaled from the records: first arrival times of the P-wave and the S-wave when possible, direction of P-wave motion, and the maximum amplitude and period in the recorded trace.

For impulsive arrivals, the first onset times for P-waves could be scaled with a precision of ±0.1 sec, while for emergent arrivals, the uncertainty in the arrival times might be as high as ±0.5 sec. For S-wave arrivals, uncertainty of the measurements is even larger.

Scaled data for each earthquake were input in appropriate format to the VAX 11/780 computer and processed by the computer program of Lahr (1982) for location purposes. The local magnitudes (M) of the earthquakes were computed by using the formula of Richter (1958) for local earthquakes, incorporating a correction factor for the instrumentation used.

The crust and upper mantle structure for western Alaska is not yet known. Thus, to compute travel times for P waves, a plane-layered P-wave velocity model for the crust, obtained from the central Alaskan data from earthquakes and quarry blasts, was used. The upper mantle section was taken from Biswas and Bhattacharya (1974). The details of this model are shown in Table 3. A ratio of 1.78 between P- and S-wave velocities, corresponding to Poisson's solid, was used for the computation of S-wave travel times.

These limitations being understood, a preliminary computer run was made and the output was examined for reading errors. If the time residuals for an earthquake (that is, the difference between the observed and computed travel times) for any station exceeded 1 sec, the records were rescaled to reduce the uncertainties to a minimum. The corrected data were then used for a second computer run, allowing all focal parameters to vary. The results indicated that for a significant number of earthquakes, the hypocenters were located at sub-crustal depths which differed from the results of Biswas et al. (1980). They used the computer program (HYPO-71) of Lee and Lahr (1975) for location purposes and interpreted the results to represent crustal seismicity for western Alaska. The location program (Hypoellipse) used in the present study is a modified version of HYPO-71.

In order to resolve the discrepancy in focal depths, the data for a group of well-recorded earthquakes distributed over Seward Peninsula were selected. For this data set, different initial focal depths were assigned in the least squares iteration used by the location program. The results are shown in Table 4.

The values in the first column in Table 4 represent the assigned initial focal depths, while those in column 2 are location program output. However, the values in columns 2-5 are averages of values obtained for all the earthquakes selected for the test case.

On the basis of the least average values obtained for both RMS and ERZ in the above test (Table 4) for 10 km as the initial focal depth, we set this depth as the starting value for all earthquakes in the location program. In addition, the earlier data gathered from 1977 through mid-1980 were reprocessed for maintaining consistency with the results obtained for the data of the later period (mid-1980 through mid-1982). The final output of the location computer program yielding the location details of the hypocenters is given in Table 5.

Out of several hundred earthquakes located with the data gathered by the local network, only for 16 events the focal depths exceeded 40 km, thereby confirming the earlier results of Biswas et al. (1980). Furthermore, only 20% of the total number of earthquakes located by the sparsely distributed stations during 1977 through mid-1980 have location errors of less than 10 km in both epicentral positions (ERH) and focal depths (ERZ). The percentage

Table 3.--P-wave velocity structure of the crust and upper mantle used to compute travel times for hypocenter locations.

Layer Thickness (km)	P-Wave Velocity (km/sec)
24.4	5.9
15.8	7.4
35.8	7.9
225.0	8.29
224.0	10.39
∞	12.58

Table 4.--Results of location test for a selected group of earthquakes. The first column shows the initial depth assigned for each earthquake in the group in locating by Hypoellipse computer programs. The values in the rest of the columns are averages of values under the headings for the events in the group selected for the test.

Starting Hypocenter Depth (km)	HYPOELLIPSE Depth (km) Output	<RMS> (sec)	<ERH> (km)	<ERZ> (km)
50	22.8	0.31	32.6	60.9
40	21.8	0.30	37.0	48.0
30	18.6	0.26	24.7	47.2
20	18.2	0.30	29.2	38.0
10	10.6	0.26	23.6	33.0
5	7.7	0.29	21.3	36.7

Table 5.--Location details of the earthquakes located from the data gathered by the local seismographic network used for this study.

DATE	ORIGIN	LAT N	LONG W	DEPTH	MAG	NO	GAP	DMIN	RMS	ERH	ERZ
770115	012 44.79	68N23.74	159W11.89	7.40	3.84	5	333	100.0	0.15	99.0	99.0
770117	14 1 3.15	66N47.65	167W33.43	25.22		5	259	268.1	1.40	26.0	41.7
770207	533 55.01	65N 3.39	162W27.91	15.91	2.41	6	164	160.2	0.10	5.6	8.3
770210	136 38.68	68N21.95	161W57.06	23.30		4	343	100.0	0.03	99.0	99.0
770211	8 6 57.86	64N28.61	168W20.05	4.27*		4	306	100.0	0.93	99.0	99.0
770212	2050 8.91	67N47.55	163W57.47	3.97	2.92	4	356	100.0	0.40	99.0	99.0
770221	21 1 49.06	65N 1.04	164W 8.33	10.00*		4	149	215.3	0.84	99.0	99.0
770221	2146 8.21	65N 1.26	163W45.43	17.20		5	137	200.5	0.10	6.3	7.7
770224	1928 2.79	64N39.12	167W40.65	10.00	3.43	7	301	100.0	0.42	27.8	14.8
770228	2120 18.40	66N 1.20	155W54.25	13.98	3.25	8	189	253.2	0.44	4.9	4.7
770302	1110 13.46	63N30.31	165W11.19	9.34	3.75	6	278	286.6	1.30	21.1	25.1
770311	212 46.25	67N 5.77	160W15.63	11.25	2.96	4	298	100.0	0.04	99.0	99.0
770318	636 38.08	63N54.69	164W48.46	48.89		4	251	100.0	0.97	30.9	53.5
770319	1 2 17.67	64N58.44	162W21.68	10.00*	3.27	3	152	150.3	0.00	99.0	99.0
770320	524 1.78	64N59.30	162W19.20	10.24	2.17	4	152	152.6	0.00	10.4	17.7
770320	1220 19.23	64N58.30	163W39.71	10.00*	2.69	6	131	193.6	0.95	6.3	13.1
770321	8 6 1.19	62N 0.96	165W10.39	10.00*	4.49	4	312	427.2	0.04	99.0	99.0
770323	1031 4.28	64N32.58	165W43.35	0.00		4	306	100.0	1.59	99.0	66.9
770323	1351 20.08	63N12.76	173W 2.15	0.26*		4	344	100.0	1.13	99.0	99.0
770402	427 52.24	65N40.94	154W34.88	11.51	2.76	4	166	100.0	0.63	99.0	99.0
770403	1433 8.50	66N17.14	161W49.23	1.33*	2.69	5	193	100.0	0.21	27.5	24.9
770406	1939 0.96	66N10.05	163W 4.23	10.00		4	258	100.0	1.46	99.0	99.0
770407	1855 24.51	66N13.80	163W15.51	31.49		4	240	225.2	0.41	99.0	99.0
770407	19 8 23.91	64N55.23	157W44.09	8.90	2.55	6	177	100.0	0.56	4.2	8.2
770408	12 2 46.00	65N14.34	167W 3.35	0.36	2.35	5	180	100.0	0.13	99.0	99.0
770409	910 55.90	65N11.84	167W11.33	10.00	2.82	5	192	100.0	0.10	34.0	24.1
770409	18 9 38.39	63N59.78	164W37.95	9.88	2.12	4	239	100.0	0.10	92.5	99.0
770409	2240 39.03	67N 0.14	163W 4.85	7.49	3.42	5	254	270.2	0.01	41.4	11.6
770410	044 19.37	65N14.29	167W 4.41	0.06		5	181	100.0	0.77	99.0	99.0
770410	1640 47.89	64N58.58	162W22.18	24.79	1.70	5	152	150.3	0.00	1.9	99.0
770411	950 10.29	64N48.80	164W 6.36	10.00*	4.01	7	127	197.1	0.42	3.3	5.7
770411	1826 12.91	64N50.89	164W 5.08	24.95	2.69	5	180	196.3	0.12	8.4	57.6
770412	028 4.97	64N55.93	167W45.87	10.00*	3.45	5	245	100.0	0.54	99.0	77.8
770412	641 31.49	64N47.41	168W15.88	4.63		4	272	100.0	1.29	24.9	31.8
770413	535 15.73	65N 1.72	164W10.31	9.61	3.17	7	104	144.5	0.55	3.1	4.5
770413	648 10.23	65N18.71	163W24.05	6.77	2.16	5	147	124.9	0.73	6.2	13.3
770413	650 38.79	65N25.67	163W54.76	23.77	2.33	4	127	124.4	0.25	2.1	8.2
770414	320 24.69	67N 3.89	164W56.83	10.00*	2.79	3	290	100.0	0.00	99.0	99.0
770414	347 45.44	67N 6.44	165W 3.73	15.82	3.38	6	246	214.8	0.36	7.6	48.3
770414	543 41.49	65N26.72	163W51.36	10.00*	2.26	4	120	121.8	0.14	73.7	99.0
770414	1858 52.28	64N48.04	162W30.27	4.39	3.10	4	125	139.7	0.00	4.6	9.2
770414	1955 4.77	65N54.44	162W41.61	0.31*	3.25	6	125	104.3	0.07	1.8	8.4
770415	13 0 42.93	65N23.69	164W 3.59	10.00*		5	127	131.4	1.06	9.9	19.0
770416	1854 33.05	66N10.87	161W41.58	5.42	2.75	5	194	133.1	0.27	17.2	18.2
770417	1920 4.76	65N15.15	167W37.83	10.00*		5	214	160.8	0.57	71.3	84.2
770419	10 4 38.43	67N 0.89	163W13.05	0.04		4	277	198.1	1.27	6.5	6.1
770419	1245 23.74	65N26.60	166W22.35	5.00*		5	134	108.7	0.39	1.0	49.9
770419	2126 12.52	65N14.12	166W44.37	10.00*	3.26	5	165	127.7	0.23	79.2	99.0
770420	1049 38.25	67N 1.66	163W11.31	0.11	2.89	4	280	198.8	0.21	6.9	8.8
770422	2319 15.22	65N31.55	167W 8.78	5.89*		5	286	135.9	0.75	24.2	33.3
770423	3 9 23.32	65N17.91	163W52.07	0.17*	2.60	5	114	123.5	0.47	1.7	6.4
770423	847 7.97	64N33.22	160W 6.65	10.00*	3.89	4	137	100.0	0.63	58.5	99.0
770423	1552 20.46	65N11.07	164W14.72	2.50*	2.45	7	91	143.1	0.60	2.8	4.6
770426	959 27.46	64N20.64	164W57.14	25.01	3.95	5	220	213.7	0.73	29.5	71.0
770427	1752 7.06	64N17.28	161W 6.30	5.00*	2.90	5	149	100.0	0.31	29.5	46.7
770428	1045 49.67	65N 6.57	165W31.24	0.46*	2.88	6	211	203.4	0.49	11.1	10.1
770429	13 2 43.81	65N 4.33	164W10.79	0.57*	2.23	4	153	143.4	0.37	2.3	11.2

Table 5.--(continued)

DATE	ORIGIN	LAT N	LONG W	DEPTH	MAG	NO	GAP	DMIN	RMS	ERH	ERZ
770429	1310 5.33	65N 4.16	164W10.82	0.64	2.24	4	153	143.5	0.35	11.4	20.2
770429	1353 29.60	65N 5.86	165W25.72	0.63*	2.63	6	118	127.0	0.38	2.1	5.2
770429	2220 45.11	65N 4.50	162W28.87	0.12*	2.58	9	193	148.6	0.73	2.0	3.1
770430	19 0 8.68	65N21.35	166W31.74	10.00*		6	142	111.6	0.55	0.9	16.8
770501	558 43.31	66N54.04	164W 6.19	10.00*	1.72	3	224	100.0	0.00	99.0	99.0
770501	739 30.65	67N 1.70	164W13.89	10.00*	2.00	3	238	100.0	0.00	99.0	99.0
770501	23 7 29.62	64N59.91	166W13.55	10.00*		4	255	130.8	2.12	68.8	83.8
770505	1110 26.48	64N39.79	164W 5.23	10.00*	2.45	4	204	159.2	0.16	12.6	17.7
770507	15 6 7.53	65N18.10	163W51.41	0.31*	3.43	5	107	122.9	0.34	1.7	7.1
770508	19 5 11.67	65N 9.47	168W16.03	0.53*		4	265	192.0	0.77	19.9	22.8
770510	1923 33.30	65N11.42	168W26.75	3.77		4	276	197.6	0.41	34.2	22.4
770511	1932 29.25	66N42.97	163W29.48	10.36	3.52	5	264	237.9	0.01	22.3	11.5
770511	22 0 16.10	64N22.51	158W12.52	10.00*		3	302	100.0	0.00	99.0	99.0
770512	532 34.66	64N12.99	171W25.16	10.00*		5	327	100.0	0.24	99.0	99.0
770513	15 2 17.38	63N16.80	156W59.93	26.41		5	332	100.0	0.07	38.2	46.6
770514	1033 29.96	66N16.69	162W29.90	13.19	3.42	5	152	111.0	0.03	7.4	12.3
770516	1735 40.63	65N 6.37	164W55.97	5.46		4	171	100.0	0.67	99.0	99.0
770519	1242 54.93	65N 9.67	164W29.06	10.44	2.49	7	145	154.6	0.54	9.5	13.0
770520	728 21.93	65N23.00	165W40.10	0.00*		4	227	100.0	0.27	10.1	11.2
770523	643 8.40	64N34.97	161W28.44	10.00		4	313	100.0	0.06	99.0	99.0
770523	14 3 22.95	65N44.51	163W26.02	11.41	2.61	4	187	128.4	0.68	21.1	19.9
770525	2046 36.42	67N16.82	163W31.02	0.82		4	320	100.0	4.89	99.0	46.4
770601	841 6.37	64N35.55	160W15.46	0.81	3.36	5	215	100.0	0.24	13.3	39.0
770604	2222 24.72	66N 5.78	166W29.77	10.00*	3.00	4	195	193.0	0.27	49.4	40.1
770612	7 5 45.69	65N22.41	164W 0.66	21.03	2.66	5	130	129.3	0.23	2.2	4.6
770613	1626 19.99	65N23.28	163W14.35	65.71	3.15	4	191	100.0	1.85	35.9	34.2
770613	1656 42.03	68N31.70	168W22.78	1.98		4	332	100.0	0.02	99.0	99.0
770616	16 4 23.76	64N59.66	162W30.14	12.24	2.36	6	111	144.6	0.12	2.6	4.7
770625	1552 4.92	64N56.07	162W25.10	1.01*	3.52	6	114	148.1	1.20	3.7	8.0
770625	1948 53.58	65N15.45	165W54.62	10.00*		3	129	99.3	0.00	12.3	99.0
770628	1255 44.23	69N 5.20	171W57.13	10.00*		4	340	580.5	0.45	99.0	96.8
770628	1315 41.60	66N 4.51	166W47.83	0.00		4	235	265.0	6.18	99.0	17.1
770630	1222 42.27	65N21.28	163W50.11	12.26	3.26	4	145	190.8	0.00	22.3	23.5
770630	1656 48.40	65N45.11	163W51.75	26.54	2.78	4	163	100.0	0.23	99.0	99.0
770707	1929 48.31	65N37.40	167W29.60	12.93	3.33	4	183	100.0	0.36	99.0	99.0
770714	1822 15.36	66N27.39	157W38.48	24.41	2.84	4	225	100.0	0.15	20.8	99.0
770715	1436 36.46	67N37.67	156W36.72	10.00	3.06	4	254	100.0	0.58	99.0	99.0
770715	1648 3.54	66N27.55	162W32.35	5.38		5	155	129.4	0.46	8.7	14.5
770720	1717 17.21	66N 0.27	157W21.34	40.76		6	174	264.2	0.74	12.7	99.0
770723	1751 50.09	65N 3.60	162W21.36	26.37	2.99	6	105	153.5	0.64	4.3	99.0
770726	2323 21.44	64N46.74	163W12.14	18.16	2.84	5	208	163.3	0.30	2.6	6.3
770806	2229 0.30	65N36.74	167W52.35	0.72*		3	250	100.0	2.24	99.0	99.0
770809	856 49.71	64N 0.53	160W12.94	10.00*		5	161	100.0	0.32	41.2	53.4
770810	729 8.33	64N24.83	163W35.90	25.47	2.59	6	238	177.4	1.34	3.7	99.0
770814	1212 9.80	64N34.77	159W26.79	0.39	3.44	6	140	303.4	0.30	6.3	5.1
770814	1424 56.07	63N 8.14	168W29.33	0.08*		6	291	100.0	0.86	75.6	78.6
770814	1429 48.57	67N19.13	163W11.89	0.59*	3.10	5	306	228.4	0.68	4.6	3.4
770909	9 2 13.12	66N45.96	162W 5.25	10.00*		4	167	100.0	0.50	99.0	86.0
770909	1021 32.58	65N37.79	163W29.06	10.00*		4	186	239.8	1.21	11.2	18.0
770910	1511 36.66	64N31.95	160W41.11	10.00	3.06	4	188	100.0	0.05	99.0	99.0
770910	1516 2.71	65N15.86	157W11.71	10.00*		3	310	100.0	0.00	99.0	99.0
770910	2318 17.18	66N 0.81	156W21.84	10.00*	3.25	4	190	232.7	0.03	99.0	99.0
770914	1546 20.97	64N44.57	165W31.90	12.95	3.31	6	151	179.4	0.17	10.4	12.8
770915	824 33.73	65N33.74	164W 3.41	5.11		4	246	100.0	0.80	99.0	99.0
770920	352 3.87	64N21.99	162W43.09	17.39	2.74	5	166	137.8	0.04	3.2	4.7
770927	640 9.67	64N55.36	164W29.76	22.62		6	133	163.0	0.27	2.2	7.4
771008	2250 2.06	64N42.96	155W59.45	10.00	2.30	6	179	237.4	0.50	13.6	99.0

Table 5.--(continued)

DATE	ORIGIN	LAT N	LONG W	DEPTH	MAG	NO	GAP	DMIN	RMS	ERH	ERZ
771011	336 52.11	64N40.66	158W16.40	10.16	1.42	4	290	100.0	1.59	99.0	99.0
771014	525 0.13	66N16.74	156W17.16	24.40	2.78	7	211	244.9	0.58	11.8	6.7
771021	1423 39.55	65N24.66	167W37.25	10.00*	2.67	5	190	172.5	0.09	63.8	77.6
771027	853 13.73	64N41.02	166W 4.45	15.81	2.97	6	208	193.7	1.35	4.3	3.1
771028	1743 52.15	68N16.53	159W 9.13	11.65	2.96	5	296	100.0	0.21	99.0	99.0
771029	737 33.60	65N19.80	167W54.82	6.55	2.64	5	235	188.8	0.18	23.7	21.0
771102	1918 21.52	65N44.58	162W15.18	0.61	1.81	7	145	123.4	0.20	2.2	7.9
771103	652 26.45	63N 7.02	167W43.60	10.00*	3.25	4	309	100.0	0.18	99.0	99.0
771105	1748 57.77	66N57.06	161W53.11	10.00	3.30	4	291	100.0	1.49	99.0	99.0
771107	513 54.63	65N55.65	159W27.03	0.81	2.68	10	137	232.5	1.04	1.8	2.5
771107	934 28.25	68N14.36	155W39.00	10.00*	3.14	7	266	371.0	0.80	30.2	25.2
771110	922 52.83	67N 2.40	156W22.35	9.97	2.14	4	358	100.0	0.99	99.0	99.0
771111	8 8 48.02	65N 3.73	160W 1.21	0.00*	1.85	4	244	248.5	5.52	8.5	6.1
771112	746 17.67	64N40.91	152W34.47	10.00	2.12	4	316	100.0	0.18	99.0	99.0
771113	2226 39.40	66N48.56	157W41.73	7.59	2.44	4	208	100.0	0.00	38.4	99.0
771120	1910 25.25	65N25.16	165W38.47	10.00*	3.65	4	120	210.1	0.65	38.7	75.7
771126	1651 6.10	65N26.08	154W54.20	9.55	3.30	5	202	318.3	0.06	42.1	58.4
771128	227 4.99	63N 9.00	162W39.94	10.00*	2.18	6	270	100.0	0.21	99.0	99.0
771128	924 3.08	66N17.50	163W 5.33	10.00*	1.86	4	227	128.2	3.50	10.9	22.5
771201	649 51.43	65N24.65	162W24.78	10.98	1.55	8	131	168.5	0.51	2.3	4.0
771202	344 6.32	64N11.23	159W23.41	20.29	1.05	4	190	100.0	0.06	99.0	99.0
771202	2327 36.61	62N49.58	163W16.14	4.32*	3.47	4	341	100.0	0.30	99.0	99.0
771205	11 3 1.57	65N 5.95	162W30.80	0.79*	1.62	7	104	162.3	0.53	2.8	5.5
771205	1143 8.06	65N 4.94	162W32.71	2.50	1.22	8	105	163.1	0.24	1.6	3.4
771206	1155 43.03	62N43.15	163W35.97	10.00*	2.54	7	289	323.4	0.55	86.9	84.7
771209	051 38.21	64N49.00	165W23.12	9.86	2.41	8	127	169.8	0.27	4.5	6.6
771210	18 1 11.84	62N44.05	162W46.43	0.50*	3.37	9	278	309.7	1.23	36.0	43.2
771211	840 27.51	64N18.18	166W35.52	0.02	2.67	7	273	242.3	0.74	12.7	11.8
771212	955 2.51	66N54.39	164W45.55	43.96	4.02	5	269	229.0	0.02	20.0	18.3
771213	556 48.57	62N35.49	162W27.03	10.00	2.88	4	337	321.9	2.69	99.0	99.0
771215	1944 40.50	66N10.28	156W26.23	19.36	1.98	6	202	100.0	0.34	53.9	14.0
771216	447 20.74	66N35.66	168W 5.75	5.28	2.59	7	284	258.8	0.99	11.6	6.5
771216	22 0 27.25	67N 1.98	161W51.93	0.06	2.29	4	355	100.0	1.92	99.0	99.0
771220	732 24.88	65N23.64	163W45.30	15.70	1.91	4	227	100.0	1.08	41.5	72.9
771221	1349 44.76	64N50.60	164W39.18	52.77	2.10	7	162	172.6	0.06	8.4	19.0
771222	12 8 10.64	65N 0.03	162W23.48	10.00*	0.98	3	156	153.1	0.00	99.0	99.0
771224	1853 20.82	66N53.10	163W56.73	1.25*	1.96	6	222	203.4	1.44	3.6	3.0
771225	12 9 3.02	65N19.49	162W32.83	1.17	1.23	6	118	158.1	0.95	11.4	16.8
771226	622 24.66	64N34.40	163W42.92	25.23	1.73	7	155	172.9	0.52	2.4	99.0
771226	639 15.08	64N35.48	160W38.26	0.18*	1.76	5	192	100.0	1.00	32.5	35.7
771227	1550 35.97	64N34.29	164W 1.94	23.33	1.40	5	158	186.7	0.25	3.2	9.0
771231	837 50.08	65N11.13	163W58.67	8.80	2.17	6	125	130.9	2.20	6.0	11.6
771231	2051 47.17	64N33.92	162W49.80	0.85*	1.99	9	148	135.2	0.84	1.1	4.5
780101	518 29.51	66N28.74	163W29.61	10.00	1.80	4	158	155.9	0.97	99.0	99.0
780101	533 33.07	65N19.48	162W42.52	3.98	1.97	4	322	100.0	0.08	99.0	99.0
780101	540 53.50	67N14.11	166W14.49	10.00	1.92	5	292	100.0	0.17	99.0	99.0
780102	1 8 20.75	67N26.55	170W 3.68	10.00*	2.97	5	343	384.8	1.50	99.0	99.0
780102	1958 40.50	65N45.27	164W23.19	25.17	1.88	7	193	150.0	0.27	2.0	99.0
780106	1935 45.36	65N 0.14	163W19.85	24.72		4	181	154.4	0.01	3.2	99.0
780106	2040 26.32	65N20.37	166W29.72	10.14	1.97	4	251	100.0	0.10	99.0	99.0
780106	22 7 38.50	64N16.51	163W39.23	25.78	2.02	4	188	172.4	0.46	5.9	99.0
780108	13 0 48.88	64N34.96	160W20.61	0.76*	2.25	4	210	100.0	0.08	15.5	43.5
780109	1748 2.07	66N31.06	157W21.91	10.00*	2.43	6	184	233.5	1.15	4.7	10.7
780111	154 58.73	67N16.93	164W19.99	10.00*	2.13	3	298	100.0	0.00	99.0	99.0
780112	510 41.64	65N 7.08	164W13.88	25.17	1.70	4	213	100.0	0.29	17.0	44.6
780112	1139 24.66	65N 3.41	164W11.04	22.07		4	206	100.0	0.43	18.1	8.8
780112	1150 49.90	65N 0.78	164W 6.99	24.48	1.85	5	148	100.0	0.51	8.8	20.2

Table 5.--(continued)

DATE	ORIGIN		LAT N	LONG W	DEPTH	MAG	NO	GAP	DMIN	RMS	ERH	ERZ
780114	445	18.90	65N12.44	161W50.65	6.89	2.11	4	107	172.7	0.00	7.1	12.2
780115	718	37.72	63N 5.53	166W43.29	14.29	2.30	4	332	100.0	0.38	99.0	99.0
780117	2344	38.64	66N58.14	163W55.16	10.00*	1.52	3	263	100.0	0.00	99.0	99.0
780118	620	12.42	61N23.82	168W12.97	10.00*	3.15	3	316	100.0	0.14	99.0	99.0
780119	2027	36.32	64N12.70	161W52.73	10.00*	0.68	4	167	173.0	0.35	12.4	20.5
780121	2249	35.03	66N16.33	157W26.72	14.05	3.73	6	168	236.9	0.30	4.8	50.1
780122	1646	30.50	66N33.80	162W12.32	10.80	2.42	4	189	134.0	0.01	99.0	99.0
780123	726	36.42	64N31.92	164W55.88	11.72	3.10	4	174	201.2	0.00	24.8	27.3
780123	1358	57.79	63N51.53	164W26.62	15.07	2.11	4	243	100.0	0.05	74.7	91.5
780125	527	31.69	64N45.04	165W36.40	10.00	1.19	5	224	219.1	0.33	40.6	44.8
780128	1941	29.09	63N26.00	165W50.50	37.60	2.85	6	203	268.6	0.12	5.5	99.0
780130	032	41.07	65N34.42	166W49.26	10.00	2.07	4	320	100.0	0.50	96.3	98.2
780130	421	10.14	64N32.93	165W27.05	0.29*	1.85	4	267	100.0	0.37	72.6	25.6
780131	0 1	37.27	65N34.82	162W48.02	0.88	1.32	4	126	141.0	0.00	4.6	10.5
780131	337	51.32	65N17.97	164W 0.88	0.64*	2.20	4	136	130.3	0.26	2.0	7.0
780131	1423	20.28	65N21.13	164W26.10	28.20	1.61	5	151	149.1	0.53	3.1	14.2
780131	1648	48.41	65N21.89	164W57.96	10.00*	1.93	3	179	100.0	0.00	99.0	99.0
780131	17 0	21.70	66N13.28	162W53.37	10.00*	1.30	3	139	116.4	0.00	99.0	99.0
780201	230	52.02	64N57.89	162W32.48	8.82	2.47	5	113	154.4	0.10	3.8	7.3
780201	2239	50.01	64N22.04	162W41.51	10.00*	1.25	3	165	137.0	0.00	3.2	99.0
780202	522	19.46	65N 6.27	157W52.24	10.00*	1.93	3	165	100.0	0.00	6.6	99.0
780204	232	13.96	64N30.30	163W45.47	22.58	2.05	4	164	171.8	0.07	4.5	99.0
780204	1832	24.57	67N 4.71	162W49.77	10.00*	1.40	3	297	100.0	0.55	99.0	99.0
780207	2147	30.50	66N39.88	161W 9.93	10.00*	1.85	3	253	155.1	0.00	99.0	99.0
780208	1439	23.43	64N39.27	162W52.95	10.00*	1.66	3	141	142.8	0.00	3.0	99.0
780209	1810	13.29	63N21.47	163W 0.44	10.00*	2.39	3	257	100.0	0.00	99.0	99.0
780209	22 5	13.02	65N 9.71	162W17.26	10.00*	1.08	4	99	162.9	0.31	5.0	8.9
780210	1428	36.73	64N21.69	162W42.55	10.00*	2.70	4	166	138.0	0.22	3.2	99.0
780215	1718	44.60	63N34.42	165W35.29	10.00*	1.78	3	289	100.0	0.00	99.0	99.0
780215	1740	3.26	66N35.27	164W13.76	10.00*	1.37	3	226	100.0	0.01	99.0	99.0
780216	751	0.11	65N17.69	167W30.94	4.80	2.32	4	282	100.0	0.23	99.0	99.0
780219	1341	22.12	65N13.04	167W48.76	0.84	2.21	4	289	100.0	0.19	99.0	99.0
780224	1750	37.68	65N36.52	163W17.79	14.09	1.62	4	224	141.1	0.23	9.2	5.3
780225	1511	7.53	65N33.57	165W10.16	10.00*	1.44	4	194	184.3	0.08	99.0	36.0
780226	2159	41.07	65N54.65	166W39.92	0.63*	2.54	5	261	209.8	0.53	18.9	6.9
780228	851	33.10	65N56.81	156W13.07	40.79	3.60	4	184	100.0	0.03	80.8	99.0
780228	1623	43.96	65N22.96	167W42.27	10.00	2.28	4	285	100.0	0.00	99.0	99.0
780228	1628	37.52	64N48.82	165W41.59	10.00*	2.30	5	227	220.4	0.10	62.3	70.2
780303	8 7	7.13	63N55.20	169W23.18	0.16	4.20	5	159	349.8	0.07	56.3	99.0
780303	1156	56.57	62N17.31	166W18.74	11.24	2.44	4	337	100.0	0.18	99.0	99.0
780304	557	5.21	65N 7.27	165W15.59	24.85	1.19	6	189	191.1	0.16	5.9	99.0
780305	1449	52.61	65N37.53	166W50.39	10.00*	1.66	5	265	100.0	0.55	99.0	99.0
780306	1411	3.69	65N 8.69	170W14.90	0.89*	2.43	5	237	292.4	1.27	11.7	17.7
780307	511	42.74	66N23.64	163W38.44	10.00*	1.00	5	148	153.7	0.22	99.0	99.0
780308	1327	52.93	67N16.41	163W32.25	11.13	1.58	4	297	100.0	0.00	54.7	16.3
780308	1424	35.92	66N38.80	163W32.15	10.00*	1.36	4	332	171.3	0.09	99.0	99.0
780310	720	30.26	65N39.54	166W23.18	10.00*	2.72	6	186	215.7	0.46	8.1	5.4
780310	1527	20.68	65N43.25	167W 4.95	9.39	1.69	4	199	237.3	0.73	42.3	99.0
780310	1531	9.06	65N41.03	166W28.51	10.00	1.66	4	255	100.0	0.45	99.0	29.3
780310	1532	22.68	65N39.79	166W19.53	10.00*	1.69	3	249	100.0	0.50	99.0	99.0
780310	2159	36.03	65N41.12	163W 9.47	10.00*	1.10	3	210	162.5	0.00	99.0	99.0
780311	1437	17.95	67N 7.49	160W37.94	4.23*	1.74	3	298	194.9	0.44	99.0	99.0
780315	751	36.98	63N43.42	163W17.33	12.54	2.90	6	233	214.1	0.61	5.5	9.0
780317	21 3	55.09	65N10.14	166W52.15	10.00*	1.53	3	267	100.0	0.02	99.0	99.0
780318	1335	57.02	64N47.71	165W24.84	10.00	1.66	7	198	208.7	0.27	30.7	40.8
780319	540	23.76	65N46.58	166W 8.18	0.03	1.90	7	246	198.6	0.35	4.6	4.3
780319	1925	18.13	65N 3.86	163W50.83	0.13*	1.88	9	114	140.9	0.64	1.2	3.7

Table 5.--(continued)

DATE	ORIGIN		LAT N	LONG W	DEPTH	MAG	NO	GAP	DMIN	RMS	ERH	ERZ
780319	2122	25.26	65N 3.71	163W51.15	0.60	1.69	6	115	141.1	0.62	2.4	5.8
780320	410	34.40	65N27.70	152W26.21	1.55	1.13	4	188	100.0	11.47	99.0	99.0
780320	14 3	57.36	64N59.61	163W55.74	23.12	1.87	6	114	147.9	0.71	3.2	8.2
780320	1743	45.35	65N25.74	167W56.93	10.00*	1.89	5	287	100.0	0.47	97.0	99.0
780320	2139	2.14	66N16.69	162W13.74	0.16	1.89	8	168	105.1	0.41	1.1	10.3
780323	124	37.88	65N22.52	169W22.10	11.67	2.37	4	222	244.0	0.12	99.0	99.0
780327	254	4.66	65N27.35	166W37.03	0.25*	3.15	7	180	238.6	0.80	4.0	3.2
780327	2246	10.27	64N46.42	164W40.25	33.03*	1.37	6	127	100.0	0.28	47.7	84.2
780329	2352	50.88	64N39.24	163W35.49	25.15	1.54	5	146	188.2	0.59	2.6	99.0
780330	127	4.03	65N12.41	157W53.35	7.95	2.16	7	136	100.0	0.36	31.5	11.3
780330	10 9	38.79	65N 0.34	164W26.06	24.64	2.16	7	136	100.0	0.60	9.5	23.4
780331	650	13.24	64N38.85	162W37.26	5.00*	3.08	4	139	203.9	0.09	6.9	99.0
780331	657	52.60	65N 7.65	164W54.38	8.56	1.52	6	172	100.0	0.20	15.1	9.9
780401	2136	44.04	65N 4.50	163W49.57	0.09	4.11	7	105	204.9	1.30	2.3	3.3
780401	2142	0.63	65N13.76	161W11.07	1.25*	2.07	4	186	211.6	0.99	7.4	16.7
780401	2151	15.72	65N 8.06	164W56.70	7.93	1.43	5	170	100.0	0.33	30.9	12.5
780401	2224	6.79	65N 1.91	164W13.41	10.00	2.35	5	128	100.0	0.60	26.7	48.5
780402	2020	42.11	64N46.91	165W32.28	10.00	1.77	5	213	100.0	0.18	68.0	63.8
780406	1927	30.20	64N41.20	166W13.42	10.00*	2.27	5	275	100.0	0.19	64.9	35.0
780407	1756	48.99	65N17.14	162W34.03	19.70	1.96	7	147	173.5	1.26	3.0	6.0
780408	2012	37.02	64N46.73	162W35.44	6.25	1.48	7	134	191.3	0.46	4.0	5.6
780408	2319	53.95	64N46.58	162W31.36	8.37	1.45	7	135	193.1	0.17	4.1	5.7
780410	338	50.29	64N33.86	164W 6.45	0.89	2.07	7	159	194.1	0.74	9.4	14.1
780413	1956	15.31	66N19.47	166W15.16	7.22	2.31	5	261	200.4	0.10	8.9	2.8
780414	1243	40.66	64N59.74	164W51.25	16.03	1.37	4	178	100.0	1.19	52.7	32.9
780414	19 4	23.56	64N47.35	165W27.14	12.40	2.06	4	203	100.0	0.44	99.0	99.0
780418	314	45.02	65N 7.73	164W50.14	17.22	1.63	4	185	100.0	0.05	99.0	99.0
780418	1137	28.57	67N39.15	160W38.77	0.31	2.35	5	247	352.8	1.16	15.0	3.0
780419	1648	43.01	64N29.94	167W22.27	8.42	2.47	4	156	240.2	0.08	99.0	99.0
780420	1835	6.71	67N 2.11	165W32.49	1.25*	2.30	6	280	275.5	0.75	4.9	3.7
780422	953	59.67	64N49.48	162W25.95	14.25	1.82	7	139	190.4	0.26	2.4	7.7
780426	232	18.62	64N46.19	165W20.57	10.44	1.57	4	189	100.0	0.14	99.0	99.0
780426	441	54.93	64N56.16	164W12.86	17.56	1.66	6	121	100.0	0.18	5.7	10.1
780430	211	32.85	61N22.53	169W20.56	15.13	3.23	4	293	100.0	0.00	99.0	99.0
780504	710	20.42	64N22.93	163W24.58	13.82	1.39	7	173	219.7	0.24	7.7	8.0
780505	2256	38.56	65N13.82	165W11.66	24.50	1.41	5	188	100.0	0.20	45.7	43.2
780507	2149	0.95	65N42.25	165W22.98	0.29*	1.79	4	210	178.5	0.07	18.3	7.5
780511	737	45.08	64N15.83	162W57.79	47.17	1.31	5	179	100.0	0.74	36.4	29.8
780513	231	51.45	65N 6.13	162W18.61	35.39	2.31	6	150	167.5	1.20	4.1	17.6
780514	2345	6.69	62N47.44	169W24.33	23.97	3.50	5	262	100.0	0.51	99.0	99.0
780518	838	20.38	65N29.68	164W15.28	22.98	1.71	6	182	167.9	0.16	3.9	3.9
780518	1336	25.94	65N44.10	165W39.96	0.60*	1.89	5	225	185.2	0.24	11.4	5.0
780520	1254	27.48	64N32.25	162W49.73	15.68	1.85	4	151	211.3	0.00	6.6	99.0
780520	1345	35.53	64N31.24	162W50.45	24.39	2.68	4	153	212.9	0.00	99.0	99.0
780523	1428	37.74	65N18.95	164W19.59	26.29	1.64	5	187	187.4	0.33	8.3	99.0
780528	1741	36.36	65N15.25	166W45.47	10.00*	2.71	5	261	258.9	0.34	99.0	51.4
780529	1441	55.51	66N34.09	163W20.66	10.00*	2.63	4	167	242.1	0.11	99.0	71.5
780530	2342	17.48	64N58.80	162W10.25	10.00	2.48	4	151	182.4	0.62	4.5	99.0
780531	1151	21.94	65N 7.79	162W42.49	1.65	2.23	6	140	173.6	0.34	3.4	8.9
780601	1759	58.81	65N 2.70	164W14.57	10.00*	1.61	3	129	100.0	0.00	99.0	99.0
780602	725	38.68	65N21.71	162W35.13	23.93	1.63	5	187	191.5	0.02	4.5	7.8
780605	1017	18.89	63N28.77	162W 0.86	10.61	2.66	4	250	100.0	0.02	99.0	99.0
780610	953	4.52	65N21.54	162W47.82	11.60	1.82	4	181	196.6	0.00	5.2	9.1
780610	1753	10.62	65N25.94	164W28.16	7.09	2.50	5	154	178.6	0.08	22.8	17.9
780612	1522	55.99	64N46.99	165W34.49	10.00	2.50	4	217	100.0	0.14	68.5	73.1
780612	1612	11.24	65N33.01	164W40.92	11.31	2.13	4	168	100.0	0.00	40.0	19.4
780612	2021	8.67	64N51.66	161W33.16	7.93		4	194	210.7	0.00	26.3	44.3

Table 5.--(continued)

DATE	ORIGIN	LAT N	LONG W	DEPTH	MAG	NO	GAP	DMIN	RMS	ERH	ERZ
780613	2020 54.04	64N53.25	162W37.69	14.67	2.02	4	165	179.8	0.00	4.5	14.3
780614	819 49.93	65N 2.28	164W 9.13	11.83	2.70	4	131	100.0	0.00	5.7	12.4
780619	513 19.35	64N20.76	167W15.99	0.29*	3.15	4	315	352.0	1.19	99.0	47.9
780630	341 37.27	65N23.86	163W 1.68	10.00	2.08	4	224	162.2	0.00	7.7	9.7
780630	1413 37.81	65N25.95	163W 0.09	10.00*	2.04	3	224	158.2	0.00	7.3	99.0
780703	19 1 12.55	64N32.91	161W32.73	35.40	2.64	4	181	100.0	1.02	83.9	99.0
780705	1128 6.41	65N45.59	160W15.71	10.00	2.05	4	329	100.0	0.21	99.0	99.0
780710	1026 17.50	64N52.95	162W48.23	24.93	2.41	5	200	100.0	0.49	29.0	42.1
780714	23 6 42.09	66N26.90	164W49.12	4.23*		3	359	100.0	7.97	99.0	99.0
780716	1050 8.96	66N23.68	163W12.59	10.00*	2.10	3	129	100.0	0.00	99.0	99.0
780718	521 38.94	65N20.15	164W14.70	9.95	2.36	4	223	100.0	0.88	99.0	99.0
780722	1835 49.71	66N22.87	161W45.36	10.00*	1.47	4	203	100.0	0.13	99.0	99.0
780802	15 8 15.72	65N14.49	163W 2.69	1.25*	2.15	4	230	179.6	0.71	14.8	9.4
780803	920 36.97	63N45.88	169W41.64	10.00*	2.86	3	194	100.0	0.00	99.0	99.0
780815	1839 19.10	65N25.87	162W58.66	10.00*	1.73	3	224	158.2	0.00	7.4	99.0
780817	1729 15.26	66N51.48	163W42.35	10.00*	1.27	3	241	100.0	0.00	99.0	99.0
780818	1741 57.33	65N24.27	162W34.67	10.00*	2.37	3	190	195.3	0.00	5.7	99.0
780827	2316 52.99	65N31.02	165W 1.84	10.00*	1.96	3	186	184.2	0.00	99.0	99.0
781007	1520 28.36	64N47.49	163W17.55	44.88	3.12	9	131	167.6	2.06	4.5	89.4
781018	1429 31.13	65N17.74	166W 2.36	12.22	2.31	5	233	100.0	0.16	99.0	99.0
781019	1712 7.30	66N21.52	162W17.01	10.00*	1.38	3	148	100.6	0.00	99.0	99.0
781021	22 6 15.37	65N36.12	170W 8.79	1.27	2.74	8	316	267.2	0.86	5.4	2.3
781023	320 53.51	66N27.59	162W24.04	0.15*	3.45	8	112	96.6	1.45	1.8	2.7
781025	1239 17.86	63N57.35	164W 1.35	10.00	1.81	5	226	100.0	0.95	99.0	99.0
781025	15 7 39.37	65N41.84	162W52.83	2.59*	2.01	4	263	128.3	0.02	2.3	99.0
781026	419 5.03	64N57.00	162W20.89	2.50*	1.33	6	131	150.2	0.39	2.8	3.8
781027	546 30.25	66N25.86	162W22.42	14.09	1.29	4	149	97.3	0.48	1.5	17.3
781028	844 49.22	64N54.07	162W27.01	10.00*	2.56	8	127	144.1	0.93	2.4	6.6
781108	245 24.06	65N36.09	167W 5.45	10.00*	1.55	4	360	141.0	2.59	7.9	13.9
781121	8 2 10.32	65N45.78	168W 2.46	1.58*	2.97	4	255	183.0	1.60	39.2	15.3
781122	5 0 47.10	65N48.18	166W 3.54	10.00*	1.93	7	158	141.7	0.85	3.5	3.8
781122	1749 44.77	65N19.31	162W 4.18	12.26	2.44	7	145	171.1	0.18	3.2	5.3
781123	1043 24.50	65N 9.57	164W35.55	10.00*	1.38	6	159	161.2	0.66	5.9	8.7
781124	028 55.50	63N42.41	156W54.69	10.00	2.90	5	313	422.6	0.88	99.0	99.0
781124	850 58.91	62N42.06	152W29.26	2.86	3.00	5	333	664.9	0.05	99.0	99.0
781127	1153 37.90	65N 0.59	163W46.49	25.46	3.40	7	109	157.2	0.43	3.5	16.0
781202	1718 44.05	66N56.69	161W48.39	10.00	0.98	5	296	100.0	0.31	99.0	99.0
781203	048 32.29	65N 6.27	157W31.84	4.32*	2.11	4	219	100.0	0.51	78.6	58.5
781204	552 8.92	64N56.21	162W23.32	10.00	1.94	5	130	147.9	0.62	2.7	99.0
781204	1057 21.27	64N58.94	163W59.37	14.30	3.27	8	196	165.9	0.76	4.8	7.8
781205	1448 40.03	65N51.17	166W10.35	5.00*	1.76	5	167	148.4	0.23	12.3	15.9
781206	833 55.14	64N47.95	165W26.16	9.95	1.80	6	159	172.2	0.30	7.4	12.3
781206	12 9 26.31	66N 7.09	163W56.88	10.00*	1.26	5	219	103.6	0.70	1.6	14.4
781210	2321 35.70	65N14.51	167W 6.82	10.00*	2.04	5	182	167.1	0.33	26.5	26.7
781211	5 7 34.94	64N57.39	166W31.54	0.49	1.69	8	189	175.6	0.42	22.3	25.9
781211	1136 26.82	65N49.24	167W27.96	9.50	1.99	5	204	170.9	0.21	64.8	72.6
781212	14 8 8.68	64N19.96	163W29.28	10.00*	3.36	4	299	216.3	1.80	22.0	32.1
781212	1512 9.87	65N51.03	159W45.41	0.16*	1.12	4	314	100.0	1.58	80.0	12.0
781212	2239 6.33	67N15.17	160W33.83	0.63	1.86	4	318	204.3	0.53	7.9	3.6
781214	1926 13.39	68N 7.99	161W21.11	16.14	1.60	6	315	246.4	0.10	15.9	19.6
781218	210 18.70	65N 6.54	156W59.93	10.00	2.62	4	315	100.0	1.32	99.0	99.0
781220	19 4 41.06	64N33.31	167W38.78	4.60	2.24	4	265	100.0	0.11	99.0	59.8
781220	21 3 50.10	66N15.62	164W27.72	10.00*	0.39	4	230	127.5	1.11	20.9	16.3
781224	7 1 57.97	67N 2.62	157W21.26	10.00	2.51	5	239	316.1	0.48	99.0	99.0
781224	1313 6.17	63N45.86	157W45.23	10.00*	4.50	12	139	321.1	0.54	4.7	44.8
781225	156 11.88	65N47.03	154W55.29	4.52	1.82	4	166	100.0	1.13	99.0	99.0
781228	1836 13.60	63N11.95	148W 3.00	10.00		4	325	100.0	2.53	99.0	99.0

Table 5.--(continued)

DATE	ORIGIN	LAT N	LONG W	DEPTH	MAG	NO	GAP	DMIN	RMS	ERH	ERZ
790101	10 2 10.03	63N54.20	164W29.26	0.58*		4	303	280.3	0.22	99.0	26.2
790101	1624 16.51	65N36.37	167W14.61	26.74	2.15	4	156	145.8	0.15	7.7	26.3
790103	150 43.04	65N17.09	166W36.50	10.00*	1.68	4	154	147.8	0.41	80.3	99.0
790103	331 31.30	64N35.98	159W35.21	10.00	1.63	4	301	100.0	0.10	99.0	99.0
790106	1542 47.56	63N33.58	157W49.91	29.42		10	130	296.2	0.42	4.6	7.2
790106	1545 33.24	63N31.63	157W54.44	10.00*		6	142	294.4	0.08	6.5	46.0
790107	1031 4.20	64N22.90	162W38.90	10.00	1.39	4	161	198.6	0.34	99.0	99.0
790108	1149 15.21	65N27.00	163W55.32	0.27*	3.15	4	222	166.4	0.41	5.7	5.9
790110	2 9 40.16	64N56.43	165W51.66	14.97	1.52	5	156	163.3	0.11	11.2	18.5
790110	438 14.60	64N53.09	165W49.02	25.08	1.96	5	159	168.4	0.16	4.7	59.9
790110	440 31.10	64N51.25	165W47.45	24.41	2.50	6	161	171.2	0.71	4.1	30.5
790111	826 30.86	64N11.64	167W 1.28	10.00*	1.53	3	283	100.0	0.24	99.0	99.0
790111	915 21.44	64N44.64	165W37.54	16.40	2.02	7	163	180.5	0.68	13.0	15.0
790115	2255 56.09	65N31.72	167W 9.94	10.00*	3.33	6	137	147.8	1.12	30.2	52.4
790117	2332 54.12	66N55.44	163W 6.53	13.15		5	249	111.0	0.12	4.5	2.5
790118	16 3 14.22	65N55.66	165W51.34	24.71	2.28	5	194	191.6	0.38	2.9	99.0
790121	1350 39.00	64N11.67	164W 9.92	44.57	1.44	4	278	100.0	0.92	63.1	86.1
790124	16 4 31.00	64N31.29	162W18.98	10.00	2.95	6	264	222.9	0.63	47.2	97.2
790126	517 23.64	65N 7.70	165W48.50	10.00	2.25	6	136	143.0	0.19	13.3	22.5
790126	558 43.59	65N13.26	160W 2.33	10.00	2.22	6	223	100.0	0.70	66.2	32.4
790126	857 4.68	64N 0.89	158W37.41	0.00	2.03	4	185	332.3	5.18	56.5	12.6
790126	12 0 13.88	65N 1.99	165W34.71	9.60	1.96	5	151	149.0	0.04	5.0	10.0
790126	1443 59.09	64N16.34	158W33.15	0.00*		9	156	330.1	1.46	7.9	10.9
790128	434 16.98	65N17.35	166W39.90	11.71	1.81	4	156	149.1	0.01	99.0	99.0
790130	736 59.05	66N25.67	167W 3.17	10.48	2.79	4	276	100.0	0.50	99.0	99.0
790207	1510 35.02	65N11.73	168W47.39	10.00	2.59	4	293	100.0	0.00	99.0	99.0
790212	1038 29.00	64N27.27	162W26.62	10.00*	2.14	5	151	188.7	0.02	99.0	99.0
790212	19 1 4.93	69N54.93	166W47.89	0.49*	4.49	4	296	694.3	14.39	99.0	99.0
790214	1016 5.23	66N24.44	162W14.73	0.69*	1.66	6	158	102.7	0.56	2.0	9.7
790214	1946 45.24	66N37.59	160W33.91	0.16	2.58	4	255	180.2	3.13	67.8	8.0
790218	1236 50.44	65N13.27	162W27.32	10.00*	1.76	5	129	156.3	0.46	3.8	7.7
790221	22 3 36.35	64N48.70	165W28.46	10.00*	2.31	6	137	171.3	0.21	11.0	18.1
790222	037 14.28	66N11.57	163W48.46	14.68	0.95	4	196	97.5	0.32	16.9	17.1
790222	21 7 6.07	64N59.13	165W41.96	10.00*	1.97	5	141	155.9	0.41	11.5	22.3
790223	11 6 45.12	65N48.84	166W 6.89	0.97*	1.67	5	160	143.5	0.45	5.8	7.9
790223	1437 17.37	64N 7.36	164W 2.83	10.00*	2.52	3	211	100.0	0.12	99.0	99.0
790223	1724 31.67	65N49.49	166W12.17	1.06*	2.16	5	163	145.8	0.59	4.2	5.0
790224	1614 18.71	65N51.33	166W12.83	10.00*	1.98	5	166	149.2	0.39	6.2	6.6
790301	1631 36.61	64N 6.56	165W13.72	10.28	2.79	6	168	224.0	0.36	6.1	5.1
790308	1815 57.29	65N 3.43	164W24.92	0.14*	1.66	5	96	172.8	0.16	3.9	4.9
790310	22 1 3.27	67N 5.65	163W14.76	11.98	0.78	5	281	130.0	0.65	4.3	1.6
790311	512 59.68	65N18.57	161W23.17	13.70	1.70	4	175	180.8	0.28	42.8	32.6
790314	1619 13.36	65N59.65	163W49.13	8.47	1.53	5	176	109.3	0.07	4.0	5.5
790321	1051 1.40	66N18.87	162W37.37	2.50*	0.78	4	153	85.2	0.11	1.7	99.0
790321	1439 34.40	65N 0.83	162W 7.06	41.73	1.64	4	141	162.6	2.86	2.5	99.0
790324	0 2 19.59	65N 1.00	162W27.12	1.14*	1.81	6	129	151.5	0.58	3.4	7.2
790403	944 11.78	65N17.96	165W 5.78	1.81*	2.16	4	131	134.2	1.55	2.5	7.5
790403	2236 56.58	66N58.64	163W29.52	6.57	1.40	4	237	126.2	0.00	55.9	8.7
790407	1117 59.65	65N45.97	162W29.40	0.26*	1.98	5	183	120.0	0.14	2.1	9.2
790409	1510 3.70	68N15.87	166W13.57	10.00*	2.80	6	299	310.6	0.29	38.8	67.3
790409	1919 38.75	64N 7.74	164W 1.16	4.22*	2.29	5	210	100.0	0.09	99.0	75.4
790411	036 18.22	65N13.21	162W56.66	10.00*	1.41	3	187	183.5	0.00	4.3	99.0
790411	1324 51.24	66N32.89	157W30.60	10.00*	2.85	3	208	100.0	0.00	93.5	99.0
790413	820 23.48	65N 8.47	162W54.32	10.00	1.70	4	114	148.7	0.63	2.9	99.0
790414	459 57.58	65N 0.48	165W49.87	10.00*	2.07	4	147	155.8	0.28	8.4	15.6
790414	1610 54.09	65N33.15	162W 4.98	1.17		6	142	145.5	0.46	2.8	4.5
790414	1719 50.79	64N48.33	165W30.69	10.00*	2.85	4	142	172.4	0.15	23.5	39.8

Table 5.--(continued)

DATE	ORIGIN	LAT N	LONG W	DEPTH	MAG	NO	GAP	DMIN	RMS	ERH	ERZ
790414	1849 5.87	66N 7.88	161W37.13	4.70	4.27	4	250	253.3	8.44	21.5	1.5
790414	19 1 52.84	64N48.68	165W26.08	8.87	1.45	4	133	170.9	0.00	22.7	39.7
790415	1316 30.43	64N45.39	165W 2.20	8.48*	1.40	4	172	173.4	0.20	25.1	33.6
790416	2042 35.56	64N57.12	163W31.26	10.00*	1.40	3	212	156.9	0.00	99.0	99.0
790417	1325 37.17	64N26.96	165W31.36	0.39*	0.98	4	276	211.2	0.36	99.0	13.0
790430	2124 16.44	65N18.49	168W25.17	3.70*	2.05	4	190	205.3	0.22	9.8	13.5
790501	1642 11.13	64N46.90	165W14.56	12.89	2.99	5	184	172.2	0.18	33.1	42.6
790504	1446 46.52	65N49.14	166W 6.92	10.00*		4	161	144.1	0.36	6.1	7.3
790506	2351 23.82	65N 6.18	166W54.63	0.31*		5	101	172.5	0.23	4.3	5.7
790507	640 45.38	64N53.75	167W26.90	10.00*	1.62	4	234	206.4	0.09	99.0	99.0
790507	1317 0.49	65N22.36	161W29.39	4.83		5	183	172.7	0.32	6.8	21.8
790509	2048 51.04	65N25.15	163W46.26	4.82	1.79	4	139	192.8	0.00	8.6	8.6
790513	436 35.86	66N18.07	164W32.08	0.27*		4	171	174.9	5.91	59.7	86.6
790513	1817 51.99	64N11.08	169W55.36	18.33	2.41	4	184	223.7	0.02	99.0	99.0
790513	1952 9.94	64N40.17	170W59.37	10.00*	2.37	4	247	100.0	0.10	99.0	99.0
790515	1724 36.23	65N12.76	168W48.10	28.85		5	200	187.5	0.02	4.4	8.2
790515	1742 19.61	65N12.63	168W48.42	27.07		5	200	187.1	0.02	4.8	11.6
790515	1844 58.24	65N10.36	168W36.27	10.00*		3	187	187.9	0.00	99.0	99.0
790515	2031 46.76	64N43.61	167W 6.90	0.00*	1.92	4	203	199.8	2.20	5.8	10.4
790516	1332 16.37	64N45.20	165W45.01	10.00*		3	173	181.2	0.00	99.0	99.0
790517	239 36.54	64N22.93	162W40.36	10.00	2.14	5	162	230.2	0.19	99.0	99.0
790517	1153 9.75	65N44.28	169W32.23	0.34	3.16	5	234	235.1	0.78	13.5	8.9
790521	1359 19.81	65N33.56	167W55.27	0.41	2.31	4	188	100.0	4.36	99.0	5.5
790526	553 50.20	67N 3.96	164W 3.86	10.00*		3	277	100.0	0.00	99.0	99.0
790526	744 37.04	67N18.07	164W 4.18	15.70	2.39	5	265	259.2	0.47	55.2	49.7
790527	140 8.82	65N16.00	170W17.16	0.28	2.64	4	318	100.0	1.51	67.3	41.7
790529	1125 22.50	65N16.37	167W54.41	0.02	1.11	5	143	192.4	1.26	5.1	7.0
790529	1650 22.02	67N47.15	164W24.31	7.45*	2.23	5	289	292.7	0.37	16.9	50.7
790530	3 0 28.93	66N45.61	162W41.71	10.00*		3	211	100.0	0.14	99.0	99.0
790530	1325 13.66	67N 1.95	163W51.22	10.00*		3	241	100.0	0.00	99.0	99.0
790616	6 4 49.85	65N11.14	168W20.57	0.32*		4	270	100.0	0.33	19.3	23.4
790622	521 18.54	65N40.13	166W 5.26	10.00*		3	142	127.6	0.00	99.0	99.0
790623	1617 46.12	69N28.92	177W 0.71	5.09	4.48	4	335	665.4	0.01	99.0	99.0
790624	1159 38.44	67N23.59	169W37.28	10.00*	3.35	5	272	311.3	0.50	16.8	60.5
790712	954 51.57	65N16.09	166W59.68	10.88	1.76	5	173	161.1	0.03	90.0	99.0
790723	1246 10.06	66N17.97	168W28.87	10.00*		3	286	100.0	0.03	99.0	99.0
790724	112 56.03	64N45.95	165W35.65	10.00*	1.61	3	156	177.7	0.00	99.0	99.0
790724	1522 52.72	66N 3.48	167W28.62	0.34*		5	216	193.2	0.76	10.4	5.3
790726	11 9 58.91	66N47.72	165W19.58	10.00*		3	225	180.7	0.00	99.0	99.0
790731	6 1 53.01	66N 0.07	166W38.41	10.00*		3	199	170.7	0.00	99.0	99.0
790802	819 10.49	64N47.25	165W26.69	10.00*		3	158	173.6	0.00	99.0	99.0
790808	448 31.89	68N15.67	161W 7.92	10.00*		3	334	100.0	0.60	99.0	99.0
790816	1944 28.93	65N21.51	166W 6.20	10.00*		4	127	127.1	0.79	52.6	90.6
790817	10 5 58.75	65N58.22	164W49.65	10.34	2.05	5	191	158.7	0.55	99.0	99.0
790818	1644 44.29	64N55.34	162W43.48	10.00		4	137	174.2	0.16	3.7	99.0
790901	151 41.11	64N53.90	165W 6.47	10.00*		4	106	158.2	0.14	22.7	36.6
790901	349 31.09	64N53.88	165W11.40	10.00*		5	108	159.0	0.07	37.8	63.0
790901	411 19.54	64N53.18	166W21.13	10.00*	2.45	3	260	100.0	0.03	99.0	99.0
790903	439 6.96	65N 5.81	165W19.11	16.16		4	151	138.7	1.16	46.5	78.3
790903	533 43.85	65N54.57	166W22.69	10.00*		3	180	94.4	10.66	99.0	99.0
790908	1412 4.89	63N39.97	155W42.33	10.00*		3	172	100.0	0.00	99.0	99.0
790911	925 22.69	64N58.45	162W22.03	10.00		4	148	177.7	0.78	2.7	99.0
790914	143 7.22	65N30.80	164W11.47	10.00*		3	214	100.0	0.00	99.0	99.0
790922	036 50.77	64N44.22	165W10.56	21.56*		4	164	100.0	0.75	99.0	99.0
791021	411 42.53	66N46.41	163W 0.84	10.00*	0.80	3	196	95.3	0.00	99.0	99.0
791024	2219 33.16	65N14.56	164W45.81	10.12		6	84	150.9	0.14	7.4	13.8
791027	032 51.51	61N36.70	168W24.16	8.46	3.79	4	324	100.0	1.96	99.0	99.0

Table 5.--(continued)

DATE	ORIGIN	LAT N	LONG W	DEPTH	MAG	NO	GAP	DMIN	RMS	ERH	ERZ
791101	653 46.23	64N12.80	163W39.21	3.52	2.79	4	206	251.7	0.01	99.0	99.0
810110	123 43.43	65N18.45	171W 8.92	25.86	2.01	6	245	209.2	0.56	11.8	21.6
810110	811 30.92	65N51.21	162W57.04	15.77*		4	169	152.7	0.85	8.8	9.2
810112	854 53.61	65N31.94	166W58.20	4.52	1.85	8	131	131.5	0.18	1.6	2.5
810120	15 5 41.96	62N43.50	150W23.94	17.10	3.08	5	342	592.8	0.16	99.0	99.0
810120	1753 2.19	65N56.37	166W 6.48	0.97		4	184	94.4	0.91	99.0	99.0
810121	336 44.93	65N52.65	166W38.65	7.03	1.77	5	182	106.8	0.05	6.0	5.2
810121	1443 51.17	66N 8.58	164W18.29	16.39	0.83	5	154	98.2	0.21	3.1	2.6
810126	2 0 37.26	62N 8.86	163W21.69	10.00	2.08	4	262	100.0	4.40	99.0	99.0
810126	236 32.72	65N46.53	166W 9.93	10.00*	1.65	9	93	94.5	0.51	3.8	4.9
810126	1150 16.68	64N41.88	164W11.72	10.00*		3	293	178.9	0.00	33.6	99.0
810126	20 9 48.76	64N26.84	165W 7.65	1.50	2.06	12	182	172.6	0.47	3.9	2.2
810128	1346 14.40	65N33.25	164W10.67	25.10	1.28	7	145	103.2	0.87	1.2	99.0
810130	831 54.22	65N32.57	164W 7.97	10.00*	1.90	6	147	105.6	0.63	2.2	3.6
810201	1339 7.27	63N17.22	168W22.07	5.01	2.22	7	233	204.7	0.53	5.1	2.7
810214	222 14.10	65N45.52	166W 7.90	0.27*	1.83	8	92	94.5	0.56	1.0	3.5
810214	1512 1.83	64N40.18	165W26.05	9.22	1.10	4	180	100.0	0.55	99.0	99.0
810214	1855 23.70	65N16.67	168W 8.99	5.53	1.63	6	256	153.6	0.50	5.6	8.5
810215	747 36.01	64N46.15	162W51.07	17.40	1.29	9	112	111.2	0.35	1.1	1.4
810216	626 13.13	64N 9.16	165W30.92	0.01	2.05	4	289	254.6	0.54	99.0	99.0
810216	710 54.50	66N 1.50	166W 6.93	2.16	0.82	4	220	166.4	0.54	99.0	99.0
810217	1514 0.86	66N 4.63	172W13.03	0.00*	2.47	8	289	290.8	0.29	20.2	23.8
810219	1426 6.02	65N58.19	166W 2.30	4.23*		3	184	182.3	4.92	99.0	99.0
810219	1849 30.40	64N13.27	170W18.14	4.23*		5	213	240.9	1.17	44.5	68.0
810221	1429 20.66	64N 3.20	162W37.01	8.79	2.44	5	267	269.6	0.18	11.7	9.3
810222	854 23.66	65N24.85	161W23.54	24.81	1.68	5	305	100.0	0.82	5.6	49.6
810222	13 4 28.20	65N25.77	165W17.94	10.00*		3	188	169.3	0.00	99.0	99.0
810222	1442 57.51	64N16.65	164W33.31	1.76	1.05	7	215	158.8	0.72	5.9	2.8
810223	4 2 9.22	65N46.00	166W12.25	1.98	2.17	9	99	139.6	0.39	2.6	4.7
810223	537 23.44	64N28.53	160W16.48	17.55	0.86	6	262	122.3	0.30	3.0	1.3
810223	713 25.21	66N 0.87	167W40.90	0.16	2.10	5	264	194.2	0.26	3.4	4.7
810224	524 33.93	66N 1.01	167W40.61	3.71	1.33	6	242	145.7	0.28	3.2	2.9
810224	22 5 2.41	66N 0.24	158W22.62	10.00*	3.02	4	360	251.1	0.65	44.6	46.7
810226	1953 33.77	64N17.93	162W20.87	11.91	1.79	11	110	96.6	0.78	1.0	1.4
810226	2138 20.69	65N19.37	162W57.33	10.00*	1.54	3	301	170.2	0.04	99.0	99.0
810227	6 2 27.19	64N 4.42	160W28.81	12.96	1.15	7	280	116.4	0.42	1.8	1.4
810227	2019 59.97	65N 2.62	167W50.02	6.00*	1.55	10	136	128.6	0.64	2.1	4.0
810228	217 18.63	65N18.85	166W57.98	10.00*	1.75	4	165	156.5	0.80	99.0	99.0
810228	556 7.61	65N16.92	167W 4.84	10.00*	2.16	8	88	113.7	0.55	3.4	5.9
810228	1033 6.84	64N21.80	162W39.50	3.73	3.05	10	86	107.7	0.29	1.8	2.2
810229	1050 6.18	63N32.27	169W 5.33	10.00*		4	239	298.4	0.48	99.0	99.0
810301	1120 49.42	65N 5.30	166W54.78	10.00*	0.91	6	190	98.0	0.72	1.3	15.3
810302	1417 0.30	65N10.46	167W43.04	11.83	1.52	5	226	130.3	0.31	26.2	22.6
810303	139 45.60	65N34.38	166W58.78	6.14	1.24	8	131	135.5	0.72	1.7	2.3
810303	639 37.60	64N54.57	162W 9.60	13.16	1.53	12	109	116.5	0.48	1.9	3.0
810303	1417 55.76	63N28.54	158W 6.03	10.00*	1.50	6	302	201.1	1.01	23.9	30.2
810303	1958 1.03	65N46.03	168W42.86	4.23*		3	311	100.0	2.49	99.0	99.0
810304	12 3 37.42	64N25.34	162W43.10	5.85	0.57	7	156	108.5	0.34	2.0	2.0
810305	1921 35.24	64N52.63	162W 9.72	13.53	0.97	8	107	93.8	0.89	2.6	3.9
810306	440 4.15	64N55.73	162W14.43	12.46	1.37	15	108	100.6	0.82	1.6	2.9
810307	919 31.67	64N24.16	163W43.00	0.35	1.34	10	135	121.0	0.49	3.1	3.1
810307	1025 10.50	65N16.40	165W43.07	10.00*	2.09	16	64	108.9	0.90	1.4	2.3
810307	19 2 21.40	64N21.11	162W42.58	8.28	0.74	4	190	130.3	0.17	28.7	6.9
810307	20 3 30.70	65N20.42	165W 3.07	5.01	1.10	4	308	100.0	0.39	99.0	99.0
810311	1017 45.12	64N47.53	163W18.38	0.51*		4	221	139.6	0.27	4.6	8.2
810311	2026 31.87	65N 9.54	165W34.91	24.61	1.28	4	191	100.0	0.13	30.5	99.0
810312	458 1.03	67N 6.44	164W34.79	30.93	1.35	8	258	151.4	0.43	2.7	4.6

Table 5.--(continued)

DATE	ORIGIN	LAT N	LONG W	DEPTH	MAG	NO	GAP	DMIN	RMS	ERH	ERZ
810312	753 35.96	63N 4.01	167W53.30	10.00*	2.23	5	238	100.0	0.25	99.0	88.2
810312	15 6 30.43	64N49.79	162W14.51	0.23*	1.69	11	101	91.0	0.34	1.5	2.7
810312	23 0 36.29	64N 3.09	160W24.36	13.95	1.42	8	225	120.5	0.46	1.6	1.4
810313	22 0 4.52	64N48.16	162W16.70	8.57	1.40	9	101	89.3	0.45	3.7	6.7
810314	2 6 57.81	65N13.02	165W54.86	8.75	1.23	9	189	136.2	0.37	8.8	7.3
810314	855 9.26	64N 3.45	160W 9.17	12.99	1.65	12	239	132.2	0.40	1.7	1.5
810314	1539 48.52	65N 6.45	169W10.25	2.99	1.47	8	208	179.0	0.28	4.7	3.1
810315	545 46.98	66N19.22	160W42.54	1.25*	2.45	13	232	171.1	1.24	3.2	2.5
810315	1243 58.45	64N31.68	160W18.49	19.31	0.80	7	244	121.4	0.44	2.7	1.1
810316	215 38.13	65N32.86	167W 3.03	5.29	1.21	10	130	135.1	0.46	1.7	2.4
810316	219 20.51	65N33.90	167W 2.30	1.00*	0.83	6	131	136.3	0.69	2.6	99.0
810316	7 2 15.21	64N42.12	164W12.33	14.05	1.30	8	135	168.3	0.45	6.4	8.6
810316	859 7.62	65N56.48	166W15.48	7.11	1.20	5	180	88.3	0.59	77.1	27.1
810316	1939 2.98	65N53.25	167W28.68	10.00*	1.05	6	218	141.3	0.57	5.5	2.8
810317	459 0.97	65N13.14	166W 4.04	14.41		7	199	139.5	0.22	13.2	6.8
810317	1831 10.78	64N54.02	162W14.52	14.19	1.26	9	106	97.8	0.36	3.0	4.4
810318	1729 11.44	67N17.03	164W28.08	10.96	1.80	10	260	171.0	0.89	5.1	4.8
810318	1731 10.78	64N54.02	162W14.52	14.19	1.33	9	106	97.8	0.36	3.0	4.4
810318	2111 14.01	65N36.67	164W11.70	10.00	1.93	4	225	100.0	0.13	99.0	99.0
810320	1910 21.39	65N 0.55	167W54.92	10.00		5	285	100.0	1.03	99.0	99.0
810323	1451 12.35	65N20.19	162W24.85	1.54	1.10	4	181	144.1	0.06	99.0	99.0
810328	9 7 12.37	63N13.49	163W54.40	10.00*	0.78	4	241	165.8	0.33	99.0	99.0
810329	351 22.94	65N18.48	164W27.67	27.66		8	153	110.3	0.47	1.2	55.8
810330	1324 15.54	65N22.36	166W40.88	0.18*	0.56	7	146	109.2	0.57	0.9	99.0
810330	1842 25.57	64N44.14	159W50.19	9.36		9	251	148.4	0.42	2.2	1.7
810402	116 10.84	62N39.47	166W 9.61	13.54	1.78	5	225	236.6	0.62	17.0	50.1
810404	1038 15.53	65N31.76	166W52.09	10.67	0.71	8	129	128.6	0.63	1.6	2.2
810404	1117 44.67	65N18.83	166W50.10	0.18	0.95	5	159	108.4	0.12	1.3	4.8
810405	1755 53.93	64N51.27	167W59.49	0.01	0.96	6	258	144.2	0.23	2.6	19.1
810406	2334 6.46	66N18.61	169W52.26	4.23*	1.66	4	278	100.0	0.21	99.0	42.3
810406	2346 23.86	64N 5.36	168W 1.15	10.00*	1.49	4	181	164.7	0.54	33.0	88.9
810407	132 25.83	65N18.48	165W30.70	5.90	0.68	9	159	117.0	0.35	1.0	2.8
810407	7 9 50.60	65N56.56	168W38.50	2.97	2.32	5	360	190.3	0.46	19.7	7.3
810410	4 7 43.51	65N50.35	166W 7.07	11.93		4	112	89.7	0.00	15.3	16.2
810410	433 55.80	65N18.53	166W45.12	0.31*		4	157	105.5	0.08	2.0	5.1
810410	545 53.69	63N 2.76	164W32.34	10.00*		3	254	100.0	0.00	99.0	99.0
810410	1142 20.79	63N 9.84	169W 1.53	21.15		4	258	272.8	1.34	99.0	99.0
810411	8 8 21.63	65N 4.22	167W20.78	10.54	0.81	6	213	109.4	1.56	1.6	5.8
810412	415 8.30	65N56.77	166W40.26	10.00	0.42	8	192	104.7	0.96	1.9	1.7
810412	1824 53.78	65N36.64	167W 9.61	2.47	1.16	12	147	142.3	0.57	1.8	2.3
810413	3 8 6.53	65N46.72	166W 6.74	6.43	0.90	7	114	92.4	0.84	4.6	7.2
810413	2041 24.02	66N 0.97	167W40.63	0.18	1.11	8	242	145.7	0.31	2.6	2.4
810413	2143 7.99	64N53.06	162W10.95	10.00*	0.50	3	208	156.1	0.00	99.0	99.0
810416	1931 36.77	65N 4.74	172W53.21	10.00	2.09	4	284	407.3	0.29	99.0	99.0
810417	253 35.22	66N32.10	164W51.71	10.00*	1.15	4	196	106.1	0.73	4.1	6.3
810417	2230 16.23	64N25.94	162W26.70	8.98	0.87	9	119	95.5	0.74	2.5	2.6
810420	1654 3.67	64N49.24	165W13.28	12.93	1.58	12	81	131.7	0.84	2.1	2.4
810424	12 8 1.25	65N25.03	167W22.68	10.00*		3	168	134.1	0.00	99.0	99.0
810425	1049 25.18	64N 2.09	160W 4.93	10.74	1.28	6	243	136.2	0.05	1.7	1.7
810425	1356 38.33	64N58.67	168W16.37	3.88		5	294	100.0	0.14	99.0	99.0
810426	150 10.71	64N34.82	166W 2.05	7.77	1.19	10	223	150.0	0.68	3.1	2.1
810426	1911 54.82	65N46.66	165W46.55	11.29	0.79	4	128	103.0	0.06	16.2	25.6
810426	1934 30.38	65N45.55	165W48.22	10.00*	0.15	3	141	134.7	0.00	99.0	99.0
810429	9 9 10.03	62N55.87	169W33.36	14.43	1.87	4	284	100.0	0.09	99.0	99.0
810430	21 3 19.38	67N18.64	164W18.07	10.00	1.66	5	263	177.1	0.82	48.0	39.0
810501	425 14.37	65N30.75	170W22.45	0.63	1.17	6	255	214.4	0.78	7.8	3.9
810501	724 0.58	65N 8.58	165W14.47	1.80	1.42	12	130	98.5	0.54	1.2	3.2

Table 5.--(continued)

DATE	ORIGIN	LAT N	LONG W	DEPTH	MAG	NO	GAP	DMIN	RMS	ERH	ERZ
810501	2041 13.07	65N31.67	166W39.12	6.23	1.25	6	108	123.1	0.38	1.6	3.5
810502	528 48.02	65N16.50	165W31.55	0.19*	1.22	7	153	117.4	0.71	1.3	99.0
810502	1749 45.02	65N16.86	166W26.91	0.63*	1.50	7	148	94.7	0.31	1.0	4.4
810503	552 29.94	65N31.71	167W 5.55	10.00*	0.49	4	134	134.6	0.42	3.7	4.7
810503	1254 11.44	65N 8.35	170W20.76	0.63*	2.46	5	241	208.8	0.85	12.4	4.9
810503	1616 44.17	65N38.62	169W29.40	0.06*	1.30	7	246	100.0	0.23	8.5	4.3
810503	2254 8.19	65N 8.70	165W15.92	2.59	0.48	9	148	132.9	0.50	1.3	3.3
810504	11 8 32.24	65N 6.30	165W 5.27	19.45	0.77	5	182	135.4	0.11	10.3	16.8
810510	920 10.27	64N25.30	164W 5.93	9.45	0.39	10	188	63.6	0.35	1.4	1.9
810510	2052 18.05	66N13.66	162W56.23	1.72	0.84	13	119	71.7	0.69	1.2	2.6
810511	920 10.55	64N25.90	164W 6.57	10.00*		3	186	64.2	0.00	99.0	99.0
810515	1441 57.74	64N44.88	168W36.15	10.00	1.52	4	282	100.0	0.64	99.0	99.0
810515	2043 40.36	64N24.66	165W23.41	12.02	1.17	11	226	125.6	0.44	3.0	1.3
810516	1424 30.83	67N15.22	157W55.16	2.50*	1.94	4	304	311.7	0.26	99.0	99.0
810518	225 27.14	64N24.05	163W18.32	0.63	0.62	6	178	101.0	0.22	4.2	13.8
810518	12 9 5.46	65N51.55	165W38.48	0.00*	1.80	4	235	175.2	11.23	19.0	3.7
810522	550 59.21	65N40.41	168W38.39	10.09	1.27	5	310	199.5	0.85	36.7	21.4
810522	2017 18.05	65N35.12	165W58.29	13.46	0.60	5	127	103.2	0.31	4.6	6.1
810522	2234 48.09	65N12.49	165W25.43	0.48*	0.11	10	118	99.2	0.89	0.9	99.0
810526	057 20.48	65N20.47	162W15.94	10.00	0.91	5	175	119.9	0.65	7.0	11.6
810526	240 43.83	63N35.25	165W10.98	10.86	1.64	6	302	144.4	0.24	6.4	5.1
810526	953 12.42	65N47.36	166W11.58	10.00*	0.90	10	98	94.5	0.62	4.4	5.5
810528	2 9 29.20	64N46.45	165W13.52	10.00*	0.16	3	174	172.8	0.00	99.0	99.0
810530	6 9 32.08	64N46.30	162W15.89	12.83	0.70	7	232	131.9	0.27	15.7	20.3
810531	2122 50.33	65N12.87	167W15.45	0.13	1.72	8	262	171.0	0.43	3.2	2.2
810605	2336 10.45	65N48.67	157W34.61	10.00*	2.54	5	306	331.6	1.10	99.0	99.0
810606	118 12.08	66N13.24	165W50.86	15.79	2.05	4	249	100.0	1.15	37.2	41.4
810606	333 35.46	67N33.40	164W24.76	10.00*		3	290	199.3	0.00	99.0	99.0
810606	22 4 37.49	65N31.65	166W15.79	13.13		4	140	116.8	0.00	3.8	5.0
810613	1725 19.92	65N 0.74	164W59.33	13.27	0.61	4	194	144.8	0.00	17.2	28.7
810621	1 4 37.17	66N40.58	163W27.82	4.59	0.61	4	196	98.7	0.00	1.7	52.6
810621	2341 58.55	64N19.79	168W39.42	10.00*		3	310	100.0	0.24	99.0	99.0
810623	1030 37.41	67N10.75	160W51.52	0.03	2.08	8	293	189.1	0.56	29.0	9.3
810625	20 0 13.81	64N55.10	162W29.34	10.00*		5	125	97.2	0.34	3.5	7.6
810626	1354 2.01	64N29.19	163W34.58	10.00		6	182	147.3	0.43	7.6	7.8
810704	745 2.14	67N39.13	161W34.59	27.80	4.80	9	244	281.6	0.41	8.0	7.2
810705	0 1 0.61	67N42.43	161W24.09	31.62		6	310	208.0	0.17	99.0	40.5
810705	0 2 20.16	67N27.11	160W24.55	0.00*	0.73	4	330	100.0	0.21	25.1	15.4
810705	0 4 34.85	66N32.73	162W39.19	20.00*	0.17	4	157	88.0	3.94	19.7	18.2
810705	0 5 9.82	66N31.67	162W35.04	20.00*	0.12	4	165	90.4	3.79	17.4	15.1
810705	0 6 33.65	66N30.47	162W58.84	20.17	0.32	4	258	72.8	0.02	17.5	21.9
810705	0 7 39.14	66N32.92	162W35.15	20.00*	0.04	4	165	90.9	3.85	16.8	14.4
810705	0 8 54.92	66N33.52	162W46.66	20.00	-0.17	4	143	83.2	4.04	20.0	26.2
810705	0 9 23.44	66N45.78	162W30.87	10.00*	-0.67	3	191	103.3	0.00	99.0	99.0
810705	010 51.59	66N32.05	162W23.38	20.00*	-0.03	4	186	98.9	3.85	12.3	8.4
810705	010 53.97	67N36.84	160W32.93	16.19*	0.80	4	330	100.0	0.16	81.9	99.0
810705	012 23.49	67N17.68	162W 9.46	32.88	2.70	6	293	152.3	0.55	99.0	19.8
810705	013 47.23	67N12.00	161W22.72	10.00*		3	355	100.0	0.34	99.0	99.0
810705	014 24.67	66N41.72	162W33.28	116.92	1.79	5	162	98.2	0.00	13.7	30.3
810712	127 54.86	67N39.82	161W38.93	37.18	5.20	9	243	197.4	0.18	8.1	5.5
810803	1329 40.40	67N45.22	161W25.86	0.03*	1.46	4	329	211.0	0.35	22.6	7.1
810803	1333 41.46	67N45.92	162W 2.08	9.35	1.47	5	318	100.0	0.02	29.8	7.4
810803	2322 56.72	64N 4.81	165W59.11	2.88	2.03	7	279	157.8	0.26	3.4	3.6
810804	14 9 16.64	67N20.45	160W38.39	10.00*	1.32	3	360	100.0	0.07	99.0	99.0
810804	1439 17.08	67N37.10	161W25.88	2.33	1.32	6	320	199.9	0.25	9.1	4.4
810804	2232 29.19	67N 2.73	161W56.09	14.65	0.30	4	310	141.6	0.00	5.3	3.4
810805	16 9 52.73	67N40.42	161W15.80	3.04		4	348	100.0	0.17	99.0	99.0

Table 5.--(continued)

DATE	ORIGIN	LAT N	LONG W	DEPTH	MAG	NO	GAP	DMIN	RMS	ERH	ERZ
810806	322 31.00	64N22.20	162W59.44	9.70		4	176	116.6	0.00	99.0	22.2
810808	1737 49.05	67N23.84	161W27.49	13.94		4	323	182.1	0.00	14.2	2.9
810808	21 6 45.93	65N 3.19	165W24.61	4.73		5	198	144.5	0.08	3.1	5.3
810808	2354 15.05	67N 2.56	160W18.55	0.74*		4	349	100.0	0.02	99.0	99.0
810810	1118 14.57	67N43.17	161W11.15	0.16	1.47	6	329	100.0	0.33	10.8	4.5
810810	1242 20.49	67N47.97	161W22.99	13.92		7	322	216.2	0.35	56.4	73.7
810811	113 30.04	64N28.28	164W44.56	10.00*		4	192	95.0	0.15	18.9	32.3
810813	1544 6.73	64N53.00	161W 2.37	10.00*	2.48	6	152	225.0	1.23	38.2	66.0
810815	7 3 8.72	67N48.99	161W41.97	6.71	2.42	8	306	209.3	0.24	5.7	2.5
810816	1120 50.66	67N 5.54	160W41.53	5.00*	2.52	5	286	270.4	0.18	99.0	15.5
810819	1120 10.46	68N25.65	160W48.10	0.31*	2.93	7	323	419.4	0.45	36.7	37.3
810819	1546 0.64	65N44.49	166W 4.98	0.20*	2.83	10	175	135.4	0.54	2.3	2.6
810902	1217 3.15	67N 7.29	164W51.39	10.00*		5	261	176.1	0.20	99.0	51.6
810902	1432 8.62	67N22.82	165W 3.11	24.68		5	280	203.2	0.43	8.1	12.0
810903	542 5.83	65N 1.14	167W26.85	39.70*		4	223	115.2	0.95	36.1	36.8
810903	2227 2.17	65N57.01	161W 5.80	10.00		4	202	206.2	0.73	10.9	99.0
810904	455 34.04	65N56.33	163W36.16	10.00	1.14	10	113	120.2	0.75	2.8	5.6
810906	1322 9.15	59N51.97	159W 1.62	8.13	3.37	5	336	618.5	0.07	99.0	99.0
810907	456 30.03	62N29.25	153W21.85	10.00	2.96	4	345	654.3	0.13	99.0	99.0
810910	11 7 8.72	65N14.72	159W53.91	8.15		4	257	100.0	0.00	85.6	99.0
810914	7 7 39.95	66N45.10	162W45.29	10.00*	0.94	3	155	181.5	0.00	99.0	99.0
810914	1336 25.27	66N27.85	161W48.81	11.31		5	236	122.6	0.16	99.0	99.0
810919	748 28.86	65N58.38	163W44.73	13.09		5	136	109.8	0.13	2.5	2.3
810919	1244 29.61	64N55.79	163W24.30	10.00		8	138	102.1	0.46	2.9	5.0
810920	2225 58.47	64N52.71	165W31.61	0.81*	1.15	7	137	121.0	0.70	2.2	4.6
810921	13 4 18.89	65N 2.66	172W23.33	0.46*	1.83	4	336	100.0	0.02	99.0	99.0
810921	1924 23.29	65N10.40	168W55.19	10.00*	1.44	4	295	100.0	0.07	99.0	99.0
810921	2144 4.68	64N14.84	170W50.09	174.79*	2.46	4	205	285.4	0.87	64.5	99.0
810925	529 56.96	67N26.30	165W 1.72	10.00	1.47	4	339	100.0	0.20	99.0	99.0
810925	13 0 36.19	64N35.44	162W29.65	7.60	1.71	11	79	77.7	0.40	1.5	2.6
810927	1659 21.89	66N43.23	163W 9.14	103.60	2.49	5	272	95.7	0.09	29.2	25.3
810928	127 20.28	65N12.37	166W42.77	10.00*	0.72	6	168	95.7	0.56	1.1	15.4
810928	1349 14.86	64N49.63	164W56.87	9.26	0.97	12	98	80.8	0.82	1.1	1.5
810928	1429 53.19	64N18.04	163W34.33	0.16	0.77	9	208	91.5	0.48	2.0	2.7
810928	1532 52.65	64N50.39	164W24.96	4.03	1.54	17	89	95.3	0.85	1.8	2.5
810928	1542 7.83	64N55.29	162W22.61	10.00*	0.89	7	108	92.2	0.52	2.8	4.5
810928	1921 14.32	66N45.12	162W45.21	20.85*		7	155	93.6	0.74	59.5	45.8
810929	511 47.99	67N10.07	164W24.50	16.83	1.86	8	251	161.0	0.61	7.5	7.7
810929	1253 57.09	67N15.79	164W26.52	10.39	1.96	12	258	169.5	0.82	3.8	2.0
810930	1858 49.68	64N51.12	165W24.32	10.00*	0.53	9	131	125.5	0.73	2.1	3.7
810930	1947 50.06	64N51.53	165W29.44	2.79	0.47	10	135	78.8	0.55	1.6	1.9
810930	2334 12.05	64N24.58	164W 6.30	10.00*	0.27	6	191	63.7	0.37	8.1	16.8
811001	827 58.39	64N52.07	165W27.17	3.45	0.93	9	133	77.6	0.63	1.7	2.2
811001	1512 32.18	66N46.62	162W35.66	19.05*	2.52	10	155	101.1	0.78	50.0	31.8
811001	21 9 4.53	67N42.13	161W29.86	5.92	0.97	6	321	204.8	0.20	9.8	4.1
811003	039 22.42	64N51.41	165W29.58	5.00*	0.35	7	157	78.8	0.51	2.1	17.5
811003	10 0 29.83	65N19.63	166W24.17	11.11	0.62	9	141	76.8	0.70	1.0	1.4
811003	1255 36.39	67N37.64	161W33.22	10.88	0.81	6	319	197.0	0.05	9.0	3.8
811003	2023 31.21	64N54.85	162W14.68	4.15	1.26	10	107	92.6	0.42	0.9	4.0
811004	23 1 50.45	64N43.27	165W45.20	0.02	0.92	7	209	85.9	0.84	2.2	99.0
811005	746 32.03	64N53.13	165W26.90	1.78*	1.58	11	130	78.3	0.52	1.6	3.1
811005	13 6 26.74	64N34.79	161W28.84	10.00*	1.59	4	122	156.8	0.26	99.0	99.0
811005	1335 7.17	64N51.34	165W30.52	0.18*	1.37	10	137	79.4	0.45	1.8	4.8
811005	1349 26.43	64N50.78	165W33.40	0.17*	0.71	7	142	81.1	0.18	1.9	99.0
811005	2255 57.31	65N37.15	167W 4.01	2.50*	0.05	6	146	51.9	0.13	0.9	34.5
811006	619 36.72	65N20.20	162W33.57	0.64	1.16	15	113	121.3	0.65	1.2	1.7
811006	7 8 29.81	65N22.62	162W33.01	10.00*	1.32	6	142	152.0	0.52	6.3	12.2

Table 5.--(continued)

DATE	ORIGIN		LAT N	LONG W	DEPTH	MAG	NO	GAP	DMIN	RMS	ERH	ERZ
811006	1732	8.13	64N51.12	165W33.70	1.27*	1.36	14	142	123.5	0.64	2.3	3.0
811006	1739	1.09	64N51.21	165W31.40	1.12*	1.15	10	139	123.8	0.51	2.4	3.5
811006	1821	37.73	64N51.85	165W28.35	2.16	1.01	10	133	123.3	0.61	1.6	1.6
811008	2241	0.86	65N30.53	168W14.71	0.12		4	296	102.9	2.87	99.0	99.0
811008	2241	40.88	65N33.04	168W 6.35	0.90	1.52	4	294	95.0	6.10	99.0	67.3
811010	1756	21.76	67N15.10	164W39.76	8.40	1.78	8	256	164.0	0.41	4.3	2.8
811011	414	25.07	64N46.04	165W35.41	0.03*	1.64	11	155	132.3	0.74	3.8	4.5
811011	1149	54.05	65N26.14	166W49.29	11.28	1.15	8	142	60.4	0.54	1.1	1.4
811014	442	41.64	67N41.70	161W23.64	1.38	2.23	6	321	207.2	0.12	9.9	4.5
811014	1010	54.09	65N19.41	162W50.46	3.45	1.52	12	128	133.0	0.29	1.1	2.0
811014	1359	50.75	66N47.04	162W37.77	20.56*	3.60	10	141	100.2	0.64	33.9	20.7
811014	1749	42.13	65N18.65	162W48.07	8.42	1.75	13	130	135.2	0.44	1.3	1.9
811015	1 7	43.81	64N51.93	165W28.58	1.38*	1.40	12	134	123.1	0.79	1.3	2.9
811015	552	49.73	67N39.70	161W29.16	27.17	3.56	9	316	201.8	0.22	7.6	8.6
811015	2020	46.25	65N26.89	164W56.50	17.07	1.51	10	127	96.5	0.32	1.6	2.1
811018	5 6	1.77	66N 5.02	166W 1.49	7.76	1.36	8	192	85.8	0.66	2.6	2.6
811018	8 2	45.11	64N23.22	163W44.58	13.60	1.30	7	182	121.9	0.59	7.1	1.5
811018	21 3	6.25	66N32.52	162W59.04	24.34	2.82	7	262	74.7	0.42	23.4	96.7
811020	622	14.04	67N27.90	167W 8.72	10.00*	3.19	5	295	276.0	0.16	99.0	99.0
811023	1542	40.67	65N17.20	166W57.01	0.63*	1.31	6	168	78.0	0.11	1.4	99.0
811023	1824	22.28	66N34.36	162W48.59	40.48*	1.89	4	269	82.4	0.50	99.0	99.0
811024	1237	3.61	67N16.06	160W52.77	1.78	2.03	6	322	193.4	0.12	7.6	5.4
811024	1917	43.24	65N46.62	166W 7.03	3.08	1.57	7	103	87.8	0.23	1.4	3.4
811025	1056	42.14	66N44.07	164W38.26	22.96	1.41	11	211	115.7	0.67	2.0	1.3
811025	1347	54.51	67N36.64	165W55.88	12.32	2.14	4	295	188.8	0.03	33.2	99.0
811026	650	37.07	66N31.83	162W31.84	42.40*	2.49	4	272	92.7	0.55	85.4	99.0
811026	7 8	43.80	66N51.20	162W 0.76	91.36	2.17	5	277	127.5	2.65	7.1	3.8
811027	537	36.41	67N27.38	160W13.86	8.96	2.33	4	357	100.0	0.11	99.0	66.6
811027	1210	28.74	63N57.49	160W11.68	10.00	2.66	4	347	100.0	0.29	99.0	99.0
811027	1248	25.18	64N58.72	162W36.97	0.38*	1.69	10	136	114.4	0.28	1.4	4.2
811030	129	25.03	67N46.18	161W 7.64	46.61		5	324	221.0	0.54	13.7	65.6
811031	1618	44.35	65N15.91	165W35.09	10.00*	0.83	6	150	79.3	0.43	2.5	4.8
811101	552	5.64	65N14.65	165W51.00	4.29	0.66	6	136	79.0	1.03	2.2	4.9
811101	1826	13.36	65N20.93	165W40.47	18.67*	0.61	6	105	88.6	0.92	6.9	7.1
811102	1220	8.03	64N28.47	160W12.52	10.00*	1.96	6	262	248.1	0.27	99.0	63.9
811102	1252	1.32	65N38.70	167W26.10	3.85	1.01	5	170	67.4	0.08	1.2	27.8
811103	758	41.61	64N47.93	165W43.26	12.45	1.22	8	191	127.6	0.54	5.5	2.0
811103	10 4	57.86	64N58.23	164W 5.41	3.12	2.18	8	96	106.8	0.36	2.1	3.1
811105	1946	56.78	67N43.16	161W42.89	32.84	3.38	9	310	200.4	0.15	6.7	6.3
811106	0 2	4.34	67N12.85	165W26.54	17.52	2.34	9	255	148.4	0.89	7.9	9.5
811107	22 4	29.53	64N58.06	164W 8.47	15.63	1.42	8	110	142.4	0.25	1.9	2.4
811108	14 6	12.12	65N20.55	162W29.35	3.17	1.52	7	146	141.3	0.30	2.4	2.2
811109	1421	56.41	65N21.28	168W 8.93	1.94	1.46	10	258	108.2	0.41	1.8	2.5
811110	1847	40.69	65N11.14	164W33.83	6.85	1.30	9	158	113.0	0.49	1.6	3.6
811110	20 9	35.10	64N58.10	163W46.53	22.73	1.24	11	113	132.3	0.64	1.2	3.3
811113	056	12.08	66N40.87	162W56.52	20.00*	1.28	4	198	87.8	4.13	99.0	99.0
811113	725	54.06	64N55.81	165W33.01	11.55	1.08	8	188	132.9	0.96	3.3	1.9
811113	929	32.38	64N58.37	166W 6.33	0.31*	1.07	7	211	106.1	0.38	6.3	5.6
811114	740	17.72	67N52.75	161W11.11	28.29	2.61	5	324	228.4	0.10	11.3	10.2
811114	839	38.40	67N41.14	161W22.62	1.81	2.80	7	321	206.9	0.59	7.6	3.7
811114	1214	0.77	65N47.92	166W10.78	9.28	1.99	9	95	85.7	0.51	1.6	2.4
811115	11 3	55.64	67N33.44	162W58.86	16.79	1.88	6	308	182.1	0.20	8.0	2.8
811115	1349	59.71	65N28.63	163W45.44	12.70	2.58	16	88	115.4	0.79	1.6	2.5
811115	1849	10.70	67N45.82	161W39.04	20.99	3.19	11	306	287.6	0.29	13.5	18.6
811115	21 5	58.24	67N53.82	161W37.53	46.36	3.50	11	308	351.9	0.72	8.4	42.8
811115	2119	2.51	66N21.88	161W 4.05	10.00	2.15	5	297	100.0	0.32	99.0	99.0
811121	2355	42.21	66N 7.62	167W51.23	4.53	3.24	10	224	117.5	0.53	6.3	4.4

Table 5.--(continued)

DATE	ORIGIN	LAT N	LONG W	DEPTH	MAG	NO	GAP	DMIN	RMS	ERH	ERZ
811122	1620 45.25	66N33.30	162W44.08	41.52*	1.78	4	269	84.9	0.53	63.2	99.0
811123	020 14.11	67N43.95	161W51.75	12.30	3.26	10	310	278.7	0.60	4.4	2.0
811123	728 2.31	62N 8.55	154W29.54	10.00	3.10	10	323	412.4	0.23	99.0	99.0
811123	9 9 21.73	65N20.41	168W 7.79	1.76	1.10	7	255	108.5	0.49	2.2	3.6
811123	2150 15.85	65N29.32	163W44.24	0.21*	1.62	12	89	116.5	0.39	0.7	4.2
811124	8 6 45.73	66N10.72	163W 8.25	74.34	1.23	6	118	143.6	0.27	3.7	5.9
811125	547 9.65	64N41.89	164W43.46	0.64*	1.25	5	141	98.5	1.81	1.6	5.3
811125	2129 20.41	63N55.28	165W19.93	9.01	1.82	10	277	132.4	0.21	2.1	1.7
811126	013 13.42	64N33.44	160W41.01	10.19	1.44	8	181	104.3	0.49	1.6	1.9
811126	320 18.47	64N54.86	168W44.77	2.14	1.75	8	176	161.7	0.23	1.9	2.5
811126	836 23.38	65N56.87	172W49.26	10.00*	3.26	5	292	299.3	0.23	84.0	81.8
811128	2153 4.03	65N48.62	166W 4.27	10.00*	1.02	5	141	88.7	0.36	2.7	4.2
811129	2118 5.37	65N35.88	167W11.04	5.00*	0.88	6	145	56.3	0.16	1.0	16.6
811130	1052 54.87	65N48.77	166W20.12	7.49	1.29	10	129	79.4	0.29	1.0	2.0
811201	1422 46.06	63N23.92	166W55.10	10.00*	2.42	7	220	216.7	0.41	16.1	14.4
811201	1851 57.89	66N30.46	162W48.90	79.51	2.19	5	140	79.9	0.15	4.4	6.7
811204	624 37.96	66N27.26	163W 9.20	10.00*	2.24	7	253	151.3	0.77	7.3	12.1
811204	22 6 4.99	65N 1.36	164W 9.13	12.04	1.13	8	132	102.0	0.81	1.8	3.6
811205	1225 32.26	65N18.34	165W16.69	5.60	1.25	6	164	82.7	0.69	2.4	5.1
811205	13 9 0.18	63N54.96	160W11.57	9.80		5	320	135.4	0.04	5.9	1.9
811207	19 6 55.54	66N49.23	162W 6.90	78.83	2.37	5	265	121.8	2.74	7.0	4.0
811207	1928 39.44	67N43.12	161W42.31	9.83	2.88	8	319	200.6	0.68	5.7	2.5
811207	2249 5.01	67N14.65	161W33.86	29.67	3.39	9	311	167.7	0.63	13.4	8.5
811208	0 5 23.47	67N50.21	160W21.99	15.37	2.65	6	329	249.3	0.17	29.8	34.4
811209	1435 51.60	65N28.92	166W 2.48	2.91*	0.90	7	126	89.0	0.29	1.5	11.1
811209	1836 52.09	65N13.22	164W16.42	0.39*	1.30	9	135	119.9	0.42	1.8	3.2
811210	10 9 5.62	65N15.36	164W14.16	11.64	1.35	11	85	116.8	0.56	1.6	2.4
811210	21 8 58.25	65N 9.46	161W15.24	17.98	1.28	6	207	116.5	0.40	5.0	3.6
811211	1644 11.38	67N30.35	161W43.32	27.56	2.68	6	318	266.3	0.52	14.3	16.1
811211	1730 52.42	65N33.72	167W39.15	10.00*	0.69	5	161	76.1	0.19	1.5	7.9
811212	1612 6.24	65N16.37	166W50.19	10.00*	0.73	4	165	105.0	0.43	2.1	36.1
811213	9 7 41.49	65N47.19	166W17.37	4.11	1.46	9	115	80.5	0.57	1.0	2.3
811213	1028 59.08	65N 1.55	162W25.42	1.00	2.12	13	107	98.3	0.59	1.2	2.3
811214	2020 40.67	65N30.67	167W 3.42	7.94	1.59	8	137	59.2	0.32	1.0	2.8
811215	140 25.82	66N27.54	163W 5.63	10.00	2.80	8	255	154.0	0.85	4.6	7.1
811215	2134 50.67	65N53.88	155W 8.15	18.86	3.36	10	153	321.1	0.26	10.0	7.2
811215	2348 45.33	65N20.88	162W28.52	4.85	1.72	11	146	113.9	0.18	1.3	1.6
811216	1042 41.29	64N55.18	162W23.59	13.13	1.10	7	144	103.2	0.43	2.5	3.5
811217	2247 33.50	65N17.85	171W22.73	0.00	2.35	5	351	100.0	0.13	99.0	99.0
811218	15 3 25.74	65N 9.56	167W39.07	5.00*	0.92	6	268	107.1	0.88	2.1	19.5
811219	13 0 59.37	64N48.09	171W14.39	10.00	2.68	10	256	243.5	0.74	45.2	37.6
811220	1021 49.92	62N11.51	171W54.49	35.58	3.54	6	331	100.0	0.13	99.0	99.0
811226	753 20.65	66N35.23	162W37.56	9.36	1.38	10	161	90.6	0.57	1.0	2.4
811227	1541 40.12	64N56.88	162W25.05	10.00*	0.97	4	144	106.5	0.24	2.3	66.0
811228	12 7 9.13	64N51.70	171W27.87	10.00*	2.77	10	262	252.1	0.87	47.4	41.8
811228	2140 40.21	64N48.31	171W27.16	33.41	2.50	8	262	253.2	0.82	99.0	99.0
811228	2145 36.20	64N43.09	162W31.92	22.04	0.98	7	131	89.0	0.26	1.1	1.4
811229	1242 8.72	65N36.33	163W 3.43	28.26	1.31	12	193	141.0	0.97	2.0	7.7
811231	621 12.97	63N29.91	161W41.79	17.32	1.36	10	190	72.0	0.54	1.3	1.1
811231	2135 15.87	65N38.04	163W20.59	14.06	2.13	10	135	136.6	0.52	1.9	2.5
820101	13 9 58.07	66N22.99	164W54.53	4.23*	1.87	4	241	132.8	2.35	12.3	3.4
820102	1359 35.17	67N32.49	164W11.36	10.87	2.01	6	279	202.0	0.32	25.9	24.8
820102	21 0 20.34	67N21.99	164W16.54	10.00*	1.63	5	279	183.0	0.34	30.3	32.0
820103	1617 1.38	67N27.74	164W13.74	5.66	1.91	5	285	190.8	0.19	11.1	10.6
820104	2353 14.11	67N22.69	160W 2.57	10.53	2.92	7	307	100.0	0.77	55.3	33.3
820105	218 5.53	65N20.68	165W41.58	10.00*		6	191	88.2	0.86	6.4	19.4
820107	633 19.30	65N 8.35	162W 2.28	10.00	1.53	4	245	118.8	0.48	11.7	7.1

Table 5.--(continued)

DATE	ORIGIN		LAT N	LONG W	DEPTH	MAG	NO	GAP	DMIN	RMS	ERH	ERZ
820107	2131	52.74	64N37.74	165W 0.44	5.71	1.26	8	142	95.6	0.55	2.0	9.1
820107	2132	25.27	67N25.70	164W 3.81	10.00*	2.44	7	284	193.6	0.75	15.2	15.4
820107	2239	43.90	65N 0.32	164W53.98	17.03	1.13	7	170	70.7	0.54	1.7	2.0
820109	1 5	31.21	64N21.28	163W56.67	11.22	1.87	6	199	72.6	0.28	3.0	2.0
820112	814	39.87	64N49.35	162W20.89	48.42	2.17	7	97	88.3	0.55	2.4	7.1
820112	2254	12.58	67N 5.23	163W53.72	25.86	2.11	6	255	166.7	0.37	23.9	99.0
820114	238	42.81	64N47.27	171W29.69	10.00*	3.43	10	262	275.2	1.38	12.9	12.5
820115	1026	34.01	64N46.37	165W12.05	0.28*	3.48	10	83	77.2	0.42	1.6	3.4
820116	634	3.71	64N54.64	171W27.42	10.00	3.48	9	261	267.1	0.58	99.0	99.0
820116	1235	8.00	64N46.46	171W24.28	4.12	3.08	10	260	272.2	1.01	16.3	15.0
820116	1633	43.54	67N 5.14	163W 5.81	18.30	2.68	7	272	132.5	0.26	5.2	3.5
820116	2041	33.72	64N46.89	171W23.33	10.00*	2.79	7	260	271.2	0.91	27.6	21.4
820116	2325	2.15	64N49.02	171W28.62	6.25	3.17	10	262	272.8	1.54	12.1	14.4
820117	545	13.24	64N53.10	162W11.21	10.00*		8	140	93.8	0.60	2.2	4.5
820117	8 5	22.56	64N45.67	171W20.72	10.00*	3.16	7	259	270.5	1.11	21.4	20.3
820119	13 3	9.72	65N 1.98	164W 4.86	0.22*	1.14	7	149	98.2	0.30	1.7	99.0
820120	1322	11.25	65N13.59	168W38.03	2.50*	3.15	9	300	171.2	0.47	2.7	4.0
820122	0 5	33.14	64N49.24	162W14.37	1.86	1.75	10	100	89.0	0.65	1.2	5.7
820122	1145	10.10	61N49.41	165W15.15	10.00*	2.73	6	336	100.0	0.09	99.0	99.0
820122	1159	41.22	65N48.11	165W44.43	7.52	2.04	5	104	78.0	0.24	2.3	4.4
820123	1458	39.17	65N58.04	164W 5.19	10.00*	1.23	8	118	98.2	0.69	2.4	2.7
820123	1814	17.37	65N 8.55	167W55.41	11.95	2.31	10	184	137.1	0.52	1.9	1.6
820125	1718	54.39	65N46.62	166W 2.27	6.80	2.56	12	141	89.9	0.65	2.3	2.5
820125	1934	46.61	65N 0.07	165W 4.71	12.81		12	108	71.4	0.77	1.8	1.7
820201	1719	5.84	67N55.70	161W40.13	4.05	3.34	8	314	300.0	0.13	92.2	33.2
820203	650	59.57	64N49.48	165W 5.04	10.00*	1.09	6	163	76.4	0.39	1.9	11.1
820204	19 7	12.53	67N41.04	164W22.91	10.00*	1.98	3	296	100.0	0.00	53.2	99.0
820205	7 0	0.83	66N 2.65	161W32.03	10.00	2.70	6	279	100.0	0.75	55.2	50.8
820205	7 4	38.62	67N50.36	164W38.28	9.24	3.00	4	302	225.0	0.02	99.0	99.0
820205	756	39.72	68N 0.88	164W40.86	2.90*	2.76	4	308	243.1	0.03	99.0	99.0
820205	812	9.56	66N 4.17	161W52.91	15.77*	2.09	5	269	198.7	0.79	41.2	40.9
820206	21 8	12.60	65N17.71	165W35.15	8.57	1.22	6	252	121.8	0.15	3.2	4.0
820206	2252	32.86	65N49.54	163W44.01	17.34		12	141	124.4	0.25	1.2	1.7
820207	1330	49.05	65N17.92	165W17.18	10.00*	0.76	5	166	82.3	0.64	2.6	4.5
820207	1916	32.36	65N49.13	163W45.81	5.42	1.48	9	123	125.6	0.57	2.4	5.4
820208	1751	53.85	67N 0.22	169W49.20	0.00	2.61	4	329	100.0	0.06	99.0	99.0
820209	1545	11.81	64N28.96	162W 0.67	5.66	2.26	13	108	95.8	0.70	1.3	1.9
820209	1717	0.75	65N50.35	163W45.02	17.47	1.66	12	140	123.3	0.31	1.1	1.6
820211	147	32.75	67N41.16	162W 7.66	10.00*	2.89	4	328	100.0	0.12	99.0	99.0
820211	12 2	58.69	65N47.66	163W49.07	10.00*	0.76	4	275	122.6	0.23	6.6	8.3
820211	1222	35.74	65N49.37	163W33.25	19.64	1.09	5	286	135.0	0.27	11.6	8.3
820211	1511	13.05	65N14.64	167W56.85	6.58	2.69	12	190	143.5	0.56	1.8	2.3
820211	23 5	46.18	65N50.18	163W40.59	21.27	1.55	9	163	122.2	0.46	1.7	2.4
820212	135	37.60	65N46.78	163W48.95	7.45	0.87	6	275	122.1	0.39	2.4	3.0
820212	2228	54.22	65N46.95	163W46.63	5.65	1.19	6	215	123.8	0.15	2.8	7.0
820213	2159	26.95	65N46.99	166W 6.65	1.17	1.81	4	154	92.0	0.03	99.0	99.0
820214	824	14.85	67N17.98	164W42.01	10.00*	2.00	4	273	168.1	0.16	99.0	99.0
820216	2310	18.74	64N48.33	165W10.76	7.15	1.07	7	137	75.0	0.40	1.1	3.4
820218	2038	0.10	64N56.10	158W24.34	58.40	2.78	6	295	320.0	0.36	99.0	99.0
820219	22 4	42.26	65N 1.97	165W39.59	0.63*	1.71	12	156	95.2	0.55	1.5	2.0
820220	1940	24.20	65N 4.97	165W 6.22	10.00*	0.83	5	221	107.4	1.36	7.7	41.8
820220	2013	49.38	64N50.26	164W47.36	11.58	1.23	8	158	85.7	0.46	1.2	2.1
820220	2125	7.34	65N 0.99	165W37.54	2.97*	0.88	6	182	105.0	0.57	6.0	46.5
820221	013	33.14	65N13.51	164W55.60	3.14	1.43	8	170	86.6	0.45	1.6	4.2
820221	524	11.65	66N46.54	165W46.02	15.69	3.04	5	253	163.7	0.09	51.3	99.0
820222	1223	30.04	65N15.26	164W50.55	10.00*	0.86	7	193	87.5	0.56	1.9	16.4
820223	218	24.20	66N48.52	165W31.05	16.07	1.60	5	249	128.8	0.07	5.6	3.2

Table 5.--(continued)

DATE	ORIGIN		LAT N	LONG W	DEPTH	MAG	NO	GAP	DMIN	RMS	ERH	ERZ
820223	856	6.84	63N42.22	167W23.93	10.00*	2.81	9	294	190.9	0.36	15.5	17.2
820224	144	7.12	66N48.91	165W34.59	16.72	2.05	6	250	131.3	0.15	4.2	1.8
820224	2217	32.22	66N 1.20	164W 2.97	18.29	0.81	8	144	112.5	0.37	1.9	1.5
820225	049	27.40	64N51.07	165W30.50	10.00*	1.39	6	160	79.2	0.33	2.2	9.4
820225	1 7	7.95	64N51.65	165W27.46	1.87*	1.10	6	153	77.4	0.19	2.1	51.8
820225	1535	50.22	65N11.75	165W21.71	10.00*	0.78	8	163	90.6	0.57	2.3	3.3
820225	23 7	8.78	64N51.30	165W28.36	1.85	1.93	13	155	77.8	0.58	1.3	1.9
820227	8 4	43.92	65N 1.63	167W49.64	10.38	1.68	8	283	127.6	0.51	2.2	1.7
820227	1036	6.05	67N26.28	162W38.05	10.00*	2.10	4	313	100.0	0.18	99.0	99.0
820228	826	29.81	64N51.43	167W31.68	9.46	1.40	5	280	133.0	0.09	4.1	3.0
820228	2118	38.71	64N52.65	162W26.01	24.45	1.33	7	220	100.2	0.79	3.2	99.0
820229	2 8	24.97	67N25.17	162W53.67	10.00*	2.05	4	305	100.0	0.17	99.0	99.0
820301	1946	35.78	65N22.19	163W58.71	17.60	1.03	10	194	106.3	0.44	1.4	2.7
820301	2147	48.93	64N51.76	162W11.68	9.20	1.01	4	263	93.1	0.01	99.0	99.0
820302	238	42.61	63N20.45	161W59.58	16.31	1.56	7	167	93.4	0.66	3.4	2.4
820302	523	59.11	65N45.89	166W14.46	3.21	0.97	6	181	97.9	0.25	2.8	3.7
820302	1356	58.57	64N41.20	160W58.44	7.78	1.57	7	190	95.3	0.37	2.0	3.2
820302	2013	39.08	64N51.46	162W15.89	1.98	1.94	11	136	89.3	0.46	2.1	2.7
820303	543	46.45	67N14.29	163W19.54	10.00	2.03	5	281	100.0	0.68	48.9	51.1
820303	1453	39.64	64N31.75	170W22.44	11.10	2.05	4	227	100.0	0.01	99.0	99.0
820305	13 1	59.51	64N52.86	162W16.43	0.87	1.28	7	224	96.7	0.46	2.0	4.8
820306	212	16.99	64N47.82	165W46.26	5.74*	1.42	6	197	88.8	0.21	4.8	12.1
820307	720	36.22	66N16.65	157W24.16	5.00*	3.78	10	169	238.6	0.25	4.8	10.6
820307	23 2	27.05	65N29.73	163W50.86	2.15	1.29	7	164	111.6	0.55	1.4	5.7
820308	028	48.31	65N 4.17	168W34.14	3.01	1.77	9	197	161.9	0.48	2.4	2.1
820310	22 9	40.05	64N51.31	165W28.99	1.23*	1.72	11	156	78.3	0.68	1.7	2.9
820310	2258	19.28	64N51.17	165W28.51	0.44*	1.58	11	155	77.8	0.53	1.8	3.0
820311	2134	30.21	64N51.50	165W29.44	2.10	1.39	8	157	78.7	0.18	1.3	4.0
820311	2345	36.90	65N10.11	164W46.36	5.00*	1.03	9	146	77.5	0.68	1.4	29.0
820312	533	16.80	64N50.51	165W30.94	5.00*	1.25	7	161	79.1	0.42	2.2	16.8
820312	1320	0.40	66N 4.41	162W29.17	10.00*	0.90	9	168	171.4	0.57	2.6	4.1
820313	057	44.12	65N13.52	167W57.50	9.64	1.56	5	285	142.9	0.01	4.6	3.9
820313	1217	34.88	64N50.02	165W34.16	0.87*	1.19	6	169	81.1	0.29	4.4	99.0
820313	22 7	16.34	64N47.23	165W50.46	0.16	1.01	4	206	127.9	0.28	16.3	99.0
820315	1233	32.98	64N51.03	165W30.28	5.72*	1.47	8	159	79.0	0.59	2.0	14.7
820315	2245	52.27	65N21.24	162W28.18	5.09	1.66	10	247	148.2	0.32	2.0	2.0
820316	1057	56.75	65N19.44	162W29.49	5.84	1.24	10	245	145.5	0.28	2.0	1.9
820316	1136	14.92	65N22.82	165W25.70	10.00*	0.57	6	210	90.9	1.31	5.7	26.2
820316	1528	36.43	65N19.83	162W26.26	20.93	2.29	17	160	143.9	0.62	1.4	2.9
820318	151	53.82	64N51.49	173W 4.43	10.00*	2.53	5	291	100.0	0.34	99.0	99.0
820319	1253	56.29	65N50.33	167W 7.77	0.00*	3.28	12	205	164.1	0.64	4.1	2.2
820321	2118	5.27	67N37.68	161W32.84	10.00*	2.26	4	338	100.0	0.06	99.0	99.0
820324	123	9.38	64N34.31	160W40.63	12.87	1.28	4	178	104.9	0.04	14.1	8.0
820325	1240	53.79	64N27.40	163W34.46	2.18	1.08	6	171	87.2	0.22	10.0	30.3
820325	1418	12.56	64N51.06	165W30.08	7.32	1.28	9	159	78.9	0.43	1.4	1.8
820325	1425	33.74	64N51.83	165W29.00	8.55	1.66	11	155	78.7	0.97	1.9	1.4
820330	1912	22.91	64N46.23	165W30.91	13.22	0.94	6	178	132.8	0.41	99.0	99.0
820331	1430	35.37	64N43.66	167W31.50	8.47	1.39	8	285	146.0	0.62	2.3	1.9
820331	1529	0.39	66N45.27	160W21.93	5.03	2.49	5	272	100.0	0.08	79.7	34.9
820331	20 2	11.41	65N30.41	164W49.70	5.00*	1.01	5	248	108.1	1.57	9.2	99.0
820401	1419	33.19	64N31.98	160W45.28	0.37*	1.89	10	175	100.4	0.26	1.5	2.4
820403	1745	15.99	68N18.49	173W33.73	23.01	3.47	5	352	100.0	0.31	99.0	99.0
820404	051	46.72	65N22.52	165W22.64	10.00	1.72	5	159	90.3	2.03	4.5	34.8
820404	1912	32.31	65N 9.28	164W31.74	10.00*	1.07	4	201	80.8	1.84	1.9	4.3
820405	2033	24.63	65N 9.80	165W20.17	10.00*	1.00	8	165	94.4	0.59	2.5	3.4
820405	22 7	40.15	64N28.56	164W26.55	14.95	2.30	12	180	80.8	0.50	2.5	1.3
820407	918	34.98	65N13.62	165W45.56	10.00*	0.84	6	141	80.7	0.36	3.3	5.1

Table 5.--(continued)

DATE	ORIGIN		LAT N	LONG W	DEPTH	MAG	NO	GAP	DMIN	RMS	ERH	ERZ
820407	1058	27.74	67N15.47	163W47.88	11.28	1.46	5	274	184.2	0.19	39.7	43.8
820408	753	39.11	65N10.30	165W39.73	3.11	2.02	9	134	87.9	0.37	2.4	2.7
820410	1552	49.66	67N19.34	164W30.09	40.36	1.72	6	275	174.1	0.21	3.3	99.0
820410	1845	46.49	64N19.41	163W33.48	3.72	1.79	13	187	91.4	0.70	1.9	2.3
820411	023	15.85	64N22.20	163W33.75	3.68	1.62	8	191	89.7	0.26	2.3	2.3
820411	722	2.89	64N38.77	163W54.13	22.59	1.22	10	122	70.9	0.38	2.0	0.8
820411	1611	51.74	67N33.01	164W 6.66	10.00*	3.00	8	291	204.4	0.82	13.1	15.2
820412	1045	34.62	65N 2.21	162W31.94	11.15	1.62	12	182	117.8	0.41	1.6	2.1
820413	256	6.66	63N28.88	164W14.24	10.00*	1.97	8	273	132.9	0.43	6.1	7.8
820414	11 5	38.43	64N25.69	165W26.03	11.53	1.64	12	242	105.9	0.74	2.7	1.4
820414	1434	12.59	65N45.74	166W 9.21	0.53*	2.17	13	164	95.0	0.49	1.5	2.4
820414	1523	58.48	65N47.39	166W13.30	6.62	1.29	6	177	95.5	0.16	1.9	3.2
820414	2216	9.01	65N52.27	162W16.71	11.16	2.19	5	260	180.8	1.32	23.7	24.3
820415	223	39.18	65N19.97	164W24.28	25.48	1.14	9	154	107.2	0.38	1.3	99.0
820415	1127	14.39	67N16.72	164W26.69	11.36	1.17	6	272	171.0	0.53	8.7	5.4
820416	2059	35.26	65N33.65	166W23.26	9.76	2.08	11	206	118.1	0.66	3.7	1.4
820417	2354	43.62	64N28.03	163W34.30	14.40	1.08	10	169	87.1	0.22	3.3	1.0
820418	21 7	37.44	66N35.12	162W39.37	10.00*	1.65	7	157	177.3	0.58	33.4	38.8
820418	2332	25.64	66N36.37	162W38.62	0.84	1.49	8	159	90.6	0.57	0.9	4.8
820419	947	57.53	64N 3.25	151W21.31	10.00*	2.82	7	330	605.4	0.10	99.0	99.0
820420	1041	11.75	65N53.77	162W11.14	0.09	1.65	5	254	114.7	0.24	20.1	16.8
820420	1051	6.78	65N12.01	164W29.72	24.94	1.29	16	76	82.1	0.49	0.8	19.6
820421	747	12.43	64N48.79	165W35.10	9.66	0.95	6	173	127.4	0.94	99.0	99.0
820422	742	19.80	63N12.48	151W42.85	10.00*	3.54	8	326	560.2	0.13	99.0	99.0
820422	852	1.10	65N30.83	163W39.16	23.50	0.86	8	208	120.8	0.19	1.8	3.1
820422	11 1	1.85	66N58.69	163W29.38	24.10	2.12	10	243	128.1	0.66	3.4	4.3
820422	2234	30.42	65N27.20	163W42.50	9.83	1.58	14	110	101.1	0.55	0.8	1.3
820423	942	21.54	67N22.72	162W52.61	17.47	1.67	6	304	100.0	0.37	7.8	2.1
820423	2036	48.31	64N56.18	162W19.06	1.27	1.82	11	148	103.1	0.64	0.9	2.2
820425	041	37.44	65N18.89	165W50.07	11.69	0.75	5	180	86.4	0.12	10.9	19.7
820425	052	42.35	65N18.46	165W54.29	5.98*	1.72	7	134	86.6	0.96	2.3	4.6
820425	053	52.01	65N13.64	166W50.75	0.16	1.93	6	244	101.6	0.28	3.8	5.1
820425	156	17.50	65N28.99	165W12.15	7.57*	1.55	5	228	95.9	0.36	10.4	99.0
820425	253	18.38	65N23.46	163W38.14	26.86	1.12	9	145	108.8	0.43	1.3	68.8
820426	12 1	28.14	64N49.22	165W21.49	9.65	0.84	8	143	71.3	0.51	1.3	1.9
820426	1256	12.66	64N48.96	163W48.74	0.63*	0.75	7	167	126.0	0.33	3.5	7.5
820426	13 5	26.02	64N24.90	161W45.84	14.07	1.61	6	152	172.8	0.26	22.3	30.4
820426	16 4	35.09	65N 8.81	167W13.03	0.01*	1.54	8	261	109.0	0.28	1.9	2.6
820427	046	11.07	67N38.13	165W53.15	10.00*	1.64	7	295	191.7	0.74	17.2	21.5
820427	131	39.34	64N59.98	166W33.30	0.16	0.99	7	238	103.9	0.36	2.9	5.8
820427	13 0	20.85	65N 3.02	164W47.45	16.56	0.98	8	140	73.0	0.70	2.6	2.4
820427	2022	24.45	64N51.60	165W15.33	6.85	1.34	11	130	68.9	0.64	1.2	1.5
820428	1447	22.24	64N51.63	163W52.01	30.86	1.06	6	159	144.7	0.16	6.6	12.1
820428	2216	48.65	65N27.75	168W40.76	10.00	1.88	9	218	185.3	0.75	4.0	6.6
820430	1955	2.29	64N54.77	161W18.30	11.59	2.11	12	145	95.2	0.82	2.3	3.1
820501	1223	10.35	65N30.22	158W20.13	9.10	2.90	4	299	100.0	0.03	99.0	99.0
820502	1729	23.34	65N47.44	166W 5.41	8.85	2.12	9	149	90.7	0.44	2.7	2.7
820503	1528	50.52	65N46.77	166W 3.80	0.16	1.88	6	145	90.6	0.24	1.5	8.2
820507	219	27.01	67N14.45	166W56.97	38.37*	2.23	8	290	195.1	0.86	26.2	55.2
820507	234	58.43	66N35.67	162W41.40	10.00*	2.00	4	153	176.4	0.22	99.0	99.0
820509	1418	13.39	66N27.89	163W39.60	10.00*	1.81	4	246	131.1	4.93	6.8	16.5
820509	2212	56.72	66N23.88	161W36.47	17.47	2.34	4	249	100.0	0.00	57.6	11.3
820509	23 2	9.43	67N38.88	161W36.88	17.60*	2.15	6	319	197.0	0.23	63.4	84.2
820510	9 3	36.39	66N 6.22	157W41.40	28.12	2.52	6	288	308.7	0.13	37.1	99.0
820511	246	50.39	63N44.73	166W58.18	0.15*	1.94	7	298	179.1	1.42	4.3	2.6
820511	329	13.89	66N11.76	162W 4.76	0.31*	0.88	7	208	110.4	0.36	1.5	4.8
820511	810	7.05	65N 2.25	164W11.02	10.64	0.85	7	129	100.1	0.20	4.1	7.4

Table 5.--(continued)

DATE	ORIGIN	LAT N	LONG W	DEPTH	MAG	NO	GAP	DMIN	RMS	ERH	ERZ
820514	1627 3.15	62N48.09	163W11.39	17.85	1.64	4	278	199.6	0.48	83.1	17.5
820523	1425 52.48	65N16.14	162W43.02	0.63*	1.45	8	296	148.1	0.48	2.1	2.3
820524	2244 16.86	64N 6.32	165W38.49	10.00	2.69	8	255	140.8	0.46	2.1	2.7
820529	1653 52.55	64N45.25	166W49.67	4.78	1.83	8	265	133.1	0.08	2.4	1.5
820530	924 30.41	65N21.64	162W38.67	0.08*	2.13	17	137	113.4	0.67	1.2	1.6
820530	941 7.77	65N21.08	162W29.48	0.16	1.39	12	146	113.7	0.73	1.1	1.9
820530	1726 39.54	64N31.43	164W14.59	10.93	1.07	6	202	128.5	0.06	5.3	2.6
820530	2258 13.60	67N18.76	164W29.37	10.00	1.64	7	274	173.4	0.56	3.0	4.8
820531	139 42.62	64N55.78	162W25.47	0.06*	1.75	11	143	104.9	0.56	0.9	2.9
820531	1335 21.10	65N33.95	165W 3.97	7.89*	1.02	6	241	112.5	1.84	5.5	45.4
820601	1724 44.37	65N27.70	164W11.94	20.39	1.71	14	93	101.4	0.72	0.9	2.6
820603	1147 23.30	65N 1.17	162W25.42	0.16	1.50	14	145	104.8	0.65	0.9	2.2
820603	1224 21.78	65N12.99	165W37.16	10.00*	1.46	11	122	83.8	0.75	1.5	2.3
820605	23 2 35.26	64N49.22	162W26.86	6.07	1.76	10	244	95.4	0.47	1.8	1.7
820607	2219 51.58	65N 7.50	164W56.53	10.15	1.49	6	291	134.3	0.42	3.9	2.9
820609	841 35.55	65N14.17	162W37.88	0.23*		7	271	139.5	0.47	5.4	2.9
820609	853 38.06	65N 6.75	162W45.94	8.25	1.65	7	262	130.8	0.17	2.4	1.7
820609	1055 7.86	64N14.49	163W37.77	10.00*		7	154	91.4	2.77	3.4	15.3
820609	1118 24.50	65N12.35	162W46.41	3.35		9	268	139.8	0.66	4.2	2.1
820609	1217 12.98	63N54.68	163W32.57	9.60		5	233	111.9	1.17	6.0	7.2
820609	1231 22.18	65N 9.84	162W49.20	3.95		9	265	137.0	0.69	2.7	2.0
820609	1233 31.92	65N 4.00	162W48.27	15.00		6	280	127.5	0.07	2.5	2.6
820611	142 25.36	65N 5.65	162W47.41	0.29*	2.16	6	285	136.0	0.23	3.0	14.2
820611	2225 17.01	65N 4.65	162W34.07	25.86		8	220	162.9	0.25	2.3	99.0
820612	111 20.69	65N 4.60	162W47.84	8.10	1.77	8	209	157.4	0.15	10.2	12.8
820615	937 17.41	65N33.45	167W 0.90	8.05	1.58	7	256	135.0	0.32	3.0	2.1
820615	1131 9.19	65N26.53	164W11.07	5.34	1.75	11	127	108.7	0.59	1.4	2.7
820615	1223 6.37	65N10.73	165W48.43	7.97		5	176	85.3	0.01	10.1	25.4
820615	1337 31.26	65N27.63	164W 9.87	20.62		12	128	108.5	0.71	1.0	2.6
820617	1851 32.72	65N16.64	164W44.80	10.00*		5	244	99.7	1.57	8.3	64.0
820618	355 0.32	65N 4.25	162W35.32	24.41		10	219	163.0	0.27	2.3	99.0
820618	5 1 15.78	63N28.68	154W 3.45	0.12	3.72	6	330	565.5	0.12	99.0	99.0
820618	2038 18.24	65N 4.40	162W46.27	12.40		11	178	158.4	0.37	5.3	8.6
820618	23 9 10.78	65N 6.67	162W47.87	6.48		10	177	154.1	0.55	5.7	9.5
820618	2356 43.55	65N 4.75	162W50.10	9.55		9	208	156.3	0.07	9.8	12.2
820619	1333 30.26	67N16.06	161W42.16	10.00*		4	344	100.0	0.12	99.0	99.0
820621	1559 24.46	67N18.06	161W57.42	10.00*		4	335	100.0	0.06	99.0	99.0
820623	1214 2.31	64N58.62	166W34.93	3.19	0.90	6	240	106.6	0.13	7.1	54.1
820624	254 1.54	65N44.77	162W20.79	5.97		8	233	179.1	0.41	2.4	3.6
820624	2138 0.67	65N11.10	164W56.21	0.74*		6	168	102.0	0.87	2.1	12.4

changed from 20 to 54 for the mid-1980 through mid-1982 period. Thus, by approximately doubling the number of stations of the network in the latter years, we achieved an improvement in the number of well-located events by more than a factor of 2.

RESULTS

A plot of the data presented in Table 5 is shown in Figure 5. In this figure, the earthquakes were not sorted by their magnitudes (M), which range from about 2.0 to 5.2. The strongest earthquake (M = 5.2) recorded by the local seismographic network is located inland and northwest of Kotzebue Sound as shown in Figure 5.

Spatial Distribution of Earthquakes

Despite considerable scatter in the distribution of earthquakes, a number of distinct clusters of epicenters are seen in Figure 5. For instance, the cluster labeled A lies close to the epicenter of the 1965 (M = 5.8) earthquake. Similarly, cluster B coincides with the 1950 (M = 6.5) earthquake. Though pre-1977 data do not show any concentration of earthquakes near the epicenter of the 1950 event (Fig. 2), from the current data it appears to be a tectonically quite active part of Seward Peninsula. Similarly, cluster C, though small in areal extent like A, lies close to the epicenter of the 1964 (M = 5.7) earthquake. Near cluster D, though no significant earthquake is found in the earthquake catalog (Fig. 2), it coincides with the position of the granitic Ear Mountains (≈ 700 m elevation) which are separated from the mountain systems on the south by low land (tundra).

To relate the earthquakes with the known tectonic features, all epicenters shown in Figure 5 were plotted on an overlay of mapped structural traces in the study area. The results are shown in Figure 6. Because dense clustering of epicenters in some areas partially obscures the structural

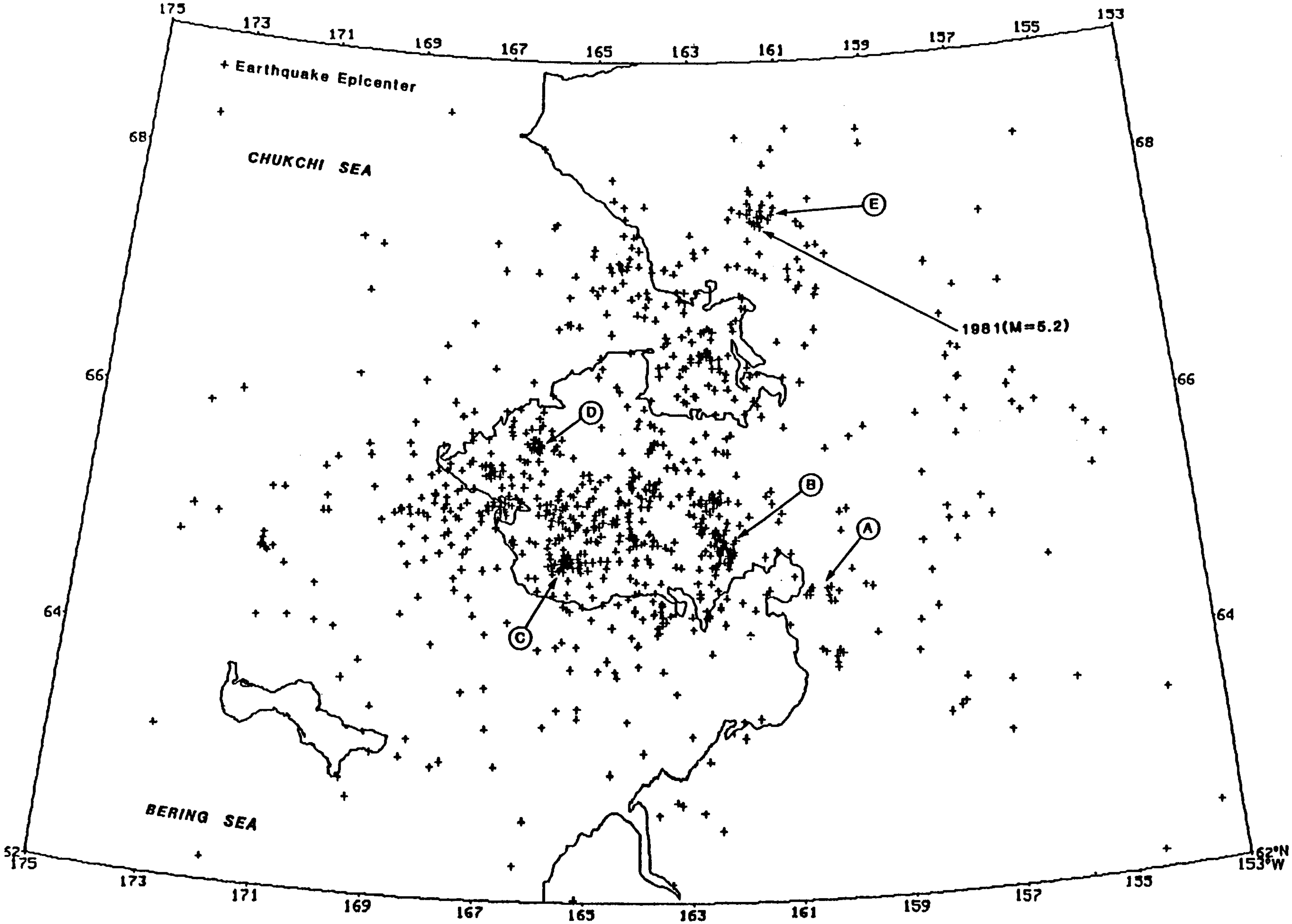

Figure 5.--Map indicating locations of epicenters of earthquakes located from 1977 through mid-1982 in western Alaska by the local seismographic network.

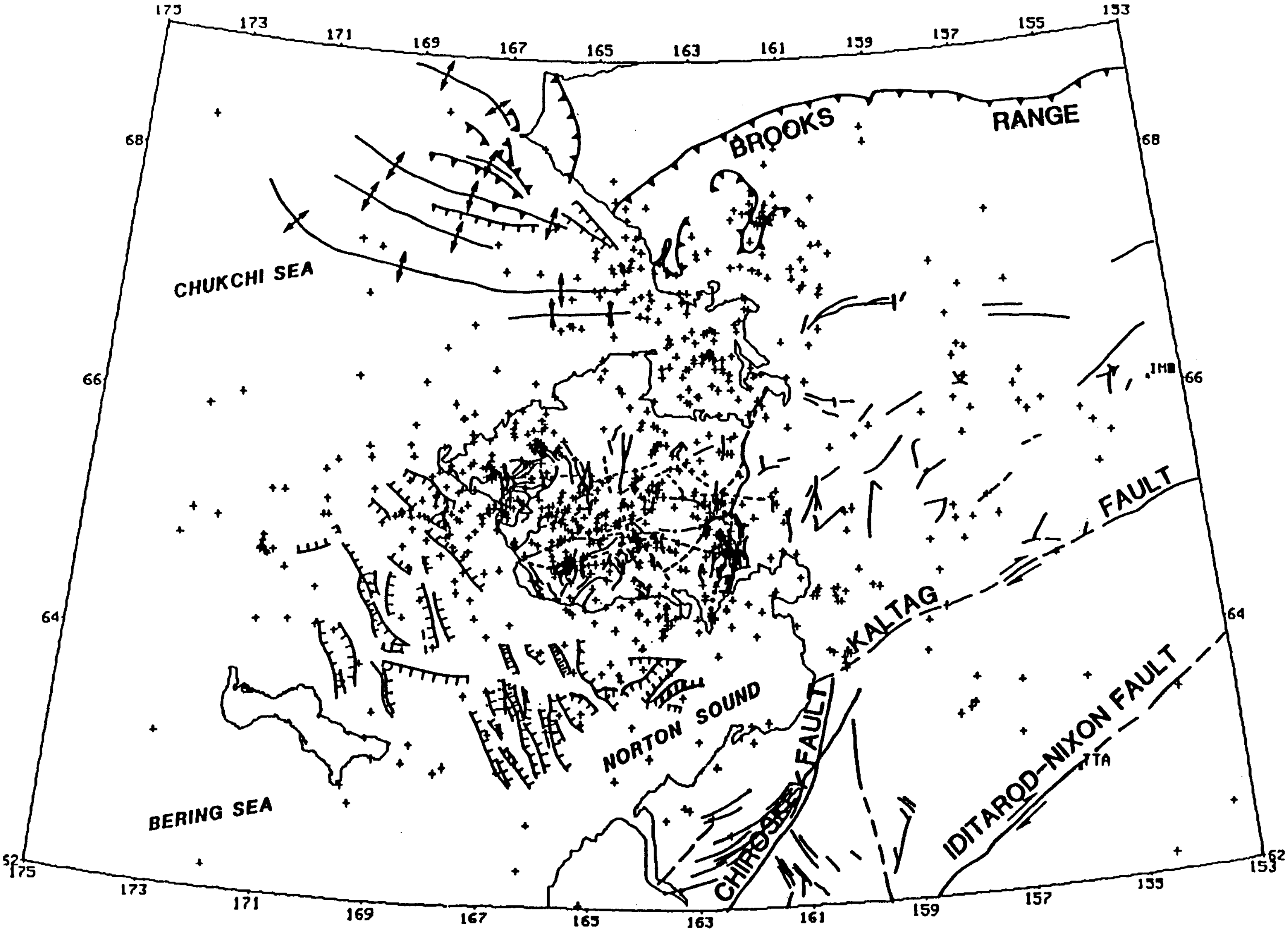

Figure 6.--Epicenters of earthquakes of Figure 5 overlayed on mapped structural traces in western Alaska.

features, these are shown separately in Figure 7. Major lineaments on Seward Peninsula as identified from satellite images are also included in Figure 7.

The mapped geologic features shown in Figure 7 were taken from Beikman (1980), Grantz et al. (1979), Eittreim et al. (1979), and Fisher et al. (1981). The traces of mapped features were digitized at close intervals, and converted to the same projection and scale as that used to plot the epicenters in the preparation of Figure 7.

From the results shown in Figure 6, it appears that the major faults in the southeast section, including a large part of the Kaltag fault, are at present tectonically inactive. This is also the case with the thrust belt of the Brooks Range and the offshore structures in the northwest section of the study area. However, these geologic features, as well as those mentioned above, lie outside the seismographic network used for the present study. Thus, an alternative interpretation would be that the network geometry and the operational gains of the stations used were inadequate in detecting earthquakes outside the network periphery. If this is true, we have to assume that the seismicity associated with the above geologic structures is relatively at a lower level.

In Kotzebue Sound, though no mapped geologic structure was found in the literature, it is associated with significant seismic activity. In Norton Sound, earthquakes scatter widely but they show a weak concentration along fault system F5 (Fig. 7). However, in Seward Peninsula, mountain axis M1 (Darby Mountains) and fault system F1 tend to follow epicentral cluster B (Fig. 5). Similar concentrations of epicenters are seen along faults F3 (Kigluaik) and F4 in the southcentral part.

In the central part of Seward Peninsula, though a number of faults and lineaments are present, the epicentral scatter is too high to associate the earthquakes there with any specific geologic feature. However, cluster D appears to lie at the northwest end of fault system F6. Cluster E coincides

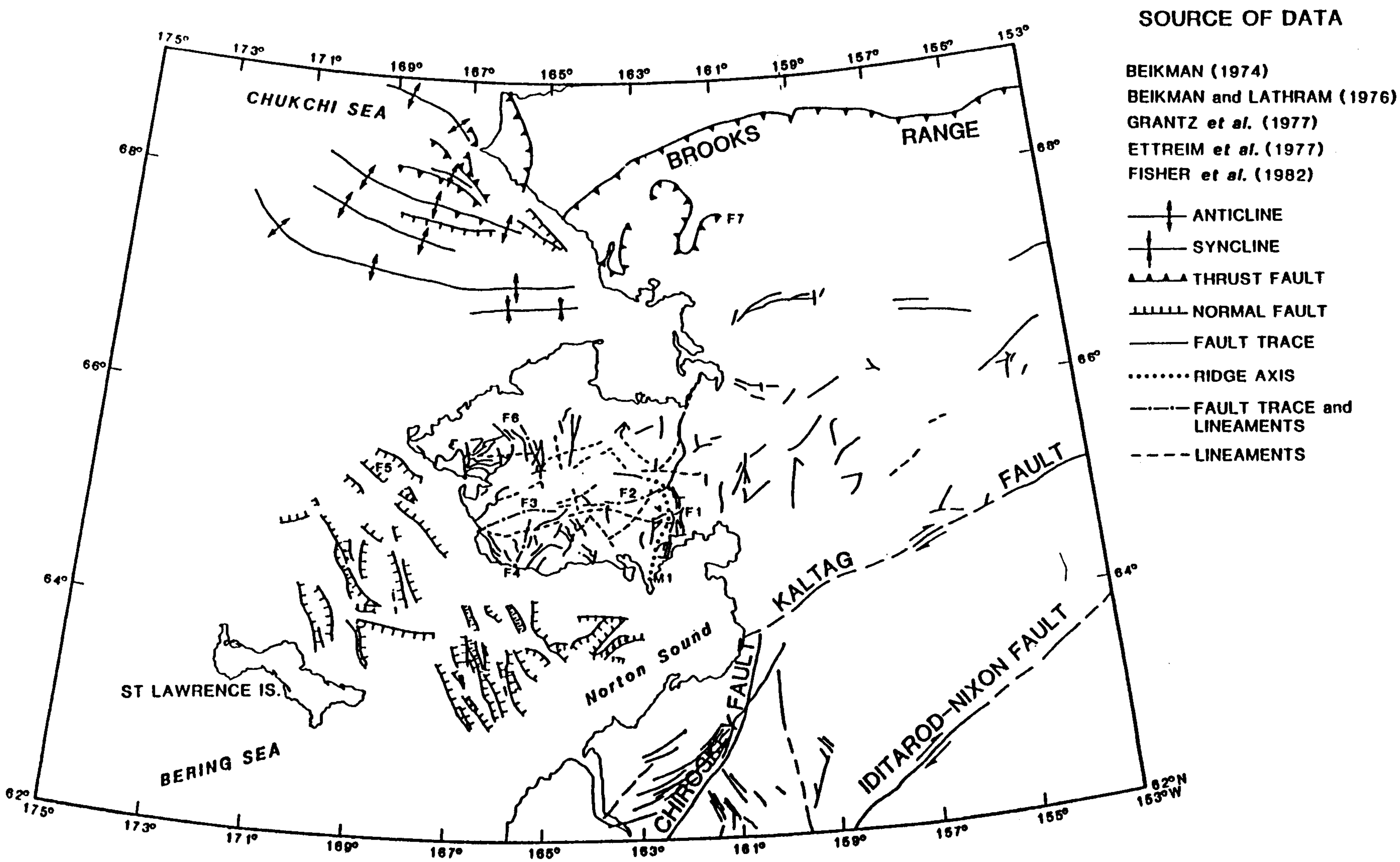

Figure 7.--Plots of mapped structural traces in Figure 6 shown separately.

with the complex thrust fault F7. It is discussed later that at present this cluster is a result of normal faulting.

Hudson and Plafker (1978) and Turner and Swanson (1981) identified the Kigluaik (F3) and Bendeleben (F2) faults as the major normal faults of Seward Peninsula with Holocene displacements. From the present study, it appears that the central part of F2 is not active.

For the sake of completeness, we digitized the Bouguer gravity map of western Alaska (Barnes and Hudson 1977). This is shown in Figure 8 in the same projection as used for the other data. The area in the northeast with prominent negative anomaly ($\Delta b > -40$ mgal) represents the Brooks Range. In general, the gravity variations closely follow the topography rather than any mapped tectonic features of significance or epicentral cluster.

Focal Mechanism

The regional stress pattern for an area can be deduced from focal mechanisms of earthquakes located in that area. It is best achieved by considering local as well as teleseismic data recorded in different azimuths for moderate sized to strong earthquakes. Due to the limited time permitted for the operation of the local network, the data gathered for western Alaska under this project do not meet, even marginally, the above requirements. We therefore used the data for an ensemble of earthquakes selected for different sections of the study area in most cases. This approach has inherent uncertainties in measuring the first-motions for small earthquakes.

To ascertain the correct recording polarity of the stations of the local network, a month-by-month polarity check was made for each station using the sense of the P-wave first-motions recorded for underground nuclear explosions in the United States and Russia. In the absence of explosion data, we used strong teleseismic earthquakes. The polarity check was made for the entire time period from 1977 through mid-1982.

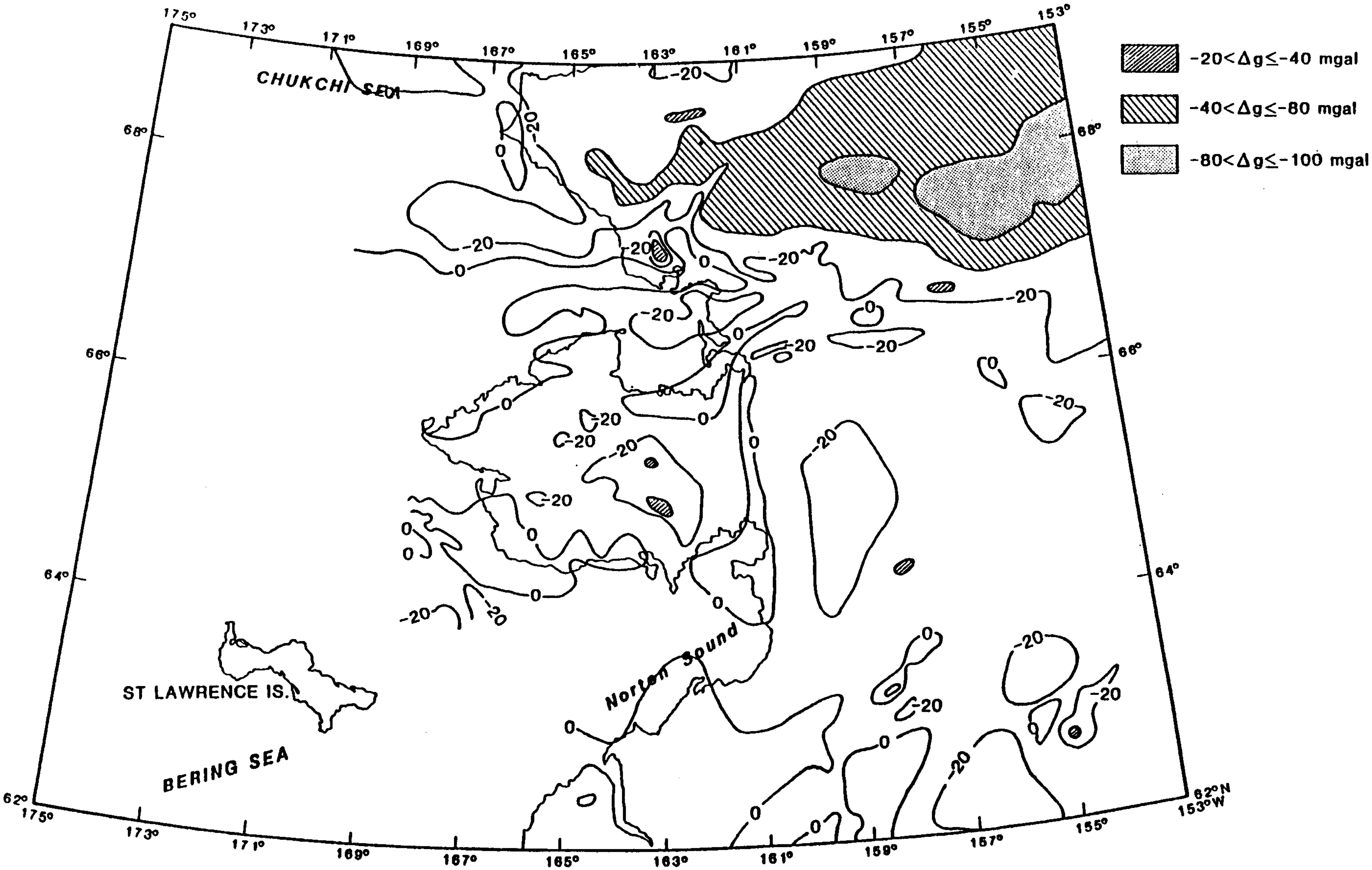

Figure 8.--Bouguer gravity distributions in western Alaska (Barnes and Hudson 1977).

After initial check of P-wave first-motions for the earthquakes listed in Table 5, we selected the earthquakes located in clusters B, C, D, and E (Fig. 5). For each cluster, we further made selection for events which were recorded by the largest number of stations. For the selected earthquakes, the angles of incidence and epicentral distances of the stations were taken from the output of the location computer program. The P-wave first-motions were then plotted on an equal area projection of lower focal sphere for each earthquake in a given cluster. For stations where the incident angle was found to be greater than $\pi/2$ radian (ray leaving the focus upward), the observed first-motion was plotted in the opposite azimuth. In doing so, we have assumed that the radiation pattern has a π radian symmetry with respect to the focus.

Clusters C and E, as mentioned before, consist of the earthquakes of 1964 ($M = 5.7$) and 1981 ($M = 5.2$), respectively. Therefore, in addition to local data, we used teleseismic data from the World Wide Standard Seismographic Network (WWSSN) and Standard Canadian Network (SCN) for these two events. In addition, we incorporated the known fault plane solutions for the other two earthquakes. The location details of these strong earthquakes are listed in Table 6. The focal mechanism solutions are discussed below.

Solution 1.--The focal mechanism solution is shown in Figure 9, which represents the Huslia earthquake. Ritsema (1962) compiled and studied the first-motion data which were also used by Wickens and Hodgson (1967) for their focal mechanism studies. The best fit nodal planes to the data as interpreted by the above authors are shown in Figure 9. Both solutions represent normal faulting for the Huslia earthquake.

Using the ENE-WSW orientation of the zone of ground breakage observed by Davis (1960), as mentioned earlier, Ritsema (1962) interpreted nodal plane a_2 as the fault plane. However, in addition to the alignment of the epicenters of earthquakes (Figs. 2 and 5) located in the Huslia area, the location of the

Table 6.--Location details for moderate sized to strong earthquakes used in focal mechanism studies.

Earthquake No.	Date Yr	Mo	Day	Origin Time Hr	Min	Sec	Latitude (N) (Degree)	Longitude (W) (Degree)	Depth (km)	M	Remarks
1	1958	04	07	15	30	40.0	66.03	156.59	Shallow depth	7.3	Location: USGS Fault Plane Soln. No. 1: Wickens and Hodgson (1967) Solu. No. 2: Ritsema (1962)
2	1965	04	16	23	22	18.6	64.7	160.1	5	5.9	Location: Rothé (1969); Fault Plane Soln.: Sykes and Sbar (1974)
4	1964	12	13	00	33	24.7	64.9	165.7	15	5.7	Location: Rothé (1969); Fault Plane Soln.: Geophys. Inst.
6	1981	07	12	01	27	56.3	67.7	161.2	37.2	5.2	Location and Fault Plane Soln.: Geophys. Inst.
7	1960	12	21	14	39	57.0	62.5	154.0		5.7	Location: USGS; First-Motion Data: ISC

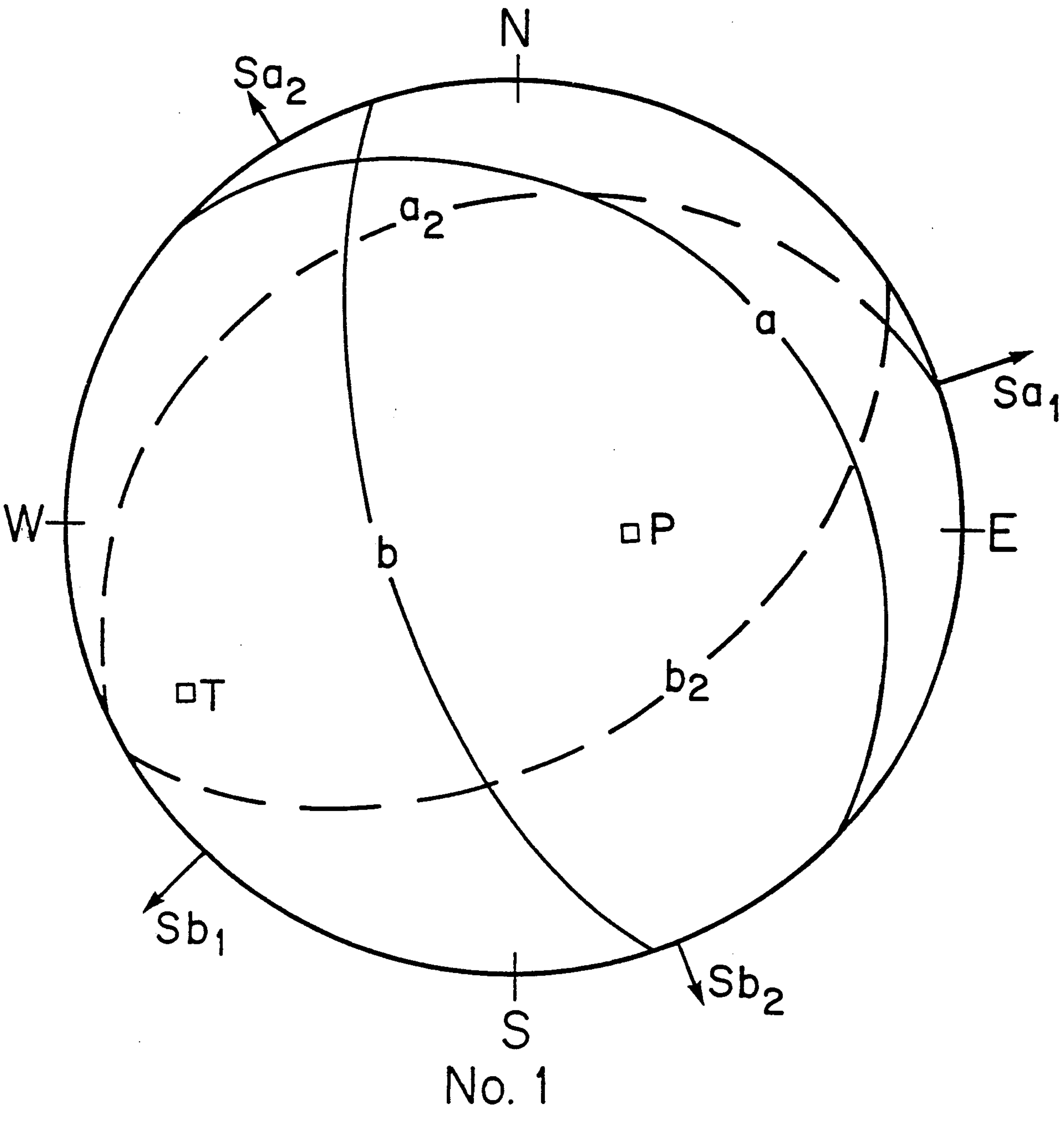

Figure 9.--Plot of nodal planes of the fault plane solutions given by Ritsema (1962) and Wickens and Hodgson (1967) for the Huslia earthquake. The solution of Ritsema is labeled a_2 and b_2 and those of the later authors, a and b.

epicenter of the strong aftershock (M = 6.7) with respect to that of the main shock, shows that a NNW-SSE oriented active fault through this area is equally possible. This orientation closely agrees with the strike of nodal plane b_1 of the fault plane solution of Wickens and Hodgson (1967). It may be noted here that Davis (1980) observed a northwesterly fault in the epicentral area of the Huslia earthquake as discussed before.

Solution 2.--This solution (Fig. 10) represents the earthquake of 1965 (M = 5.8). It is given by Sykes and Sbar (1974) which shows normal faulting. Though any of the two nodal planes (a and b) may represent the fault planes, from their similar strike direction we interpret a NW-SE oriented fault.

For the above earthquake, using the fault plane solution of Sykes and Sbar (1974), we analyzed the long-period Rayleigh wave data recorded by WWSSN and SCN stations to compute phase velocities by the single-station method. These values were used to study the focal mechanisms of the 1964 (M = 5.7) earthquake, the results of which are discussed later.

Solution 3.--This solution is a composite solution representing selected small earthquakes from cluster B (Fig. 11). Though two possible fits to the data (a_1, b_1 and a_2, b_2) are shown, other orientations of the nodal planes seem to be possible. However, dilational first-motions being the dominant ones occupying the central part of the figure, the earthquakes in cluster B are probably primarily associated with normal faults.

Solution 4.--The first-motion data for the 1964 (M = 5.7) earthquake were measured on the short and long-period seismograms of WWSSN and SCN stations (Fig. 12). As these data concentrate around the center of the figure and fail to constrain the fault plane solution well, they have been supplemented by the first-motion data for other small earthquakes selected from the population of cluster C. These data have been plotted with those of the 1964 event in the same figure (Fig. 12). It shows mostly compressional first-motions along the

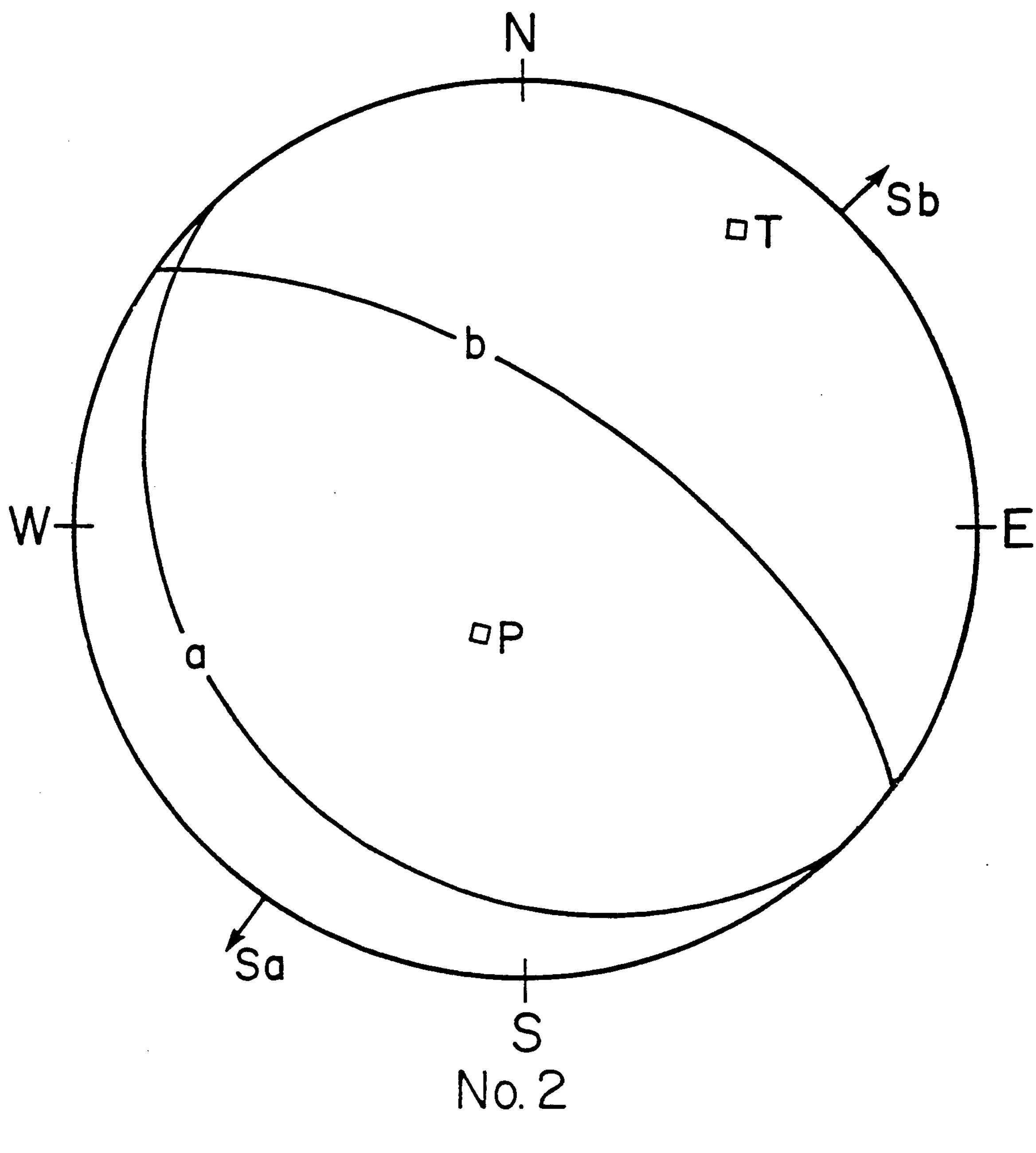

Figure 10.--Plot of nodal planes of the fault plane solutions given by Sykes and Sbar (1974) for the 1965 (M = 5.8) earthquake located near 64°N, 160°W.

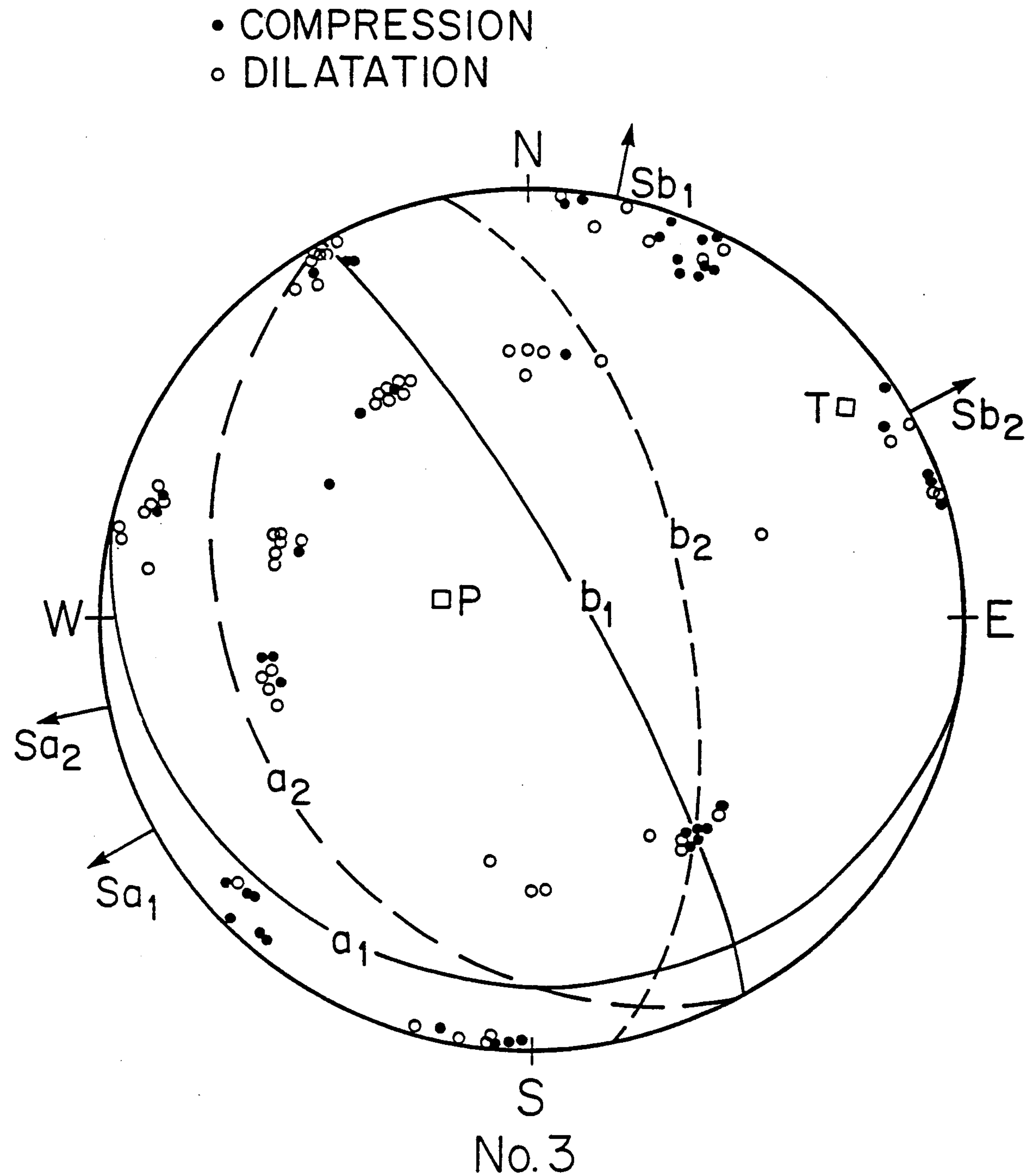

Figure 11.--Composite fault plane solution for earthquakes selected from the cluster labeled B in Figure 5. Two pairs of nodal planes (a_1, b_1 and a_2, b_2) show fit to the first-motion data.

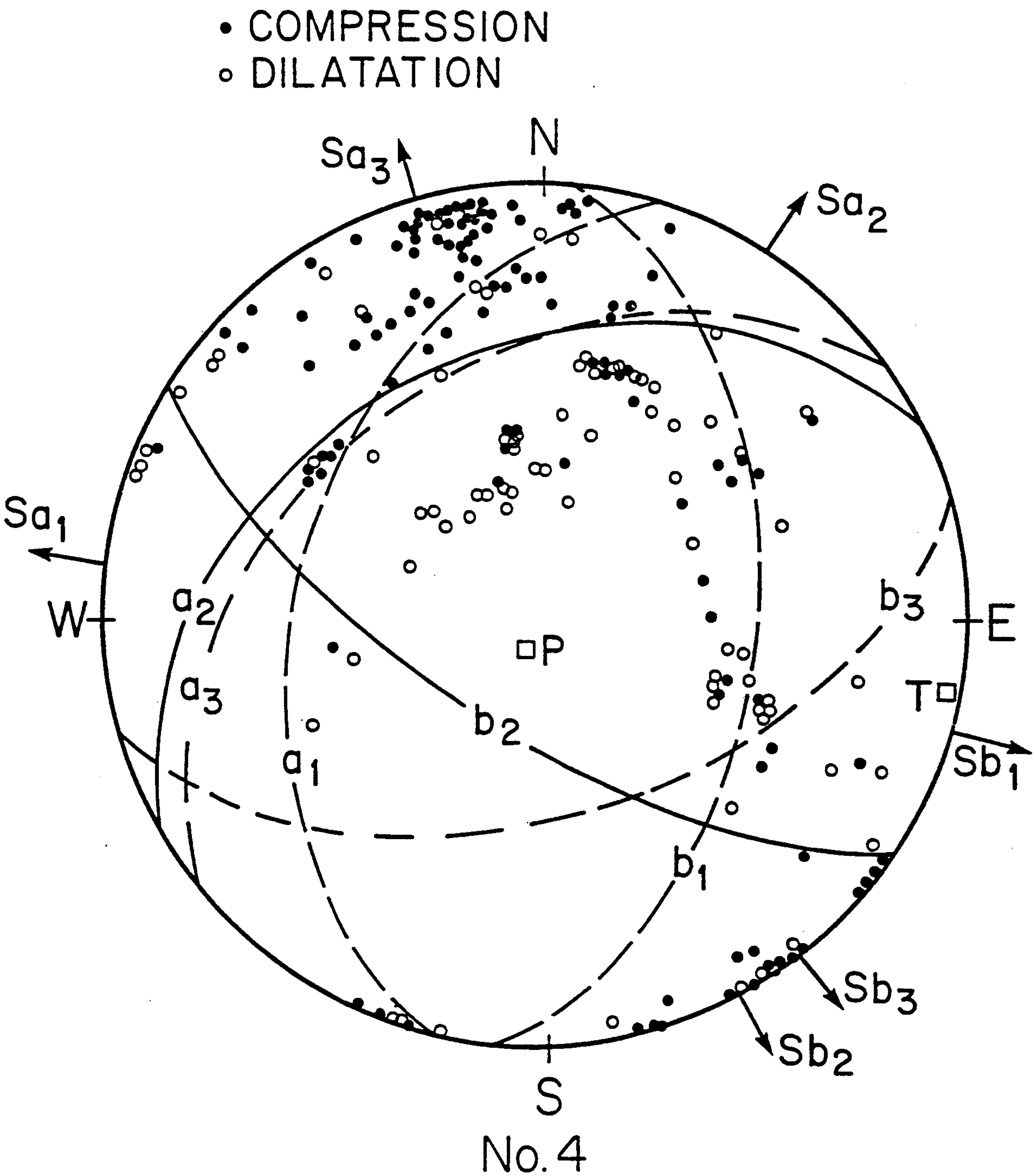

Figure 12.--Composite fault plane solution for earthquakes selected from the cluster labeled C in Figure 5. The first-motion data around the center were measured on the seismograms of WWSSN and CSN stations for the 1964 (M = 5.7) earthquake located in cluster C. Three pairs of nodal planes (a_1, b_1; a_2, b_2; a_3, b_3) show fit to the data. The solution represented by nodal planes a_1 and b_1 was obtained from moment tensors computations using long-period Rayleigh wave data.

circumference with dilatational motions around the center and thus represents a normal fault mechanism.

In order to study the fault plane mechanism more closely, the long-period Rayleigh wave seismograms of WWSSN and SCN stations acquired in 35 mm or 70 mm films were analyzed. The phase velocities computed for wave travel paths between western Alaska and the worldwide stations computed for solution 2 were utilized for Rayleigh wave studies. The focal mechanism solution represented by Rayleigh wave data was derived by computing the moment tensors (Patton 1978; Suarez 1982). The details of this study will be given elsewhere. The solution obtained is shown by nodal planes a_1 and b_1 (Fig. 12.)

It must be noted here that the focal mechanism solutions represented by moment tensors is completely independent of the first-motion data. However, this solution shows good fit to the first motion data except to some of the compressional data in the northern azimuths. These first-motion data were measured for small earthquakes in cluster C (Fig. 5).

Assigning equal weights to the local and teleseismic first-motion data, it is seen that two more solutions can be fitted to the data equally well. The nodal planes of these two solutions are shown, respectively, by nodal planes a_2, b_2 and a_3, b_3 in Figure 12. However, out of the three possible solutions, whichever solution is preferred, from the dominance of dilational first-motions around the center we interpret that the earthquakes in cluster C are associated with normal faulting mechanisms. This interpretation of the focal mechanism is in agreement to the nearly vertical maximum (P) and horizontal minimum (T) stress axes, represented by the solution derived from moment tensors.

<u>Solution 5.</u>--The plot of the first-motion data is shown in Figure 13. Three possible composite solutions are shown by three pairs of nodal planes (a_1, b_1; a_2, b_2; and a_3, b_3). Although none of the solutions are well

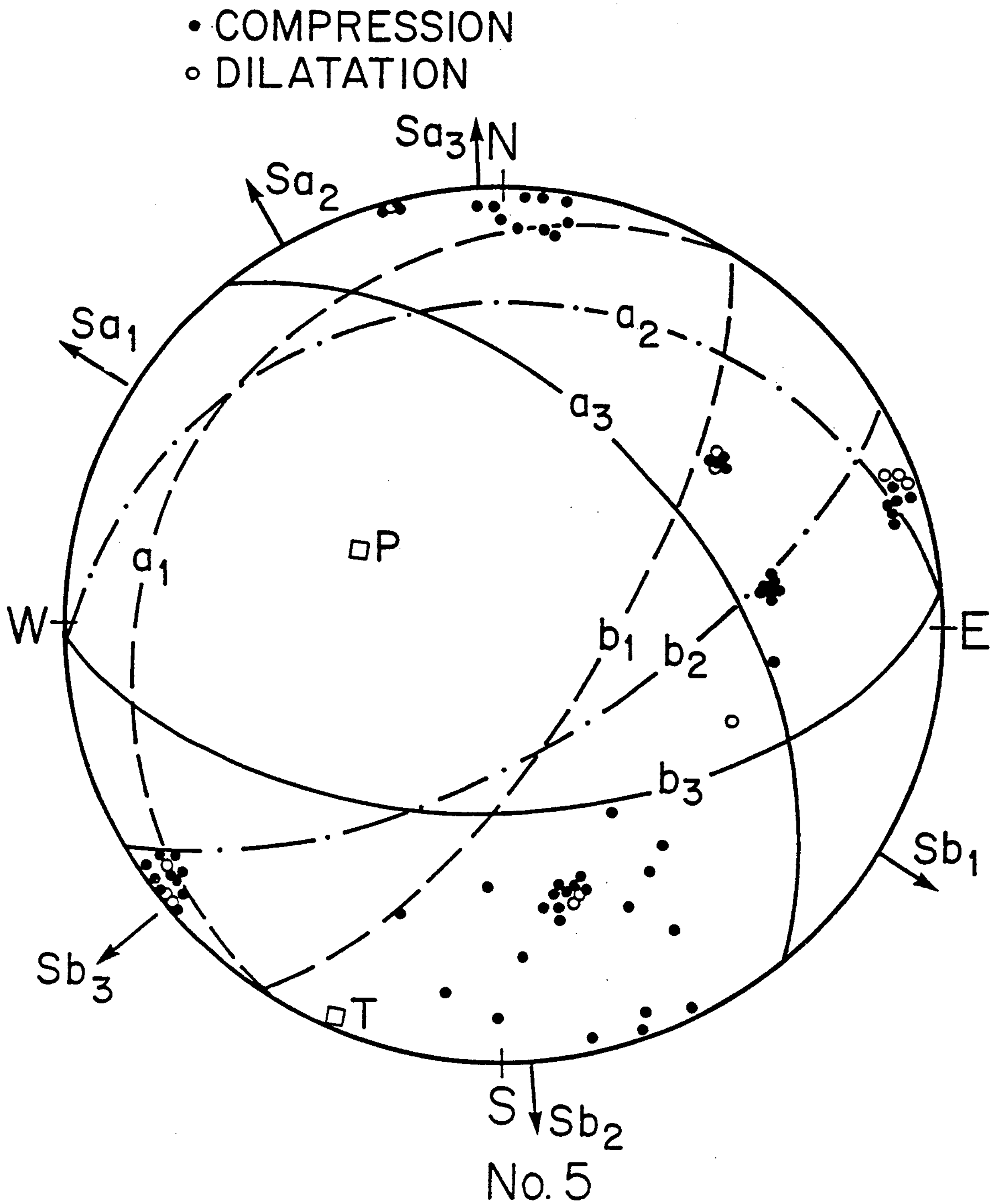

Figure 13.--Composite fault plane solution for earthquakes selected from the cluster labeled D in Figure 5. Three pairs of nodal planes (a_1, b_1; a_2, b_2; a_3, b_3) show fit to the data.

constrained by the data, all of them represent normal faulting as the principal type of focal mechanism for the earthquakes in cluster D.

Solution 6.-- The solution deduced from the first-motion data for selected earthquakes in cluster E (Fig. 5) is shown in Figure 14. The data around the center were measured on the seismograms of WWSSN and SCN stations for the 1981 (M = 5.2) earthquake while those around the circumference represent small earthquakes in cluster E. Most of the compressional first-motions around the center of Figure 14 were noted from the ISC bulletin; they differ from the dilatational motions measured on the seismograms recorded by the WWSSN and SCN stations. Assigning zero weight to the teleseismic data reported by the non-WWSSN and non-SCN stations, we interpret that the solution represents normal faulting.

In addition to the above solutions, the first-motion data for the 1960 (M = 5.75) earthquake located in the southeast corner in Figure 2 were noted from the ISC bulletin. The plot of these data, shown in Figure 15, appeared to be insufficient for drawing any nodal plane. However, from the concentration of compressional first-motions in the center, we infer that the above earthquake was associated with thrust faulting. The details of the solutions (Figs. 9-14) are given in Table 7.

DISCUSSION

Fisher et al. (1981) studied the geology of Norton Sound using multi-channel seismic, gravity, and magnetic data. The traces of the major faults mapped by them, as mentioned before, have been incorporated in the structural compilation of Figure 7. Due to the high scatter in the epicenters of earthquakes located on the south of Seward Peninsula (Fig. 5), we could not relate the earthquakes to any specific fault mapped by the above authors. Nevertheless, the dominance of normal faults as identified by them shows that tensional stress is the primary stress operative in Norton Sound.

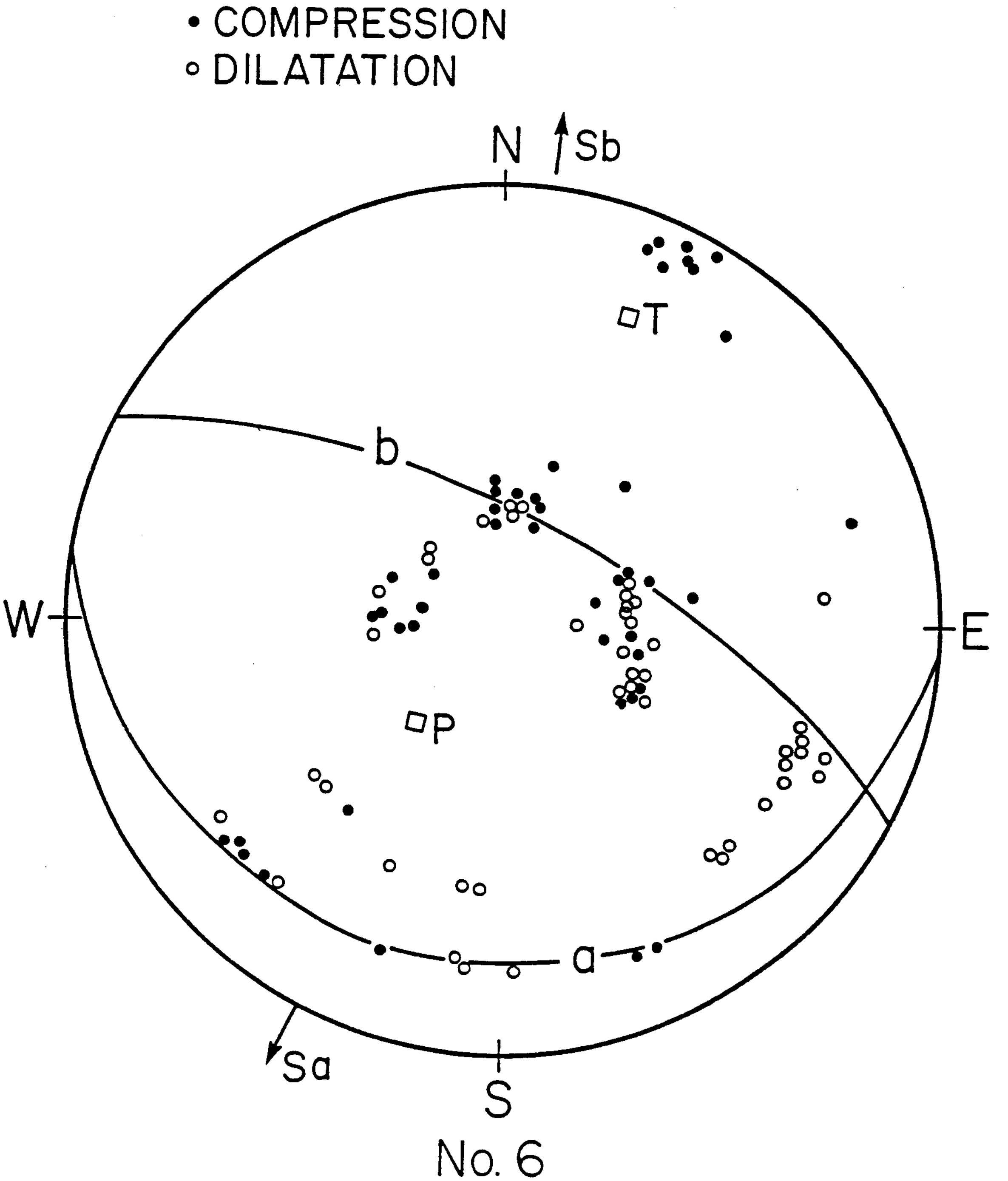

Figure 14.--Composite fault plane solution for earthquakes selected from the cluster labeled E in Figure 5. The data around the center were measured on the seismograms of WWSSN and CSN stations for the 1981 (M = 5.2) earthquake located in the cluster.

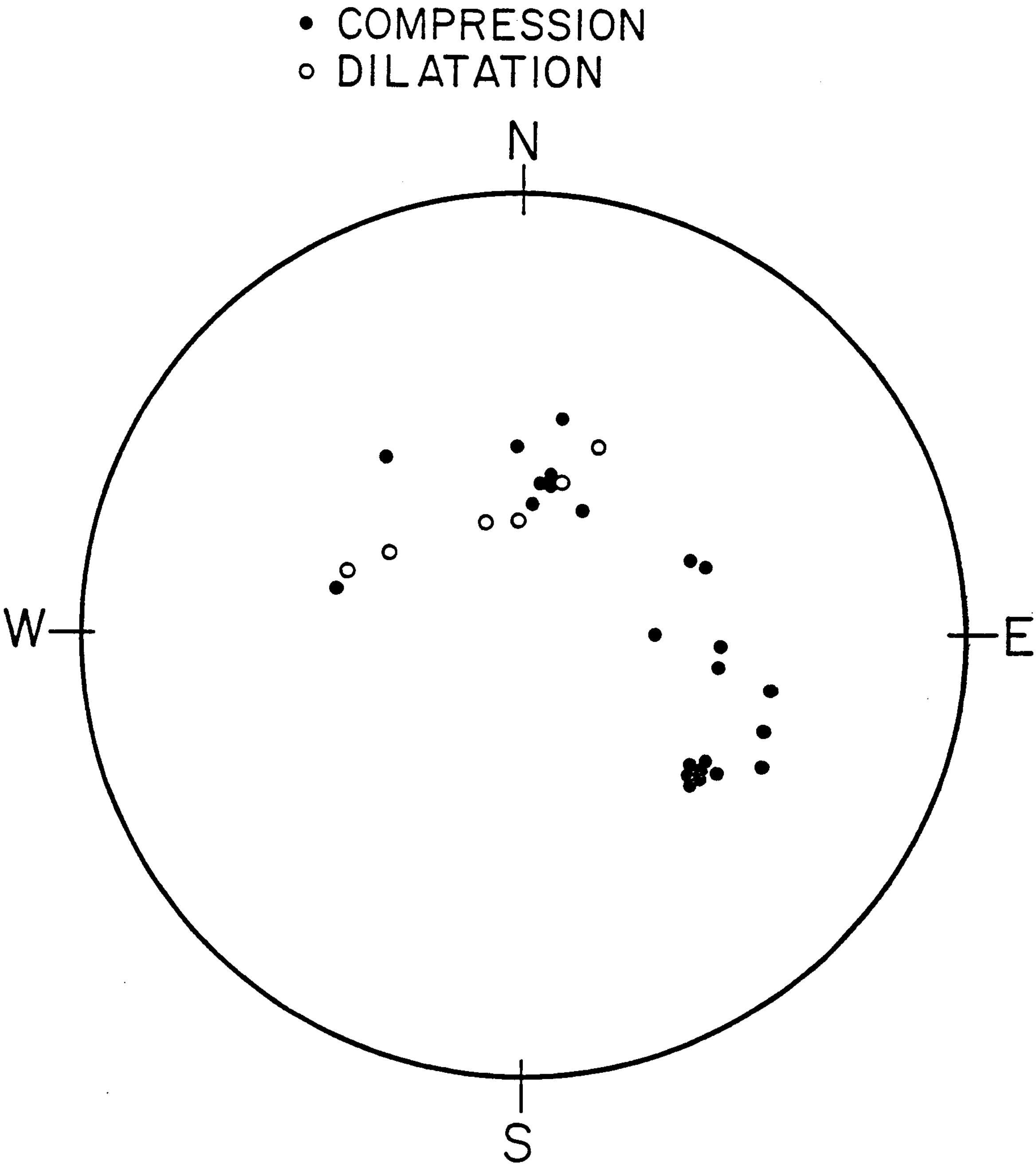

Figure 15.--Plot of first-motion data for the 1960 earthquake located near 62°N, 154°W. The first-motion data were assembled from the ISC bulletin.

Table 7.--Details of fault plane solutions. The preferred solutions are shown by asterisks.

Earthquake or Earthquake Cluster	PLANE a Trend	PLANE a Plunge	PLANE a Trend (pole) Degree	PLANE a Slip Angle	PLANE b Trend	PLANE b Plunge	PLANE b Trend (pole) Degree	PLANE b Slip Angle	P-AXIS Trend Degree	P-AXIS Plunge	B-AXIS Trend	B-AXIS Plunge	T-AXIS Trend	T-AXIS Plunge
No. 1														
*Soln. 1 (a_1, b_1)	312	27	72	64	161	66	222	76	92	68	334	10	243	16
Soln. 2 (a_2, b_2)	250	26	159	80	57	48	328	82	265	82	62	2	151	2
No. 2	136	24	215	78	304	66	45	85	202	69	304	2	40	21
No. 3														
*Soln. 1 (a_1, b_1)	102	16	11	30	330	80	240	11	283	72	148	11	56	10
Soln. 2 (a_2, b_2)	152	30	61	75	348	60	258	82	283	72	165	6	73	13
No. 4														
Soln. 1 (a_1, b_1)	195	44	106	85	8	46	278	75	204	86	11	3	101	1
*Soln. 2 (a_2, b_2)	240	36	152	37	124	69	34	58	78	54	290	28	192	16
Soln. 3 (a_3, b_3)	234	40	143	74	76	52	344	78	34	78	246	10	155	5
No. 5														
Soln. 1 (a_1, b_1)	212	20	121	87	32	70	303	90	302	65	213	1	122	30
Soln. 2 (a_2, b_2)	266	27	177	66	60	66	329	77	308	68	65	10	159	19
*Soln. 3 (a_3, b_3)	319	50	230	52	88	54	4	90	297	60	111	29	203	1
lo. 6	96	21	5	90	296	70	208	84	220	64	115	8	22	25

For the inland areas, a number of fault plane solutions could be obtained. With the exception of solutions 2 and 6, first-motion data for others show fit to more than a pair of nodal planes (Figs. 9, 11, 12, and 13). Despite this problem, the solutions show normal faulting as the principal component of focal mechanism. However, for the integration of the tectonic framework of western Alaska with the neighboring areas, it is necessary to select one of the pairs of nodal planes for each solution and next to identify one of the nodal planes which most likely represents the fault plane.

The nodal planes of solutions 2 (Sykes and Sbar 1974) and 6 are relatively better constrained by the first-motion data. For these two cases, if we select the nodal planes dipping southwest at low angles as the fault planes, the horizontal projection of their slip vectors orient, approximately, in the southwest direction. This is roughly the direction of the absolute velocity of motion ($\approx$ 2 cm/yr) of the overriding plate at the Aleutian trench as noted by Uyeda and Kanamori (1979). The identification of fault planes from the first-motion data on this basis seems logical as the back arc plate between the Aleutian trench and St. Lawrence Island in the north (Bering Sea) is largely aseismic and thus can be considered as rigid. The direction of motion of such a plate should be the same over its entire extent.

Following the above procedure, if the NNW-SSE steeply dipping nodal plane for the Huslia earthquake (solution 1) is chosen as the fault plane, the direction of the horizontal projection of the slip vector conforms to those obtained for solutions 2 and 6. Thus, using the same criterion, we have chosen the fault planes for solutions 3, 4, and 5. The preferred solutions are identified in Table 7.

In order to illustrate the interrelationships of the preferred solutions, their plots along with the epicenters of all earthquakes compiled for western Alaska are shown in Figure 16. The trends of the fault planes together with the horizontal projection of slip vectors are shown in Figure 17. Some

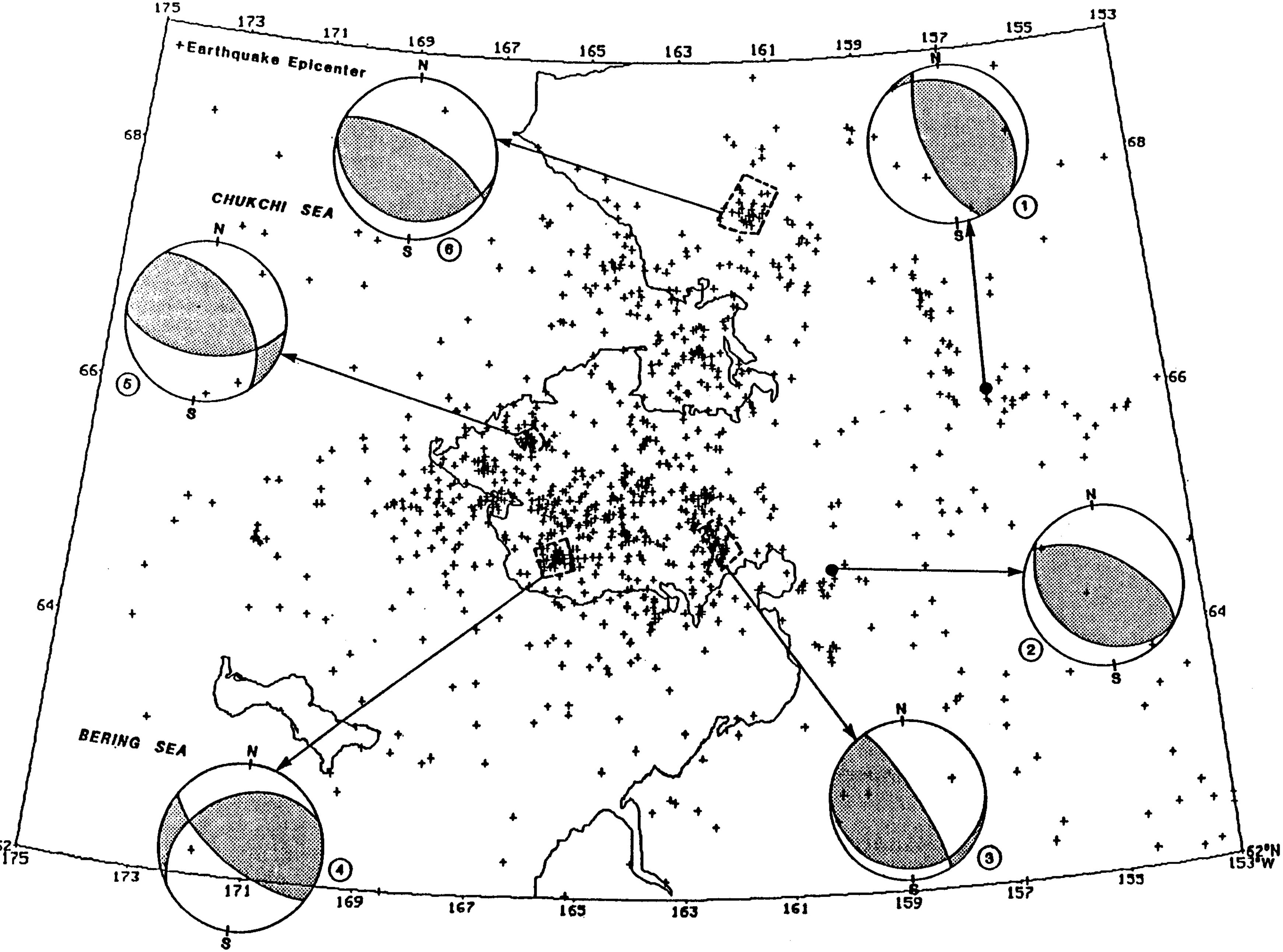

Figure 16.--Plot of preferred fault plane solutions shown in Figures 9-14. Also shown are the epicenters of all earthquakes located in western Alaska.

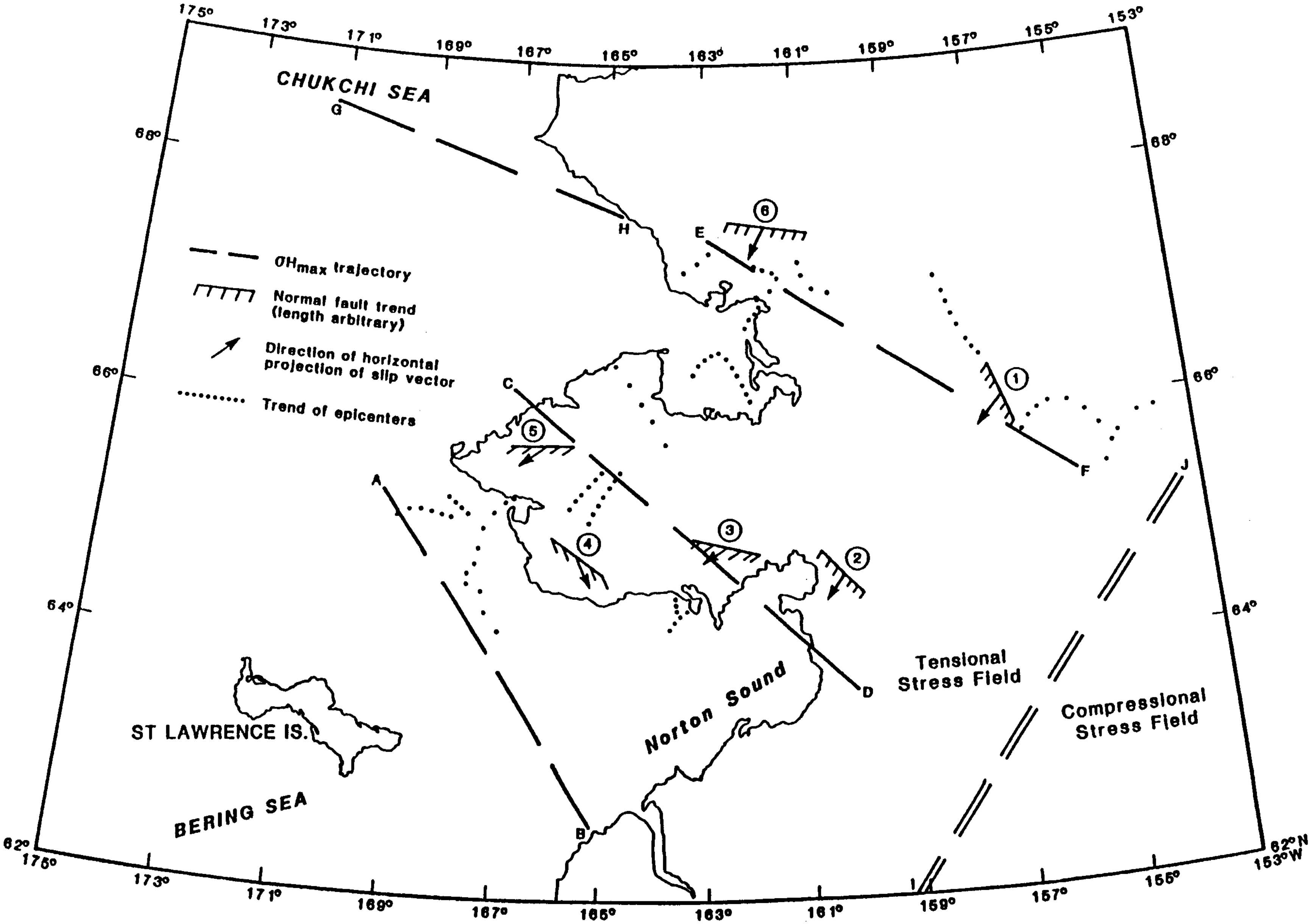

Figure 17.--Plot of the trends of faults and slip vectors for the solutions shown in Figure 16. The broken lines show the trends of the maximum horizontal stress trajectories deduced from fault plane solutions and trends of mapped normal faults and axes of anticlines. The double broken line marks, approximately, the transition from compressional to tensional stress regimes in western Alaska.

identifiable trends in epicenters are also shown in this figure. With the exception of solution 4, the slip vectors of others more or less align in the same direction.

In Figure 17, the average trends of the B-axis (σH_{max}) for solutions 1 and 6 and for solutions 2, 3, 4, and 5 are shown by broken lines EF and CD, respectively. The line AB represents the average of the strike directions of normal faults mapped in the center and west of Norton Sound by Fisher et al. (1981). Similarly, GH represents the average trend for the strikes of normal faults and the directions of the anticlinal axes mapped by Eittreim et al. (1979) in and around Hope basin in the Chukchi Sea. Thus, lines AB and GH may also be interpreted as the trends of σH_{mas}. Moreover, the double broken line IJ, though located approximately, separates areas under tensional stress from those under compressional stress. This separation is inferred from the first-motion data (Fig. 15) for the 1960 (M = 5.75) earthquake located near 62°N, 154°W.

Nakamura et al. (1980) studied the stress trajectories for the Alaska-Aleutian region from the characteristics of post-Miocene volcanoes and Quaternary faults. Their results are reproduced in Figure 18. A comparison of these results with those given in Figure 17 shows that the location of the zone of transition in western Alaska from compressional to tension stress regimes is in good agreement. As regards the stress trajectories (σH_{max}), the results of the present study show northwest orientation in and around Seward Peninsula and ENE in the Chukchi Sea in comparison to the westerly direction of Nakamura et al. (1980). But the two results (Figs. 17 and 18) have an important common feature, namely, the predominance of tensional stress for western Alaska. Note that the two studies are based on the analysis of different sets of data.

As discussed earlier, some uncertainties in fitting the first-motion data with the nodal planes remained. A somewhat larger error in the focal

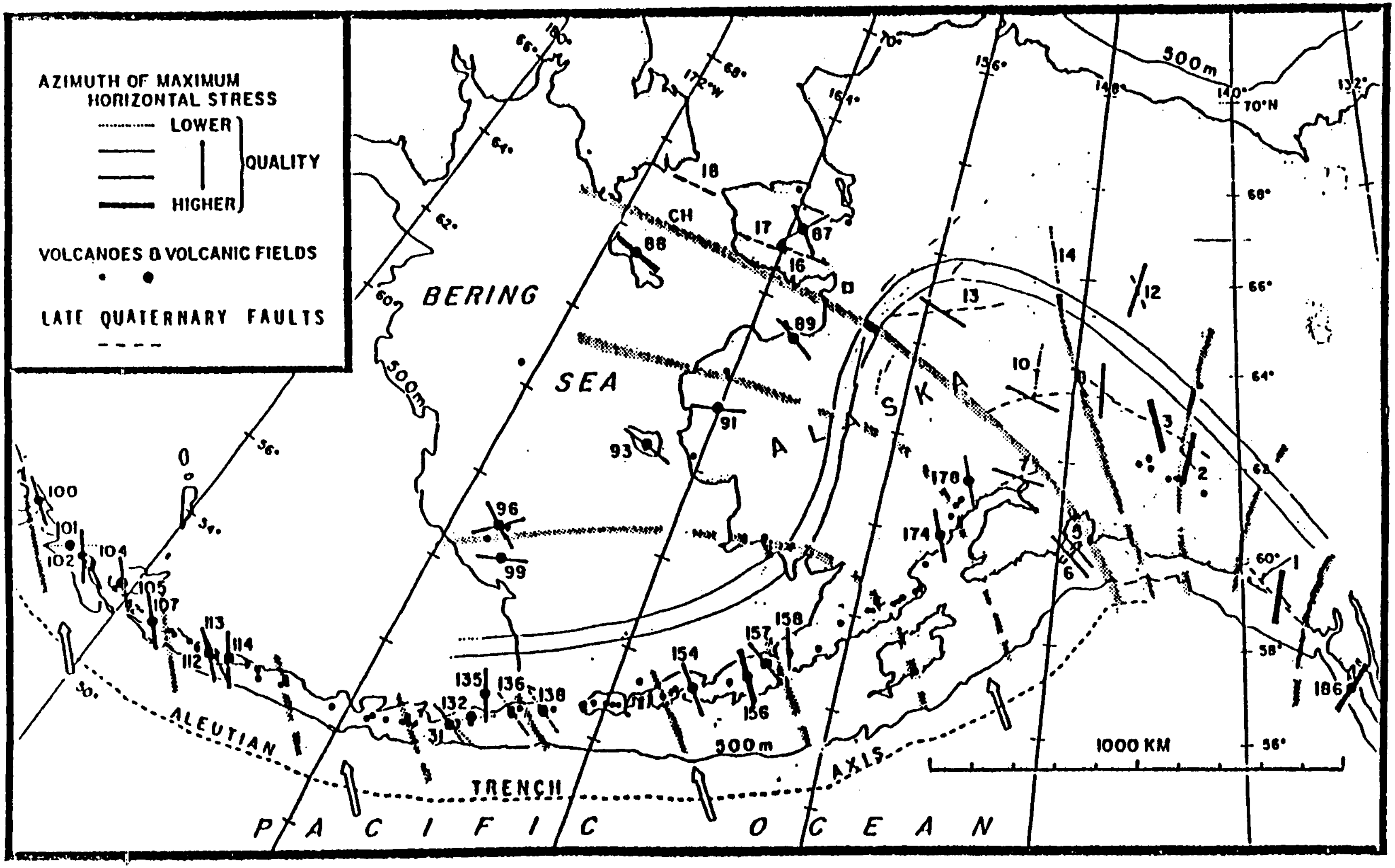

Figure 18.--A σH_{max} trajectory map of the Alaska-Aleutian region (Nakamura et al. 1980). Trajectories are shown by shaded lines. Sinuous double line locates approximate boundary between northern region, where σH_{max} represents σ_2, and trench side region, where σH_{max} represents σ_1; σH_{max} is indicated by a short bar. Faults and volcanoes are shown by dashed lines and solid circles. Open arrows indicate directions of plate convergence after Minster et al. (1974).

mechanism solutions might have been caused by the uncertainties in the velocity model adopted for the crust and upper mantle. Thus, the differences in the direction of stress trajectories noted above may not be considered as significant.

Uyeda and Kanamori (1979) and Nakamura and Uyeda (1980) classified the back arc region of the Aleutian trench as the Mariana type, i.e., actively opening without the formation of new crust. However, they did not identify any specific area in the back arc region as the zone of opening or spreading. On the other hand, in view of the predominance of normal faults, current southward motion along some of these faults as shown by focal mechanism solutions and trends in earthquakes, it seems logical to locate the above zone of spreading through Seward Peninsula on the west of 155°W.

CONCLUSION

Within the last 25 years, the strongest instrumentally recorded earthquake in western Alaska was a magnitude 7.3 earthquake located near Huslia in the Koyukuk River basin. Several earthquakes of magnitude greater than 5.0 have occurred on and around the Seward Peninsula, with four events located about 400 km offshore in the Chukchi Sea. Because the areas around the epicenters of these earthquakes are thinly populated, their seismic impact passed largely undocumented.

Crustal earthquakes commonly migrate with time along a fault or fault system. This means that if a given section of an active fault yields (resulting in an earthquake), then at a later time a somewhat distant point of the same fault may yield to accumulated stresses. This points to the necessity of determining the trend of the faults both in offshore and onshore areas for an appropriate geohazard assessment for an area.

Since the installation of a local seismographic network, several hundred earthquakes, predominantly of crustal origin and in the magnitude range of

$2.0 < M_L < 5.2$ have been located. Despite location uncertainties due to unknown crust-upper mantle velocity structure, the epicenters of these earthquakes are found in some cases to follow closely some traces of mapped faults. Some of these seismic trends traverse the epicentral areas of the past strong earthquakes.

Studies of fault plane solutions for a few selected earthquakes and clusters of small earthquakes located inland show that normal faulting is the principal mode of strain energy release in western Alaska. Supplementing the fault plane solutions with the trends of mapped offshore faults and anticlinal structures, trajectories of the maximum horizontal stress operative in western Alaska are obtained. The zone of transition from compressional to tensional stress fields appears to lie in the southeastern part of the study area. These features are more or less in agreement with those given by Nakamura et al. (1980).

From the above results, we postulate that the areas in and around Seward Peninsula represent the active break arc spreading zone of the Aleutian subduction processes. From the trends of earthquakes located in northeast Siberia (Wetmiller and Forsyth 1978), it appears that the zone of spreading extends from western Alaska through the southern part of the Chukchi Sea and farther northwest along the coast of Chukotsk Peninsula to about 170°E. Moreover, we propose that the earthquakes located in the above zone, including those in western Alaska, are the direct consequence of southward spreading of the back arc rigid lithospheric plate. The largely aseismic Bering Sea lying between the trench and the spreading zone constitutes the largest part of the rigid plate. Since no large scale volcanism is in evidence in the spreading zone, the formation of new crust along it may be ruled out.

REFERENCES CITED

Barnes, D. F., and T. Hudson. 1977. Bouguer gravity map of Seward Peninsula, Alaska. U.S. Geological Survey Open-File Rep. 77-796-C.

Beikman, H. 1980. Geologic map of Alaska. U.S. Geological Survey, Reston, VA.

Bhattacharya, B., and N. N. Biswas. 1979. Implications of North Pacific plate tectonics in central Alaska: focal mechanisms of earthquakes. Tectonophysics 53: 99-130.

Biswas, N. N., and B. Bhattacharya. 1974. Travel-time relations for the upper mantle P-wave phases from central Alaskan data. Bull. Seism. Soc. Am. 64: 1953-1965.

Biswas, N. N., and L. Gedney. 1979. Seismotectonic studies of northern and western Alaska. U.S. Dep. Commerce and U.S. Dep. Interior, OCSEAP, Environmental Assessment of the Alaskan Continental Shelf 10: 155-189.

Biswas, N. N., L. Gedney, and J. Agnew. 1980. Seismicity of western Alaska. Bull. Seism. Soc. Am. 70: 873-883.

Biswas, N. N., and Aki. 1983. Characteristics of coda waves: central and southcentral Alaska. In press.

Davis, T. N. 1960. A field report on the Alaskan earthquakes of April 7, 1958. Bull. Seism. Soc. Am. 50:489-490.

Eittreim, S., A. Grantz, and O. T. Whitney. 1979. Cenozoic sedimentation and tectonics of Hope Basin, southern Chukchi Sea. In The relationship of plate tectonics to Alaskan geology and resources. Proc. 6th Alaska Geological Society, B-1 to B-11.

Fisher, M. A., W. W. Patton, Jr., and M. L. Homes. 1981. Geology and petroleum potential of the Norton Basin, Alaska. U.S. Geological Survey Open-File Rep. 81-1316.

Grantz, A., S. Eittreim, and D. A. Dinter. 1979. Geology and tectonic development of the continental margin north of Alaska. Tectonophysics 59: 263-291.

Hudson, T. 1977. Geologic map of Seward Peninsula, Alaska. U.S. Geological Survey Open-File Rep. 77-796A.

Lahr, J. C. 1980. Hypoellipse/Multies: a computer program for determining local earthquake hypocentral parameters, magnitude and first motion pattern. U.S. Geological Survey Open-File Rep. 80-59.

Lee, W. H. K., and J. C. Lahr. 1975. A computer program for determining hypocenter, magnitude and first motion patterns of local earthquakes. U.S. Geological Survey Open-File Rep. 75-311.

Meyers, H. 1976. A historical summary of earthquake epicenters in and near Alaska. U.S. Dep. Commerce, NOAA, Tech. Memo. EDS NDSDG-1.

Nakamura, K., G. Plafker, K. H. Jacob, and J. D. Davies. 1980. A tectonic stress trajectory map of Alaska using information from volcanoes and faults. Bull. Earthquake Res. Inst. 55: 89-100.

Nakamura, K., and S. Uyeda. 1980. Stress gradient in arc-back arc regions and plate subduction. J. Geophys. Res. 85: 6419-6428.

Patton, H. 1978. Source and propagation effects of Rayleigh waves from central Asian earthquakes. Ph.D. thesis, M.I.T., Cambridge.

Richter, C. 1958. Elementary seismology. W. H. Freeman and Co., San Francisco.

Ritsema, A. R. 1962. P and S amplitudes of two earthquakes of the single force couple type. Bull. Seism. Soc. Am. 52: 723, 746.

Sykes, L. R., and M. L. Sbar. 1974. Focal mechanism solutions of intraplate earthquakes and stress in the lithosphere. In L. Kristjanssen, ed., Geodynamics of Iceland and the North Atlantic area. Proc. NATO Advanced Study Inst. Reykjavik, Iceland. D. Reidel Publishing Co., U.S.A.

Suarez, G. 1982. Seismicity, tectonics, and surface wave propagation in the central Andes. Ph.D. thesis, M.I.T., Cambridge.

Turner, D. L., and S. Swanson. 1981. Continental rifting--a new tectonic model for the central Seward Peninsula, Alaska. Univ. Alaska, Fairbanks, Geophys. Inst. Rep. UAGR-284.

Uyeda, S., and H. Kanamori. 1979. Back-arc opening and the mode of subduction. J. Geophys. Res. 84: 1049-1061.

Wetmiller, R. J., and D. A. Forsyth. 1978. Seismicity of the Arctic, 1908-1975. In J. F. Sweeney, ed., Arctic Geophysical Review, Earth Physics Branch 45(4). Ottawa, Canada.

Wickens, A. J., and J. H. Hodgson. 1967. Computer re-evaluation of earthquake mechanism solutions. Pub. Dominion Obs. 33(1). Ottawa, Canada.

BOTTOM AND NEAR-BOTTOM SEDIMENT DYNAMICS IN NORTON SOUND, ALASKA

by

David A. Cacchione and David E. Drake

Pacific–Arctic Branch of Marine Geology
U.S. Geological Survey
345 Middlefield Road
Menlo Park, California 94025

Final Report
Outer Continental Shelf Environmental Assessment Program
Research Unit 430

April 1979

TABLE OF CONTENTS

I. SUMMARY

A. Overview

An investigation of sediment dynamics in Norton Sound and other sections of the northern Bering Sea was conducted to define the principal pathways and mechanisms of bottom and suspended materials transport. A major topic of this research is the complicated interrelationships of sediment movement and hydrodynamic stresses that occur in the marine environment. Temporal contrasts like those caused by seasonal cycles and quiescent versus storm conditions are of particular interest. This research is pertinent to two major impact areas of petroleum development in the marine environment: (1) transport of materials including pollutants; and (2) hazardous sea floor conditions caused by wave and current erosion.

B. Results

Distributions of suspended matter in July 1977 and February–March 1978 were essentially the same as those found in September–October 1976. The pattern is dominated by a broad tongue of turbid water trending northwest across the mouth of Norton Sound from the Yukon Delta. Mixed Yukon and Alaska Coastal Water carrying large amounts of suspended silt extends through the entire water column along this transport pathway.

Mud deposits in the eastern part of the area are supplied by weak or intermittent surface currents which transport Yukon River detritus eastward along the southern coast of Norton Sound. The presence of remnant winter water (low temperature, high salinity) in inner Norton Sound probably is important in the accumulation of a blanket of mud in this area. Pollutants entering this "cul-de-sac" may be retained for relatively long periods owing to the limited water exchange with the outer part of Norton Sound.

The GEOPROBE results demonstrate that storms play a major part in the transport of sediment in Norton Sound. Suspended sediment transport during one 1977 storm exceeded transport during the 2 months of fair weather preceding the storm. Thus, sediments (and potentially pollutants) which have been temporarily deposited on the sea floor can suddenly be remobilized during a short storm.

During relatively quiescent conditions characterized by insignificant surface wave activity, the currents generated by the mixed astronomical tides dominate the bottom stress field. These currents are able to maintain fine silt and clay in suspension, but bedload transport probably occurs only during spring tide cycles or in shallow (<5 m) areas where waves become significant. On balance, the months of June, July, and August are characterized by deposition of very fine sand and silt delivered during the peak discharge of the Yukon River. Late summer storms disrupt the system and cause substantial erosion of the surficial sediment on the Yukon prodelta. Bottom stress measurements show that these high-energy events are responsible for the spread of sand north across the prodelta and we estimate that one 2–3-day storm transports a volume of sediment equal to 4 months of quiescent hydrodynamic conditions.

Although our data suggest that variations in sea floor elevation caused by erosion–deposition "events" are typically less than 2 cm on the Yukon prodelta, such short-term variations (storm-related) should be substantially greater in the shallow areas surrounding the delta. Depressions in the delta front have been discovered by Nelson (1978) and it is possible that these features are produced and maintained by storm currents.

Nelson and Creager (1977) have discussed the relatively low growth rate of the modern Yukon prodelta. In addition to the erosive action of storms, major causes for the low accumulation rates are the absence of large low-energy basins near the Yukon Delta and the lack of any measurable subsidence of the modern delta. Also, the low clay content of the Yukon sediment limits the development of cohesive mud deposits; exceptions to this are the fine-grained deposits in the eastern part of Norton Sound and in Norton Bay.

Conversely, a substantial amount of Yukon silt and sand has been incorporated in the prodelta and the eastern part of Norton Sound during the past several thousand years. Accumulation of this material is directly related to the absence of significant surface wave-generated currents during most of the year. Except for the brief periods of intense wave action during storms, the transport of sediment is controlled by the tides and the mean flow. The latter are capable of sustaining a flux of fine silt and clay but leave the coarser particles behind on the Yukon prodelta, delta front, and sub-ice platform.

II. INTRODUCTION

A. General Nature and Scope

This research unit is designed to investigate the transport of sediments and other materials in the northern Bering Sea, with special attention on Norton Sound. This work is part of a larger program of continental margin sediment dynamics in which the principal investigators have been involved since July, 1975. The overall program is directed at increasing our understanding of the pathways, rates, and mechanics of sediment movement in a variety of geological settings. A major topic of this research is the complicated interrelationships of sediment movement and hydrodynamics stresses that occur in the marine environment. Temporal contrasts like those caused by seasonal cycles and quiescent versus storm conditions are of particular interest.

The northern Bering Sea is characterized by several unique and extreme environmental conditions: (1) sea ice covers the sea surface over 50 percent of the year, (2) late summer to early fall storms that travel along the polar front often bring severe local weather to the area, and (3) the Yukon River effluent, second largest of North American rivers, enters the system at the southwestern side of Norton Sound (Fig. 1).

A comprehensive picture of the geological and geophysical setting for this region has been developed by Nelson (1977, 1978) from several years of data collected under OCSEAP support. His work has provided the in-depth background that is a necessary prerequisite for the more topically focused research in this project. For example, Nelson

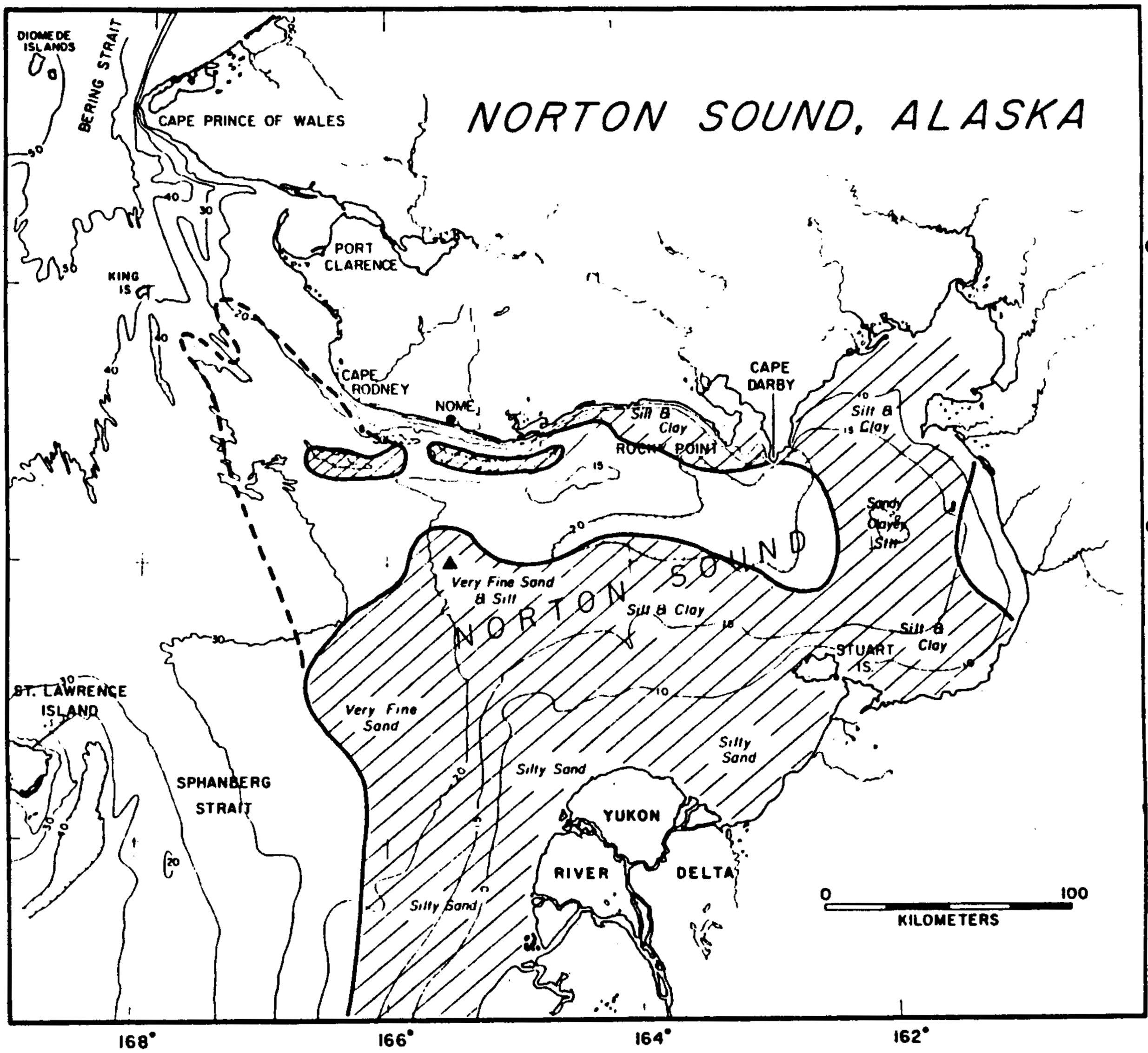

Figure 1.—Bathymetry of Norton Sound and adjacent area in meters. The cross-hatched area defines the area of modern deposition of Yukon River sediment. The triangle 60 km south of Nome is the GEOPROBE site.

and Creager (1977) and others have shown that the enormous flux of sediment introduced at the mouth of Norton Sound annually by the Yukon River has not yielded sediment accumulations commensurate with the rate of supply. The causes and modes of transport for this apparent exit of Yukon River materials from the immediate region of Norton Sound are topics included in this investigation.

The scope of research in this project also includes topics such as (1) patterns and rates of transport of sediments, nutrients, and pollutants as suspended load in the northern Bering Sea; (2) patterns and rates of transport in the sedimentary bedforms located west of the Seward Peninsula; and (3) wintertime suspended sediment concentrations in western Norton Sound.

B. Specific Objectives

The principal objective of this work is to develop an understanding of the relationships between suspended and bottom sediment transport in Norton Sound and the hydrodynamic regime that causes this transport. Specific objectives are:

1. Completion of maps showing the spatial distributions of suspended particulate matter during the summer and winter seasons and interpretation of these data in terms of sources, transport pathways and hydrography.
2. Production of site-specific temporal histories of sediment transport parameters and hydrodynamic values; these data would include analysis of bottom currents, bottom stress, roughness coefficients, flux vectors and the comparison of quiescent versus storm conditions.
3. Development of quantitative relationships between bottom velocity shear and sediment entrainment for specific sites in Norton Sound.

This research unit addresses "Task D" (transport) described in the OCSEAP Technical Development Plan (1978).

C. Relevance to Problems of Petroleum Development

Our research is pertinent to two major impact areas of petroleum development in the marine environment: (1) transport of materials including pollutants; and (2) hazardous sea floor conditions produced by erosion caused by currents and waves.

The data and analyses produced in this work will enable future engineers, scientists, and other personnel to make better estimates of transport pathways for oil that is spilled in Norton Sound and the northwestern Bering Sea. The transport patterns of suspended fine materials (like Yukon River silts and clays) are indicators of the paths oil will take in the average or mean sense (long times >1 month); the transport vectors produced at specific sites will better define the temporal variability of the oil and sediment transport.

This information is immediately useful to chemists and biologists who are assessing the impact that oil and trace metals might have on the local Norton Sound and Bering Sea environment. Oil that is absorbed by the fine suspended organic and inorganic material and is mixed into the bottom sediments will be transported by the regional mean currents. The higher frequency currents such as tidal flow and surface wave-induced currents add local complications to the transport effects. For example, a tidal current average of about 10 cm/s during the ebb stage in Norton Sound (typical for the data) will produce transport over about 4.5 km during the 12 hour half-cycle. Biota over this distance would be affected by the local transport of pollutants and nutrients.

The ability to predict accurately the movements of pollutants in the sea is strongly dependent on our knowledge of local transport processes. The mechanisms which control the paths and amounts of material that is moved will have unique aspects in specific geographic regions, like Norton Sound. This study attempts to identify and elaborate upon the most important transport-producing mechanisms in this region, and to relate these mechanisms to entrainment and movement of near-bottom materials.

The eventual understanding which this study has as its goal will hopefully permit an accurate description of bottom transport of sediments, pollutants, nutrients, and other particulate matter in Norton Sound.

III. CURRENT STATE OF KNOWLEDGE

The suspended sediments found in Norton Sound are nearly all derived from the Yukon River, which discharges 70–100 million tons of material per year into the southwestern corner of this area (Fig. 1). Despite this enormous sediment source, Nelson and Creager (1977) and McManus et al. (1977) show that in recent times (<5,000 years B.P.) modern Yukon fine sands and silts have been accumulating on the Yukon subdelta in southern Norton Sound at a surprisingly low rate. The thin accumulation of sediments has been attributed to the erosive action of storms that occur in the early fall prior to the formation of ice cover (Nelson and Creager 1977). The fine-grained fraction of Yukon-derived materials is presumably transported through the northern Bering Sea with the Alaska Coastal Water and deposited in the southern Chukchi Sea (McManus et al. 1974; Nelson and Creager 1977).

Modern Yukon very fine sands and silts do not form a continuous blanket in Norton Sound. Despite the proximity of this large sediment supply, the modern muds tend to deposit along the southern border of the sound, leaving substantial areas in the north-central area with little or no recent cover (<20 cm). The explanation for the slow rates of accumulation in the northern half of the sound was not known prior to our work. We now believe this situation is the result of strong tidal and storm currents along with an advective transport pattern that diverts the bulk of the Yukon silt to other areas.

Investigations of the large-scale current patterns in the northern Bering and Chukchi Seas have been summarized by Coachman et al. (1975). When viewed in a regional sense, the mean circulation is relatively simple. Bering Sea shelf water flows toward the Arctic Ocean and the magnitude of this transport is modulated primarily by atmospheric pressure changes. Owing to topography, the current speed increases toward the north; the effect of flow constriction is particularly apparent north of 64°30'N latitude. Bottom sediments in the approaches to Bering Strait are predominantly sands which have been molded into a progression of bedform types that are characteristic of progressively stronger bottom currents. There is little chance for permanent deposition of fine-grained sediments in this area (north of 64°30') and suspended material moves rapidly through Bering Strait and into the Chukchi Sea (Drake et al., in press).

Whereas the gross aspects of the regional flow field are reasonably well known, the physical oceanography of Norton Sound has only recently been examined. As is typical of most investigations of "unknown" areas the initial gains in knowledge tend to come easily but the detail needed to achieve a quantitative understanding comes only after several years of intensive research.

Studies in 1976 by Muench, Charnell, and Coachman (1977) and Cacchione and Drake (1977) were the first adequate investigations of the physical oceanography of Norton Sound. Among many results the following should be noted:

1. Muench et al. (1977) suggested that the circulation in the outer part of Norton Sound is characterized by a cyclonic gyre.
2. Exchange of water between the outer Sound and the eastern "cul-de-sac" is limited. In fact, the bottom water in the cul-de-sac late in the summer of 1976 was probably remnant from the previous winter (Muench et al. 1977).
3. GEOPROBE data for September–October 1976 showed that tidal currents were surprisingly strong in 18 m of water (60 km south of Nome). Sediment transport calculations suggested that the tidal currents plus the mean flow should produce bed shear stresses close to those needed to initiate sand motion (Cacchione and Drake 1977).
4. The regional sampling by Cacchione and Drake revealed a pronounced tongue of turbid water originating near the Yukon Delta and extending across the mouth of Norton Sound toward the Nome coast.

Geologic studies by Nelson (1978) have revealed the presence of a number of circular depressions on the Yukon delta front. The origin of these features is presently unknown but it is possible that they are related to intense currents during storms. The delta front is an area of rapid sand and silt deposition in the summer and these materials should be readily eroded during the late summer storms.

IV. STUDY AREA

Norton Sound is a shallow arm of the northern Bering Sea, located on the western margin of Alaska, south of the Seward Peninsula (Fig. 1). It is approximately rectangular in shape, 250 km long east to west, and 130 km long north to south. Water depth everywhere is less than 24 m; average depth is 18 m. Nome, population 2,400, is situated along the northwest coast.

The geologic history of Norton Basin and the Yukon delta complex have been discussed by Nelson et al. (1974) and Dupré (1978). A complete description of the bottom sediments in the northern Bering Sea is presented by McManus et al. (1977). Seasonal climatic variations are briefly discussed in Appendix B.

Although we have concentrated our work within Norton Sound we have also collected data in Bering Strait and in the region of sand waves west of Port Clarence. In addition, Nelson (USGS, pers. commun.) collected water samples for suspended sediment analysis in previously unsampled areas north of Saint Lawrence Island.

V. DATA COLLECTION

We employed two complementary methods of data collection in our Norton Sound work. The first method involved regional sampling of hydrographic parameters and suspended particulate matter in order to examine the spatial variation in sediment transport. Sampling cruises were conducted in September–October 1976, July 1977, and February–March 1978. The second method focused on temporal variation in transport and employed an instrumented, bottom tripod system (GEOPROBE). The GEOPROBE system is designed to measure bottom currents and pressure, temperature, and light transmission and scattering for periods of about 3 months. In addition, bottom photographs are taken at a fixed time-interval and also at times when the bottom current exceeds preselected speeds. GEOPROBE operation and data analysis are described in Appendix A.

Specific methods of sample collection and analysis have been discussed in detail in Cacchione and Drake (1977) and Appendixes A–D.

VI. RESULTS

A. Suspended Particulate Matter

Distributions of total suspended matter (TSM) during September–October 1976, July 1977, and February–March 1978 are shown in Appendixes B and C. In each case the distribution reflects the dominance of the Yukon River sediment supply in Norton Sound and the advective transport of this material across the mouth of the sound. Combustion analysis of the suspended matter shows that inorganic components compose the bulk of the material during both summer and winter seasons. The TSM during fair weather conditions (negligible surface wave action) is principally finer than 16 μm, although coarser material was in suspension near the delta in July 1977 and February 1978.

Subsurface distribution of TSM in the summer reveals a two-layer stratification which corresponds closely to the water density stratification (Appendix B). The bulk of the suspended matter is located in the lower layer within a few meters of the sea floor and the concentrations and texture of this material reflect the balance between turbulent energy and particle settling. In the winter the discharge of fresh water is negligible, and vertical mixing due to surface water cooling and ice formation leads to the destruction of the two-layer system and formation of a single, nearly homogeneous layer in western Norton Sound (Appendix C). Vertical mixing of suspended matter is not restricted in the winter, and the TSM concentrations show only slight increases at depth. When the winter TSM values are integrated over the entire water column and compared to the depth-averaged suspended load in summer, it is evident that seasonal variation in "wash load" is negligible on the prodelta (Appendix C). The suspended matter in winter is dominated by fine silt and clay and is essentially the same as the suspended matter in summer (quiescent conditions).

B. Temporal Variations—GEOPROBE Results

GEOPROBE tripods were deployed in 1976 and 1977 at a site 60 km south of Nome (64°06'N latitude, 165°30'W longitude) near the northern margin of Yukon prodelta deposits (Fig. 1). Both deployments resulted in successful measurements of bottom currents, pressure, temperature and the optical parameters, transmission and scattering. The 1977 record covered an 80-day period, July 8–September 26, and this data set provides an excellent comparison between fair weather and storm conditions. The 1977 GEOPROBE data are discussed in Appendixes B and D. In addition, a complete presentation of these data was included in our annual report for 1978 (Cacchione and Drake 1978). The significant aspects of the GEOPROBE results which were presented in the 1978 report are reproduced here.

Hourly Average Current Measurements

Currents are measured at five positions on each GEOPROBE tripod as shown in Figure 2. As discussed in Section V, the rotor/vane values represent average currents for each 1-hr interval; each e–m current sensor produces "burst" measurements taken one per second for 60 seconds during each 1-hr interval. The hourly averages for each current sensor over the entire 80-day period are shown in Appendix E. Also shown for each sensor are the statistics and histograms of speed and direction for the entire record (July 8–September 26, 1977).

Several significant results are obvious in the current data and are pointed out here. Refer to Appendix E for the figures.

(1) The speed and direction records are dominated by a tidal periodicity for the first 57 days (to about September 5). The tidal current has a mixed periodicity with a dominant diurnal component prevalent in the more intense E–W motion. A distinct spring-neap fortnightly cycle is evident, with relatively low currents with confused direction occurring during the neap stage. For example, CM 4 has weak, neap tidal current-speeds during the period around July 10 and again 2 weeks later on July 24, August 8, and so on. The strongest tidal currents occur during peak springs, achieving speeds of about 25 cm/s at CM 1 to about 35 cm/s at CM 4. The E–W tidal currents are very energetic; these records compare favorably with the current meter record taken by PMEL near site G1 (not shown).

(2) The current records show events that are longer in duration than the daily tidal cycle. For example, on July 24–25, September 4–7, and especially during September 13–16 and subsequently the current speed records show prolonged periods (>1 day) of increased, non-tidal flows. As will be discussed below, these events are correlated with increased wind speeds and wind direction shifts.

(3) The dominant low frequency non-tidal flow (daily-averaged) is generally northward, with added eastward component at CM 1 and CM 4 (Appendix E—"stick" diagrams). The small magnitudes of the daily averages, denoted by the short "sticks" in the daily vector records are statistically insignificant. However, the large northward daily component during September is significant and occurs during strong southerly winds. The progressive vector plots essentially estimate the daily drift over the 80-day record at each sensor, and show the north-northeastward motion (about 2.5 km/day or 3 cm/s at CM 4).

(4) The storm-intensified bottom flow during September 13–15 has hourly average values (i.e., burst-averaged) of nearly 25 cm/s at 20 cm above the bed (CM 1) and greater

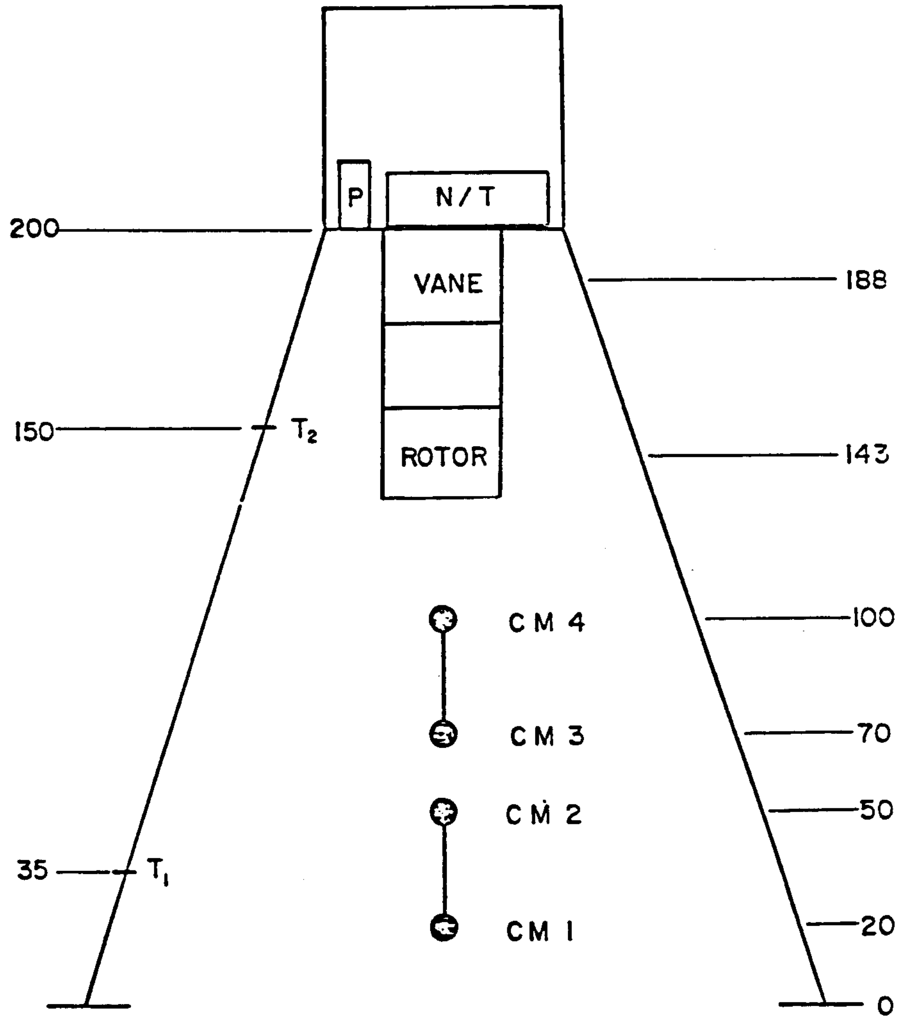

Figure 2.—Schematic of GEOPROBE tripod.
All distances are given in centimeters from the base of the foot pads.

than 40 cm/s at 100 cm above the bed (CM 4).

(5) Strong non-tidal flows subsequent to the September 13–15 storm event are evident. The N–S component has a marked northward component of about 10 cm/s at CM 4 throughout the period September 21–22 and the diurnal overtones. The other sensors show a similar northward polarization during the post-storm period.

Graphs of the power spectra for each time-series record of burst-averaged currents are given in Appendix E. The kinetic energy spectrum for each sensor shows that the diurnal and semi-diurnal components dominate the motion field; however, a lower frequency peak (not significant at 95% confidence interval) is present at a period of about 140 hr (5.8 days). The spectral plots for E–W and N–S components generally show largest power at the diurnal period.

Burst Data

The e–m current sensors were sampled each second over a single 60-s burst to obtain measurements of the surface wave-induced currents. The data are too numerous to present as time series plots for the entire 1,900 burst sequences. The total number of burst data points for each e–m current sensor is about 1.2×10^5.

The most significant finding is that the large surface waves and swell (1–2 m) during September 13–14 occurred during strong southwesterly winds (~20 knots) that persisted for over 24 hr. Additionally, this was a period of high spring tides. The combined wind-driven, wave-induced, and tidal currents produced near-bottom currents of 60–70 cm/s at the times of measurements.

The maximum periods of the wave motion derived from the pressure data were 5 s, 7 s, and 11 s. The relatively long periods during the strong winds of September 13–14 are particularly significant because of the shallow water depth of 20 m at site G1. These waves probably were swell that had propagated into the areas from the southwest.

Other Current Data

Figure 3 contains GEOPROBE sensor data for the first 30 days (July 8–August 7) of the 1977 experiment. The uppermost graph shows hourly averages of current speed obtained with the rotor/vane sensors. Semi-diurnal tidal motion and two fortnightly tidal cycles are quite obvious in this record. Spring tidal current speeds have daily maxima of 25–32 cm/s; neap tidal current maxima are 10–15 cm/s.

The plots of light transmission (TRANS) and light scattering (NEPHEL) in Figure 3 are presented as relative units of measurement taken once each hour (basic interval). The relatively persistent, low levels of scattering, about 0.24 relative, correspond to about 3–5 mg/liter as derived from calibration data (not shown here). These levels are representative of the quiescent conditions in the region of measurement as determined by independent shipboard sampling (about 4.4 mg/liter).

Light transmission is more sensitive to turbidity fluctuations than scattering at relatively low levels of suspended concentrations. Therefore, the diurnal fluctuations in light transmission, not apparent in the scattering record (July 8–July 21), correspond to real changes in the turbidity levels (about 1–2 mg/liter peak-to-peak). These tidal fluctuations in turbidity are correlated with similar diurnal oscillations in the temperature data. A more detailed examination of these results shows several significant features:

1. The oscillations are distantly diurnal, not semi-diurnal.
2. Periods of low temperatures ("cold") are correlated with values of low turbidity ("clear").
3. During times of neap tide (July 8, July 23, August 6), both turbidity and temperature are relatively steady.

The above features suggest that tidal advection, specifically the E–W diurnal motion evident in the current speed (E–W) values transports water into and out of Norton Sound, sweeping past site G1. This mechanism is a more plausible explanation for the

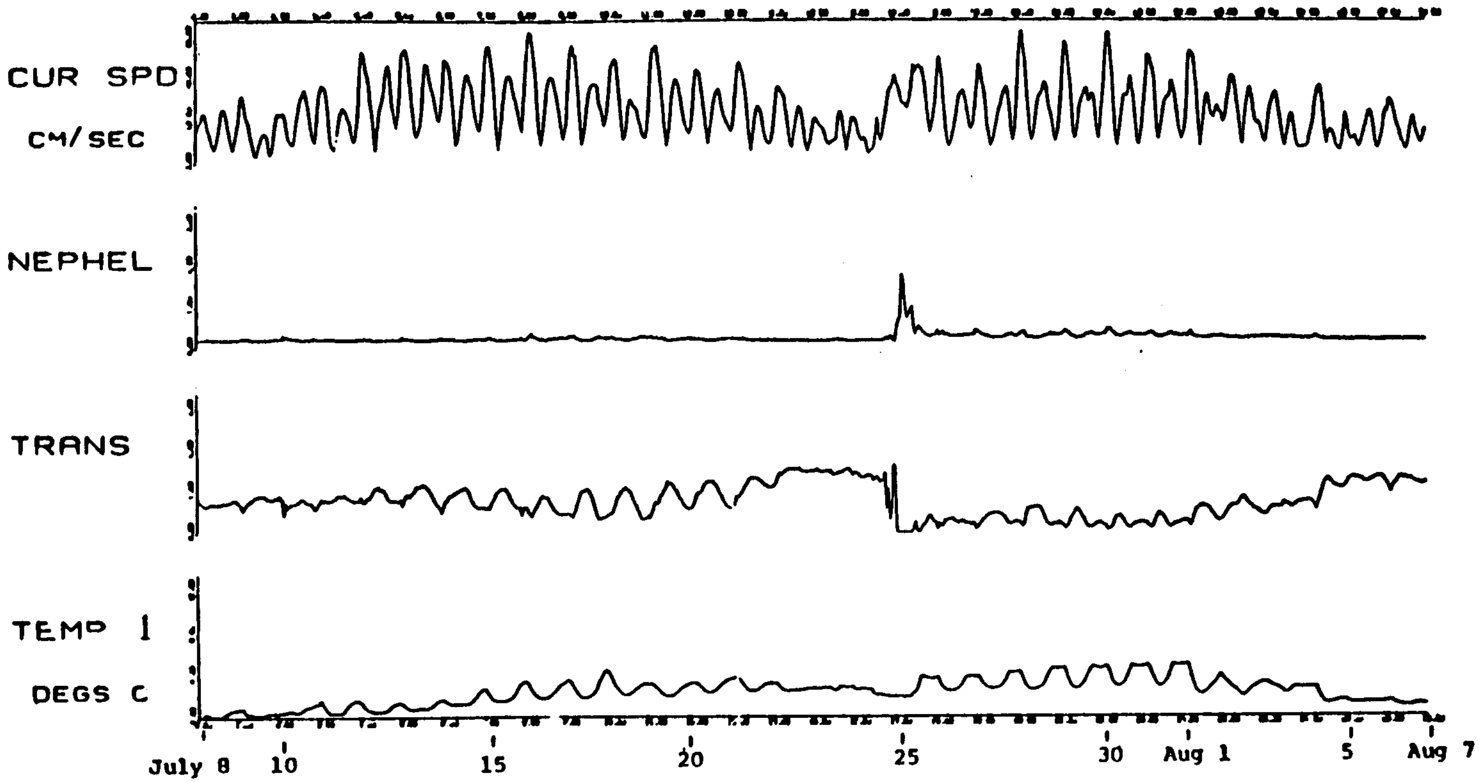

Figure 3.—Hourly GEOPROBE data taken over the 30-day period from 0000, July 8, to 0000, August 7, 1977. Current speeds (CUR SPD) at top are hourly averages obtained with the Savonius rotor. Light scattering (NEPHEL) and light transmission (TRANS) are in relative units; value for these and for temperature (TEMP 1) were taken once each hour. Horizontal axis is in days.

observed values than vertical advection or mixing caused by the internal tide because of the correlation of "cold" with "clear" water. Since the bottom water is colder and more turbid than the surface layer, a vertical mixing or advection process would presumably cause a correlation of "cold" with "turbid" values. The horizontal tidal advection implies, then, that with a rms diurnal tidal speed of about 10 cm/s, reversing lateral E–W transport of about 4.5 km will occur every 12 hr.

Even more noteworthy in Figure 3 is the unusual "event" that occurs on July 25, characterized by a sudden increase in scattering speed increase due to a non-tidal current. The peak NEPHEL value of 2.0 relative corresponds to about 50 mg/liter in sediment concentrations, an order of magnitude increase over the "normal" levels.

Figure 4 shows the weather data recorded at the National Weather Service station at Nome (about 30 miles to the north) during the period of this unusual event. Hourly values of wind speed, wind direction, and air pressure are plotted in this figure. The wind data show a regular diurnal cycle, with wind speeds generally lower during the late evening–early morning hours. During July 24, wind speeds increased to 9–10 m/s (about 20 knots) and became persistent, about 12 knots, over the next several days. Wind direction also became steadier from the southeast during this period. Air pressure dropped off, suggesting the passage of a low pressure center through the region. The larger surface waves caused by the increased wind stress produced maximum oscillatory bottom currents as high as 35 cm/s (Fig. 5). The increased, sustained wind stress, occurring at the end of a neap stage in the tidal regime, apparently also caused an increase in magnitude and duration of the mean bottom current speed. The combined effect of higher wave-induced and wind-driven currents produced a bottom stress competent enough to cause the relatively large increase in concentrations of suspended materials (~50 mg/liter). The sudden onset and equally sudden decrease in the concentration values are probably a result of initial resuspension of fine-materials that had settled out locally during the preceding time of neap tide, and to increased upward turbulent mixing of the higher near-bottom suspended load by vigorous wave activity.

The effects on sediment movement at site G1 caused by the passage of a moderate storm were even more vividly demonstrated in September 1977. A detailed analysis of this storm is presented in Appendix D.

VII. DISCUSSION

A. Transport Pathways of Suspended Matter

Three transport pathways are important in the dispersal of terrigenous silt and clay delivered by the Yukon River (see Appendix B for detailed discussion):

1. Initial transport (during the summer months at least) is characterized by westerly and southerly flow within 20 km of the Yukon Delta. Turbid water commonly extends south to Cape Romanzof and on June 29, 1977, a NOAA satellite image suggests transport as far south as Hazen Bay. This transport pattern, evident on satellite images, is rather surprising because one would expect that the density

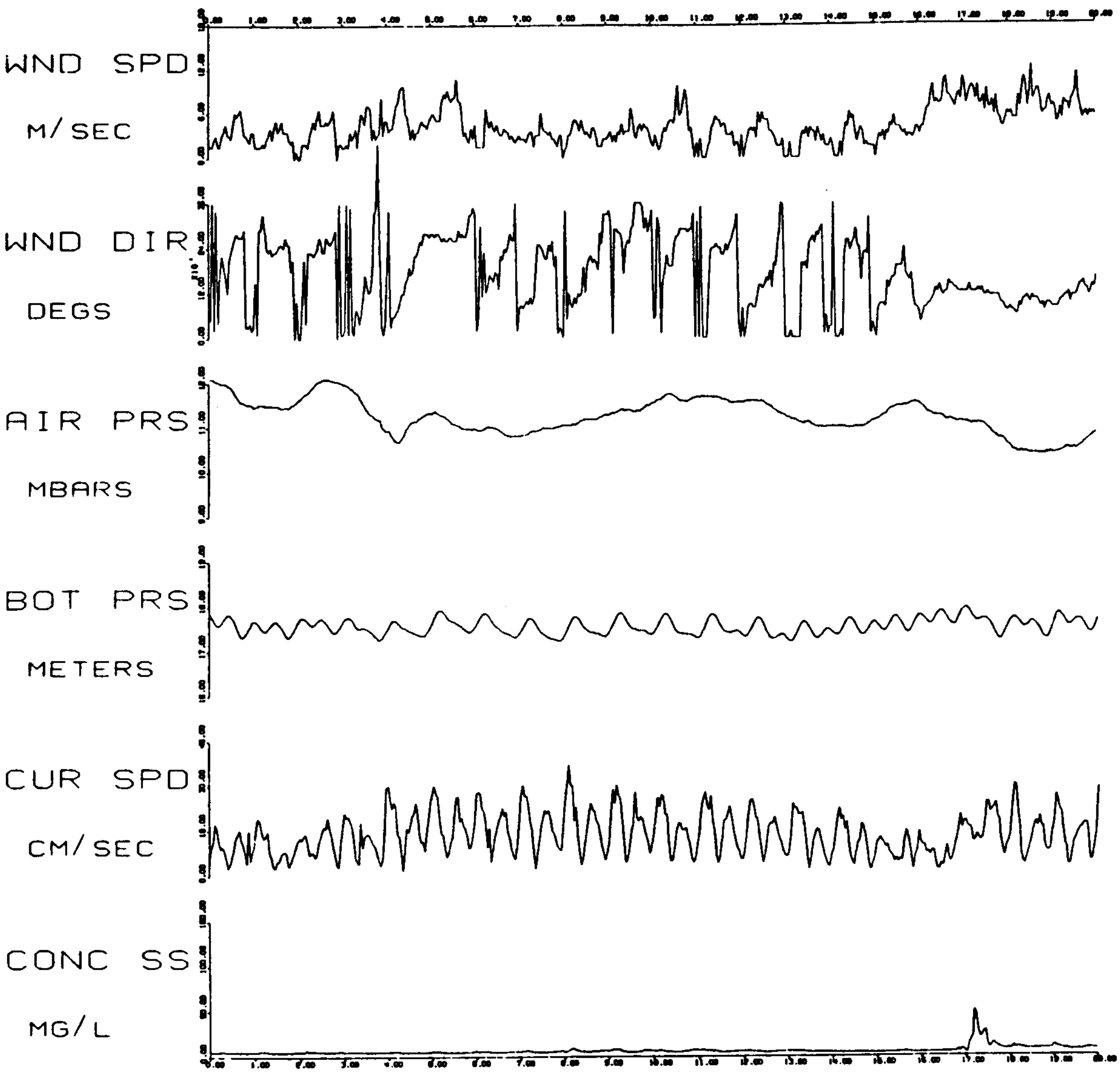

Figure 4.—GEOPROBE data obtained during July 8–28, 1977, and meteorological data recorded at Nome, Alaska (National Weather Service). The data show an increase in wind speed on July 24 which was followed by a sudden increase in suspended matter concentration. The current speed data are hourly averages obtained with the Savonius rotor. See Figure 5 for wave-generated currents on July 25.

distribution would generate currents to the north and east around the delta front (owing to Coriolis effect). We suspect that the observed current is the result of entrainment of nearshore water by the Alaska Coastal Water as it flows northward past Cape Romanzof. Dupré (RU 208) has found that embayments to the south of the major Yukon River distribution contain large amounts of modern Yukon silt. This finding provides independent evidence to support the importance of southward nearshore flow.

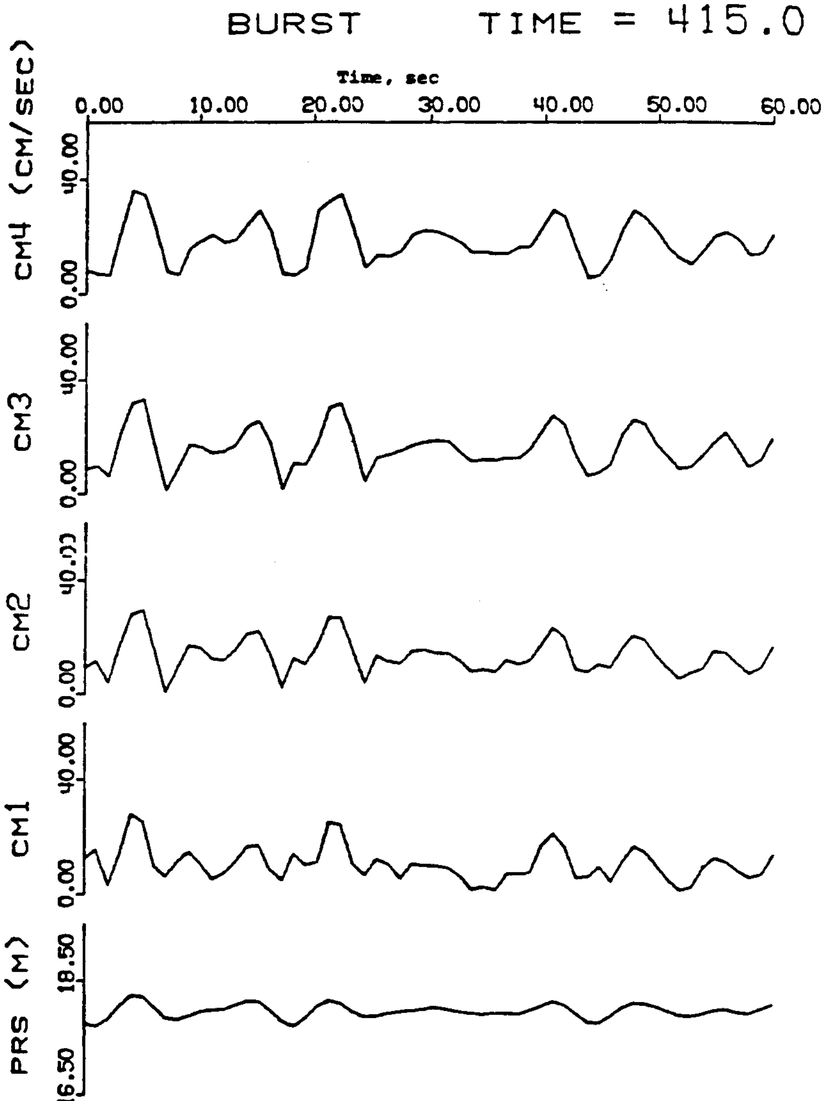

Figure 5.—"Burst" current (CM) and pressure (PRS) data taken on July 25, 1977.

2. The suspended matter that is moved southward along the west shore of the delta either accumulates in "low energy" lagoons and bays or returns with the Alaska Coastal Water. Our studies, the studies of Muench et al. (1977), and a large body of data collected over the years by L. Coachman and his associates (University of Washington) demonstrates a nearly "unidirectional" flow of shelf water northward between the mainland and St. Lawrence Island. This flow is driven by the difference in sea level between the Bering Sea and the Arctic Ocean and the need to replace water lost from the Arctic Ocean to the Atlantic Ocean.

As this shelf current flows past Norton Sound it tends to mix with turbid Yukon water in the vicinity of the delta. This mixed water then extends across the mouth of the sound toward the coast at Nome. There is no question that the currents immediately north and northwest of the delta are complex. Nevertheless, the distributions of both surface and near bottom suspended matter demonstrate the existence of this important northward transport pathway. Muench et al. (1977) have postulated a mean circulation system that includes a cyclonic gyre centered in the outer part of the sound north of the delta. In order to obtain agreement between our results and this circulation pattern, it is necessary to postulate a split in the northward flow near the Yukon Delta with part of the water moving directly across the sound and another part moving into the sound to feed the cyclonic gyre. Obviously, more long-term current measurements are needed to fully describe the flow field over the Yukon prodelta.

3. Bottom sediments in the inner part of Norton Sound are derived from the modern Yukon River (Nelson and Creager 1977). In fact, accumulation rates of mud in this area (east of Cape Darby and Stuart Island) are among the highest on the northern Bering Sea shelf. Suspended matter distributions in 1977 and in 1976 (Cacchione and Drake 1977) suggest transport of Yukon silt and clay eastward past Stuart Island. However, the available data do not support a strong interchange of water between the inner and outer parts of Norton Sound (Drake et al. 1977; Muench et al. 1977. Satellite images tend to show a steep gradient decrease in TSM at the surface near Stuart Island such that the bulk of the suspended matter is confined to Pastol Bay (west of Stuart Island).

   The effects of wind stress on the circulation in Norton Sound are not well understood but it seems likely that periods of westerly winds would drive surface water eastward along the southern coast and into the inner sound. West and southwest winds exceeding 15 knots occur on about 3–4 days during each of the summer months (based on weather records at Nome); winds come from the southwest quadrant approximately 40% of the time. It is possible that flow into the inner sound occurs whenever the wind stress is sufficient to overcome the effects of other forcing mechanisms.

   The volume transport of suspended matter eastward from the delta is not as important as other transport pathways. However, the sediment that is carried into the inner part of Norton Sound tends to remain there. We believe that key factors in this sediment retention are the low energy of bottom currents in this area and the limited exchange of bottom water with the outer sound (as shown by the presence of remnant, winter bottom water well into the ice-free season). Of these two factors we suspect that the latter is the more significant because TSM concentrations in the remnant water are relatively high, indicating that this water, although isolated, is not motionless. For example, current data collected by R. Muench within the postulated remnant water body southwest of Cape Darby (Fig. 1) show tidal currents of up to 30–40 cm/s but essentially no net motion. It seems likely that a similar but less vigorous current regime also would characterize the bottom water within the inner sound. Additional data are needed.

B. Comparison of 1976 and 1977 Results

Suspended sediment distributions on many continental shelves exhibit a large degree of spatial and temporal variability. It is probable that much of the variability is caused by wind-driven transport combined with variable rates of fine sediment resuspension by wave action.

The data for Norton Sound in late summer of 1976 and early summer of 1977 reveal strikingly similar suspended sediment patterns (Cacchione and Drake 1977). In both cases the distributions at the surface and near the bottom are dominated by a broad tongue of turbid water that originates along the western side of the Yukon Delta and extends across the mouth of Norton Sound. Temperature and salinity values show that this water is a mixture of Alaska Coastal and Yukon River water.

These results along with the GEOPROBE measurements indicate that current patterns and speeds in the outer part of Norton Sound are caused principally by the tides and the regional transport of Bering Sea shelf water toward the Chukchi Sea. In particular, it appears that the regional flow establishes, to a large degree, the mean circulation pattern in the sound whereas the tidal currents (primarily constrained to flow E–W) serve to maintain particles in suspension and to resuspend materials at times of spring tides. Tidal excursions are approximately 4–5 km with only a small net motion. Consequently, they act as a diffusing element. The "clarity" of the observed suspended matter distributions (i.e., the sharpness of boundaries between clear and turbid waters) suggests the importance and consistency of the advective flow regime in Norton Sound.

The situation is different in the inner part of Norton Sound (east of Cape Darby and Stuart Island). Here the suspended matter distribution tends toward greater horizontal uniformity, particularly in September 1976. This suggests that tidal and wind-driven currents are more significant compared to advection. As discussed above, the inner part of Norton Sound is strongly two-layered and the lower layer is water, formed during the winter months. Substantial advective motion must be restricted to the low density surface layer and mixing across the pycnocline must be minimal (Muench et al. 1977).

The results of our winter sample collections (February–March 1978) confirm our conclusion that the bottom currents generated by the astronomical tides are sufficient to maintain the transport of fine silt and clay through Norton Sound; i.e., the continuous sediment flux which we term "wash load." More significantly, the concentration levels observed in the winter demonstrate that a reservoir of Yukon River silt must exist near the delta. Furthermore, the currents near the delta (below the shorefast ice) must be strong enough to resuspend silt and feed particulate matter to the advective flow across the prodelta (Appendix C).

C. Temporal Variability

The GEOPROBE tripod data provide a valuable time history of near-bottom measurements of fluid and sediment parameters at site G1 (Appendix D) for the 80-day deployment period. A complete listing and plot of all data is not included here because of the large volume of numbers that are generated by one GEOPROBE station tape. Only the most pertinent information is given in Section VI.

One of the most significant results is the contrast in dynamic conditions that occurs during "normal" and stormy periods. The normal near-bottom flow field at G1 is characterized by the data shown in Figures 3 and 4 for July 8–24. During this time, tidal forcing dominates the hourly mean values of pressure, bottom current, temperature, and turbidity. Small perturbations in the tidally dominated normal regime occur, principally due to short periods of increased wind-driven currents and waves.

The tidal bottom currents are most intense during spring tides, commonly achieving values of greater than 30 cm/s at 1 m above the sea floor. During neap, the daily maximum currents at 1 m are much reduced, typically less than 15 cm/s during the smallest tides. As Figure 4 shows, the bottom pressure has a definite change in pattern during the fortnightly cycle. The spring tides are strongly mixed, with two unequal highs during each daily cycle; the neaps are more nearly a diurnal type.

Figures 6 and 7 point out the extreme importance of storm conditions in affecting the sediment transport pattern in this area. The relatively high, sustained values of hourly averaged bottom current speed and the persistent northward directions are indicative of active, large transport of materials. These wind-generated events appear to overwhelm the rhythmic pattern that is the "normal" condition.

In terms of evaluating the fluid motion at the sea floor for its effect in the transport of sediments, two of the most critical parameters are shear velocity, u_*, and bed roughness, z_0, where

$$u_* = (\tau_0/\varrho)^{1/2}; \qquad (1)$$

τ_0 is the bottom shear stress, ϱ is fluid density, and z_0 is the roughness length in the Karman-Prandtl turbulent boundary layer equation

$$u/u_* = \frac{1}{k} \ln \left(\frac{z + z_0}{z_0}\right) \qquad (2)$$

u is the velocity at a distance z above the bed; $k \sim 0.4$ is von Karman's constant.

To compute u_* and z_0 from equation (2), u can be measured at several levels (z) above the bed. If more than two levels are used then the validity of equation (2) can also be estimated. Since the four GEOPROBE e–m current sensors are operated within the bottom tidal boundary layer, these measurements afford a unique data set to derive u_* and z_0 values. Figure 8 shows examples of the hourly current speed profiles obtained during neap, spring, and storm conditions. The maximum values of u_* and the maximum speed at 1 m are highest during the storm; spring tide values are significantly greater than during neap.

The threshold values of u_* to initiate movement on non-cohesive sediment can be estimated from the modified Shields Diagram (Madsen and Grant 1976), even when

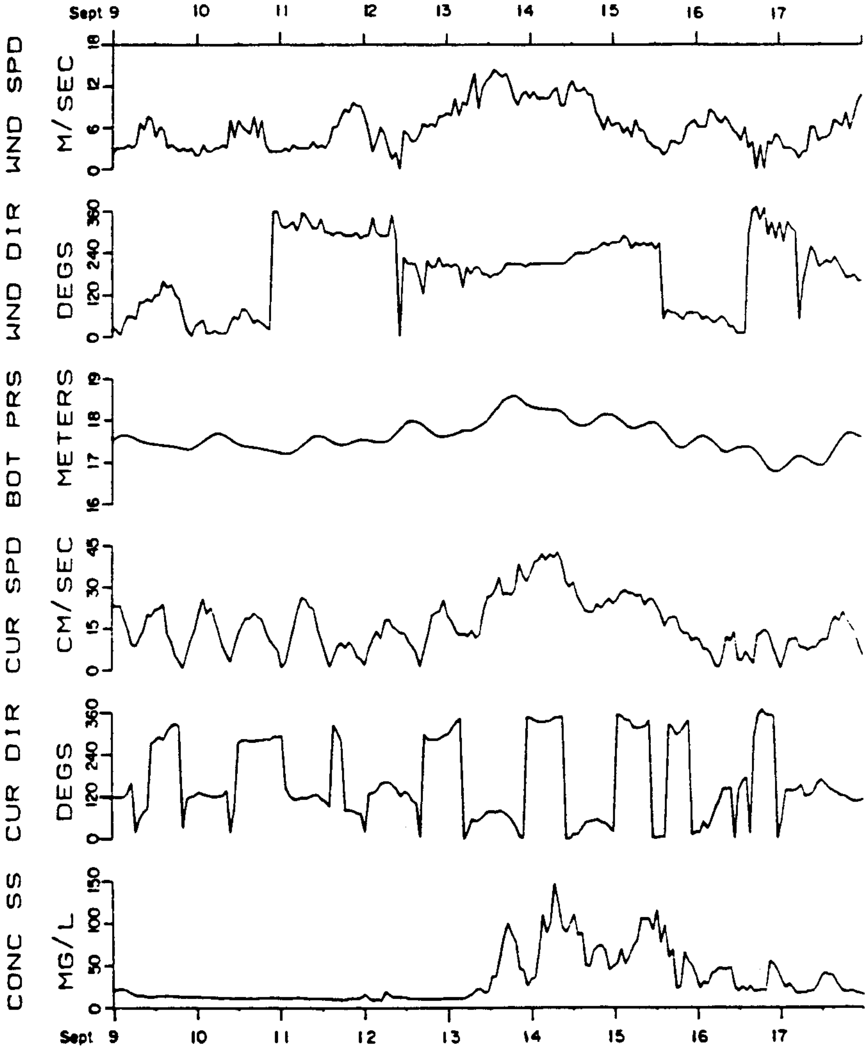

Figure 6.—GEOPROBE and meteorological data during September 9–18, 1977, in Norton Sound. Current speed and bottom pressure are hourly averages and the suspended matter concentrations at 2 m above the sea floor are derived from light scattering values using calibration data. See Figure 7 for examples of the wave-generated currents on September 15.

the flow is unsteady. The critical, or threshold, value of u_* for the mean particle size of 0.07 mm at site G1 is 1.3 cm/s. This value, together with u_* values in Figure 8, suggests that incipient sediment motion in the vicinity of site G1 occurs during storms and spring tides. The added effects of organic materials (cohesive) and finer-grained sediments ($<62\ \mu$) are not well understood; Jumars (1977) and Southard (1977) have discussed these problems with regard to sediment transport and pointed out the poor state of knowledge in this area. Possibly the binding caused by mucoid surface materials explains the patchiness of the sediment ripples throughout the central western Norton Sound area. Also, the high silt content would tend to inhibit ripple formation and bedload transport. The clay fraction at G1 is less than 5% of the sediment.

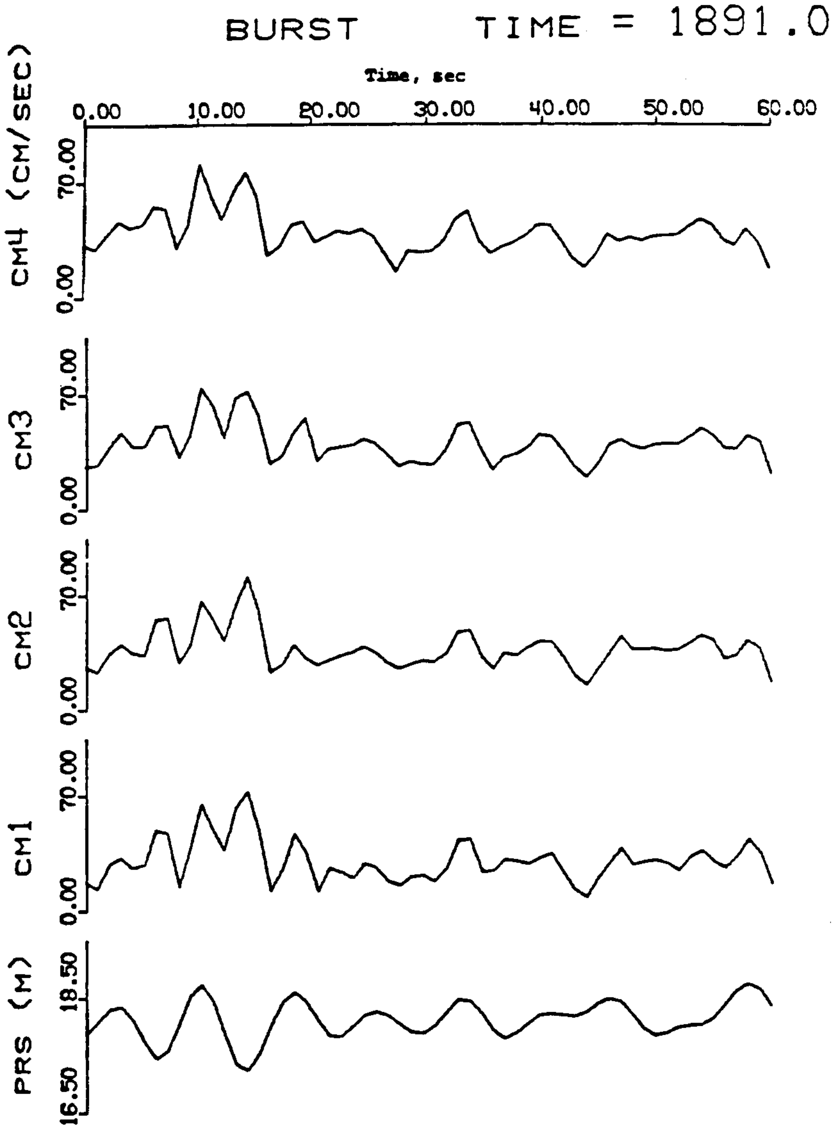

Figure 7.—"Burst" current (CM) and pressure (PRS) data taken on September 15, 1977.

Another important part of the overall transport pattern in this region is demonstrated by Figure 9. Daily average values of u_* and z_0 were computed by first taking averages of u at each level over consecutive 24-hr periods. These new daily-averaged values of u, called $<u>$, were then used in equation (2) to derive daily averaged values of u_* and z_0, which are shown in Figure 9. Throughout the 80-day period, all vertical profiles of $<u>$ fit a logarithmic curve to within 2%. The maximum standard error of estimate of any single value of $<u>$ that derives from using the logarithmic profile is 0.03 cm/s.

Figure 9 clearly shows the effect of the fortnightly tidal cycle on shear velocity. The dashed line is the estimated critical value of u_* of 1.3 cm/s. During times of peak

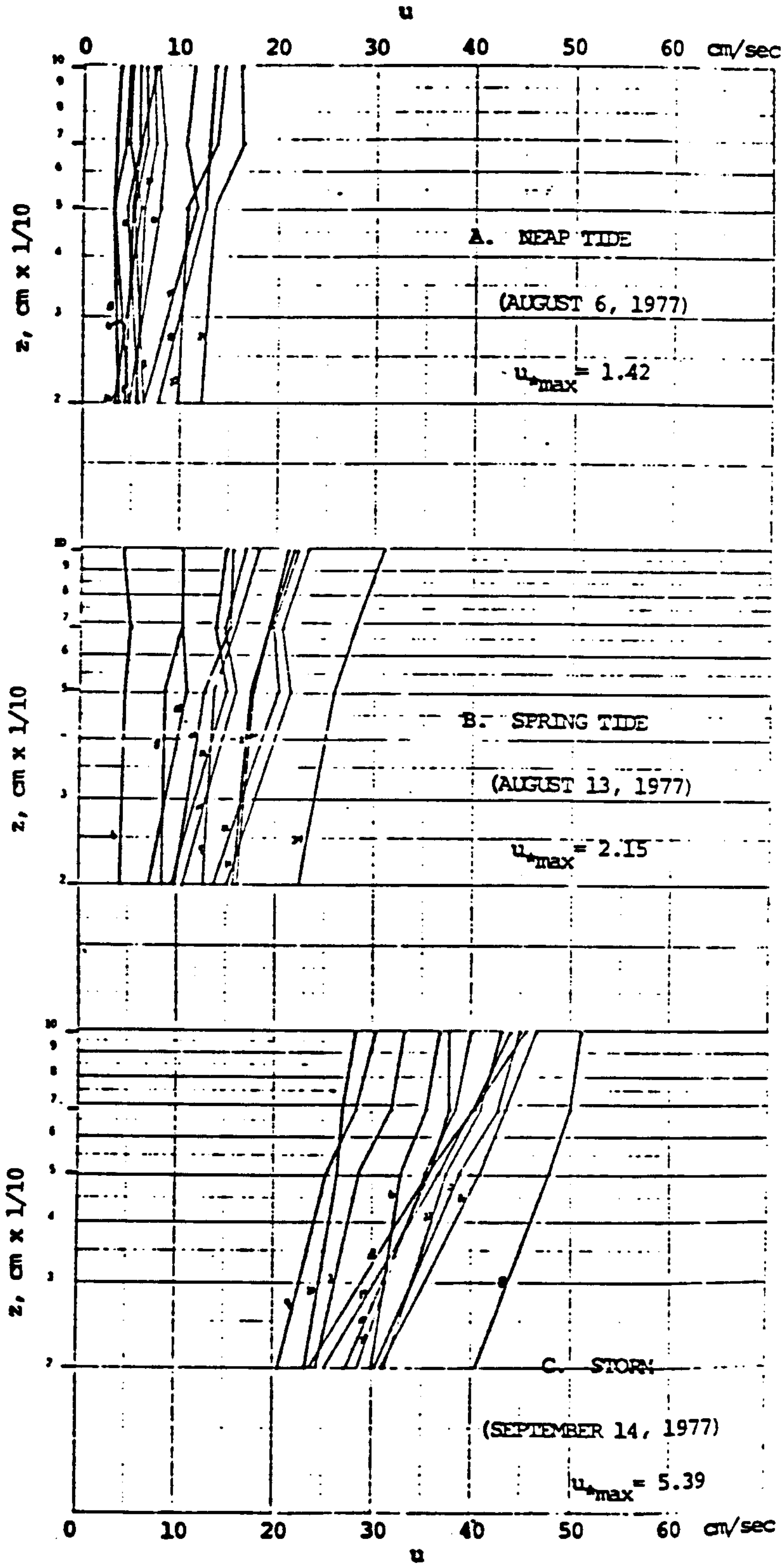

Figure 8.—Current speed, u, in cm/s measured at 4 levels with the electromagnetic current sensors plotted against the natural logarithm of distance above the sea floor (ln z) at different times during the 80-day period, July 8–September 27, 1977, in Norton Sound, Alaska. Maximum values of shear velocity, u_*, are shown.

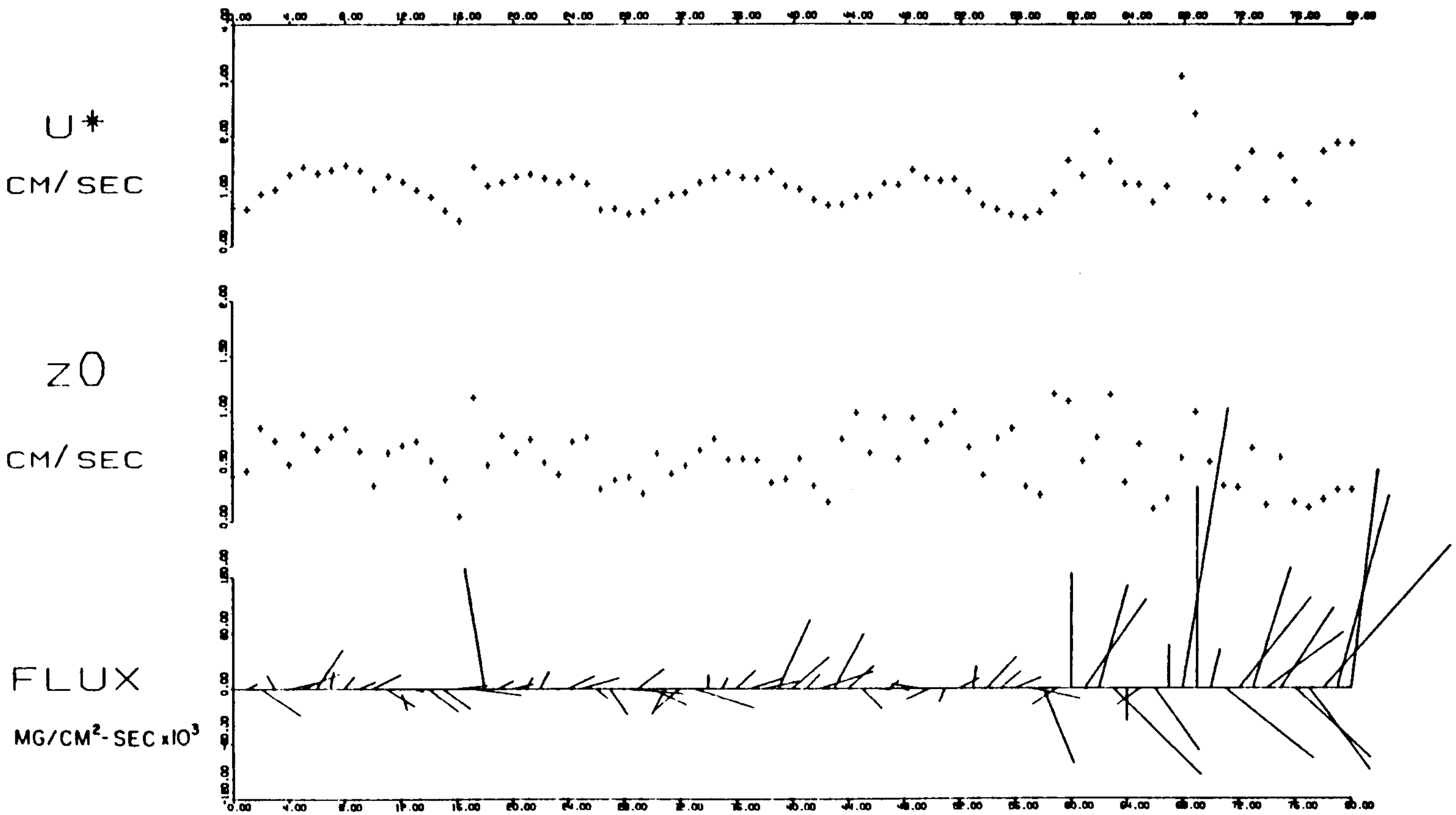

Figure 9.—Daily average values of u_* and z_0 are shown in top two panels. Suspended matter flux is shown in lower panel and was computed using the mean current at 1 m above the bottom and the suspended matter concentrations determined from the nephelometer values.

spring tides, u_* exceeds or equals the critical value. Storm periods during September generate the highest shears. The relatively small change in z_0, even during the storm period is interesting and somewhat surprising (see Appendix D for more complete discussion).

The above discussion did not directly assess the effects of surface waves. Obviously, during times of high winds, the larger waves would be expected to contribute a substantial increase to the instantaneous bed shear stress. In Section VI and Appendix D, examples of the wave-induced currents are shown. The added stress from these waves will produce local resuspension when the combined wave-induced and lower frequency components cause u_* to exceed the critical value. In a water depth of about 20 m, waves of 0.5 m in height with periods of 6 s, typical of this area over normal conditions, produce maximum wave-induced bottom currents of about 7–8 cm/s. The bottom stresses contributed by these normal wave conditions, when combined with spring tidal currents, certainly would produce initial motion and resuspension of bottom sediment. Yet when compared to the shear velocities and transport during storms, the quiescent period is not characterized by important bed load transport on the Yukon prodelta.

VIII. CONCLUSIONS

The transport of sediment in Norton Sound can be conveniently described in terms of the distinctly different quiescent and storm regimes. The quiescent or fair weather regime is characterized by generally low levels of sediment transport caused principally by the tides and mean flow augmented by surface waves during spring tide cycles. The quiescent regime is characterized by surface winds of <8–10 m/s, short period surface waves (<6 s), and a predominance of fine silt and clay moving as "wash load." Bedload transport is negligible except in shallow areas where the surface waves become important (for example, on the "2 m bank" which surrounds the Yukon Delta). Although calm weather conditions appear to occur for about 90% of the year in the northern Bering Sea, our GEOPROBE data suggest that less than 50% of the sediment transport occurs under these conditions (see Appendix B). In fact, the GEOPROBE measurements show that critical shear stresses on the prodelta are reached only briefly during spring tides during quiescent periods. This implies that much of the fine-grained suspended matter present over the prodelta is material that was resuspended at shallow depths near the delta and moved northward with the mean current.

During about 30–40 days of each year the surface wind approaches or exceeds 10 m/s, although National Weather Service records for Nome, Alaska, show that sustained winds >15 m/s recur with less than annual frequency. The 2-day storm in September 1977 appears to be representative of the more energetic late summer atmospheric events in Norton Sound. In September, October, and November the polar front migrates south and tends to steer low pressure weather systems from the southwest to the northeast across the northern Bering Sea (see Appendix D). Norton Sound is commonly exposed to strong southerly and southwesterly winds generated by the low pressure cells. Winds from this quadrant can generate 1–3-m waves with periods of 8–11 seconds because of the essentially infinite fetch southwest of Norton Sound. It is waves like these which cause severe damage along the northern coast of the sound (Fathauer 1975).

The instantaneous shear velocity (u_*) at the GEOPROBE during the September storm reached >6 cm/s and the light scattering data demonstrate a 20-field increase in TSM at 2 m above the bottom. As shown in Appendix B the amount of sediment transported during this brief event was approximately equal to the transport that would occur during 4 months of quiescent conditions.

Although the amount of sediment eroded during storms does not represent a foundation hazard at depths of 15 m or greater, the impact of storms (particularly the surface wave scour) could be highly significant at depths less than 10 m. Indeed, the morphology of the Yukon Delta shows that wave and current energy is concentrated on the western margin of the delta, which is exposed to the open Bering Sea and the full impact of southwesterly storm winds and waves.

IX. NEEDS FOR FURTHER STUDY

Our understanding of sediment transport vectors is largely dependent on our knowledge of the physical oceanography of a region. The circulation on any segment of the shelf cannot be understood without a sufficient number of long-term current meter records. In Norton Sound this requirement is even more acute because of the complexities introduced by the Yukon discharge (which must produce important density effects) and the topography (which must introduce significant frictional effects). The following points need clarification through additional research.

(1) Dynamic considerations suggest that the Yukon "fresh" water surface plume should produce important baroclinic flow around Stuart Island and into the head of the sound. The nature of the sediments show that this is the case. Because the flushing of the inner part of Norton Sound may depend largely on this advection, a more complete knowledge of flow into and out of the area is needed.

(2) There are strong indications in the temperature and salinity data that "east–west" components of advection (in addition to the reversing tidal currents) are significant in the western half of Norton Sound. A denser array of current meter moorings extending across the sound along several meridians would substantially improve our understanding of the mean circulation and the effects of wind (which presently are largely unknown).

(3) The characteristics of the flow field in the winter in Norton Sound remain unknown. However, indirect evidence (see Appendix C) from suspended sediment measurements and bottom sediment properties suggests that the currents near the Yukon Delta below the shorefast ice are strong and important to the fate of particulate materials. Current measurements in the winter would be most useful.

(4) Wind-driven currents are not discussed in detail in this report because of the nearly total lack of data on this mechanism. The GEOPROBE data show that these currents are important during storms, but we know very little about the wind stress

and wind-generated currents during less energetic times. This data gap is significant and will require further collection of current meter and meteorologic data.

X. REFERENCES

Butman, B. 1976. Sediment transport on east coast continental shelves: Proc. of NSF/IDOE workshop, Vail, Colorado.

Cacchione, D. A., and D. E. Drake. 1977. Sediment transport in Norton Sound, northern Bering Sea, Alaska. Annual Report to NOAA/OCSEAP, Juneau, Alaska. 19 p.

Coachman, L. K., K. Aagaard, and R. B. Tripp. 1976. Bering Strait, the regional physical oceanography. Seattle, Univ. Washington Press. 186 p.

Drake, D. E., R. L. Kolpack, and P. J. Fischer. 1972. Sediment transport on the Ventura–Oxnard Shelf, California. Pages 307–331 *in* D. J. P. Swift, D. B. Duane, and O. H. Pilkey, eds., Shelf sediment transport: process and pattern. Dowden, Hutchison and Ross, Inc., Stroudsburg, Pa.

Drake, D. E., D. A. Cacchione, and R. Muench. 1977. Movement of suspended and bottom sediment in Norton Sound, Alaska (abs.). Geol. Soc. Am. Abstracts with Programs 9(7): 956.

Gust, G., and E. Walger. 1976. The influence of suspended cohesive sediments on boundary-layer structure and erosive activity of turbulent seawater flow. Mar. Geol. 22: 189–206.

Jumars, P. 1977. Sediment flux and animal foraging patterns (abs.). Trans. Am. Geophys. Union 58(12): 1161.

Madsen, O. S., and W. D. Grant. 1976. Sediment transport in the coastal environment. Tech. Report 209, Ralph M. Parsons Laboratory for Water Resources and Hydrodynamics, Mass Inst. of Technology. 105 p.

McManus, D. A., V. Kolla, D. M. Hopkins, and C. H. Nelson. 1974. Yukon River sediment of the nothernmost Bering Sea shelf. J. Sed. Petrol. 44: 1052–1060.

McManus, D. A., V. Kolla, D. M. Hopkins, and C. H. Nelson. 1977. Distribution of bottom sediments on the continental shelf, northern Bering Sea. U.S. Geol. Survey Prof. Paper 759-C. 31 p.

Muench, R. D., R. L. Charnell, and L. K. Coachman. 1977. Oceanography of Norton Sound, Alaska, September–October 1976. Tech. Report, Pacific Marine Environmental Lab., NOAA, Seattle, Wash. 18 p.

Nelson, C. H., and J. S. Creager. 1977. Displacement of Yukon-sediment from Bering Sea to Chukchi Sea during Holocene time. Geology 5: 141–146.

Nelson, C. H. 1977. Faulting, sediment instability, erosion, and deposition hazards of the Norton Basin sea floor. Annual Report to NOAA/OCSEAP, Juneau, Alaska. 129 p.

Nelson, C. H. 1978. Faulting, sediment instability, erosion, and deposition hazards of the Norton Basin sea floor. Annual Report to NOAA/OCSEAP, Juneau, Alaska.

Smith, J. D., and T. S. Hopkins. 1972. Sediment transport on the continental shelf off of Washington and Oregon in the light of recent current measurements. Pages 143–180 *in* D. J. P. Swift, D. B. Duane, and O. H. Pilkey, eds., Shelf sediment transport: process and pattern. Dowden, Hutchinson and Ross, Inc., Stroudsburg, Pa.

Smith, J. D., and S. R. McLean. 1977. Boundary layer adjustments to bottom topography and suspended sediment. *In* J. C. J. Nihoul, ed., Bottom turbulence. Elsevier Scientific Publishing Company, New York. 306 p.

Southard, J. B. 1977. Erosion and transport of fine cohesive marine sediments (abs.). Trans. Am. Geophys. Union 58(12): 1161.

APPENDIX A.

A New Instrument System to Investigate Sediment Dynamics on Continental Shelves

D. A. Cacchione and D. E. Drake

ABSTRACT*

A new instrumented tripod, the GEOPROBE system, has been constructed and used to collect time-series data on physical and geological parameters that are important in bottom sediment dynamics on continental shelves. Simultaneous in situ digital recording of pressure, temperature, light scattering, and light transmission, in combination with current velocity profiles measured with a near-bottom vertical array of electromagnetic current meters, is used to correlate bottom shear generated by a variety of oceanic processes (waves, tides, mean flow, and others) with incipient movement and resuspension of bottom sediment. A bottom camera system that is activated when current speeds exceed preset threshold values provides a unique method to identify initial sediment motion and bedform development.

Data from a 20-day deployment of the GEOPROBE system in Norton Sound, Alaska, during the period September 24–October 14, 1976, show that threshold conditions for sediment movement are commonly exceeded, even in calm weather periods, due to the additive effects of tidal currents, mean circulation, and surface waves.

---

*The full text of Appendix A is available as: Cacchione, D. A., and D. E. Drake. 1979. A new instrument system to investigate sediment dynamics on continental shelves. Mar. Geol. 30: 299–312.

APPENDIX B.

Sediment Transport in Norton Sound, Alaska

D. E. Drake, D. A. Cacchione, R. D. Muench, and C. H. Nelson

ABSTRACT*

The Yukon River, the largest single source of Bering Sea sediment, delivers more than 95% of its sediment load at the southwest corner of Norton Sound during the ice-free months of late May through October. During this period, surface winds in the northern Bering Sea area are generally light from the south and southwest, and surface waves are not significant. Although wind stress may cause some transport of low-density turbid surface water into the head of Norton Sound, the most significant transport of Yukon River suspended matter occurs within advective currents flowing north across the outer part of the sound. The thickest accumulations of modern Yukon silt and very fine sand occur beneath this persistent current.

We monitored temporal variations in bottom currents, pressure, and suspended-matter concentrations within this major transport pathway for 80 days in the summer of 1977 using a Geological Processes Bottom Environmental (GEOPROBE) tripod system. The record reveals two distinctive periods of bottom flow and sediment transport: an initial 59 days (July 8–September 5) of fair-weather conditions, characterized by tidally dominated currents and relatively low, stable suspended-matter concentrations; and a 21-day period (September 5–26) during which several storms traversed the northern Bering Sea, mean suspended-matter concentrations near the bottom increased by a factor of 5, and the earlier tidal dominance was overshadowed by wind-driven and oscillatory wave-generated currents.

Friction velocities (u_*) at the GEOPROBE site were generally subcritical during the initial fair-weather period. In contrast, the 21-day stormy period was characterized by u_* values that exceeded the critical level of 1.3 cm/s more than 60% of the time. The GEOPROBE data suggest that the very fine sand constituting about 50% of the sediment on the outer part of the Yukon prodelta is transported during a few late-summer and fall storms each year. A conservative estimate shows that suspended-matter transport during the storms in September 1977 was equal to 4 months of fair-weather transport.

---

* The full text of Appendix B is available as: Drake, D. E., D. A. Cacchione, R. D. Muench, and C. H. Nelson. 1980. Sediment transport in Norton Sound, Alaska. Mar. Geol. 36: 97–126.

APPENDIX C.

Sediment Transport During the Winter on the Yukon Prodelta, Norton Sound, Alaska

D. E. Drake, C. E. Totman, and P. L. Wiberg

ABSTRACT*

Winter in the northern Bering Sea brings a drastic reduction in terrestrial runoff and a substantial decrease in air–sea momentum transfer (wind and waves) owing to the formation of shorefast and pack ice. Despite these changes, quantities of suspended silt and clay over the Yukon prodelta in the winter of 1978 were essentially the same as those observed during fair weather summer periods, when the sediment discharge of the Yukon River is at its maximum and there is no ice layer to inhibit surface waves. Furthermore, the regional transport pattern involving northward mean flow across the prodelta in Norton Sound remains unchanged in the winter.

Bottom current and light scattering measurements obtained during the summer of 1977 showed that spring tides are capable of resuspending fine sediment at depths of about 18 m on the prodelta in the absence of significant surface wave action. We conclude that during the winter the suspended matter transport system is driven by tidal current reworking of sediments which were introduced by the Yukon River during the previous summer.

---

* The full text of Appendix C is available as: Drake, D. E., C. E. Totman, and P. L. Wiberg. 1979. Sediment transport during the winter on the Yukon prodelta, Norton Sound, Alaska. J. Sed. Petrol. 49: 1171–1180.

APPENDIX D.

Storm-Generated Sediment Transport on the Bering Sea Shelf, Alaska

D. A. Cacchione and D. E. Drake

ABSTRACT*

GEOPROBE measurements of bottom stress on the outer margin of the Yukon prodelta in Norton Sound show periods of intensified bottom sediment transport during the passage of a subarctic storm. Wave-induced bottom currents significantly increase the local bed shear stress, exceed the threshold conditions for entrainment of bottom sediments, and effectively increase the local mean roughness scale (z_0). Although maximum tidal stresses during spring tides have values above threshold, average conditions for sediment entrainment are subcritical during spring tides and fair weather. Storm conditions generate mean stresses of about 10 dynes/cm^2, with instantaneous maximum wave stresses of about 10 dynes/cm^2, and cause considerable resuspension and northward transport of Yukon-derived materials.

---

* The full text of Appendix D is available as: Cacchione, R. D., and D. E. Drake. 1980. Storm-generated sediment transport on the Bering Sea shelf, Alaska. Geophys. Res. Lett.

APPENDIX E.

Bottom Currents on the Yukon Prodelta, July 8–September 25, 1977

The data were obtained by the electromagnetic current sensors on the GEOPROBE tripod. The raw data consist of "burst" measurements of horizontal current speeds taken once per second for 60 consecutive seconds each hour.

STATISTICS AND HISTOGRAMS OF CURRENTS AT CM1 - GEOPROBE, NS77
LOCATION = LAT 64 00N, LONG 165 00W, DEPTH = 17.5 METERS
OBSERVATION PERIOD = 0000 8 JUL 77 TO 2300 25 SEP 77 (80.0 DAYS)
N = 1920 DT = 1.00 HOURS, UNITS = (CM/SEC)

	MEAN	VARIANCE	ST-DEV	SKEW	KURT	MAX	MIN
S	8.93	25.96	5.10	0.622	2.862	28.18	0.03
U	2.14	78.95	8.89	0.279	2.281	28.01	-18.94
V	1.60	19.53	4.42	0.920	4.804	21.92	-16.12

S = SPEED
U = EAST-WEST COMPONENT OF VELOCITY, EAST =POSITIVE U
V = NORTH-SOUTH COMPONENT OF VELOCITY, NORTH = POSITIVE V

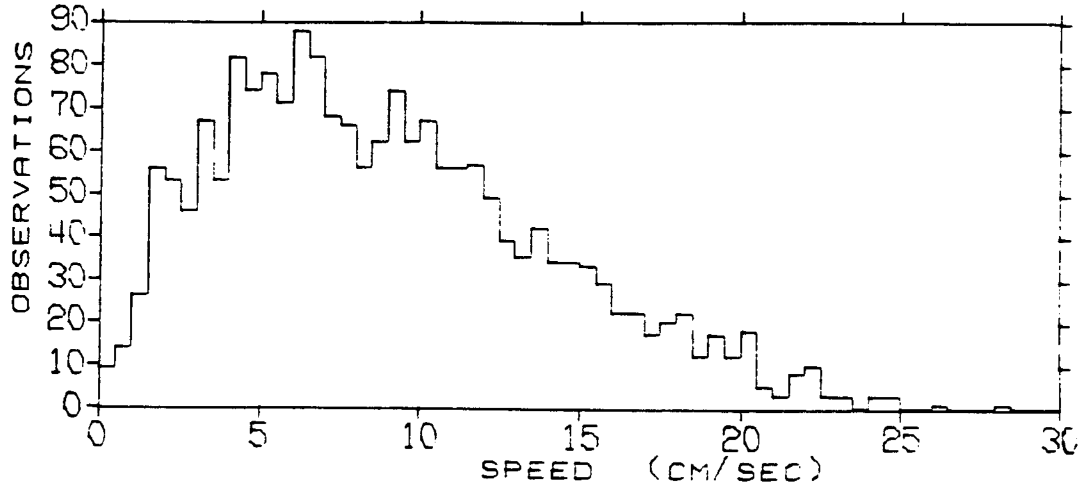

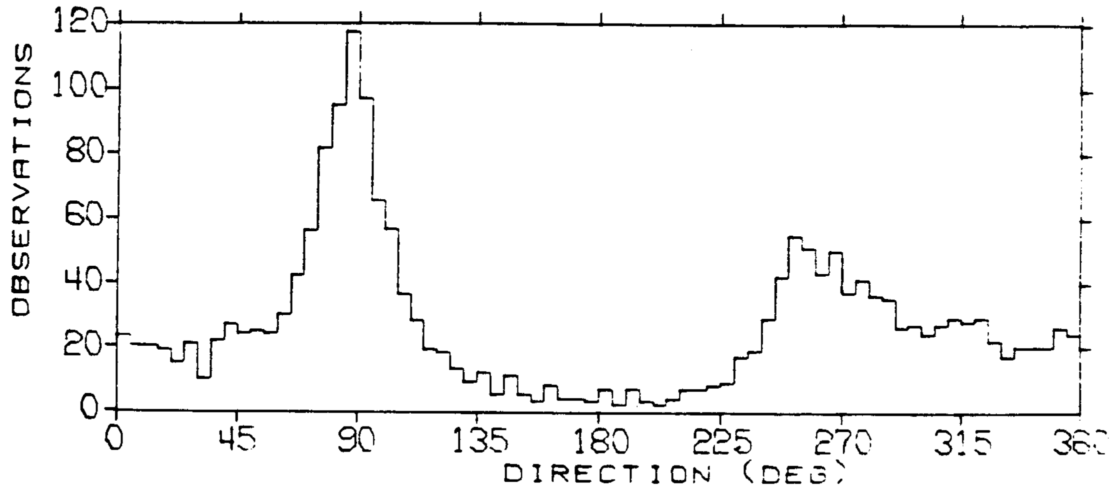

TIME SERIES OF VECTOR AVERAGED CURRENTS AT CM1 - GEOPROBE, NS77
LOCATION = LAT 64 00N, LONG 165 00W, DEPTH = 17.5 METERS
OBSERVATION PERIOD = 0000 8 JUL 77 TO 2300 27 JUL 77 (20.0 DAYS)
AVERAGING INTERVAL = 1.0 HOURS (1 POINTS)

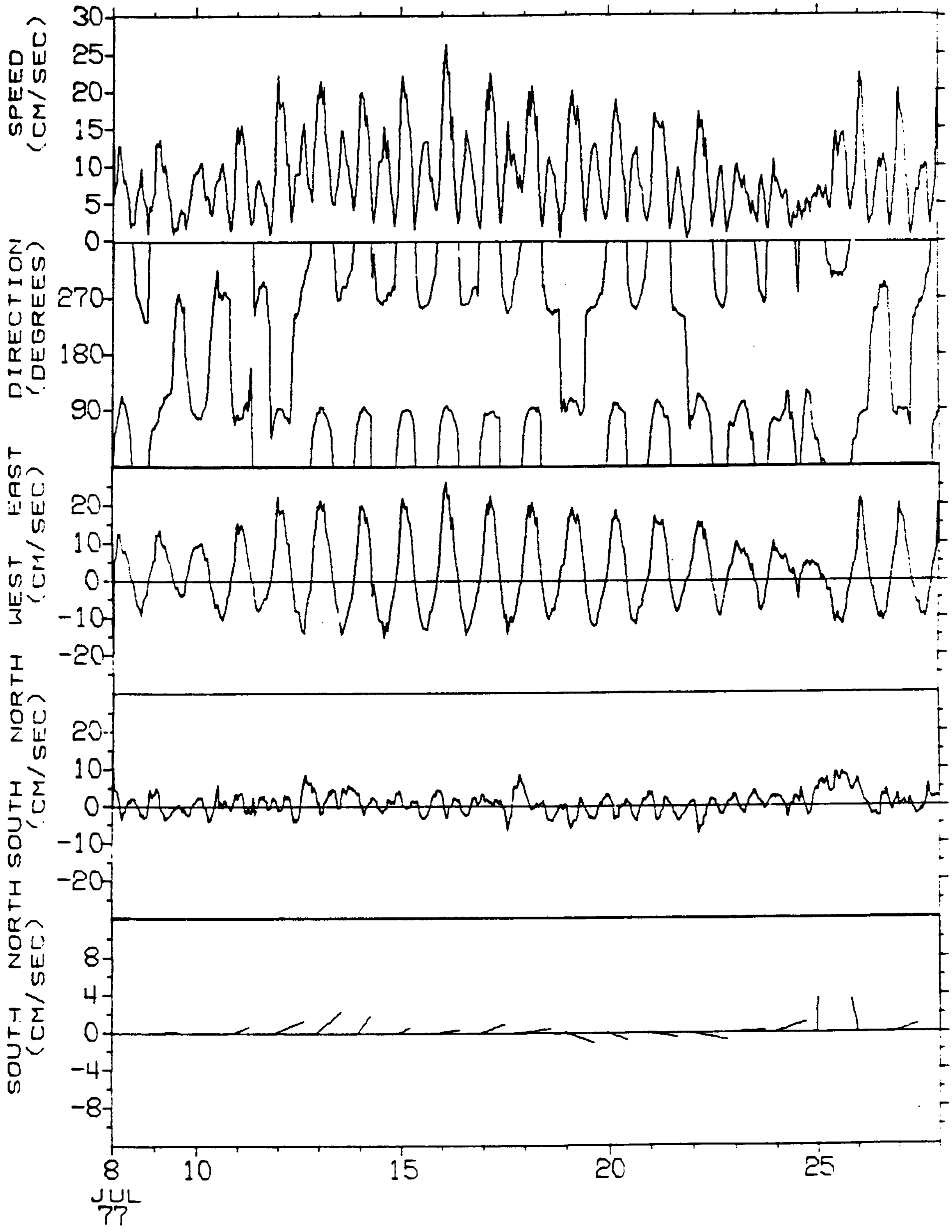

TIME SERIES OF VECTOR AVERAGED CURRENTS AT CM1 - GEOPROBE, NS77
LOCATION = LAT 64 00N, LONG 165 00W, DEPTH = 17.5 METERS
OBSERVATION PERIOD = 0000 28 JUL 77 TO 2300 16 AUG 77 (20.0 DAYS)
AVERAGING INTERVAL = 1.0 HOURS (1 POINTS)

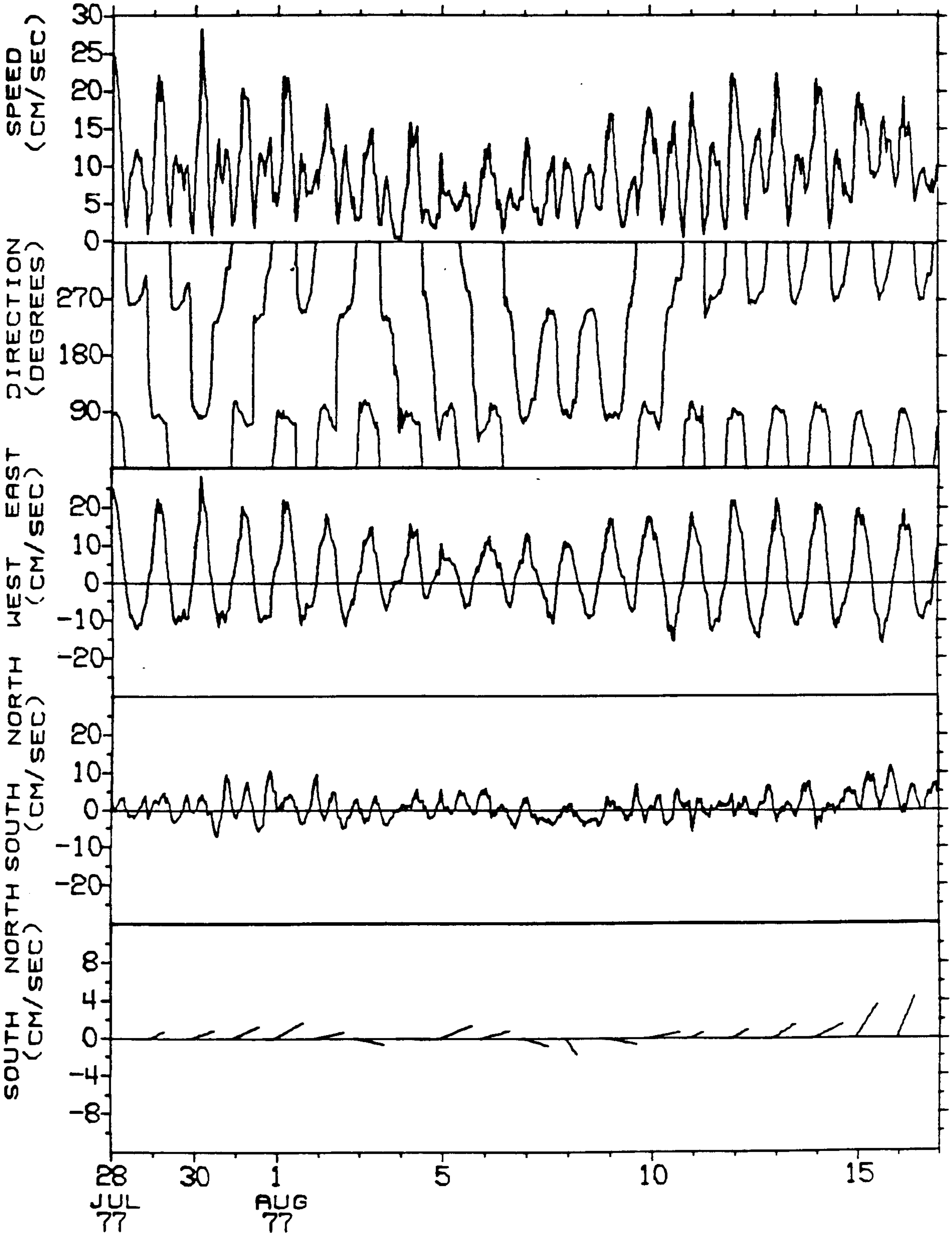

TIME SERIES OF VECTOR AVERAGED CURRENTS AT CM1 - GEOPROBE, NS77
LOCATION = LAT 64 00N, LONG 165 00W, DEPTH = 17.5 METERS
OBSERVATION PERIOD = 0000 17 AUG 77 TO 2300 5 SEP 77 (20.0 DAYS)
AVERAGING INTERVAL = 1.0 HOURS (1 POINTS)

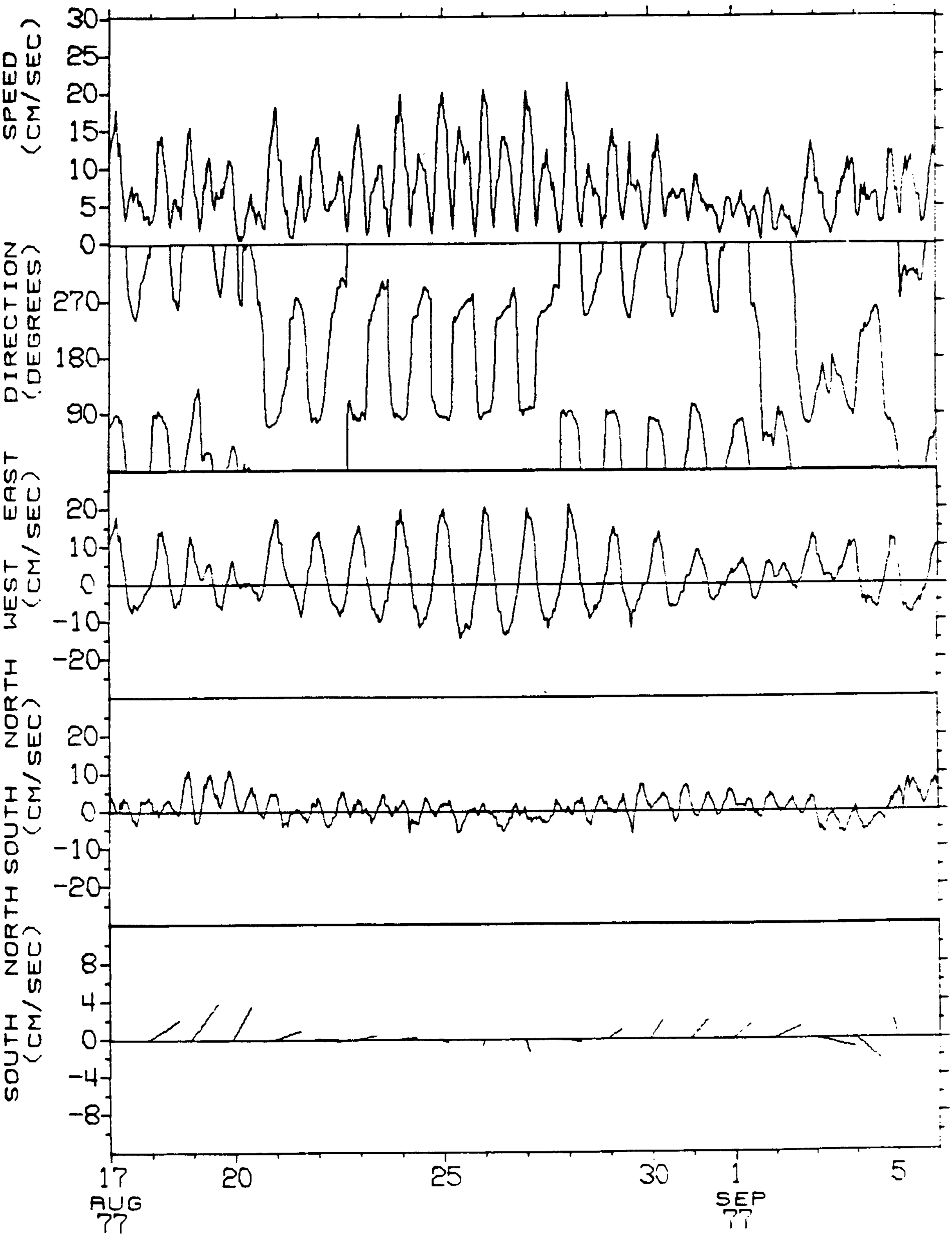

TIME SERIES OF VECTOR AVERAGED CURRENTS AT CM1 - GEOPROBE, NS77
LOCATION = LAT 64 00N, LONG 165 00W, DEPTH = 17.5 METERS
OBSERVATION PERIOD = 0000 6 SEP 77 TO 2300 25 SEP 77 (20.0 DAYS)
AVERAGING INTERVAL = 1.0 HOURS (1 POINTS)

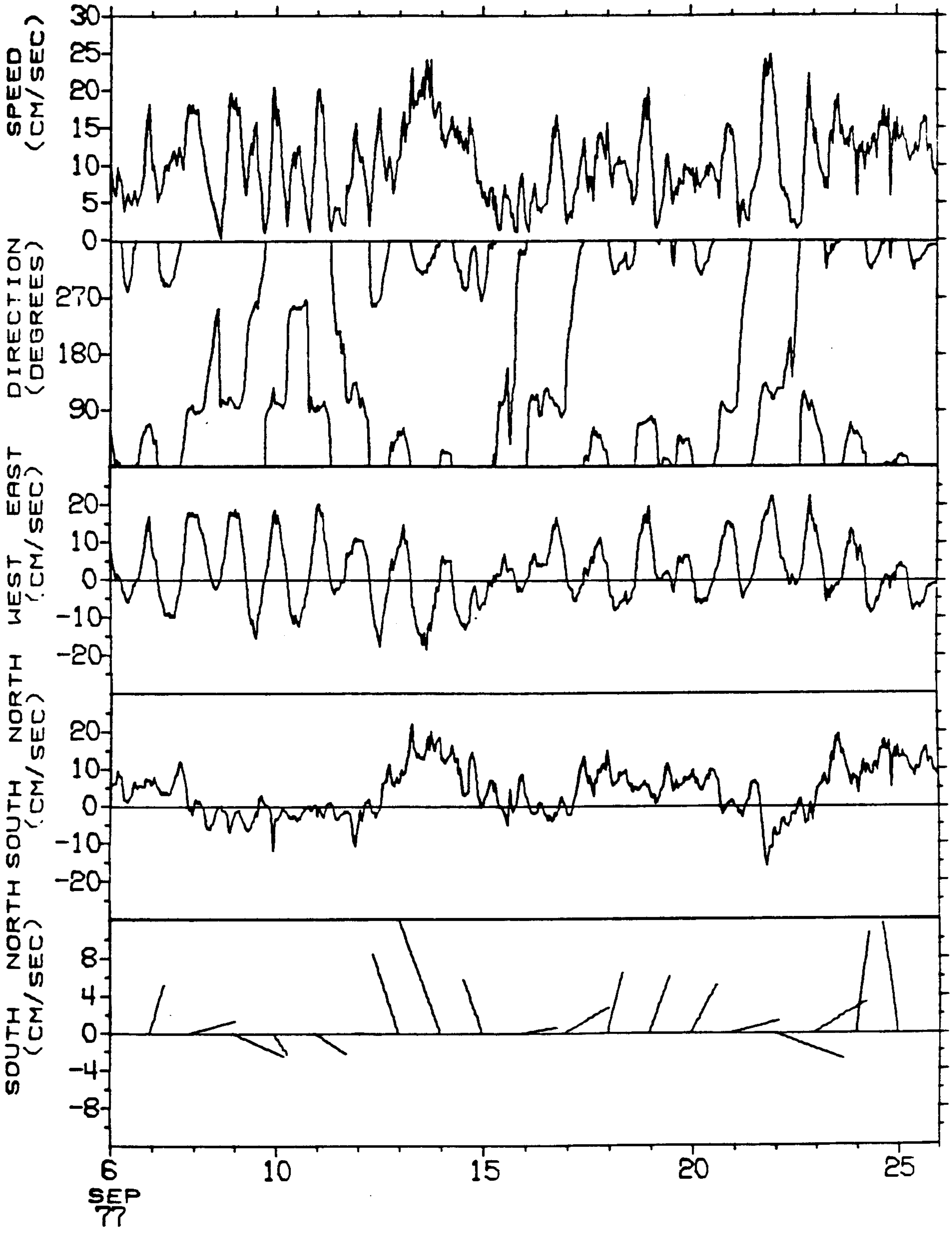

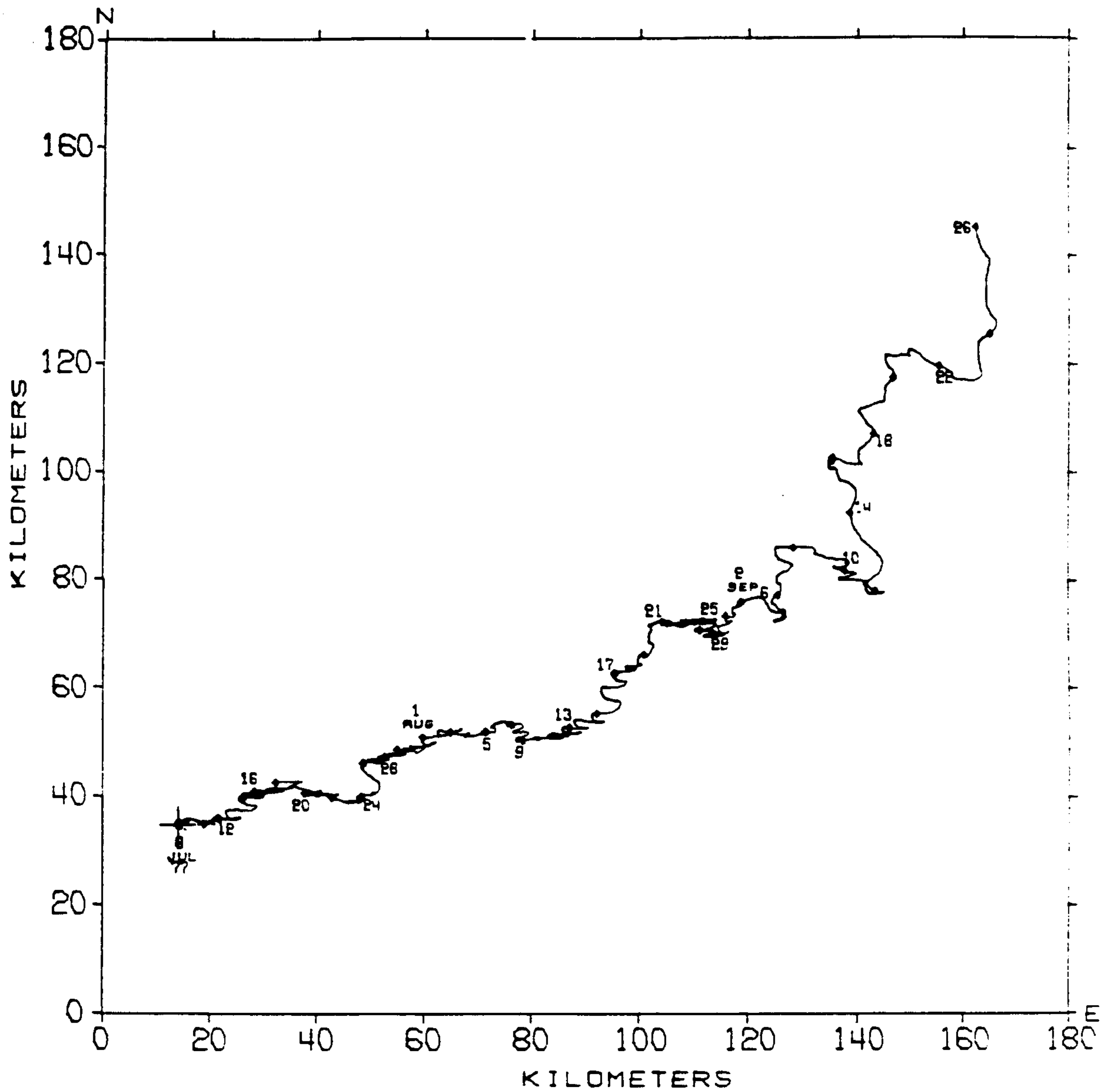

PROGRESSIVE VECTOR DIAGRAM OF CURRENTS AT CM1 - GEOPROBE, NS77
LOCATION = LAT 64 00N, LONG 165 00W, DEPTH = 17.5 METERS
OBSERVATION PERIOD = 0000 8 JUL 77 TO 2300 25 SEP 77 (80.0 DAYS)
◆ EVERY 2.0 DAYS BEGINNING AT 0000 8 JUL 77

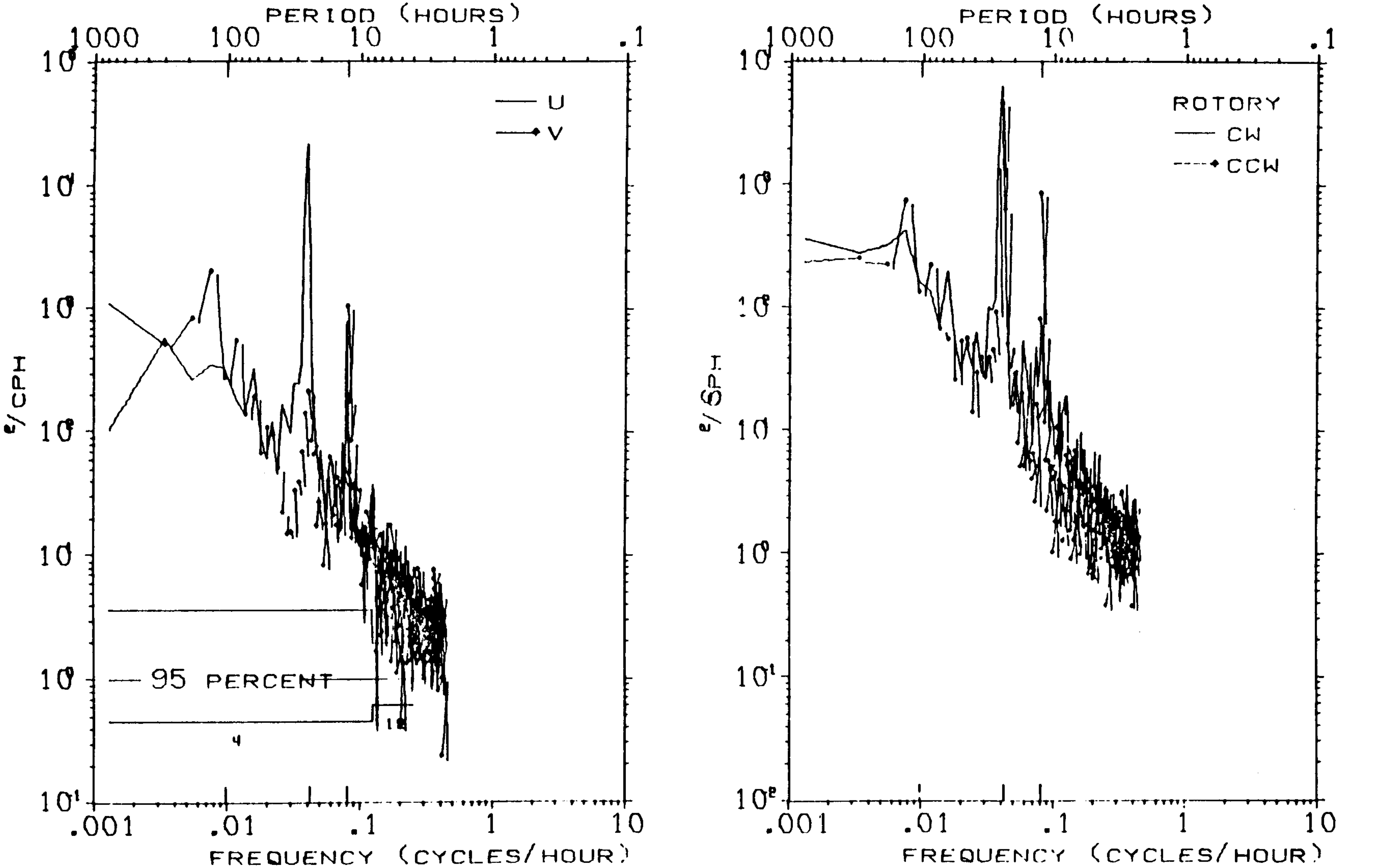

U, V AND ROTORY SPECTRA OF CURRENTS AT CM1 - GEOPROBE, NS77
LOCATION = LAT 64 00N, LONG 165 00W, DEPTH = 17.5 METERS
OBSERVATION PERIOD = 0000 8 JUL 77 TO 2300 25 SEP 77 (80.0 DAYS)
N = 1920, DT = 1.0 HOURS, SMOOTHING - DANIELL WINDOW

KINETIC ENERGY SPECTRUM OF CURRENTS AT CM1 - GEOPROBE, NS77
LOCATION = LAT 64 00N, LONG 165 00W, DEPTH = 17.5 METERS
OBSERVATION PERIOD = 0000 8 JUL 77 TO 2300 25 SEP 77 (80.0 DAYS)
N = 1920, DT = 1.0 HOURS, SMOOTHING - DANIELL WINDOW

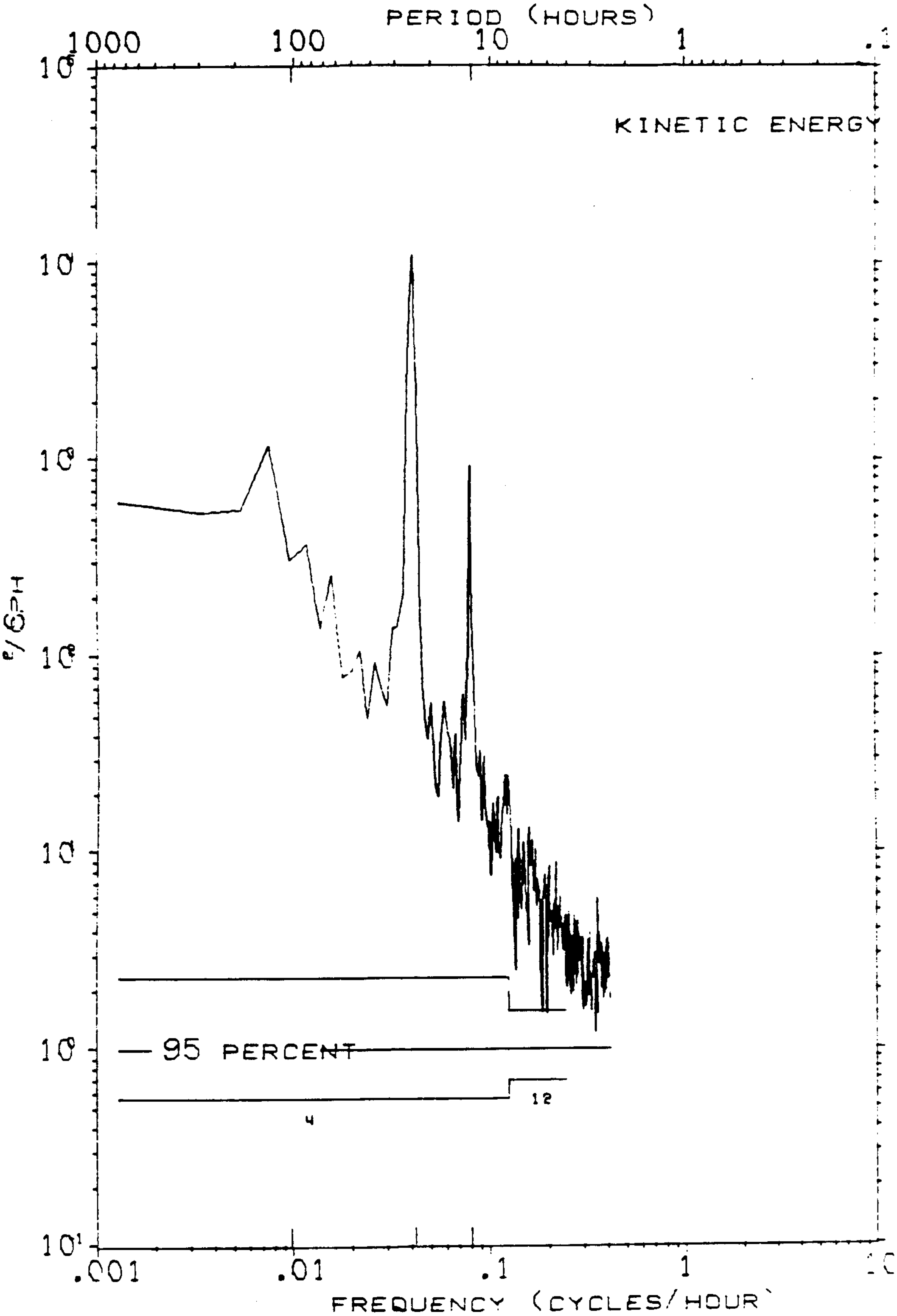

STATISTICS AND HISTOGRAMS OF CURRENTS AT CM2 - GEOPROBE, NS77
LOCATION = LAT 64 00N, LONG 165 00W, DEPTH = 17.5 METERS
OBSERVATION PERIOD = 0000 8 JUL 77 TO 2300 25 SEP 77 (80.0 DAYS)
N = 1920 DT = 1.00 HOURS, UNITS = (CM/SEC)

	MEAN	VARIANCE	ST-DEV	SKEW	KURT	MAX	MIN
S	12.11	40.29	6.35	0.465	2.896	36.99	0.23
U	0.96	122.97	11.09	0.173	2.144	32.11	-23.48
V	2.81	55.16	7.43	0.684	4.509	35.84	-27.62

S = SPEED
U = EAST-WEST COMPONENT OF VELOCITY, EAST =POSITIVE U
V = NORTH-SOUTH COMPONENT OF VELOCITY, NORTH = POSITIVE V

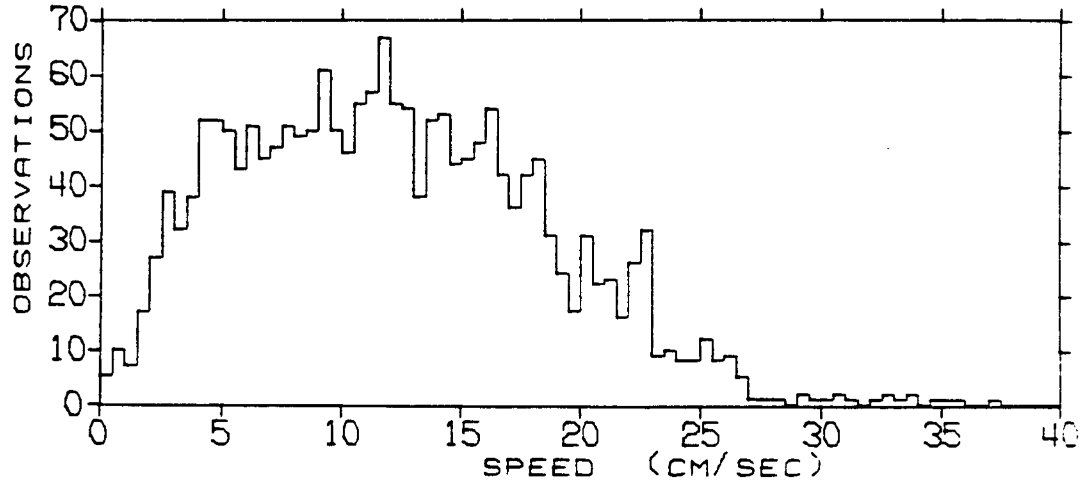

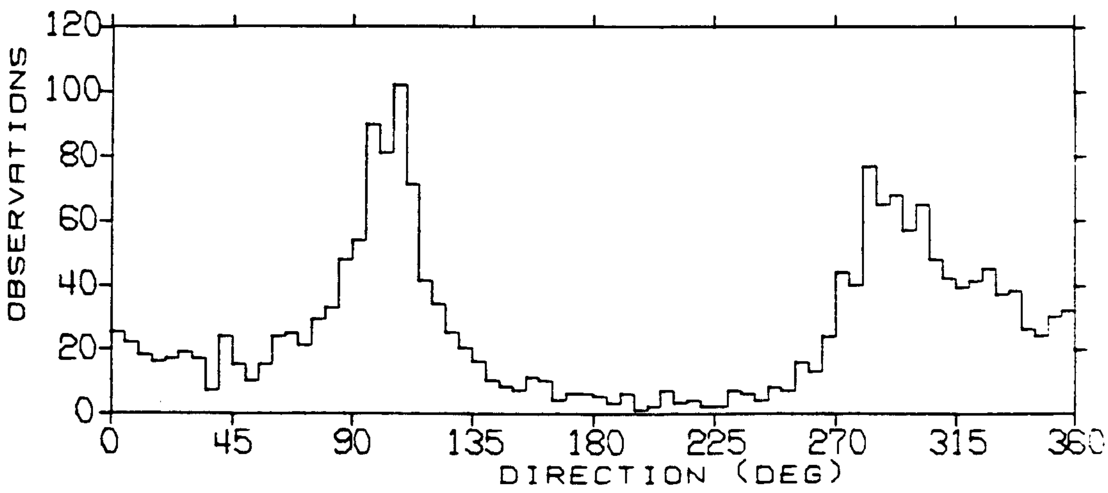

TIME SERIES OF VECTOR AVERAGED CURRENTS AT CM2 - GEOPROBE, NS77
LOCATION = LAT 64 00N, LONG 165 00W, DEPTH = 17.5 METERS
OBSERVATION PERIOD = 0000 8 JUL 77 TO 2300 27 JUL 77 (20.0 DAYS)
AVERAGING INTERVAL = 1.0 HOURS (1 POINTS)

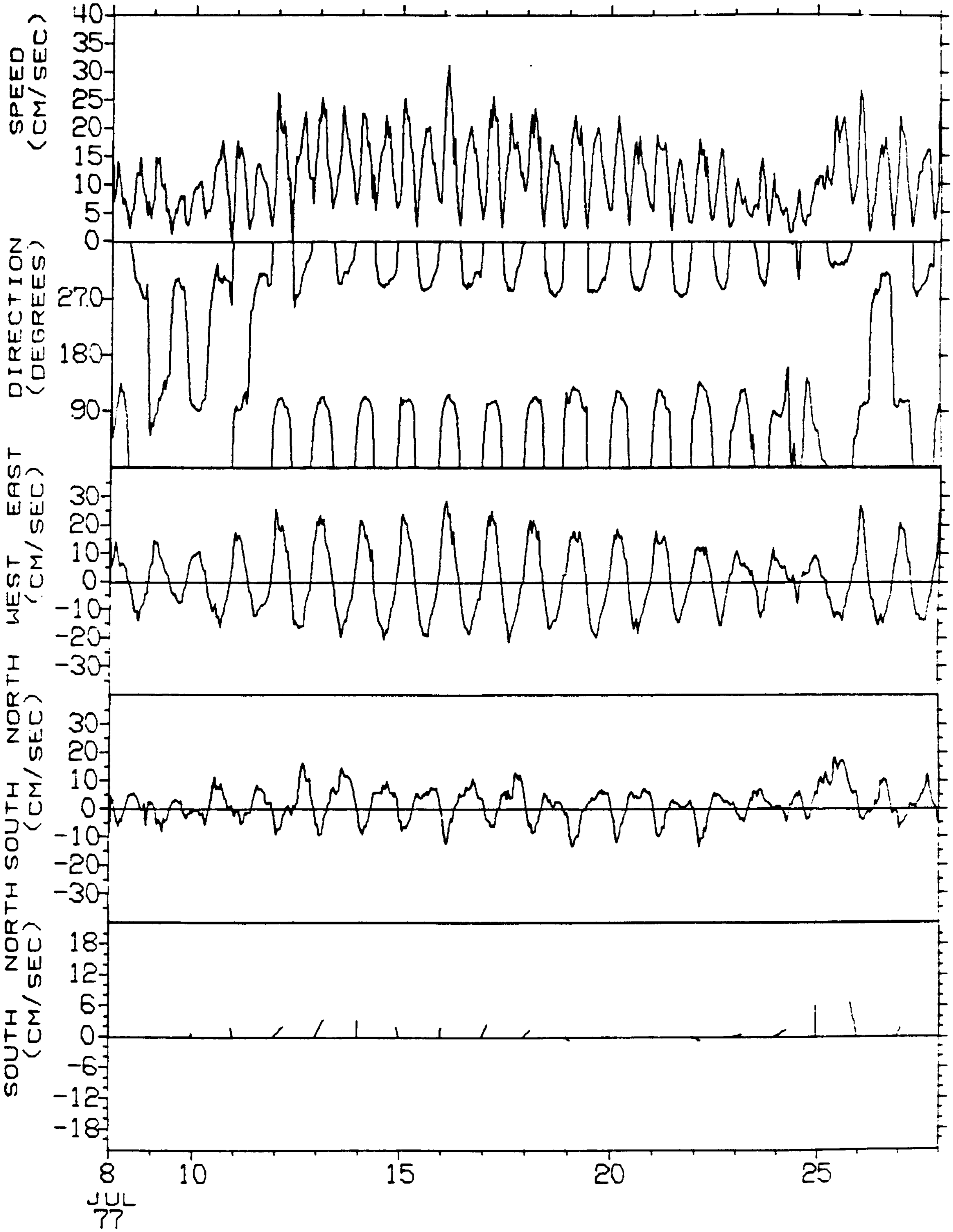

TIME SERIES OF VECTOR AVERAGED CURRENTS AT CM2 - GEOPROBE, NS77
LOCATION = LAT 64 00N, LONG 165 00W, DEPTH = 17.5 METERS
OBSERVATION PERIOD = 0000 28 JUL 77 TO 2300 16 AUG 77 (20.0 DAYS)
AVERAGING INTERVAL = 1.0 HOURS (1 POINTS)

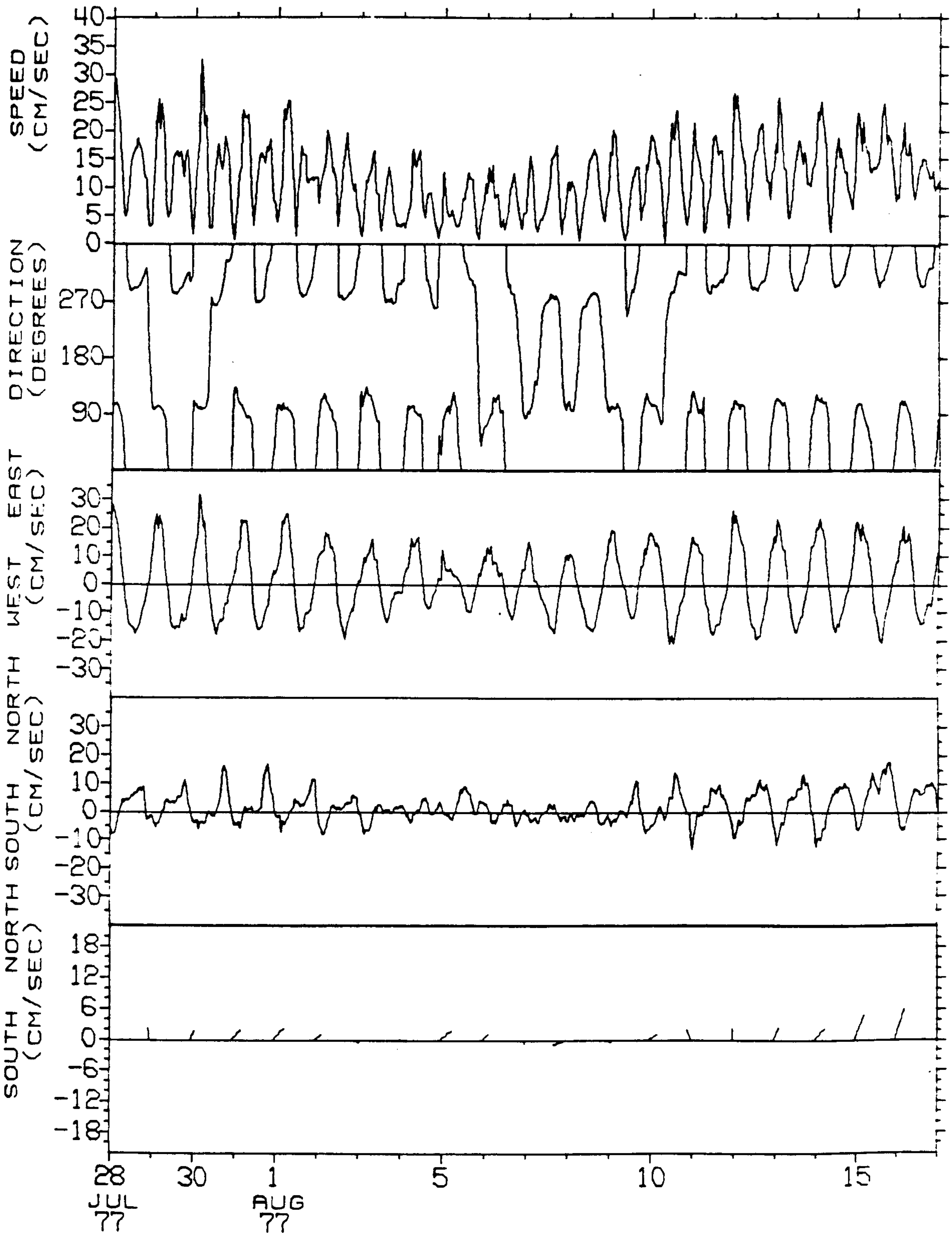

TIME SERIES OF VECTOR AVERAGED CURRENTS AT CM2 - GEOPROBE, NS77
LOCATION = LAT 64 00N, LONG 165 00W, DEPTH = 17.5 METERS
OBSERVATION PERIOD = 0000 17 AUG 77 TO 2300 5 SEP 77 (20.0 DAYS)
AVERAGING INTERVAL = 1.0 HOURS (1 POINTS)

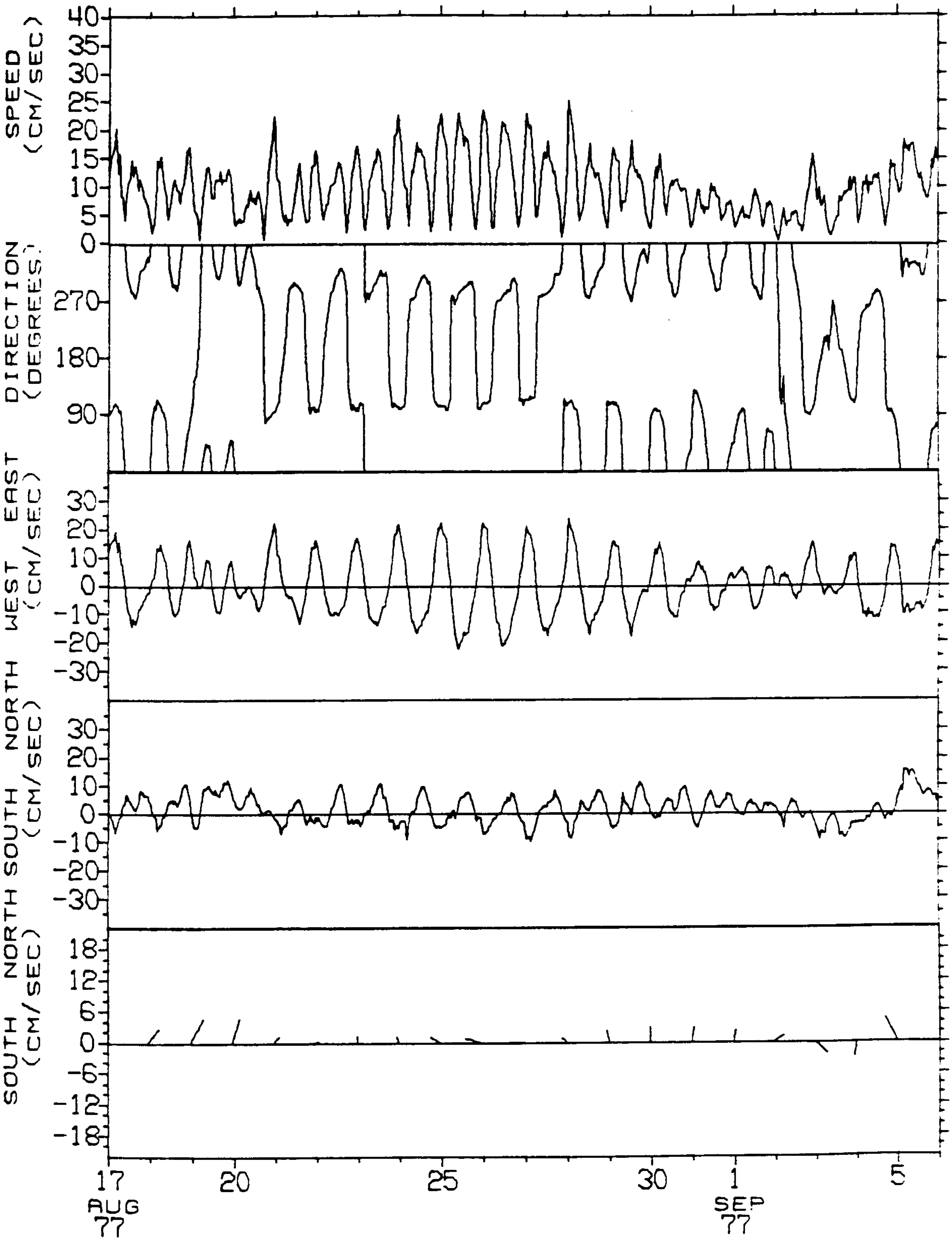

TIME SERIES OF VECTOR AVERAGED CURRENTS AT CM2 - GEOPROBE, NS77
LOCATION = LAT 64 00N, LONG 165 00W, DEPTH = 17.5 METERS
OBSERVATION PERIOD = 0000 6 SEP 77 TO 2300 25 SEP 77 (20.0 DAYS)
AVERAGING INTERVAL = 1.0 HOURS (1 POINTS)

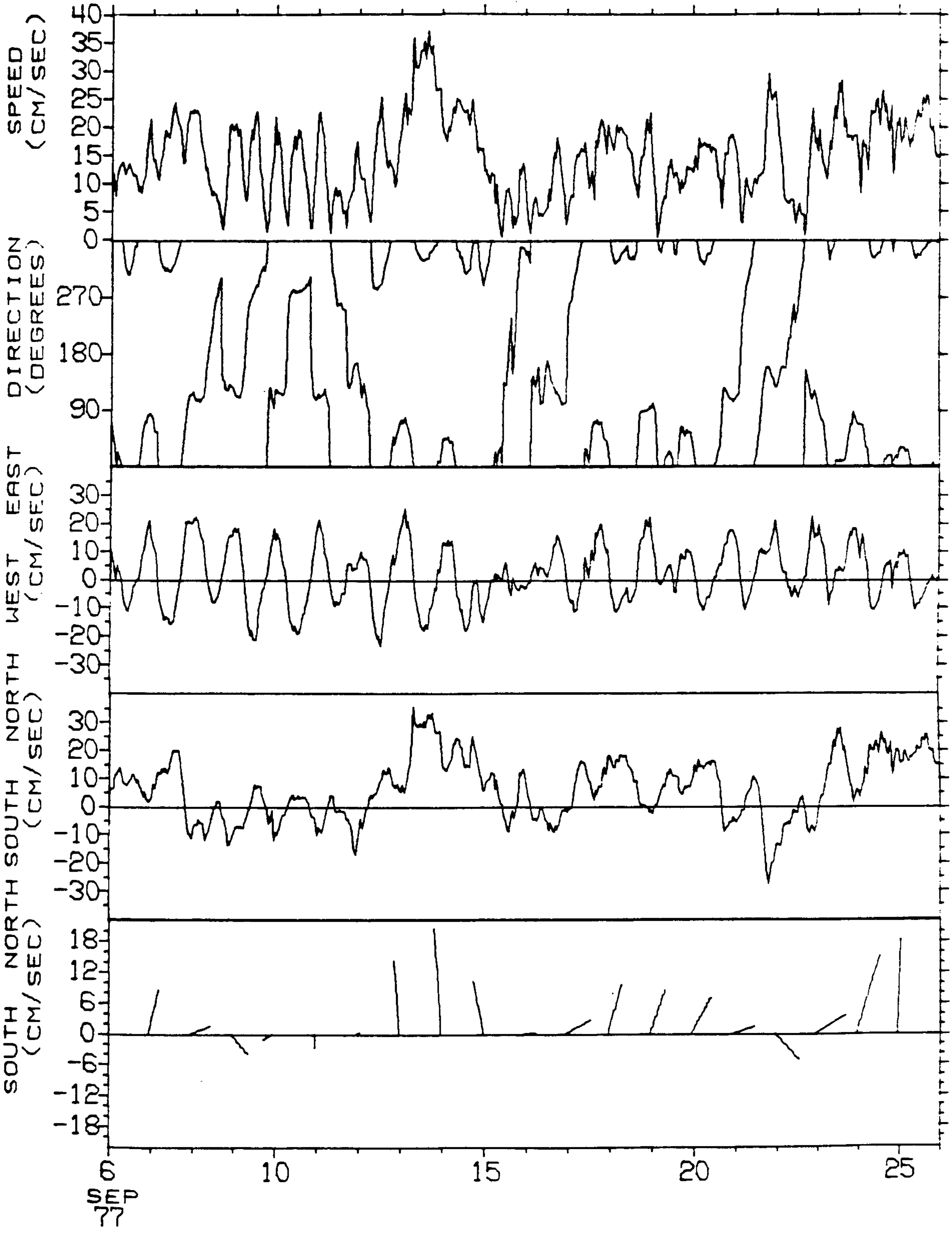

PROGRESSIVE VECTOR DIAGRAM OF CURRENTS AT CM2 - GEOPROBE, NS77
LOCATION = LAT 64 00N, LONG 165 00W, DEPTH = 17.5 METERS
OBSERVATION PERIOD = 0000 8 JUL 77 TO 2300 25 SEP 77 (80.0 DAYS)
• EVERY 2.0 DAYS BEGINNING AT 0000 8 JUL 77

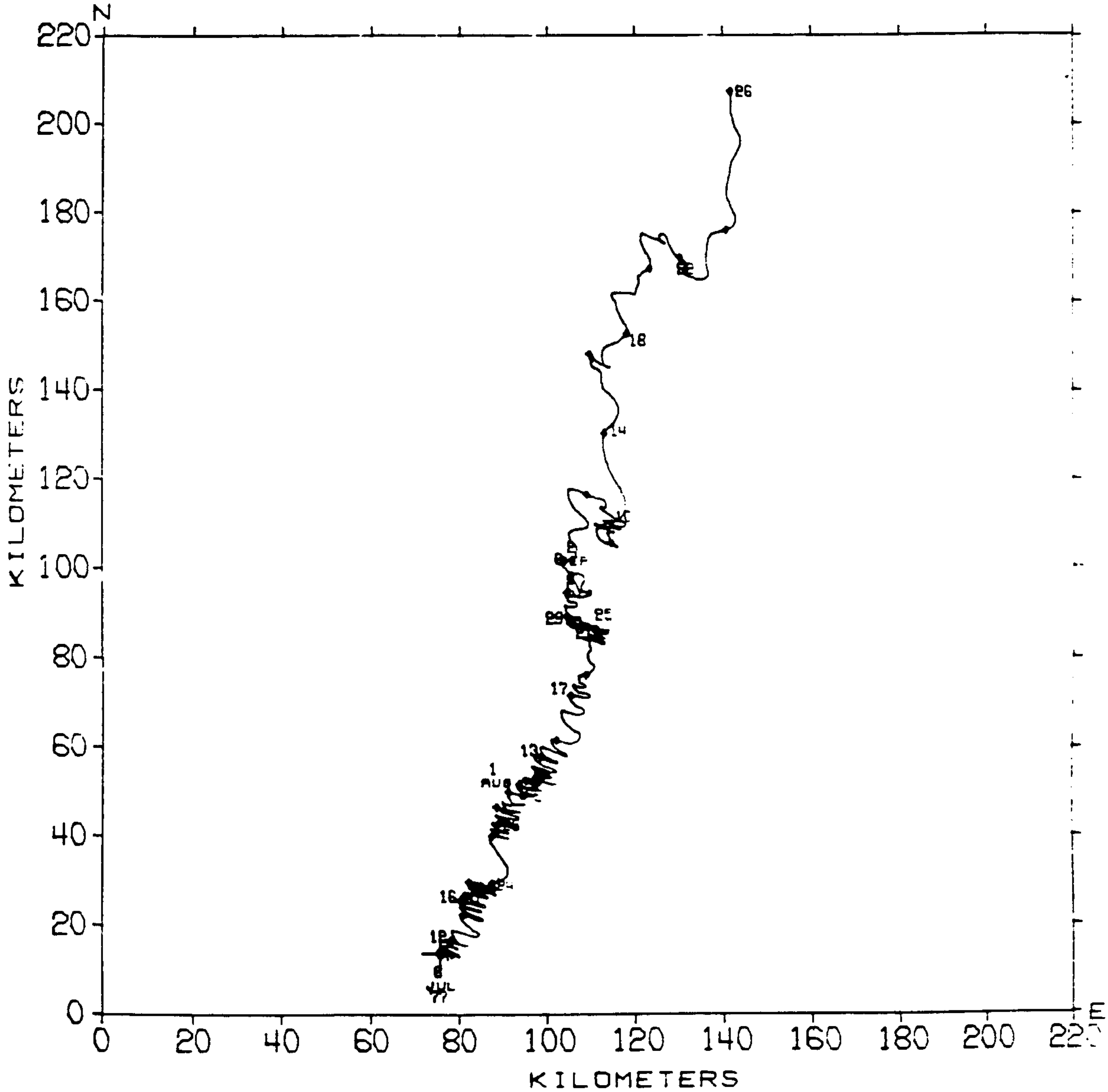

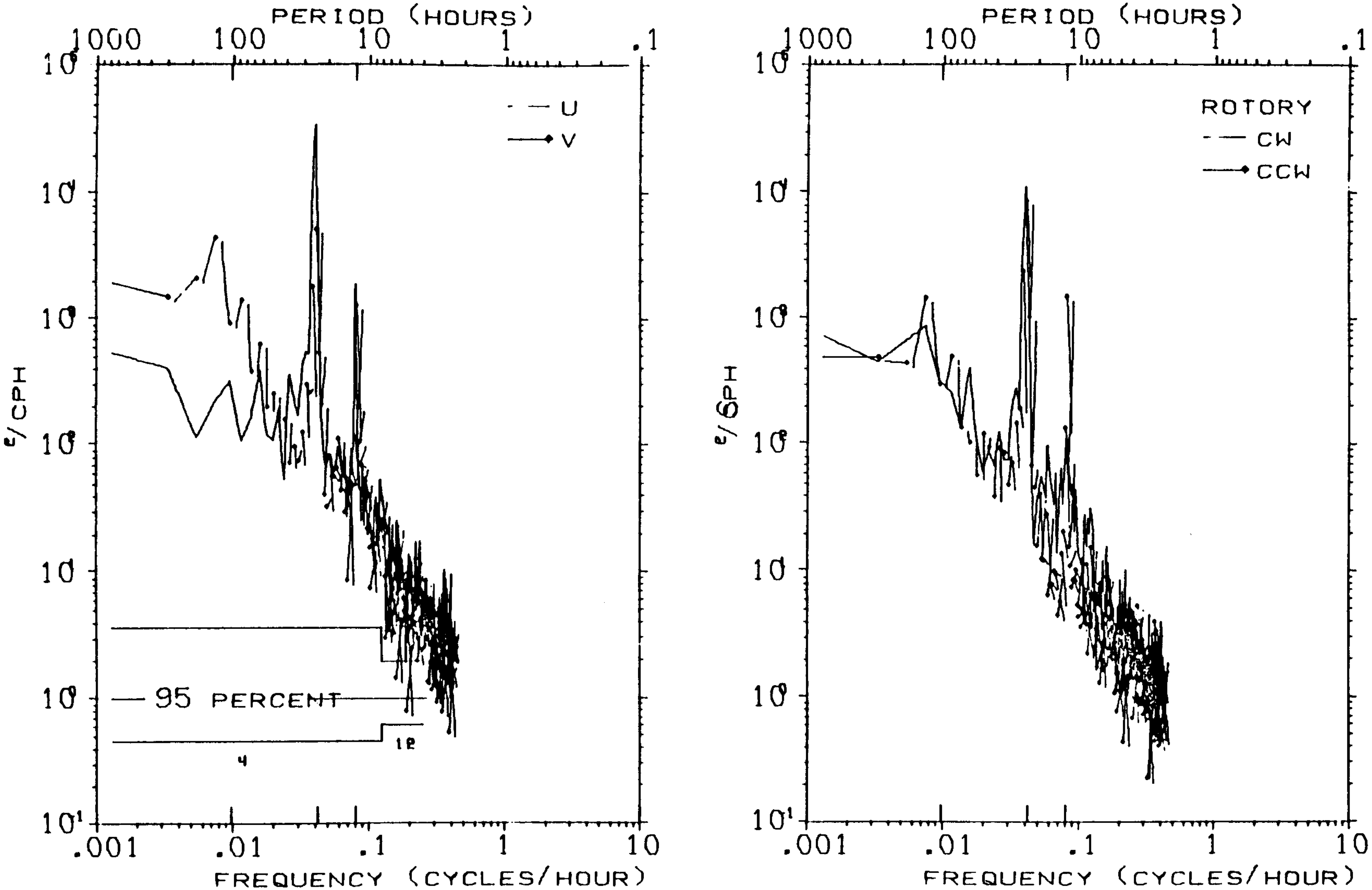

U, V AND ROTORY SPECTRA OF CURRENTS AT CM2 - GEOPROBE, NS77
LOCATION = LAT 64 00N, LONG 165 00W, DEPTH = 17.5 METERS
OBSERVATION PERIOD = 0000 8 JUL 77 TO 2300 25 SEP 77 (80.0 DAYS)
N = 1920, DT = 1.0 HOURS, SMOOTHING - DANIELL WINDOW

KINETIC ENERGY SPECTRUM OF CURRENTS AT CM2 - GEOPROBE, NS77
LOCATION = LAT 64 00N, LONG 165 00W, DEPTH = 17.5 METERS
OBSERVATION PERIOD = 0000 8 JUL 77 TO 2300 25 SEP 77 (80.0 DAYS)
N = 1920, DT = 1.0 HOURS, SMOOTHING - DANIELL WINDOW

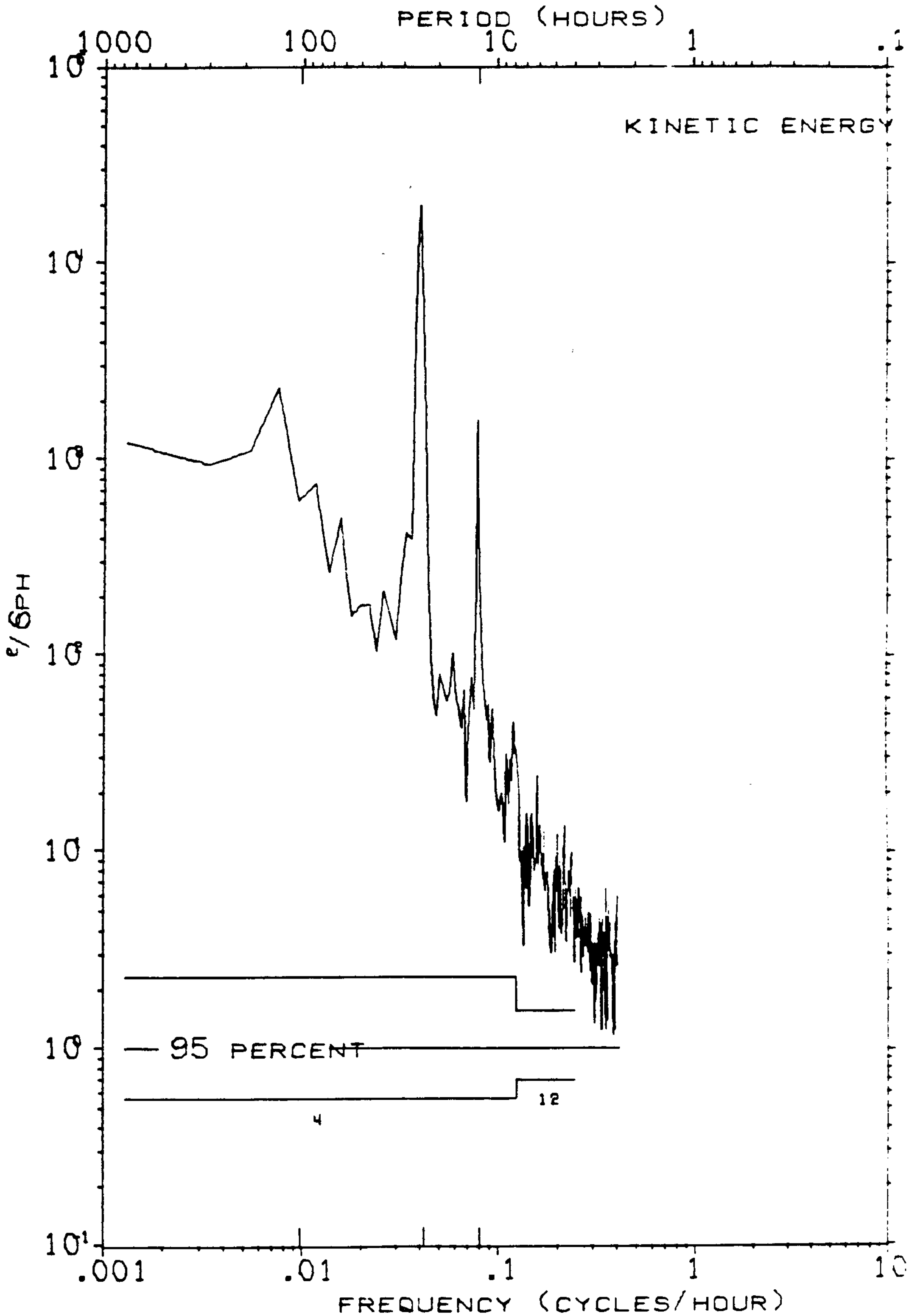

STATISTICS AND HISTOGRAMS OF CURRENTS AT CM3 - GEOPROBE, NS77
LOCATION = LAT 64 00N, LONG 165 00W, DEPTH = 17.5 METERS
OBSERVATION PERIOD = 0000 8 JUL 77 TO 2300 25 SEP 77 (80.0 DAYS)
N = 1920 DT = 1.00 HOURS, UNITS = (CM/SEC)

	MEAN	VARIANCE	ST-DEV	SKEW	KURT	MAX	MIN
S	13.00	47.84	6.92	0.558	3.020	39.68	0.66
U	1.42	155.17	12.46	0.209	2.107	34.77	-27.55
V	3.62	46.52	6.82	1.113	5.413	37.24	-23.09

S = SPEED
U = EAST-WEST COMPONENT OF VELOCITY, EAST =POSITIVE U
V = NORTH-SOUTH COMPONENT OF VELOCITY, NORTH = POSITIVE V

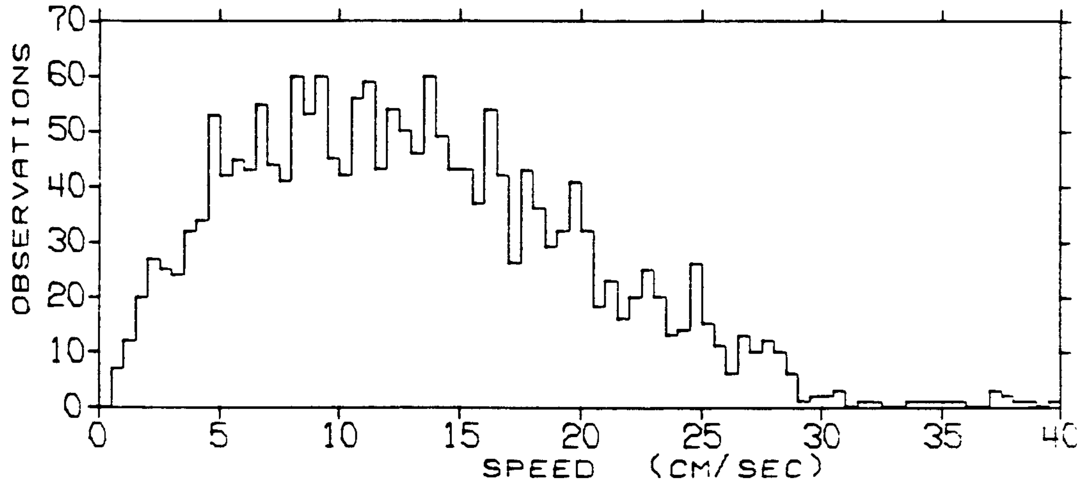

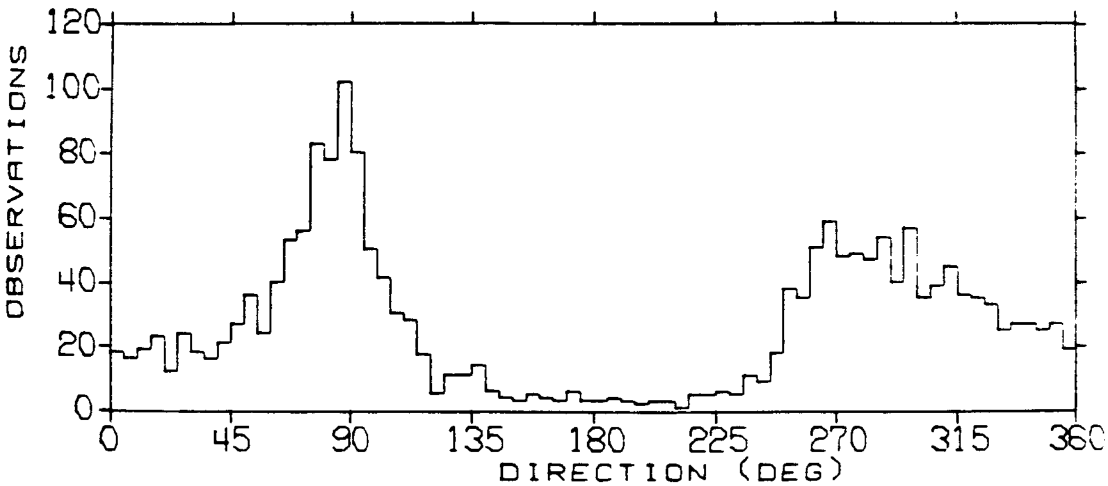

TIME SERIES OF VECTOR AVERAGED CURRENTS AT CM3 - GEOPROBE, NS77
LOCATION = LAT 64 00N, LONG 165 00W, DEPTH = 17.5 METERS
OBSERVATION PERIOD = 0000 8 JUL 77 TO 2300 27 JUL 77 (20.0 DAYS)
AVERAGING INTERVAL = 1.0 HOURS (1 POINTS)

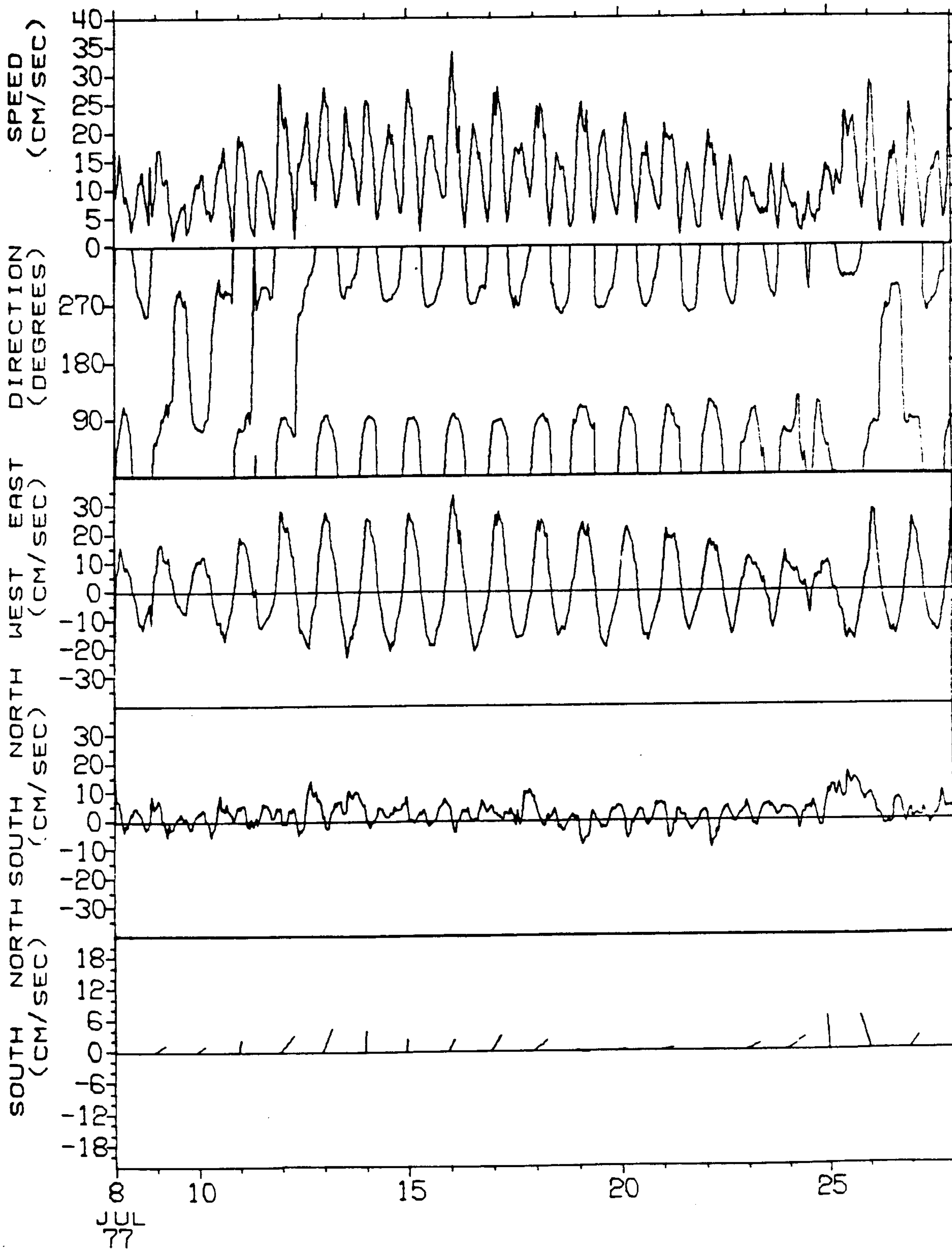

TIME SERIES OF VECTOR AVERAGED CURRENTS AT CM3 - GEOPROBE, NS77
LOCATION = LAT 64 00N, LONG 165 00W, DEPTH = 17.5 METERS
OBSERVATION PERIOD = 0000 28 JUL 77 TO 2300 16 AUG 77 (20.0 DAYS)
AVERAGING INTERVAL = 1.0 HOURS (1 POINTS)

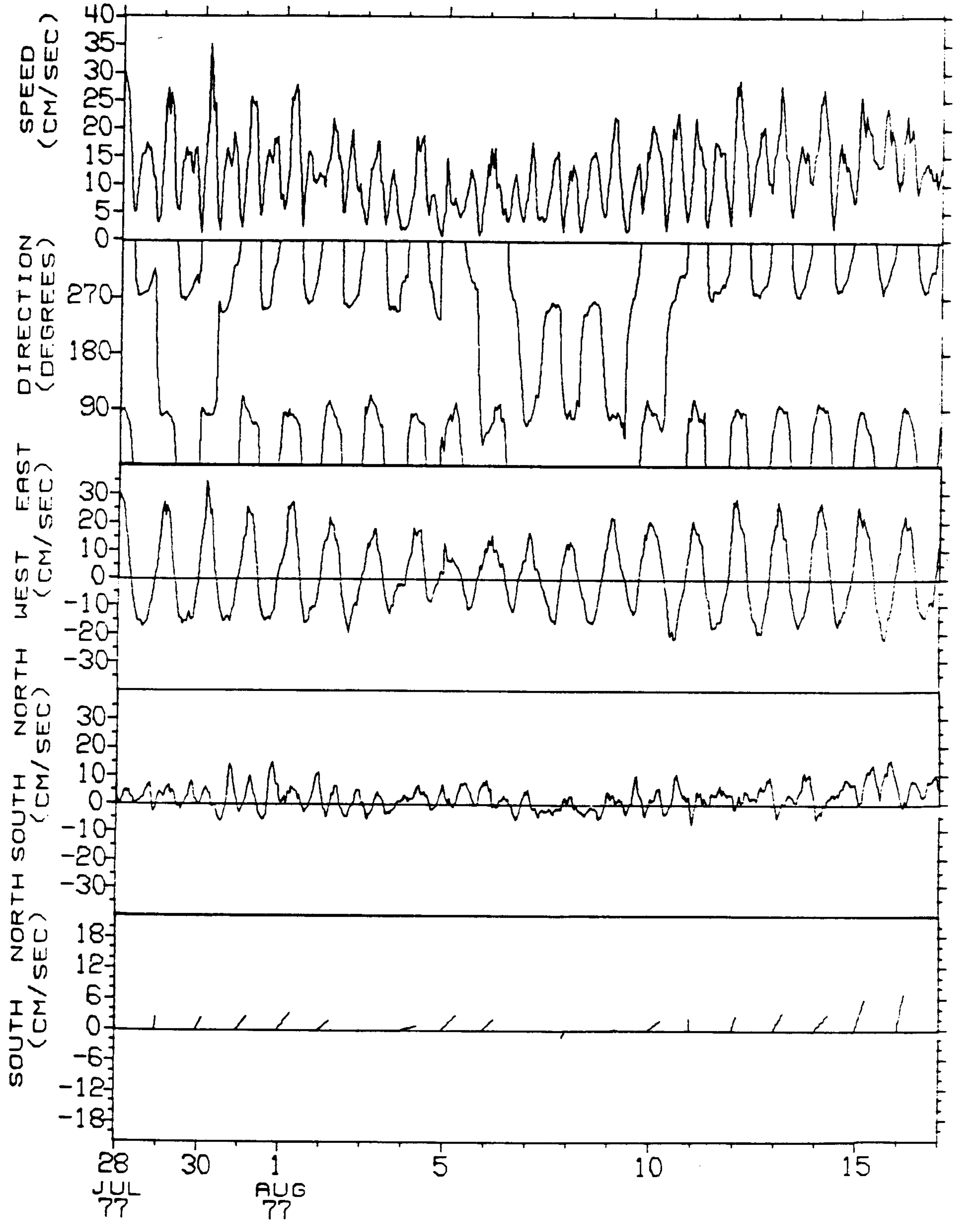

TIME SERIES OF VECTOR AVERAGED CURRENTS AT CM3 - GEOPROBE, NS77
LOCATION = LAT 64 00N, LONG 165 00W, DEPTH = 17.5 METERS
OBSERVATION PERIOD = 0000 17 AUG 77 TO 2300 5 SEP 77 (20.0 DAYS)
AVERAGING INTERVAL = 1.0 HOURS (1 POINTS)

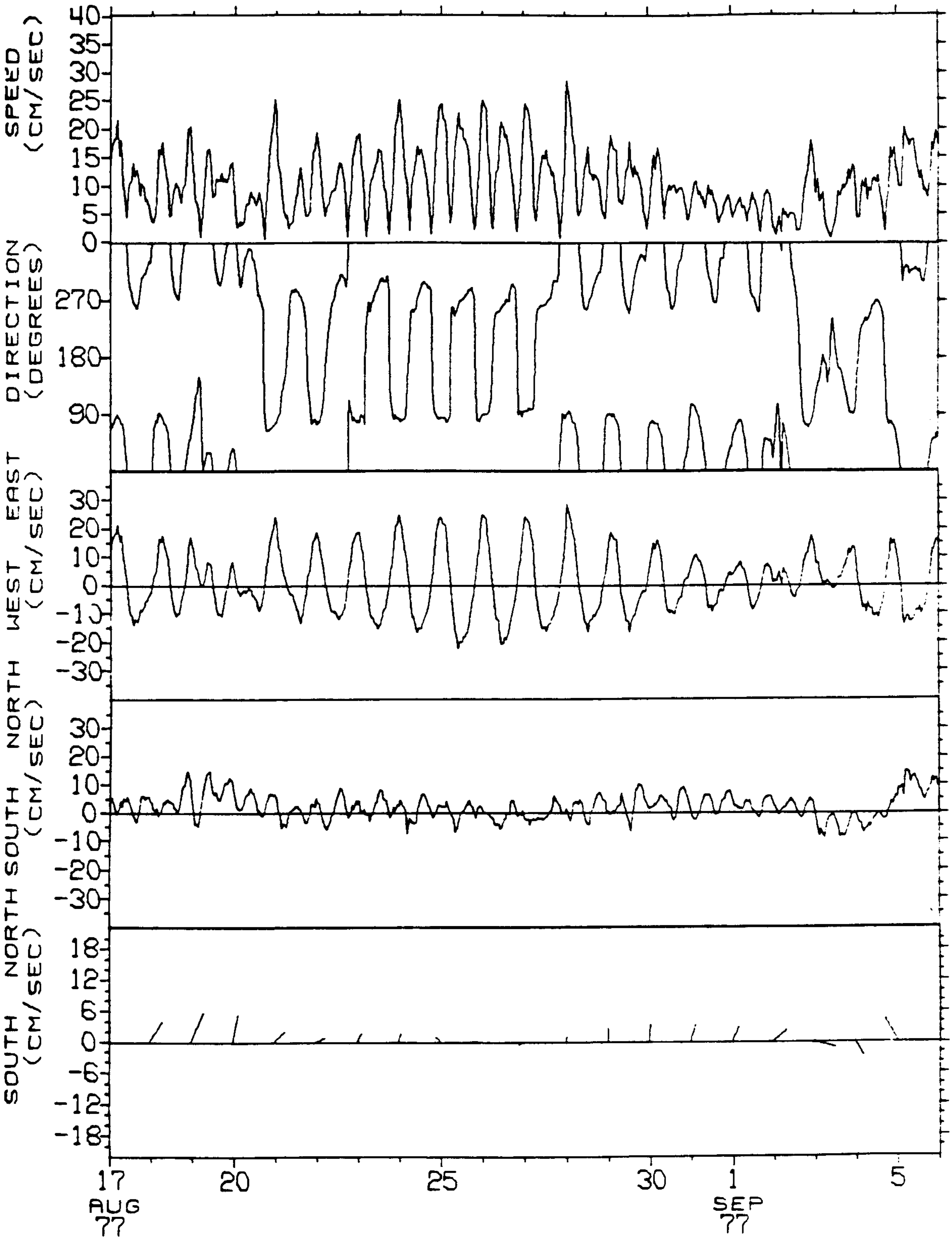

TIME SERIES OF VECTOR AVERAGED CURRENTS AT CM3 - GEOPROBE, NS77
LOCATION = LAT 64 00N, LONG 165 00W, DEPTH = 17.5 METERS
OBSERVATION PERIOD = 0000 6 SEP 77 TO 2300 25 SEP 77 (20.0 DAYS)
AVERAGING INTERVAL = 1.0 HOURS (1 POINTS)

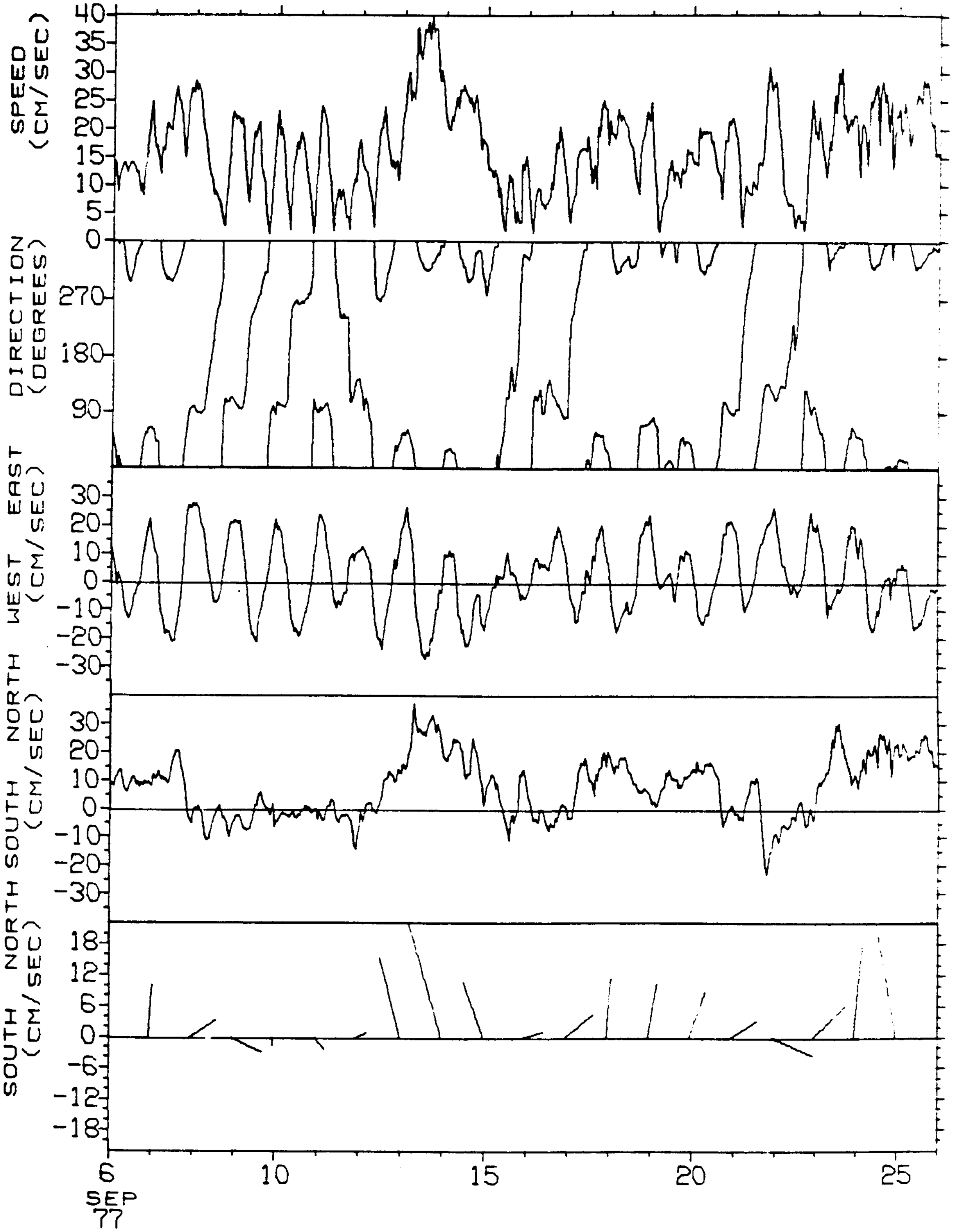

PROGRESSIVE VECTOR DIAGRAM OF CURRENTS AT CM3 - GEOPROBE, NS77
LOCATION = LAT 64 00N, LONG 165 00W, DEPTH = 17.5 METERS
OBSERVATION PERIOD = 0000 8 JUL 77 TO 2300 25 SEP 77 (80.0 DAYS)
◆ EVERY 2.0 DAYS BEGINNING AT 0000 8 JUL 77

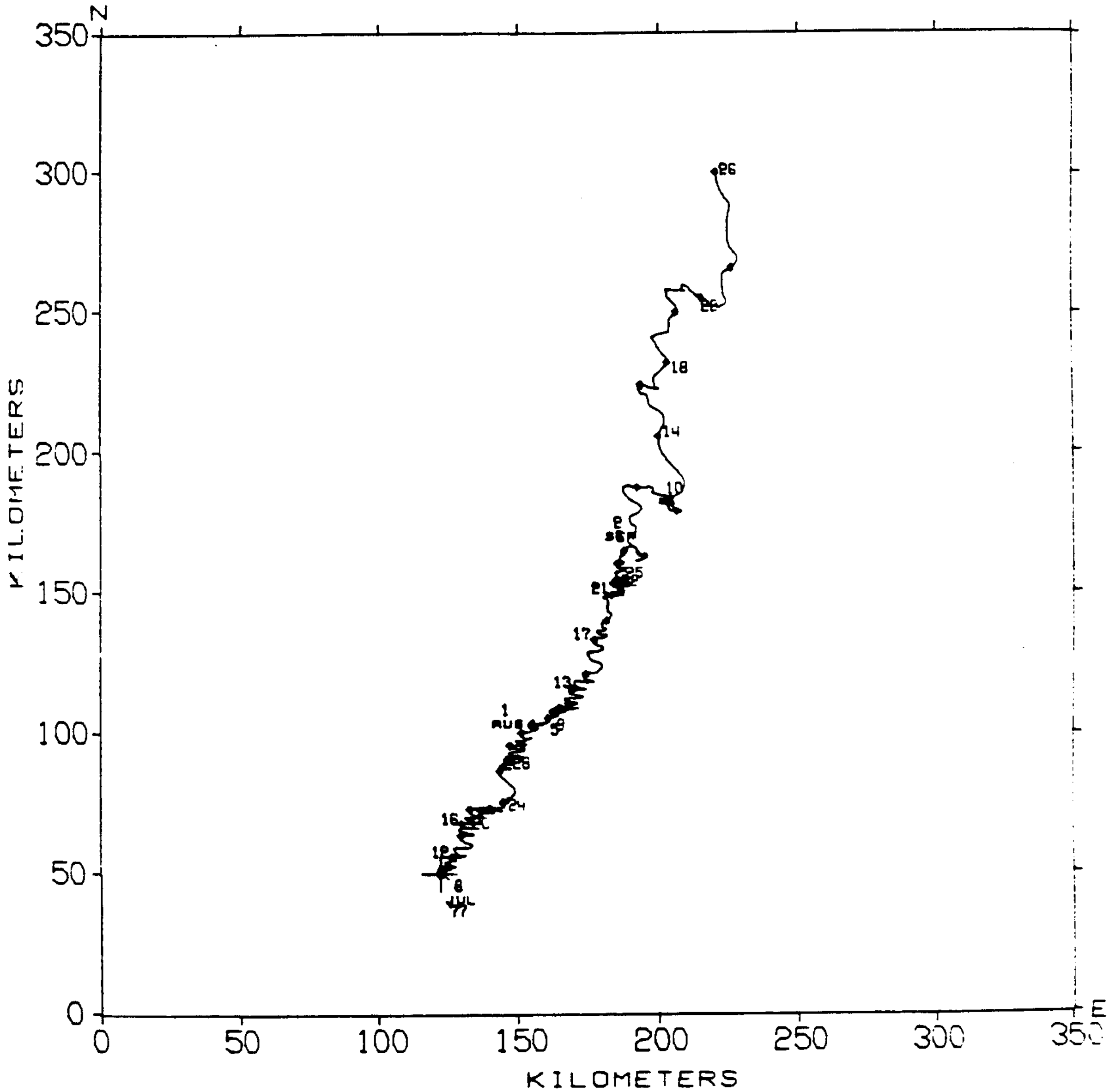

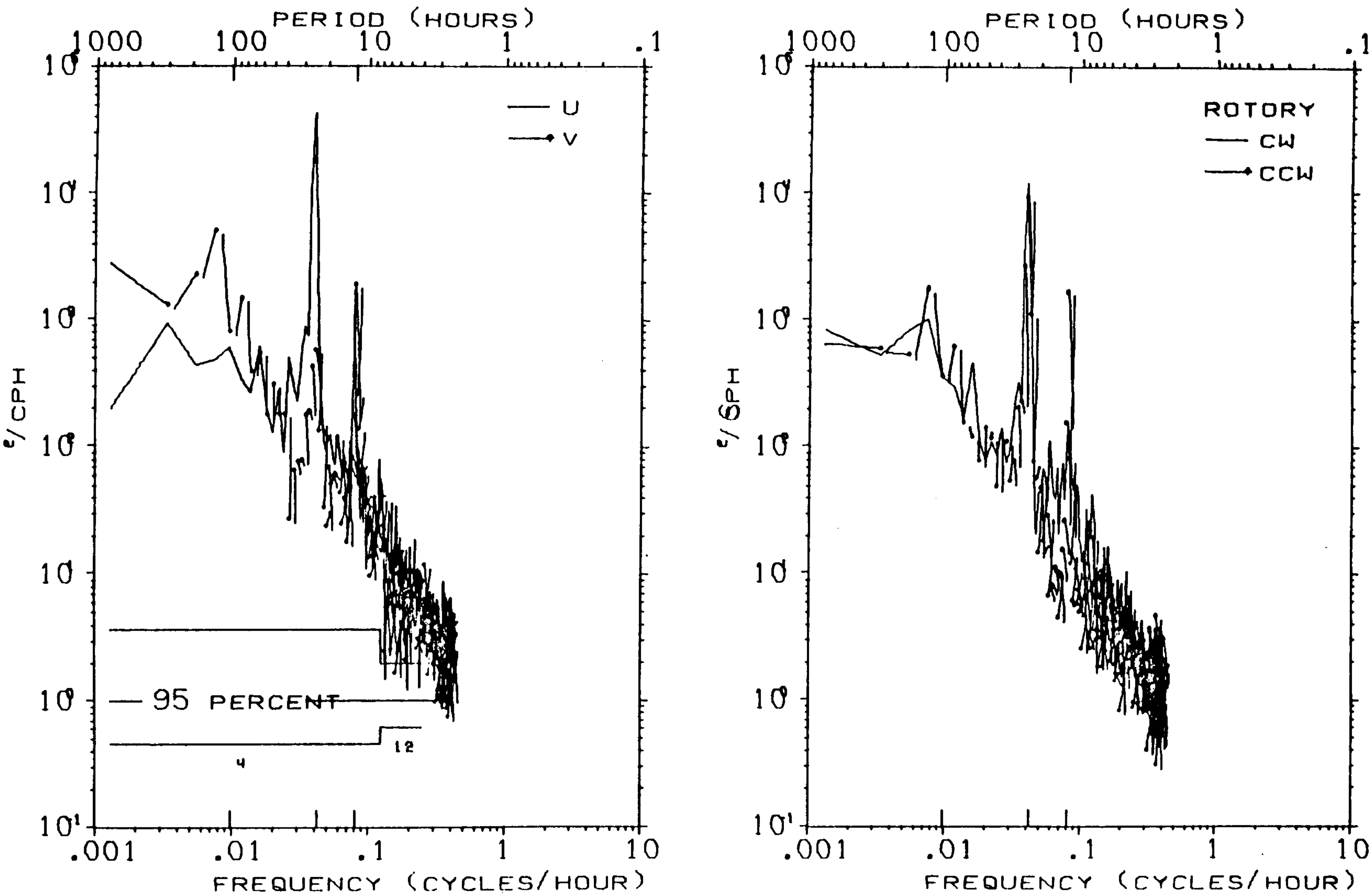

U, V AND ROTORY SPECTRA OF CURRENTS AT CM3 - GEOPROBE, NS77
LOCATION = LAT 64 00N, LONG 165 00W, DEPTH = 17.5 METERS
OBSERVATION PERIOD = 0000 8 JUL 77 TO 2300 25 SEP 77 (80.0 DAYS)
N = 1920, DT = 1.0 HOURS, SMOOTHING - DANIELL WINDOW

KINETIC ENERGY SPECTRUM OF CURRENTS AT CM3 - GEOPROBE, NS77
LOCATION = LAT 64 00N, LONG 165 00W, DEPTH = 17.5 METERS
OBSERVATION PERIOD = 0000 8 JUL 77 TO 2300 25 SEP 77 (80.0 DAYS)
N = 1920, DT = 1.0 HOURS, SMOOTHING - DANIELL WINDOW

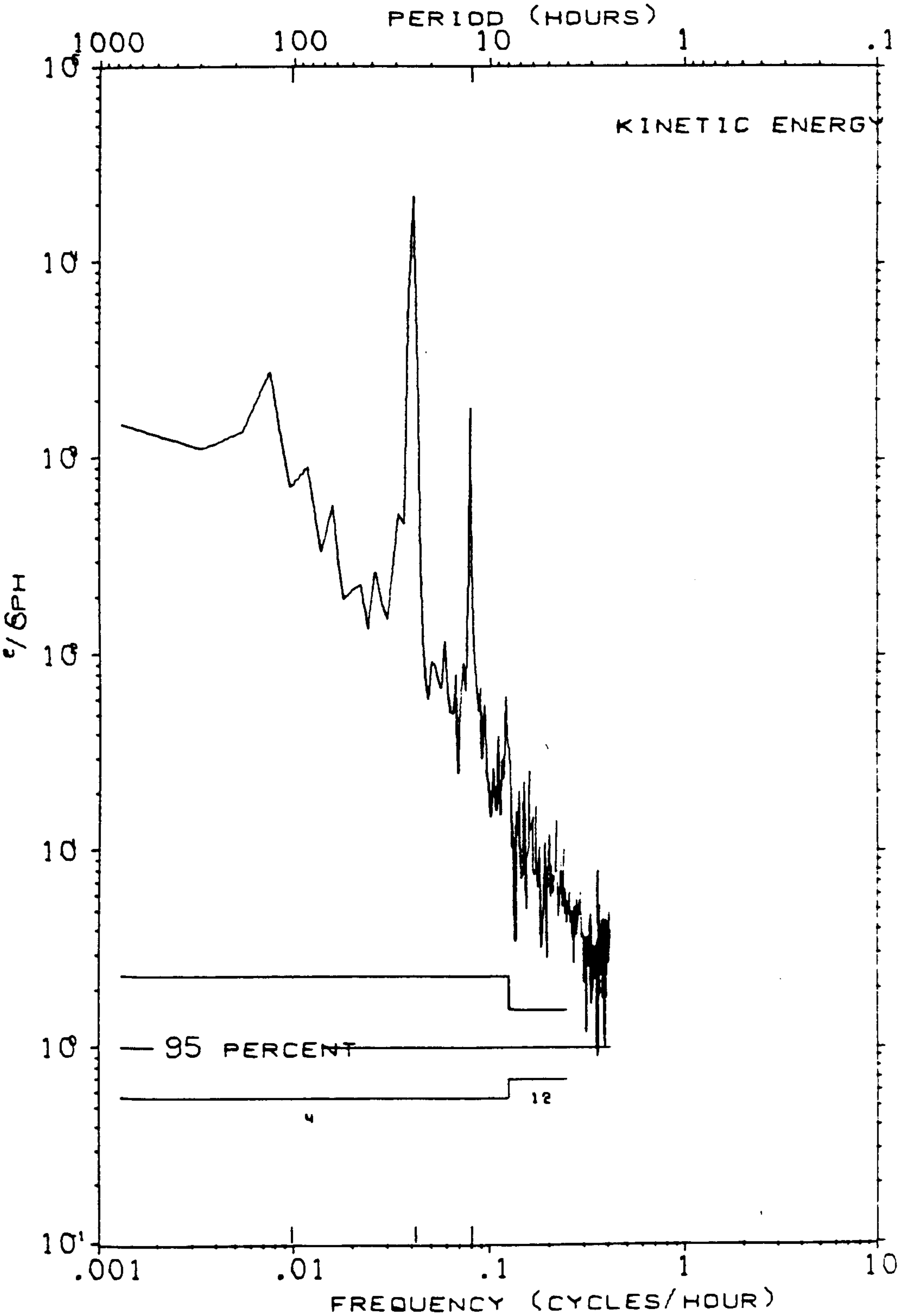

STATISTICS AND HISTOGRAMS OF CURRENTS AT CM4 - GEOPROBE, NS77
LOCATION = LAT 64 00N, LONG 165 00W, DEPTH = 17.5 METERS
OBSERVATION PERIOD = 0000 8 JUL 77 TO 2300 25 SEP 77 (80.0 DAYS)
N = 1920 DT = 1.00 HOURS, UNITS = (CM/SEC)

	MEAN	VARIANCE	ST-DEV	SKEW	KURT	MAX	MIN
S	14.05	56.05	7.49	0.543	2.966	43.10	0.16
U	2.43	159.37	12.62	0.135	2.099	36.86	-24.59
V	2.03	84.10	9.17	0.678	4.407	42.22	-32.04

S = SPEED
U = EAST-WEST COMPONENT OF VELOCITY, EAST =POSITIVE U
V = NORTH-SOUTH COMPONENT OF VELOCITY, NORTH = POSITIVE V

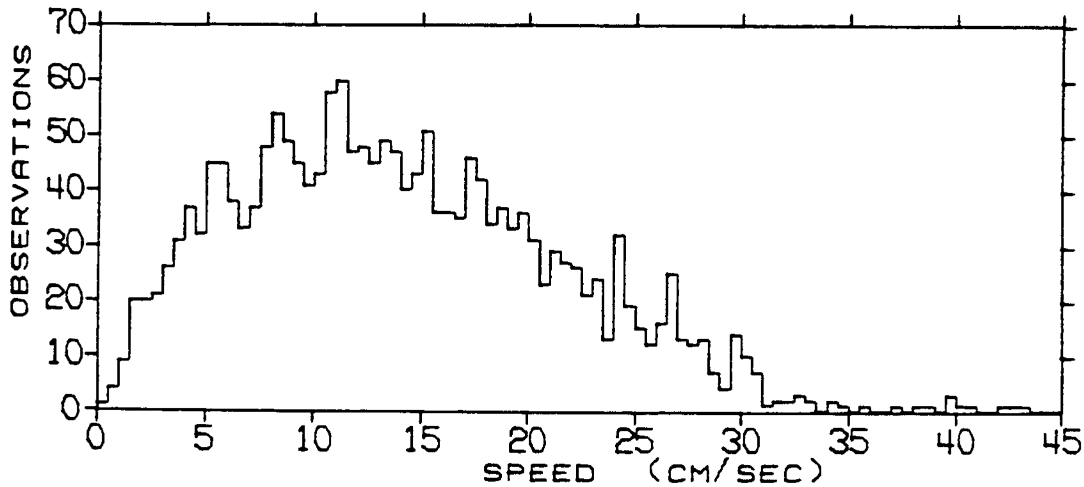

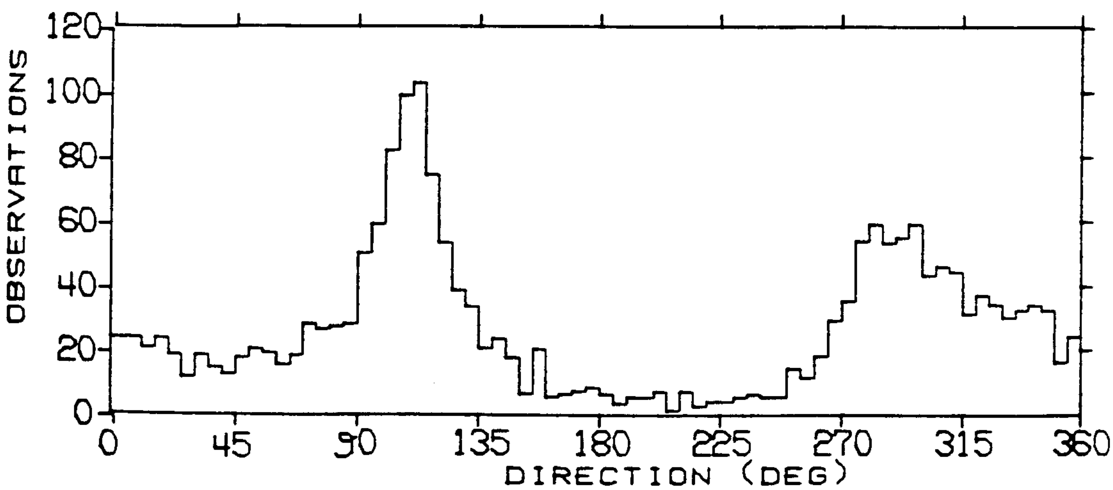

TIME SERIES OF VECTOR AVERAGED CURRENTS AT CM4 - GEOPROBE, NS77
LOCATION = LAT 64 00N, LONG 165 00W, DEPTH = 17.5 METERS
OBSERVATION PERIOD = 0000 8 JUL 77 TO 2300 27 JUL 77 (20.0 DAYS)
AVERAGING INTERVAL = 1.0 HOURS (1 POINTS)

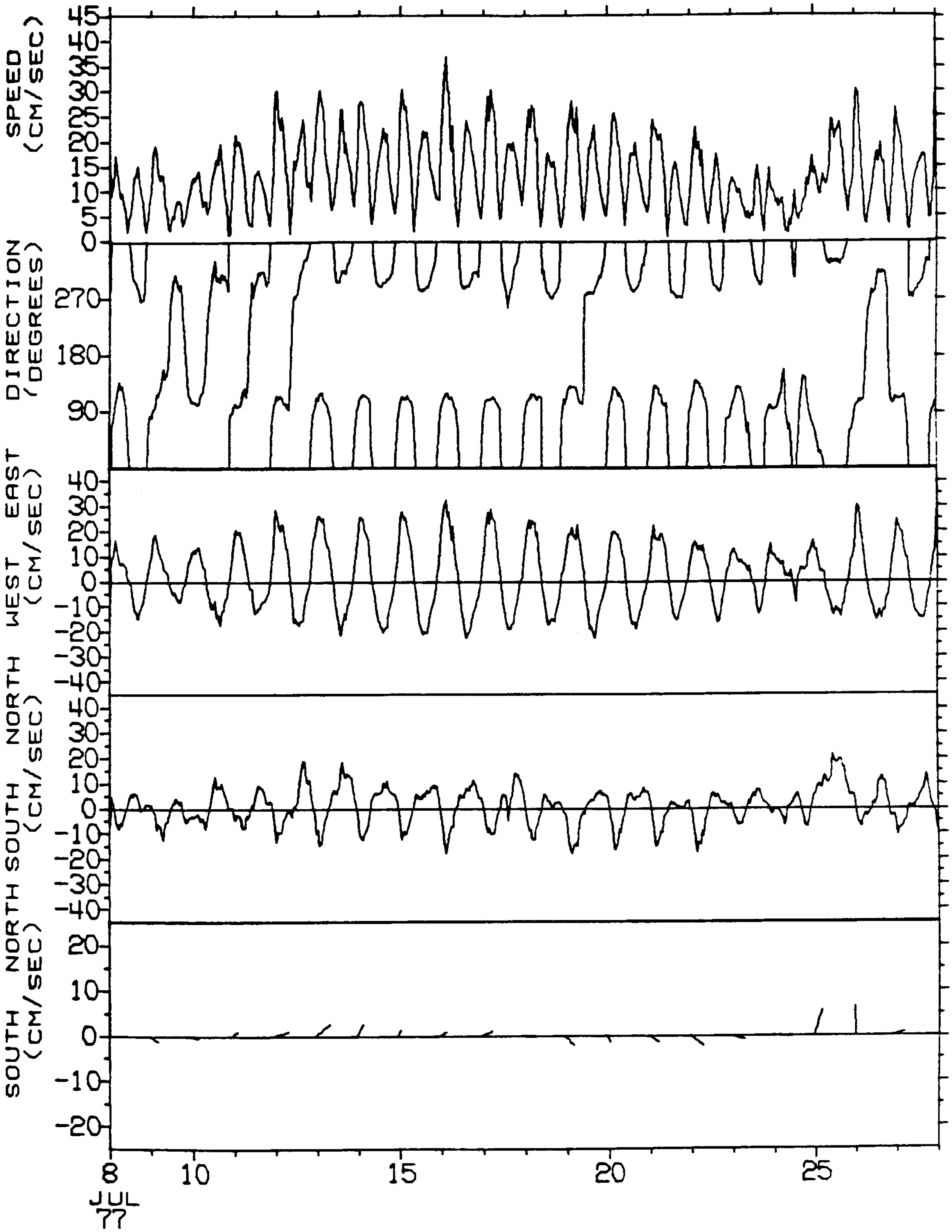

TIME SERIES OF VECTOR AVERAGED CURRENTS AT CM4 - GEOPROBE, NS77
LOCATION = LAT 64 00N, LONG 165 00W, DEPTH = 17.5 METERS
OBSERVATION PERIOD = 0000 28 JUL 77 TO 2300 16 AUG 77 (20.0 DAYS)
AVERAGING INTERVAL = 1.0 HOURS (1 POINTS)

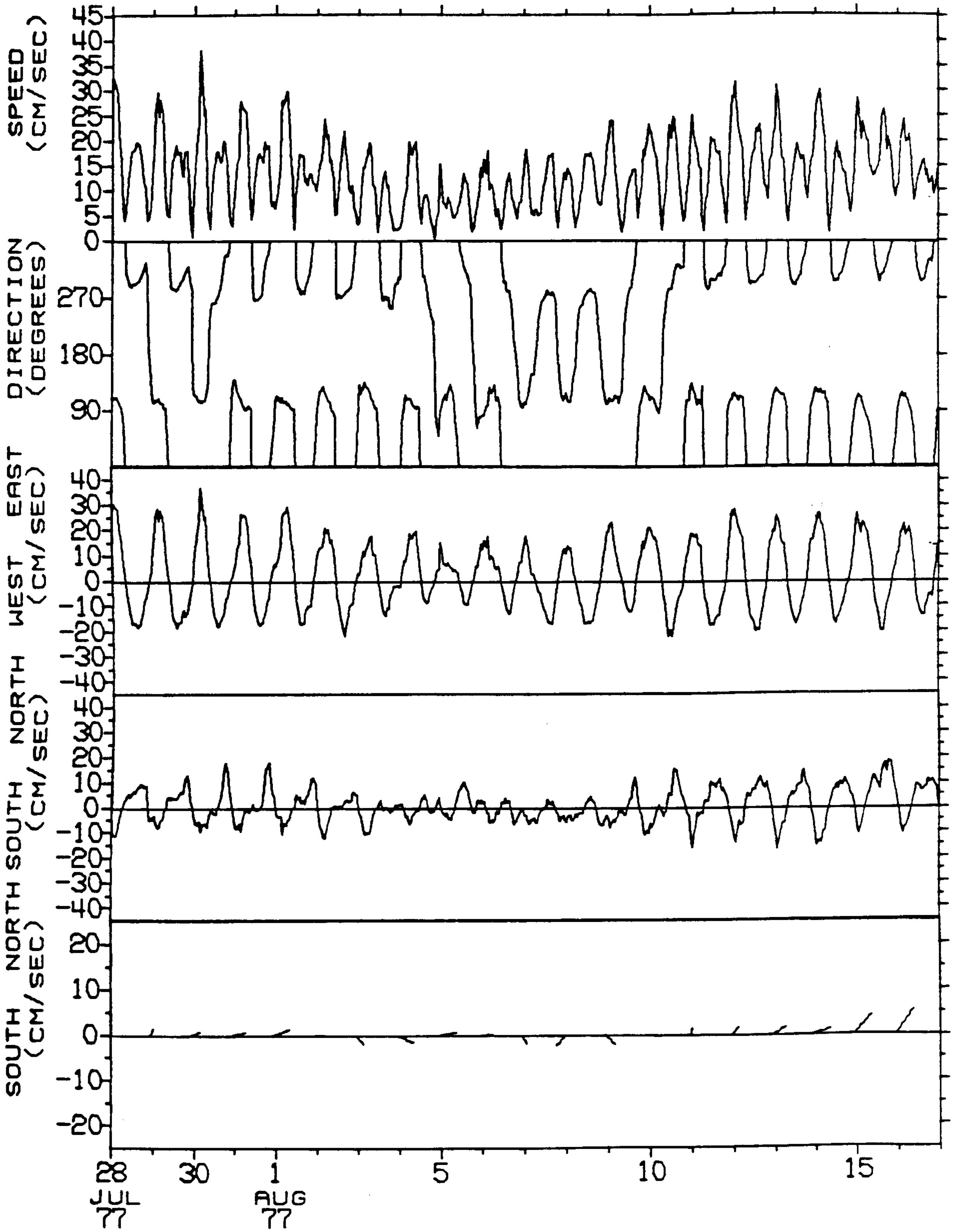

TIME SERIES OF VECTOR AVERAGED CURRENTS AT CM4 - GEOPROBE, NS77
LOCATION = LAT 64 00N, LONG 165 00W, DEPTH = 17.5 METERS
OBSERVATION PERIOD = 0000 17 AUG 77 TO 2300 5 SEP 77 (20.0 DAYS)
AVERAGING INTERVAL = 1.0 HOURS (1 POINTS)

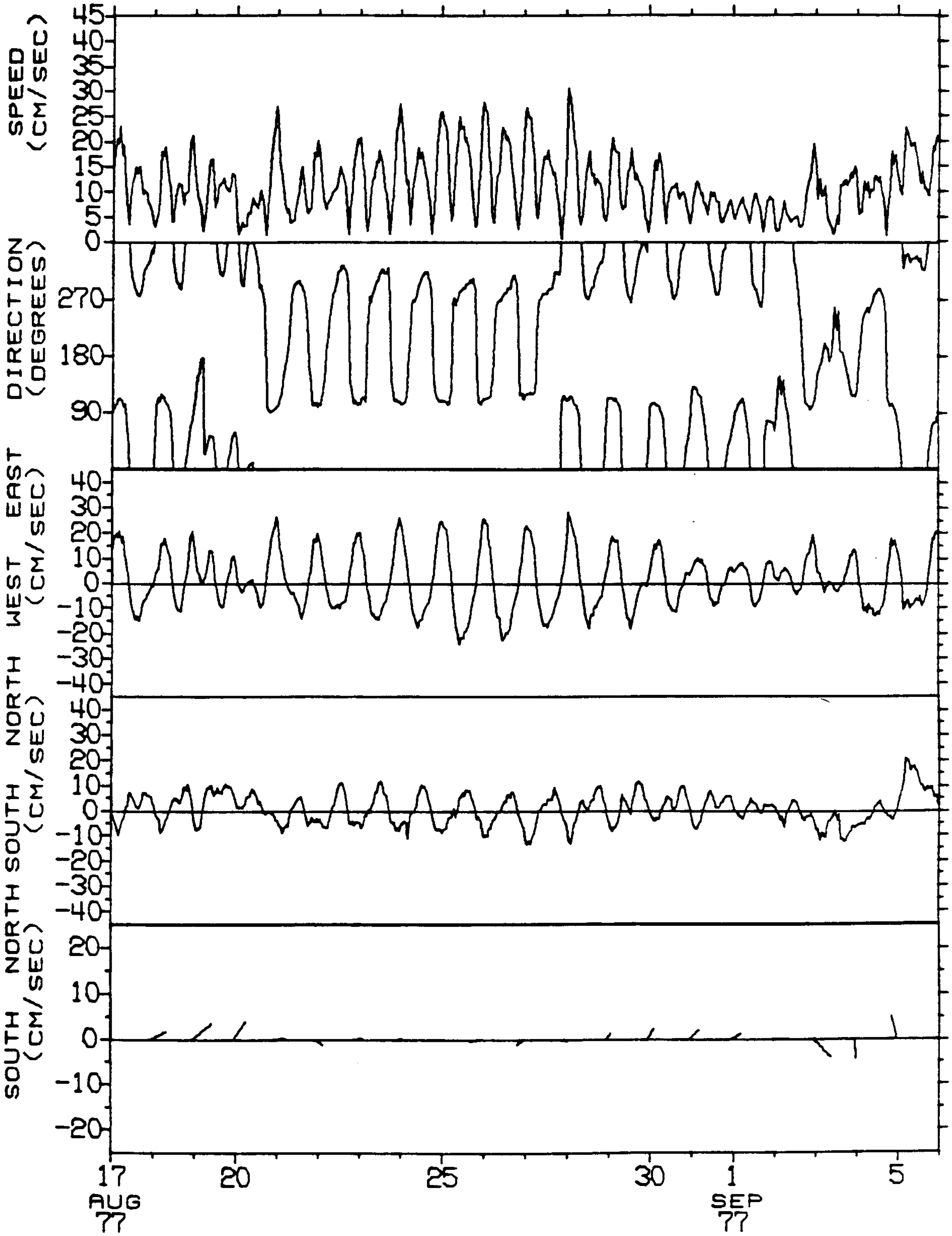

TIME SERIES OF VECTOR AVERAGED CURRENTS AT CM4 - GEOPROBE, NS77
LOCATION = LAT 64 00N, LONG 165 00W, DEPTH = 17.5 METERS
OBSERVATION PERIOD = 0000 6 SEP 77 TO 2300 25 SEP 77 (20.0 DAYS)
AVERAGING INTERVAL = 1.0 HOURS (1 POINTS)

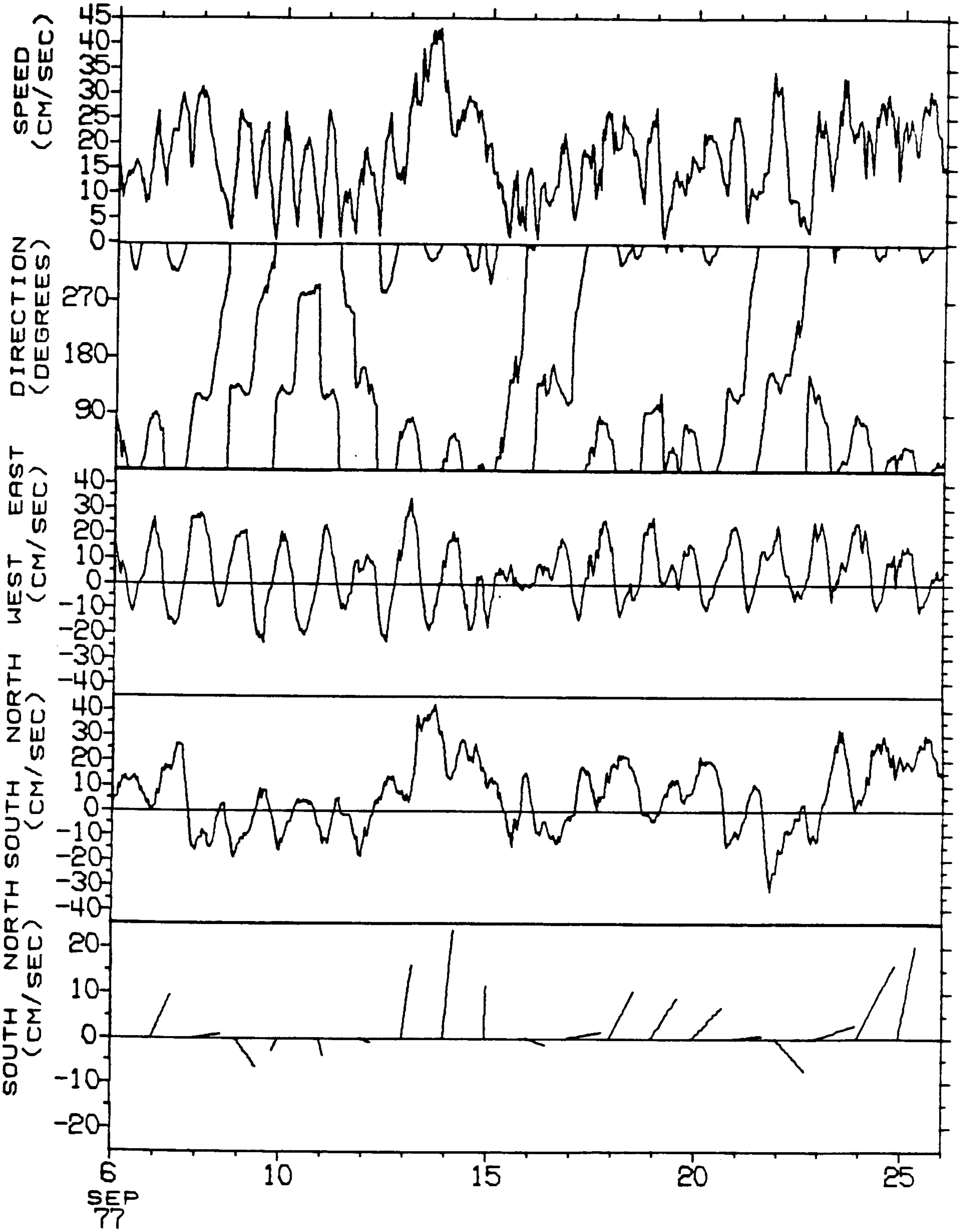

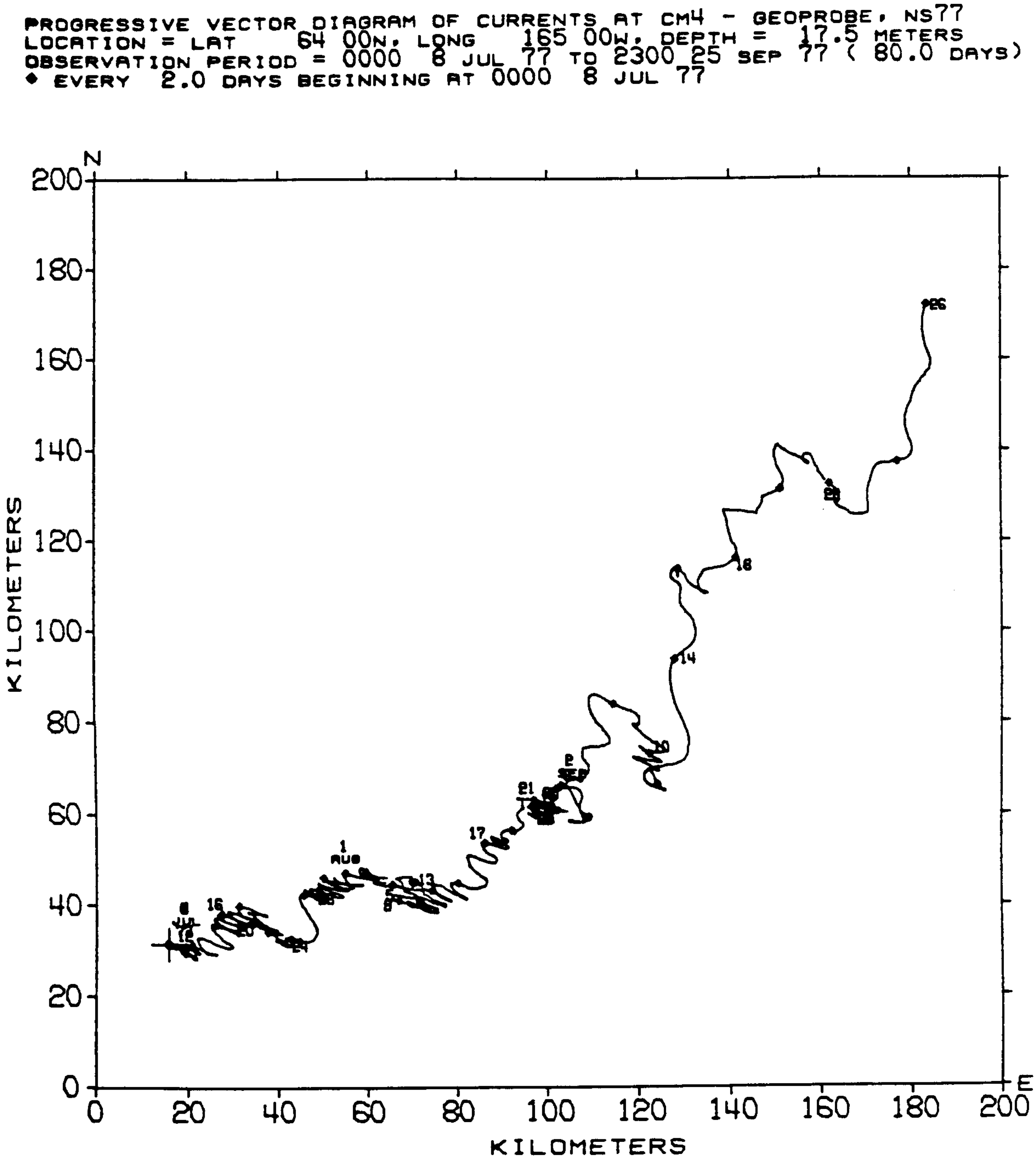
PROGRESSIVE VECTOR DIAGRAM OF CURRENTS AT CM4 - GEOPROBE, NS77
LOCATION = LAT 64 00N, LONG 165 00W, DEPTH = 17.5 METERS
OBSERVATION PERIOD = 0000 8 JUL 77 TO 2300 25 SEP 77 (80.0 DAYS)
◆ EVERY 2.0 DAYS BEGINNING AT 0000 8 JUL 77
N
E
KILOMETERS
KILOMETERS
1 AUG
2 SEP

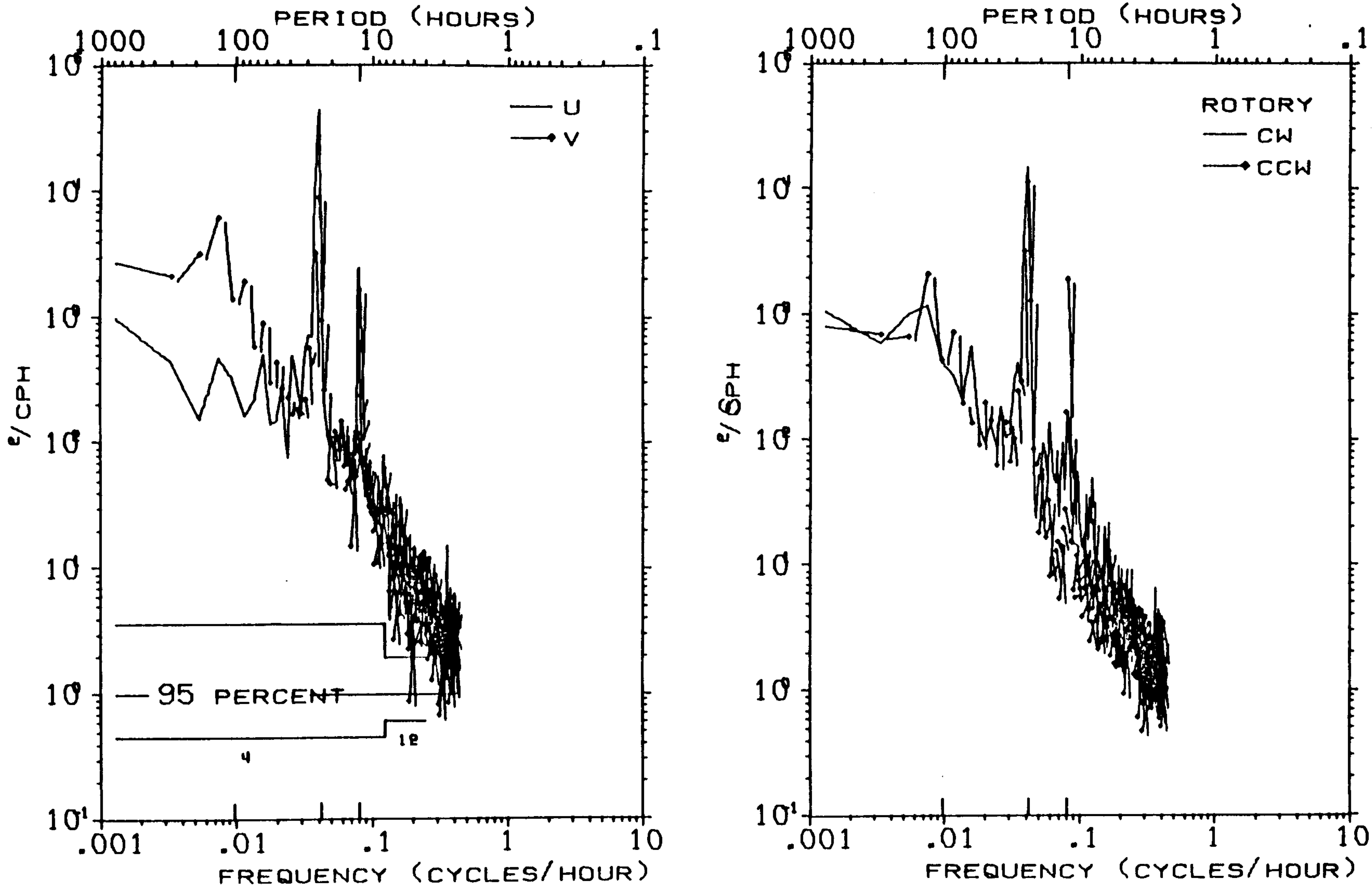

U, V AND ROTORY SPECTRA OF CURRENTS AT CM4 - GEOPROBE, NS77
LOCATION = LAT 64 00N, LONG 165 00W, DEPTH = 17.5 METERS
OBSERVATION PERIOD = 0000 8 JUL 77 TO 2300 25 SEP 77 (80.0 DAYS)
N = 1920, DT = 1.0 HOURS, SMOOTHING - DANIELL WINDOW

KINETIC ENERGY SPECTRUM OF CURRENTS AT CM4 - GEOPROBE, NS77
LOCATION = LAT 64 00N, LONG 165 00W, DEPTH = 17.5 METERS
OBSERVATION PERIOD = 0000 8 JUL 77 TO 2300 25 SEP 77 (80.0 DAYS)
N = 1920, DT = 1.0 HOURS, SMOOTHING - DANIELL WINDOW

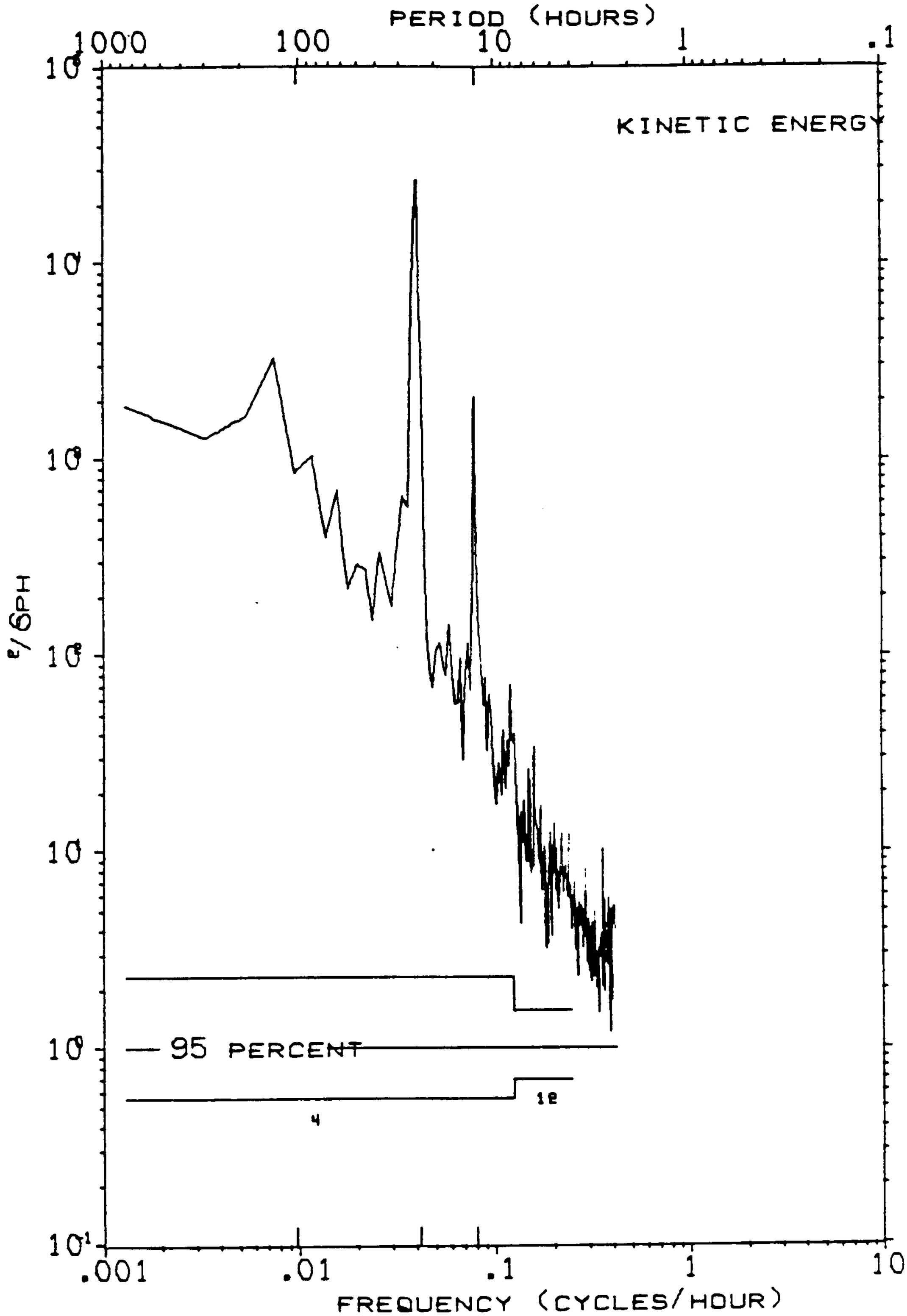

INTEGRATION OF CIRCULATION DATA IN THE BEAUFORT SEA

by

Dennis Hanzlick, Kent Short, and Lon Hachmeister

EBASCO ENVIRONMENTAL
10900 NE 8th Street
Bellevue, Washington 98004-4405

Final Report
Outer Continental Shelf Environmental Assessment Program
Research Unit 715

November 1990

ABSTRACT

Wind and oceanographic data from the nearshore area of the Beaufort Sea along the north coast of Alaska between Pt. Barrow and Demarcation Point were identified, catalogued, and, where possible, acquired. Selected current records from several different years were analyzed, and the relation between winds and nearshore currents and between nearshore and offshore (represented by Beaufort Sea Mesoscale Circulation Study) currents was investigated. Nearshore current records were from the open water season and primarily from depths of 6 m or less. Current meter data obtained shoreward of the barrier islands were excluded from the analysis because of shallowness and the sheltering effects of the islands.

A total of 56 data sets, collected during the period 1948-1989, were cataloged. Of these, 29 data sets (some incomplete) were acquired and incorporated into the project data base. The bulk of data acquired was from oil company sponsored studies in the Prudhoe Bay/Stefansson Sound region. NODC provided additional data sets. Attempts to acquire the remaining data sets were unsuccessful due to proprietary constraints and data inaccessibility.

Complex regression analyses showed that the wind accounted for approximately 40 to 50 percent of the variance of the nearshore currents measured at sensor depths of 3 m or less, and markedly less at sensor depths greater than 3 m. Comparison of current records from similar locations and depths indicated comparable wind-explained variance from year-to-year. Current direction was strongly rectified by bottom topography and proximity to the coastline. Current fluctuations consistently lagged the wind by one to three hours. Current spectra were often inconclusive, but generally indicated energy in the 3- to 8-day period range, which includes meteorological time scales. Tides did not constitute a significant source of signal variance. Current records were not adequate to identify and study other potential sources of current variability such as trapped waves or instabilities.

Comparisons between nearshore and offshore open water currents were limited by the very small number of current meter pairs available. In one comparison of 1987 data, nearshore currents were highly correlated (r=0.66) with currents 70 km offshore and led offshore currents by 14 hours. The highest coherence between the currents was at a frequency of 0.0274 cph (37-hour period). For the period from late July to early September 1987, the nearshore currents were highly correlated with Resolution Island winds (r=0.91 at lag=2 hours), while the offshore currents were less strongly correlated with the winds (r=0.69 at lag=16 hours). It is not clear whether the nearshore/offshore current correlation in this particular case was due to direct wind forcing of both or to a combination of direct and indirect meteorological forcing. While the periodicity of 37 hours for maximum coherence seems short for atmospheric phenomena, no other dynamic mechanism is evident from the data.

CONTENTS

CONTENTS, continued.

*Appendix A (one volume) and Appendix B (two volumes) are not included in this publication. Copies are on file at the NOAA, OAD Alaska Office, Anchorage, and NTIS, 5285 Port Royal Road, Springfield, VA 22161.

FIGURES

FIGURES, continued.

TABLES

1.0 INTRODUCTION

1.1 OBJECTIVES

Exploration and production of oil from lease-sale areas off the north coast of Alaska have prompted a large number of studies of the Beaufort Sea environment by both government and private industry. As a result of these investigations, a significant oceanographic database exists for the nearshore Beaufort Sea (depths <20m) as well as for regions farther offshore over the shelf and slope. Results of the recently-completed Beaufort Sea Mesoscale Circulation Study (BSMCS) (Aagaard et al., 1989) provide a valuable contribution to the database and to knowledge of long-term, synoptic ocean circulation and relation to the wind beyond the nearshore area. While the BSMCS data have been analyzed and interpreted, much of the data from the nearshore area was collected for descriptive purposes and has not been subjected to rigorous analysis.

The first objective of this work is to identify and compile existing current meter, hydrographic, and meteorological data from the nearshore area of the Beaufort Sea. The second is to analyze existing data to investigate the relation between currents in the nearshore area and winds. The third is to relate the nearshore circulation results with those of the offshore-oriented BSMCS. The area of study extends from Point Barrow, Alaska to Demarcation Point (see Figure 2-1).

1.2 GENERAL COASTAL CURRENT REGIME

Aagaard (1984) examined circulation over the shelf and slope of the southern Beaufort Sea and included a brief background description of the coastal current regime. The description presented here draws heavily from Aagaard (1984) and is meant to provide a context for considering the results of various analyses detailed in this report.

There is ample evidence of wind-driven circulation in the inner shelf area, particularly during summer. In general, water movement is westward under the influence of easterly winds, although fluctuations in current direction reflect fluctuations in wind direction. Nearshore circulation also responds to seasonal riverine input during the warm season and brine rejection during the cold part of the year, and the resulting density-driven currents modify the wind-driven circulation and circulation due to large-scale pressure gradients.

Presence of ice cover suppresses kinetic energy levels in currents over the inner shelf relative to those in summer during open water. Even so, there appears to be a weak meteorologically-driven flow component during winter. This flow component is likely a combination of direct wind stress and coastal setup.

Seaward of approximately the 50-m isobath is a relatively strong eastward current that Aagaard (1984) terms "the Beaufort undercurrent." It is speculated that the flow extends from the near surface to the bottom between the 50- and 2500-m isobaths. The surface circulation is of mean westward motion and represents the southern edge of the anticylonic gyre in the Canadian Basin of the Arctic Ocean.

Previous investigations have not detailed the transition and communication between the inshore or nearshore regime and circulation farther offshore. The encroachment of ice remains a formidable obstacle to obtaining adequate data records. A small number of individual current records indicate substantial cross isobath water motions between the offshore and nearshore regimes, so that there is potential for exchange between the two regimes.

1.3 ORGANIZATION OF THIS REPORT

The structure of this report reflects the near-independence of the three objectives. Three primary sections describe the work associated with the three objectives and are intended to stand alone, largely independent of each other. Within each respective section, methods, results and discussion, and other pertinent details are presented. The comprehensive summary condenses the results of all three project aspects, and a short Recommendations section follows.

2.0 DATA IDENTIFICATION, DOCUMENTATION, COMPILATION, AND EVALUATION

2.1 METHODS

2.1.1 Data Identification

This element of the program included a comprehensive review of oceanographic literature, project reports, data reports, and existing published data inventories for the nearshore Alaska Beaufort Sea region. Basic procedures involved manual and automated literature searches, and direct inquiries to appropriate investigators, agencies (federal, state, and local), academic institutions, and private organizations (e.g., oil companies, consulting firms) known to have conducted studies in the region. More than 150 published and unpublished references were screened as possible sources of information on historical data sets. From all of these sources, a list of past experiments in the region was generated, and served to target the data sets to be sought for incorporation into the project data base. Approximately 80 references containing relevant information on the data sets uncovered in this search are listed in Section 8.0. An additional useful resource in this task was an arctic data compilation and appraisal report prepared by the Canadian Institute of Ocean Sciences (IOS) (Birch et al., 1984).

2.1.2 Data Documentation

The data documentation step included acquisition of information on where, when, why, how, and by whom individual data sets were collected. For each of the data sets identified, all available information of this type was extracted from the reference material or via direct contact with the original investigator(s). A series of standardized data set documentation forms was used to record the information. Individual data sets were inventoried according to location within the study region and types of data collected, as described below.

Although NOAA's primary interest in this program was the integration of historical measurements inshore of the 20 m isobath, a larger area encompassing the entire Alaskan Beaufort Sea continental shelf was adopted in the identification and documentation phases of the study (Figure 2-1). This was done because the nearshore measurements were often part of larger scale continental shelf experiments, and it was felt that without the entire picture, the relevance of certain data sets might be lost. Five subregions within the overall study area were defined for the purpose of documenting the location of data collected in past experiments. These subregions were delineated partly on the basis of geographic features (i.e., major bays and capes), and partly on the basis of known concentrations of past oceanographic activity.

Data types documented included current meter (moored and profiling), Lagrangian drifter, hydrographic (temperature and salinity), sea level (tide gauge), and meteorologic. For sea level and meteorologic data, only those data sets from temporary stations installed as part of discrete experiments were documented in this study (i.e., long-term station data from permanent weather stations or NOS tide stations were not documented).

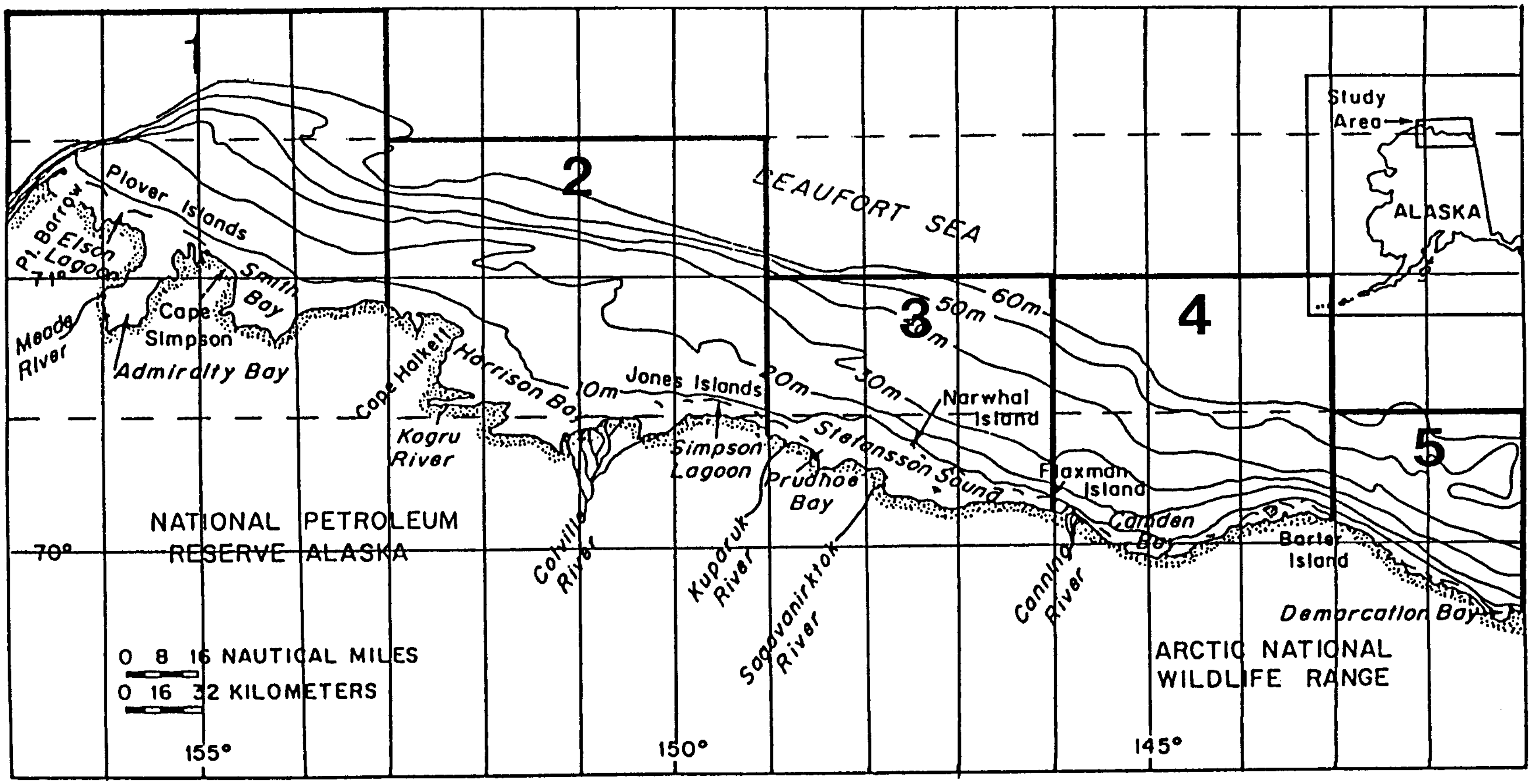

Figure 2-1. Map of the study area. Heavy lines delineate study subregions, labeled 1-5.

The final aspect of the documentation task included listing pertinent references for each data set so that subsequent investigators will be able to locate more information on a particular data set if desired. These key references were selected from the full set of references uncovered during the identification task (see section 2.1.1 above).

2.1.3 Data Compilation

Data compilation consisted of the acquisition, organization, and reformatting of all available historical data sets identified by the study. Data sets available in digital format on computer storage media were the primary target for acquisition, although in a few cases, optical scan-digitization of hardcopy tabular data listings allowed incorporation of data sets not previously available on computer media.

The computer system selected for storage and manipulation of the project data base was a 386 microcomputer, equipped with a 322 megabyte hard disk and a 150 megabyte streaming tape cartridge backup system. Data received on 9-track magnetic tape were read temporarily onto a VAX 11/780 computer, then downloaded to the 386 microcomputer. Each incoming data set was reformatted to standard NODC format (if necessary), then copied into permanent data directories organized by year, experiment, and data type. The data base was periodically backed up using the cassette tape storage backup system.

Since a considerable volume of data was available from the National Oceanographic Data Center (NODC), it was decided to ship the 386 microcomputer to NODC for the purpose a direct data transfer from the NODC archives to the hard disk on the 386. Approximately 50 megabytes of data were obtained from NODC in this manner. The types of data transferred included: current meter resultants and components (file types F005 and F015), low and high resolution S/CTD (file types C002 and F002), Lagrangian drifter (file type F156), Nansen bottle cast (file type C100), sea level (pressure gauge) (file type F017), and wind (file type F191).

A large volume of historical data from the Prudhoe Bay/Stefansson Sound region already on hand in the Ebasco Environmental data archives was transferred into the project data base, as were a number of smaller data sets acquired from individual investigators or from scan-digitization of tabular listings in reports.

Finally, although the data collected during the BSMCS appeared to be complete in the NODC holdings, a separate data transfer of all data collected during that experiment was accomplished by direct access to the NOAA/PMEL computer system. In this manner, the completeness of the BSMCS data set was assured.

The volume of oceanographic and accompanying meteorologic data from all sources acquired during the compilation phase of this program was approximately 90 megabytes.

Additional effort was expended in attempts to track down and acquire data sets not readily available from the sources noted above. Despite these efforts, many of the known historical data sets remained unavailable, due to proprietary constraints or data inaccessibility. These restrictions are discussed further in Section 2.2.

2.1.4 Data Evaluation

One of the secondary goals of Task 1 of this study was to include, with the data set documentation, a subjective estimate of the data quality (i.e., accuracy, completeness, consistency) inherent in each data set identified. A numerical data quality rating scale developed by the IOS (Birch et al., 1984) was intended for use in this effort.

Unfortunately, the unavailability of a large number of historical data sets, combined with incomplete documentation on experimental methods, data processing, and quality control on many others led us to conclude that such a numerical evaluation would be ineffective. In their arctic data inventory, Birch et al. (1984) did assign numerical ratings to each data set, but in many cases the number given was 2, which was their designation for indeterminate data quality.

During the course of the data analyses conducted in Task 2, an evaluation of each data set used was made during preparation of the data for input into the analysis routines. Some data quality problems became apparent in these evaluations. These are noted in Section 3.2.

2.2 RESULTS AND DISCUSSION

The number of data sets uncovered during the identification phase exceeded our expectations. Some of these data sets were relatively small and obscure. One cannot, however, categorize such data as insignificant, since in this data sparse region, even a limited data set may provide key information on spatial and temporal variability. Furthermore, some of these data sets were poorly documented and presumably unknown to many contemporary arctic investigators. As such, they have the potential to shed new light on results derived from more recent studies, and may guide planning efforts for future field experiments.

A total of 56 distinct project data sets encompassing physical oceanographic data from some part of the study area were identified. The earliest documented experiment occurred in 1948 and the most recent in the summer of 1989. Table 2-1 summarizes the available information on each of these data sets, including sampling areas (refer to Figure 2-1 for subregions), data types, and data status (archival status and availability). A reference is listed to direct the interested reader to a source of further information on the experiment (except in a few cases where no appropriate reference was found). For ease of association, each experiment has been named according to common usage (e.g.,

Table 2-1. Summary of project data set information. Subregion designations are as shown in Figure 2-1. Data type abbreviations are as follows: H = hydrographic, C = current meter, D = drifter, P = current profile, M = meteorologic, S = sea level.

Project Name/Year	Reference	Subregions Sampled	Data Types	Data Status
COAST GUARD 1948*	None found	1	H	NODC; project data base
NAVY 1950*	U.S. Navy Hydrographic Office (1954)	1, 2, 3, 4, 5	H	NODC; project data base
NAVY 1951*	Mountain (1974)	1, 2, 3, 4,	H	NODC; project data base
COAST GUARD 1955*	None found	1, 3, 4, 5	H	NODC; project data base
NAVY 1955*	U.S. Navy Hydrographic Office (1958)	1, 2	H	NODC; project data base
NAVY 1956*	U.S. Navy Hydrographic Office (1960)	1, 3	H	NODC; project data base
NAVY 1957*	U.S. Navy Hydrographic Office (1959)	1,2, 3, 4, 5	H	NODC; project data base
NAVY 1958*	U.S. Naval Oceanographic Office (1963)	1, 2, 3, 4, 5	H	NODC; project data base
NAVY 1959*	U.S. Naval Oceanographic Office (1963)	1, 2, 3, 4	H	NODC; project data base
NAVY 1960*	U.S. Naval Oceanographic Office (1964)	1, 2, 3, 4	H	NODC; project data base
PAQUETTE 1960*	Paquette and Bourke (1974)	1, 2, 3	H	NODC; project data base
KINNEY 1968-69*	Kinney et al. (1970)	1, 2, 3, 4	H	NODC; project data base
KINNEY/DYGAS 1970-72*	Dygas (1975)	2	C, D, M	unavailable [(4)]
MIZPAC 1971*	Paquette and Bourke (1974)	1, 2	H, C	unavailable [(3)]

Project Name/Year	Reference	Subregions Sampled	Data Types	Data Status
WEBSEC 1971*	Hufford (1973)	1, 2, 3, 4	H, C	NODC; project data base (H only)
WEBSEC 1972*	Hufford (1975)	1, 2, 3, 4	H, C	NODC; project data base (H only)
WISEMAN 1972*	Wiseman et al. (1973)	2	D, M	unavailable (4)
WEBSEC 1973*	Horner (1981)	1, 2, 3	H	unavailable (6)
HORNER 1974*	Horner (1981)	1, 2, 3, 4	H	NODC; project data base
BARNES (1971-76)*	Barnes et al. (1977)	2, 3	H, C, S	unavailable (2)
GARRISON (1973-77)*	Garrison et al. (1979)	1, 2	H	unavailable (2)
OCS/CALLAWAY 1975*	Callaway and Koblinsky (1976)	3	S	unavailable (4)
BSIMS 1975-76	Oceanographic Services Inc. (1976)	2, 3	C, M	unavailable (1), (2)
OCS/AAGAARD 1975-80*	Aagaard (1984)	2, 3, 4, 5	C, H	NODC; project data base (most)
OCS/HORNER 1976-78*	Horner (1981)	1, 2, 3, 4, 5	H	unavailable (6)
OCS/CARSEY 1976*	Carsey (1977)	1, 2, 3	M	NODC; project data base
WEST DOCK 1976-77	Grider et al. (1978)	3	H	unavailable (6)
OCS/MATTHEWS 1977-81*	Matthews (1981)	2	H, C, P, S	NODC; project data base (1977 and part of 1978 - C only) (4)
MIZPAC 1977*	Paquette and Bourke (1978)	1	H	unavailable (3)
OCS/LEAVITT 1977*	Leavitt (1978)	2, 3, 4	M	NODC; project data base

Project Name/Year	Reference	Subregions Sampled	Data Types	Data Status
OCS/MUNGALL 1977*	Mungall et al. (1978)	2	H	unavailable (4)
MIZPAC 1978*	Paquette and Bourke (1979)	1	H	unavailable (3)
WEST DOCK 1978-79	Chin et al. (1979)	3	H, C, D	unavailable (4)
OCS/MUNGALL 1978*	Mungall et al. (1979)	2	H, C, D	unavailable (4)
OCS/KOZO 1978-80*	Kozo (1981)	1, 2, 3	M	NODC; project data base
BEAUMOP 1978-83	Oceanographic Services Inc. (1979)	3	H, C, M, S	unavailable (1),(2)
REINDEER IS. 1979	Northern Technical Services (1981)	3	H, C, M	unavailable (1)
OCS/WILSON 1979-80*	Wilson et al. (1981)	2, 3	D	unavailable (2)
SAI 1980*	None found	1, 2	H	unavailable (4)
MURPHY 1980-81*	Murphy et al. (1983)	3, 4, 5	D	unavailable (6)
GREISMAN 1981*	Greisman and Blaskovich (1984)	3, 4	H, C	unavailable (4)
OCS/WILSON 1981*	Wilson et al. (1981)	1	H, C	unavailable (2)
DUCK IS. 1981	Colonell and Weingartner (1982)	3	H, C, D, M, S	unavailable (2)
YO191 1981	Toimil and England (1982)	3	C	unavailable (6)
OLIKTOK 1981-82	Woodward-Clyde (1983)	2	H, C, M, S	unavailable (5)
WATERFLOOD 1981*	Mangarela et al. (1982)	3	H, C, D, M, S	unavailable (5)

Table 2-1. (continued)

Project Name/Year	Reference	Subregions Sampled	Data Types	Data Status
WATERFLOOD 1982-84*	Savoie and Wilson (1986)	3	H, C, M, S	project data base
PRE-ENDICOTT 1982	Britch et al. (1983)	3	H, C, M, S	project data base
OCS/HACHMEISTER 1982*	Hachmeister and Vinelli (1983)	5	H, C	NODC; project data base
TERN IS. 1982	Northern Technical Services (1983)	3	C	project data base
MUKLUK 1983-84	Northern Technical Services (1985)	2	C	project data base
LISBURNE 1983-84	Berry and Colonell (1985)	3	H, C, D, M, S	project data base (except H - 1984)
ENDICOTT 1985-87*	Short et al. (1988)	2, 3	H, C, D, P, M, S	project data base
ENDICOTT 1988-90*	Morehead et al. (1990)	3	H, C, M, S	unavailable (5)
OCS/BSMCS 1986-88*	Aagaard et al. (1989)	1, 2, 3, 4, 5	H, C, D, M, S	NODC; project data base
ANWR 1988-89*	Fruge et al. (1989)	4, 5	H, C, M	project data base (1988 only)

*Collected under U.S Government agency funding or regulation.
For unavailable data:
(1) Data unavailable due to proprietary restrictions or excessive cost.
(2) Investigator or institution indicated that the data are inaccessible or would require excessive effort to locate and retrieve.
(3) Investigator indicated data sent to NODC, but not found in the archive.
(4) Investigator or knowledgeable party could not be reached.
(5) No response received to request for data.
(6) Data not archived in digital form.

MIZPAC, WATERFLOOD, BSMCS) where such exists, or by the investigator/institution that conducted the experiment. In some cases, one experiment was broken down into two or more data sets, if the principal investigator(s) or some other major aspect of the experiment changed (e.g., ENDICOTT 1985-87, ENDICOTT 1988-89). Those experiments that were elements of the OCSEAP program were designated by the prefix "OCS". A total of 43 of the 56 data sets (77 percent) were either funded or controlled by public agencies.

Of the 56 documented data sets, only 21 were present in their entirety (or nearly so) in the NODC holdings. In one additional case (OCS/MATTHEWS 1977-81) only a small fraction of the data known to have been collected was found in the NODC data base. An additional seven data sets (some incomplete) were acquired from other sources. Thus, 27 of 56 documented data sets were unavailable for acquisition. The reasons for the unavailability of these data sets generally fell into two categories. First, in some cases it was either impossible to locate the original investigator(s), or if located, the investigator indicated that the data set was no longer accessible. Second, many of the data sets collected by private funding sources (primarily oil companies) were unavailable due to proprietary constraints. In such cases, the funding company or companies maintains confidentiality on the data for a specified number of years (typically 10). Even when the restriction is lifted, an exorbitant cost may still be imposed for anyone wishing to purchase the data. These proprietary restrictions generally applied to studies conducted in conjunction with oil exploration activities (e.g., BEAUMOP), but not necessarily to privately funded monitoring studies associated with EIS assessments or permit requirements for oil development activities (e.g., WATERFLOOD, ENDICOTT, LISBURNE).

Certain of the missing data sets, due to their documented extensive data coverage in space and/or time, were deemed high priority for additional efforts at retrieval. These efforts, within the scope of the present study, met with limited success. If additional data compilation efforts are attempted in the future, it is suggested that special attention be given to the location, retrieval, and incorporation of the following high priority data sets into the available public record: OCS/MATTHEWS (1977-81); BARNES (1971-76); BEUMOP (1978-83); and ENDICOTT (1988-90).

The absence of the OCS/MATTHEWS 1977-81 data set deserves special note. According to Matthews (1978, 1979, 1980, 1981), more than 35 current meter deployments were carried out in the Simpson Lagoon area during this five-year period. Several of Matthews' deployments resulted in lost instruments with no data recovery. Only data from 1977 and 1978 were present in the NODC archives, and upon close inspection, even they proved to be unusable due to sampling or recording interval problems. Several of Matthews' data tapes, provided by the University of Alaska, were found to be indecipherable, even by the current meter manufacturer. The loss of Matthews' data is an unfortunate and disappointing gap in the historical data record.

3.0 DATA ANALYSIS AND INTERPRETATION

3.1 METHODS

3.1.1 Data Input/Output Management

3.1.1.1 Standard Input Format

In view of the variety of formats of obtained data sets, NODC data format was chosen as a standard input format, and each analytical program included a subroutine that served as the data input section. This subroutine accepted parameters that selected oceanographic or meteorological format and wrote header information to the computer file defined to accept computed results.

3.1.1.2 Interactive Input of Parameters

Analytical programs included a standard input query sequence. Analyses required items of information such as file names for selecting particular data records, data type, desired velocity component, whether or not to rotate into principal axis orientation, total number of data points to interpolate for fast fourier transforms (FFT's), and smoothing intervals for output plots. For ease of use of the programs even by individuals unfamiliar with the routines, the decision was made to use an interactive exchange rather than require modification of an input file for each analysis run.

3.1.1.3 Real-time On-screen Plot Display

A real-time on-screen plot display feature allowed the analyst to display output plots on the computer screen upon completion of computer runs. This feature played an extremely important role in previewing the results of the large number of analytical runs required by the program. This preview allowed the option of re-specifying input parameters to improve the information content of plots and computed results before producing hardcopy output. It also improved data analysis efficiency by providing immediate results that could be used to choose subsequent avenues of analysis of a given suite of data.

3.1.1.4 Production of Output Disk Files

Output sections of all programs wrote both computed and graphical outputs to user-specified disk files. The feature provided results for record in an easily readable format and files of plot instructions that could be used to make multiple original copies of graphs without rerunning analytical programs. Plot files were of two types, one of instructions for a Hewlett-Packard model 7475A pen plotter and the other of instructions for an Imagen laser printer. Output disk files were intended as a means of maintaining permanent records of results of all the various computer runs.

3.1.2 Data Manipulation

3.1.2.1 Conversion to NODC Format

Many of the data sets obtained were in non-standard formats and required conversion into NODC format before analysis. Programs for each different format conversion were written in C and produced output files of header information and data in either oceanographic or meteorological NODC format.

3.1.2.2 Checking for Missing Data

Missing data in original data sets were entered either as blanks or as entries of -999, depending on the source. Format conversion routines scanned for either type of entry and wrote -999 as the entry for any missing data. The data records that were chosen for analysis were then edited to search out any -999 entries. Very few blocks of missing data were found. Data records were truncated if a block fell near either end, and in one case, missing data from one data record (1985 Resolution Island MET data) were replaced by two blocks of comparable data (Deadhorse MET data) slightly longer than 24 hours.

3.1.2.3 Subsampling

A sampling rate of one hour was selected as standard for all data used by the program. Some of the data sets obtained had sampling intervals other than one hour. Those data sets were subsampled to yield time series with one-hour sampling interval at the top of each hour.

3.1.2.4 Truncating

Data sets contained time series of various lengths. Time series were truncated, either beginning or end, in order to achieve start times and record lengths matching other records with which correlations or other joint calculations were made. Calculations made with individual records generally used the entire record length as long as the record corresponded approximately with typical deployments in a given data set. Where specific calculations were desired for a given time series for an interval concurrent with another data record, only the corresponding segment was used, regardless of record length.

3.1.3 Selection of Data Sets for Analysis

3.1.3.1 Oceanographic Data

Current meter records selected for analysis came from the years 1982 and 1984 through 1988. The criteria considered when selecting data sets for analysis included length of record, geographic location, concurrence with other data records on the same mooring, and existence of records from the same location in successive years. Only current meter records from the open water season (mid/late-July to mid-September) were available and were thus limited to a maximum of about eight weeks. Many were shorter due to instrument malfunction or damage. Preference was given to longer records for analysis. In view of the shallow depths (1-2 m) inside the barrier islands, the strong constraint imposed on current direction by lateral barriers on two sides, and the sheltering effect of barrier islands against offshore motions, current records from outside the barrier islands were given preference. The potential for investigating the variation with depth of current response to wind forcing led, whenever possible, to the choice of vertically separated current records from the same mooring. Current records separated either in the alongshore or offshore direction were chosen in order to investigate the presence of propagating signals not directly attributable to local wind forcing. In summary, current records selected for analysis were chosen on the basis of potential for investigating current-wind relationships and illuminating other dynamical processes that might contribute to current variability in the nearshore area.

3.1.3.2 Meteorological Data

Meteorological data sets were chosen on the basis of proximity to (and concurrence with) the selected current records. For current records from the Prudhoe Bay area, the first choice for wind-current analyses was Resolution Island, slightly northeast of Prudhoe Bay. Winds from Deadhorse and Gull Island were also used. For the analysis of 1988 current meter data from Camden Bay, wind data were from a temporary meteorological recording shore station south of Camden Bay.

3.1.4 Analytical Tools

3.1.4.1 Autocorrelation

Lagged autocorrelations were calculated for most of the data records. One use of autocorrelations was to estimate the approximate time interval necessary for current motions to be independent. A second was to supplement the results of autospectral calculations by means of lending visual confirmation for spectral peaks, but perhaps the most important was simply to provide a simple descriptive representation of the frequency content of a given current record.

The autocorrelation routine comes from Bendat and Piersol (1971, chapter 9). Ninety-five percent confidence limits were calculated using the Fischer Z-transform (Otnes and Enochson, 1978) and were plotted as dashed lines on the output graphs.

3.1.4.2 Cross Correlation

Lagged cross correlations were calculated between winds and currents and between selected current record pairs. The basic routine is analogous to that for autocorrelation, with the exception that both negative and positive lags were used.

Cross correlations were used to investigate the lead/lag relation between pairs of data records, particularly winds and currents. In addition, cross correlations provided evidence of periodicities at which winds and currents or current record pairs were potentially related.

3.1.4.3 Autospectra

Autospectra are the frequency domain counterparts of autocorrelations and yield an estimate of the distribution of variance as a function of frequency. Autospectra were calculated for wind and currents in order to identify frequencies at which energy associated with fluctuations was concentrated, thus to aid in isolating potential dynamic mechanisms.

Spectra were estimated by linearly interpolating data series to an integral multiple power of 2, tapering by applying a half-cosine bell to the first and last 10 percent of the data series, calculating the Fourier coefficients using an FFT routine, and then manipulating the coefficients to produce spectral estimates. The artificial production of high frequency information by interpolation was inconsequential because frequencies of signals of interest were tidal and lower and because there was very little energy to begin with in signals with time scales of a few hours or less.

Spectral plots were smoothed using a boxcar window whose width varied logarithmically with frequency (Irish et al., 1976). Thus, at low frequencies, very few successive spectral estimates were averaged together, and the number increased with increasing frequency.

3.1.4.4 Coherence and Phase

Coherence and phase calculations are the frequency domain counterpart of cross correlations. The coherence calculations represent the joint distribution of energy of two data series as a function of frequency, and the phase calculations quantify the lead/lag relation of two data series also as a function of frequency. While cross correlation gives an indication of the overall relation of two time series, coherence and phase calculations isolate particular frequencies at which the relatedness is strongest.

Coherence and phase routines follow a method presented in Jenkins and Watts, 1968, chapter 9. Co- and quad-spectra were calculated from Fourier coefficients (computed as for autospectra) and then manipulated to obtain estimates of coherence and phase. These were smoothed using a fixed-length linear boxcar window, the 95 percent confidence limit for coherence determined, and finally, the results plotted against a linear frequency scale.

3.1.4.5 Rotary Spectra

Rotary spectra were calculated in a limited number of cases. As the name implies, this type of analysis investigates the rotational nature of a given vector time series, yielding the energy in clockwise and counterclockwise motions as a function of frequency. This technique is useful in examining possible dynamic mechanisms as sources of observed variability. For instance, inertial motions in the northern hemisphere would show up as a concentration of energy in clockwise rotations as opposed to counterclockwise rotations.

The routine is based upon the method of Gonella (1972) and Mooers (1973). The foundation for calculating rotary spectral densities rested upon manipulating the Fourier coefficients for the U and V velocity components of a given record. The rotary spectral densities were then smoothed using the same techniques as for autospectra and plotted as solid and dashed lines against frequency on a single graph.

3.1.4.6 Complex Linear Regression

Complex linear regression is the regression of one vector time series onto another. It is used to recover the fraction of variance of one time series (dependent variable) that is accountable by a linear relation to another (independent variable). The technique also produces a scale factor relating the speeds and an angle relating the directions of the two vector time series (the indraft angle). Complex regression was one of the primary tools used to examine the relation between wind and currents and between pairs of current and wind records. The program produced a file of computed results, but no graphical output.

3.1.4.7 Rotation into Principal Axis Orientation

All analytical programs included a query option of rotating input time series into principal axis orientation before performing computations. Rotation into principal axis orientation means rotating the coordinate system so that one axis lies in the direction of maximum current variability, and the other lies perpendicular to it. The convention used throughout was that the velocity component in the direction of the principal axis was termed the U component, and that perpendicular was the V component. This option was exercised as a matter of consistency, since the proximity to the coastline and shallow depths generally constrained current directions. Thus, comparisons between U components of time series had a consistent meaning regardless of the actual geographical orientation of the coordinate system.

3.2 SUMMARY AND ASSESSMENT OF ANALYZED DATA

3.2.1 1982 Data

Data records from four current meters deployed as part of a baseline study near the mouth of the Sagavanirktok River (Britch et al., 1983) were chosen for analysis (Figure 3-1, Table 3-1). For the deployment interval, meteorological data used were from a recording station on Resolution Island, an artificial drilling island within 3 to 11 km of the moorings (Figure 3-1, Table 3-1).

One problem that immediately became apparent from cross correlations between wind and current records and between current record pairs was that start times listed for moorings L1 and L3 were incorrect and offset by slightly more than two days. Cross correlations between L4, L5 and the wind indicated apparently correct listed start times for those two current time series. Under the assumption that L1 and L5 were in phase because of their close proximity, as

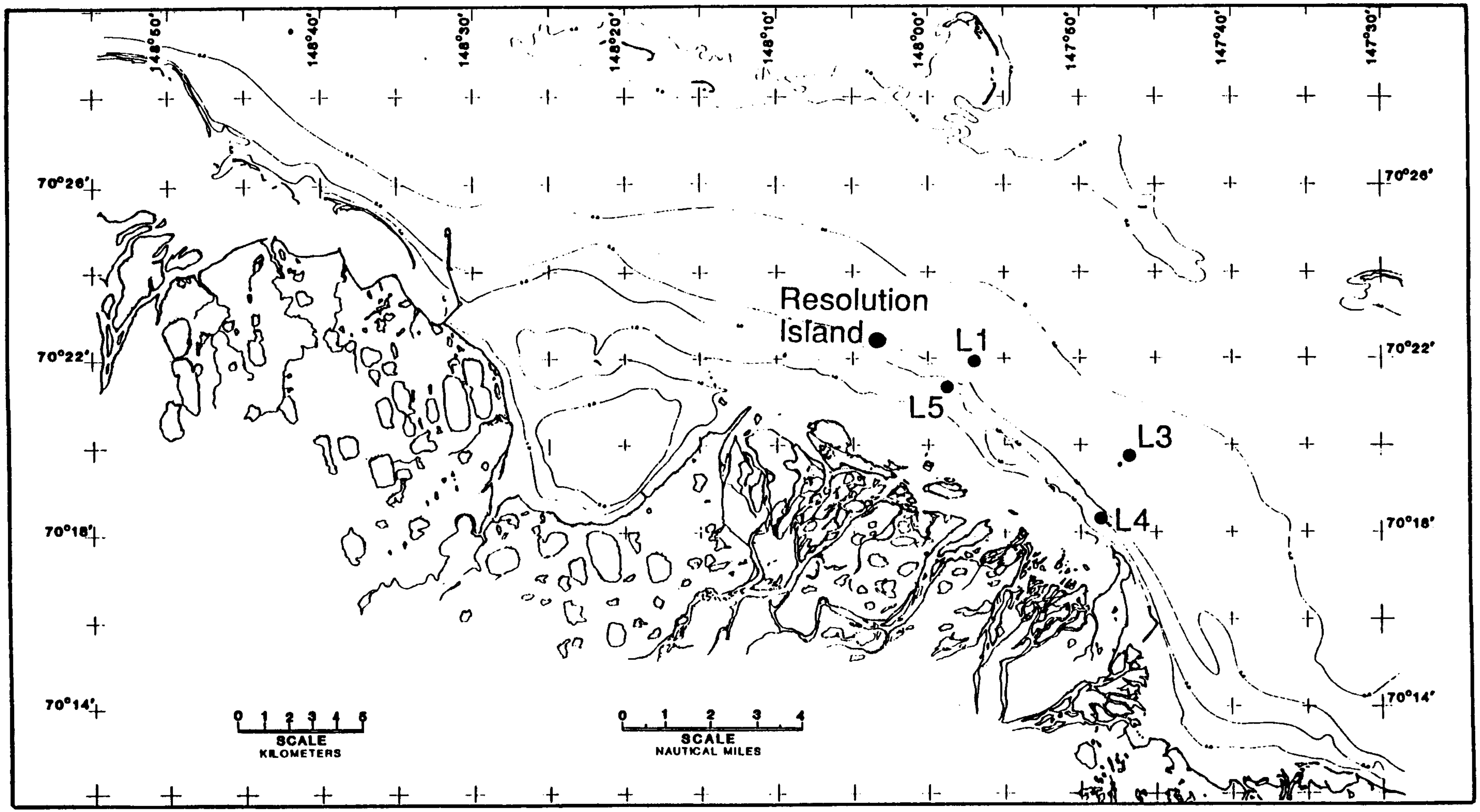

Figure 3-1. Location of 1982 current meter and meteorological data records selected for analysis.

Table 3.1. Details of current records and meteorological data, 1982

File name is the name of the computer disk file for the data and identifies each respective data record on output plots and computed results files.

		Current Record		Mooring Location		Depth (m)
I.D.	File Name	Begin	End	Latitude (N)	Longitude (W)	sensor/bottom
L1	L1.C82	07/29 1100	09/13 0600	70°21.9'	147°56.7'	3.0/5.0
L3	L3.C82	07/31 1900	09/13 0600	70°19.7'	147°47.0'	3.0/5.0
L4	L4.C82	07/31 1200	09/15 0800	70°18.3'	147°48.8'	1.0/2.0
L5	L5.C82	07/30 1700	09/15 0800	70°21.4'	147°59.0'	1.0/2.0
Resolution Is. Met Data	RI.W82	06/21 1800	09/15 1400	70°22.3'	148°03.1'	

were L3 and L4, start times for L1 and L3 were adjusted by 53 and 57 hours, respectively, based upon the results of cross correlation calculations. This adjustment approximately aligned the data points of the four time series and compensated for the incorrect times associated with the acquired L1 and L3 data. Even so, the potential errors in adjustments to start times are 1-3 hours, which corresponds to typically observed phase lags between winds and currents analyzed for this project. Thus, no strong conclusions were attempted on the basis of cross-calculations between L1, L3, and the wind.

3.2.2 1984 Data

Three current meter records from 1984 were chosen for analysis (Figure 3-2, Table 3-2). They were obtained during a monitoring program in the Prudhoe Bay area (Berry and Colonell, 1985). These three current records were from deployments that were among the deepest in the nearshore area and provided simultaneous measurements separated in both alongshore (L32 and L36) and cross-isobath (L32 and L34) directions. There were no gaps in the records and no apparent discrepancies in start times. However, the subsequent data report (Berry and Colonell, 1985) indicated that all three moorings had been struck and dragged by ice. Simple calculations showed that the vector-averaged mooring velocities were 0.5 cm/s for L34 and 0.2 cm/s for L32 and L36. These are comparable to the observed vector-averaged velocities, and therefore, relative velocities induced by mooring movements bias investigations of means for these records. On the other hand, the contribution from mooring movement will not greatly affect spectral results, since the means are removed before commencing calculations. In view of the spatial distribution and of the validity of spectral calculations in spite of mooring translations during the deployment intervals, these current records were included in the analysis.

Meteorological observations from Deadhorse Airport were used in the analysis. Meteorological data were also available from Gull Island, located in the north part of Prudhoe Bay. Complex regression calculations between the two data sets indicated that wind directions at the two locations differed by only seven degrees, and that Gull Island wind speeds averaged about 70 percent of Deadhorse wind speeds. Gull Island winds led by one to two hours. Deadhorse winds were selected on the basis of longer record overlap with the current records and continuous year-to-year coverage, should current predictions for the general area covered by the three mooring locations mentioned above be attempted for other years.

3.2.3 1985 Data

Numerous current meters were deployed in the Prudhoe Bay area during the 1985 open-water season as part of the Endicott Environmental Monitoring Program (Hachmeister et al., 1987). Many yielded short data records, some were deployed in water 2 m or less deep, and some were located inshore of a manmade gravel causeway stretching several kilometers alongshore and connected to shore by another causeway with several breaches in it. Three current records were included in the analysis (Figure 3-3, Table 3-3). Two of the current records (ED2 upper and lower) provided an opportunity to study vertical

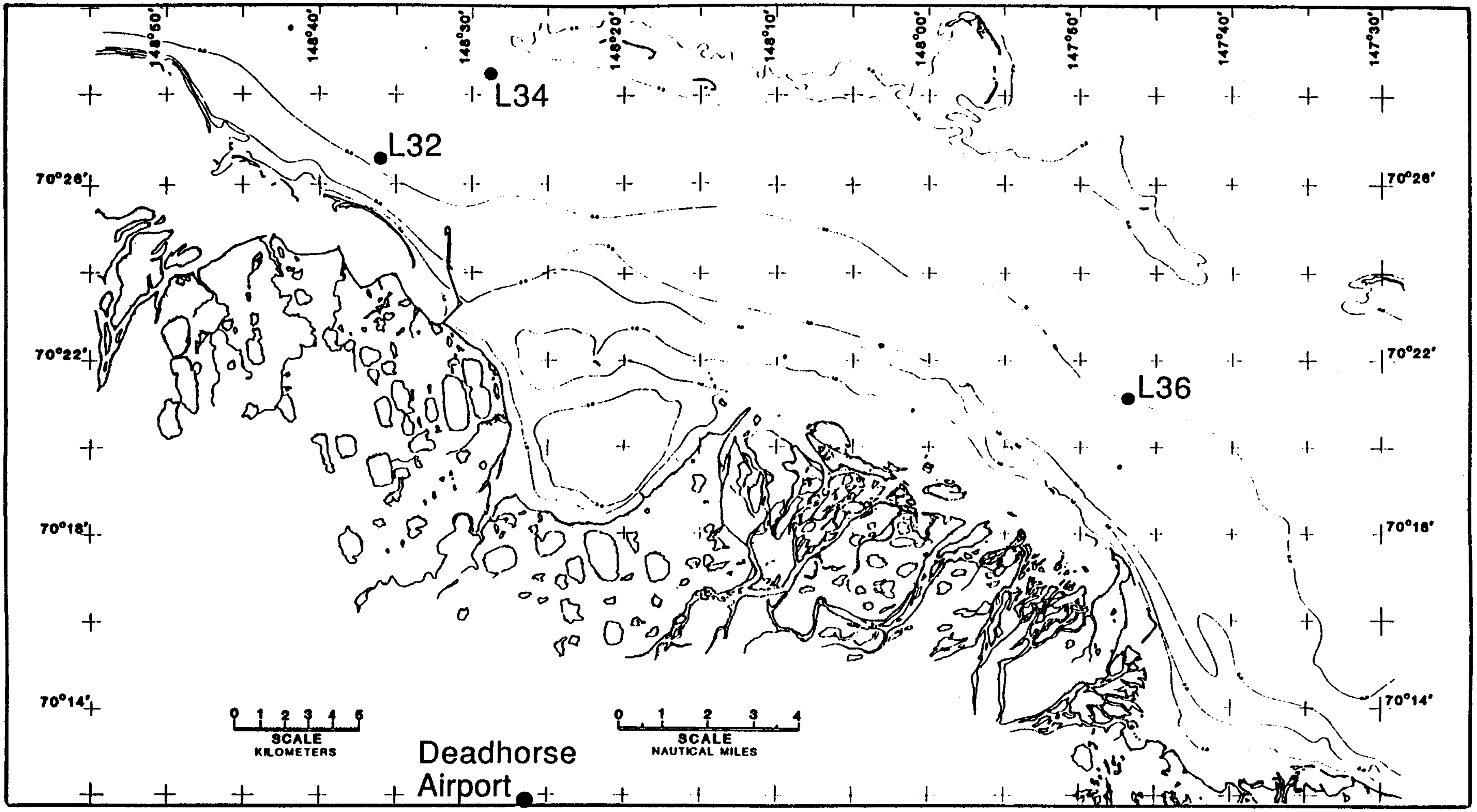

Figure 3-2. Location of 1984 current meter and meteorological data records selected for analysis.

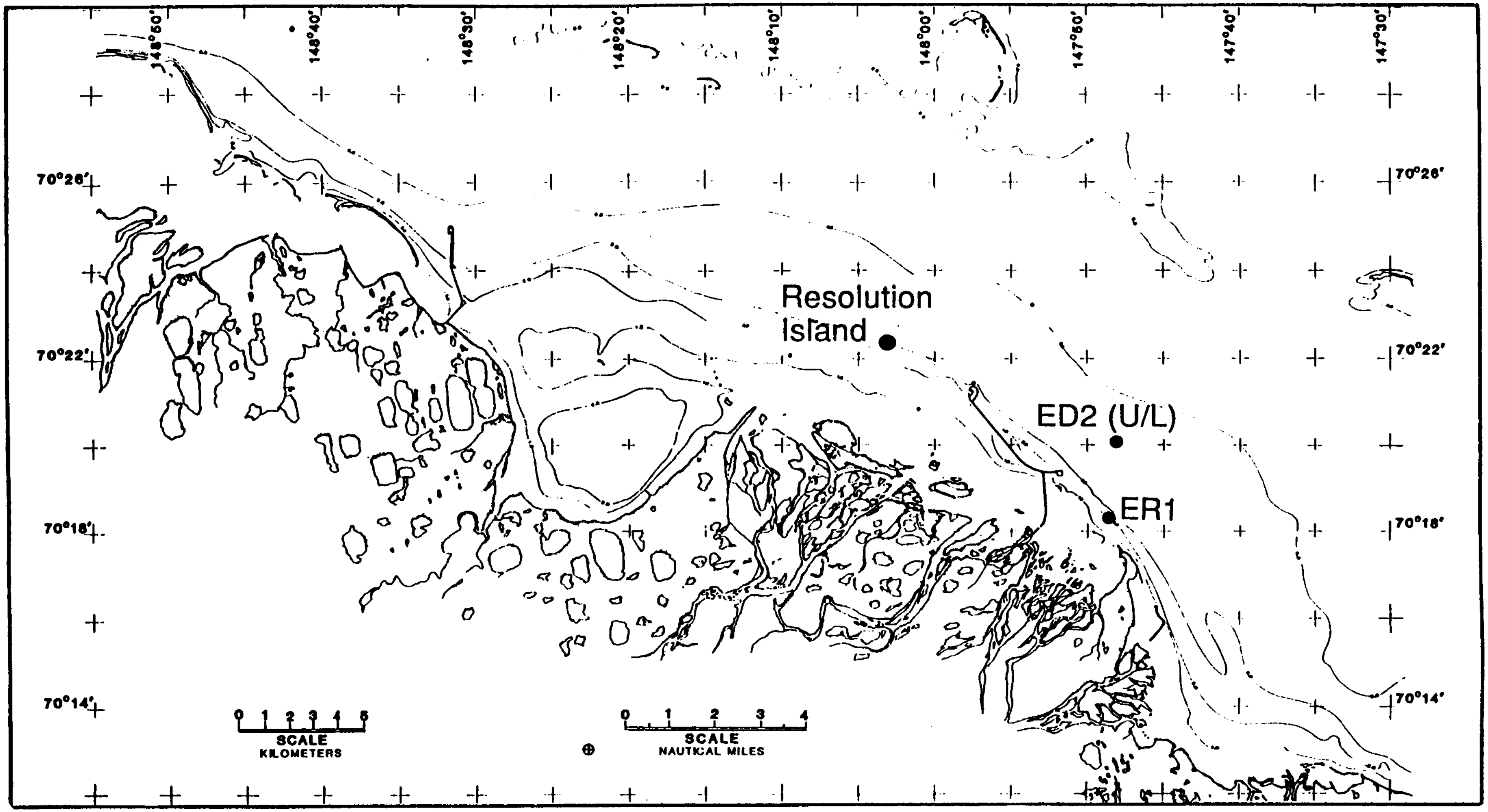

Figure 3-3. Location of 1985 current meter and meteorological data records selected for analysis.

Table 3.2 Details of current records and meteorological data, 1984

File name is the name of the computer disk file for the data and identifies each respective data record on output plots and computed results files.

I.D.	File Name	Current Record Begin	Current Record End	Mooring Location Latitude (N)	Mooring Location Longitude (W)	Depth (m) sensor/bottom
L32	L32.C84					
or	L32.S84	08/06 0600	09/17 2200	70°26.3'	148°36.1'	4.6/6.4
L34	L34.C84					
or	L34.S84	08/05 0500	08/29 0800	70°28.3'	148°28.5'	7.3/9.1
L36	L36.C84					
or	L36.S84	08/06 0200	09/12 0500	70°21.4'	147°46.6'	4.6/6.4
Deadhorse Airport						
Met Data	DH.W84	06/01 0100	09/30 2400	70°11.92'	148°26.47'	
Gull Island						
Met Data	GI.W84	06/22 0100	09/15 1500	70°22.0'	148°43.9'	

Table 3-3. Details of current records and meteorological data, 1985

File name is the name of the computer disk file for the data and identifies each respective data record on output plots and computed results files.

I.D.	File Name	Current Record Begin	Current Record End	Mooring Location Latitude (N)	Mooring Location Longitude (W)	Depth (m) sensor/bottom
ER1	ER1H.C85	07/25 1159	09/13 1059	70°18.3'	147°48.8'	1.0/2.0
or	ER1.C85					
ED2upper	ED2UH.C85	08/08 1205	08/25 1705	70°20.5'	147°48.3'	2.0/5.0
or	ED2U.C85					
ED2lower	ED2LH.C85	08/08 1158	09/13 1158	70°20.5'	147°48.3'	4.0/5.0
or	ED2L.C85					
Resolution Is.						
Met Data	RMETL.W85	07/16 0100	09/19 1200	70°22.3'	148°03.1'	
or	RI.W85					

relationship between currents at the same location and, in addition, were obtained seaward of the shielding effect of the artificial barrier. Record lengths were 18 and 36 days, respectively. While current record ER1 was measured at a depth of 1.0 meter, it was included because its 50-day record length provided the best opportunity of detecting long-period current fluctuations. None of these current records had any apparent errors.

Resolution Island meteorological observations supplied the wind data for the 1985 analysis. These data contained two gaps, 08/03 1800 to 08/05 2000 and 09/08 1100 to 09/09 1400. The relation between Resolution Island and Deadhorse Airport observations were deemed sufficiently close that Deadhorse Airport observations were substituted directly into the two gaps in the Resolution Island data. Resolution Island data were favored over Deadhorse data because of closer proximity to the current meter moorings.

3.2.4 1986 Data

Several current records were chosen from the 1986 Endicott Monitoring Program (Short et al., 1987) nearshore data set obtained in Stefansson Sound near Prudhoe Bay (Figure 3-4, Table 3-4). These current records were chosen because of their long duration and distribution both in shallow water and in nearshore locations offshore of the gravel causeway. All the current records were complete and showed no apparent deficiencies. Data collection was terminated by ice encroachment just prior to deployment of current meters farther offshore that initiated the Beaufort Sea Mesoscale Circulation Study (Aagaard et al., 1989). Nearshore data were not available for comparison with offshore data in 1986.

As in 1985, meteorological data were available from a recording station on Resolution Island. These data supplied wind information used in the 1986 analysis.

3.2.5 1987 Data

A third-year continuation of the Endicott monitoring program in Stefansson Sound near Prudhoe Bay (Short et al., 1988) supplied nearshore current records for analysis. Current records came from three mooring locations seaward of the alongshore barrier lying off the mouth of the Sagavanirktok River (Figure 3-5, Table 3-5). These records provided the opportunity to investigate the relation of currents both vertically at a single location (the same as in 1985) and horizontally alongshore at separations of approximately 6 and 12 km.

One current record, ED1, contained a gap from 08/17 0600 to 08/17 1800, the interval for recovery of one current meter and deployment of another in the same location. In view of the gap length relative to the total record length of 48 days, the gap was bridged by linear interpolation, the assumption being that calculated results would differ little from those obtained if a more sophisticated method were used to bridge the gap. Indeed, calculations made with the gap filled with zeroes were nearly identical with those made after bridging by linear interpolation.

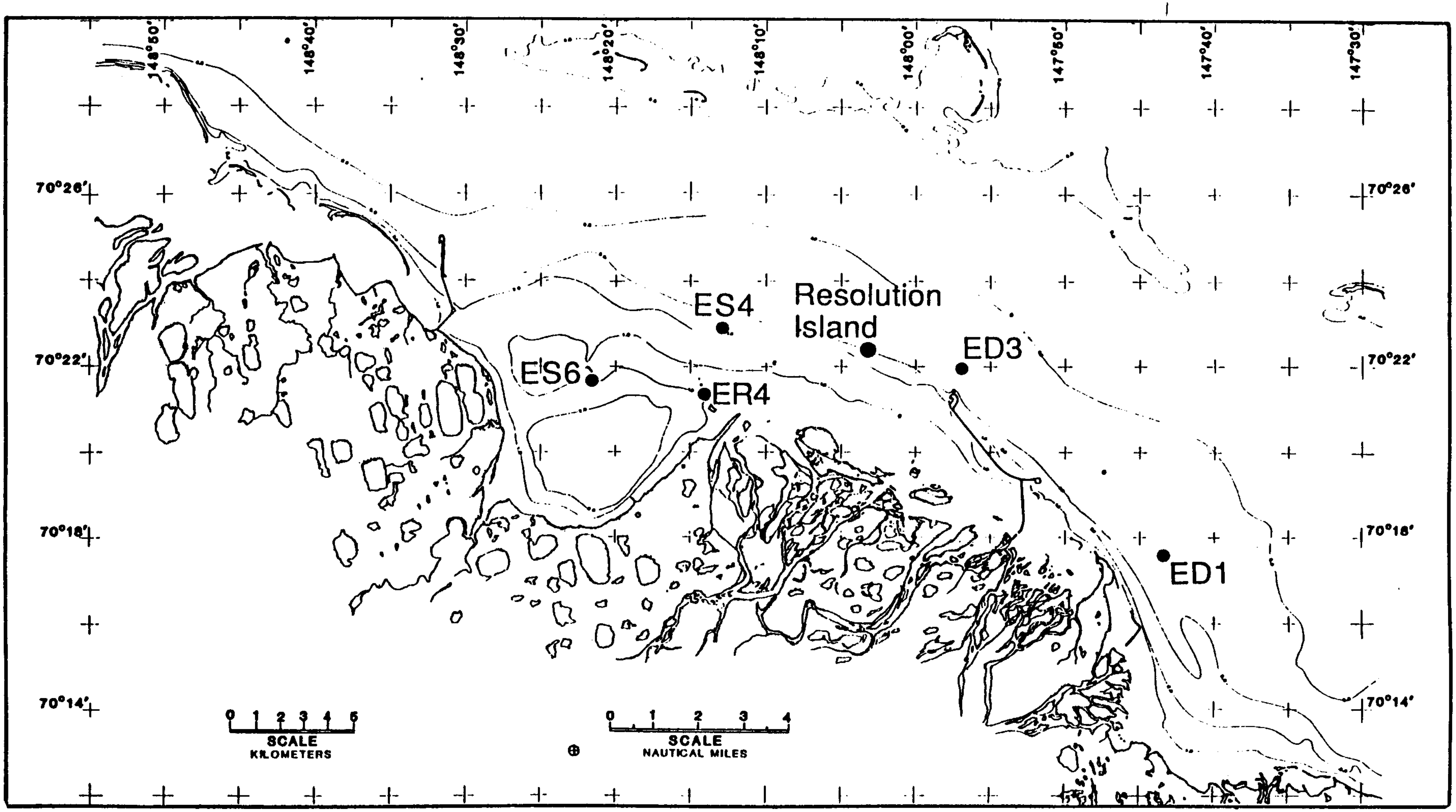

Figure 3-4. Location of 1986 current meter and meteorological data records selected for analysis.

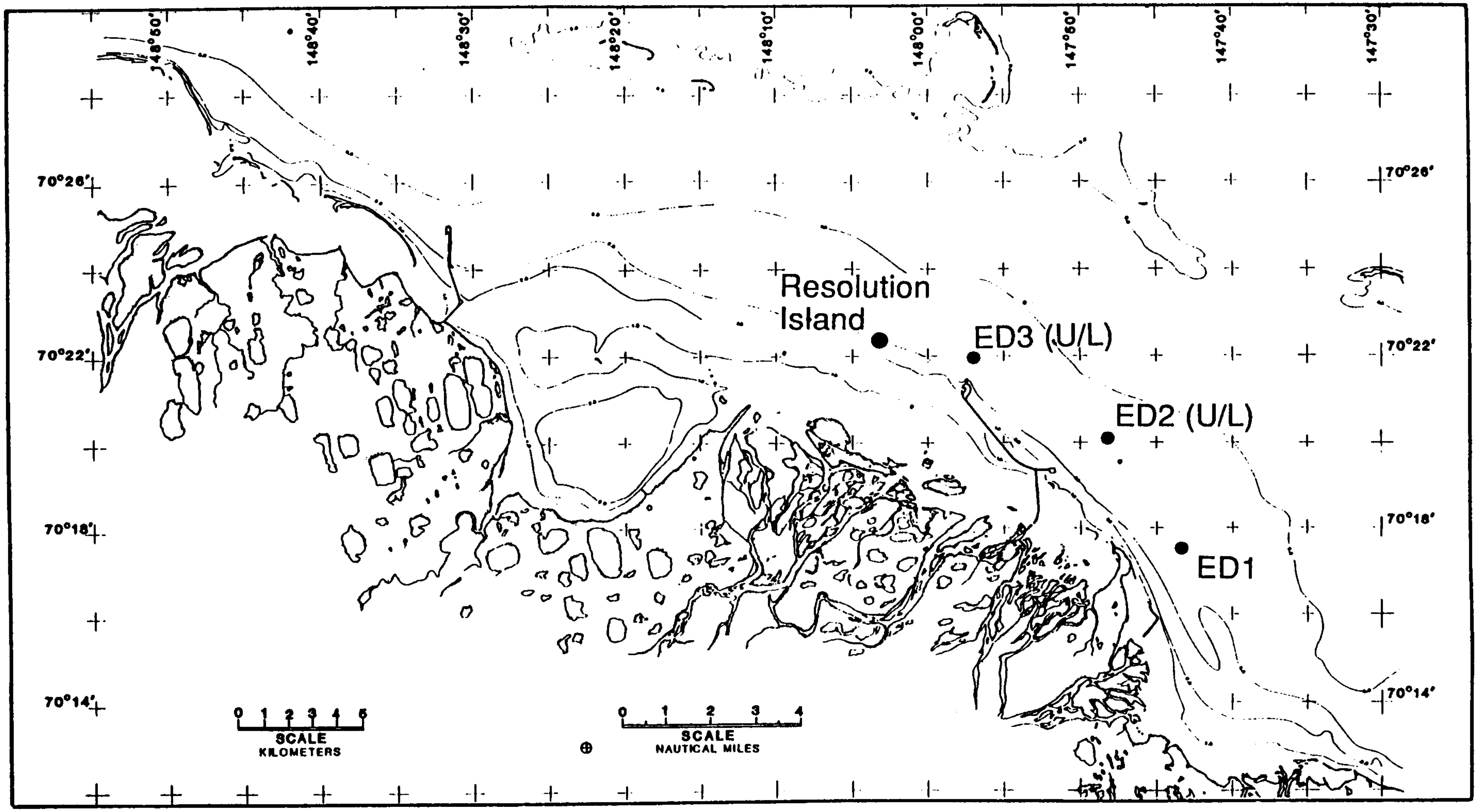

Figure 3-5. Location of 1987 current meter and meteorological data records selected for analysis.

Table 3-4. Details of current records and meteorological data, 1986

File name is the name of the computer disk file for the data and identifies each respective data record on output plots and computed results files.

I.D.	File Name	Current Record Begin	Current Record End	Mooring Location Latitude (N)	Mooring Location Longitude (W)	Depth (m) sensor/bottom
ED1	ED1.C86	07/27 1200	08/23 0800	70°17.6'	147°43.0'	2.7/4.0
ED3upper	ED3.C86	07/27 1200	09/10 1100	70°21.9'	147°56.7'	2.7/5.0
ER4	ER4.C86	07/29 1800	09/11 1200	70°21.1'	148°14.4'	0.9/1.0
ES4	ES4.C86	07/29 1800	09/11 1300	70°22.9'	148°13.0'	1.5/2.0
ES6	ES6.C86	07/29 1800	09/04 1000	70°21.7'	148°22.0'	0.6/1.0
Resolution Is. Met Data	RI.W86	05/31 1300	09/30 1600	70°22.3'	148°03.1'	

Table 3-5. Details of current records and meteorological data, 1987

File name is the name of the computer disk file for the data and identifies each respective data record on output plots and computed results files.

I.D.	File Name	Current Record Begin	Current Record End	Mooring Location Latitude (N)	Mooring Location Longitude (W)	Depth (m) sensor/bottom
ED1	ED1.C87	07/25 0000	09/11 0000	70°17.6'	147°43.0'	3.1/4.0
ED2upper	ED2U.C87	07/24 1100	09/11 1000	70°20.5'	147°48.3'	2.4/4.2
ED2lower	ED2L.C87	08/12 2100	09/11 1100	70°20.5'	147°48.3'	4.0/4.2
ED3upper	ED3U.C87	08/25 1700	09/11 0700	70°21.9'	147°56.7'	3.0/5.0
MB2B-1		04/05/87	04/04/88	70°55.1'	146°45.8'	72/185
MB4B-1		04/03/87	03/30/88	70°52.6'	146°57.3'	52/60
Resolution Is. Met Data	RI.W87	05/29 1800	09/30 1200	70°22.3'	148°03.1'	

These current records overlapped current records obtained further offshore as part of the BSMCS. They were used subsequently to investigate the relation between nearshore wind and currents and offshore currents about 70 to 80 km north-northeast of the Stefansson Sound sites.

A recording station that was installed on Resolution Island provided wind data used in 1987 calculations. The wind data contained no gaps or deficiencies and totally bracketed the current meter deployment intervals.

3.2.6 1988 Data

Current meter data available to the program from 1988 were limited. A single current record, from a monitoring project in the area just offshore of the Arctic National Wildlife Refuge (ANWR), was chosen (Figure 3-6, Table 3-6). While other current meters were deployed, they were very near shore or in protected areas, and it was felt that calculated results would be of very limited use, if any. Current meters deployed as part of the Beaufort Sea Mesoscale Circulation Study were recovered in March and April 1988, so there were no overlapping nearshore and offshore current records for analysis.

A temporary MET station installed on the spit at Simpson's Cove in Camden Bay was the source of meteorological data for the ANWR current meter data comparison. The length of the meteorological data record was slightly shorter than the current meter record, but contained no gaps or other problematic features.

3.2.7 1989 Data

Data from 1989 chosen for analysis were two current meter records from mooring location CB6, the same as the 1988 ANWR data, and a nearshore current record CB2 (Table 3-7). Locations are indicated on Figure 3-6. Choosing the 1989 CB6 current records allowed comparison with 1988 data from the same location and examination of currents separated vertically in the water column. There were no current meters deployed offshore simultaneously with the 1989 ANWR deployments, so no nearshore/offshore comparison was possible.

As in 1988, a temporary MET station installed on the spit at Simpson's Cove in Camden Bay provided meteorological data for the 1989 deployments in Camden Bay.

3.3 RESULTS AND DISCUSSION

3.3.1 Wind and Nearshore Currents

3.3.1.1 Wind-explained Current Variance

The percentage of current variability explained by the wind varied both spatially and temporally, and showed a distinct depth dependence (Table 3-8). Generally, the wind accounted for approximately 40-50 percent of the variance of nearshore currents at current meter depths of 3 m or less in water that was less than about 6 m. In contrast, wind explained only about 1-10 percent of the variance at depths greater than 3 m (Table 3-8, 1984 entries) where bottom

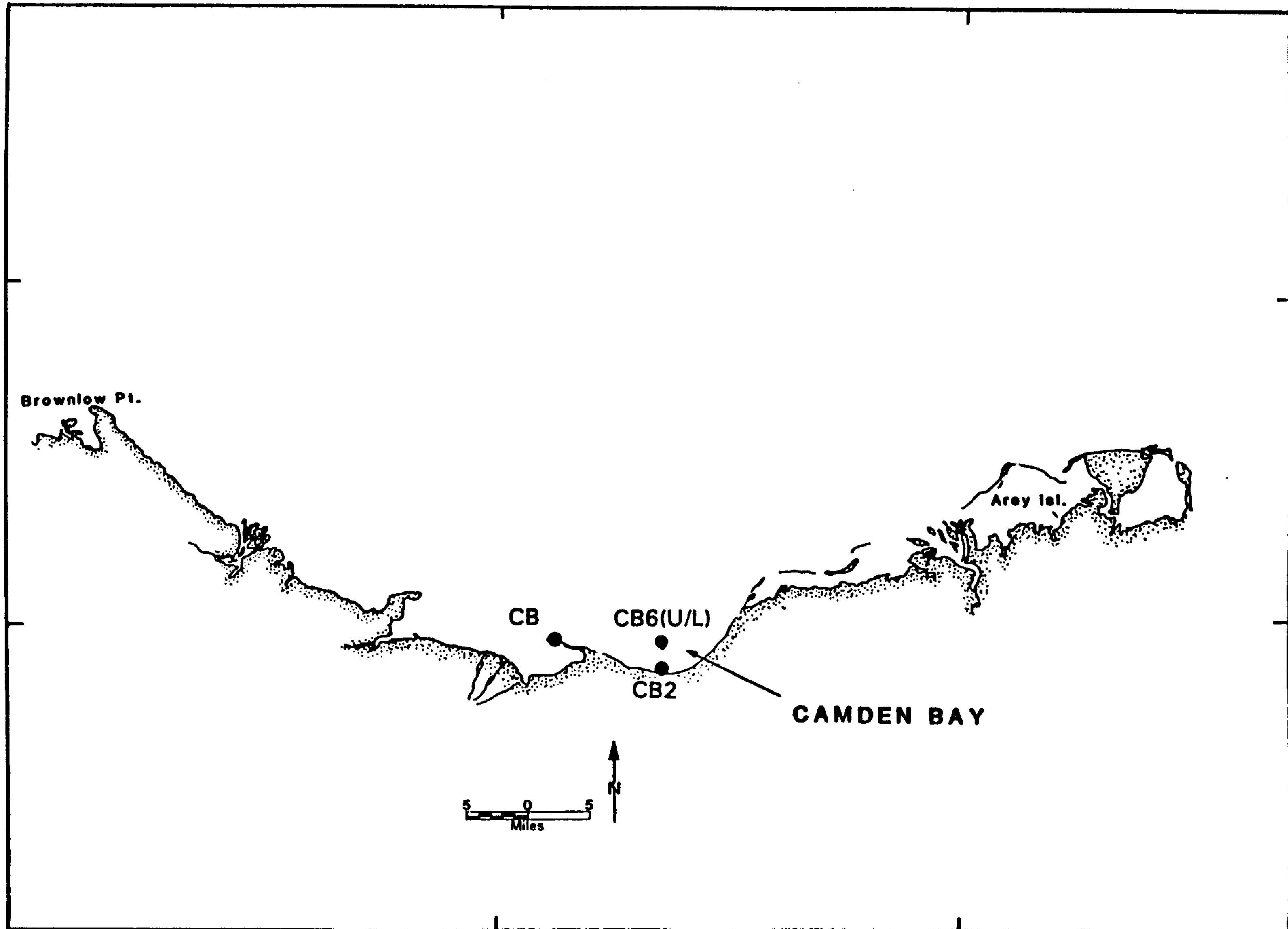

Figure 3-6. Location of 1988 and 1989 current meter and meteorological data records selected for analysis.

Table 3-6. Details of current records and meteorological data, 1988

File name is the name of the computer disk file for the data and identifies each respective data record on output plots and computed results files.

I.D.	File Name	Current Record Begin	End	Mooring Location Latitude (N)	Longitude (W)	Depth (m) sensor/bottom
CB6lower	CL.C88 or CB6L.C88	08/06 2200	09/12 1700	69°59'	144°43'	6.6/7.6
Camden Bay Met Data	CB.W88	08/05/1300	08/28 1300	69°59'	144°52'	
Pokok Bay Met Data	PK.W88	08/10 0000	09/13 1500	69°59'	142°33'	

Table 3-7. Details of current records and meteorological data, 1989

File name is the name of the computer disk file for the data and identifies each respective data record on output plots and computed results files.

I.D.	File Name	Current Record Begin	End	Mooring Location Latitutde (N)	Longitude (W)	Depth (m) sensor/bottom
CB2	CB2.C89	08/03 0000	09/09 1900	69°58'	144°43'	2/3
CB6upper	CB6U.C89	08/03 0000	09/10 1200	69°59'	144°43'	5/8
CB6lower	CB6L.C89	08/03 0000	09/10 0500	69°59'	144°43'	7/8
Camden Bay Met Data	CB.W89	08/03 1200	09/10 1900	69°59'	144°52'	

Table 3-8. Summary of regression and U-component correlation calculations between wind and currents.

Year Data File Name	Current Variance Explained by Wind (%)	Cross[1/] Correlation Maximum(lag/hr)	Factor Relating Correlated Wind and Current Speeds	Indraft Angle of Current Relative to Wind L or R	Depth (m) sensor/bottom
1989					
CB6U.C89	28	0.65(1)	.018	73°R	3/8
CB6L.C89	15	0.48(5)	.009	18°R	7/8
CB2.C89	10	0.41(4)	.006	51°R	2/3
1988					
CB6L.C88	19	0.56(2)	.007	48°L	6.6/7.6
1987					
ED1.C87	35	0.76(3)	.013	53°R	3.1/4.0
ED2U.C87[2/]	55	0.91(2)	.027	43°R	2.4/4.2
ED2L.C87	33	NC[4/]	.014	22°R	4.0/4.2
ED2U.C87[3/]	45	NC	.026	45°R	2.4/4.2
ED3U.C87	47	NC	.025	40°R	3.0/5.0
MB4B-1.C87		0.69(8)			52/60
1986					
ED1.C86	39	NC	.013	48°R	2.7/4.0
ED3.C86	39	NC	.021	33°R	2.7/5.0
ER4.C86	53	NC	.020	46°L	0.9/1.0
ES4.C86	27	0.82(3)	.008	4°R	1.5/2.1
ES6.C86	45	NC	.011	31°R	0.6/1.0
1985					
ER1.C85	32	0.49(1)	.009	63°R	1.0/2.0
ED2U.C85	41	0.73(3)	.009	46°R	2.0/5.0
ED2L.C85	3	0.38(6)	.002	14°R	4.0/5.0
1984					
L32.C84	3	NC	.001	10°L	4.6/6.4
L34.C84	0	NC	.0001	90°R	7.3/9.1
L36.C84	9	0.43(6)	.007	13°R	4.6/6.4
1982					
L1.C82	50	0.82(2)[5/]	.018	82°R	3.0/5.0
L3.C82	52	0.83(-2)[5/]	.023	59°R	3.0/5.0
L4.C82	43	0.81(1)	.015	83°R	1.0/2.0
L5.C82	49	0.77(3)	.014	23°R	1.0/2.0

1/ Wind leads for positive lags.
2/ Record starts at 0000 on 25 July 1987.
3/ Record starts at 2100 on 12 August 1987.
4/ NC = Not computed.
5/ Exact lag is dubious because of start-time errors.

depths were greater than about 6 m. However, in two cases in 1987, wind explained 33 percent and 35 percent of variance of deeper currents at mooring locations ED1 and ED2, respectively. Note that the same is not true for 1985, ED2, when wind explained only 3 percent of the variance of the deeper currents. These comparisons, along with comparisons of the scale factors relating winds and deeper currents (Table 3-8) in 1985 and 1987 indicate a notable difference in wind-forcing of the deeper currents. The reason for the difference in this example is that stratified conditions persisted throughout the 1985 open water season, while well-mixed conditions characterized the majority of the 1987 open water season (Short et al., 1989). Stratification presented a buoyancy barrier that inhibited vertical transfer of momentum from the surface layer downward. The differences in the degrees of mixing were largely due to wind direction and persistence, affecting hydrographic conditions through either onshore or offshore Ekman drift.

Wind accounted for a comparable fraction of current variance at a depth of approximately 7 m at mooring location CB6 in Camden Bay in 1988 (19 percent) and 1989 (15 percent). During the 1989 deployment, wind accounted for 28 percent of the current variance at a depth of about 3 m, which is consistent with increasing fraction of wind-explained variance with increasing distance above the bottom. Vector-average wind speed and direction were similar during those two respective deployment intervals.

While the wind-explained current variance near the bottom at location CB6 in 1988 and 1989 is comparable, one striking difference is that the vector-average current direction was eastward in 1988, roughly in opposition to the wind, but north-northwestward in 1989, which may reflect geographic steering and westward wind component. In 1989, near-surface vector-average currents at location CB6 were east-southeastward, roughly opposite the near-bottom currents and also somewhat in opposition to winds. Vector-average currents at CB2 in 1989 were also eastward along the coastline, confirming a component of circulation in Camden Bay in opposition to direct wind-stress forcing. Fluctuations in wind affected fluctuations in currents similarly in both years, but there apparently were other influences such as recirculation in Camden Bay or presence of local or large-scale pressure gradients that were different between the two years.

The retarding action of bottom friction will also influence deeper currents. However, bottom friction is a passive influence that depends on current speed, which in turn is related to external forcing. The implication is that annual variability of meteorological conditions, which subsequently affect hydrographic conditions, exerts a primary influence on the degree to which wind drives deeper currents.

3.3.1.2 Correlation Analysis

Wind consistently led nearshore currents by 1-3 hours (Table 3-8). Cross correlations between wind and current major axis velocity components in the principal axis coordinate system (henceforth termed U components) ranged from 0.38 to 0.91, averaging 0.69. Cross correlation functions decayed to zero within a lagged interval of about 40 to 60 hours (Figure 3-7 is typical). The maximum cross correlation between minor axis velocity components (henceforth

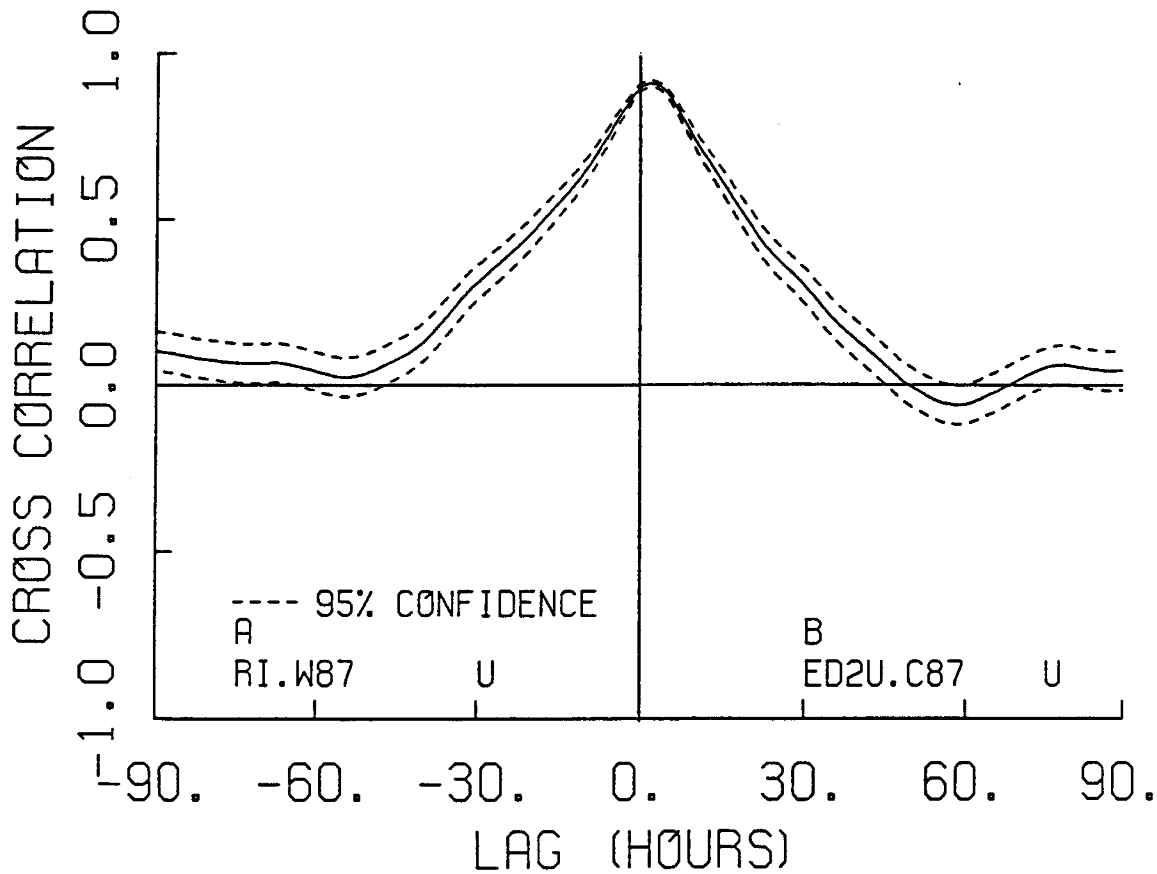

Figure 3-7. Cross correlation between U-components of Resolution Island wind and ED2 upper currents, 1987. Wind leads for positive lags.

termed V components) of wind and currents was typically between -0.4 and zero, and decayed to zero within a lag of about 10 hours (Figure 3-8). The negative correlation between wind and V components of currents indicates that the relation may be secondary within several kilometers of the coast. Coherence and phase calculations between wind and ED2 upper, 1987 confirm the intuitive expectation that the strongest relation is at low frequencies and that the wind and near surface currents are nearly in phase (Figure 3-9).

3.3.2 Vertical Relation between Currents

Analysis of current records from mooring location ED2, 1985 and 1987 shows interannual differences in the relation between currents measured at two depths. In 1985, wind accounted for 41 percent and 3 percent of the current variance at depths of 2 m and 4 m, respectively (Table 3-8). In 1987, however, wind accounted for 55 percent and 33 percent of the current variance at 2.4 m and 4 m, respectively (Table 3-8).

While there is a lower percentage of the current variance explained by the wind at the lower depths in both years, it is especially apparent in 1985. One significant difference is that in 1985, meteorological patterns were such that well-mixed conditions in the water column were never consistently established over the open-water season, while 1987 was a year in which the water column was either weakly stratified or well-mixed for much of the open water season (Short, et al., 1989). The direct consequence is that in 1985, stratification tended to weaken the coupling between the surface layer and the deeper part of the water column, weakening the influence of direct wind action on deeper currents. The absence of a buoyancy barrier to vertical momentum transport in 1987 led to greater wind influence on deeper currents compared to the more stratified case observed in 1985. The difference in the scale factor relating wind and currents speeds at depth in 1985 and 1987 reflects the increased coupling of wind effects to deeper currents in 1987.

Maximum U-component cross correlation coefficients between the upper and lower currents at ED2 were also different in 1985 and 1987 (Figures 3-10 and 3-11). The maximum of 0.64 in 1985 relative to 0.91 in 1987 indicates a stronger coupling of the upper and lower layers of the water column in 1987, as do the lags of 1 to 2 hours in 1985 versus 0 to 1 hour in 1987 for maximum correlation.

The V-component cross correlation between upper and lower currents was distinctly influenced by tidal signals (cf. Figure 3-12). While the tidal signal is obvious, the cross correlation is only marginally different from zero at the 95 percent confidence limit. There is only weak evidence of longer-term correlation, shown by the broad positive peak at lag of about -45 hours and negative peak at lag of +45 hours (Figure 3-12). Coherence and phase calculations for the V-components of upper and lower current records from ED2 in 1985 (Figure 3-13) confirm the correlation at semi-diurnal tidal frequencies (0.08 cph) but show no indication of significant relation at lower frequencies. Analogous calculations for 1987 yield coherence and phase plots (Figure 3-14) surprisingly similar to those for 1985, implying that variance along the minor axis is relatively independent of stratification and wind patterns.

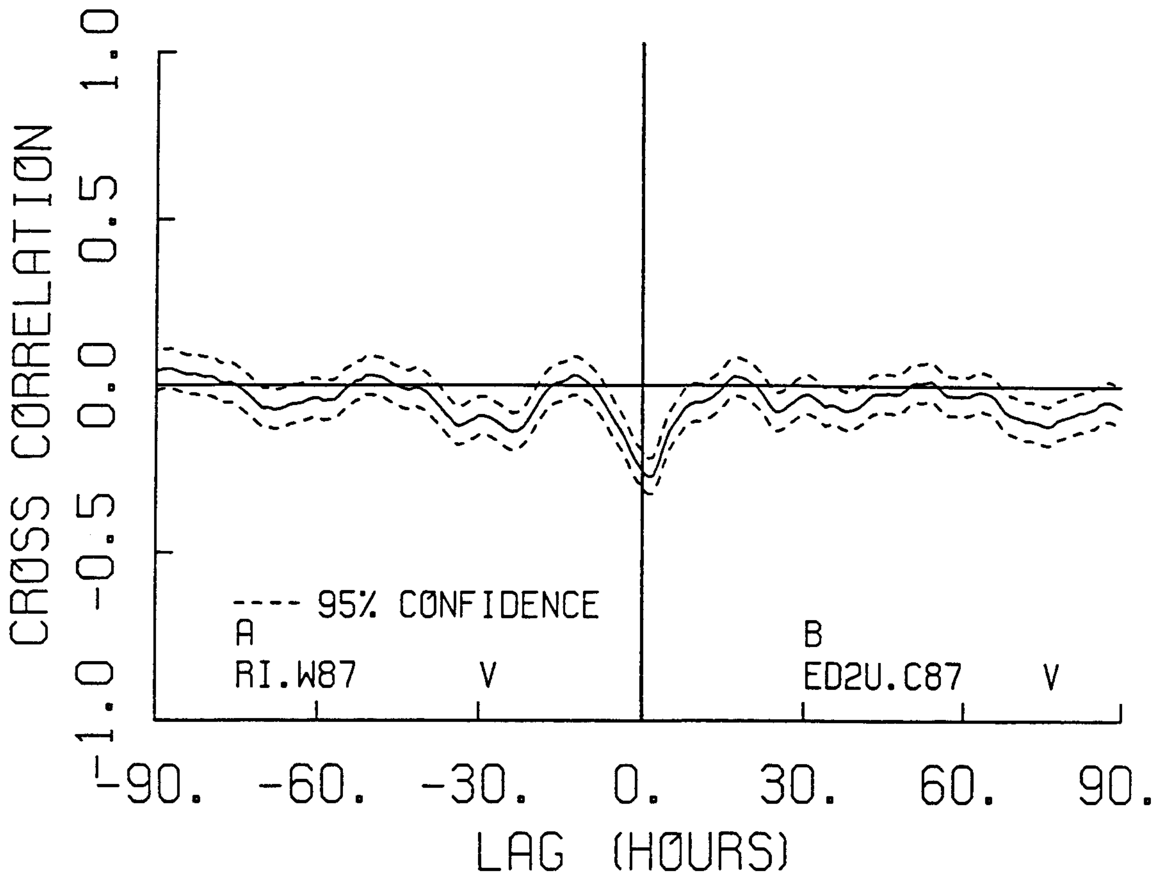

Figure 3-8. Cross correlation between V-components of Resolution Island wind and ED2 upper currents, 1987. Wind leads for positive lags.

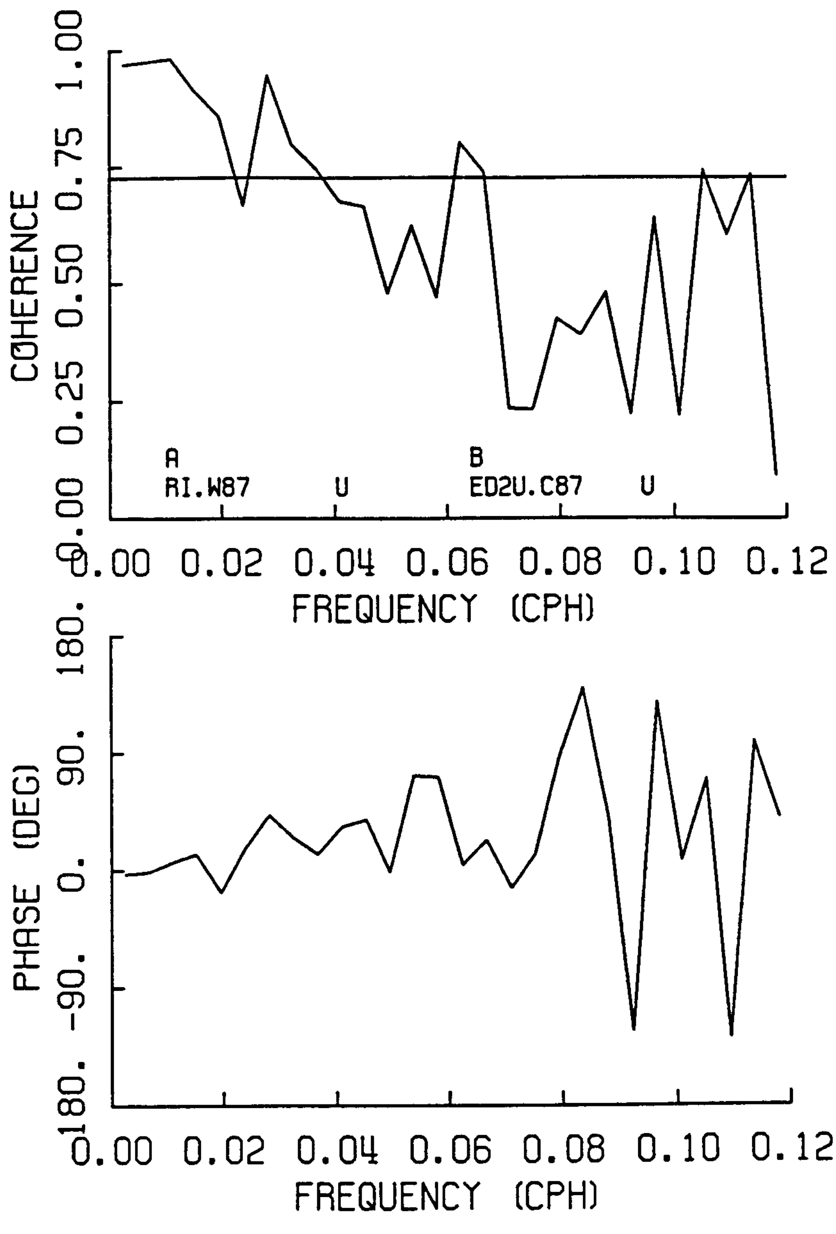

Figure 3-9. Coherence and phase between U-components of Resolution Island wind and ED2 upper currents, 1987. Positive phase indicates wind leads currents.

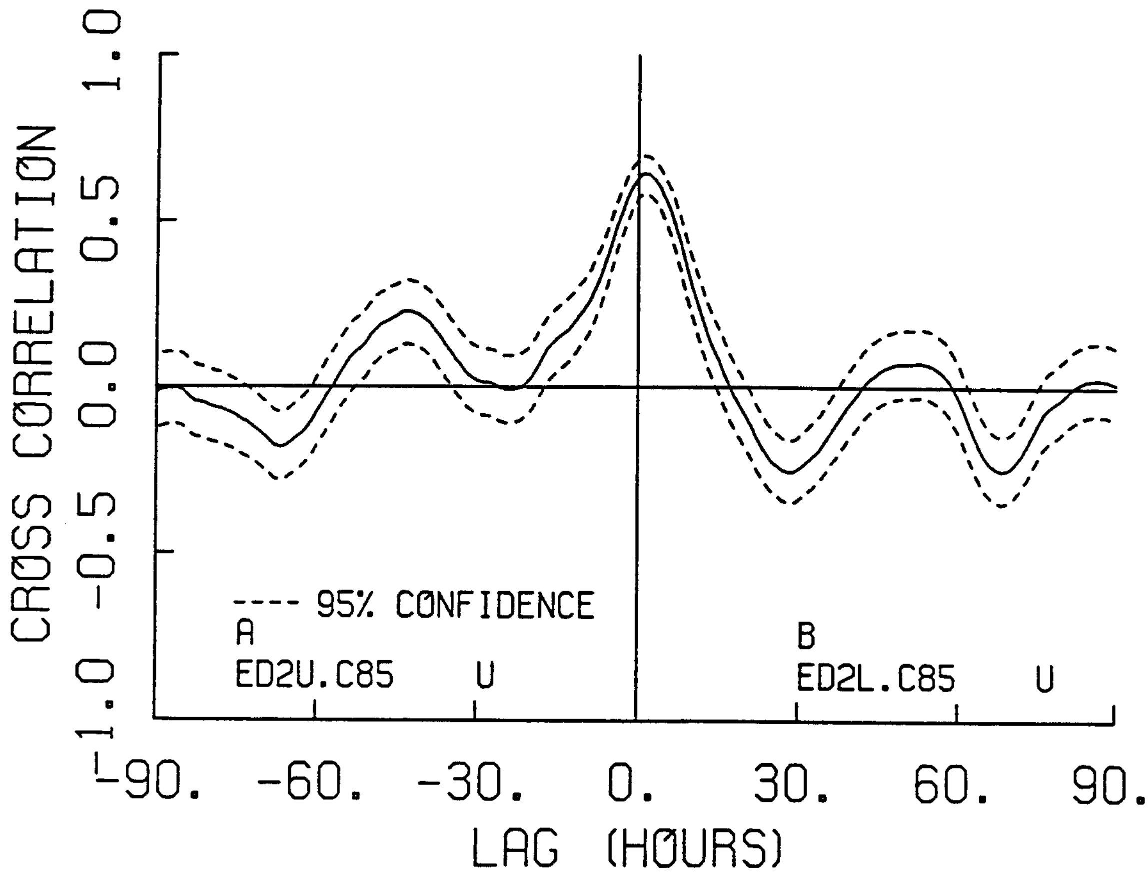

Figure 3-10. Cross correlation between U-component currents at ED2 upper and ED2 lower, 1985. For positive lags, ED2 upper leads.

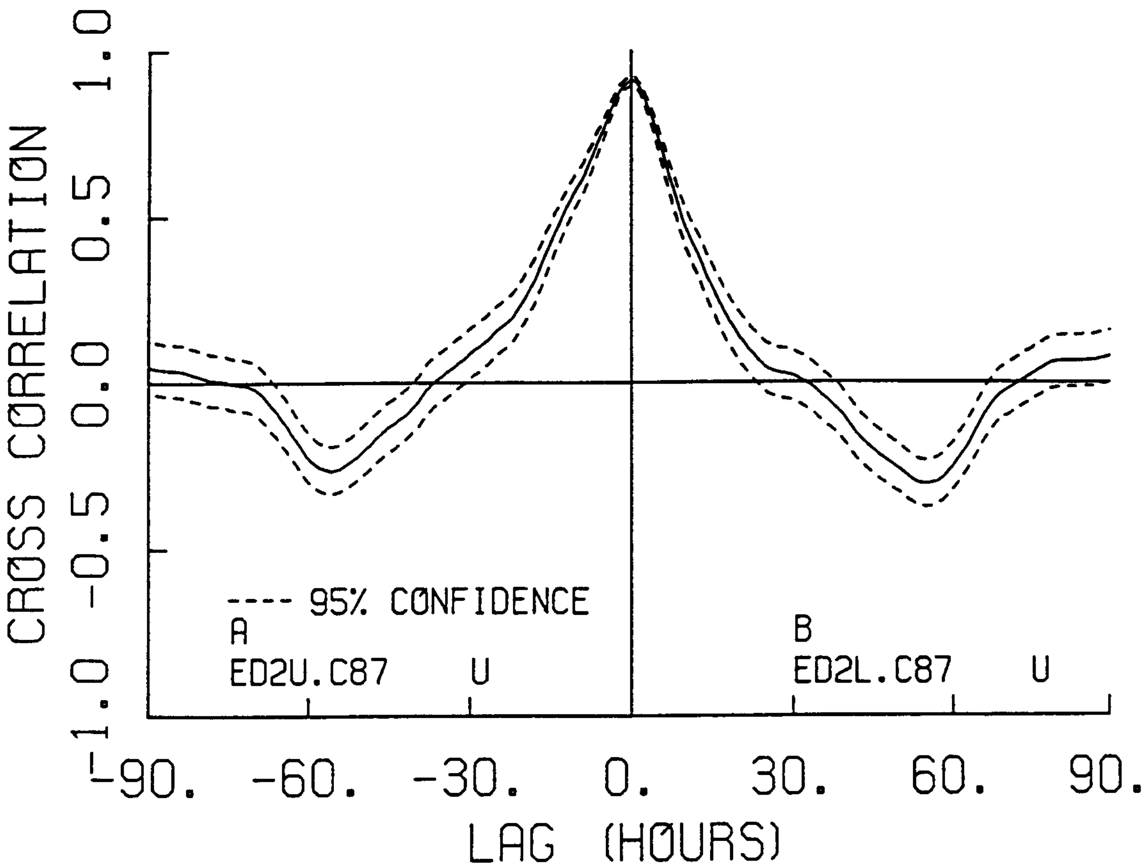

Figure 3-11. Cross correlation between U-component currents at ED2 upper and ED2 lower, 1987. For positive lags, ED2 upper leads.

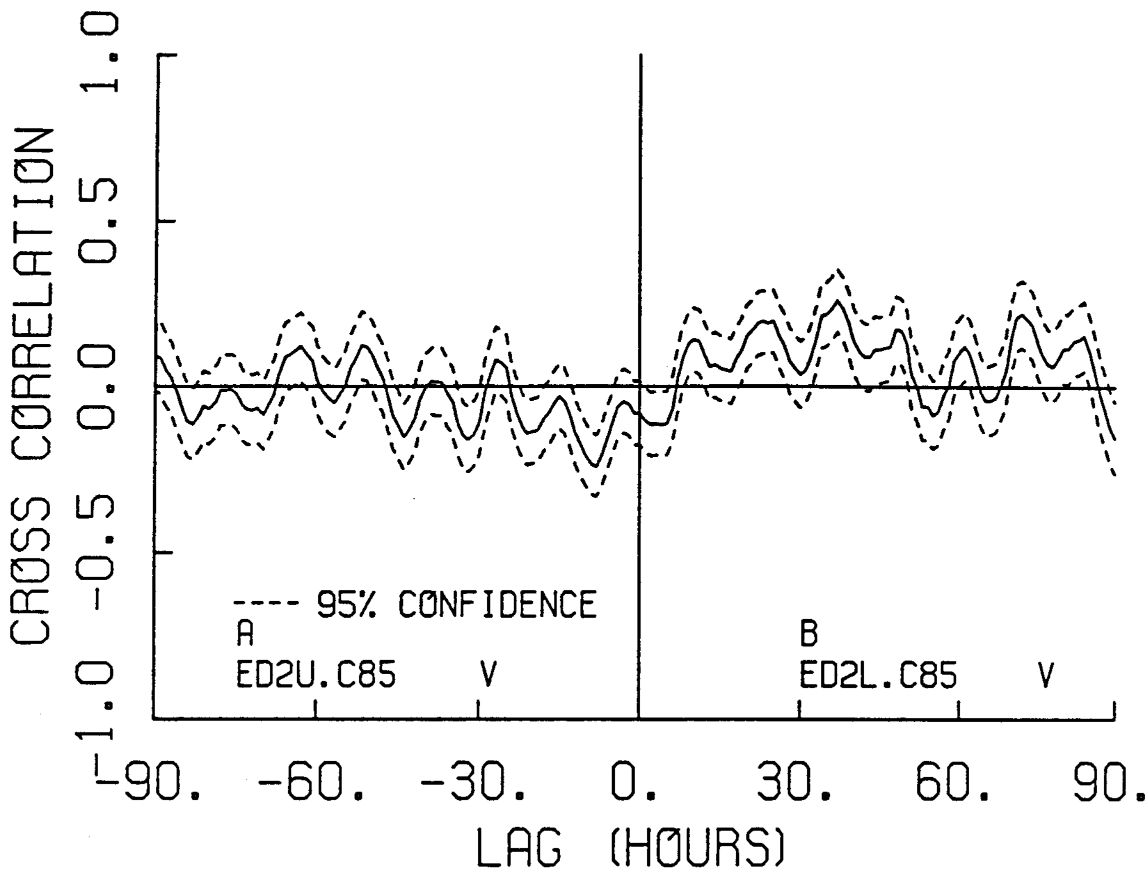

Figure 3-12. Cross correlation between V-component currents at ED2 upper and ED2 lower, 1985. For positive lags, ED2 upper leads.

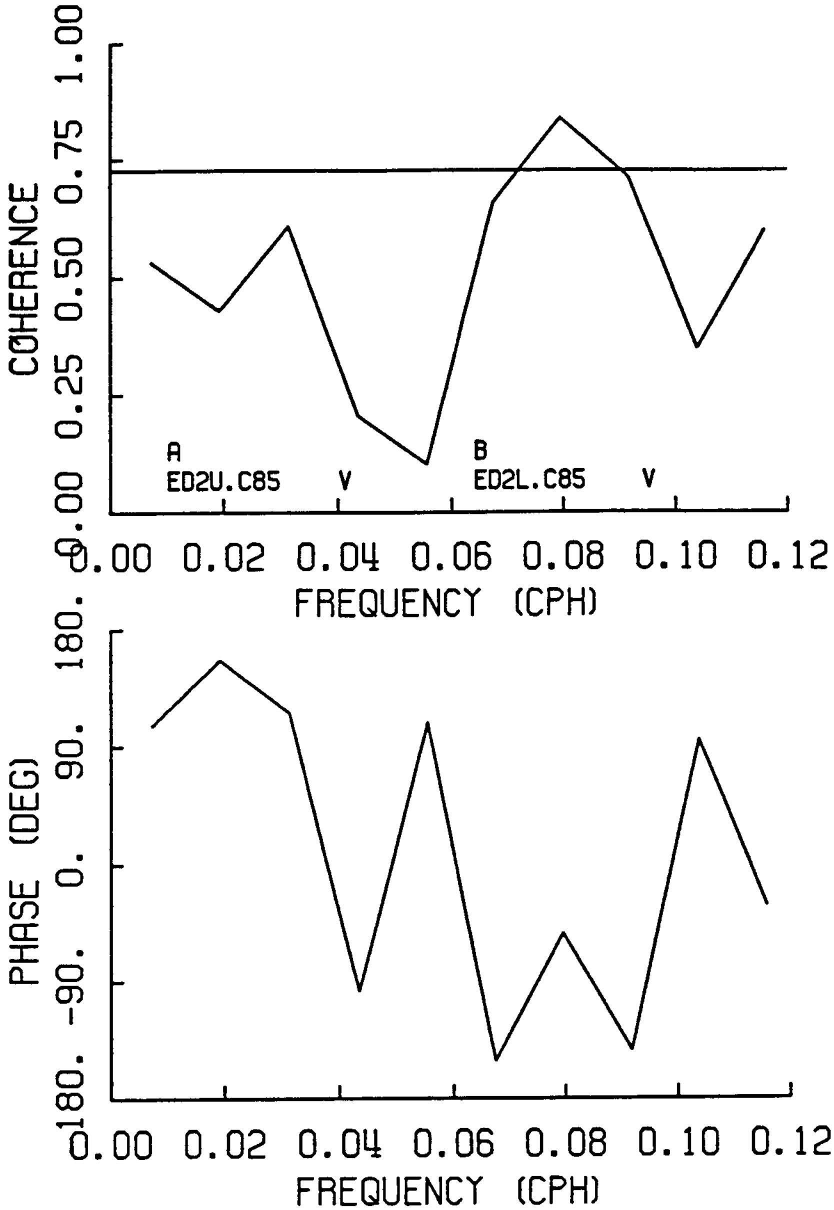

Figure 3-13. Coherence and phase between V-component currents at ED2 upper and ED2 lower, 1985. Positive phase indicates ED2 upper leads.

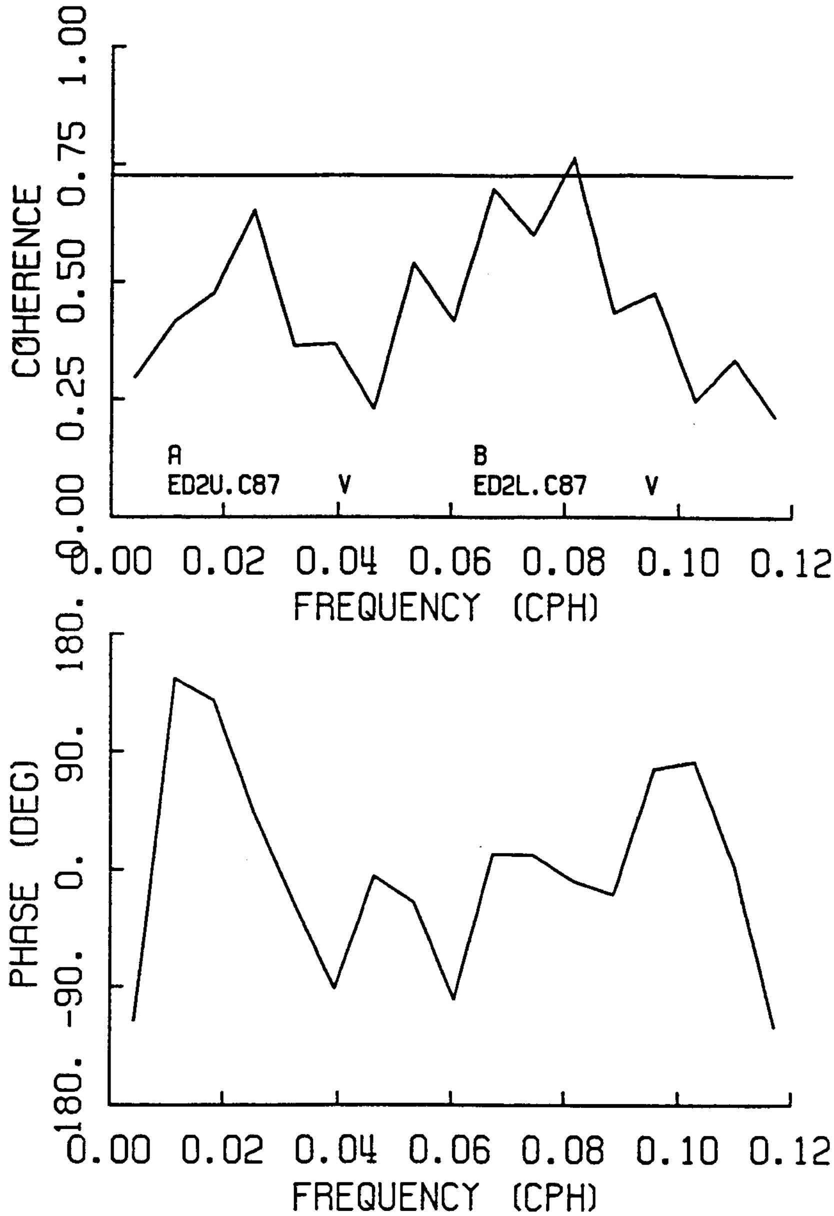

Figure 3-14. Coherence and phase between V-component currents at ED2 upper and ED2 lower, 1987. Positive phase indicates ED2 upper leads.

Cross correlation between U-components of upper and lower current meters at location CB6 (Camden Bay) in 1989 indicates the deeper current leading the upper current by 0 to 1 hours at maximum correlation of 0.59 (Figure 3-15). This result is opposite that in 1985 and 1987, when upper currents led deeper currents. In 1989, wind led upper currents by one hour, maximum correlation of 0.65 (Figure 3-16). For the same time interval, wind led lower current by five hours, maximum correlation of 0.48 (Figure 3-17). Based upon comparison of cross correlations between wind and currents at CB6 in 1989, upper current should lead lower current by approximately four hours, which disagrees with results of cross correlation calculations between the two current time series themselves.

One explanation for the apparent inconsistency is that wind and currents possess joint variance in one portion of the frequency spectrum, while the currents possess joint variance in another portion of the spectrum, and that the phasing is different between these two portions of the spectrum. Coherence and phase calculations indicate strong relation between the current records (Figure 3-18) in the low frequency band where wind and currents are generally related, but also between 0.10 and 0.11 cycles per hour. The autospectrum of the upper current meter U-component shows a relative energy deficit for periods between approximately 16 and 50 hours (Figure 3-19) while the autospectrum for the lower current meter (Figure 3-20) shows a constant slope (no deficit) over the same range. Corresponding V-component spectra reflect the same feature, but less clearly.

The implication is that there is sufficient covariance in CB6 currents in the 0.10 to 0.11 cph frequency band, prticularly because of the spectral content of the upper current, to dominate the cross correlation between upper and lower current records. Dimensions of Camden Bay, response to fluctuations in local riverine input, and the sheltered nature of location CB6 to the east are all potential factors influencing the correlation between upper and lower currents at CB6 in 1989.

3.3.3 Periodicities

3.3.3.1 Meteorological

Spectra for the U-component of wind for various analyzed years show no consistent significant spectral peaks, although the spectral content may indicate the presence of a given frequency in a given year. The strongest hint of a consistent interannual signal is at a frequency of about 0.007 cph, which corresponds to a period of approximately six days (Figure 3-21 from 1987 is representative; others, e.g., 1982 L1, L3, L4, L5, 1985 ER1 appear in Appendix A).

A signal at period of about 110 to 120 hours appears in autospectra of 1986 current records, particularly V-component (e.g., Figure 3-22), where the feature is not masked by other low-frequency energy, as is the case for corresponding U-component spectra. The corresponding local wind U-component autospectrum (Figure 3-23) also exhibits a peak at approximately this period, and at this period, it seems likely that wind forcing is the source of current variance.

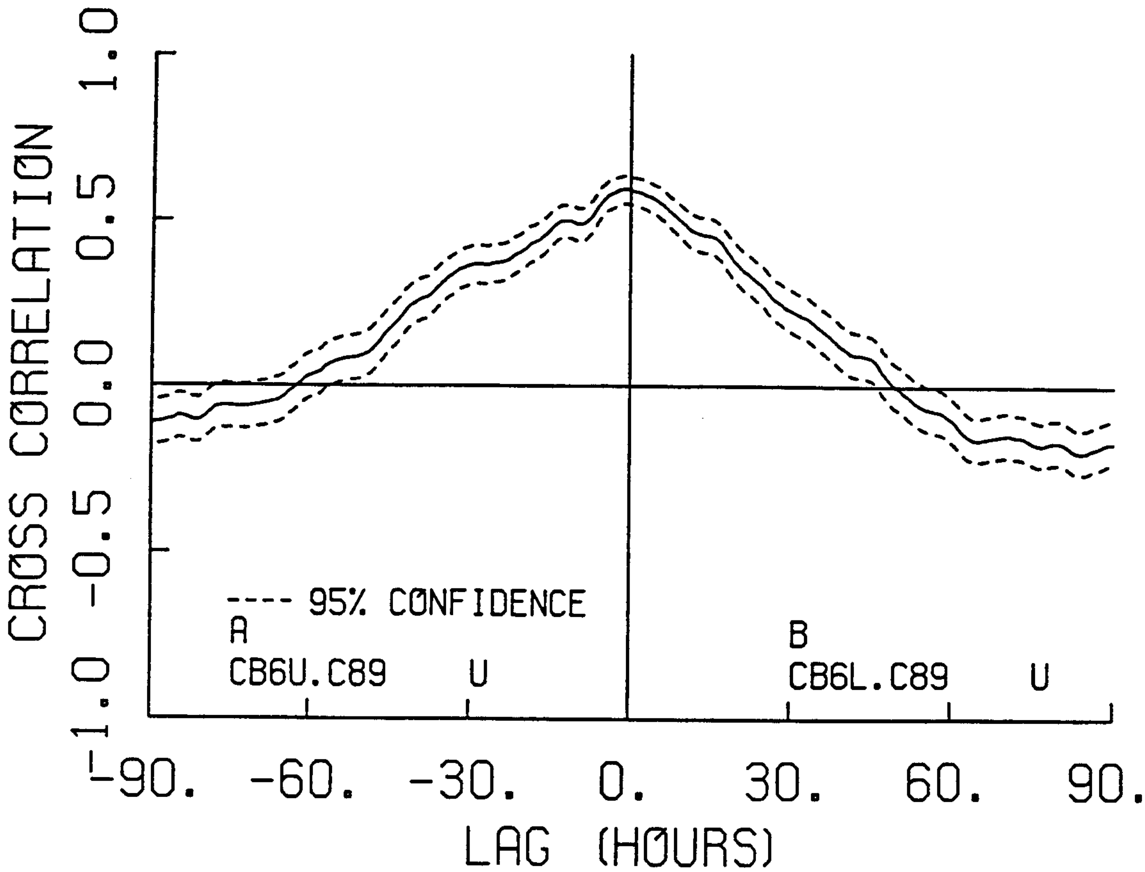

Figure 3-15. Cross correlation between U-component currents at CB6 upper and CB6 lower, 1989. For positive lags, CB6 upper leads.

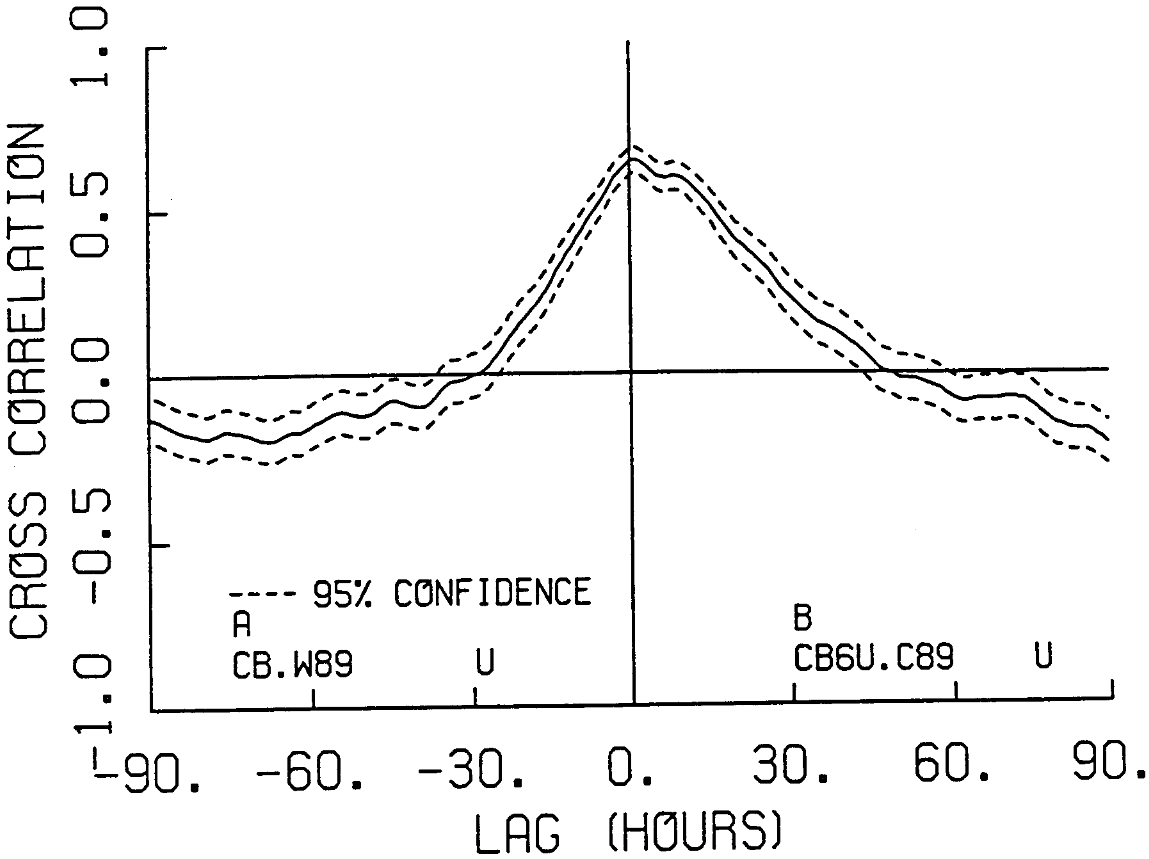

Figure 3-16. Cross correlation between U-components of Camden Bay wind and CB6 upper currents, 1989. Wind leads for positive lags.

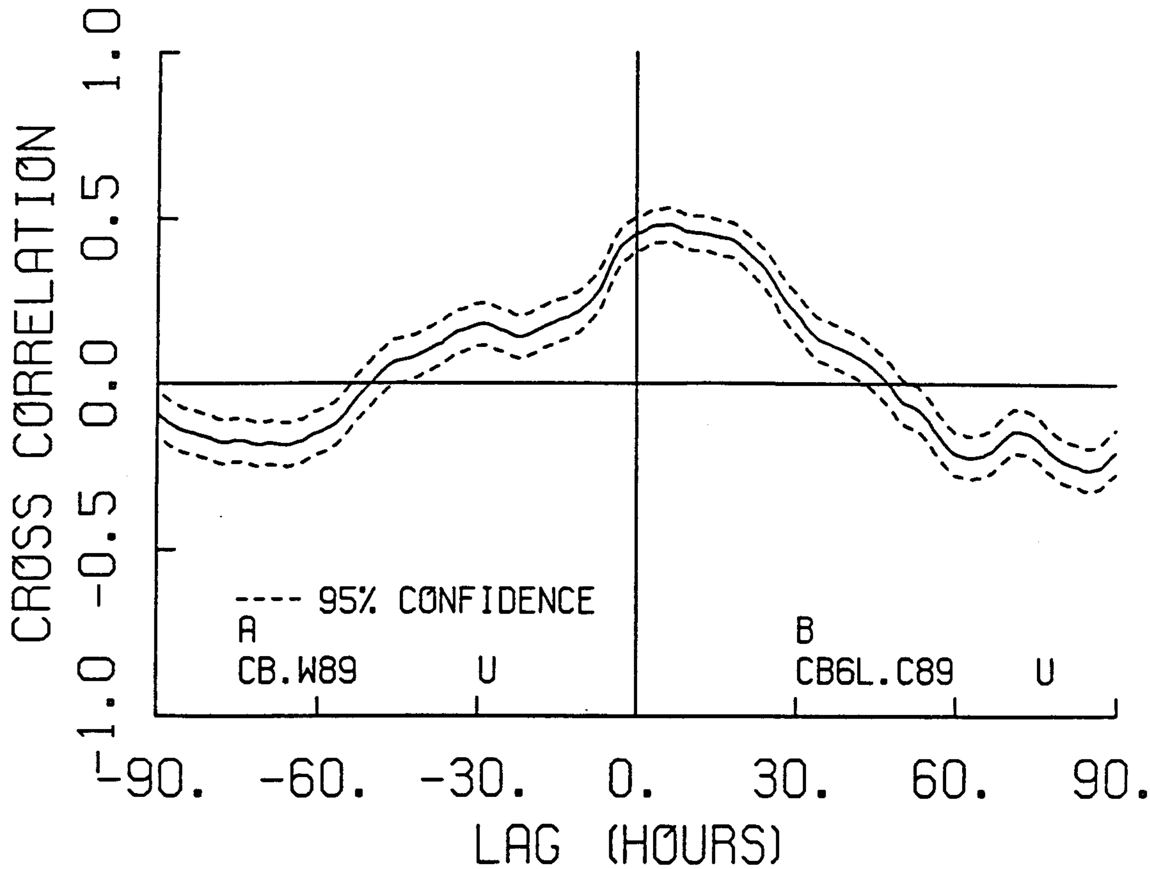

Figure 3-17. Cross correlation between U-components of Camden Bay wind and CB6 lower currents, 1989. Wind leads for positive lags.

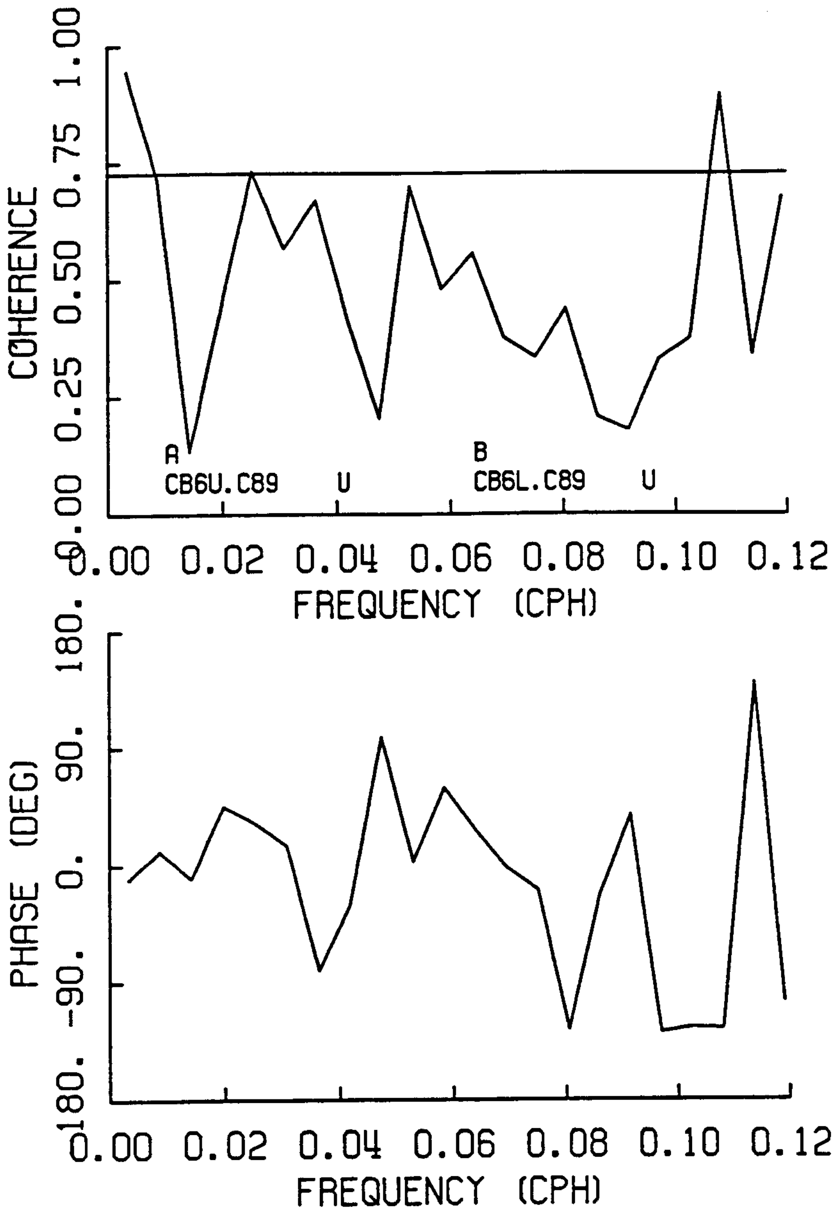

Figure 3-18. Coherence and phase between U-component currents at CB6 upper and CB6 lower, 1989. Positive phase indicates CB6 upper leads.

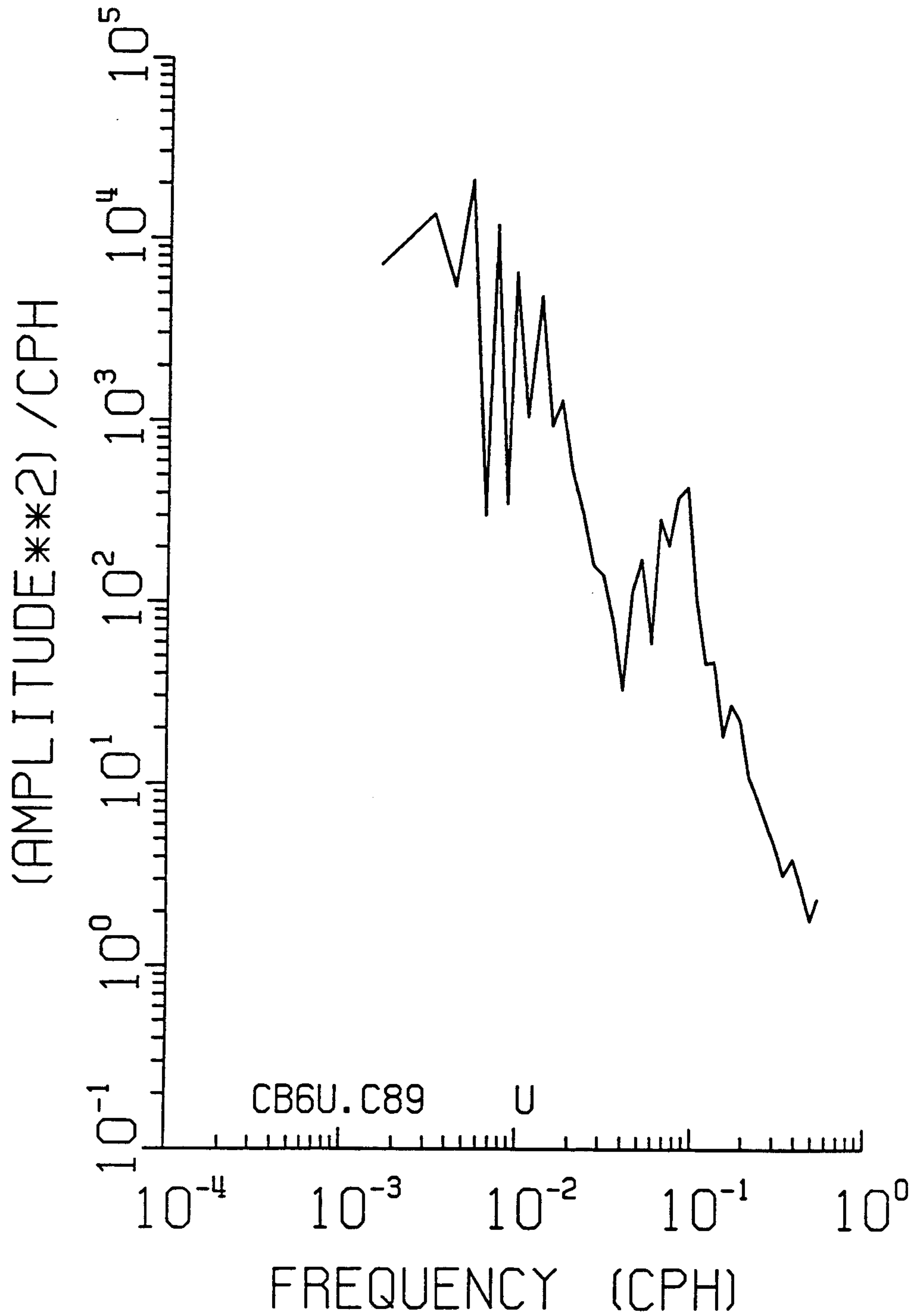

Figure 3-19. Autospectrum of U-component CB6 upper currents, 1989.

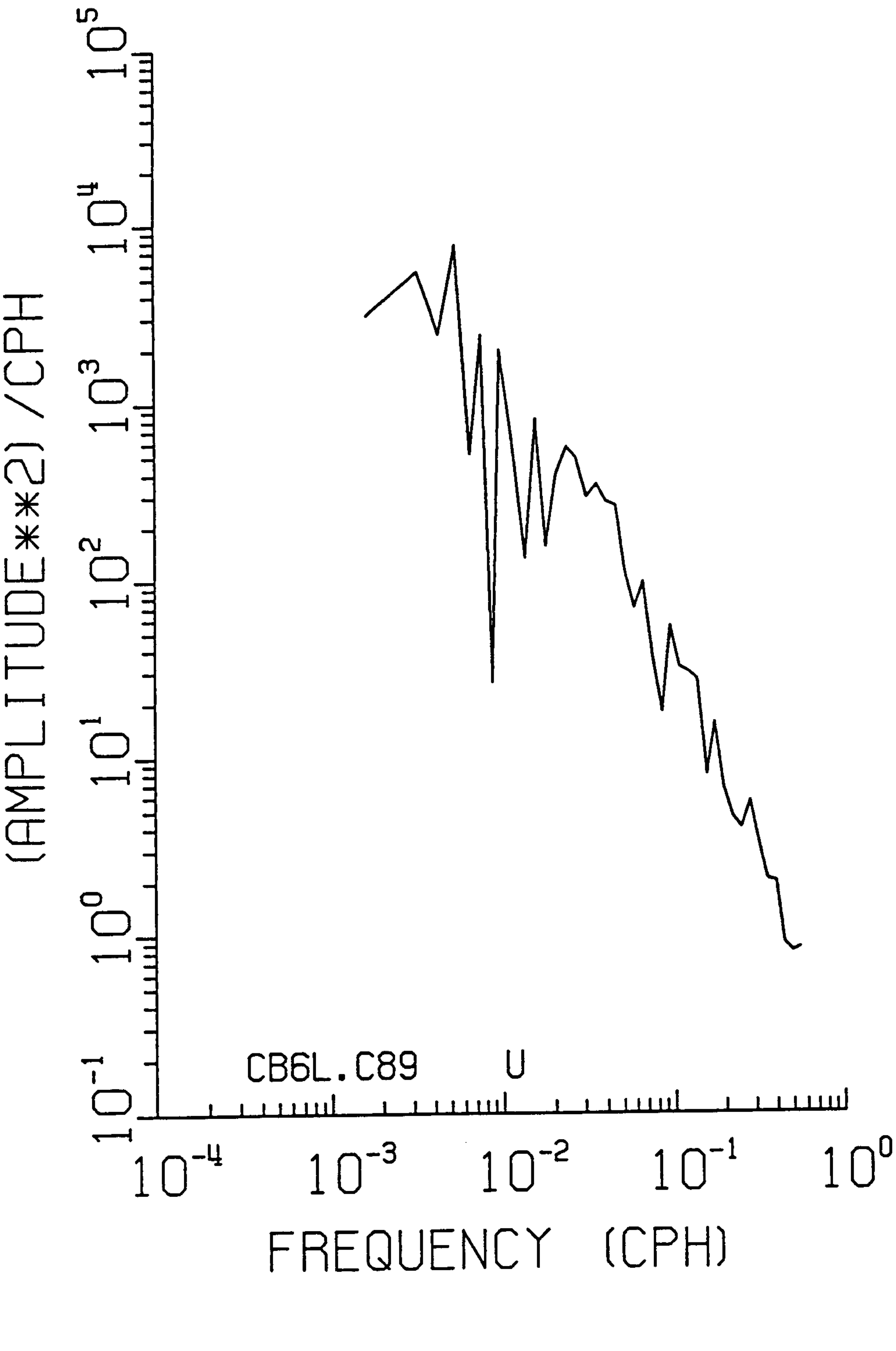

Figure 3-20. Autospectrum of U-component CB6 lower currents, 1989.

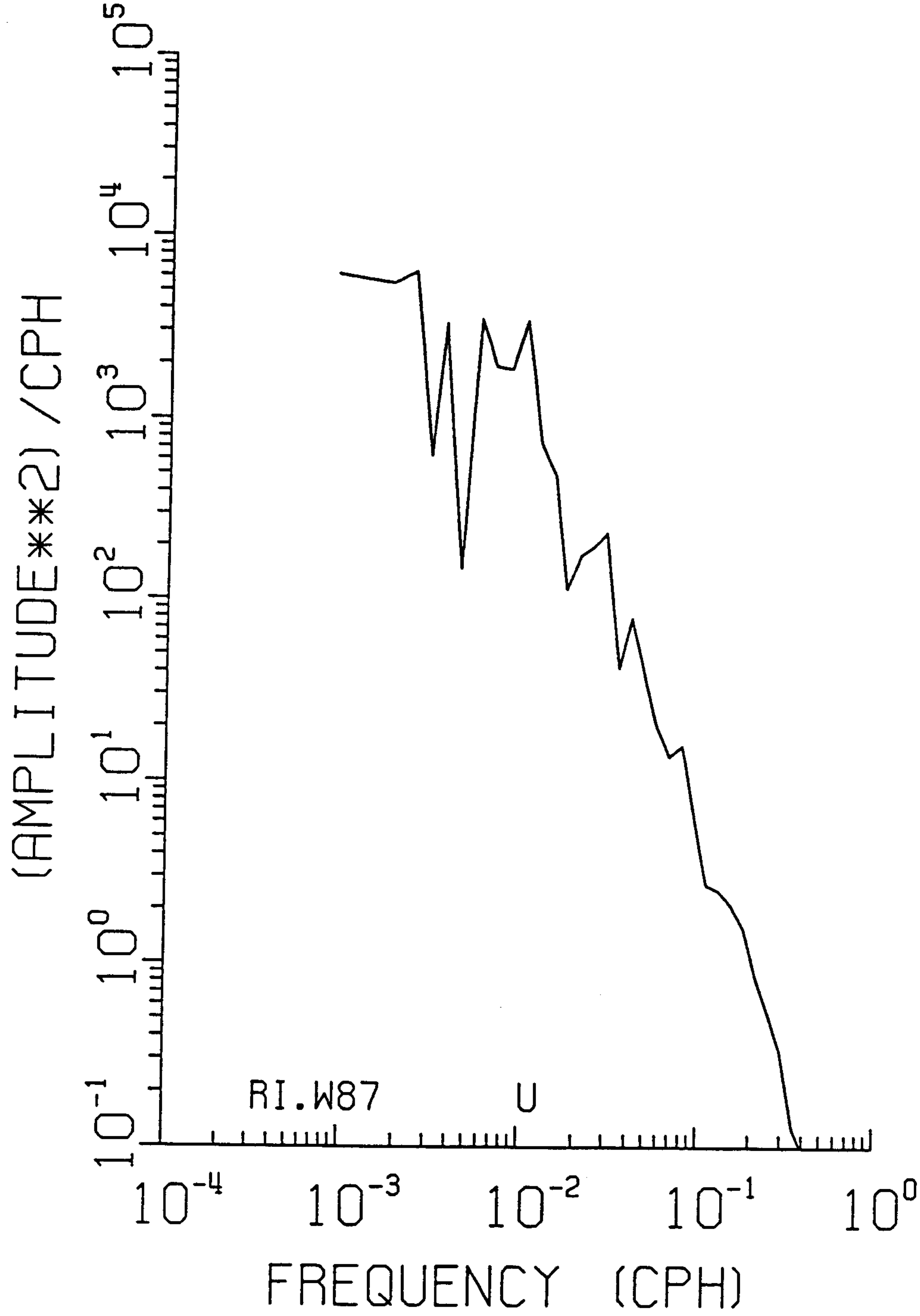

Figure 3-21. Autospectrum of U-component Resolution Island wind, 1987.

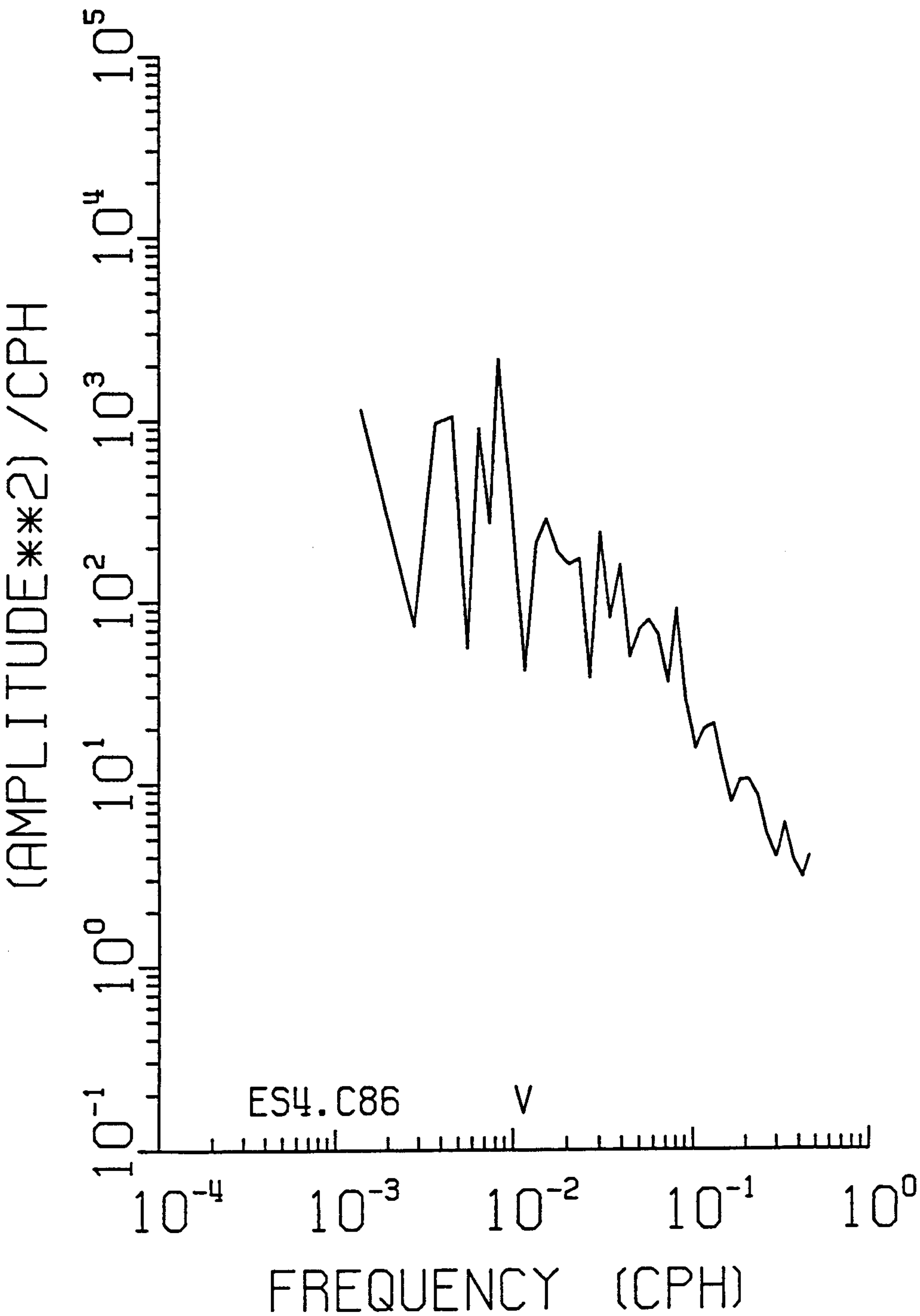

Figure 3-22. Autospectrum of V-component ES4 currents, 1986.

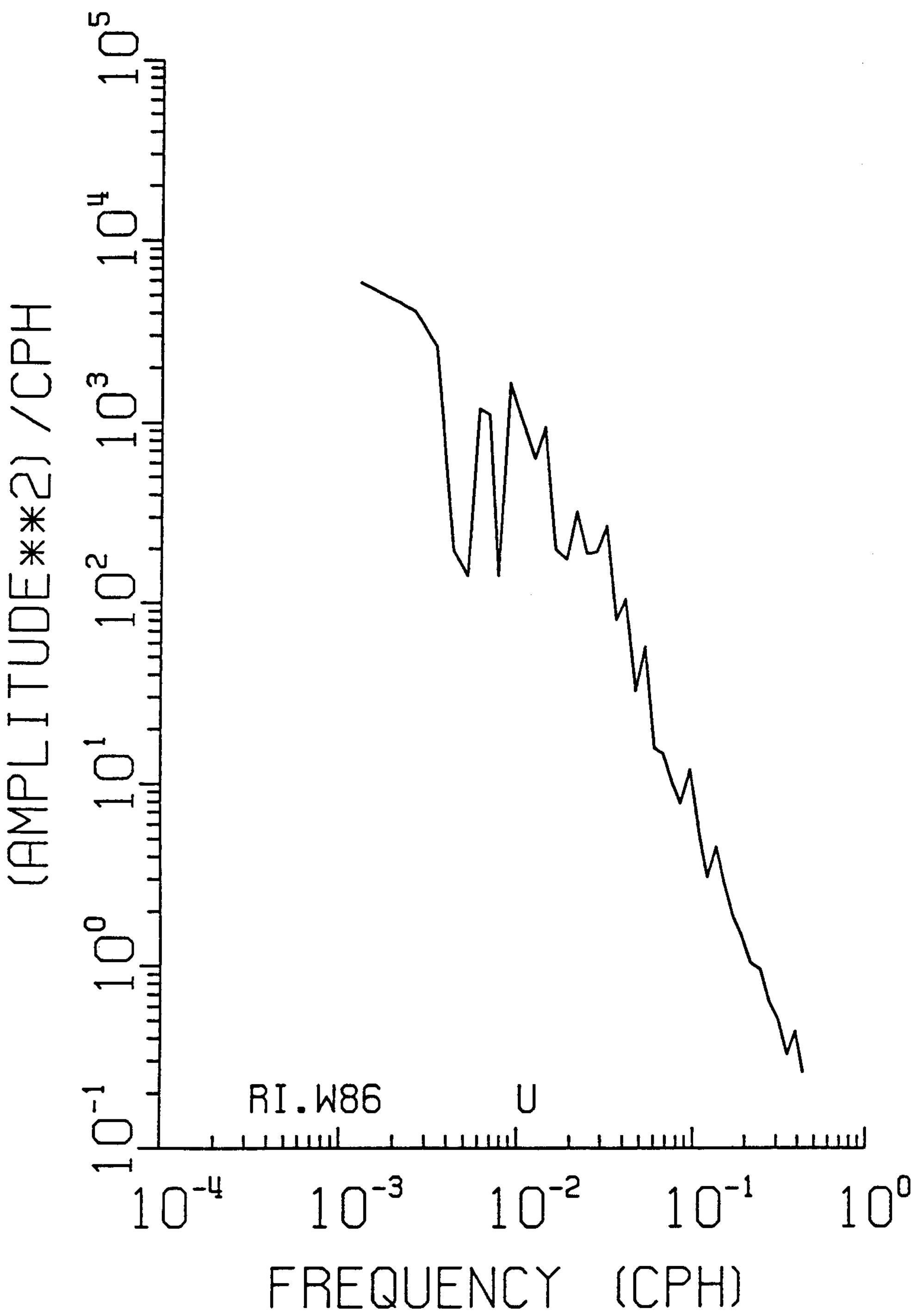

Figure 3-23. Autospectrum of U-component Resolution Island wind, 1986.

Similarly, there is a discernible peak in U- and V-component autospectra of the ED2 upper current meter data from 1987 at about 0.0078 cph, or 128 hour period (Figures 3-24 and 3-25). The corresponding local wind U-component spectrum (Figure 3-21) has a rather broad spectral peak that encompasses that same frequency. As in the 1986 data, it appears likely that wind forcing is the source of current variance in this case.

These cases are individual examples drawn from different years. While the periods may be consistent with typical meteorological spectral characteristics, the very low frequency spectral values calculated here are not statistically significant. Thus, evidence and intuition point to wind being the major factor in current fluctuations in the nearshore area at periods greater than roughly 100 hours, but the inference is far from conclusive and caution should be used in interpreting the wind-current relation implied in the cases discussed above. The broadband nature of meteorological phenomena, with energy distributed over a period band ranging from a few days to more than a week can mask the presence of other low-frequency phenomena that contribute to current variability.

Coherence and phase calculations (Figures 3-9 and 3-26) from 1987 show that the major spectral relation between U-components of wind and currents is at frequencies of approximately 0.02 cph and less, which correspond to periods longer than a few days. Coherence diminishes between frequencies of 0.02 to 0.04 cph. Corresponding phase spectra indicate that wind and currents are approximately in phase at low frequencies, but the general increase in phase angle with increasing frequency implies a lag of currents behind wind fluctuations as frequency increases. While confidence limits were not calculated for the phase plots, it is likely that they are on the order of plus or minus 15 degrees. This estimate assumes an average of five successive raw values for each phase estimate (10 degrees of freedom), corresponding coherence (not coherence squared) values of 0.8 or greater, and reference to Fig. 9.3 of Jenkins and Watts 1968. Because of the potential error of several degrees in phase estimates, caution should be used in trying to determine exact phase relations between wind and currents.

The low-frequency relation indicated by coherence and phase results is borne out by the shape and initial decay of the respective cross correlation functions between wind and currents (Figures 3-7 and 3-27), in which the functions have maxima at near-zero lag and decay to zero within lags of about plus or minus 50 hours. The phase lag at maximum correlation evident from the cross correlations is 1-3 hours, with wind leading currents. This phase lag should approximately correspond to the actual phase difference at the maximum coherence value between wind and currents, which is at about 0.01 cph.

In view of the fact that wind accounts for up to about half the observed current variance in the analyzed records, there is no question that the low-frequency ends of the current spectra reflect low-frequency fluctuations in the wind. That there are not necessarily consistent sharp peaks at common frequencies in wind and current spectra indicates the broad band nature of wind forcing rather than the absence of a strong connection between the two.

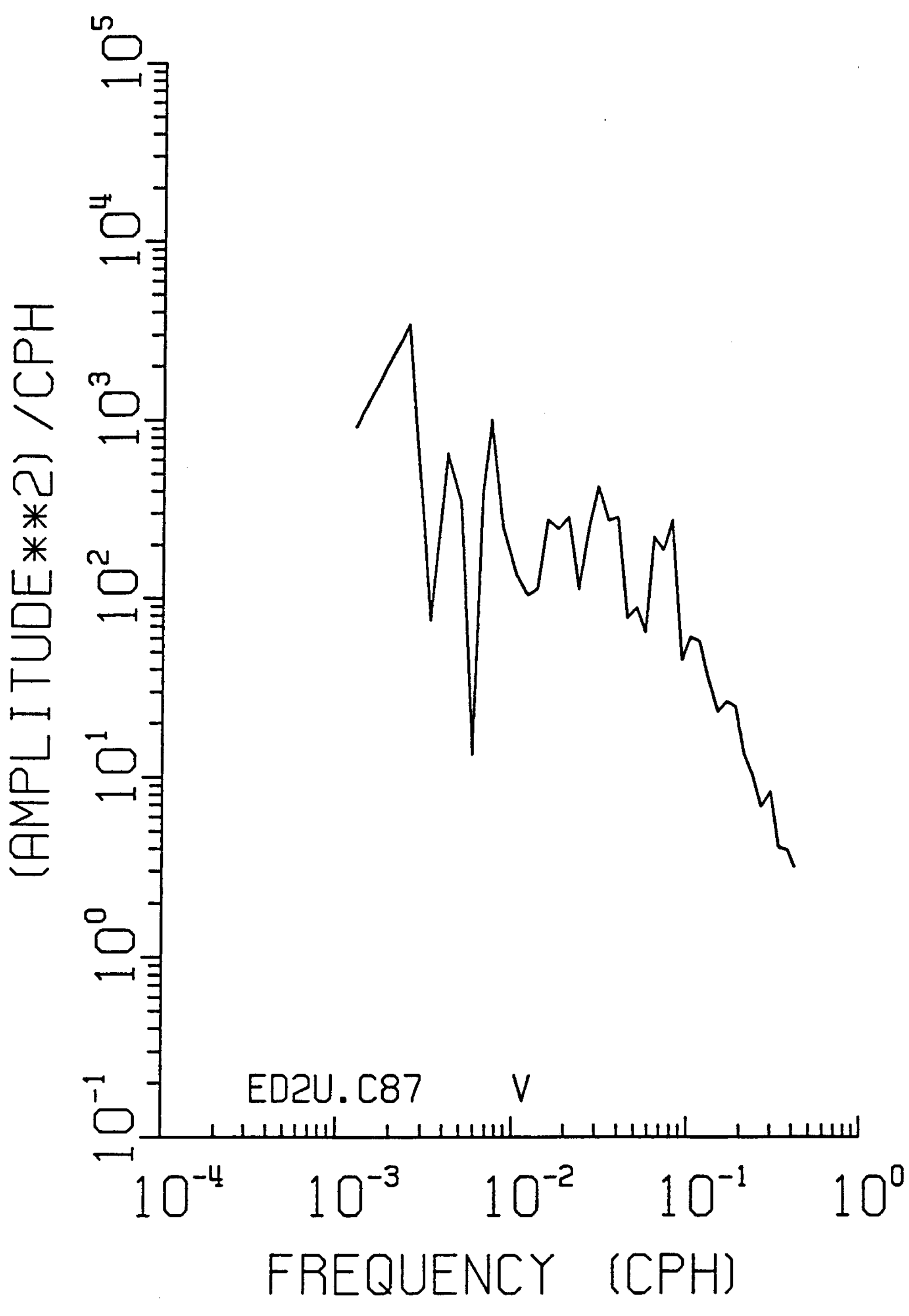

Figure 3-24. Autospectrum of V-component ED2 upper currents, 1987.

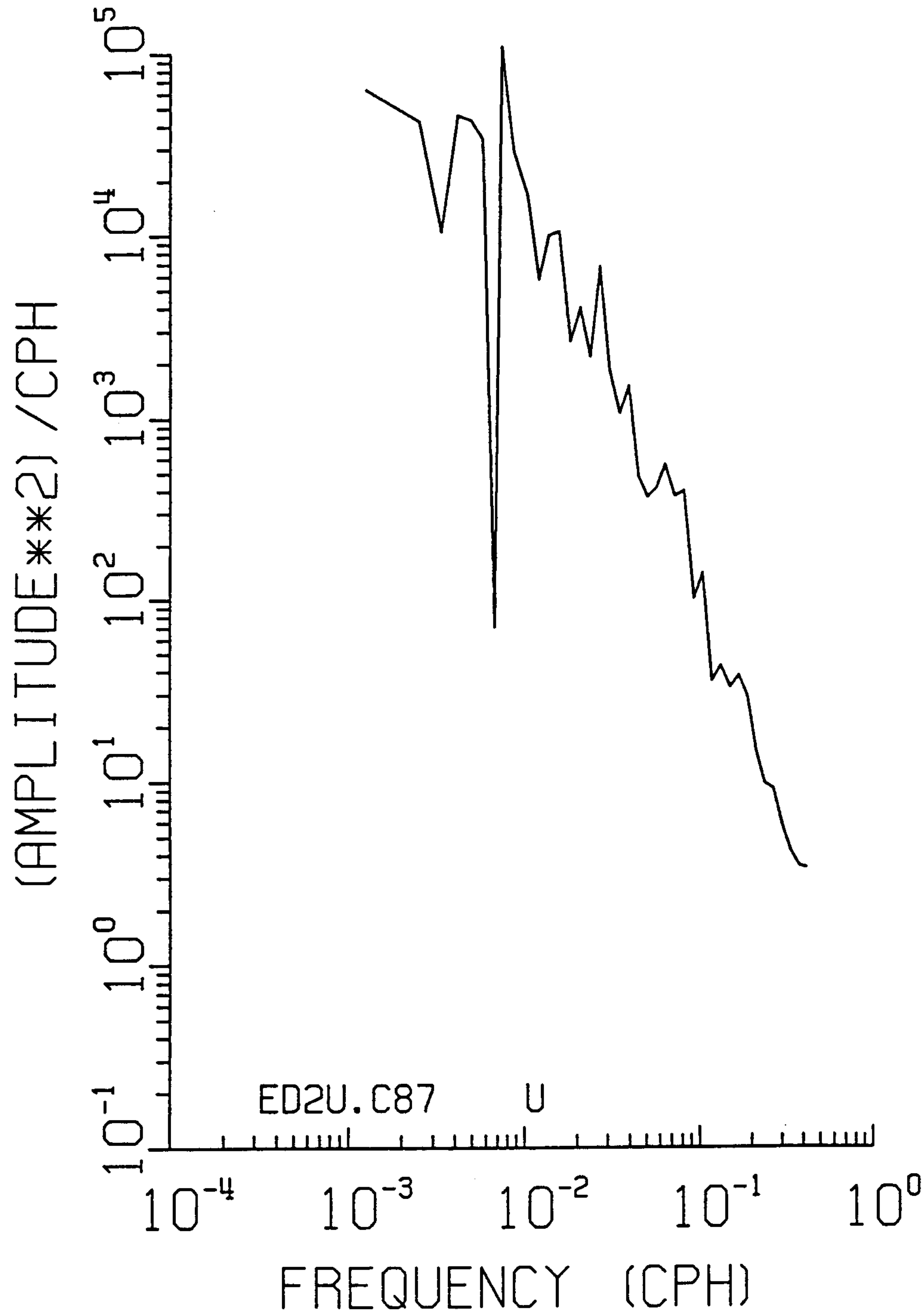

Figure 3-25. Autospectrum of U-component ED2 upper currents, 1987.

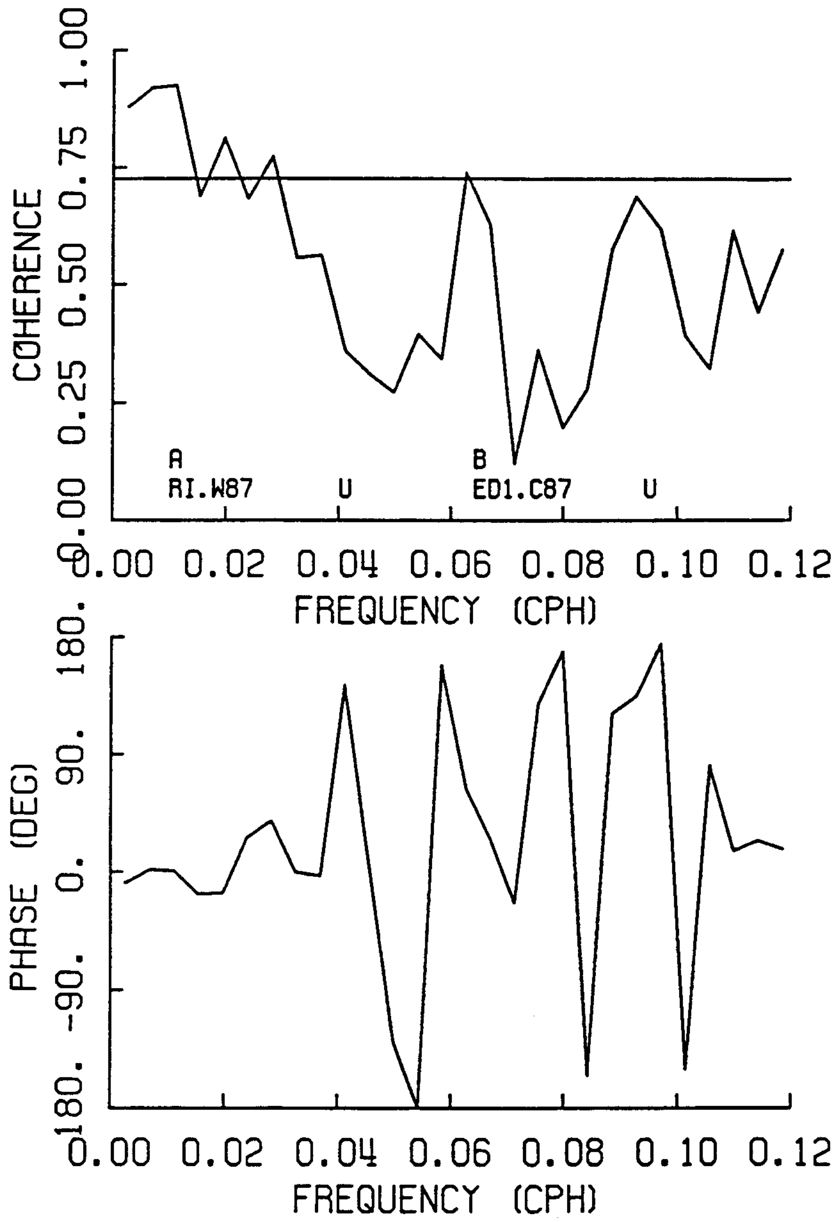

Figure 3-26. Coherence and phase between U-components of Resolution Island wind and ED1 currents, 1987. Positive phase indicates wind leads currents.

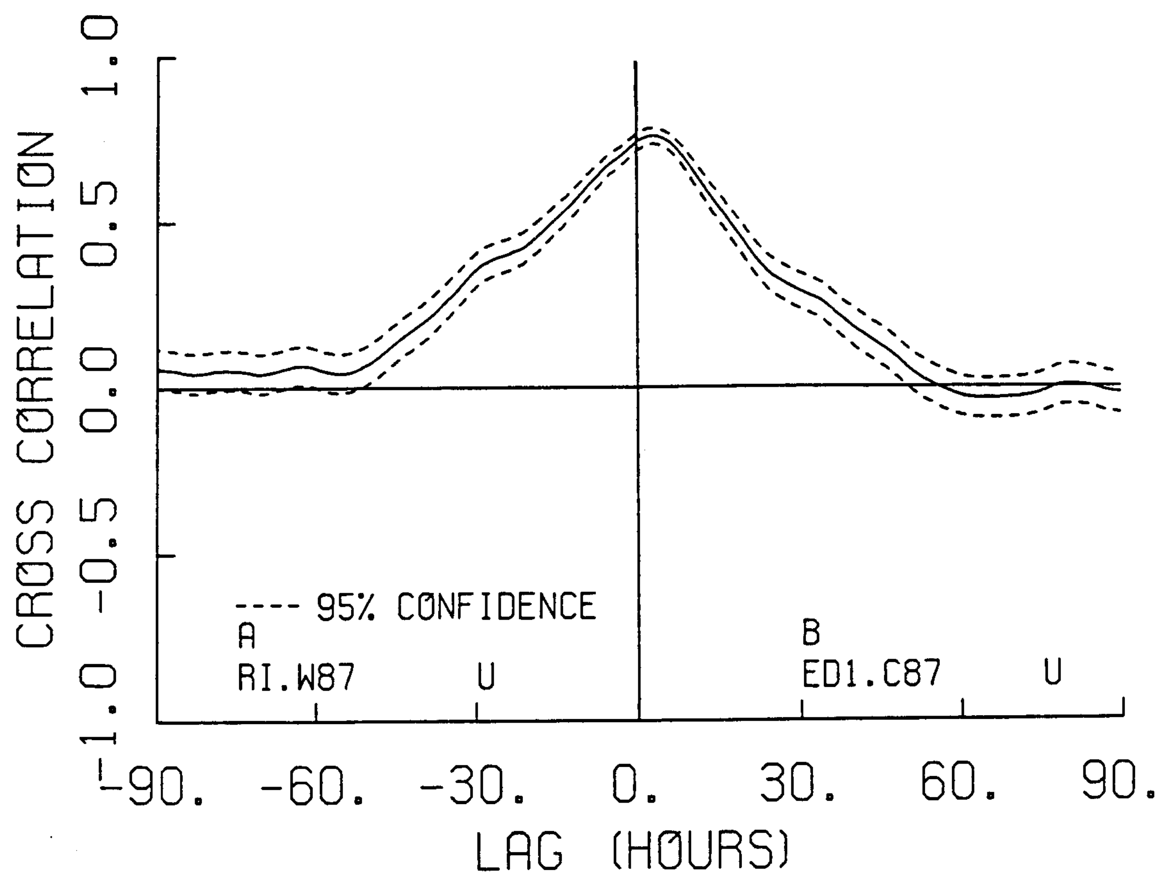

Figure 3-27. Cross correlation between U-components of Resolution Island wind and ED1 currents, 1987. Wind leads for positive lags.

3.3.3.2 Tides

Tidal signals, particularly semi-diurnal as opposed to diurnal, appear in many of the current records, but primarily in the V-component along the minor axis, where meteorological influences are not as dominant. Energy at the semi-diurnal frequency is more apparent in the V-component autospectrum from ED2 (upper), 1987 (Figure 3-24) than in the corresponding U-component autospectrum (Figure 3-25). The appearance is deceptive because the semi-diurnal tidal energy in those respective autospectra is comparable, and the difference is due to the fact that distribution of energy over the low-frequency end of the U-component autospectrum masks the semi-diurnal tidal energy. In contrast, the energy content in the low-frequency portion of the V-component autospectrum decreases with decreasing frequency. Whereas, coherence and phase calculations between V-components of ED2(upper) and ED2(lower), 1987 (Figure 3-14) show the absence of coherent low-frequency energy in the upper and lower layers of the water column, they also show the expected presence of coherent tidal energy throughout the water column.

Autospectra of U- and V-components measured at L1, 1982 (Figures 3-28 and 3-29) display the same general tidal nature as those for ED2, 1987, namely comparable semi-diurnal energy but with the U-component masked by the presence of low-frequency energy. Cross correlation from 1985 (Figure 3-12) reflects that the dominant common V-component signal in the shallow water column at ED2 is the semi-diurnal tidal signal.

3.3.3.3 Other

Signals of other periodicities can be identified in current records from the various years sampled. Unlike tides, however, explanations for these other signals are more difficult to assign because of the transitory nature both of currents and potential external forcing mechanisms. Thus, a given mechanism may be active only part of a deployment interval or perhaps one year but not the next, and therefore the measured currents may not reflect its presence.

The results of various types of calculations suggest the year-to-year presence of a signal with a period of approximately 35 to 45 hours. For example, autospectra of U-components measured at L34 and L36, 1984 (Figures 3-30 and 3-31) display common peaks at periods of about 43 hours (or 0.023 cph). Autospectra of U-component data from ED2, 1985 upper (Figure 3-32) and lower (Figure 3-33) current meters also have peaks at approximately the same period, but the cross correlation function for the two (Figure 3-10) and the autocorrelation function for ED2 lower, U-component, 1985 (Figure 3-34) show the periodicity more graphically. Autospectra of U- and V-components at ED2 upper, 1987 (Figures 3-25 and 3-24) show similar peaks, and a corresponding rotary spectrum (Figure 3-35) indicates that energy is primarily in counter-clockwise motions.

The source of 35- to 45-hour periodicity is unclear. Autospectra of the U-components of local wind data for 1984 (Figure 3-36), 1985 (Figure 3-37), and 1987 (Figure 3-21) have peaks at periods of 50, 60, and 33 hours, respectively. Only in 1987 do the spectral characteristics of wind and currents coincide at

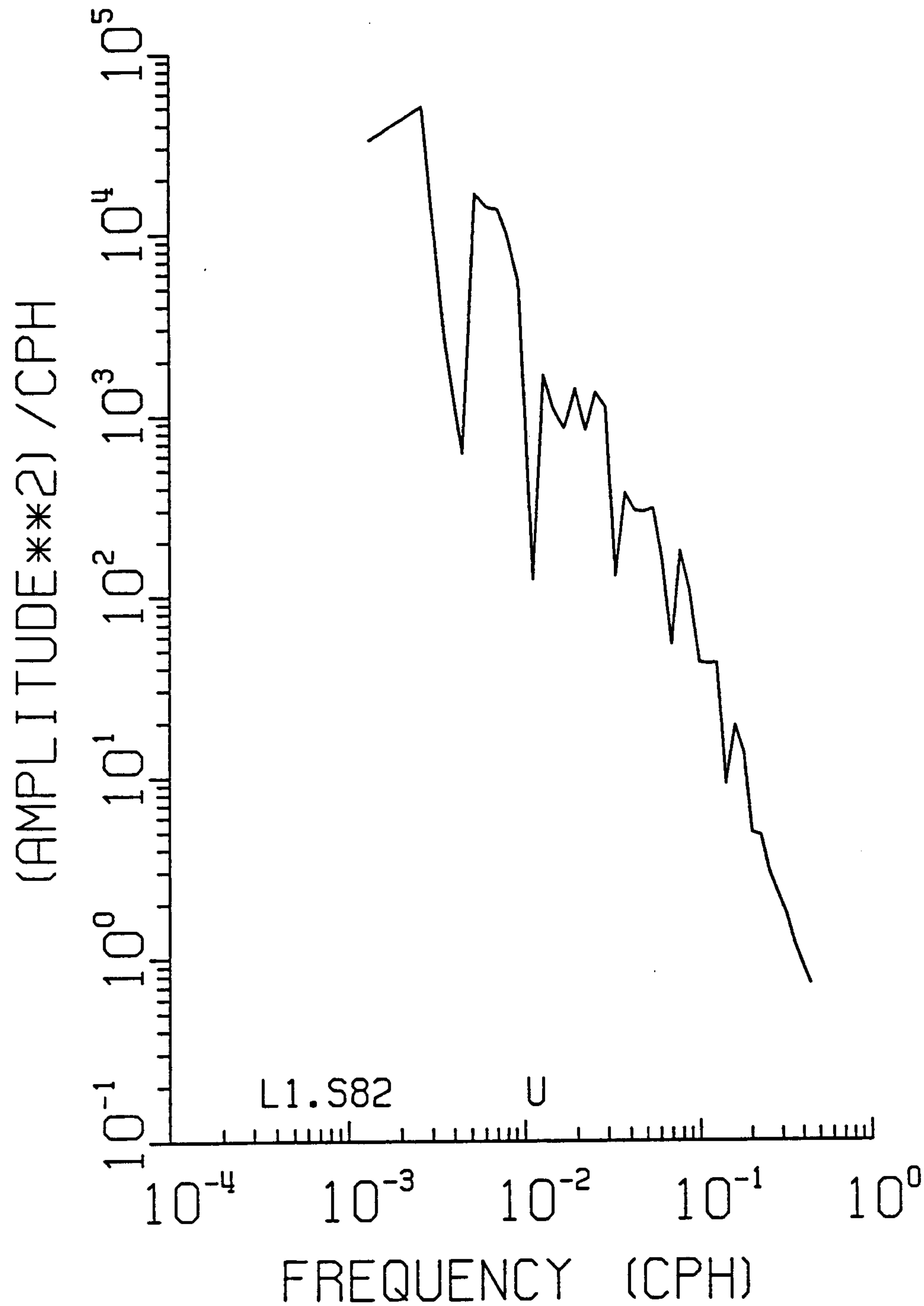

Figure 3-28. Autospectrum of U-component L1 currents, 1982.

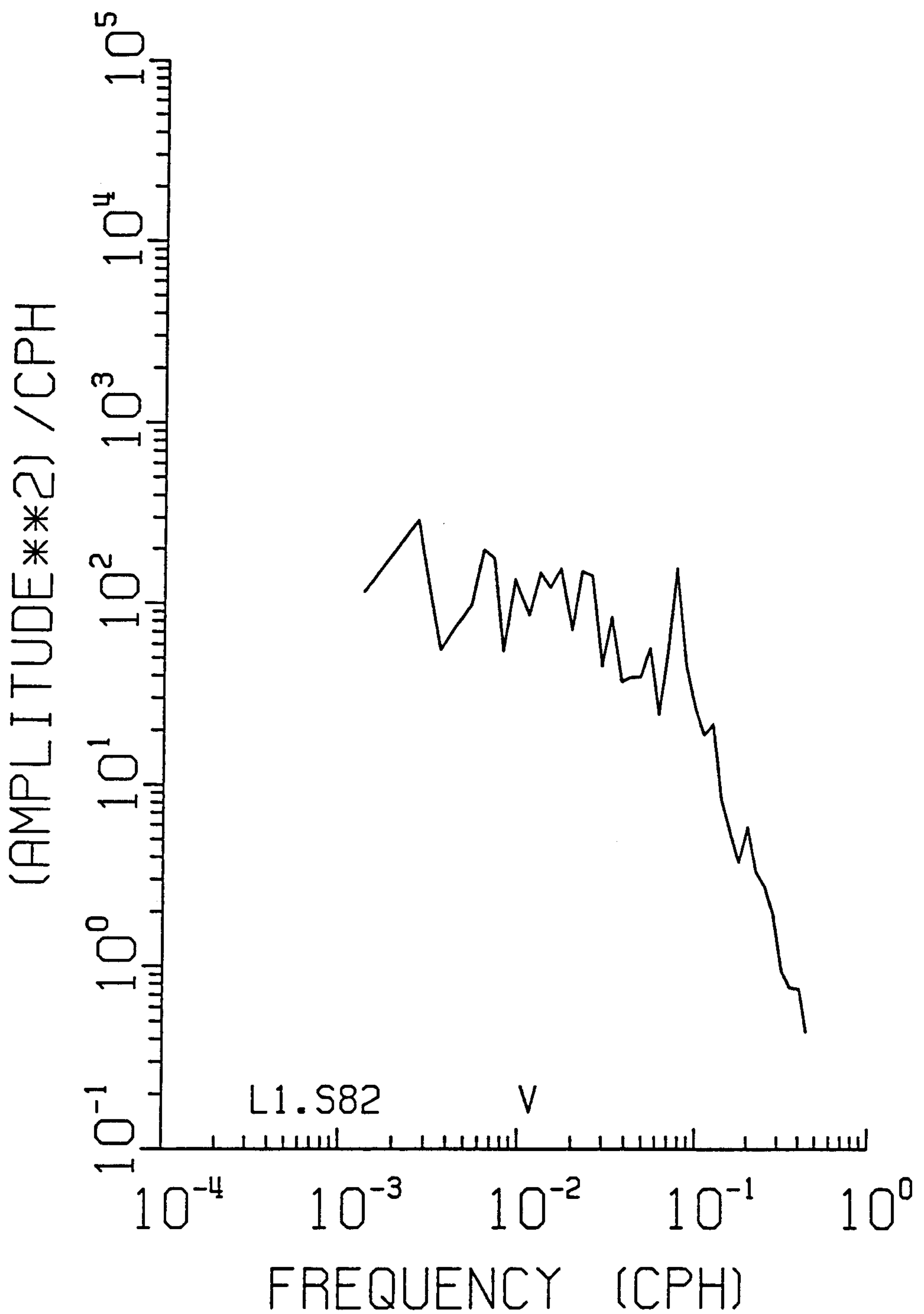

Figure 3-29. Autospectrum of V-component L1 currents, 1982.

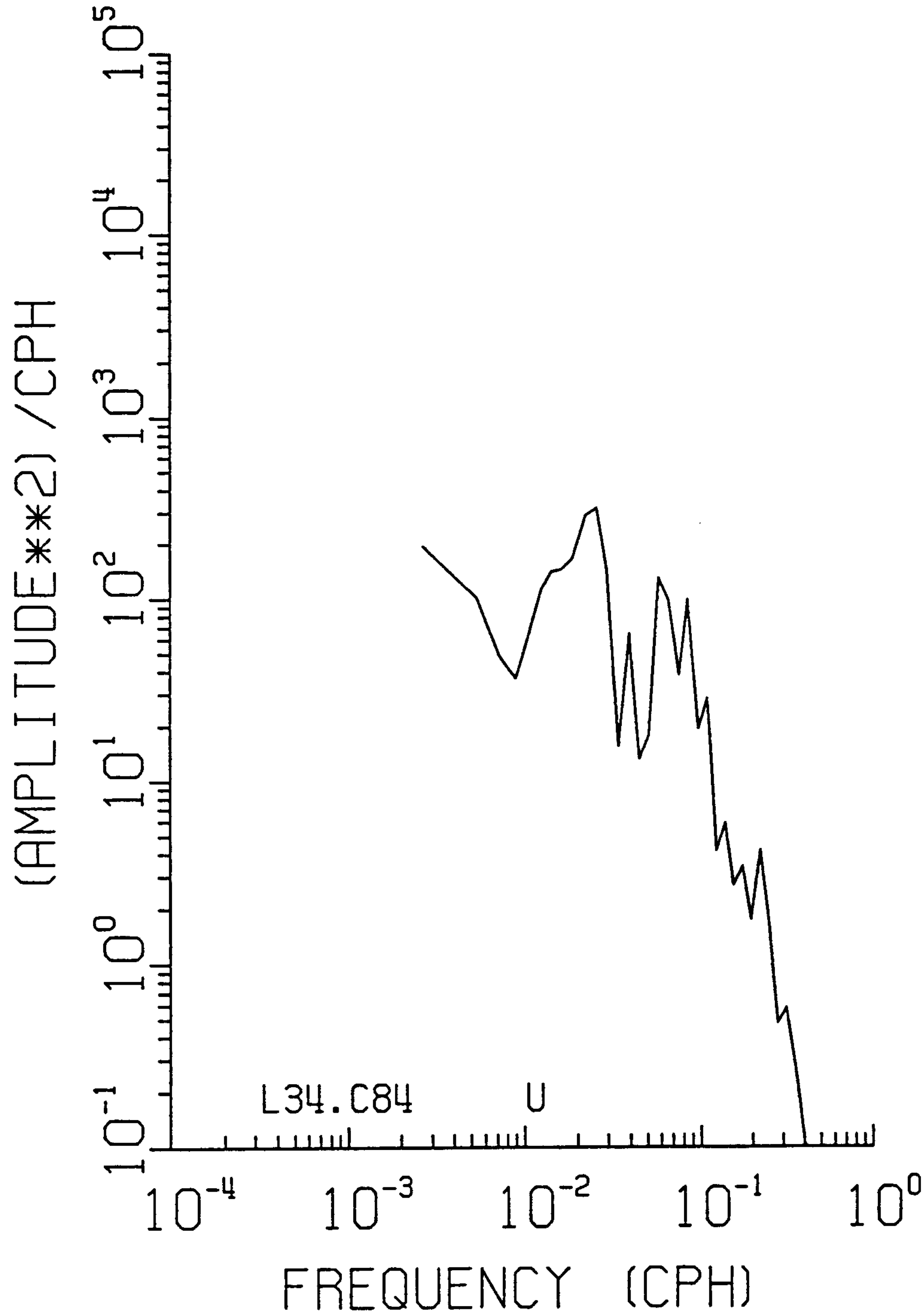

Figure 3-30. Autospectrum of U-component L34 currents, 1984.

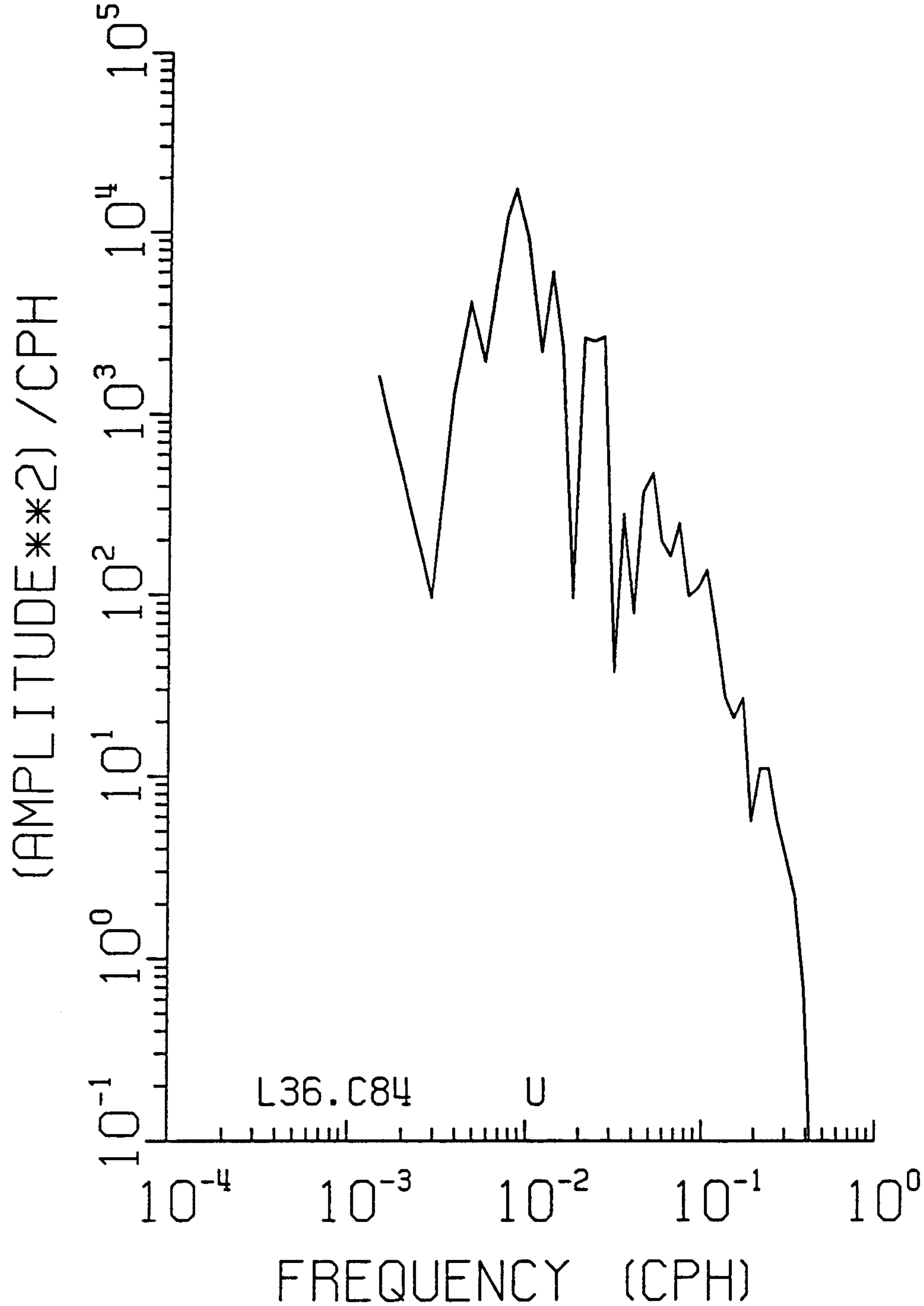

Figure 3-31. Autospectrum of U-component L36 currents, 1984.

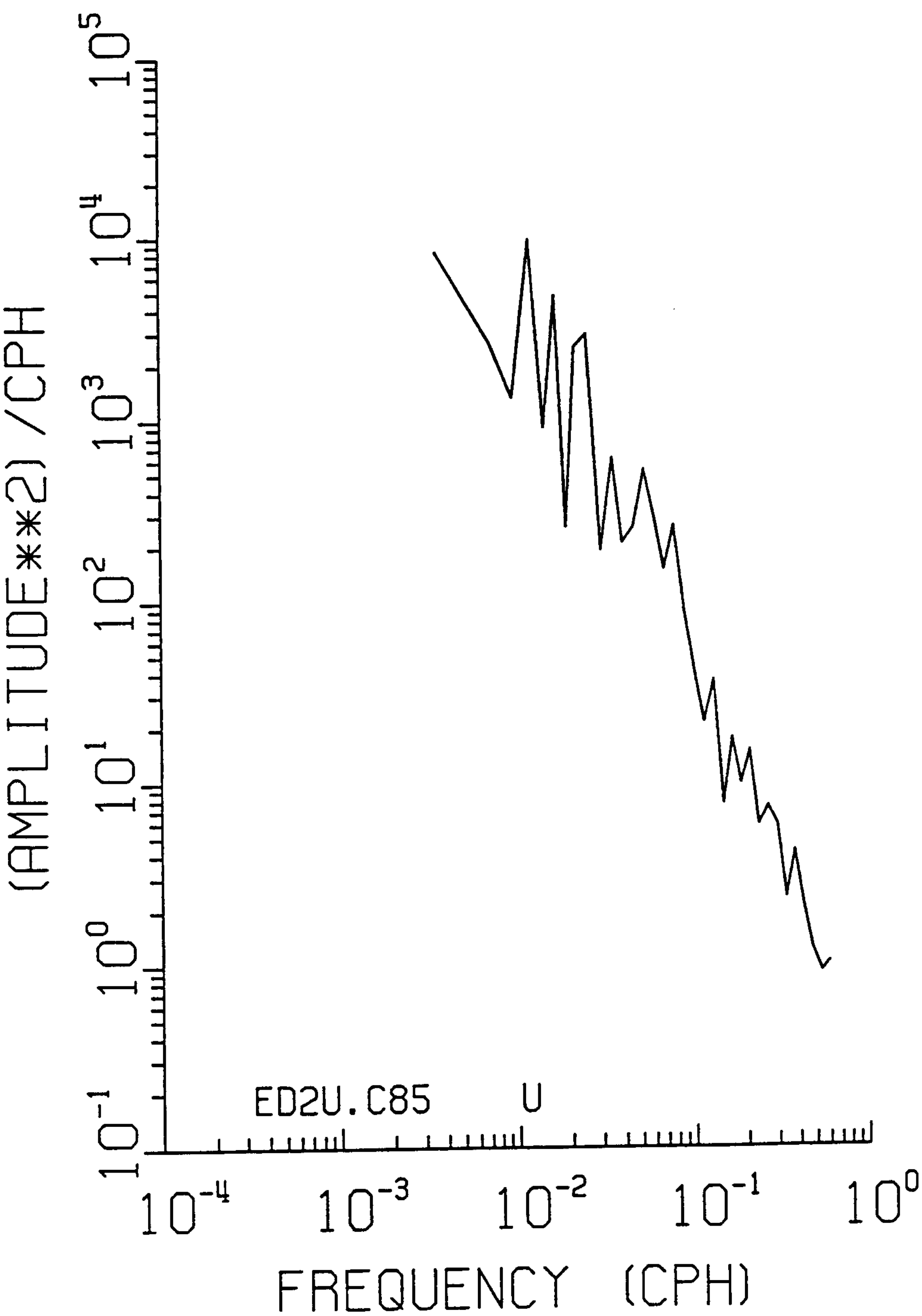

Figure 3-32. Autospectrum of U-component ED2 upper currents, 1985.

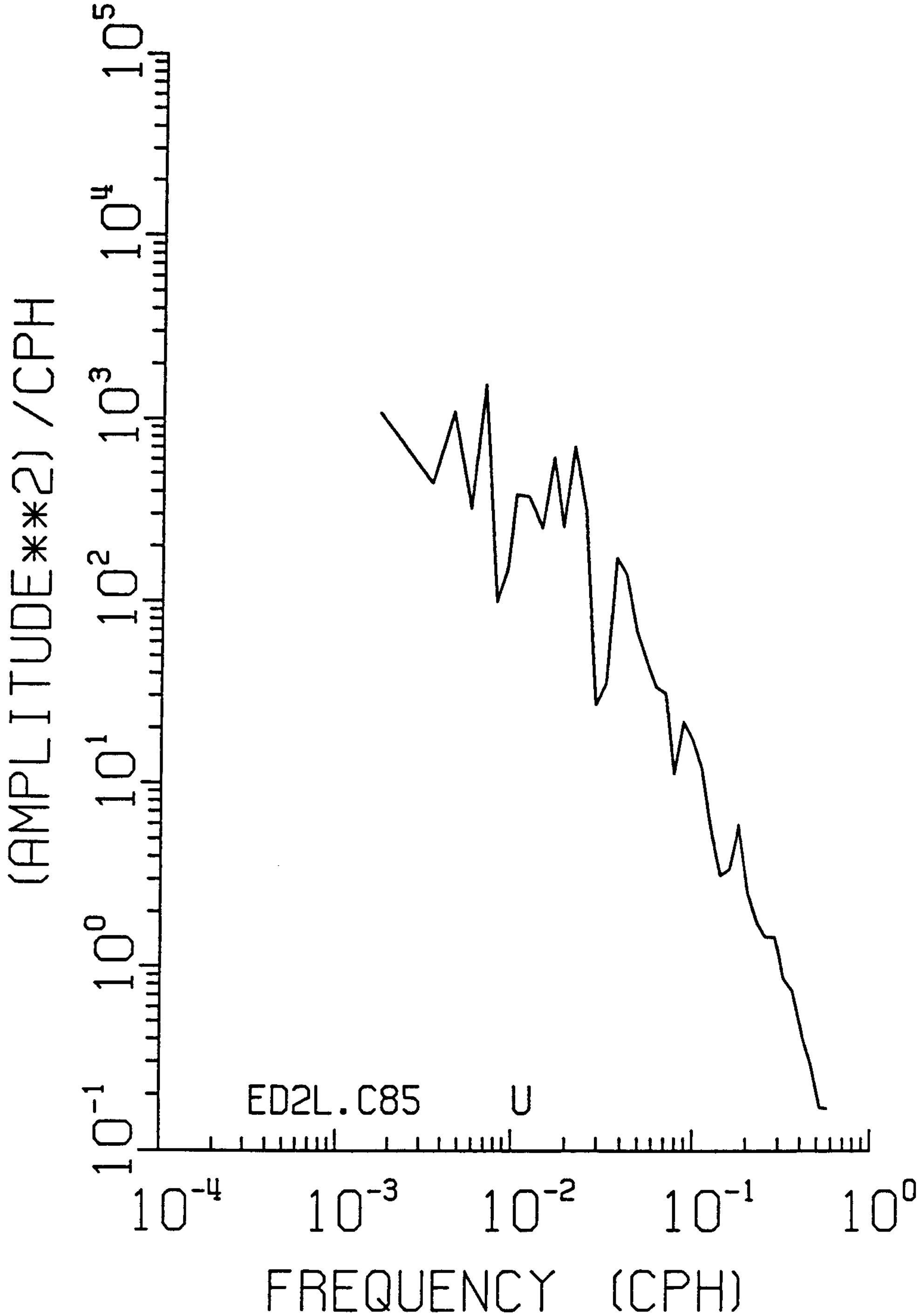

Figure 3-33. Autospectrum of U-component ED2 lower currents, 1985.

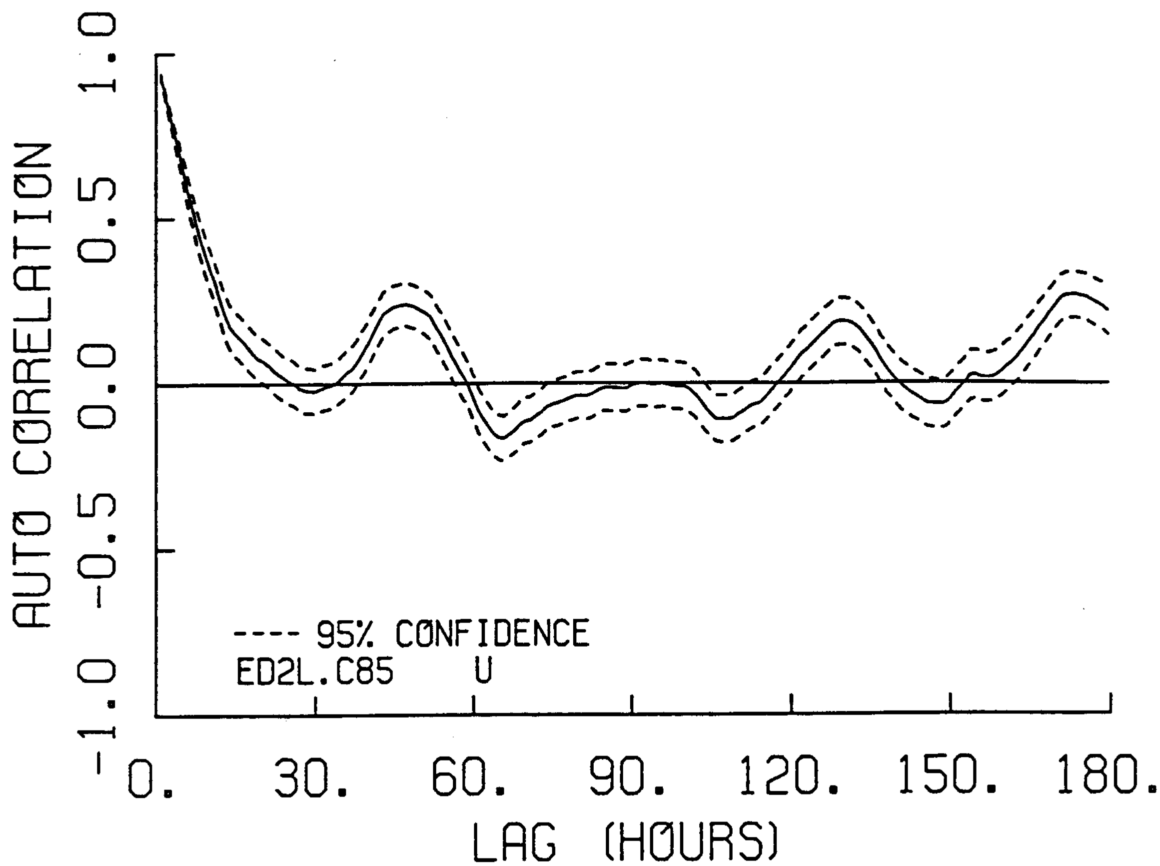

Figure 3-34. Autocorrelation of U-component ED2 lower currents, 1985.

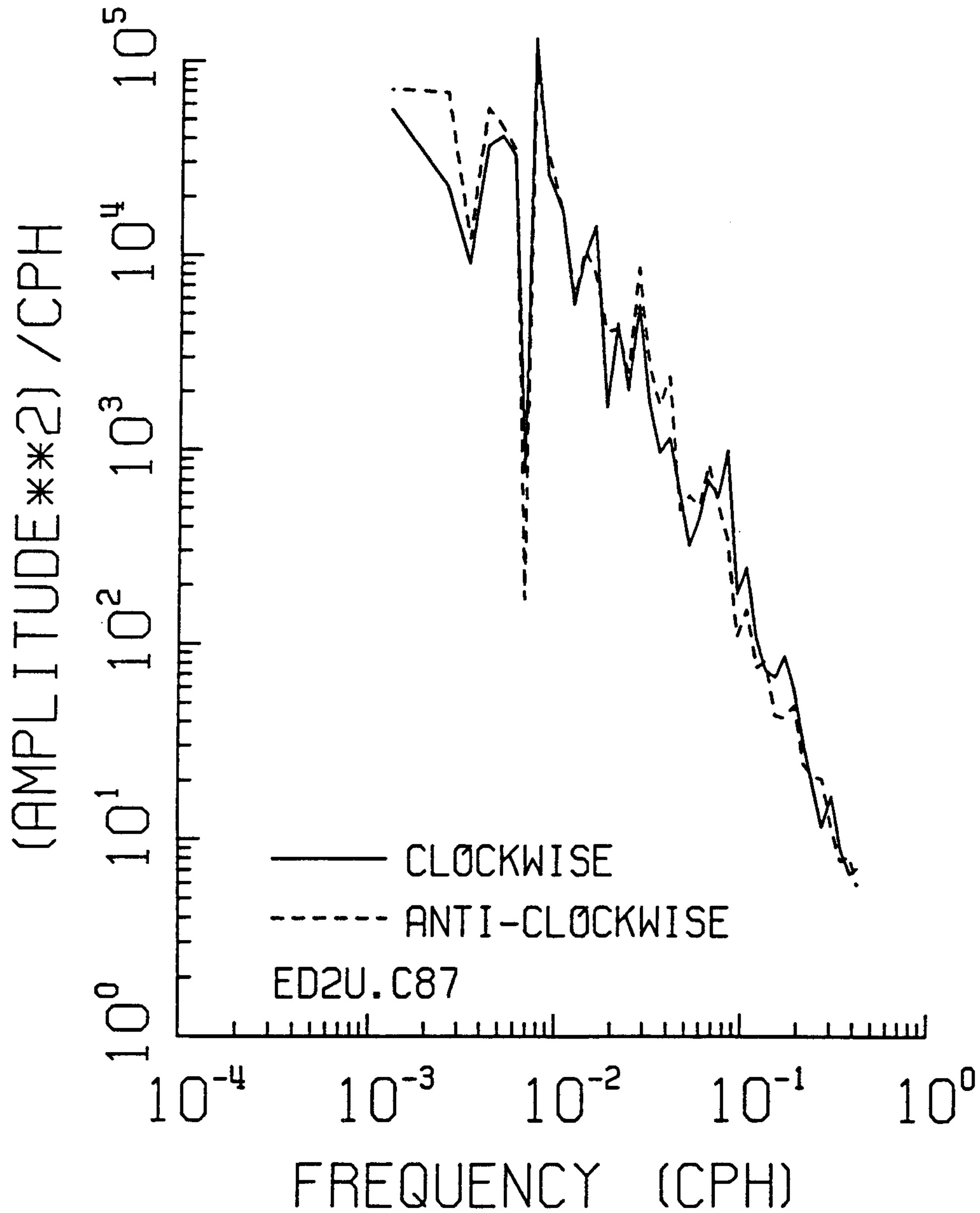

Figure 3-35. Rotary spectrum of ED2 upper currents, 1987.

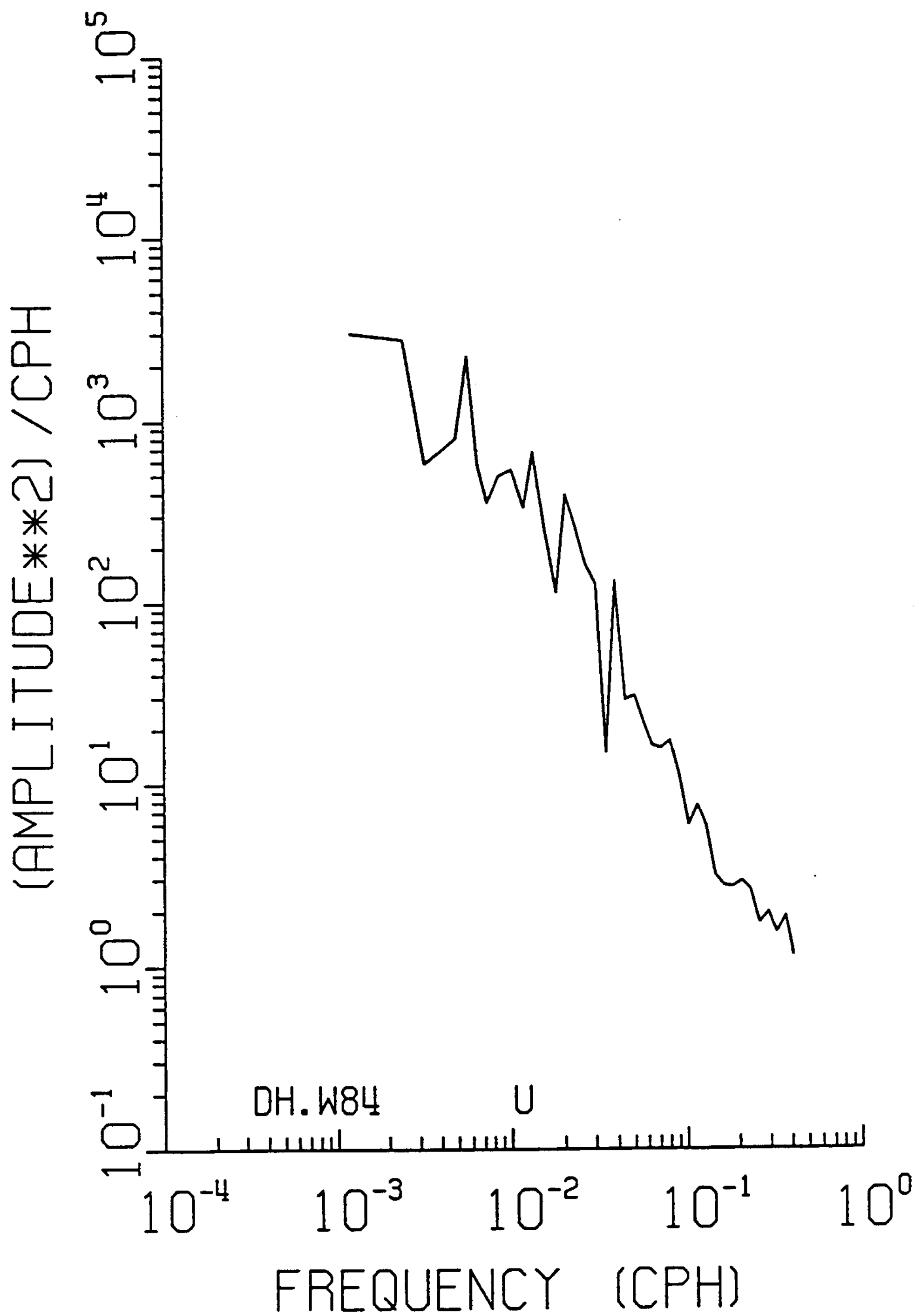

Figure 3-36. Autospectrum of U-component Deadhorse Airport wind, 1984.

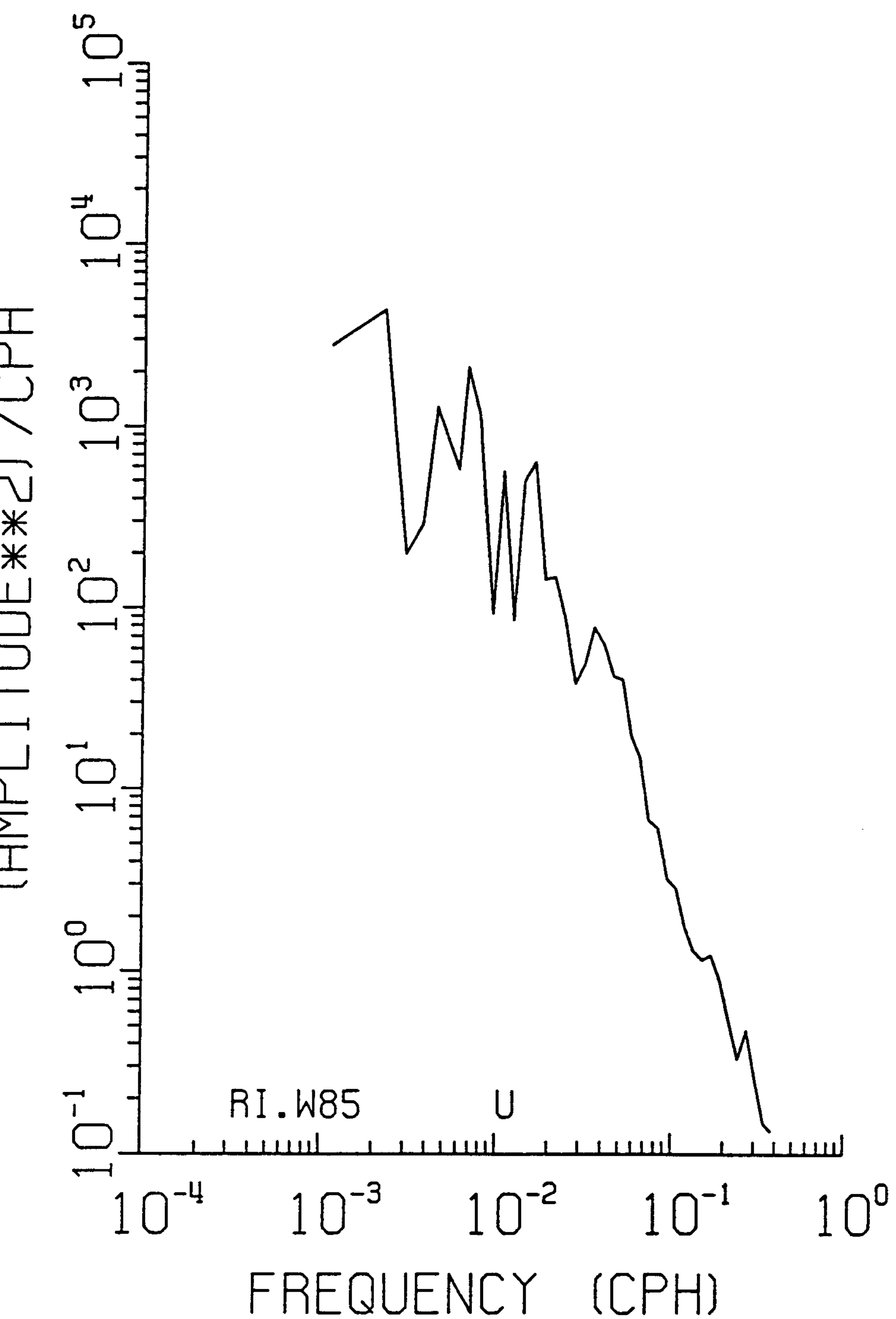

Figure 3-37. Autospectrum of U-component Resolution Island wind, 1985.

approximately the 35- to 45-hour period range, and the significance of the peak at 33-hour period is questionable. Also, in 1984 and 1985, wind accounted for less than 10 percent of the variance of deeper currents (Table 3-8), so that direct wind-forcing in that period range might not be expected to be significant. On the other hand, it is important to point out that, in 1987, local wind and currents at ED2 upper were significantly coherent at 0.0274 cph, which corresponds to a period of 36 hours. Thus, wind forcing can neither be confirmed nor denied as the source of variance in the 35- to 45-hour period range, even though periods in this range seem short compared with expected meteorological periodicities. Another possibility is an eastward-propagating trapped-wave disturbance, and indeed, coherence and phase calculations for 1984 data show significant coherence between currents separated in the alongshore direction, with currents at the western mooring leading by a few hours. Existing data do not allow unequivocal isolation of the source of observed variance in the 35- to 45-hour period range.

3.3.4 Topographic Effects

3.3.4.1 Principal Axis Orientation

In the nearshore area, the combination of bottom topography and proximity to the coastline clearly influence current direction. Approximate orientation of local bottom contours and principal axis directions for the respective current records show a close correspondence in most cases (Table 3-9). Thus, the most energetic fluctuations tend to be along bottom contours, which also roughly coincide with the coastline. All tend to be oriented northwest-southeast.

3.3.4.2 Vector-averaged Direction

In many cases, the vector-averaged current direction also aligns with local bottom contours, but not with the same consistency as principal axes (Table 3-9). (Principal axis angles are reported between 0 and 180 degrees true, so an addition of 180 degrees is necessary when comparing with current directions between 180 and 360 degrees true.) Disparity between vector-averaged directions and bottom contours in part reflects low frequency background motion that may be due to an alongshore pressure gradient, for example.

3.3.4.3 Wind and Currents

In contrast to principal axis orientations of currents, which tend to be northwest-southeast, principal axes for wind lie between 60 and 93 degrees true (Table 3-9). While wind fluctuations tend to have a strong cross-isobath component, currents are rectified into the alongshore direction, although it is important to keep in mind that wind-forcing is far from being the sole source of current motions. In spite of this caveat, and taking into consideration previous results showing that wind does indeed account for a large portion of current variance in near-surface current meter records, the role of topography in steering wind-forced currents is apparent.

Table 3.9 Summary of wind and current principal axes, means, and approximate bottom contour orientation.

Note: All directions are in degrees true and represent direction toward which the velocity vector points for both wind and current. Speeds are in centimeters per second except where entered as meters per second (m/s) for wind. Bottom contour directions are in degrees clockwise from north.

YEAR	PRINCIPAL AXIS			VECTOR AVERAGE		BOTTOM CONTOUR
Record	Length	Dir	% Variance	Speed	Dir	Dir
1989						
CB.W89	3.4	43	87	1.4 m/s	213	
CB6U.C89	10.8	110	75	1.2	129	75
CB6L.C89	6.9	93	62	0.9	336	75
CB2.C89	7.0	104	96	2.8	103	100
1988						
CB.W88	5.0	76	87	1.6 m/s	228	
CB6L.C88	6.5	50	59	2.5	97	75
1987						
RI.W87 1/	6.1	80	77	1.0 m/s	191	
ED2U.C87 1/	24.2	129	95	3.2	91	130
RI.W87 2/	5.6	77	73	1.5 m/s	96	
ED2U.C87 2/	24.6	130	94	8.1	110	130
ED2L.C87 2/	13.9	107	82	4.3	123	130
ED1.C87	14.3	140	88	5.2	278	140
ED3U.C87	25.9	126	96	7.8	110	120
1986						
RI.W86	5.5	93	77	1.6 m/s	241	
ED1.C86	12.1	139	88	3.5	344	140
ES6.C86	10.5	124	92	6.0	314	85
ED3.C86	21.1	125	96	2.9	328	125
ES4.C86	8.5	93	78	1.9	314	105
ER4.C86	17.3	44	93	3.1	202	120
1985						
RI.W85	3.8	82	80	3.1 m/s	235	
ED2U.C85	12.5	130	95	6.8	311	140
ED2L.C85	4.2	102	72	2.0	7	140
ER1.C85	6.6	160	81	3.2	18	140

(continued)

Table 3-9, continued. Summary of wind and current principal axes, means, and approximate bottom contour orientation.

Note: All directions are in degrees true and represent direction toward which the velocity vector points for both wind and current. Speeds are in centimeters per second except where entered as meters per second (m/s) for wind. Bottom contour directions are in degrees clockwise from north.

YEAR	PRINCIPAL AXIS			VECTOR AVERAGE		BOTTOM CONTOUR
Record	Length	Dir	% Variance	Speed	Dir	Dir
1984						
DH.W84	4.7	72	79	1.7 m/s	233	
GI.W84	4.9	74	81	2.0 m/s	232	
L32.C84	3.3	93	90	0.7	102	110
L34.C84	3.5	104	70	0.6	82	100
L36.C84	11.3	110	90	0.1	200	115
1982						
RI.W82	5.2	61	84	2.3 m/s	231	
L1.C82	14.1	146	95	2.3	333	125
L3.C82	17.9	121	97	1.9	256	130
L4.C82	11.8	153	79	4.4	4	135
L5.C82	10.2	102	86	4.2	275	125

1/ Record starts at 0000 on 25 July 1987.
2/ Record starts at 2100 on 12 August 1987.

3.3.5 Spatial Current Correlations

3.3.5.1 Alongshore

Analysis of the small number of data records separated alongshore indicates that the currents at the westernmost of a mooring pair tend to lead those at the mooring farther east. In one example from 1987, ED3 upper U-component leads that of ED1, about 11 km east, by one to two hours (Figure 3-38). This represents a phase speed of about 2 m/s. Similarly, in 1982, L5 U-component leads L4 by one to two hours. Mooring L5 is about 8 km west of L4. However, from 1982, L1 U-component lags L3 by three hours, which is opposite the expected trend. In view of errors in recording true start times for L1 and L3, the deviation may simply be due to a lag pre-imposed by erroneous start times. From 1984, L32 U-component leads L36, about 33 km farther east, by only about an hour at maximum positive cross correlation of +0.35, but by 55 hours at maximum negative correlation of -0.42. These two current records are both from depths of 4.6 m in water 6 m deep, and direct wind-forcing does not appear to contribute significantly to the variance (Table 3-8), so the cross correlation may indicate propagating disturbances or phased response to indirect wind effects such as upwelling and surges. In all these examples, the data are adequate only to illustrate lead/lag relationships, but fall short of providing a firm basis for isolating the underlying dynamic cause.

3.3.5.2 Cross-isobath

Only one example, from 1984, provides a basis for cross-isobath comparisons in the nearshore area. In this case, L34 U-component, leads that of L32 by 12 hours (cross correlation of +0.37) and by 52 hours (cross correlation of +0.41) (Figure 3-39). The cross correlation thus provides some confirmation of the presence of a 35 to 45-hour period signal.

On the basis of existing data, the implication is of a disturbance propagating slowly onshore from L34 to L32, about 6 km apart. One possibility is a slow meandering of the mean eastward alongshore flow.

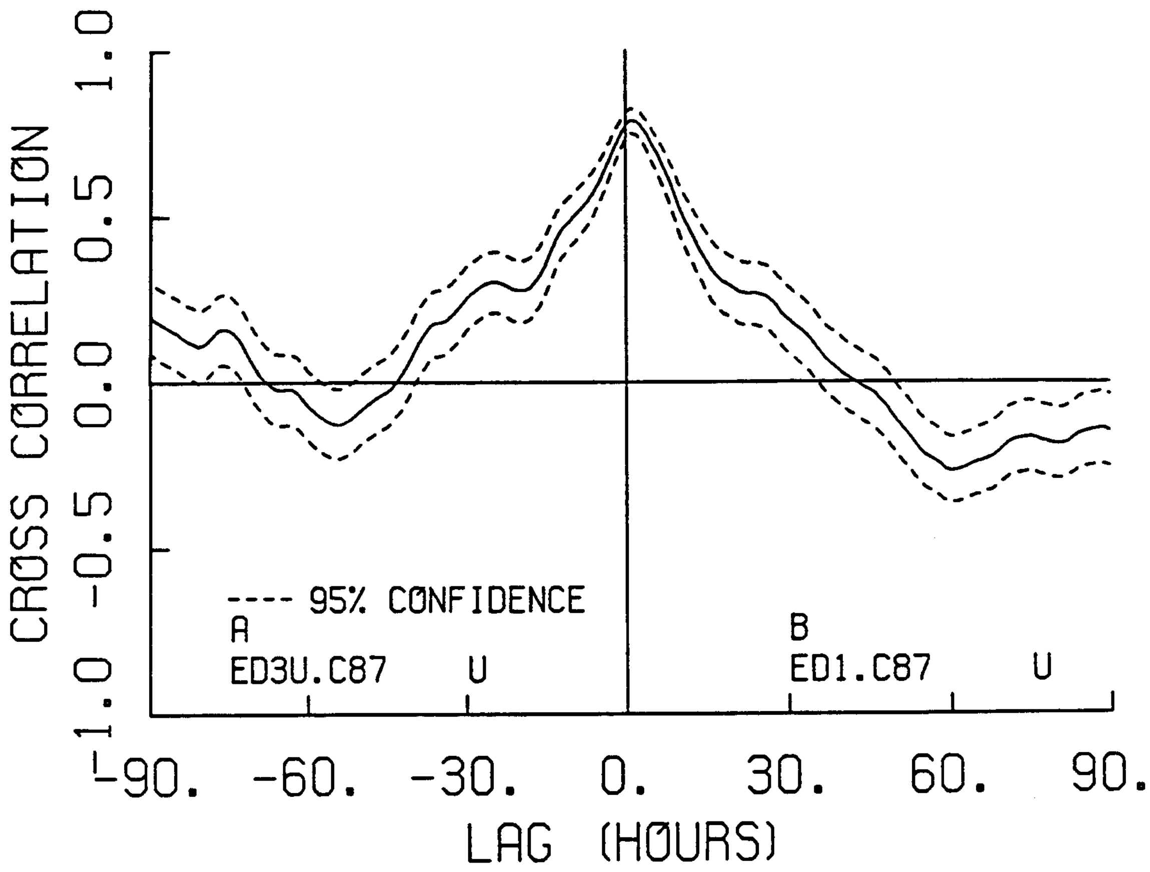

Figure 3-38. Cross correlation between U-component currents at ED3 upper and ED1, 1987. For positive lags, ED3 upper leads.

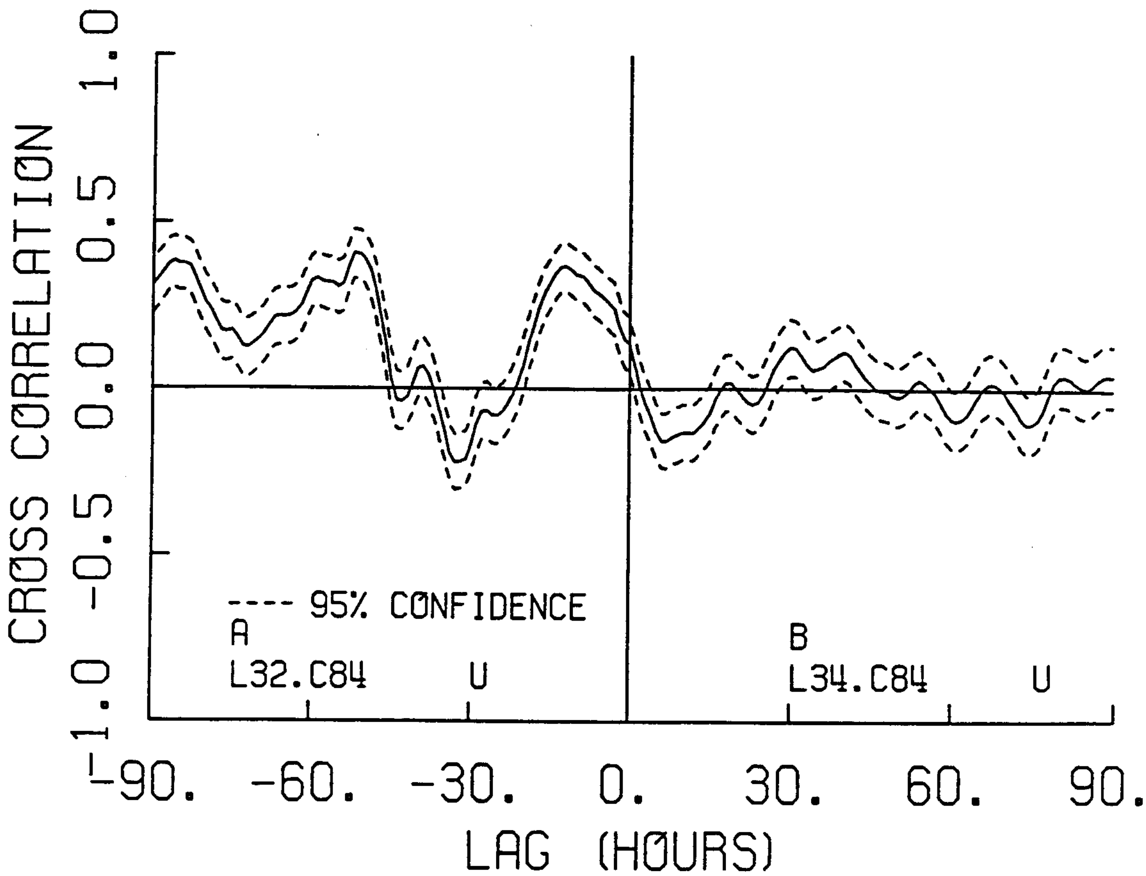

Figure 3-39. Cross correlation between U-component currents at L32 and L34, 1984. For positive lags, L32 leads.

4.0 INTEGRATION OF RESULTS WITH THE BEAUFORT SEA MESOSCALE CIRCULATION STUDY (BSMCS)

4.1 METHODS

4.1.1 Data Manipulation

BSMCS data were obtained from NOAA PMEL, Seattle, Washington, and were converted to NODC format prior to using the data analysis programs. Since the data were presented at a one-hour interval, no subsampling was done. Because the data records were in excess of a year long, the BSMCS data were truncated to approximately the same length as the nearshore data records in order to save file space and scan time on the computer.

4.1.2 Selection of Data Sets for Analysis

4.1.2.1 BSMCS Data

The BSMCS data sets chosen for analysis with nearshore current records were 1987-1988 MB4B-1 and MB2B-1, approximately 73 km and 82 km, respectively, NNE of Prudhoe Bay. Current record MB4B-1 sensor depth was 52 m in water 60 m deep, and MB2B-1 sensor depth was 72 m in water 185 m deep. These current records were coincident with the summer 1987 Endicott Environmental Monitoring Program. No other BSMCS data corresponded in time with available nearshore data records. Other 1987 BSMCS data records were about 230 km west or 160 km east from Prudhoe Bay and were not used in this analysis. Data from MB4B and MB2B were considered much more useful in making onshore/offshore current comparisons.

4.1.2.2 Nearshore Data

Data from mooring ED2 represented nearshore currents in the nearshore/offshore analysis. The choice was made on the basis of record length and location outside of nearshore causeway systems to the east and west of Prudhoe Bay. In view of the high correlation between ED2 and ED1, the only other nearshore record of suitable length and location, the use of both was considered redundant.

4.2 SUMMARY AND ASSESSMENT OF DATA

4.2.1 BSMCS Data

Current record MB4B-1 spanned 03 April 1987 to 30 March 1988, easily bracketing the 1987 nearshore current records. Current record MB2B-1 spanned 05 April 1987 to 04 April 1988. Both were judged to be of high quality and appeared to contain no missing data. Figure 4-1 shows these two mooring locations, and Table 3-5 lists general details.

4.2.2 Nearshore Data

Description of the nearshore data (1987 ED2) appears in Section 3.2.5.

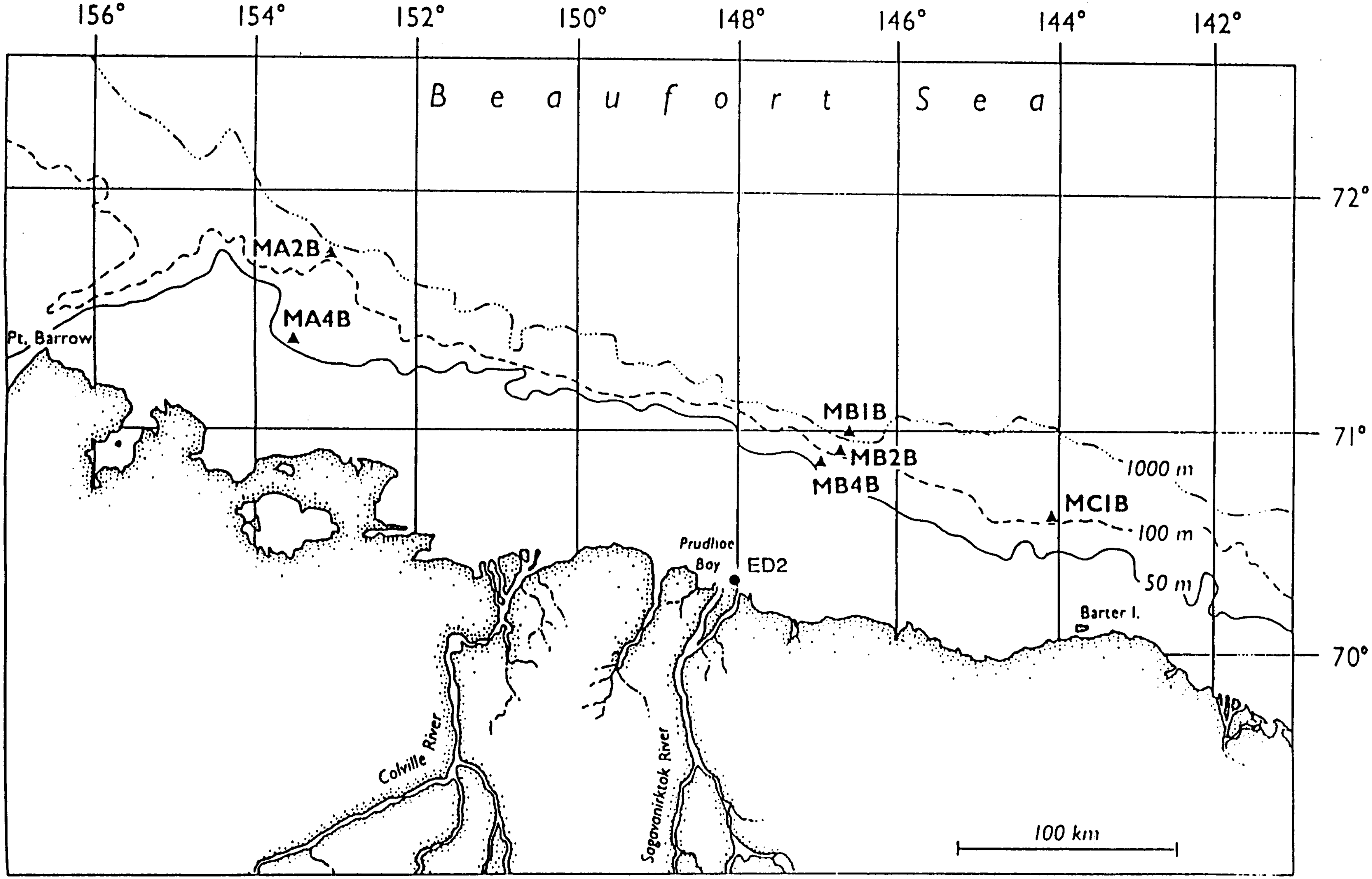

Figure 4-1. Location of 1987 current meter and meteorological data records selected for nearshore/offshore analysis and integration (Aagaard et. al. 1989).

4.3 RESULTS AND DISCUSSION

4.3.1 Wind and Offshore Currents

Resolution Island winds were well correlated with MB4B U-component (Figure 4-2). The maximum correlation was +0.69 with wind leading by eight hours, and the two remained significantly correlated about 45 hours either side of the maximum. Because of the depth of MB4B, it is unlikely that direct wind forcing is a significant source of current motions, but rather, the correlation likely represents the joint influence of large-scale atmospheric pressure distribution on both currents and wind.

In comparison, cross correlation showed MB4B U-component leading MB2B by 28 hours at the maximum correlation of +0.60. Considering that MB4B and MB2B are separated by only about 9 km, a phase difference of 28 hours is surprising.

4.3.2 Nearshore and Offshore Currents

The maximum correlation between currents at ED2 and MB4B was +0.65, with ED2 leading by six hours (Figure 4-3). This is consistent with previous correlations between wind and currents at ED2 and MB4B. The two time series remain significantly correlated within about 45 hours either side of the maximum. The maximum correlation between ED2 and MB2B was +0.57, with ED2 leading by 43 hours. Both results indicate significant correlation between nearshore and offshore currents, but do not suggest an explanation of the underlying cause.

Coherence and phase calculation between U-components of ED2 upper and MB4B-1 show a pronounced coherence peak at 0.028 cph, which corresponds to a period of 35 hours (Figure 4-4). The phase difference is about three hours, in rough agreement with the lag of six hours at maximum cross correlation. The average of phase difference over the six lowest frequencies (each itself a linear average of five successive values) is slightly less than seven hours. The near agreement with the lag for maximum cross correlation suggests that low frequency motions clearly dominate the common nearshore/offshore signals.

Interestingly, a 37-hour period was identified in ED2 upper U-component autospectrum, as well as others. That period also appears clearly in the MB4B-1 U-component autospectrum (Figure 4-5). Incidentally, so does a peak at period of about 4.5 to 5 days. The five-day period is apparent in the MB2B-1 autospectrum, but the 37-hour signal is much less distinct. Aagaard et al., 1989, also identified the 4.5- to 5-day signal and speculated that it might represent an eastward-propagating trapped wave. Whether or not the 37-hour signal has a similar explanation requires further work to determine beyond speculation. The period seems too short to be attributable to purely meteorological causes.

Cross correlations and spectra serve to establish the strength of nearshore-to-offshore relations and potentially identify major periodicities of common signals. However, the current meter data, in themselves, speak only weakly to the issue of momentum exchange and not at all to that of mass exchange between the nearshore and offshore circulation.

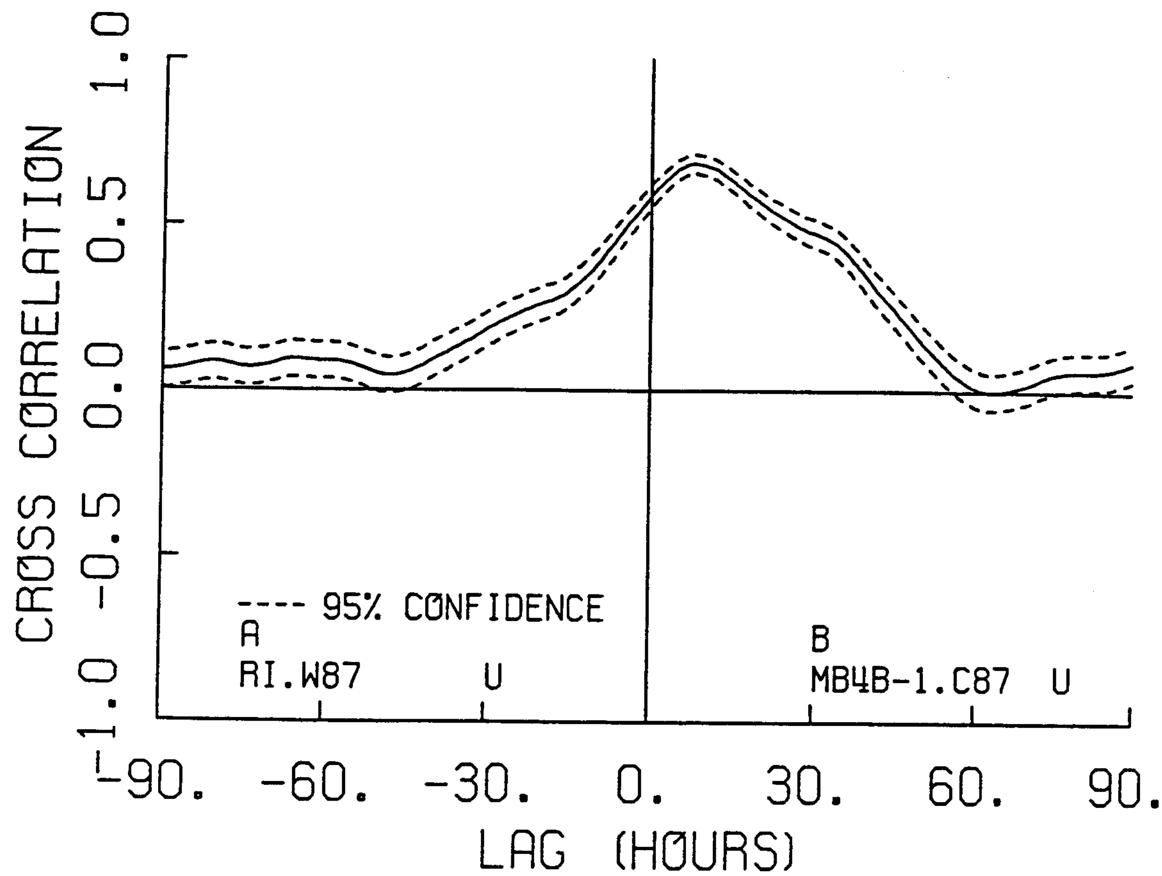

Figure 4-2. Cross correlation between U-components of Resolution Island wind and MB4B-1 currents, 1987. Wind leads for positive lags.

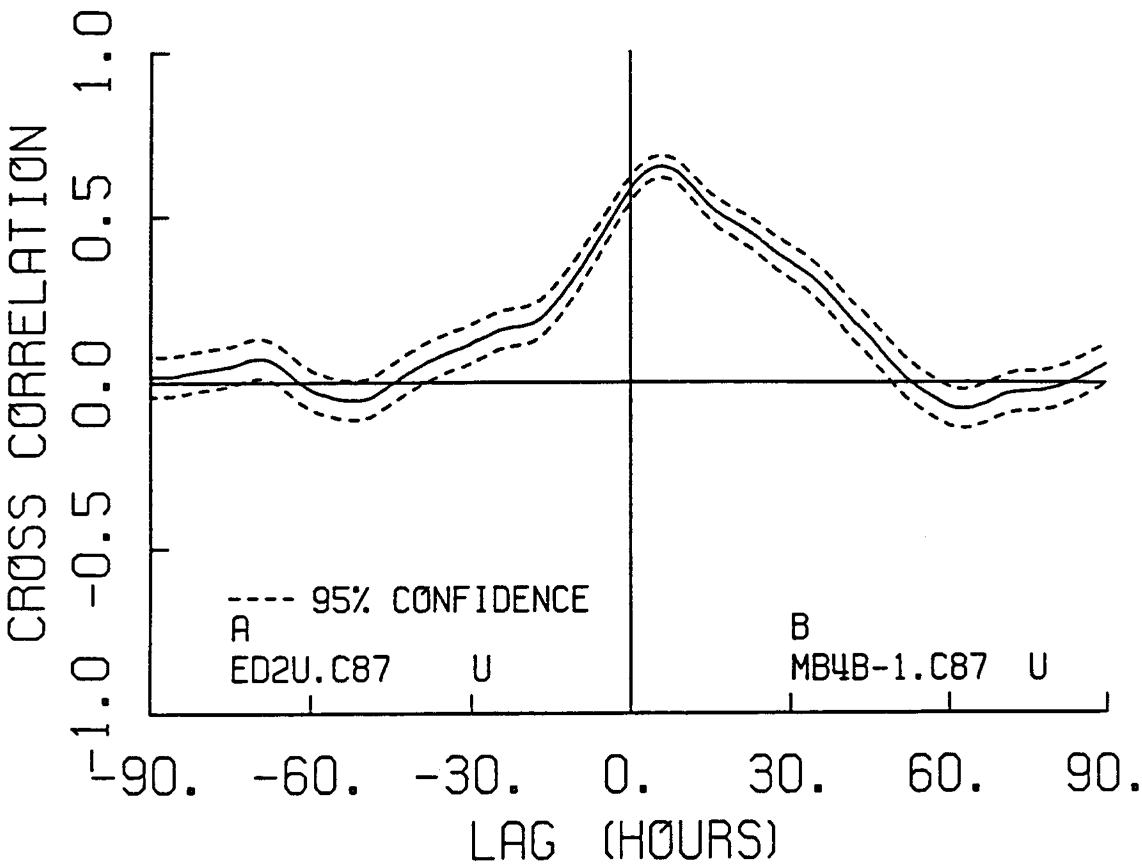

Figure 4-3. Cross correlation between U-component currents at MB4B-1 and ED2 upper, 1987. For positive lags, MB4B-1 leads.

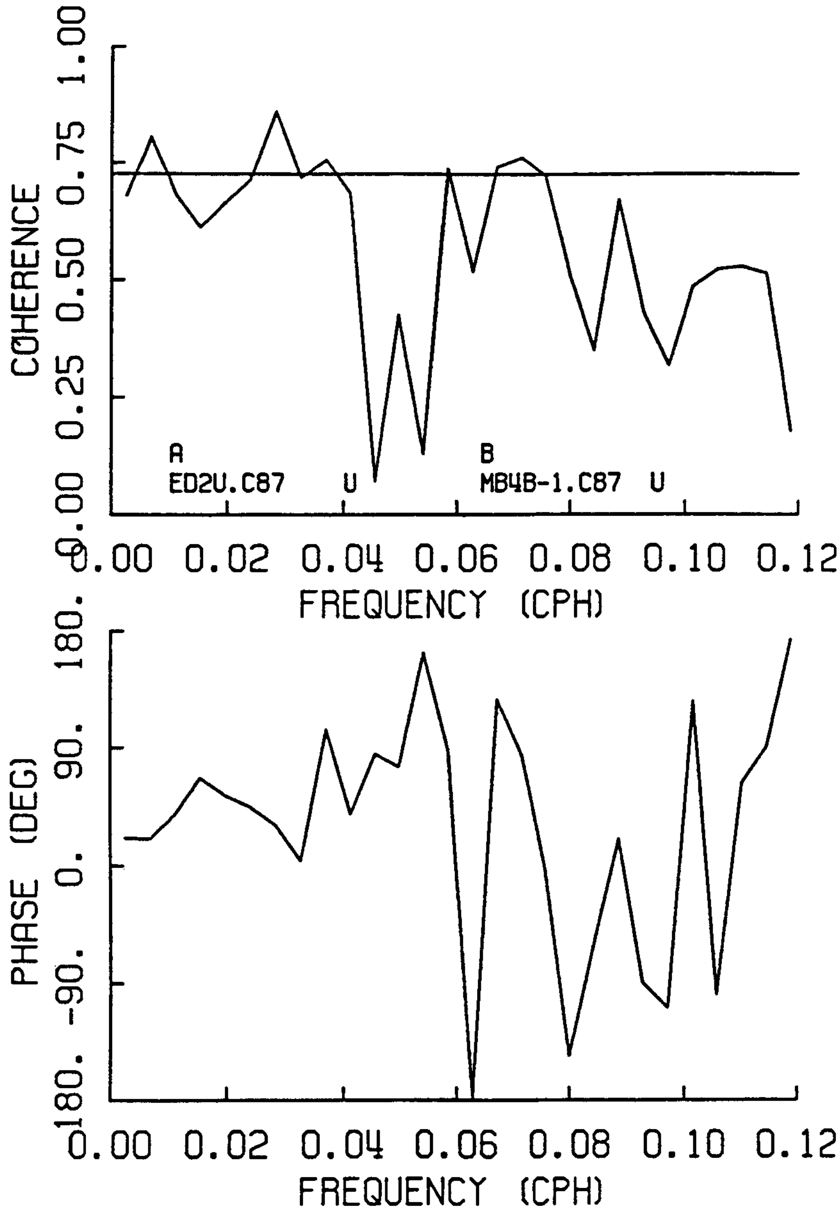

Figure 4-4. Coherence and phase between U-component currents at ED2 upper and MB4B-1, 1987. Positive phase indicates ED2 upper leads.

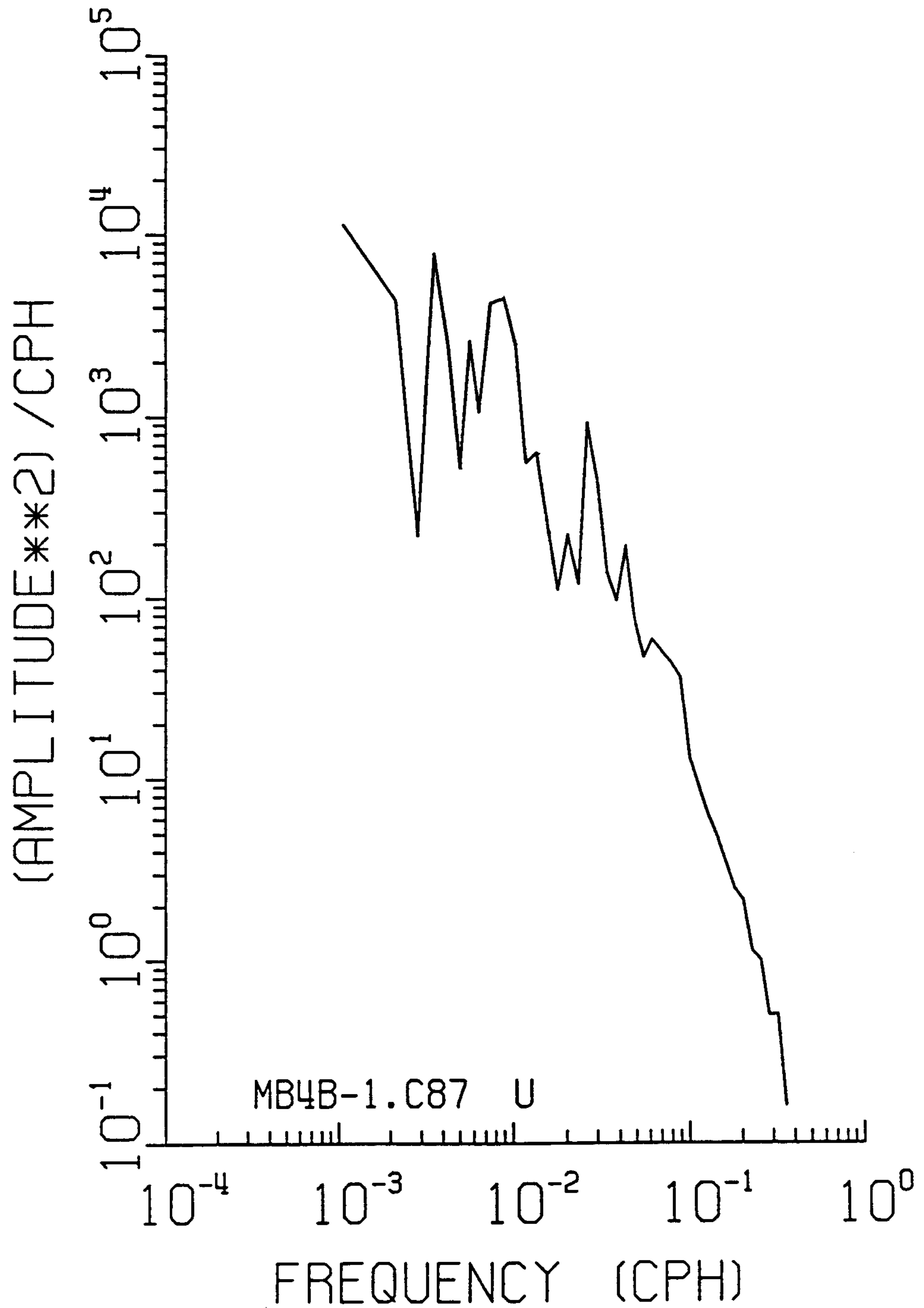

Figure 4-5. Autospectrum of U-component MB4B-1 currents, 1987.

5.0 COMPREHENSIVE SUMMARY

5.1 DATA IDENTIFICATION, DOCUMENTATION, COMPILATION, AND EVALUATION

The objectives of this task were: (1) to identify, document, and summarize all available information on historical data sets collected in the nearshore Alaskan Beaufort Sea region; and (2) to compile and evaluate the actual data from these historical data sets to the maximum extent possible.

This task began with a comprehensive review of oceanographic literature, project reports, data reports, and existing published data inventories. Direct inquiries were also sent to appropriate investigators, agencies, academic institutions, and private organizations known to have conducted studies in the region. Through these means, a total of 56 distinct project data sets encompassing physical oceanographic data from some part of the study area were identified. For each data set, documentation on where, when, why, how, and by whom individual data sets was acquired. Data types documented included current meter (moored and profiling), Lagrangian drifter, hydrographic (temperature and salinity), sea level (tide gauge), and meteorologic.

After the data sets were identified and documented, the compilation phase began, wherein all available historical data were obtained, organized, and reformatted (into standard NODC formats). A considerable volume of data was obtained from NODC via direct computer transfer from NODC's archival system to an Ebasco Environmental 386 microcomputer. Another large volume of historical data from the Prudhoe Bay/Stefansson Sound region already on hand in the Ebasco Environmental data archives was transferred into the project data base. A number of smaller data sets obtained from individual investigators or from optical scan-digitization of hardcopy tabular data listings in reports comprised the remainder of the project data base.

Of the 56 documented data sets, only 29 (some of these incomplete) were available for acquisition and subsequent analysis. Despite additional efforts to track down and acquire the missing data sets, many remained unavailable due to proprietary restrictions, inability to locate the original investigators, or inaccessibility of the original data.

Formal evaluation of the data quality associated with each data set proved to be impractical, due to the unavailability of a large number of historical data sets, combined with incomplete documentation on experimental methods, data processing, and quality control on many others. During the course of the data analysis task, an evaluation was made of each data set used, and any apparent data quality problems were noted.

One recommendation arising from this task is a suggestion that government funding agencies be more diligent in ensuring that oceanographic data collected under public funding be submitted to NODC. Furthermore, we recommend that if possible, regulations be implemented to require submission to NODC of any data collected by private concerns (e.g., oil companies) operating under agency permits. In the latter case, confidentiality could be stipulated for a specified time period, after which the data would become publicly available.

5.2 DATA ANALYSIS AND INTERPRETATION

Nearshore current records (depths <20 m) from 1982 and 1984-1989 were selected and analyzed using statistical and spectral techniques. Corresponding meteorological data for the various years were also obtained and used in the investigation of the relation between nearshore currents and wind.

Linear regression indicated that wind accounted for about 40 to 50 percent of current variance at current meter depths of 3 m or less. The percentage of explained variance of currents measured at sensor depths greater than 3 m was generally 10 percent or less, although two exceptions were noted in 1987 where the percentage of explained variance was as high as 35 percent. Density stratification, which itself is strongly influenced by wind direction and persistence, appears to be an important factor in the relation between direct wind forcing and deeper currents in the nearshore area.

Nearshore currents consistently lagged wind by one to three hours. Cross correlation coefficients between major-axis components (U-components) of wind and currents averaged 0.69 but ranged as high as 0.91 for one case in 1987. Correlation coefficients between minor axis components (V-components) were typically between -0.4 and zero and decayed within lags of about 10 hours. Coherence and phase calculations between wind and current show that the major contribution to high correlation was at low frequencies, generally less than 0.02 cph. Current speeds were 2.7 percent of wind speed or less for all wind/current analyses, and the indraft angle between wind and currents was meaningless because of rectification of currents in the alongshore direction.

The vertical relation of currents at the same mooring location varied markedly between 1985 and 1987. Maximum cross-correlation coefficients between current records at depths of 2 m and 4 m were 0.64 and 0.91, respectively, in 1985 and 1987. These values occurred at one to two hours lags in 1985 and zero to one hour in 1987, with the shallower currents leading in both cases. Stratification appeared to be a factor in the difference. In contrast, the V-component cross correlation functions were only slightly different from zero, although a tidal fluctuation was obvious in the plot. Analogous coherence and phase calculations between the V-components of the currents at 2 m and 4 m for 1985 and 1987 were similar, implying that variance along the minor axis is a weaker function of depth or stratification than variance along the major axis direction.

There was notable vertical shear in currents at location CB6 in Camden Bay in 1989. Vector-average currents at location CB6 were east-southeastward in the upper part of the water column and north-northwestward one meter above the bottom. Vector-average wind was toward the south-southwest. Thus, bottom currents were primarily in the same direction as wind, but currents nearer the surface were in rough opposition to the wind. Wind explained less than 30 percent of the current variance at both depths. At the same location in 1988, currents 1 m above the bottom were eastward, but vector-average wind was approximately the same as in 1989. The implication is that local dynamics influenced currents at location CB6 in 1989. Circulation probably reflects recirculation in Camden Bay and fluctuations in buoyancy input due to freshwater influx. Cross correlation and coherence and phase calculations between wind and CB6 currents and between upper and lower CB6 currents in 1989 suggest the possibility that localized dynamic factors in Camden Bay dominate wind effects in determining circulation and vertical shear in Camden Bay.

Autospectra indicate the presence of low-frequency signals in the U-component of nearshore currents. While the spectra exhibit general energy content throughout the band of frequencies less than about 0.02 cph, there is a strong hint of identifiable signals at frequencies of 0.007 cph (6-day period), at 0.0078 cph (5.3-day period), and at 0.0087 cph (4.8-day period). These are all in the range of frequencies likely attributable to wind forcing, but data are not comprehensive enough to conclude that no other dynamic mechanisms contribute. These signals are apparent in some years, but not universally in all the years analyzed. The broadband nature of wind forcing complicates the conclusive identification of any low-frequency signals.

Semi-diurnal tidal signals are particularly apparent in V-component current autospectra, although closer inspection shows comparable tidal energy in the U-component spectra that is masked by the general concentration of energy at low frequencies. Overall, the energy at tidal frequencies is a small fraction of the total energy in current motions.

Autospectra also indicate the year-to-year presence of a signal at frequencies of .029 to .022 cph (35-hour to 45-hour period). In one case, the spectrum of corresponding wind data also indicated a peak in approximately the same frequency range, while other wind spectra contained no similar peak. One possible explanation is a wavelike disturbance propagating alongshore, but a conclusive explanation awaits an experimental program designed to identify such phenomena.

Comparisons between the orientation of local isobaths and principal axis directions for currents suggests strong influence of bottom topography and proximity to coastline in steering currents alongshore. This is the case even when prevailing wind had a significant cross-isobath component. For two examples from 1985 and 1987, the principal axes of the deeper currents tended to be about 25 degrees offshore of the shallower currents. The difference may reflect the influence of layered-flow effects or friction near the bottom.

Cross correlations generally indicated that westernmost currents led currents farther east. This is likely related to the mean eastward flow in the nearshore area.

Interpretation of the analytical results is complicated by the fact that wind forcing is a broadband phenomenon and is aperiodic, for the most part. This means that spectral investigations can rarely yield conclusive results. It also means that analyses of successive segments of a given data record may yield results that differ markedly from each other and from analyses using the entire record length. Furthermore, the contributions of other potential dynamic mechanisms to observed currents may overlap those of the wind, making discrimination between them difficult, if not impossible without specific experimental design.

5.3 INTEGRATION OF RESULTS WITH THE BSMCS

Only during the open-water season of 1987 did available nearshore and offshore current measurements (BSMCS) coincide, so the number of data records available for nearshore/offshore comparison was limited. Those offshore current records closest to the location of the nearshore current records were chosen. Other offshore current records 230 km to the west and 160 km to the east were excluded under the assumption that comparison of nearshore/offshore current records with the smallest spatial separation would yield the most representative results.

The maximum correlation between nearshore (ED2) and offshore (MB4B-1) U-components was 0.65 with the nearshore currents leading by six hours. Corresponding coherence and phase calculations showed a distinct peak at 0.028 cph (35-hour period) with nearshore current leading by three hours. Low-frequency components are the primary contributors to the correlation between nearshore and offshore currents.

Resolution Island wind was also well correlated with MB4B-1 U-component current (0.69 with wind leading by eight hours). This is more likely due to wind and currents both responding to large-scale atmospheric pressure distributions rather than direct wind forcing of currents at a depth of 52 m at MB4B-1.

Autospectra of U-component currents indicated spectral peaks at about 0.027 cph (37-hour period) for both MB4B-1 and ED2U in 1987. This frequency is virtually the same as that apparent in coherence and phase calculations, suggesting a common mechanism coupling both the nearshore and offshore areas.

6.0 RECOMMENDATIONS

This section contains some brief recommendations regarding data acquisition/archiving as well as the nature of future oceanographic efforts in the region.

This study found that only about half of the historical data sets known to have been collected in the region were available for general use. This may be attributed to several factors. First, with respect to the incompleteness of the data holdings at NODC, it must be realized that in many cases the investigators were under no obligation to submit final data to that facility. In cases where such a requirement did exist (as a stipulation in some government funding agency contracts, for example), the funding agencies were apparently not diligent in verifying the data transmittals. The case of OCS/MATTHEWS 1977-81 (see section 2.2) is an apparent case in point. Understandably, both investigators and funding agencies assign a high priority to the collection and analysis of data and the reporting of scientific results. Data archiving and transmittal to NODC is often the last, and by perception, least important task of any project. A second problem is the unavoidable circumstance of personnel turnover. The departure of a principal investigator, graduate student, or key data manager before project completion strongly reduces the chance of orderly data archiving and transmittal. The inaccessibility of proprietary data sets for many years (see section 2.2) is a third reason for gaps in the available archived data base. By the time the proprietary restriction is lifted from a data set, the original data may be lost or degraded, and the investigator may be unlocatable.

We present two recommendations with respect to the data accessibility question. First, we suggest that stronger emphasis be placed on ensuring the submission of data to NODC in all projects funded by public agencies. Second, we suggest that a mechanism be put in place whereby data collected under private funding, but associated with government-regulated activities (e.g., permitted exploration and development activities), be required to be submitted to NODC in a timely fashion. In the latter case, it could be stipulated that the data shall remain confidential for a specified amount of time, after which it would become publicly available. At least in such a system, the data would not be ultimately lost.

One of the apparent impediments in characterizing the relation between wind and nearshore currents and between nearshore and offshore currents is the absence of oceanographic data between roughly the 10-m and 100-m isobaths. The obvious difficulty is seasonal encroachment of ice and probable damage or loss of moored instruments. Data from this segment of the shelf are necessary to investigate the transition between nearshore and offshore regimes, which likely involves transition from primarily wind-forced to ocean-forced dynamics. This is not to say that the realms of influence do not overlap, but rather that the degree of influence changes. Whether or not the change is abrupt at a particular depth contour, for instance, or gradual is not within the resolution of existing data.

In order to investigate dynamic processes, concurrent moorings separated both alongshore and offshore are necessary. This allows identification of propagating disturbances as well as determination of phase speeds, wave-lengths, and possibly, cross-isobath structure. Continuation of data recording to include ice-covered intervals as well as open-water intervals is desirable as a means of looking at seasonal and annual circulation patterns.

Another approach to supplementing observations is to apply computer models to the shelf and slope regions of the Beaufort Sea coast. While such model investigations could not be expected to be conclusive, they might serve to provide preliminary indications of types of dynamic mechanisms supported by the topography, stratification, and external forcing that typify the area.

7.0 ACKNOWLEDGEMENTS

This study was funded by the Minerals Management Service, U.S. Department of the Interior, through an Interagency Agreement with the National Oceanic and Atmospheric Administration, U.S. Department of Commerce, as part of the Alaska Outer Continental Shelf Environmental Assessment Program. The authors extend thanks to Mr. David Hale of NOAA for his aid and support throughout this project, and to Mr. Sid Stillwaugh of the Northwest Ocean Service Center for his help in sleuthing existing data sets from the study area.

8.0 LITERATURE CITED

Aagaard, K. 1984. The Beaufort Undercurrent. In: The Alaskan Beaufort Sea: Ecosystems and Environments, P. W. Barnes et al. (eds.). Academic Press.

Aagaard, K. 1976. STD mappings of the Beaufort Sea shelf. In: Envir. Assess. of the Alaskan Cont. Shelf, Ann. Rep., 11, 249-266.

Aagaard, K. 1977. STD mappings of the Beaufort Sea shelf. In: Envir. Assess. of the Alaskan Cont. Shelf, Ann. Rep., 14, 473-507.

Aagaard, K., C.H. Pease, A.T. Roach, and S.A. Salo. 1989. Beaufort Sea Mesoscale Circulation Study - Final Report. Pacific Marine Environmental Laboratory, NOAA, Seattle, WA.

Aagaard, K., C.H. Pease, and S.A. Salo. 1988. Beaufort Sea Mesoscale Circulation Study - preliminary results. NOAA Technical Memorandum ERL PMEL-82.

Barnes, P.W., and R. Garlow. 1976. Surface current observations - Beaufort Sea, 1972. In: Envir. Assess. of the Alaskan Cont. Shelf, Ann. Rep., 12, 591-599.

Barnes, P.W., E. Reimnitz, and D. Drake. 1977. Marine environmental problems in the ice covered Beaufort Sea shelf and coastal regions. In: Envir. Assess. of the Alaskan Cont. Shelf, Ann. Rep., 17, 1-229.

Barnes, P.W., D.M. Schell, and E. Reimnitz (eds). 1984. The Alaskan Beaufort Sea: Ecosystems and Environments. Academic Press.

Bendat, J.S. and A.G. Piersol, 1971. Random data: Analysis and measurement procedures, John Wiley & Sons, New York.

Berry, A.D., and J.M. Colonell. 1985. Oceanography. In: Lisburne Development Environmental Studies: 1984. Prep. by Woodward-Clyde Consultants for ARCO Alaska, Anchorage.

Birch, J.R., D.B. Fissel, A.B. Cornford, and H. Melling. 1984. Arctic Data Compilation and Appraisal, Volume 7, Canadian Basin-Arctic Ocean: Physical Oceanography-Temperature, Salinity, Current, and Water Levels. Canadian Data Report of Hydrography and Ocean Sciences No. 5. Institute of Ocean Sciences, Sidney, B.C.

Britch, R.P., R.C. Miller, J. Downing, T. Petrillo, and M. Veit. 1983. Physical processes. In: Environmental Summer Studies (1982) for the Endicott Development. Prep. by LGL Alaska Research Assoc. and Northern Technical Services for SOHIO Alaska Petroleum Co.

Callaway, R., and C. Koblinsky. 1976. Transport of pollutants in the vicinity of Prudhoe Bay, Alaska. In: Envir. Assess. of the Alaskan Cont. Shelf, Ann. Rep., 11, 427-475.

Carsey, F. 1977. Coastal meteorology of the Alaskan arctic coast. In: Envir. Assess. of the Alaskan Cont. Shelf, Ann. Rep., 15, 538-578.

Chin, H. 1979. Physical/chemical measurements taken in the Beaufort Sea, July/August 1979. Unpub. data report.

Chin, H., M. Busdosh, G.A. Robilliard, and R.W. Firth Jr. 1979. Physical oceanography and benthic ecology. In: Environmental Studies Associated with the Prudhoe Bay Dock, 1978 Studies, Final Report. Prep. by Woodward-Clyde Consultants for ARCO Alaska.

Colonell, J., and T. Weingartner. 1982. Physical oceanographic studies in the Beaufort Sea near the Sagavanirktok River delta. In: Duck Island Development - Marine Environmental Studies. Prep. by Woodward-Clyde Consultants for Exxon Co.

Dygas, J.A. 1975. A study of winds, waves, and currents in Simpson Lagoon. In: Environmental Studies of an Arctic Estuarine System - Final Report. Inst. of Marine Science, Univ. Alaska. EPA Ecology Res. Ser. EPA-660/3-75-026, 15-44.

Dygas, J.A., D.C. Burrell. 1976. Response of waves and currents to wind patterns in an Alaskan lagoon. In: Assessment of the Arctic Marine Environment : Selected Topics. D. W. Hood and D. C. Burrell, eds. Inst. of Marine Science, Univ. Alaska, Occas. Pub. No. 4, 263-285.

Feder, H.M., D.G. Shaw, and A.S. Naidu. 1976a. The arctic coastal environment in Alaska: the nearshore marine environment in Prudhoe Bay, Alaska. Inst. of Marine Science, Univ. Alaska, Sea Grant Rep. 76-3.

Feder, H.M., D.G. Shaw, and A.S. Naidu. 1976b. The arctic coastal environment in Alaska: a compilation and review of scientific literature of the arctic marine environment. Inst. of Marine Science, Univ. Alaska, Sea Grant Rep. 76-9.

Fruge, D.J., D.W. Wiswar, L.J. Dugan, and D.E. Palmer. 1989. Fish population characteristics of Arctic National Wildlife Refuge coastal waters, summer 1988. U.S. Fish and Wildlife Service, Progress Report, Fairbanks, AK.

Garrison, G.R. 1976. Chukchi Sea oceanography: 1975 measurements and review of coastal current properties. Applied Physics Lab., Univ. Washington, Rep. No. APL-UW 7614.

Garrison, G.R. 1977. Oceanographic measurements in the Chukchi Sea and Baffin Bay, 1976. Applied Physics Lab., Univ. Washington, Rep. No. APL-UW 7710.

Garrison, G.R., and P. Becker. 1975. Marginal ice zone measurements: Bering and Chukchi Seas, 1973 and 1974. Applied Physics Lab., Univ. Washington, Rep. APL-UW 7505.

Garrison, G.R., and E.A. Pence. 1973. Studies in the marginal ice zone of the Chukchi and Beaufort Seas: a report on Project MIZPAC-71B. Applied Physics Lab., Univ. Washington, Rep. No. 7223.

Garrison, G.R., M.L. Welch, and J.T. Shaw. 1979. Oceanographic measurements in the Chukchi Sea and Baffin Bay, April-August 1977. Applied Physics Lab., Univ. Washington, Rep. No. APL-UW 7824.

Gonella, J. 1972. A rotary component method for analyzing meteorological and oceanographic time series. Deep-Sea Research, 19, 833-846.

Greisman, P., and A. Blaskovich. 1984. Analysis and interpretation of current measurements from the Beaufort Sea. Prep. by Dobrocky SeaTech Ltd. for the U.S. Coast Guard. Rep. No. CG-D-18-84.

Grider, G.W. Jr., G.A. Robilliard, and R.W. Firth. 1977. Coastal processes and marine benthos. In: Environmental Studies Associated with the Prudhoe Bay Dock - Final Report, 1976 . Prep. by Woodward-Clyde Consultants for ARCO Alaska.

Grider, G.W. Jr., G.A. Robilliard, and R.W. Firth. 1978. Coastal processes and marine benthos. In: Environmental Studies Associated with the Prudhoe Bay Dock - Final Report, 1977. Prep. by Woodward-Clyde Consultants for ARCO Alaska.

Hachmeister, L.E., K.S. Short, G.C. Schrader, K.B. Winnick, and J.W. Johannessen. 1987. Oceanographic monitoring, 1985. In: Endicott Environmental Monitoring Program, Annual Report - 1985. Prep. by Envirosphere Co. for U.S. Army Corps of Engineers, Alaska Dist.

Hachmeister, L.E. and J.B. Vinelli. 1983. Environmental characterization of lagoons and nearshore shelf regions in the eastern Beaufort Sea: physical oceanography. Prep. by Science Applications Inc. for LGL Ecological Research Assoc.

Horner, R.A. 1981. Beaufort Sea plankton studies. In: Envir. Assess. of the Alaskan Cont. Shelf, Final Rep., 13, 65-314.

Hufford, G.L. 1973. Warm water advection in the southern Beaufort Sea, August-September 1971. Journ. Geophysical Res., 78(15), 2702-2707.

Hufford, G.L. 1974. On apparent upwelling in the southern Beaufort Sea. Journ. Geophysical. Res., 79(9), 1305-1306.

Hufford, G.L. 1975. Some characteristics of the Beaufort Sea shelf current. Journ. Geophysical Res., 80(24), 3465-3468.

Hummer, P.G. 1987. Meteorology 1985. In: Endicott Environmental Monitoring Program, Annual Report - 1985. Prep. by Envirosphere Co. for U.S. Army Corps of Engineers, Alaska Dist.

Hummer, P.G. 1987. Meteorology 1986. In: Endicott Environmental Monitoring Program, Draft Annual Report - 1986. Prep. by Envirosphere Co. for U.S. Army Corps of Engineers, Alaska Dist.

Hummer, P.G. 1988. Meteorology 1987. In: Endicott Environmental Monitoring Program, Draft Annual Report - 1987. Prep. by Envirosphere Co. for U.S. Army Corps of Engineers, Alaska Dist.

Irish, J.D., D.J. Bendiner, M. Levine and J. Zeh. 1976. WHIMPER: A library of time series programs. Univ. of Washington Dept. of Oceanography technical report #343, Univ. of Washington Applied Physics Laboratory Report #7508, Seattle, Washington.

Jenkins, G.M. and D.G. Watts, 1968. Spectral analysis and its applications, Holden-Day, San Francisco, 525 pp.

Kinney, P.J., D.C. Burrell, M.E. Arhelger, T.C. Loder, and D.W. Hood. 1970. Chukchi Sea data report: USCGC Northwind, July-August 1968; USCGC Staten Island, July-August 1969. Univ. Alaska, Fairbanks, R-70-23.

Kinney, P.J., D.M. Schell, J. Dygas, R. Nenahlo, G.E. Hall. 1972. Nearshore currents. In: Baseline Data Study of the Alaskan Arctic Aquatic Environment. Inst. of Marine Science, Univ. Alaska, Rep. R-72-3, 29-48.

Kozo, T.L., and R.A. Brown. 1979. Meteorology of the Alaskan arctic coast. In: Envir. Assess. of the Alaskan Cont. Shelf, Ann. Rep., 8, 1-56.

Kozo, T.L. 1981. Meteorology of the Alaskan arctic coast. In: Envir. Assess. of the Alaskan Cont. Shelf, Ann. Rep., 5, 109-127.

Leavitt, E. 1978. Coastal meteorology of the Alaskan arctic coast. In: Envir. Assess. of the Alaskan Cont. Shelf, Ann. Rep., 10, 580-607.

MacDonald, B.C. 1983. Meteorological monitoring program for 1982. In: Prudhoe Bay Waterflood Project Environmental Monitoring Program, 1982, Final Report. Prep. by Envirosphere Co. for U.S. Army Corps of Engineers, Alaska Dist.

Mangarella, P.A., J.R. Harper, and T.J. Weingartner. 1982. Prudhoe Bay Waterflood Project, physical processes monitoring program. In: Prudhoe Bay Waterflood Project Environmental Monitoring Program, 1981, Final Report. Prep. by Woodward-Clyde Consultants for U.S. Army Corps of Engineers, Alaska Dist.

Matthews, J.B. 1978. Characterization of the nearshore hydrodynamics of an arctic barrier island-lagoon system. In: Envir. Assess. of the Alaskan Cont. Shelf, Ann. Rep., 10, 607-617.

Matthews, J.B. 1979. Characterization of the nearshore hydrodynamics of an arctic barrier island-lagoon system. In: Envir. Assess. of the Alaskan Cont. Shelf, Ann. Rep., 8, 57-97.

Matthews, J.B. 1980. Characterization of the nearshore hydrodynamics of an arctic barrier island-lagoon system. In: Envir. Assess. of the Alaskan Cont. Shelf, Ann. Rep., 6, 577-601.

Matthews, J.B. 1981. Characterization of the nearshore hydrodynamics of the Beaufort Sea and Chukchi Sea and summer studies of the physical oceanography of the Beaufort Sea for sale #71. In: Envir. Assess. of the Alaskan Cont. Shelf, Ann. Rep., 5, 129-150.

Mooers, C.N.K., 1973. A technique for the cross spectrum analysis of pairs of complex-valued time series with emphasis on properties of polarized components and rotational invariants. Deep-Sea Research, 201, 1129-1141.

Morehead, M.D., J.T. Gunn, G.D. Pollard, C.B. Wilson. 1990. Oceanography. In: Endicott Environmental Monitoring Program, Draft Annual Report - 1988. Prep. by Science Applications International Corp. for U.S. Army Corps of Engineers, Alaska District.

Mountain, D.G. 1974. Bering Sea water on the north Alaskan shelf. Ph.D. dissertation, Univ. Washington, Seattle.

Mungall, J.C.H., R.W. Hann Jr., D.J. Horne, R.E. Whitaker, and C.E. Abel. 1978. Oceanographic processes in a Beaufort Sea barrier island-lagoon system: numerical modeling and current measurements. In: Envir. Assess. of the Alaskan Cont. Shelf, Ann. Rep., 10, 732-830.

Mungall, J.C.H., R.E. Whitaker, and S.D. Pace. 1979. Oceanographic processes in a Beaufort Sea barrier island-lagoon system: numerical modeling and current measurements. In: Envir. Assess. of the Alaskan Cont. Shelf, Ann. Rep., 8, 182-287.

Murphy, D.L., I.M. Lissauer, and J.C. Myers. 1983. Movement of satellite-tracked buoys in the Beaufort Sea. U.S. Coast Guard Res. and Devel. Center, Rep. No. CG-D-30-83.

Northern Technical Services. 1981. Beaufort Sea drilling effluent disposal study. Prep. for Reindeer Island Stratigraphic Test Well Participants, under direction of SOHIO (BP), Anchorage, Alaska.

Northern Technical Services. 1983. Open-water drilling effluent disposal study, Tern Island, Beaufort Sea, Alaska. Prep. for Shell Oil Co., Anchorage, Alaska.

Northern Technical Services. 1985. Environmental effects of below-ice drilling effluent discharges, Mukluk Island Well No. 1, Beaufort Sea, Alaska. Prep. for SOHIO (BP), Anchorage, Alaska.

Oceanographic Services Inc. 1976. Beaufort Sea Ice Movement Study, final report. Prep. for AMOCO Production Co. (and other participants).

Oceanographic Services Inc. 1979. Beaufort Sea Meteorological and Oceanographic Program (BEAUMOP), summer 1978, final report. Prep. for Gulf Res. and Devel. Co. and other participants.

Oceanographic Services Inc. 1981. Summer oceanographic measurement program, Beaufort Sea-1980, phase II, August 1980-August 1981. Prep. for AMOCO Production Co. and other participants.

Otnes, R.K. and L. Enochson, 1978. Applied time series analysis: Volume 1 - basic techniques, John Wiley & Sons, New York, 449 pp.

Paquette, R.G. and R.H. Bourke. 1974. Observations on the coastal current of arctic Alaska. Journ. of Marine Res., 32(2), 195-207.

Paquette, R.G. and R.H. Bourke. 1978. The oceanographic cruise of the <u>USCGC Burton Island</u> to the marginal sea-ice zone of the Chukchi Sea - MIZPAC 77. Dept. of Oceanography, U.S. Naval Postgrad. School, Monterey, Tech. Rep. NPS68-78-001.

Paquette, R.G. and R.H. Bourke. 1979. The oceanographic cruise of the <u>USCGC Glacier</u> to the marginal sea-ice zone of the Chukchi Sea - MIZPAC 78. Dept. of Oceanography, U.S. Naval Postgrad. School, Monterey, Tech. Rep. NPS68-79-003.

Reed, J.C. and J.E. Sater (eds). 1974. The Coast and Shelf of the Beaufort Sea; Proc. of Symposium on Beaufort Sea Coast and Shelf Research, Arctic Inst. of N. America.

Savoie, M.A. and D.E. Wilson. 1983. Physical processes monitoring program. In: Prudhoe Bay Waterflood Project Environmental Monitoring Program, 1982, Final Report. Prep. by Envirosphere Co. for U.S. Army Corps of Engineers, Alaska Dist.

Savoie, M.A. and D.E. Wilson. 1984. Physical processes monitoring program. In: Prudhoe Bay Waterflood Project Environmental Monitoring Program, 1983, Final Report. Prep. by Envirosphere Co. for U.S. Army Corps of Engineers, Alaska Dist.

Savoie, M.A. and D.E. Wilson. 1986. Physical marine processes monitoring program. In: Prudhoe Bay Waterflood Project Environmental Monitoring Program, 1984, Final Report. Prep. by Envirosphere Co. for U.S. Army Corps of Engineers, Alaska Dist.

Short, K.S., C.D. Janzen, C.J. Van Zee, and D.J. Hanzlick. 1988. Oceanography 1987. In: Endicott Environmental Monitoring Program, Draft Annual Report - 1987. Prep. by Envirosphere Co. for U.S. Army Corps of Engineers, Alaska Dist.

Short, K.S., G.C. Schrader, L.E. Hachmeister, and C.J. Van Zee. 1987. Oceanography 1986. In: Endicott Environmental Monitoring Program, Draft Annual Report - 1986. Prep. by Envirosphere Co. for U.S. Army Corps of Engineers, Alaska Dist.

Toimil, L.J. and J.M. England. 1982. Environmental effects of gravel island construction, OCS-Y0191 (BF-37), Beechey Point block 480, Stefansson Sound, Alaska. Prep. by Harding-Lawson Assoc. for Exxon Co.

U.S. Navy Hydrographic Office. 1954. Oceanographic observations, arctic waters, USS Burton Island cruises, summer 1950, winter 1951, summer 1952, summer, 1953. H. O. Pub. 618-C.

U.S. Navy Hydrographic Office. 1958. Oceanographic atlas of the polar seas, part II, arctic. H. O. Pub. 705.

U.S. Navy Hydrographic Office. 1959. Oceanographic observations, arctic waters. Technical Report TR-59.

U.S. Navy Hydrographic Office. 1960. Oceanographic observations, arctic waters. Technical Report TR-58.

U.S. Naval Oceanographic Office. 1963. Oceanographic data report, arctic 1958. Informal Manuscript Report No. 0-26-63.

U.S. Naval Oceanographic Office. 1963. Oceanographic data report, arctic 1959. Informal Manuscript Report No. 0-43-63.

U.S. Naval Oceanographic Office. 1964. Oceanographic data report, arctic 1960. Informal Manuscript Report No. 0-62-63.

Wiseman, W.J., J.M. Coleman, A. Gregory, S.A. Hsu, A.D. Short, J.N. Suhayda, C.D. Walters Jr., and L.D. Wright. 1973. Alaskan arctic coastal processes and morphology. Coastal Studies Inst., Louisiana State Univ., Tech. Rep. No. 149.

Wilson, D.E., J.C.H. Mungall, S. Pace, P. Carpenter, H. Teas, T. Goddard, R. Whitaker, and P. Kinney. 1981. Numerical trajectory modeling and associated field measurements in the Beaufort Sea and Chukchi Sea nearshore areas. In: Envir. Assess. of the Alaskan Cont. Shelf, Ann. Rep., 5, 299-378.

Woodward-Clyde Consultants. 1983a. Oliktok Point and vicinity: 1982 environmental studies. Prep. for ARCO Alaska.

Woodward-Clyde Consultants. 1983b. Physical oceanography. In: Lisburne Development Area - 1983 environmental studies. Prep. for ARCO Alaska, Anchorage.

NUMERICAL MODELING OF STORM SURGES IN THE BEAUFORT AND CHUKCHI SEAS

by

Zygmunt Kowalik

Geophysical Institute
University of Alaska
Fairbanks, Alaska 99701

Final Report
Outer Continental Shelf Environmental Assessment Program
Research Unit 627

May 1984

ACKNOWLEDGMENTS

I would like to express my gratitude to A. Thorndike (Polar Science Center, University of Washington) for his help in preparing the atmospheric pressure data for the wind calculation and discussion of the air-ice interaction problems.

I am grateful to the following for offering me unpublished data on sea level variation in the Chukchi and Beaufort seas: D. Bain (State of Alaska, Department of Natural Resources), B. Matthews (University of Alaska, Fairbanks), F. E. Stephenson (Institute of Ocean Sciences, Sidney, Victoria, B.C.), and J. Nasr (Fisheries and Oceans, Ottawa).

Discussions with T. Fathauer (National Weather Service, Fairbanks) and Al Comiskey (University of Alaska, Anchorage) helped me understand the climatology of the storm surges and discussions with R. F. Henry and T. Murty (Institute of Ocean Sciences, Sidney, Victoria, B.C.) elucidated the problems related to the surge modeling in the polar seas.

I am greatly indebted to M. Pelto (NOAA, OCSEAP, Juneau) and G. Weller (University of Alaska, Fairbanks) for help and discussions throughout the work.

This is the final report of OCSEAP Research Unit 627, Contract Number NA-81-RAC-00048.

ABSTRACT

Specific problems of storm-surge modeling in ice-covered seas are analyzed and discussed. First, the system of equations of motion and continuity in the ice-covered sea is introduced. The idea is to apply the vertically integrated equations of motion and continuity to the prediction of the storm surge wave both in ice-free and ice-covered seas. The interaction of atmosphere, ice, and water is expressed by the normal and tangential stresses. To include ice in the storm surge model we have to formulate the equations of motion and continuity for the ice cover. It is reasonable to assume that the storm surge is a phenomenon of relatively short duration; the thermodynamic behavior of ice can, therefore, be neglected and only the mechanical properties of ice are included in the equations. This brings into the scope of this work the various methods to describe interactions between the ice floes. A few possible ways to express the internal ice stresses are listed. Because the system of equations will be solved by numerical methods, the new numerical problems are scrutinized and criteria of numerical stability are examined. Before starting the computation of a storm surge in the Beaufort and Chukchi seas, a simulated surge is investigated in a square basin. The computations are performed with the same wind distribution for both ice-free and ice-covered areas.

In the next step a numerical grid is set over the Chukchi and Beaufort seas and three storm surges are simulated and described. The charts of the sea level, current and ice distribution are related to the large scale of the wind pattern used to simulate the driving force for the surge. The charts also allow estimates of the potential for the storm surge at various locations along the Chukchi and Beaufort coasts. First, a positive surge of October, 1963, generated by a low pressure center traveling from Siberia to Banks Island, is studied. On its way the storm was a source of the strong northwest and west winds which caused the sea level to rise to a record height of about 3 m along the Alaskan coast of the Chukchi Sea. Next we simulated a negative surge which occurred in the fall of 1979. This surge was

generated by the stationary high pressure system centered between Barrow and the North Pole. This is a typical wind pattern which feeds the Beaufort Gyre motion. Comparison of the measured and computed sea level and observed and computed ice edge position proves that the model is suitable to reproduce both water and ice motion. Finally, the storm surge in the late summer of 1981 is studied and the results are compared against eight tide gauges deployed along the Beaufort coast. Temporal variations of the recorded and computed sea level support the application of the model for short time predictions of the sea level during storms.

Results from the storm surge computations show relation of the sea level and current distribution. Due to the depth and shoreline geometry the pattern of motion in the Beaufort Sea is quite different from that in the Chukchi Sea. In both basins the storm surge tends to develop a dome structure in the sea level distribution. The negative sea level at the center of the dome in one sea basin is coupled with a positive level at the dome in the second basin. Velocity tends to be parallel to the sea level contours according to the geostrophic adjustment; therefore, two gyres are observed in which motion takes place around the domes. In the Chukchi Sea both current and sea level display strong variations not only at the shore but at large distances from the coast as well. In the Beaufort Sea, on the other hand, the changes are usually confined to the nearshore region. Also during major surges a coastal jet current develops along the shelf from Mackenzie Bay to Point Barrow.

All simulations are done for the ice-free and ice-covered sea surface, but the influence of the ice is practically negligible because major surges took place in summer and fall when the Chukchi and Beaufort seas were only partly covered by ice.

TABLE OF CONTENTS

1. Formulation of basic equations

Storm surge modeling is a subject area where numerical-hydrodynamical methods are quite successful. The storm surge propagation is usually studied through the vertically integrated equations of motion; therefore, complicated problems of exchange of momentum along the vertical direction are diverted to simpler problems of defining the tangential stresses at the sea surface and at the bottom.

The air-sea interaction in the polar seas is impeded by the presence of ice. The prediction of the pack ice influence on the storm surge propagation would not be so complicated if fairly general laws of the ice floe mechanics had been specified and tested experimentally (Rothrock, 1975).

The basis of calculations presented here will be the vertically integrated equations of water motion and continuity, written in the Cartesian coordinate system $\{x_i\}$, with x_1 directed to the east and x_2 directed to the north:

$$\frac{\partial u_i}{\partial t} + \varepsilon_{ij}u_j + \frac{\partial}{\partial x_j}(u_i u_j) = -g\frac{\partial \zeta}{\partial x_i} + \frac{(1-c)\tau_i^a}{H\rho_w} + \frac{c\tau_i^w}{H\rho_w}$$

$$-\frac{\tau_i^b}{\rho_w H} + A\frac{\partial u_i^2}{\partial x_j^2} \tag{1}$$

$$\frac{\partial \zeta}{\partial t} + \frac{\partial (Hu_i)}{\partial x_i} = 0 \tag{2}$$

The ice motion induced by wind will be studied through the following equations of motion:

$$m\frac{\partial v_i}{\partial t} + m\frac{\partial}{\partial x_j}(v_i v_j) + m\,\varepsilon_{ij}v_j = -mg\frac{\partial \zeta}{\partial x_i} + c\,(\tilde{\tau}_i^a - \tau_i^w) + F_i \tag{3}$$

Rate of change of the ice mass (m) over specific area is equal to the net influx of mass to that area plus all sources and sinks (ϕ)-Rothrock (1970). The equation of continuity for the ice mass consistent with the above considerations is

$$\frac{\partial m}{\partial t} + \frac{\partial (m v_i)}{\partial x_i} = \phi \tag{4}$$

In the above equations the following notation is used:

- i,j - indices, $(i,j = 1,2)$ where 1 stands for east coordinate, and 2 for west coordinate;
- t - time;
- u_i - components of the water velocity vector;
- v_i - components of the ice velocity vector;
- $\tau_i{}^a$ - components of the wind stress vector over the sea;
- $\tilde{\tau}_i{}^a$ - components of the wind stress vector over the ice;
- $\tau_i{}^w$ - components of the water stress;
- $\tau_i{}^b$ - components of the bottom stress;
- F_i - components of the force due to internal ice stress;
- ε_{ij} - Coriolis tensor;
- ζ - variation of the sea level or the ice around the undisturbed level;
- c - ice compactness;
- H - water depth;
- ρ_w - water density;
- A - lateral eddy viscosity, usually will be taken as $5 \cdot 10^4$ m^2/s;
- m - ice concentration or mass per unit area;
- g - gravity acceleration.

Throughout all indexed expressions Einstein's summation convention will be applied.

Assuming that the ice is not spread evenly over the whole sea surface, the mass of ice can be expressed through the ice compactness (c), ice thickness (h), and ice density (ρ):

$$m = \rho hc \tag{5}$$

A storm surge is a phenomenon of a relatively short duration, therefore thermodynamical sources and sinks linked to ϕ in equation (4) can be neglected. The equation of mass balance can be divided into two separate equations, i.e. a continuity equation for the ice compactness and an equation of thickness balance:

$$\frac{\partial c}{\partial t} + \frac{\partial (v_i c)}{\partial x_i} = 0 \tag{6}$$

$$\frac{\partial h}{\partial t} + v_i \frac{\partial h}{\partial x_i} = 0 \tag{7}$$

Both equations (6) and (7) will be applied along with equations (1) through (3) to obtain the ice thickness and the ice compactness distributions. It is reasonable to assume when the ice is not packed closely (c<1) that the ice thickness is not changed due to the ice motion. If, on the other hand, due to internal ice stress, the ice compactness will grow beyond c=1, the excess of compactness will lead to a change of the ice thickness. In such a case the new ice thickness distribution is computed through equation (7).

To derive a solution to equations (1) through (7) suitable boundary and initial conditions should be stated. Among all possible sets of the boundary conditions the chosen one should lead to a unique solution to the above system of equations. Such a set of conditions is still undefined for the ice-ocean interaction; therefore,we shall assume (since the ice flow equations), that the specification of the normal and tangential velocities along the boundaries is sufficient to derive the unique solution (Marchuk et al., 1972). Usually at the open boundaries (i.e. water boundaries) the storm surge velocity distribution is unknown. To overcome this hindrance the conditions at the opening boundary are specified for the simplified hyperbolic problem in which the horizontal exchange of momentum is neglected. Simplified problems, solved along the open boundary, define the velocity distribution. This velocity is the new boundary condition when solution of the complete system of equations is sought.

2. Short discussion of certain terms in the equations of motion

The aim is to discuss those terms in the equations of motion which still are not clarified with adequate precision, due mainly to the lack of suitable experimental knowledge. The interaction of the atmosphere, ice, and water is generally expressed through the normal tangential stresses. The definition of tangential stress over the ocean

$$\tau_i{}^a = C_{10}\ \rho_a |W_i| W_1 \tag{8}$$

includes the wind-drag coefficient C_{10}. Recently Garrat (1977) analyzed almost all measured data and found that C_{10} under a neutral atmospheric stability depends linearly on the wind velocity (W):

$$C_{10} = (0.75 + 0.067W)\cdot 10^{-3} \tag{9}$$

In (9) wind velocity is expressed in m/s.

In practice in storm surge computations (Henry and Heaps, 1976), the wind drag is usually set as constant and as large as $2.7 \cdot 10^{-3}$. Applying Garrat's expression one can see that this drag coefficient occurs at wind speeds close to 30 m/s, a speed which is too high even for average storm conditions. The large value of C_{10} was introduced into storm surge computations through comparison of the computed and observed sea level distributions in the coastal zone. Since the coastal effects are not always resolved properly, this may be the source of discrepancy. On the other hand measurements performed under strong wind conditions over the open ocean are quite rare. One can, therefore, argue that C_{10} should grow much faster with the wind speed due to the high roughness of the sea surface. Facing the necessity of choice of C_{10} as a constant value equal to $2.7 \cdot 10^{-3}$ and according to Garrat's expression (9) we take the former value in ensuing storm surge computations.

Definition of the wind stress over the pack ice,

$$\tilde{\tau}_i{}^a = \tilde{C}_{10}\, \rho_a |W_i| W_i \tag{10}$$

again leads to the same kind of problem. If one tries to scrutinize all data gathered during AIDJEX (Pritchard 1980) and the data dispersed in a few additional references, the dependence of $\tilde{C}_{10}$ on wind will be probably close to the expression (9). Again the same flaw occurs, namely that the measurements were made over smooth ice which does not properly characterize the high roughness of the sea ice due to the hummocking processes- Leavitt (1980), McPhee (1980). In the ensuing computations the wind drag coefficient over the ice, $\tilde{C}_{10}$, will be assumed to be equal to the one over the sea, i.e. $2.7 \cdot 10^{-3}$.

Interaction of the water and ice in equations (1) through (7) is described by two forces - the pressure gradient and the water stress. The former is fully defined if the sea level distribution is given; the latter we take as,

$$\tau_i^W = R_W \, |v_i - u_i| \, (v_i - u_i) \tag{11}$$

Water stress is sensitive both to the relative motion of the water and the ice, and to the magnitude of the coefficient R_W. The water drag coefficient is a function of the aerodynamic properties of the ice-water interface and the relative motion, its magnitude ranges from $3 \cdot 10^{-3}$ to $5.5 \cdot 10^{-3}$. For the pack ice drift in summer due to wind, McPhee (1980) estimated the water drag magnitude to be from $4 \cdot 10^{-3}$ to $5.5 \cdot 10^{-3}$. He also postulated that the ratio of the water drag coefficient to the wind drag coefficient is close to two ($R_W/C_{10} \approx 2$). The water drag coefficient is quite close to the above value. The drag coefficient under smooth first-year sea ice may be as small as $1.32 \cdot 10^{-3}$ (Langleben, 1982).

At the bottom of the sea a quadratic dependence of bottom stress on the velocity is also well recognized;

$$\tau_i^b = R \, |u_i| \, u_i \tag{12}$$

The bottom drag coefficient (R) is a function of the bottom roughness and the properties of the bottom boundary layer (Komar, 1976); R is usually taken in the range $(2 \div 4) \cdot 10^{-3}$.

The important problem to be clarified before the ice-water interaction can be studied is the formulation of a constitutive law which relates the stress (σ_{ij}) transmitted between floes to the variables in the problem formulated by equations (1) through (7). Only the mechanical behavior of ice is considered. We shall assume that during the storm surge the ice distribution will change due only to the ice motion; the influence of the thermodynamic processes will be neglected.

Due to the internal ice stresses the force F_i (see equation 3) acts on the ice floes. The components of the force are given by the divergence of the stress tensor (σ_{ij});

$$F_i = \frac{\partial \sigma_{ij}}{\partial x_j} \tag{13}$$

The stress-strain relationship is defined as follows;

$$\sigma_{ij} = 2\eta\varepsilon_{ij} + (\lambda-\eta)\,\varepsilon_{kk}\,\delta_{ij} - \frac{p}{\rho}\,\delta_{ij} \tag{14}$$

Here i,j are indices and they take the value 1 or 2. The strain-rate in (14) is expressed by the ice velocity;

$$\varepsilon_{ij} = \frac{1}{2}\left(\frac{\partial v_i}{\partial x_j} + \frac{\partial v_j}{\partial x_i}\right) \tag{15}$$

Introducing (14) and (15) into (13) the components of the force due to the internal ice stress are derived

$$F_1 = \eta\Delta v_1 + \lambda \frac{\partial}{\partial x_1}\left(\frac{\partial v_1}{\partial x_1} + \frac{\partial v_2}{\partial x_2}\right) - \frac{1}{\rho}\frac{\partial p}{\partial x_1} \tag{16a}$$

$$F_2 = \eta\Delta v_1 + \lambda \frac{\partial}{\partial x_2}\left(\frac{\partial v_1}{\partial x_1} + \frac{\partial v_2}{\partial x_2}\right) - \frac{1}{\rho}\frac{\partial p}{\partial x_2} \tag{16b}$$

In the ensuing computations, bulk (λ) and shear (η) viscosity coefficient are taken as equal, i.e. $\lambda = \eta$. The constitutive law has been applied a few times to investigate the under-ice tide propagation, but it has never been used in storm surge models. In this law at least two empirical constants which express the mechanism of the floe interaction are unknown, i.e. the viscosity coefficient (η) and pressure (p). Due to its discrete structure the pack ice is able to transmit compressive stresses only; the tensile stresses cannot propagate through the pack ice. It should be underlined that the ice mechanics expressed by the constitutive law do not take into account each individual ice-floe and its history. Sea ice cover is considered an aggregate of the ice floes, i.e. pack ice. The internal ice stress derived from the constitutive law is, therefore, a statistical average of the stresses between individual ice floes.

3. Constitutive laws to express internal ice stresses

Ice motion and ice compactness display close inter-relation, because nonuniform distribution of the ice velocity leads to variations in the ice compactness. Ice movement, practically unrestricted at a small compactness, is constrained at high compactness. The growth of compactness increases the internal stresses and if a critical value of stress is reached, deformation processes like hummocking, ridging or breaking will occur. This picture indicates that a simple frictional model of the ice flow interaction is unable to describe correctly the internal interaction over a wide range of compactness. From a certain value of compactness the frictional model should be aided by a model which is able to reproduce the high internal stresses in closely packed sea ice. Nonetheless, it is useful to consider the ice as a viscous fluid superposed over the water. A simple mechanism of the ice flow interaction is given by a linear viscous material, in that case the ice stress is proportional to the strain rate tensor (see Campbell, 1965, and Glenn,1970).

If, further, the fluid is considered as noncompressible, the relation between strain and stress (14) simplifies to:

$$\sigma_{ij} = 2\epsilon_{ij} \tag{17}$$

Inserting (15) into the above expression, and calculating the divergence of the stress tensor by (13) the internal force becomes:

$$F_i = \eta \frac{\partial^2 v_i}{\partial x_j \, \partial x_j} \tag{18}$$

The magnitude of the kinematic viscosity coefficient (η) is difficult to evaluate. In the Arctic Ocean and in the Weddel Sea, Campbell (1965) and Ling et al. (1980) found the coefficients by tuning the computed pattern of the mean ice circulation to the observed pattern. The estimated values ranged from $5 \cdot 10^6$ m^2/s to $5 \cdot 10^8$ m^2/s. To evaluate the influence of viscosity on tidal waves a sequence of investigation was carried out by Kowalik (1981) in the Arctic Ocean. The viscosity coefficients found for the steady motions when applied to the tide led to the suppression of the tide and, therefore, are unsuitable to describe time-dependent motion.

Closer to the natural conditions is the assumption that the viscosity coefficient is a function of the ice compactness. Linear dependence proposed by Doronin (1970)

$$\eta = \alpha c; \quad \alpha \approx 5.10^6 \text{ m}^2/\text{s}, \tag{19}$$

proved to be valuable in the prediction of the ice drift. However, since a long period was considered by Doronin it is not clear whether the success of the prediction was due to correct choice of ice mechanics or ice thermodynamics. According to Shirokov (1977) the internal ice friction starts to play an important role when the ice compactness is close to 0.8 and one may argue that starting from this value Doronin's expression can be applied.

It is possible to approach a description of stresses between floes from a different point of view and to consider the elastic properties only. Internal pressure, due to the ice floe interactions, will be expressed as a function of the ice compactness. Kheisin (1971) postulated a linear dependence of the pressure on the compactness;

$$p = k_p \frac{\delta c}{c_o} \tag{20}$$

with constant coefficient of the ice compression (k_p). The internal ice pressure is only present when variations of compactness are positive ($\delta s>0$); on the other hand, if $\delta s<0$, $p=0$. According to Kheisin (1971) the magnitude of k_p in closely packed ice ($c \approx 1$) varies from 10^4 kg/m·s^2 to 10^5 kg/m·s^2. In a two-layered system: ice-water, a pressure signal is not only transmitted through the water with velocity of the long waves ($\sqrt{gH}$), but also an elastic wave propagates with velocity $\sqrt{\frac{k_p}{\rho}} \approx 10$ m/s. In shallow water (H<10 m), the speed of elastic waves can exceed the speed of gravity waves.

A model of the ice drift with the ice mechanics based on the elastic constitutive law, has been developed and tested for the Caspian Sea by Ovsienko (1976, 1978). Internal ice pressure was set as a power function of the compactness

$$p = p_o \left(\frac{c}{c_o}\right)^{\kappa} \quad \theta\left(\frac{dc}{dt}\right) \tag{21}$$

where,

$$\theta\left(\frac{dc}{dt}\right) = \begin{cases} 1\,, & \text{if } \frac{dc}{dt} > 0 \\ 0\,, & \text{if } \frac{dc}{dt} < 0 \end{cases}$$

The magnitude of p_0 is close to the coefficient of the ice compression in (20), exponent $\kappa = 4 \div 6$.

Models to include both viscous and elastic properties were introduced by Rothrock (1975) and Kheisin and Ivchenko (1973). Rothrock's constitutive law contains pressure terms as a function of divergence of the ice velocity;

$$\left.\begin{array}{ll} \dfrac{p}{\rho} = -A_p \dfrac{\partial v_i}{\partial x_i} , & \text{if} \dfrac{\partial v_i}{\partial x_i} < 0 \\ p = 0 , & \text{if} \dfrac{\partial v_i}{\partial x_i} > 0 \end{array}\right\} \tag{22}$$

Analyzed constitutive laws contain rather simple mechanical properties of the ice, but they seem to describe the interaction of a storm-surge or tide with the pack ice in a quite satisfactory manner. For the long period processes, sophisticated models of the ice floe interaction, with both mechanical and thermodynamical properties have been proposed by Coon et al. (1974) and Hibler (1979).

4. Numerical problems related to the storm surge modeling in the polar seas

A few numerical schemes were constructed to predict the time dependent water-ice interaction. Hibler (1979) investigated slow seasonal variations of the ice cover in the Arctic Ocean by an implicit numerical scheme. Ovsienko (1976) employed particle-in-cell methods to predict the ice distribution and especially the position of an ice edge. We shall apply the scheme of Hansen (1962), which is explicit in time and staggered in space, to search for the solution of equations (1) through (7). The reason is that the explicit method has been employed in various oceanographical problems and its properties are quite well recognized (Kagan, 1970). It is of interest to understand how the ice cover will change the stability conditions of an explicit scheme.

Principal stability condition (Ramming and Kowalik, 1980)

$$T < \frac{L}{\sqrt{2gH}} \tag{23}$$

relates time step (T) to the distance (L) between grid points of a numerical scheme. If elastic properties of the ice cover are taken into account the inequality (23) must be modified accordingly, but the modification is necessary only in a very shallow basin ($H < 10$ m).

A significant difficulty of preserving numerical stability of the explicit scheme is created by internal friction, expressed by the lateral exchange of momentum. The ice kinematic viscosity coefficient, an analogue of kinematic eddy viscosity of water has high values up to 10^8 m^2/s. Kowalik (1981) demonstrated dependence of the stability condition on the magnitude of the horizontal viscosity. The general condition (23) should be assisted by two conditions related to the frictional forces:

$$T < (r_1 + 2A/L^2)/2f^2 \tag{24}$$

and

$$T < 1/(r_1 + 2A/L^2) \tag{25}$$

Coefficient r_1 is expressed as $r|u_i|/\rho_w H$, and in the deep ocean ($H \to \infty$), its value is negligible. Combining (24) and (25) for the deep ocean case, the range of variations of the horizontal viscosity is easily defined;

$$T(fL)^2 < A < \frac{L^2}{2T} \tag{26}$$

Viscosities defined beyond the range of inequality (26) will lead to the instability of the explicit numerical scheme.

5. Storm surges in ice-covered sea basins

Before starting the storm surge computation in the ice-covered Beaufort and Chukchi Seas one may investigate a similar process in a somewhat simple basin where complicated problems related to the open boundary conditions can be discarded. We take a square basin of 1000 km length with the depth variable along the x_1 (horizontal) direction from 50 m (at $x_1=0$) to 30 m (at x_1 = 1000 km). At the initial moment wind starts to blow along the (x_2) vertical coordinate with the speed constant in time but variable in space. The speed varies linearly along the x_1 direction from 4 m/s at $x_1=0$, up to 20 m/s at $x_1=1000$ km. A series of experiments was carried out with the above distribution of wind to compare different distributions of the sea level and current related to the presence or the absence of the ice and to the various constitutive laws of the ice mechanics. Three cases of the ice behavior were tested:

a) Internal stress was neglected ($F_i=0$),

b) Internal stress was expressed through the horizontal exchange of momentum with a constant viscosity coefficient, and with the viscosity coefficient according to Doronin's expression (19), and,

c) Internal stress was given by the elastic constitutive law according to expression (21).

The ice leads to redistribution of the energy transmitted from air to sea. This is clearly seen both in the current and sea level distributions derived from the computations - Figure 1 to Figure 6. The computations with the various constitutive laws show that the influence of the internal ice stresses on the ice distribution, sea level and mean current is of secondary importance. The dominant features of the ice motion are well described by the ice model.

without internal ice stresses (F_i=0). Figures 1 and 2 display the sea level and the mean current at 2 hours and 90 hours from the onset of winds over the ice-free sea. Steady motion occurs after about 70-80 hours of the process. The asymmetry of the sea level distribution is due mainly to the strong wind torque. The horizontal grid distance is scaled as 25 cm/s, therefore the largest velocities are of the order of 30 cm/s. In Figures 3, 4, 5 and 6 the same situation is depicted when the sea surface is covered by ice. Ice with a high compactness (c = 0.95) covers the eastern portion of the sea and over the remaining are the ice compactness is quite small (c = 0.1) (Figure 4). A comparison of Figures 1 and 3 shows the variations of the sea level and current. Close to the southern edge of the ice field the change in the sea level is especially noticeable. Since ice is situated on the sea surface where wind acts and also because the ice is thinner than the water, the ice velocity (Figure 4) exceeds the water velocity (Figure 3). In case of steady motion represented by Figures 5 and 6 the motion of ice and water is completely adjusted to the wind stress distribution. In these figures one can find areas where the ice velocity is smaller than the water velocity, and therefore, the energy is transmitted from water to ice. Such situations occur where the water and ice motion is reverse to the wind direction. The current in that area is not related to the wind stress but to the water slope.

6. Storm Surges in the Beaufort and Chukchi Seas - Introduction

The importance of the storm surges and associated water and ice motion is related to the recent exploitation of the North Slope oil. The shore of the Beaufort Sea is generally of low relief; therefore, coastal plains can be inundated by the surge and waves. The knowledge of the sea level variation along the Alaskan Beaufort and Chukchi coasts is scant. Until now tide gauges were installed in this region for a short time only and the present set of data is too small to estimate statistically valid distribution of the sea level variations. Only those surges which caused extensive flooding of the coastal communities were recorded. In the eastern Beaufort Sea in Tuktoyaktuk, Canada, a tide gauge was installed more than 20 years ago. Therefore some facts related to the storm surges in the Beaufort Sea can be inferred from this set of data. In Table 1, storm surges in excess of ± 0.9 m for the 11 year period (1962-73) are given after Henry (1974). Frequency of the major surges was not distributed uniformly in time and the highest sea level ever recorded at Tuktoyaktuk occurred on October 4, 1963. The same surge was observed at Barrow one day earlier. Sea level rose up to 3 m and this is historically known as the highest level ever observed at Barrow.

One can therefore conclude that sea level variations due to the storm surges are highly correlated along the Beaufort Sea coast. The storm in October 1963 caused damage of $3 million to Barrow. Hume (1964) studied topography variation after the storm surge and concluded that the sediment transport during storm in the vicinity of Barrow was equivalent of 20 years normal transport. We shall simulate the surge of October 1963 by numerical modeling, and the relation of the weather pattern and the sea level variations will be studied.

Due to the lack of the sea level data the range of the surge was studied by examining associated events like the driftwood distribution. In such a way Reimnitz and Maurer (1978) found a 3 m surge along the coast of Alaskan Beaufort Sea. They tracked the driftwood distribution due to the storm surge in the fall of 1970. The driftwood was stranded 20 m to 2000 m from the water line. The storm occurred over the southern Beaufort Sea, with wind up to 40 m/s-50 m/s. During this storm the Tuktoyaktuk gauge was not in operation and the surge was estimated as 3 m; even higher than the one recorded in October 1963. From Harrison Bay to MacKenzie Bay both wind and sea level were strongly correlated, and only in the

TABLE 1

Storm surges (in excess of 0.9 m) at Tuktoyaktuk (Canada) during summer 1962 to fall 1973.

Date	Surge Amplitude (m)	Date	Surge Amplitude (m)
July 28, 1962	1.37	Sept. 22, 1963	1.01
Aug. 29, 1962	1.04	Oct. 4, 1963	1.89
Aug. 31, 1962	1.43	Oct. 16, 1963	0.91
Sept. 4, 1962	1.83	Aug. 7, 1965	1.37
Oct. 13, 1962	-0.91	Nov. 12, 1965	0.94
Oct. 25, 1962	-1.01	July 18, 1966	0.91
Nov. 14, 1962	-1.16	Sept. 10, 1966	1.13
July 5, 1963	1.19	Oct. 4, 1966	-0.91
July 27, 1963	0.94	Oct. 15, 1966	-1.10
July 28, 1963	1.13	July 24, 1967	1.13
July 30, 1963	1.55	Aug. 13, 1967	1.07
Aug. 4, 1963	0.91	Oct. 3, 1967	0.91
Aug. 10, 1963	1.01	Oct. 12, 1973	1.01
Aug. 17, 1963	1.37		

vicinity of Barrow was this surge not observed.

Hunkins (1965) was probably the first to measure an open sea surge in the Chukchi Sea, when Ice Island (T-3) was aground. In the spring and summer of 1961 for 7 weeks a tide gauge was installed on the Ice Island. A negative storm surge (i.e., sea level below mean sea level) recorded on 30 May 1961 was caused by the high pressure system - fig. 7. A positive surge of about 40 cm occurred on June 18 due to the passage of a low pressure system - fig. 8. Both pressure systems traveled from Siberia across Chukchi Sea into the Arctic Ocean. Matthews (1971) installed recorders at Point Barrow for 3 years, and was able to show seasonal variation of the surges, and the presence of negative surges. These surges can produce important effects in winter, causing fracture of shore-fast ice, and underwater structures previously in water under the ice may have to bear the full weight of an ice sheet.

During various measurements organized by OCSEAP in the Beaufort Sea the sea level records were taken at random both during the open ice season and from under ice (Matthews, personal comm.). Some of these data we shall use later in the testing and validation of the numerical model. The need to improve prediction of the storm flooding over the North Slope has been recognized long ago. Fathauer (1978) compiled a summary of storm surges and gave a thumb-rule procedure to forecast floods along the Western and Northern shores of Alaska. Wise et al. (1981) identified about 90 major storm surges and developed a forecast procedure which is based on frequency of the wind occurrence. Assuming that the wind frequency (f) is inversely proportional to the frequency interval (fi) for the storm surges,

$$Fi = K/f, \tag{27}$$

a constant (K) can be determined for any given location. In the vicinity of Barrow, with 5 storm surges recorded, and assuming a frequency interval of 125 years for 12 foot surges with wind frequency of 0.013 for the related wind range (42-47 Kts), K equals 1.63. Although these relations are derived from the best available data one has to be very careful in drawing conclusions from these results. No one knows how often 12 foot surges occurred. The distribution of the wind frequency is known better through various observations, but again the wind during the storm peak is measured rarely. At the time of storm in October 1963 winds up to 20 m/s to 30 m/s were reported at Barrow. In the storm during fall of 1970 winds were 40 m/s - 50 m/s along the Beaufort Sea coast. In actual fact wind and atmospheric pressure over the Arctic Ocean until 1979 were extrapolated from the coastal and a few ice drifting stations. When modeling the October 1963 storm surge we have found that the pressure maps are often misleading. The possibility to model storm surges by applying realistic surface wind distribution was created only in 1979 through the Arctic Ocean Buoy Program carried out by Thorndike and Colony (1980). An array of buoys was placed on the ice in the Arctic Ocean to measure atmospheric pressure, air temperature and buoy position.

In one respect surges in the Beaufort and Chukchi Seas differ from those at the moderate latitudes. The whole area is ice-covered for 8 months in the year. In summer and early autumn only the southern part of the Beaufort and Chukchi Seas is ice-free and there the major storm surges are generated. One generally assumes that the ice cover diminishes the sea level variation and such behavior can be expected from the atmosphere-ice-water interaction described by eqs. (1)-(4). Sea level recorded under the ice in Tuktoyaktuk (Henry, 1975) reveals the existence of mainly negative storm surges. The range of the positive sea level variations compared against summer-fall season is quite small. Therefore one can reasonably assume that the ice cover suppresses the positive surges. This conclusion is supported by the observations, but certain waves can also be amplified under the ice. The amplitude of the M_4 component in Tuktoyaktuk is about two times larger in winter than in summer - (Barber et. al, 1983). This is caused by fast ice which may lead to the essential difference between the water depth in summer and winter. A summary of the influence of the ice cover on various tidal constituents in Tuktoyaktuk is given in Table 2 (Barber et. al, 1983). Storm surges usually occur together with the astronomical tides and it is essential to understand how much the surge is altered by the tide. Various measurements taken along the coasts of the Beaufort and Chukchi Seas show that major surges would not be essentially altered by the tides (Huggett et. al, 1975). The maximum amplitude of the tides varies from 5 cm to 20 cm. In fig. 9 the distribution of M_2 constituent (amplitude and phase) computed by Kowalik and Matthews (1982) is given. The amplitude of the tide is small relative to those in the major surges and consequently we shall neglect the tides in the numerical simulation of the major surges.

7. Numerical Modeling - Area, Grid and Boundary Conditions

Two efforts to model the storm surges in the Beaufort and Chukchi Seas ought to be mentioned. P. J. Schafer (1966) computed the surge distribution at Barrow by simulating the storm surge of October 3, 1963. It was truly a pioneering effort which allowed to elucidate the interaction of the coast and the atmospheric low.

Henry and Heaps (1976) applied numerical method to the storm surges in the Southern Beaufort Sea. The model was based on the vertically integrated equations of motion and continuity (1) and (2); but the influence of ice cover was neglected.

We shall study the storm surge generation and propagation by applying the full system of equations (1)-(4). By applying the storm surge model with equations of ice motion and continuity we hope to answer several questions. First, the influence of the pack ice on the sea level and current can be studied, secondly one can see whether the storm surge model is suitable to describe ice motion or at least the motion of the ice edge. To include ice in the storm surge model

TABLE 2

Summary of the Influence of Ice Cover on Various Tidal Constituents

Tidal Constituent	Frequency C.P.H.	Amplitude (ft.) Yearly	Amplitude (ft.) Winter 1962	Amplitude (ft.) Summer 1962	Amplitude (ft.) Winter 1963
M_2	0.0805	0.420	0.360	0.533	0.370
S_2	0.0833	0.176	0.145	0.243	0.158
K_1	0.0418	0.116	0.070	0.123	0.080
O_1	0.0387	0.089	0.071	0.078	0.086
M_4	0.1610	0.006	0.012	0.006	0.013
MS_4/MK_4	0.1639	0.003	0.008	0.005	0.010
MG	0.2415	0.002	0.005	0.002	0.006
$2MS_6$	0.2444	0.003	0.008	0.004	0.008

we assumed that variations of the pack ice distribution are due entirely to the wind and not due to the thermodynamical processes. The assumption is based on Wendler's (1973) analysis of an actual summer situation for a 5-day period in the Beaufort Sea. He was able to show that the ice conditions were strongly correlated to the wind direction.

The response of the sea level to the storm passage we shall consider in the domain depicted in fig. 10. Due to the large dimension of the area the spherical shape of the Earth cannot be neglected and we introduce a spherical system of coordinates to the system of equations (1)-(4). The grid intervals of the numerical lattice in Fig. 10 are 1/3 of a degree of latitude and 1 degree of longitude; i.e. at latitude 70°N the grid length is about 38 km. The open boundary follows the 74°N parallel from Banks Island to 180°W, then south along this meridian to the Siberian coast; the second open boundary is set in the Bering Strait. To derive unique solutions to equations (1)-(4) both initial and boundary conditions ought to be specified. On the open boundary (for the water) a radiating condition proposed by Reid and Bodine (1968) is selected. It allows for all waves propagating out of the domain to pass the boundary without restrictions. Velocity perpendicular to the boundary (say, along positive x_1 direction) is defined through the relationship between amplitude(ζ) and velocity (u_1) in the long wave - Lamb (1945);

$$\frac{\zeta}{H} = \frac{u_1}{\sqrt{gH}} \tag{28}$$

By changing u_1 to u_2 in (28) the velocity along the x_2 direction will also be defined. The radiating boundary condition has been extensively applied in the modeling of storm surges, from the time it was introduced by Reid and Bodine (1968).

Setting as the open boundary condition $\zeta = 0$ leads to different patterns of the surge in the vicinity of an open boundary, but the surge at the coast is usually quite similar to the case when sea level is defined by open radiating condition (28). Usually sea level changes substantially at the shore and over the shallow water area; therefore, if the open boundary condition is set beyond the shelf it should only insignificantly influence the surge distribution at the coast. This conclusion can be readily applied to the Southern Beaufort Sea, where the shelf is narrow and the largest depth is about 4 km. In the Chukchi Sea the depth is almost everywhere less than 200 m and even at large distances from the shore a strong sea level variation can be generated.

Open boundary conditions for the ice velocity and compactness are not easily specified. One set of conditions can be defined by assuming continuity of the ice velocity and compactness across the boundary and setting first and second derivatives equal to zero. This condition, though numerically feasible, assumes that the motion in the domain is defined completely by internal processes and is not influenced by the motion from outside of the domain. Such an approach is obvious for the storm surges, when the open boundary condition is set beyond the shelf, but whether it is right for the ice motion remains to be proven. Another set of boundary conditions can be taken from the measurements through the buoys deployed in the Arctic Ocean if the buoys are in the proximity of the boundary during simulated storm surge.

To start numerical computation with radiating boundary conditions or with any condition which is not related to the uniqueness theorem of the problem, one has to check if the model works "reasonably" well, i.e. whether the specific boundary conditions do not create sources or sinks. Therefore,in the first experiment a steady and uniform wind was applied over the Chukchi and Beaufort Seas. After about 3 days steady state was reached. When the integral of the sea level over the surface of the Chukchi and Beaufort Seas was estimated, it was close to zero, thus indicating the lack of sources and sinks.

8. Storm Surge of October 1983

8.1 Short analysis of the storm

Meteorological observations at the time of the storm were very scant. Surface pressure maps for the six hour intervals from the Canadian Meteorological Centre allowed reconstruction of the storm track - fig. 11. One has to understand that the numbers given on the maps are extrapolated from the few coastal stations. Our work was greatly facilitated by weather analysis of the storm performed by Schafer (1966).

The low pressure center travelled from Siberia (00Z, October 3) to the northern shores of Banks Island (06Z, October 4), where it stayed for about 24 hours. The low on its way was a source of unusually strong winds. Record high surges of about 3 m were reported along the Alaskan coast of the Chukchi Sea (Schafer, 1966) and a very high surge of about 2 m was recorded in Tuktoyaktuk at the eastern coast of the Mackenzie Bay. In both cases the high surges were due to NW winds, and it is obvious that the direction of the shoreline in both areas is quite similar. An additional factor which might have influenced the sea level in the Chukchi Sea was the high velocity of the pressure center. The center travelled a distance of about 2100 km in 30 hours, with an average velocity of about 19.5 m/s. The velocity of the long free waves defined as $c = \sqrt{gH}$ is quite large in the Beaufort Sea due to the large depth, but in the Chukchi, the average depth is about 50 m, therefore the velocity of the long wave is 22 m/s. Because the velocity of the atmospheric pressure center in the Chukchi Sea was close to the velocity of the free waves, the large sea level variations can be related to the resonance effects (Lamb, 1945).

8.2 The results of numerical simulation

Every 6 hours starting October 3, 00Z till October 6, 00Z the wind distribution has been computed from the surface pressure maps. Between 6 hour readings the wind velocity was interpolated linearly in time. A typical surface pressure map which served for the calculation of the wind velocity is given in fig. 12; it depicts the situation on October 3, 18Z. To compute geostrophic winds, the region was subdivided into lattices of 2 degree latitude and 10 degree longitude and atmospheric pressure was taken from the grid points. Based on the data gathered during the AIDJEX experiment (Albright 1980) we have applied the cross-isobar turning angle ($\alpha = 24°$) and the ratio of the surface wind (W) to the geostropic wind (G); W/G = 0.6, in computing surface wind distribution.

The results of storm surge simulations will be given as the distributions of sea level, current, ice velocity, ice compactness and wind velocity over the area of the Chukchi and Beaufort Seas. Usually two types of computation were attempted. First, the sea surface was assumed to be ice-free and only equations describing water motion were applied. In the second case, the actual ice distribution has been taken as the initial condition and the storm surge was computed by applying the complete set of equations of ice and water motion. By comparing two simulations one can conclude that even an ice cover of about 4/10 is practically equivalent to open water when storm surge generation or propagation is studied. The four sets of figures at hour 6, 1 day, 2 days and 3 days from the onset of computations, will be given to describe the propagation of the surge from the Siberian coast to Banks Island.

The situation on October 3, 06Z is described in fig. 13 - fig. 19. The atmospheric pressure center was situated at that time to the East of Wrangell Island. Winds computed from the pressure distribution over rectangular 2° by 10° grids are constant (fig. 13). The velocity scale is defined by the horizontal distance between grid points and equals 5 m/s. We did not attempt to smooth the spatial distribution of the wind, but linear interpolation in time was necessary to preserve stability of the computations. Due to NW and W winds the sea level (fig. 14, fig. 15) rose about 50 cm along the Alaskan coast of the Chukchi Sea and a smaller surge occurred in the Mackenzie Bay.

Velocity (fig. 16, fig. 17) defined as an average velocity from the surface to the bottom is stronger in the Chukchi Sea, obviously due to the small depth of this area. Ice compactness (fig. 18) 6 hours after onset of computation is actually very close to the initial distribution. In the ice-free regions we assumed a 2% ice cover for the continuous application of the equations of motion and continuity. Therefore the ice velocity is plotted everywhere in the area of computation including "ice-free" areas - fig. 19. The ice motion can be taken as an indicator of the motion at the sea surface.

The second set of figures describes the storm surge distribution on October 4, 1963, 00Z; fig. 20-fig. 26. A report of observations made at the Arctic Research Laboratory at Barrow (Schafer, 1966) pointed out that between 1300 and 1600 AST the storm reached its peak with winds of 45 mph and gustiness up to 65 mph. Water level was about 3 m above normal sea level.

The wind computed from the surface pressure at Barrow shows NW winds up to 40 m/s - fig. 20. The maximum of the set-up along Alaskan Beaufort Sea is about 2.5 m - fig. 21, fig. 22. It is obvious that sea level rises toward the South from Barrow. This tendency was confirmed by observation at Wainwright, where the sea level at the peak of the storm was as high as 3.5 m (Schafer, 1966). On the other hand the sea level along the Beaufort Sea does not show any conspicuous variations. We shall later on describe sea level as a function of time at Barrow and at two locations, one in the Chukchi Sea and another in the Beaufort Sea at the distance of one grid (36 km) from Barrow. This will demonstrate the special nature of the geographical location of Barrow between two water basins of different dynamics related to the shore line geometry and depth distribution. The sea level in the Chukchi Sea (fig. 21, fig. 22) displays the large sea level variation at the open sea, while in the Beaufort Sea large variations are confined to the near-shore area. Strong currents (fig. 23, fig. 24) form a coastal jet with speeds up to 1 m/s. Both water and ice movement (fig. 26) changed the ice compactness along the southern coast of the Beaufort Sea to a value smaller than 0.25 - fig. 25.

On October 5, 00Z, the low pressure center was situated to the North from Banks Island and only in the Mackenzie Bay area did the NW wind (fig. 27) set sea level about 2 m above the mean sea level - fig. 28 and fig. 29. Sea level in these figures displays a characteristical pattern which will often occur in major surges. Both in the Beaufort and Chukchi Seas the sea level contours, away from the shore, tend to develop the dome-like structures. According to the geostrophic flow pattern the velocity vectors tend to be parallel to the sea level contour lines. Two domes in the sea level structure divide the flow into two large gyres - fig. 30 and fig. 31. The division line runs from Point Barrow to the North. Ice velocity in fig. 33 also displays a similar pattern of circulation. Obviously, because of the negligible wind speed in the Chukchi Sea, the ice motion is induced there only by the water motion. Due to the easterly flow along the southern coast of the Beaufort Sea the boundary between the ice and ice-free area has moved further toward the east and the ice compactness continued to diminish along the shore - fig. 32.

The final set of figures describes the storm surge 3 days after the start of computation. The center of the low pressure is not moving any longer. It stayed for about 24 hours to the north of Banks Island, producing quite low winds in the Southern Beaufort Sea so that the sea level subsided to the mean sea level - fig. 34, fig. 40.

To observe the propagation of the storm surge along the coast of the Beaufort Sea the temporal variations of the sea level at a few geographical locations are given in fig. 41 - fig. 46. Both cases, i.e. with an ice cover and without one,are plotted, therefore the influence of the ice on the surge can be defined. Actually only at the peak of the surge is the difference noticeable. The largest difference at Barrow West (fig. 41) amounts to about 20-25 cm. The level at Barrow and at two other points, one in the Chukchi Sea (Barrow West) and another in the Beaufort Sea (Barrow East) each situated at distance of about 40 km from Barrow, is plotted in fig. 41, 42, 43. At the time when at Barrow West the sea level rose up to 3 m, at Barrow East the level was close to the mean sea level. The sea level difference between these two points is obviously due to the special location of Barrow which is situated between two sea basins. In some other locations along the Beaufort Sea coast the computed maximum sea level was: 80 cm at Simpson Cove (fig. 44) and 50 cm at Demarcation Bay (fig. 45). The largest surge of about 2 m occurred on October 5, 00Z (fig. 46) at Tuktoyaktuk; this figure compares well with actual observations.

An example of the temporal variations of the wind velocity during 3 days of computations at the point $\lambda = 135° \ 30'W$, $\phi = 70° \ 30'N$ is given in fig. 47. As we mentioned before,velocity is linearly interpolated between 6-hr intervals.

9. Negative surges - open water season 1979

During the open water season of 1979 from May to November a tide gauge was deployed by OCSEAP in Harrison Bay. Due to ice conditions, the three tide gauges in Canada were not in operation during major storm. The storm surges occurred only in September and October and all major surges were negative. We shall reproduce two surges; a smaller one between September 12 and September 19 when sea level dropped about 30 cm and a negative surge of about 50 cm from September 26 to October 7. The latter storm we shall describe in detail. The storm started on September 26 and was due to an atmospheric high pressure system with the center situated between Point Barrow and the North Pole. The surface pressure distribution over the Arctic Ocean during the storm surge is represented by the weather chart from Oct. 4, 1979, 12Z (fig. 48) - Thorndike and Colony (1980). This is a typical weather situation which generates patterns of ice and surface water motion often observed through the ice drift and is responsible for the so-called Beaufort Gyre. The pressure systems during the storm of 1979 for about 10 days occupied nearly the same position. Basing on geostrophical wind computation E and NE winds from 7 m/s to 15 m/s, were found. Atmospheric pressure data used in calculation were stored at 3-hr intervals on magnetic tape by Thorndike and Colony (1980). Temporal variation of the wind speed (fig. 49) in Harrison Bay has a time dependence which is similar to the sea level variations (fig. 50). Measured sea level (continuous line) compares well with computed values (broken line), although due to the M_2 constituent the recorded level is more variable. In fig. 50 the results of computations for both surges are plotted but we will only examine sea level, current and ice motion associated with major surge. As before, two sets of experiments were run, i.e., with and without an ice cover. To describe the wind influence on the ice distribution we abandon the ice compactness charts and only plot the position of the ice edge at the start and end of the storm as observed by satellite. The ice edge position on October 7 computed by the model is also plotted in the same figure (fig. 51). Both computed and observed positions of the ice edge along the Siberian coast show its movement towards the East. Initially ice cover along the Beaufort coast was negligible but the E and NE wind piled pack ice against the shore. It is obvious from the buoys drift (fig. 48) that the ice velocity beyond our domain had a strong southerly component along the Canadian islands toward the Beaufort Sea. To introduce this component into the numerical model the ice velocity from the buoys was applied at the open boundary. The storm surge computation spanned 12 days from 00Z, September 25 till 00Z October 7. Four sets of figures are given to represent the development of the storm surge after 12 hours, 4 days, 8 days and 12 days (fig. 52 - fig. 67).

As we have seen previously, the results for the ice-free and ice-covered sea are very close, therefore we shall describe only the ice-covered situation. Both the Chukchi and Beaufort Seas were practically ice free (fig. 51); a situation conducive to storm surge generation. For the period 26 September to 7 October the wind direction was practically constant, thus the flow and sea level pattern after a few days was quasi-steady. Throughout the whole period both current and sea level show consistent distribution related to the wind. Strong currents and sea level variations again occurred in the shallow coastal area. After about 3-4 days, along the shelf from Mackenzie Bay to Point Barrow a current, somewhat reminiscent of a "coastal jet" (Csanady, 1974) develops. In the vicinity of Barrow, due to the shape of the shore-line and probably due to the depth difference between the Beaufort and Chukchi Seas, the coastal current partly branches off into open water and partly follows the coastal contour into the Chukchi Sea. This division line again splits the motion into two gyres which are closely associated with the dome structure of the sea level. Because the direction of the current in the gyres is correlated to the sea level distribution it is obvious that only in the initial period of the wind action the current at the sea surface can be associated with the wind; after the initial period the sea level variations can change conspicuously the dynamics of the flow.

10. Storm surge, August 30 - September 1, 1981

At the end of August 1981 a low pressure center moved southward along the Canadian Islands from the high latitude region. For 2-3 days the low maintained strong NW winds over the western Beaufort Sea (fig. 68). According to the Beaufort Weather and Ice Office (1981) it was the second longest storm of the season with wind speeds up to 40 knots. While the Western and Central Beaufort Sea were under the influence of the strong low, the winds over the Chukchi and Eastern Beaufort Sea were due to a shallow high with its center over Siberia.

In August and September, 1981, some 11 gauges were installed along the Beaufort coast both in the United States and Canada. A positive surge of about 60 cm was recorded in the Canadian Beaufort Sea, further westward the surge was mixed, it was negative at the beginning and changed to positive when winds changed their direction to NW. The storm occurred between August 30 and September 1, 1981, only, but to study the whole process we extended the computation for 10 days, from August 27, 00Z to September 6, 00Z. Again, to compute the temporal and spatial distribution of the wind, the data compiled by Thorndike et al. (1982) were used; unfortunately the atmospheric pressure was stored for 12-hour intervals only. For comparison with computed sea levels the eight tide gauges along the Beaufort coast were used (fig. 69). The measured levels compare well with computed sea level, with the ice included into the model or with an ice-free surface (fig. 70 - fig. 77). During the peak of the surge, in four cases the observed level exceeds the computed level, in four other cases the reverse situation occurred. Surge maximum was observed on 30, 31 August and October 1; i.e. on day 4, 5, 6 from the start of computation. Needless to say, the sea level is "repeating" the temporal variation of the wind speed (fig. 78). At the peak of the storm between August 30 and October 1 both sea level and wind show two maxima and the minimum occurred on August 31. We were unable to resolve very accurately this feature due to the long time intervals (12-hour) between consecutive wind computation. The low temporal resolution of the wind is also possibly associated with the time difference (up to 12 hours) between calculated and recorded sea level. We shall not discuss the ice motion and ice compactness during this storm because ice conditions did not change distinctly from the initial distribution (fig. 79).

At the peak of the storm the patterns of the wind, sea level and velocity are plotted in fig. 80, fig. 81, fig. 82. It is interesting to observe again the dome structure in the sea level chart. With negative values at the center of the dome in the Beaufort Sea and positive values in the Chukchi Sea, the associated gyres display counter-clockwise motion in the Beaufort Sea and clockwise motion in the Chukchi Sea. As we found from the previous computation usually two gyres are generated, but the rotation in the gyres will depend on the type of pressure center (low or high), geographical position of the center and its direction of travel.

REFERENCES

Albright, M., 1980. Geostrophic wind calculations for AIDJEX. Sea Ice Processes and Models, Ed. by R. S. Pritchard, Univ. of Washington Press, Seattle and London, 474 pp.

Barber, F. G., Taylor, J. D., Bolduc, P. A., Murty, T. S., 1983. Influence of the ice cover on resonance phenomena in Tuktoyaktuk Harbour, Proc. of 34th Alaska Science Conference, Whitehorse, CANADA.

Beaufort Weather and Ice Office 1981 Report. Atmospheric Environment Service, Western Region, Arctic Weather Center, 172 p.

Campbell, W. J., 1965. The wind-driven circulation of ice and water in a Polar Ocean. Journ. Geoph. Research. 70, 14, pp. 3279-3301.

Csanady, T. T., 1974. Barotropic currents over the continental shelf. Journ. Phys. Ocean. 4, 3, p. 357-371.

Coon, M. D., Maykut, G. A., Pritchard, R. S., Rothrock, D. A., and Thorndike, A. S., 1974. Modeling the pack ice as an elastic-plastic material. AIDJEX Bulletin, 24 pp. 1-105.

Doronin, Yu. D., 1970. On the method of calculate compactness and drift ice. Trudy Arctic-Antarctic Inst., Leningrad, 291, 5-17.

Fathauer, T. F., 1978. A forecast procedure for coastal floods in Alaska, NOAA technical memorandum NWS AR-23, 27 p.

Garrat, J. R., 1977. Review of drag coefficients over oceans and continents. Month. Weath. Rev. 7, 105, pp. 915-929.

Glen, J. W., 1970. Thoughts on a viscous model for sea ice. AIDJEX Bulletin, 2, pp. 18-27.

Hansen, W., 1962. Hydrodynamical methods applied to the oceanographical problems. Proc. Symp. Math.-Hydrodyn. Meth. Phys. Oceanography. Mitt. Inst. Meeresk., Univ. Hamburg, 1, pp. 25-34.

Henry, R. F., 1974. Storm surges in the Southern Beaufort Sea. Interim Report, Dec. 1974, Beaufort Sea Project, Institute of Ocean Sciences, Patricia Bay, Sidney, B. C., Canada, 14 p.

Henry, R. F., 1975. Storm surges. Beaufort Sea Technical Report #19. Institute of Ocean Sciences, Sidney, B. C., Canada, 41 p.

Henry, R. F., and N. S. Heaps, 1976. Storm surge in the southern Beaufort Sea. Journ. Fisher Res. Board of Canada 33(10), 2362-2376.

Hibler III, W. D., 1979. A dynamic-thermodynamic sea ice model. J. Phys. Oceanogr., 9, pp. 815-846.

Huggett, W. S., Woodward, M. J., Stephenson, F., Hermiston, F. V., Douglas, A., 1975. Near bottom currents and offshore tides. Beaufort Sea Proj. Tech. Rept. #16, Inst. of Ocean Sciences, Sidney, B. C., Canada, 38 p.

Hume, J. D., 1964. Shoreline changes near Barrow, Alaska, caused by the storm of October 3, 1963. Report of the 15th Alaskan Science Conference, Fairbanks.

Hunkins, K. L., 1965. Tide and storm surge observations in the Chukchi Sea. Limn. Oceanogr. 10, pp. 29-39.

Johannessen, O. M., 1970. Note on some vertical current profiles below ice floes in the Gulf of St. Lawrence and near the North Pole, J. Geoph. Res. 75, 2857-2862.

Kagan, B. A., 1970. On the features of some finite-difference schemes used at numerical integration of tidal dynamics equations, Izv. Atmospheric and Oceanic Physics, 6, 7, pp. 704-717.

Kheisin, D. E., 1971. On the excitation of ice compression forces at the hydrodynamic stage of drift of close ice pack. Trudy AANII v. 303, pp. 89-97.

Kheisin, D. E., and Ivchenko, V. O., 1973. A numerical model of tidal ice drift with allowance for the interaction between floes. Izv. Atmospheric and Oceanic Physics, 9, 4, pp. 420-429.

Komar, P. D., 1976. Boundary layer flow under steady unidirectional currents. In Marine Sediment Transport and Environmental Management. John Wiley and Sons Publ. Ed. D. J. Stanley and D. J. P. Swift., pp. 91-106.

Kowalik, Z., 1981. A study of M_2 in the ice-covered Arctic Ocean. Modeling, Identification and Control v.2.N.4, 201-223.

Kowalik, Z., Matthews, J. B., 1982. The M_2 tide in the Beaufort and Chukchi Seas. Jour. Phys. Ocean. 12, 7, pp. 743-746.

Lamb, H., 1945. Hydrodynamics. New York. Dover Publ. 738 p.

Langleben, M. P., 1982. Water drag coefficient of the first-year sea-ice. Jour. Geophysical Research. v. 87, NC1, 573-578.

Leavitt, E., 1980. Surface-based air stress measurements made during AIDJEX. In Proceedings of the AIDJEX Symposium, Univ. of Washington Press, pp. 419-429.

Ling, C. H., Rasmussen, L. A., and Campbell, W. J., 1980. A continuum sea ice model for a global climate model. In Proceedings of the AIDJEX Symposium, University of Washington Press, pp. 187-196.

Marchuk, G., Gordev, R., Kagan, B., et al., 1972. Numerical method to solve tidal dynamics equation and results of its testing. Novosybirsk: Comput. Centre., pp. 78.

Matthews, J. B., 1971. Long period gravity waves and storm surges on the Arctic Ocean continental shelf. Proc. Joint Oceanogr. Assembly, Tokyo, p. 332.

McPhee, M. G., 1980. An analysis of pack ice drift in summer. In Proceedings of the AIDJEX Symposium. University of Washington Press, pp. 62-75.

Ovsienko, S. N., 1976. On the numerical modelling of the ice drift. Izv. Atmospheric and Oceanic Physics. T.12,N.11, pp. 1201-1206.

Ovsienko, S. N., 1978. Numerical model of the ice drift due to the wind in Caspian Sea. Trudy Gidrometeorologiceskogo Naucno-Issledov. Centra SSSR, Leningrad, 194, p. 53-58.

Pritchard, R. S. (editor), 1980. Sea Ice Processes and Models. Proceedings of the AIDJEX Symposium. University of Washington Press, pp. 474.

Ramming, H. G., and Kowalik, Z., 1980. Numerical modelling of marine hydrodynamics. ELSEVIER. Amsterdam - New York, pp. 148-154.

Reid, R. O., and B. R. Bodine, 1968. Numerical model for storm surges in Galveston Bay. J. Waterway and Harbour Div., 94 (WWI), p. 33-57.

Reimnitz, F., and D. K. Maurer, 1979. Effect of storm surge on the Beaufort Sea coast, northern Alaska. Arctic 32, pp. 229-344.

Rothrock, D. A., 1970. The kinematics and mechanical behaviour of pack ice: the state of subject. AIDJEX Bulletin, 2, pp. 1-10.

Rothrock, D. A., 1975. The mechanical behaviour of pack ice. Annual Review of Earth and Planetary Sciences, 3, pp. 317-342.

Schafer, D. J., 1966. Computation of a storm surge at Barrow, Alaska. Archiv für Meteorologie, Geophysik and Bioklimatologie, Ser. A, 15, N. 3-4, pp. 372-393.

Shirokov, K. P., 1977. Influence of compactness on the wind-driven ice drift. Sbornik Rabot Leningradskoi CMO 9, pp. 46-53.

Thorndike, A. S., Colony, R., 1980. Arctic Ocean Buoy Program. Data Report. Polar Science Center, University of Washington, Seattle, 131 p.

Thorndike, A. S., Colony, R., Munõz, E. A., 1982. Arctic Ocean Buoy Program Data Report. Polar Science Center, University of Washington, Seattle, 137 p.

Wendler, G., 1973. Sea ice observation by means of satellite. Journ. Geoph. Res., 78, 9, pp. 1427-1448.

Wise, J. L., Comiskey, A. L., Becker, R. 1981. Storm surge climatology and forecasting in Alaska. Arctic Environment Information and Data Center, Anchorage. 26 p.

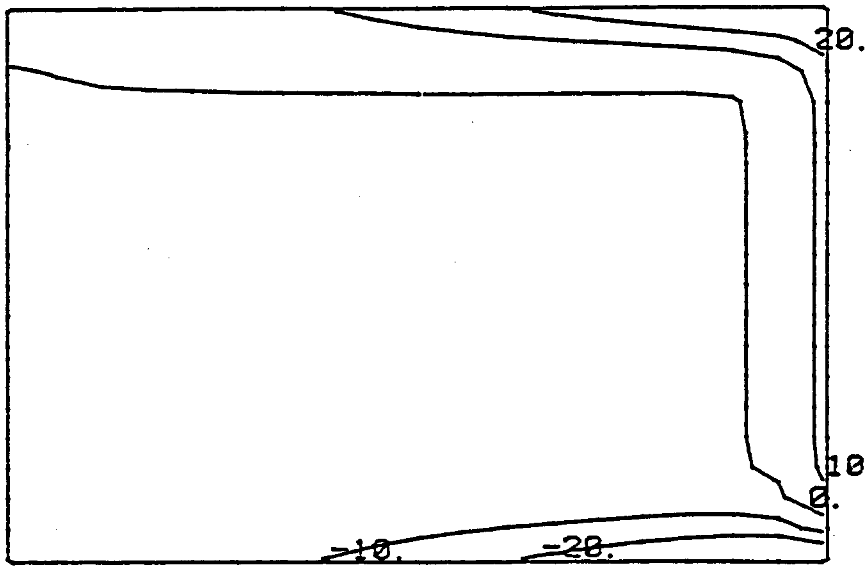

SEA LEVEL HOUR 2

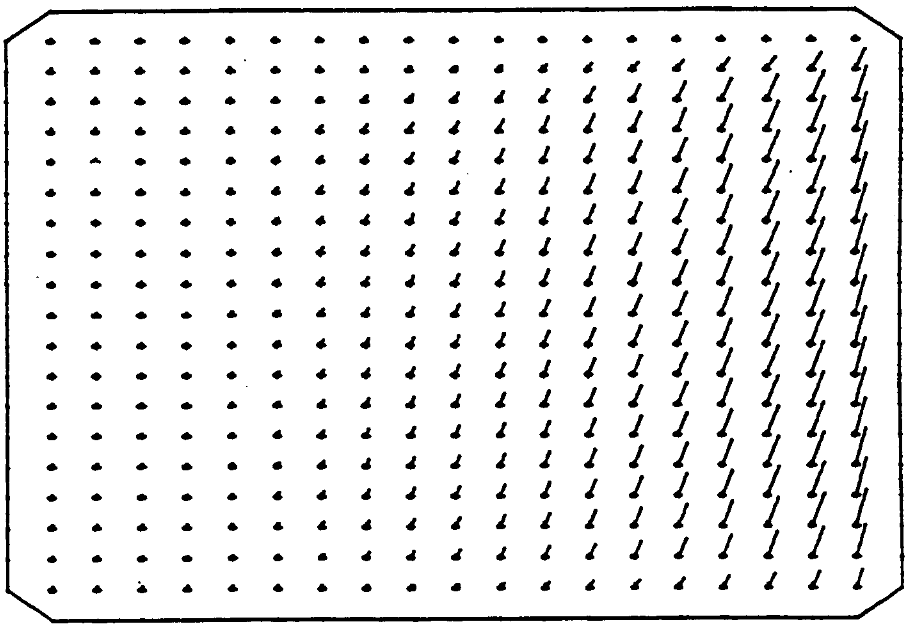

VELOCITY HOUR 2

Figure 1.--Wind blows along the vertical coordinate only. Wind speed is constant in time but varies along the horizontal direction from 4 m/s (at $x_1 = 0$) to 20 m\s (at $x_1 = 1{,}000$ km). Sea level variation is expressed in centimeters. For velocity, the grid distance along the horizontal direction is scaled to 25 cm/s. In this experiment, velocity vectors are not identified by arrows; therefore, direction of the flow is away from the grid point. Ice compactness is measured in relative units from 0 to 1.

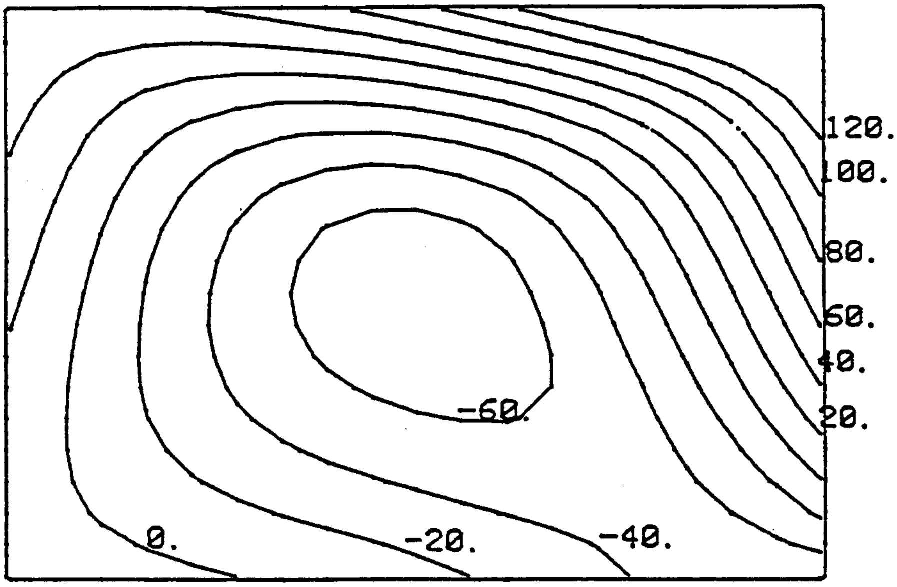

SEA LEVEL HOUR 90

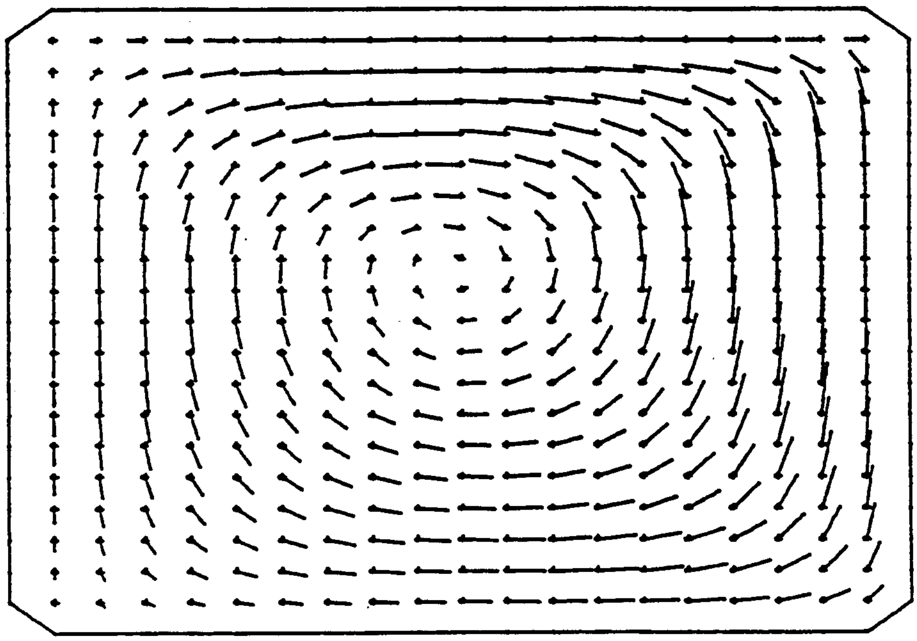

VELOCITY HOUR 90

Figure 2.--(See caption for Fig. 1.)

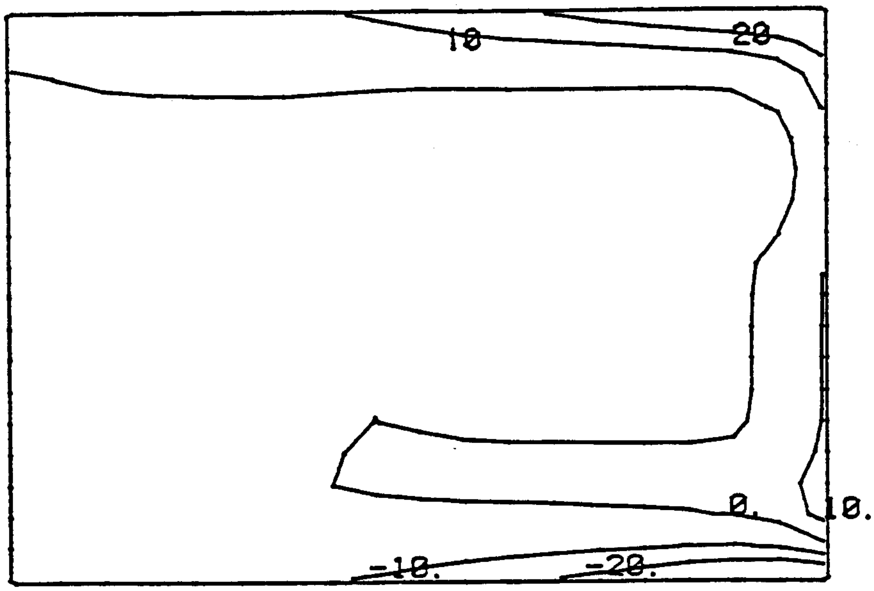

SEA LEVEL HOUR 2

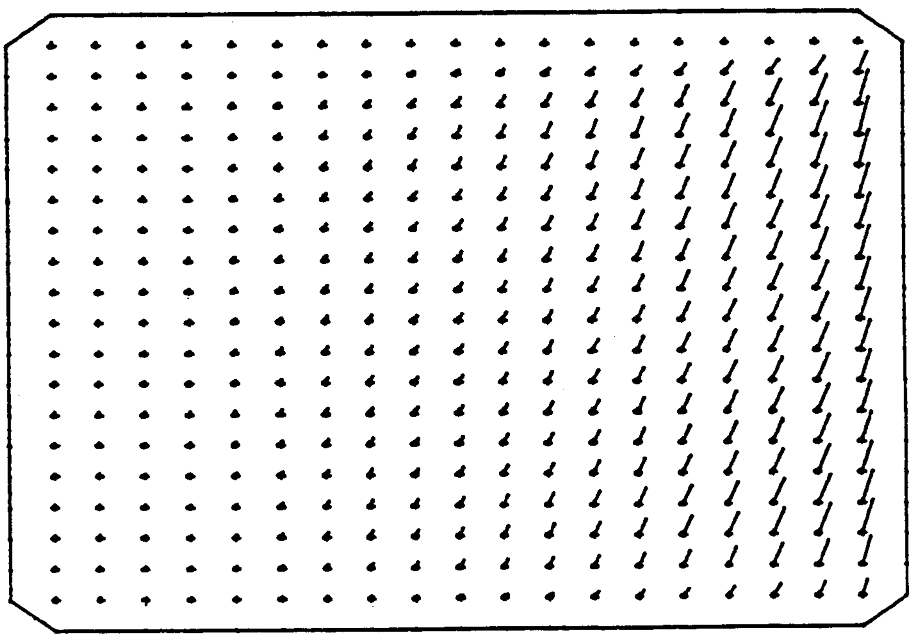

VELOCITY HOUR 2

Figure 3.--(See caption for Fig. 1.)

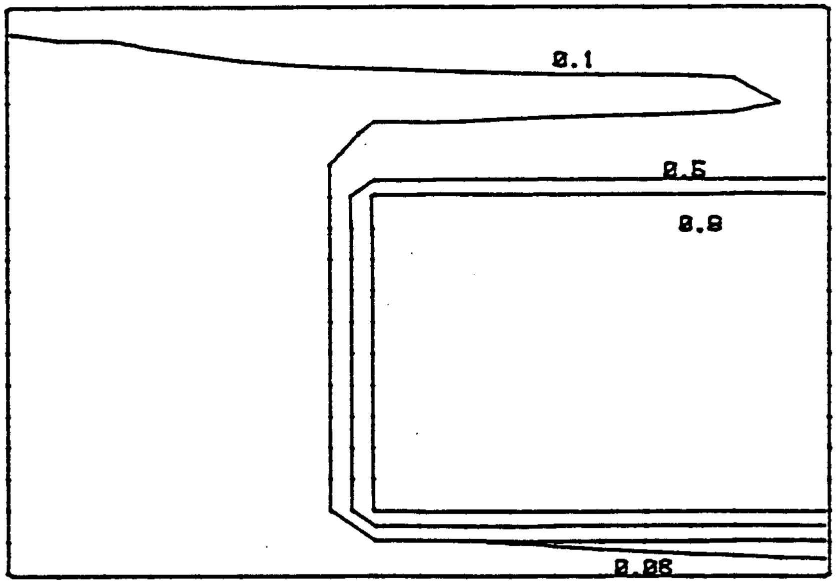

ICE COMPACTNESS HOUR 2

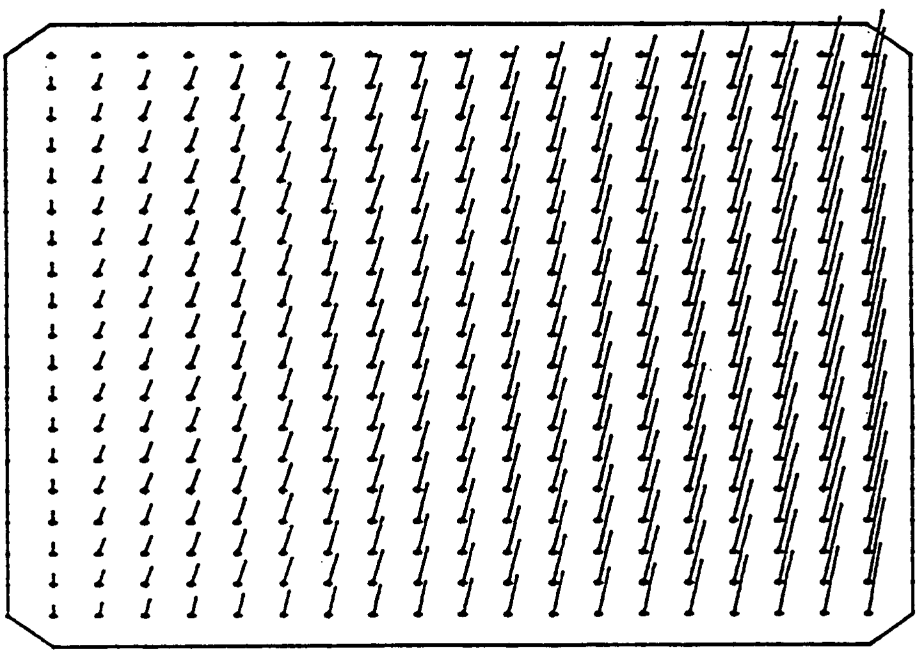

ICE VELOCITY HOUR 2

Figure 4.--(See caption for Fig. 1.)

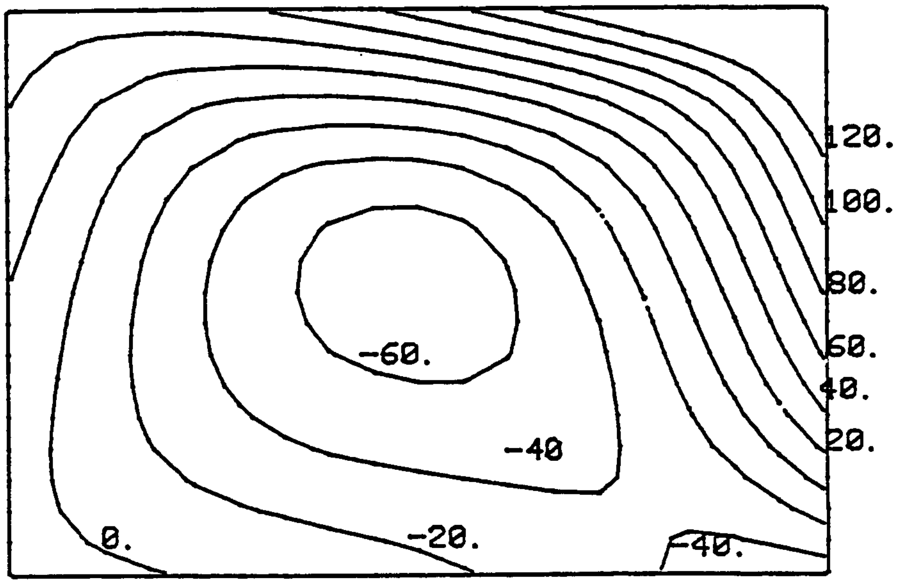

SEA LEVEL HOUR 90

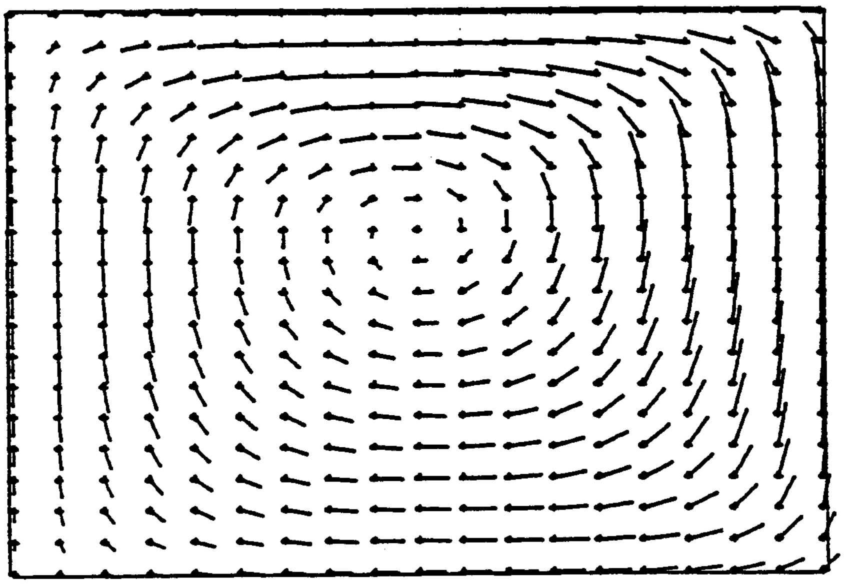

VELOCITY HOUR 90

Figure 5.--(See caption for Fig. 1.)

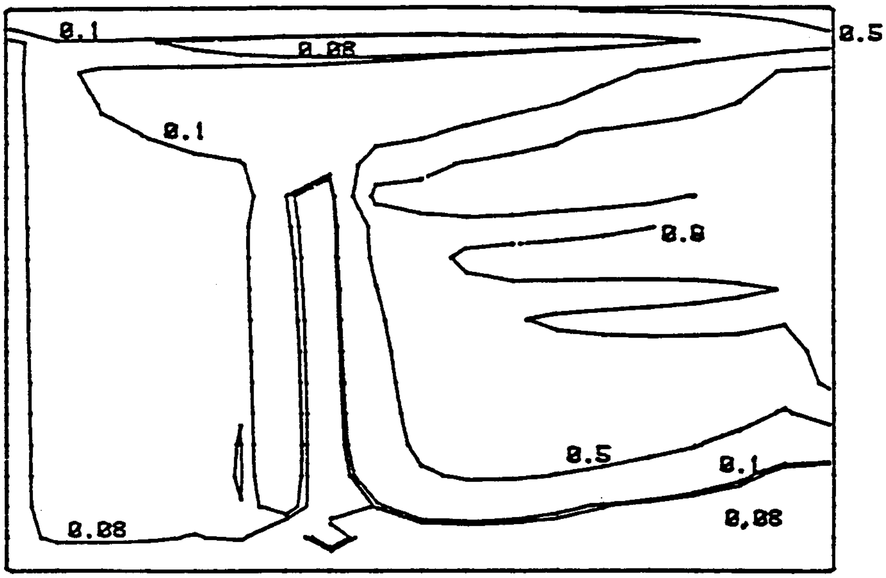

ICE COMPACTNESS HOUR 90

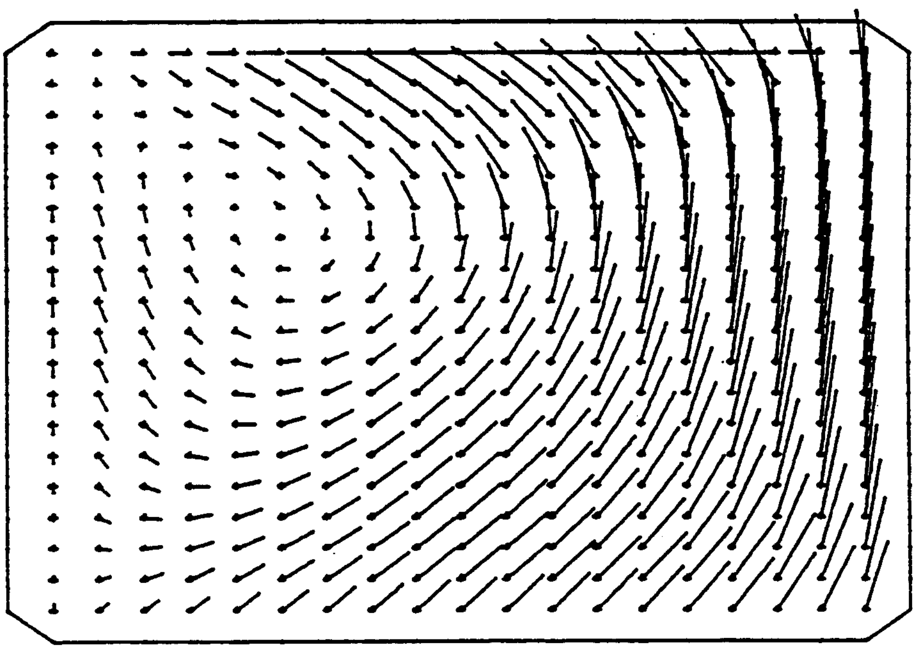

ICE VELOCITY HOUR 90

Figure 6.--(See caption for Fig. 1.)

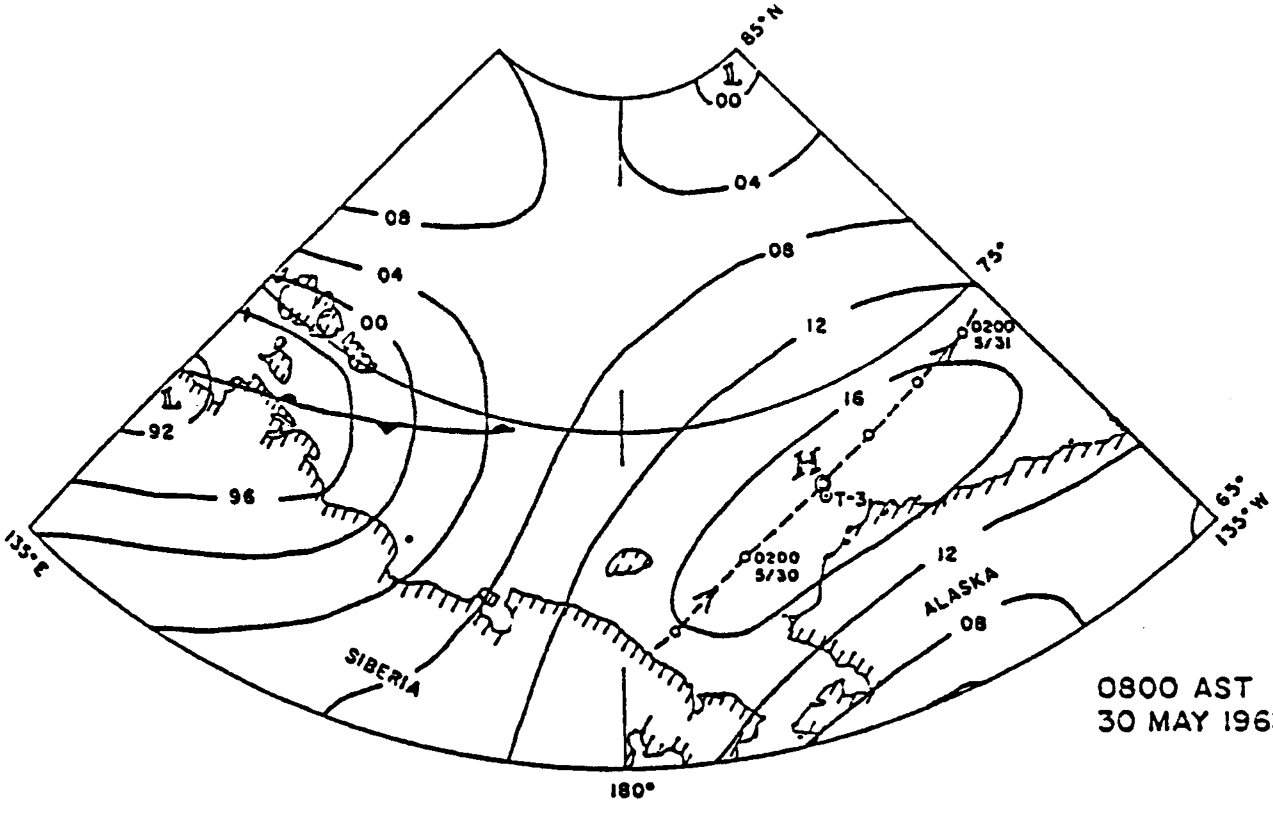

Figure 7.--Surface weather chart for 0800 AST, 30 May 1961, at approximately the time of the closest passage to T-3 of the high. Pressure in millibars. Dashed line represents the track of the high. Open circles represent positions of the high-pressure center at 6-h intervals. From Hunkins (1965).

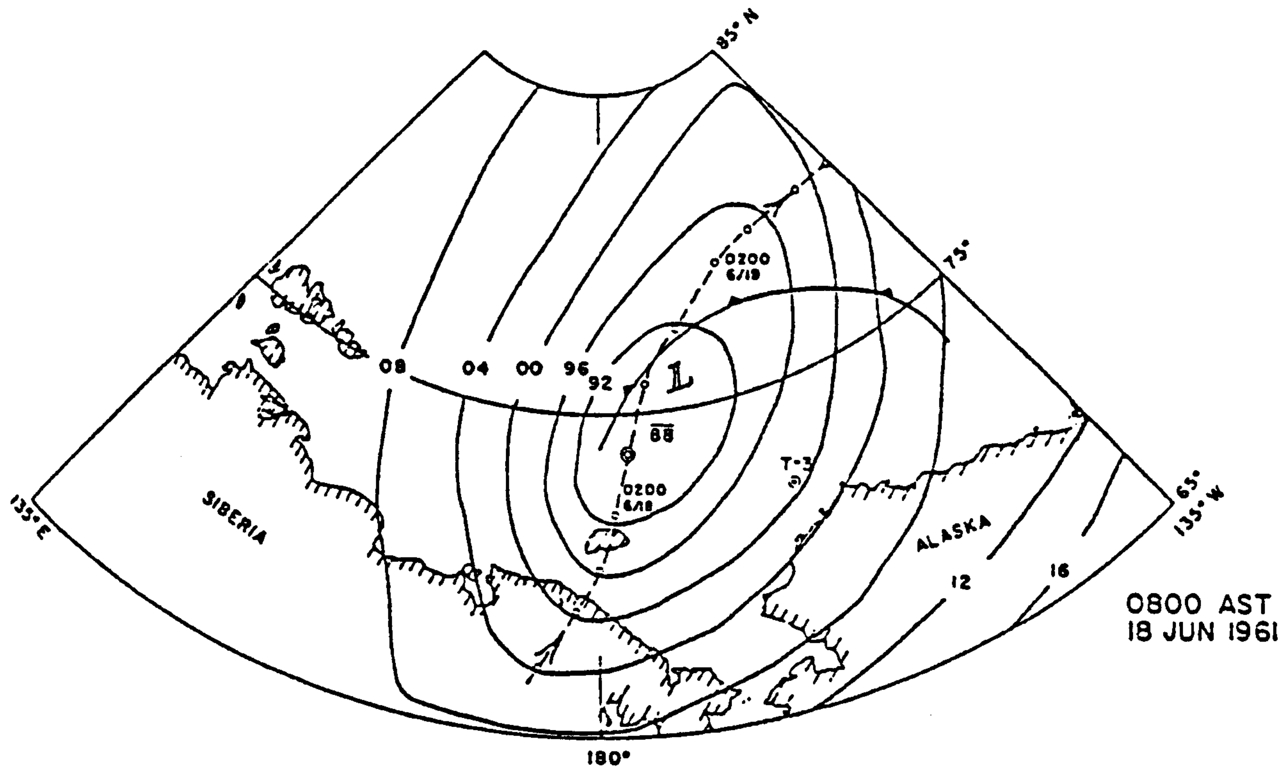

Figure 8.--Surface weather chart for 0800 AST, 18 June 1961. Pressure in millibars. Dashed line represents storm track. Open circles represent positions of the low-pressure system at 6-h intervals. From Hunkins (1965).

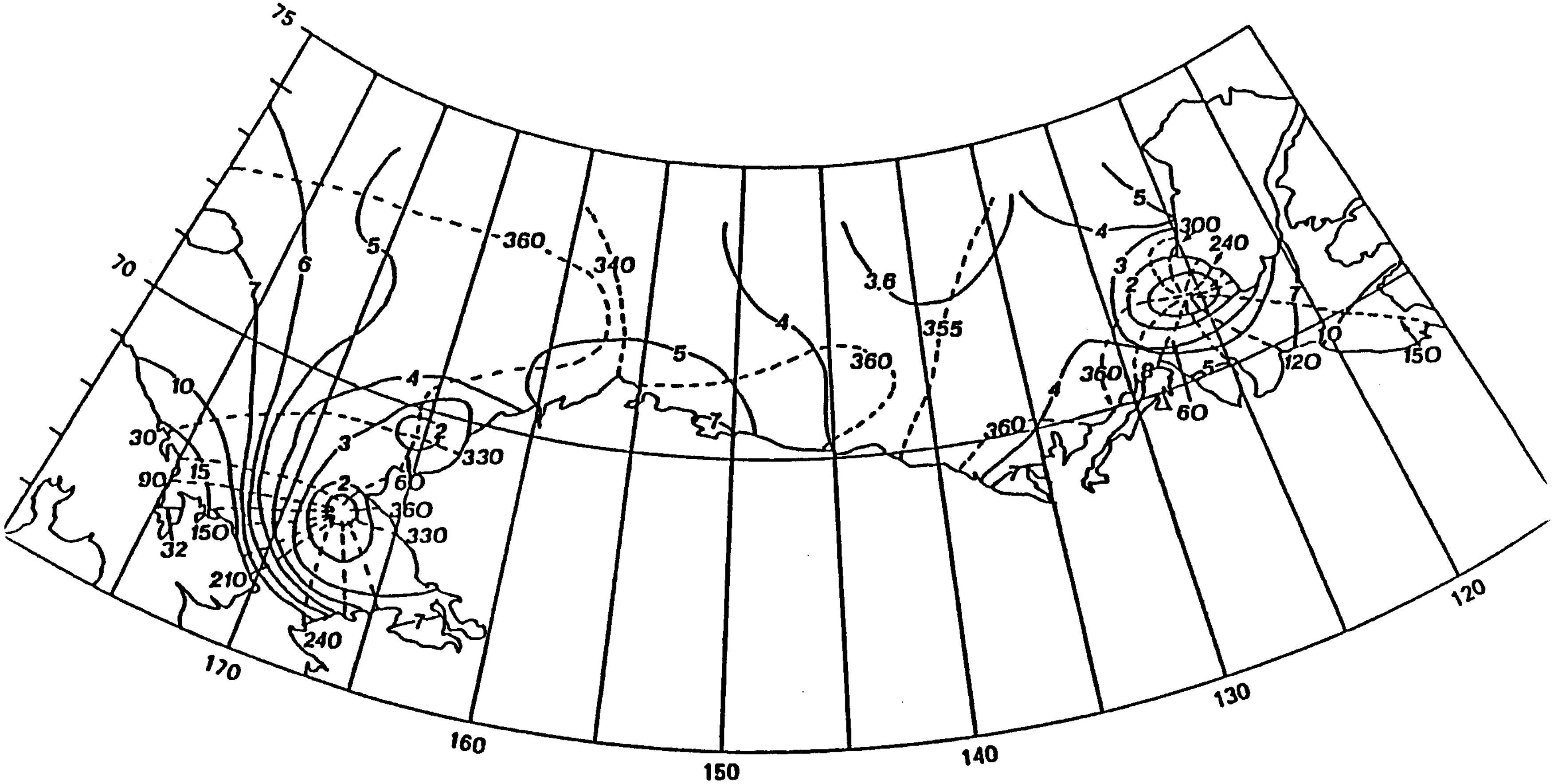

Figure 9.--Co-tidal (broken) and co-range (continuous) lines of the M_2 tide. Phase angles in degrees are referred to Greenwich (solar time); amplitudes are given in centimeters. From Kowalik and Matthews (1982).

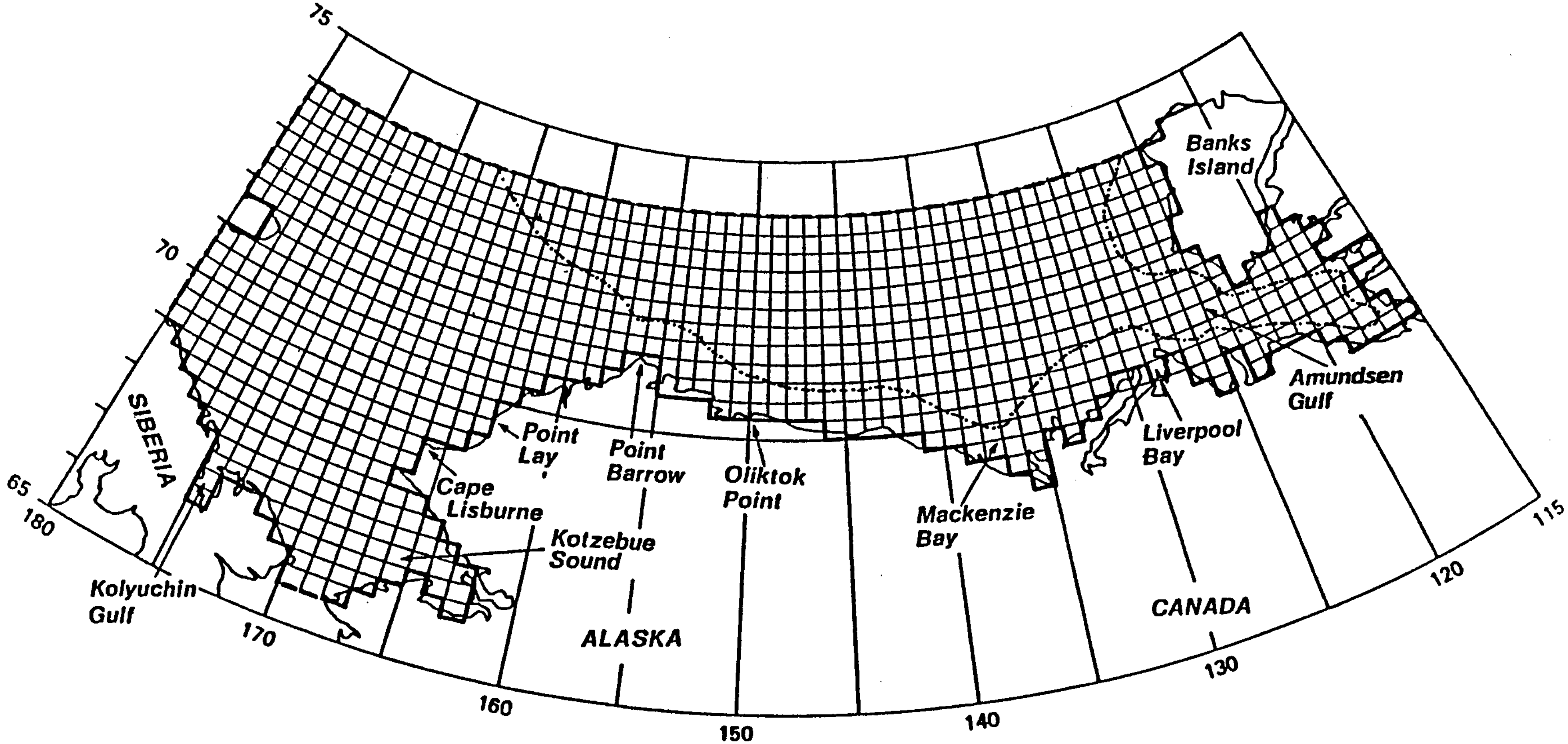

Figure 10.--Grid net for the numerical computation of the M_2 tide in the Beaufort and Chukchi seas. Dashed line represents open boundary, solid line is land boundary, dotted line is 200-m depth contour.

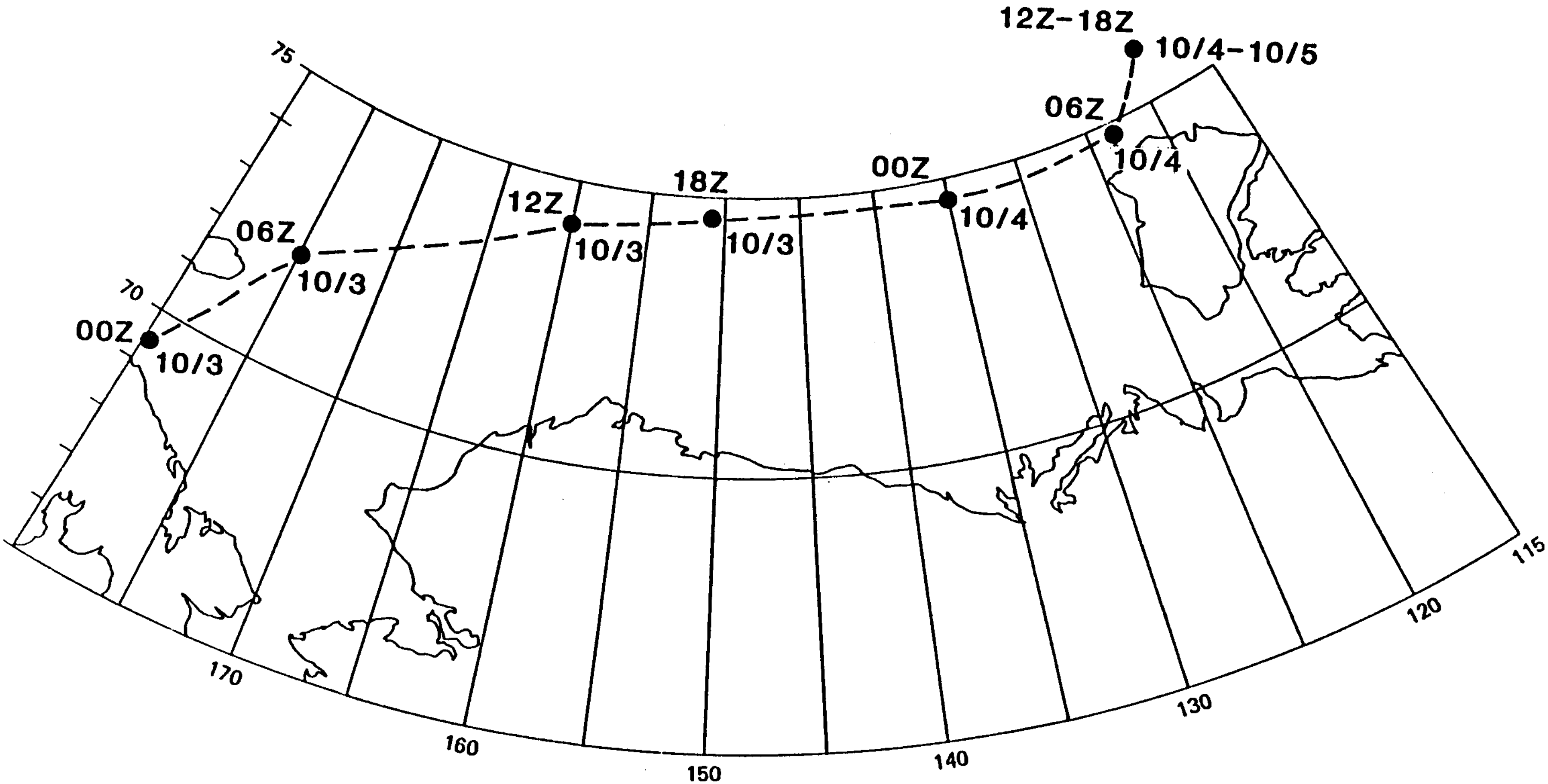

Figure 11.--Positions of the low pressure system from October 3, 00Z, to October 5, 18Z.

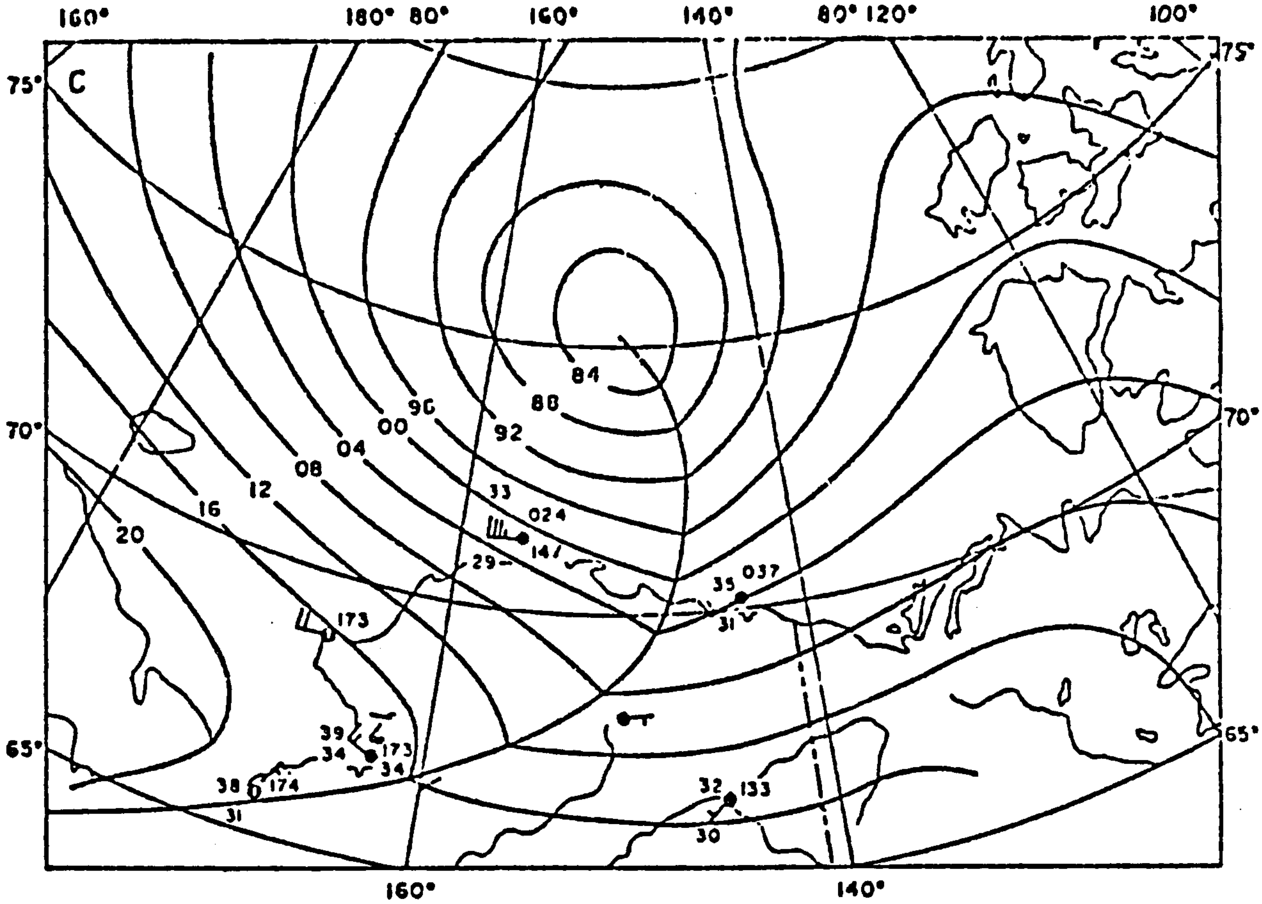

Figure 12.--Synoptic weather chart, 3 October 1963, 18Z. Pressure in millibars. From Schafer (1966).

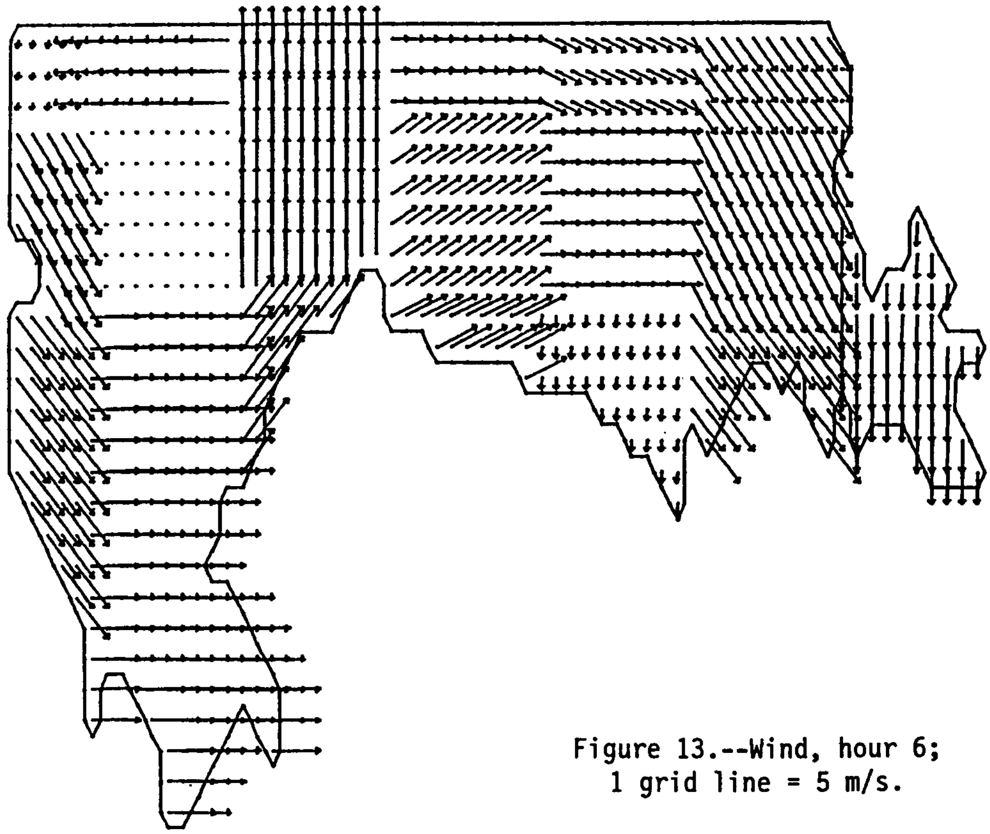

Figure 13.--Wind, hour 6;
1 grid line = 5 m/s.

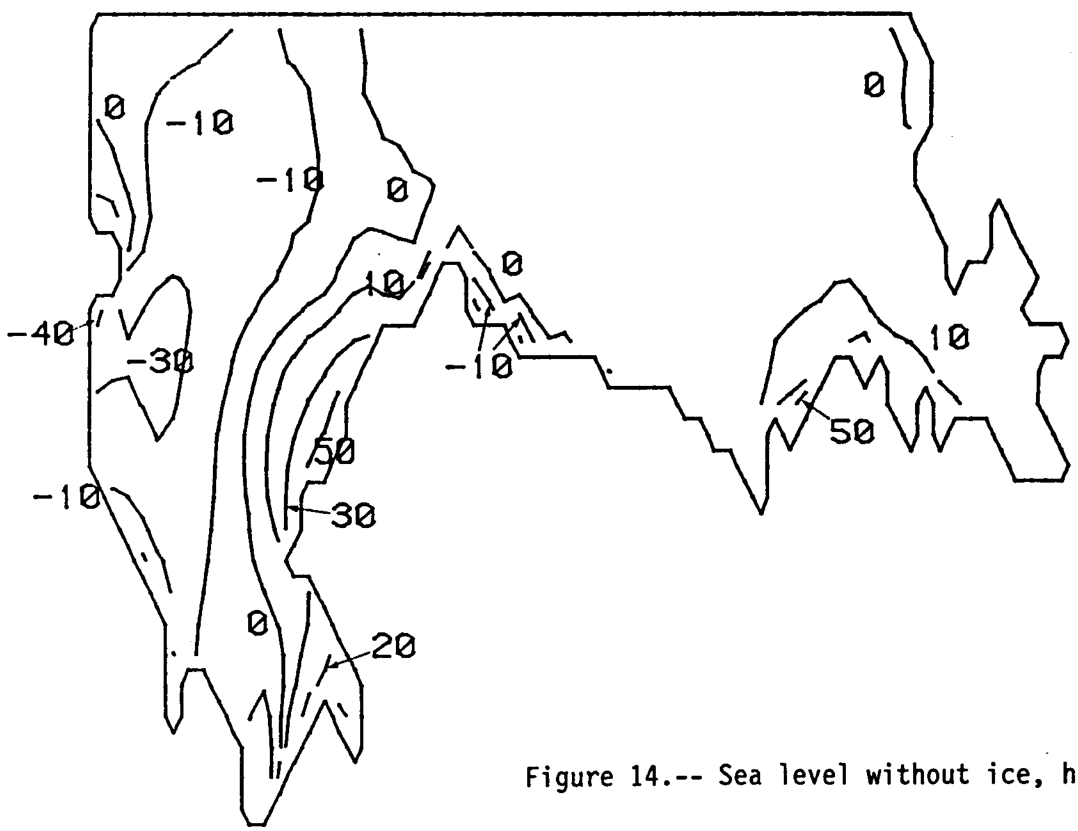

Figure 14.-- Sea level without ice, hour 6.

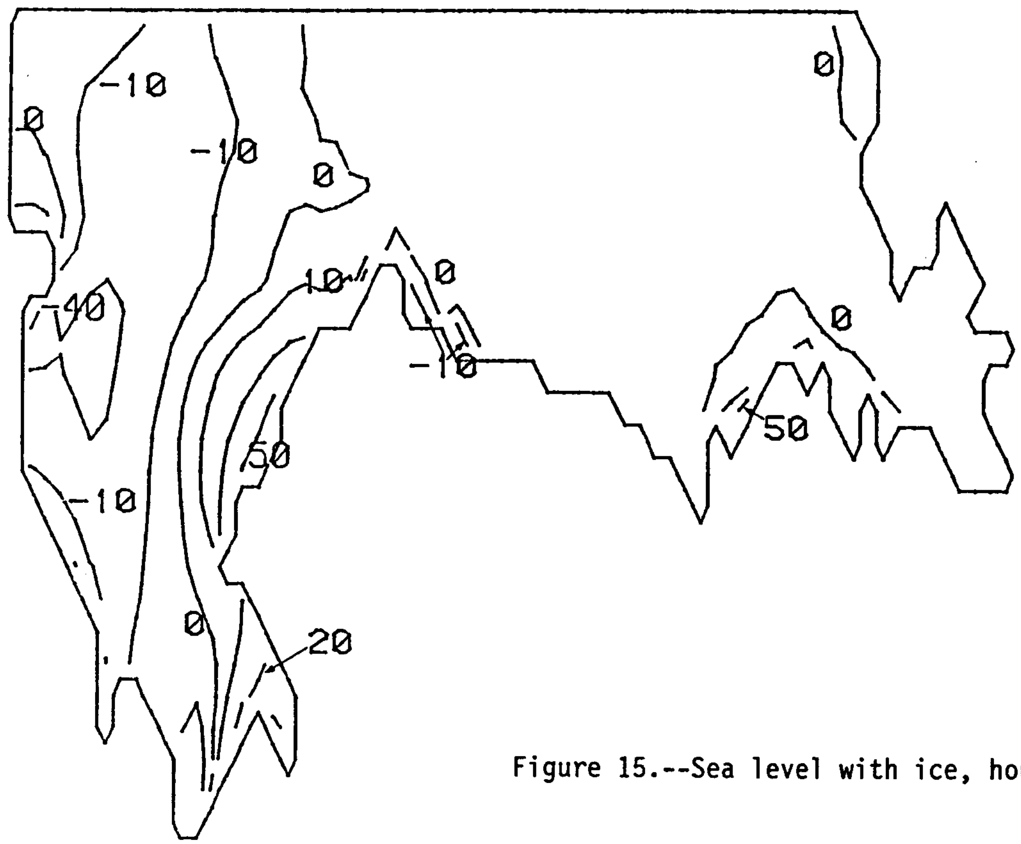

Figure 15.--Sea level with ice, hour 6.

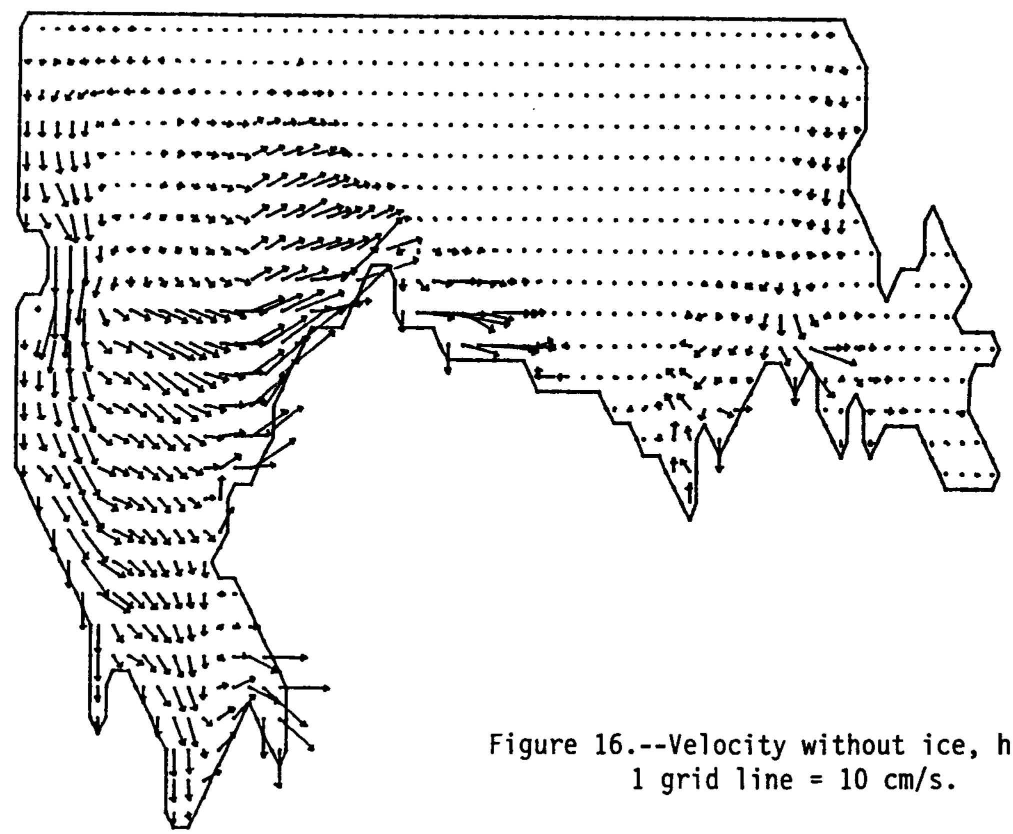

Figure 16.--Velocity without ice, hour 6;
1 grid line = 10 cm/s.

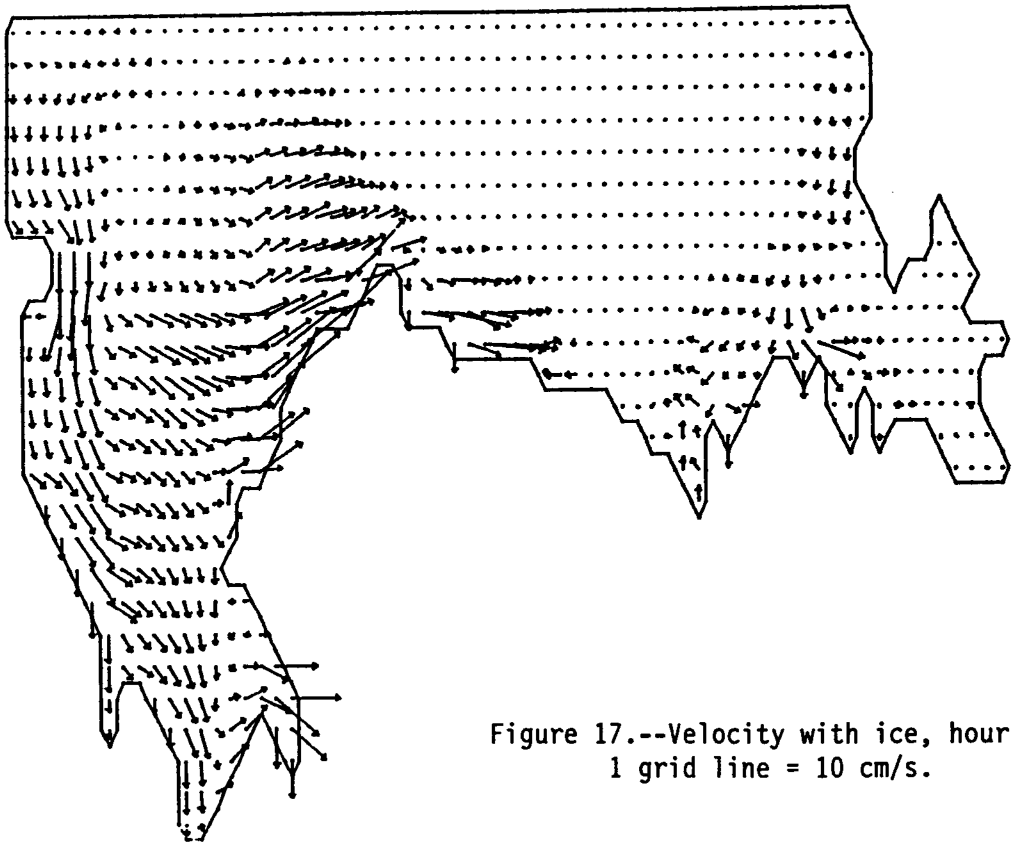

Figure 17.--Velocity with ice, hour 6;
1 grid line = 10 cm/s.

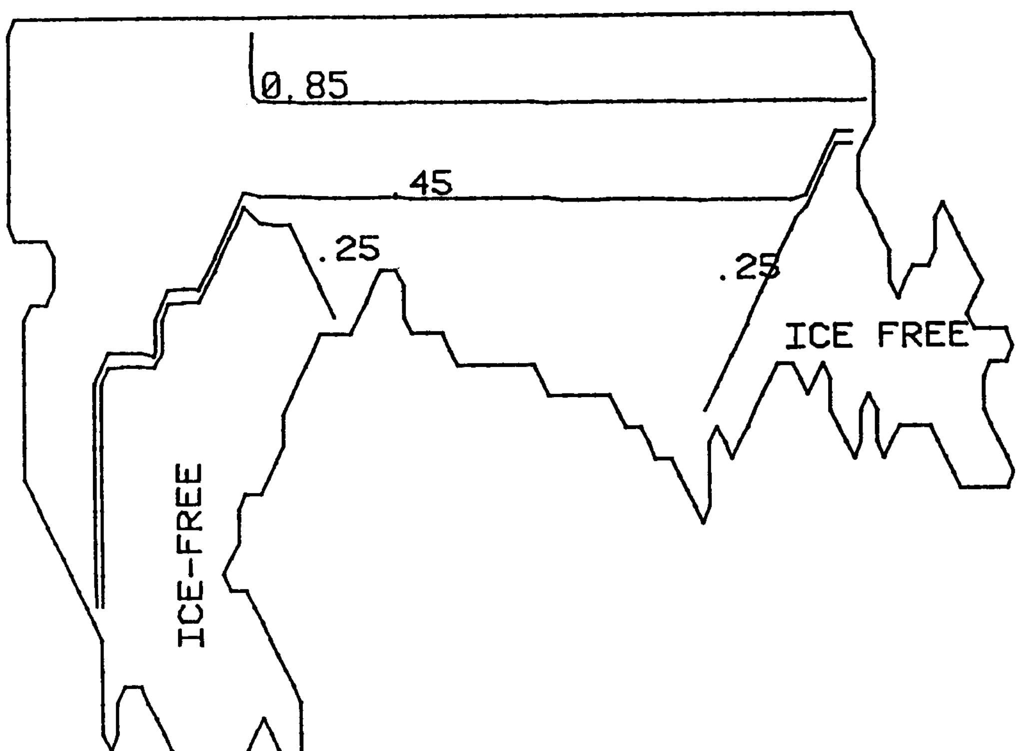

Figure 18.--Ice compactness, hour 6.

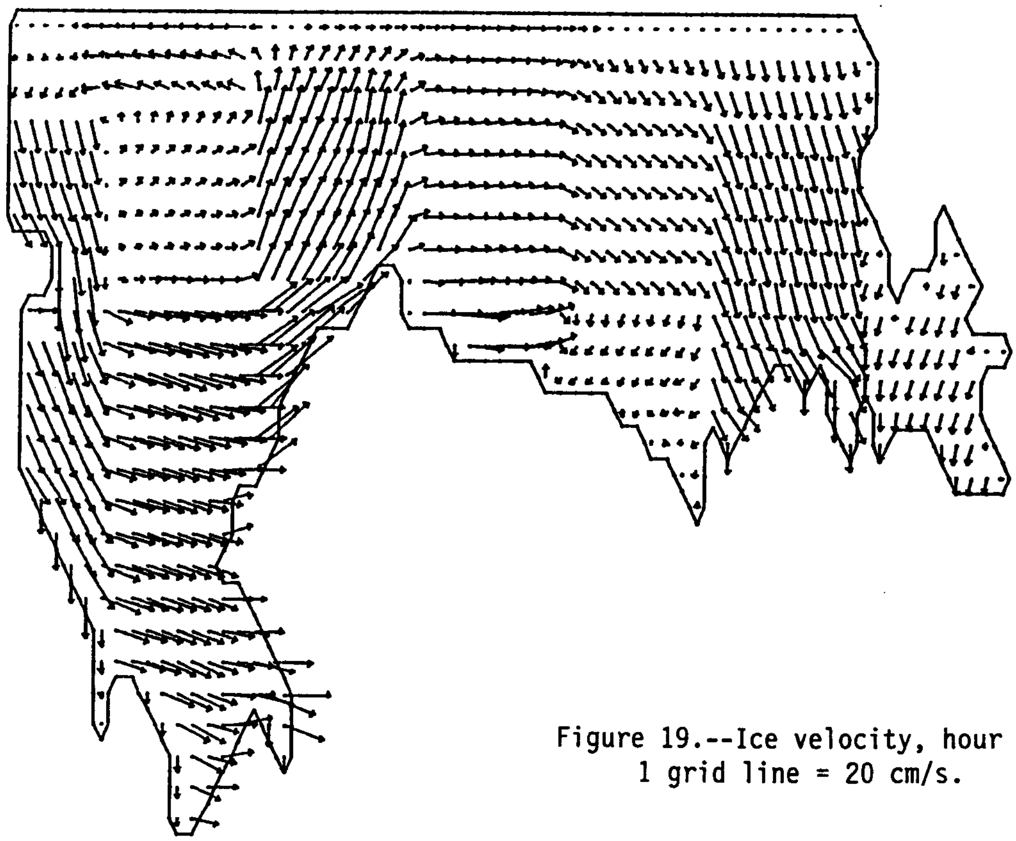

Figure 19.--Ice velocity, hour 6;
1 grid line = 20 cm/s.

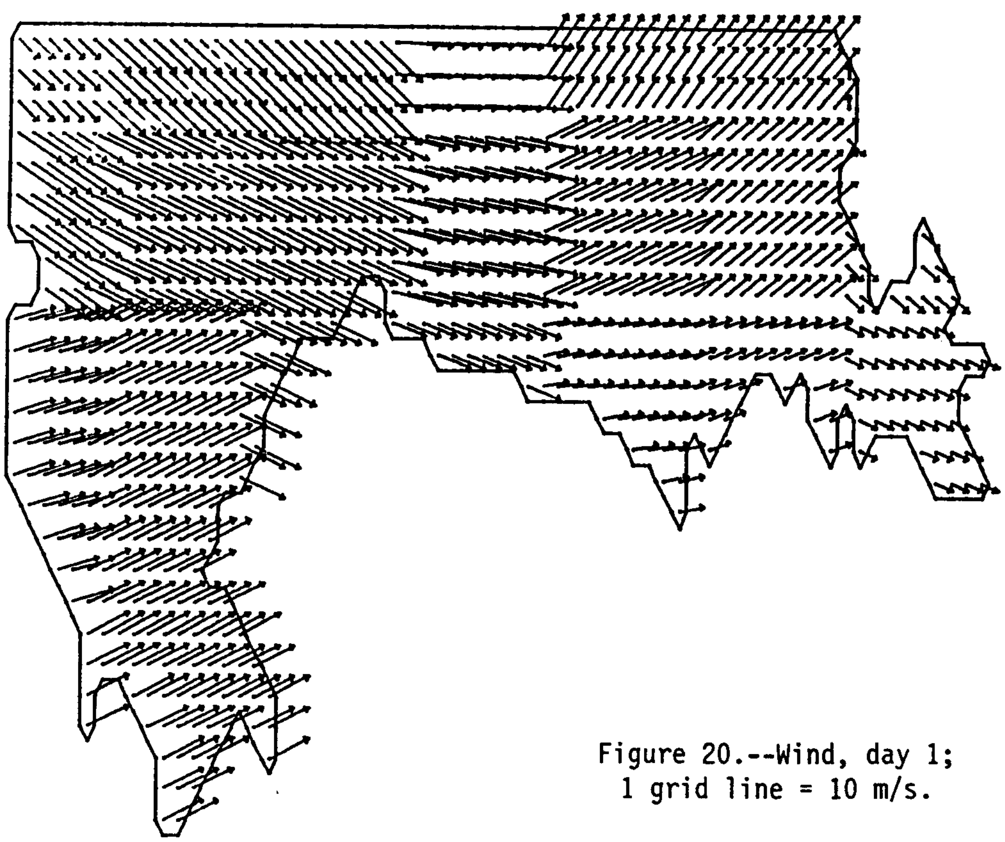

Figure 20.--Wind, day 1;
1 grid line = 10 m/s.

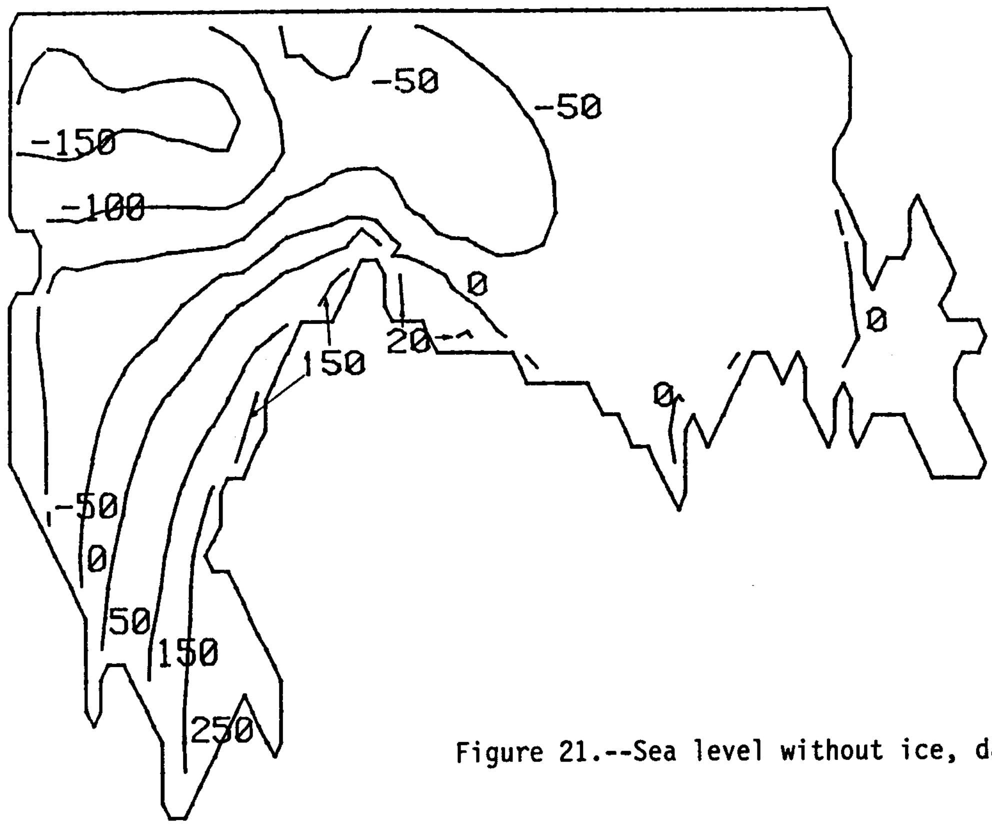

Figure 21.--Sea level without ice, day 1.

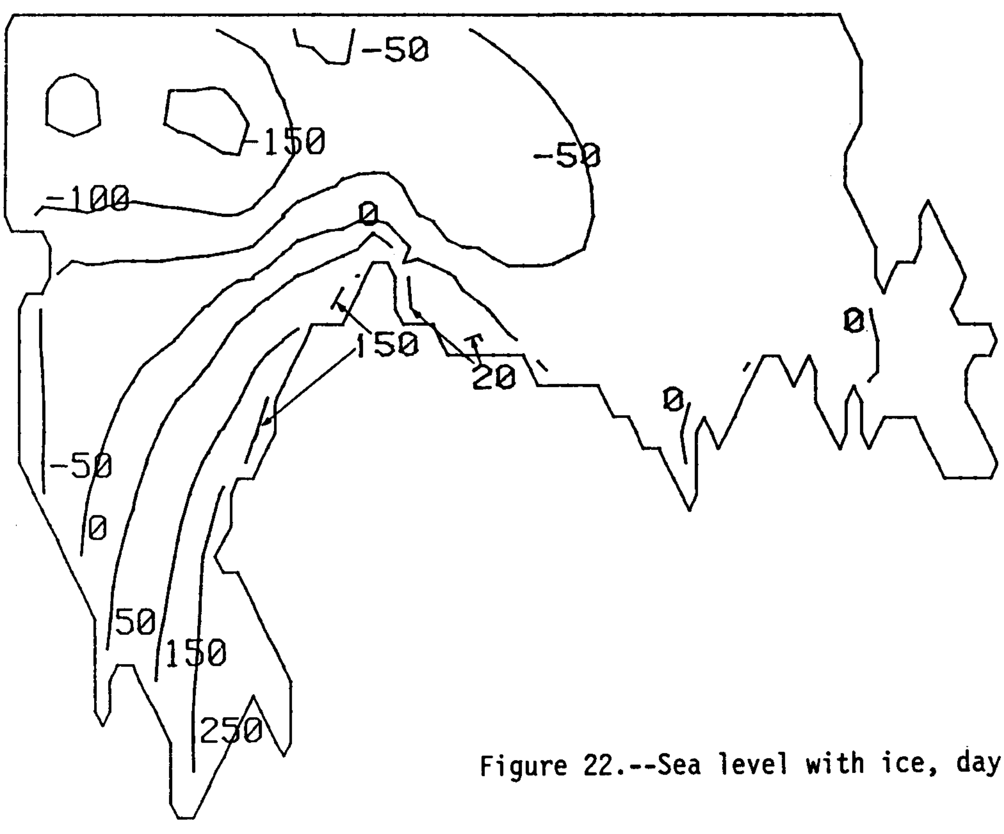

Figure 22.--Sea level with ice, day 1.

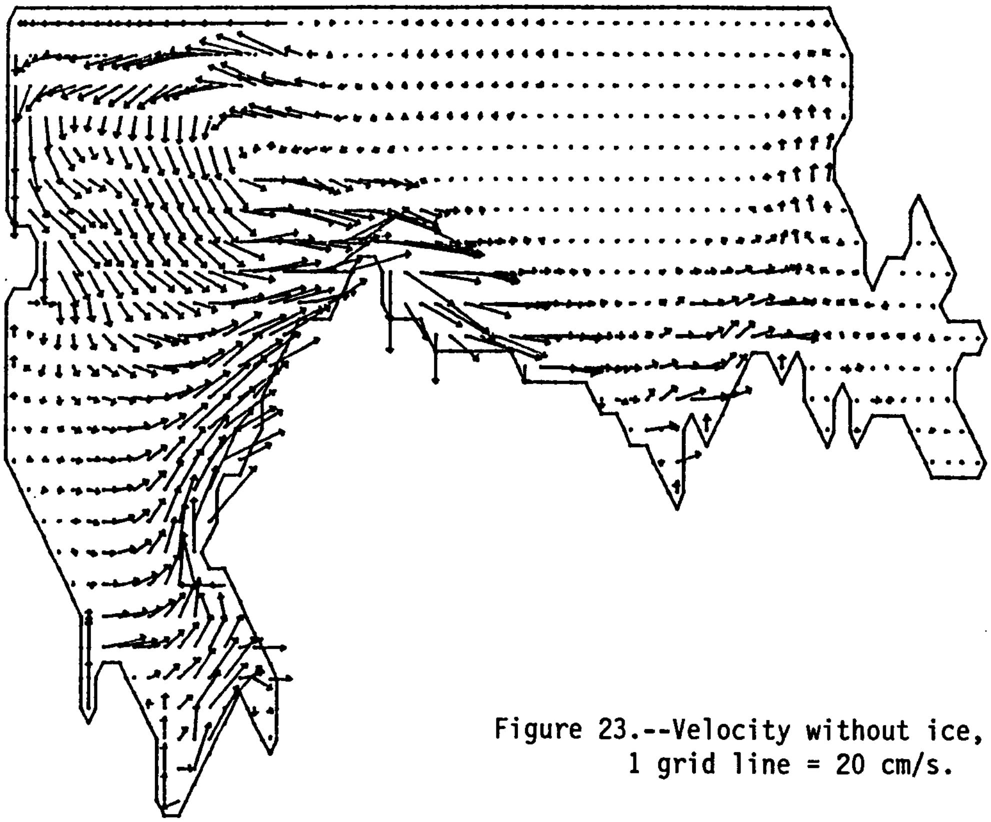

Figure 23.--Velocity without ice, day 1;
1 grid line = 20 cm/s.

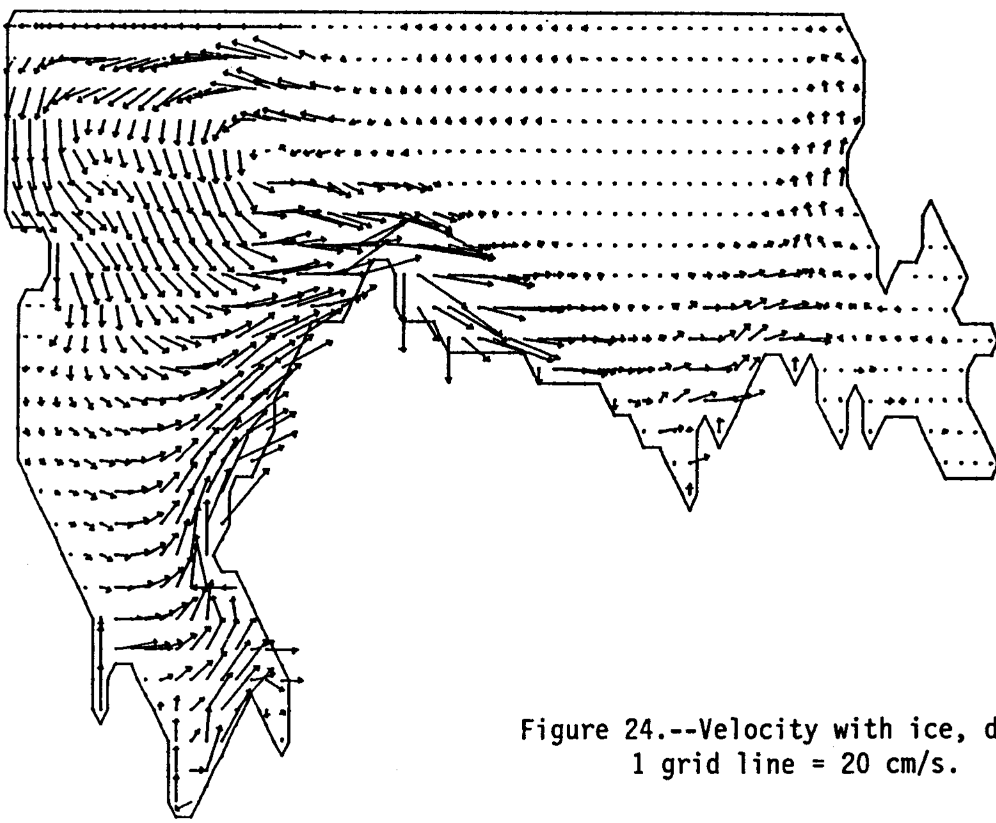

Figure 24.--Velocity with ice, day 1;
1 grid line = 20 cm/s.

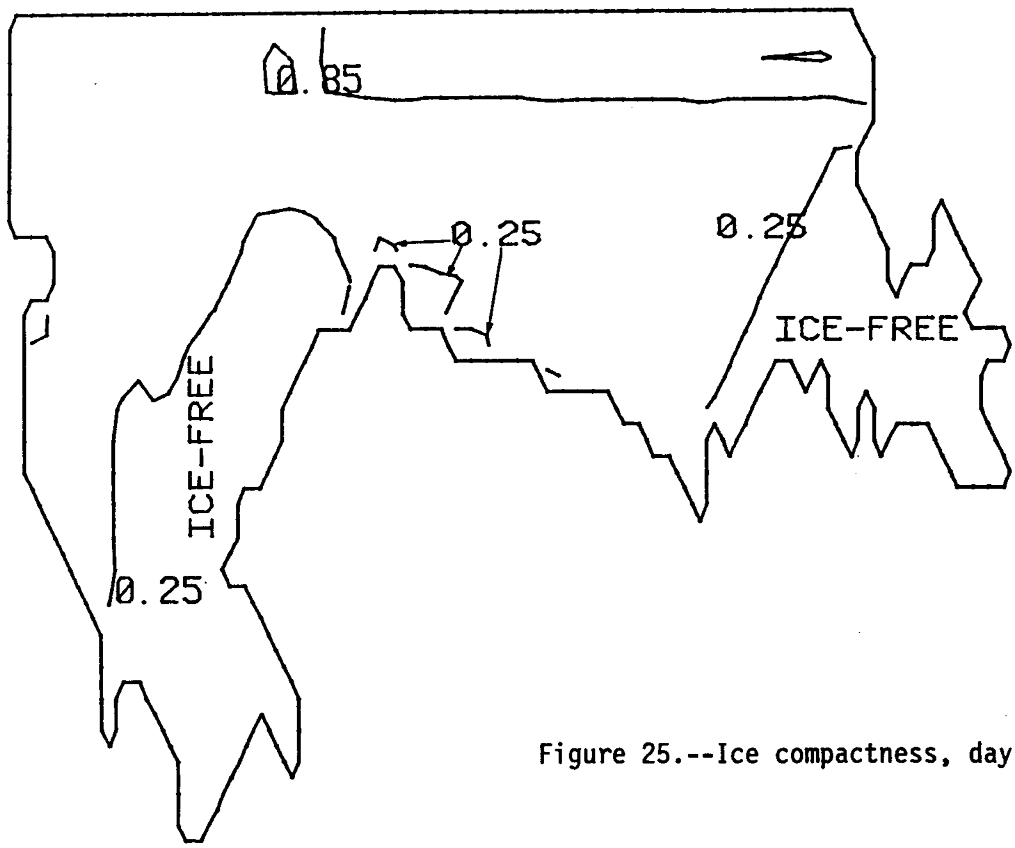

Figure 25.--Ice compactness, day 1.

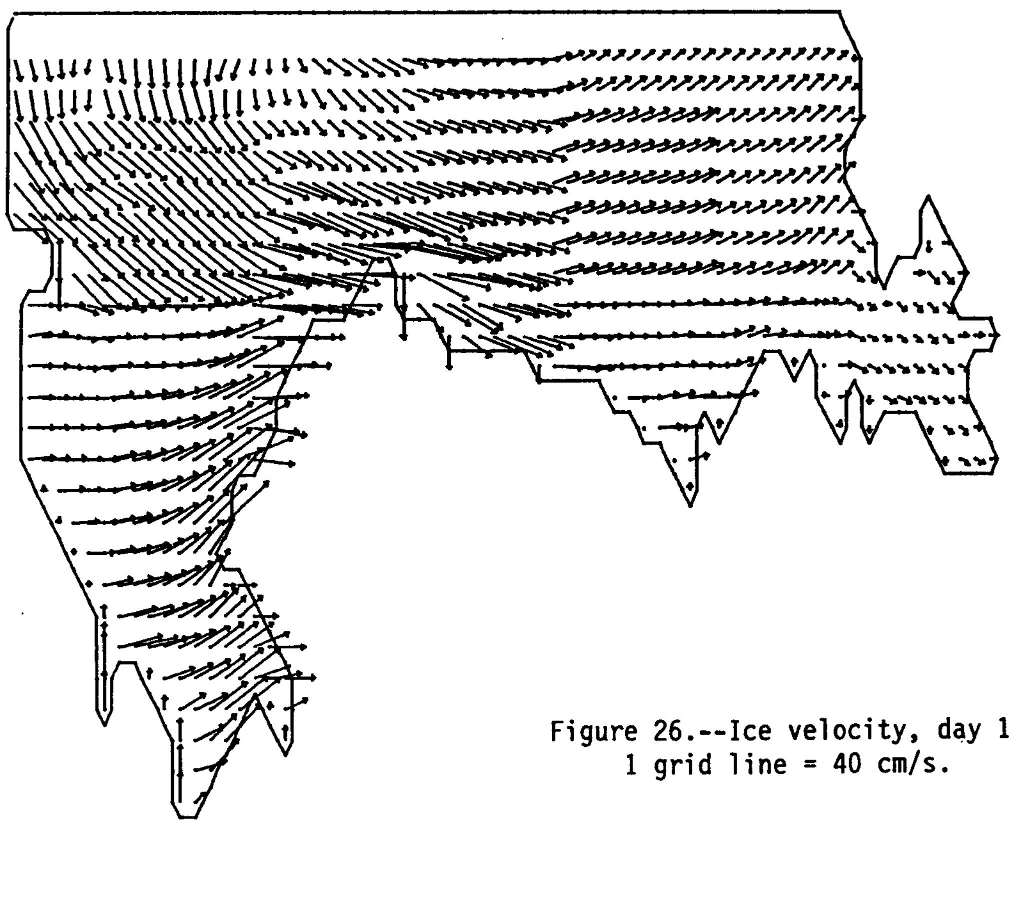

Figure 26.--Ice velocity, day 1;
1 grid line = 40 cm/s.

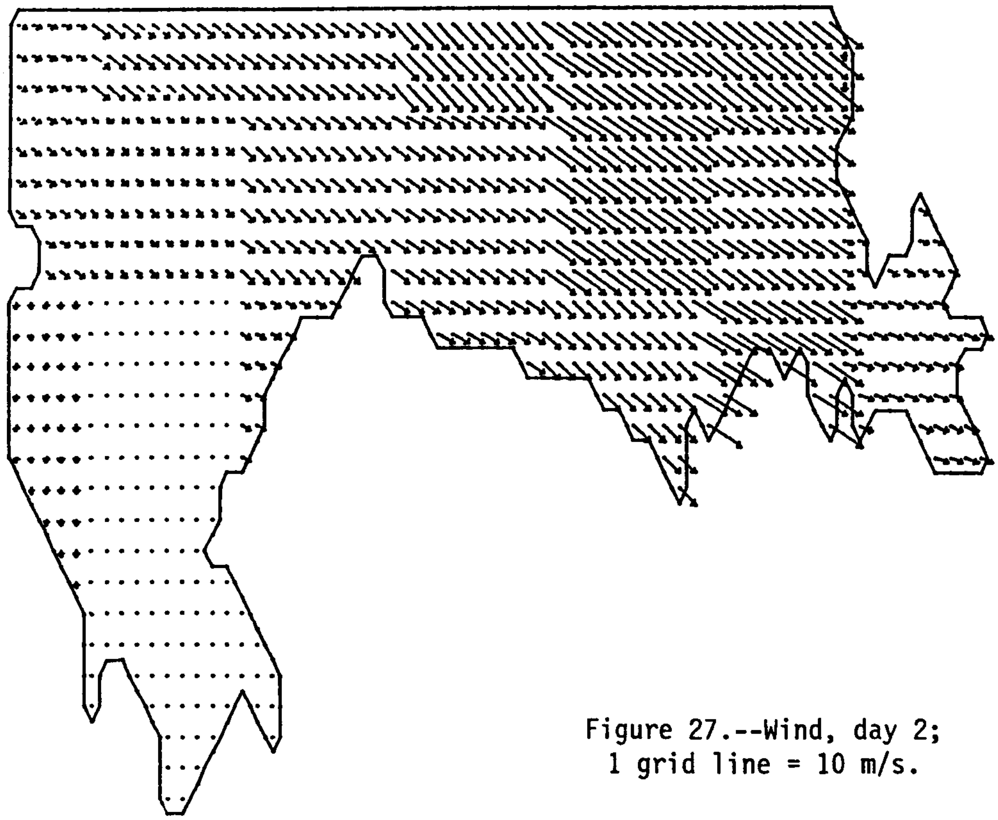

Figure 27.--Wind, day 2;
1 grid line = 10 m/s.

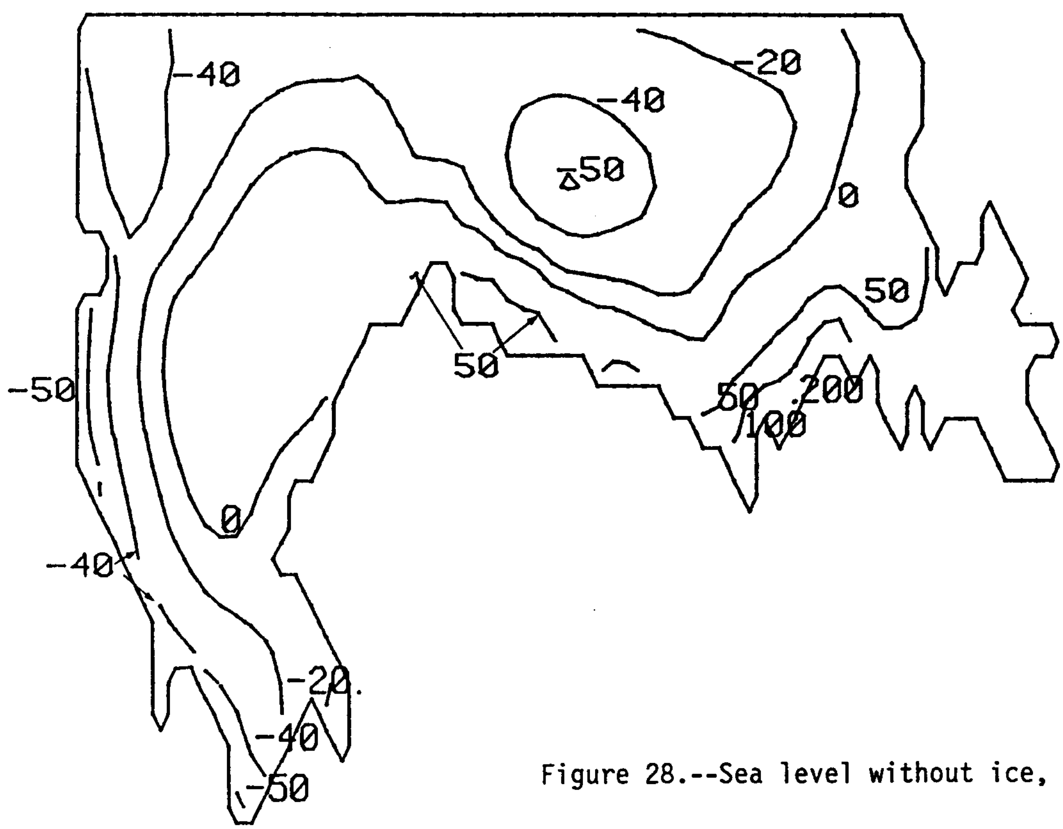

Figure 28.--Sea level without ice, day 2.

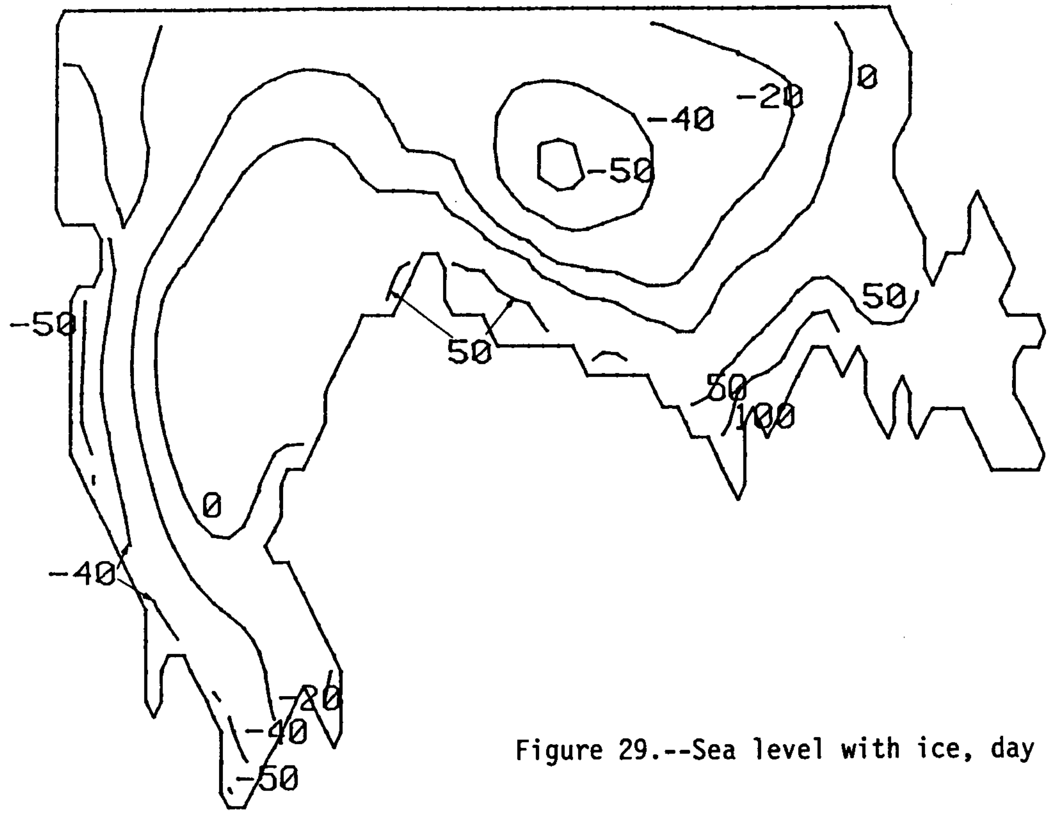

Figure 29.--Sea level with ice, day 2.

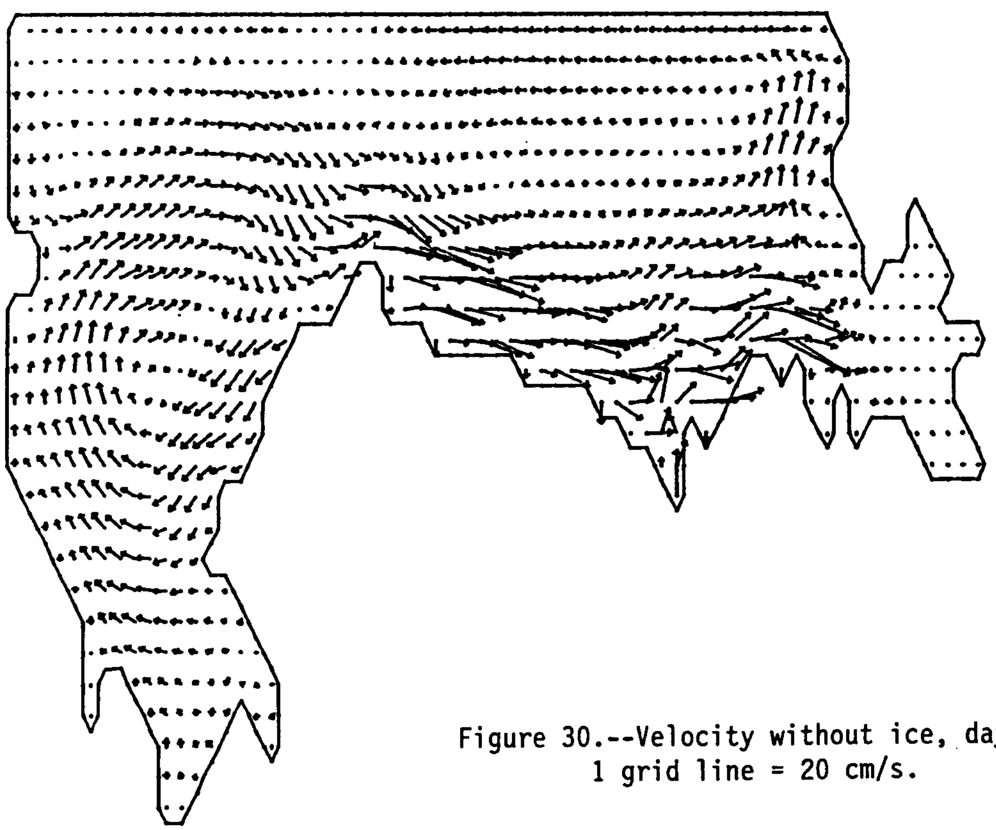

Figure 30.--Velocity without ice, day 2;
1 grid line = 20 cm/s.

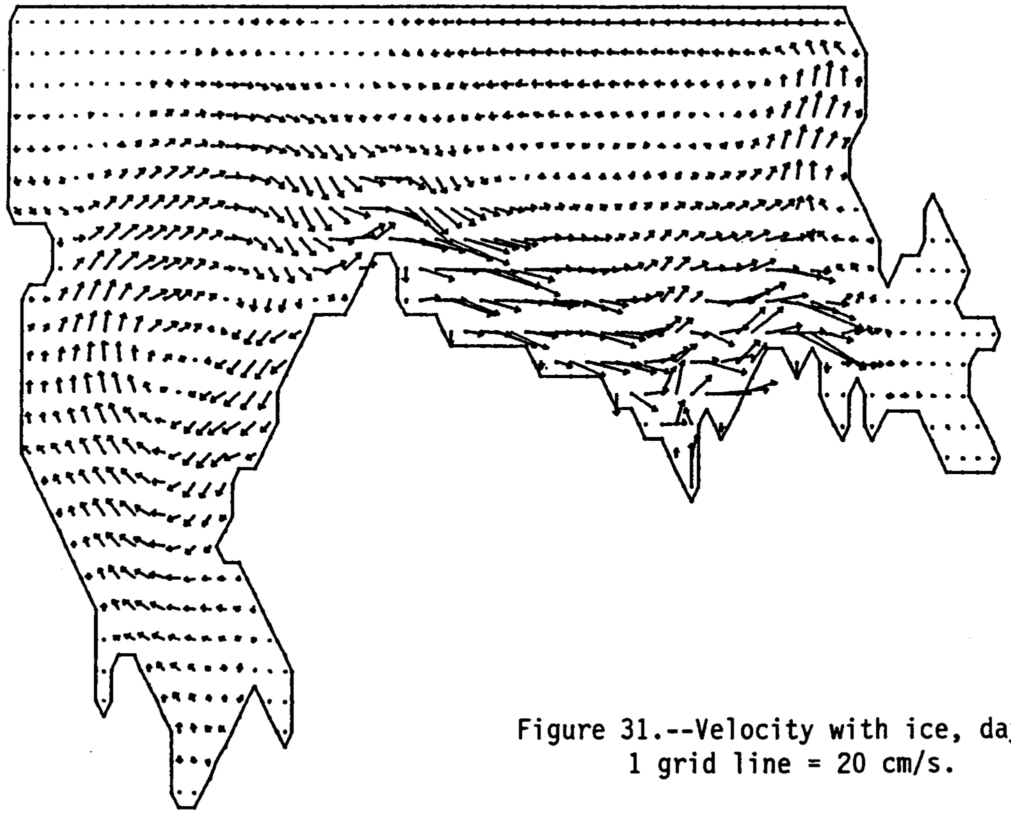

Figure 31.--Velocity with ice, day 2;
1 grid line = 20 cm/s.

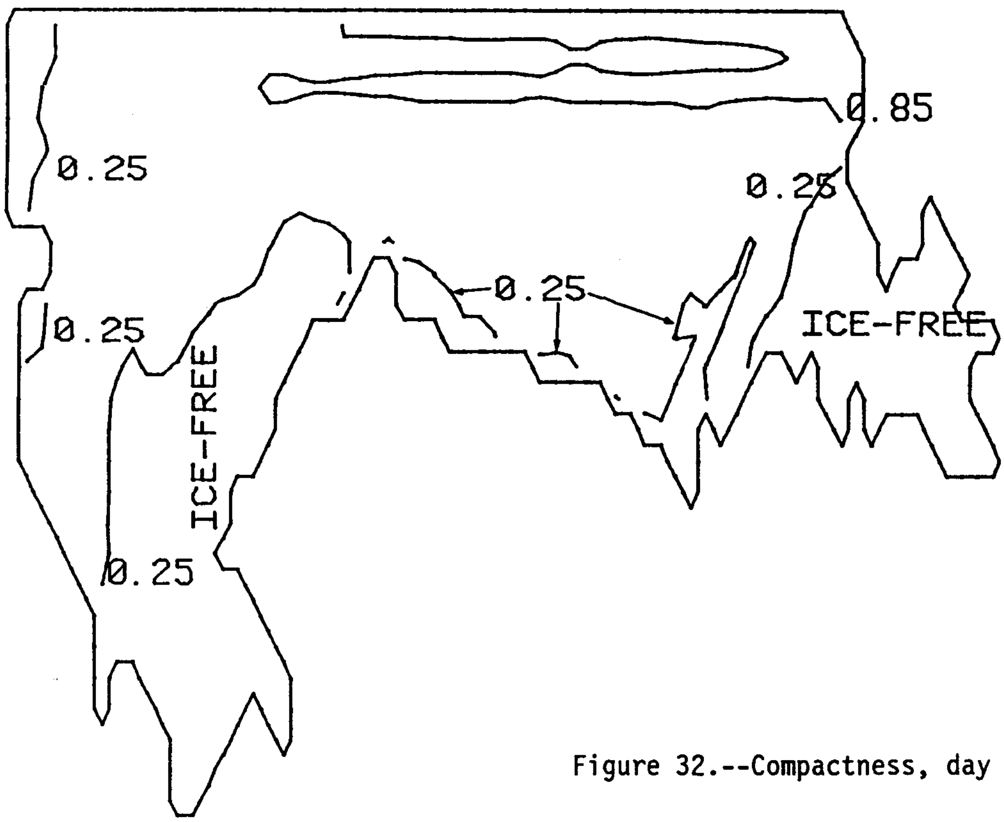

Figure 32.--Compactness, day 2.

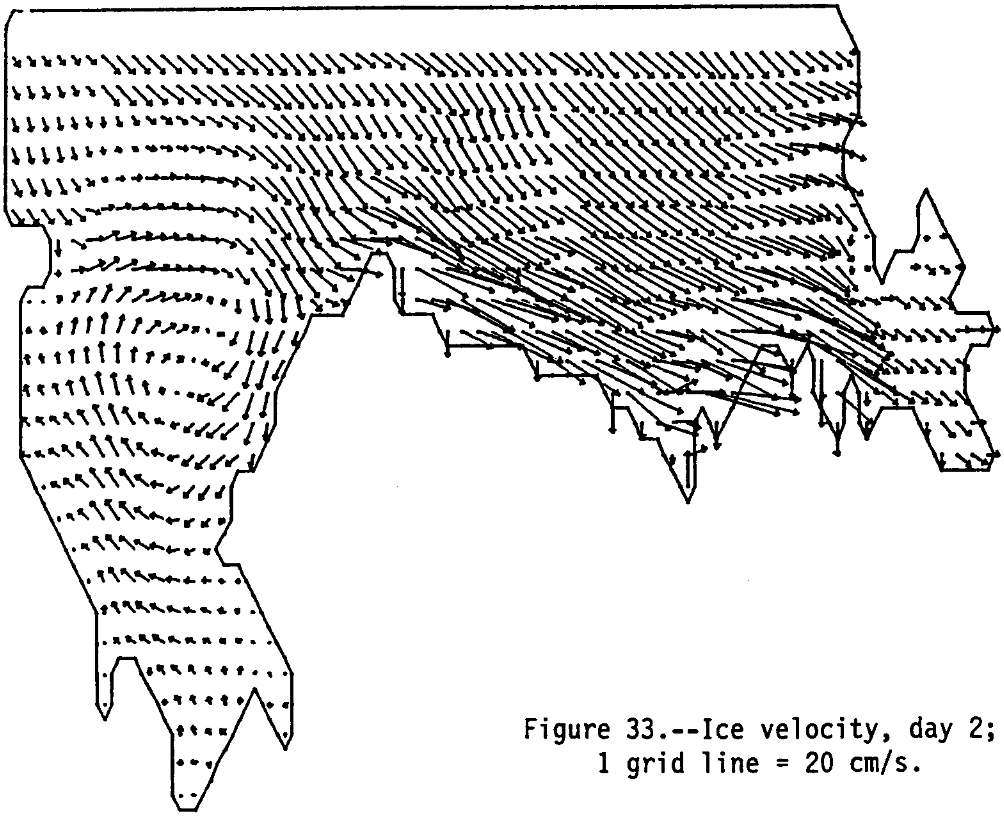

Figure 33.--Ice velocity, day 2;
1 grid line = 20 cm/s.

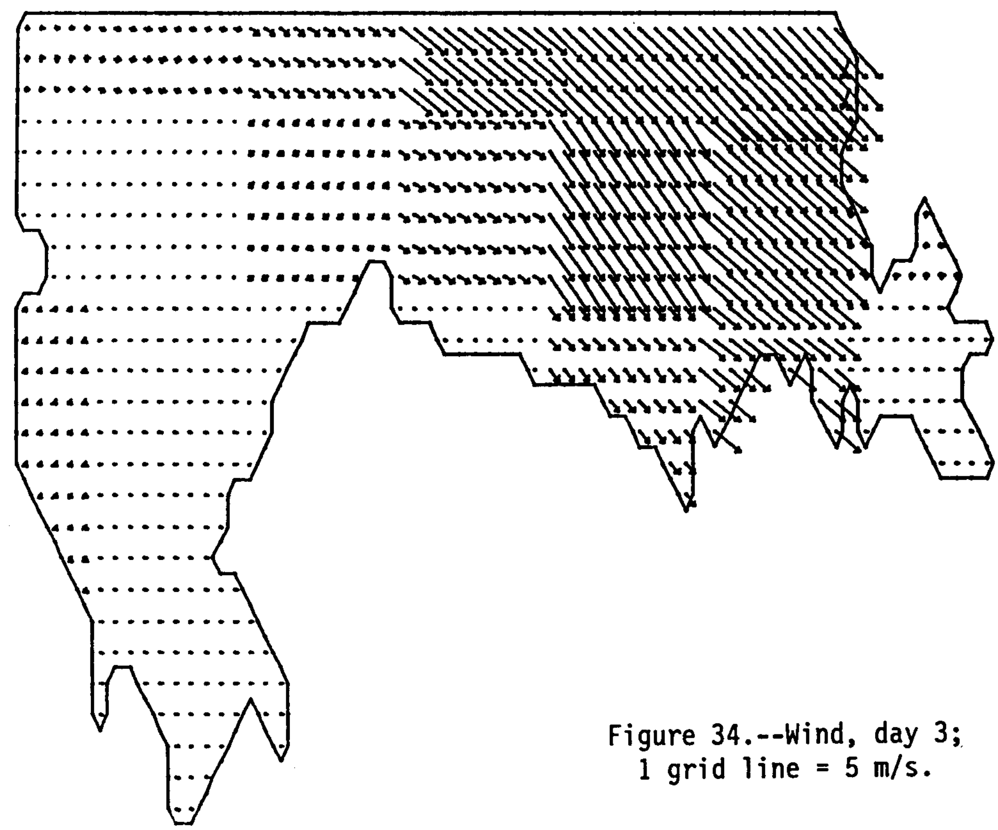

Figure 34.--Wind, day 3;
1 grid line = 5 m/s.

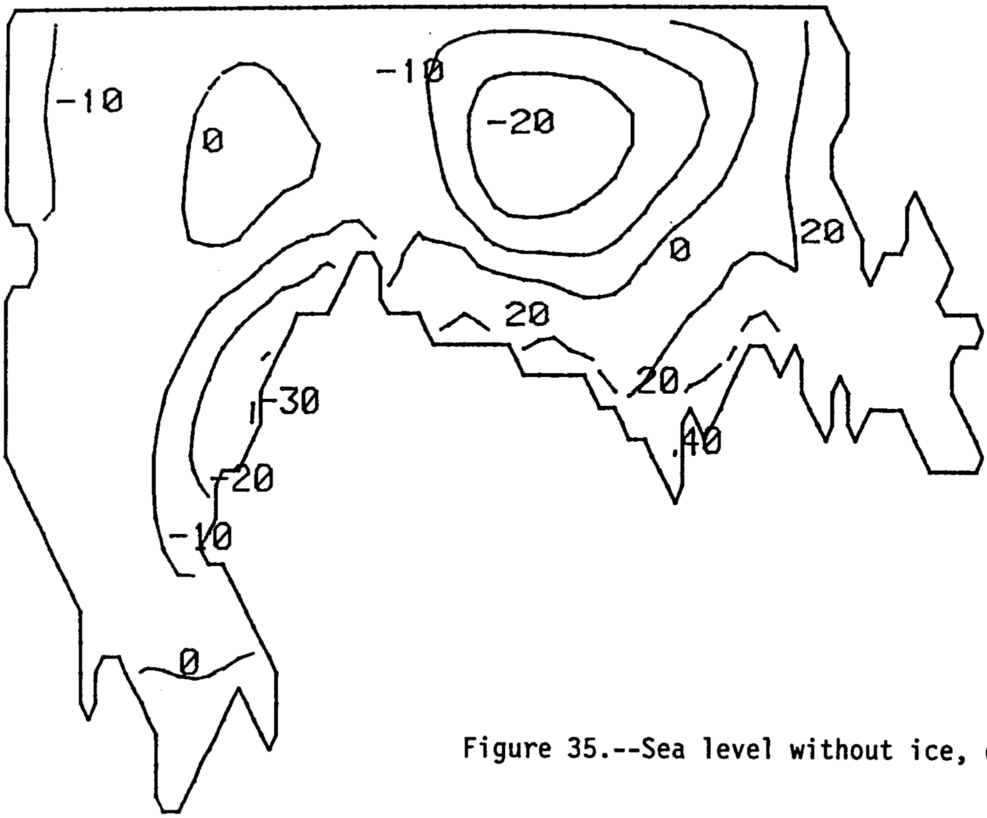

Figure 35.--Sea level without ice, day 3.

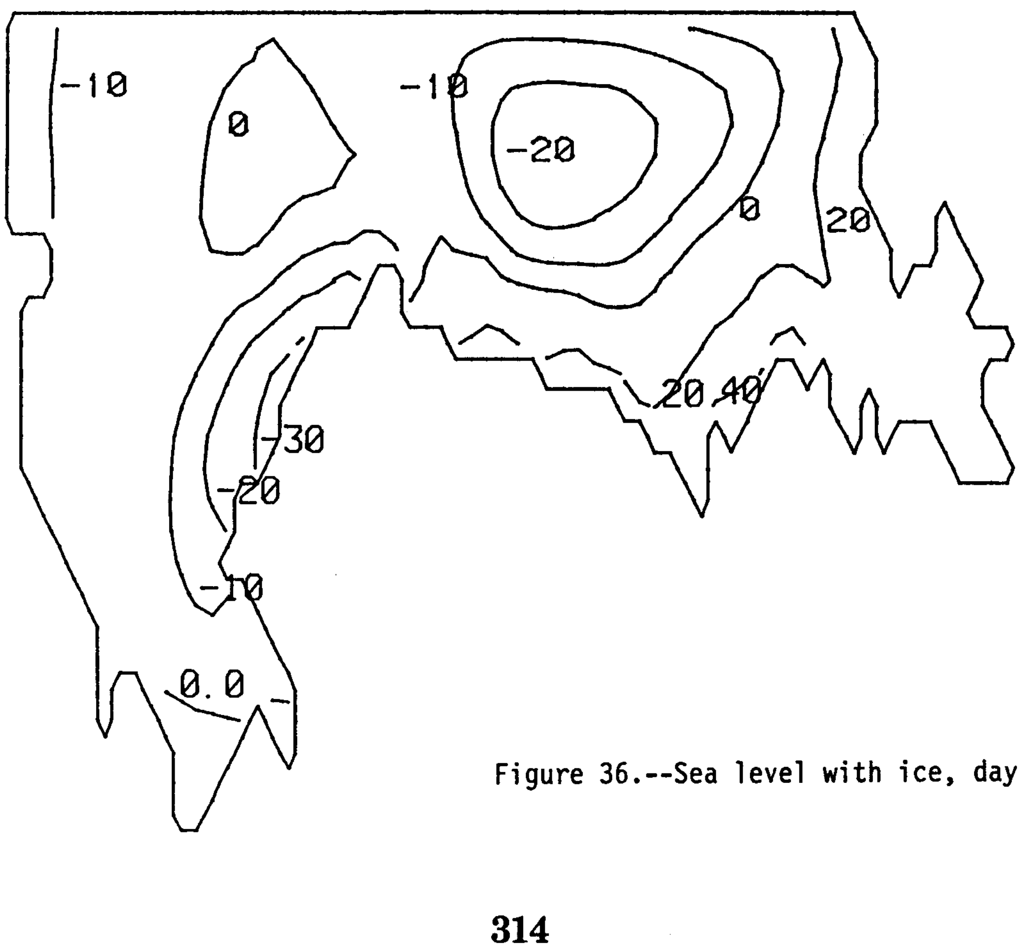

Figure 36.--Sea level with ice, day 3.

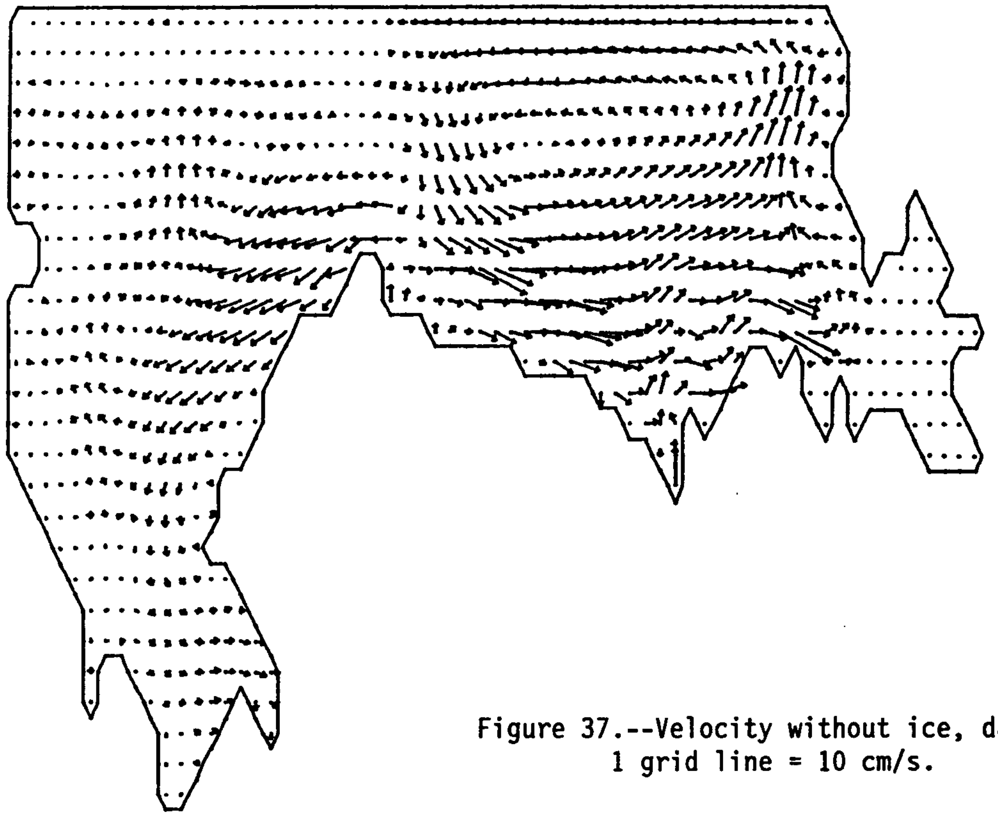

Figure 37.--Velocity without ice, day 3;
1 grid line = 10 cm/s.

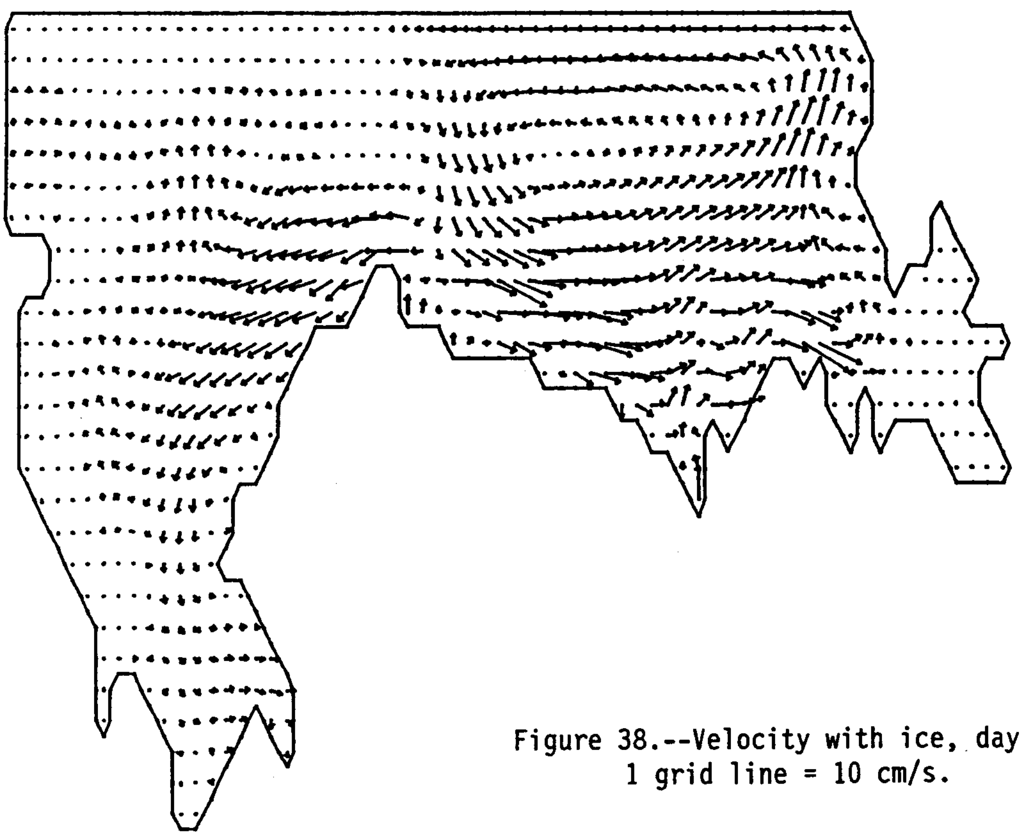

Figure 38.--Velocity with ice, day 3;
1 grid line = 10 cm/s.

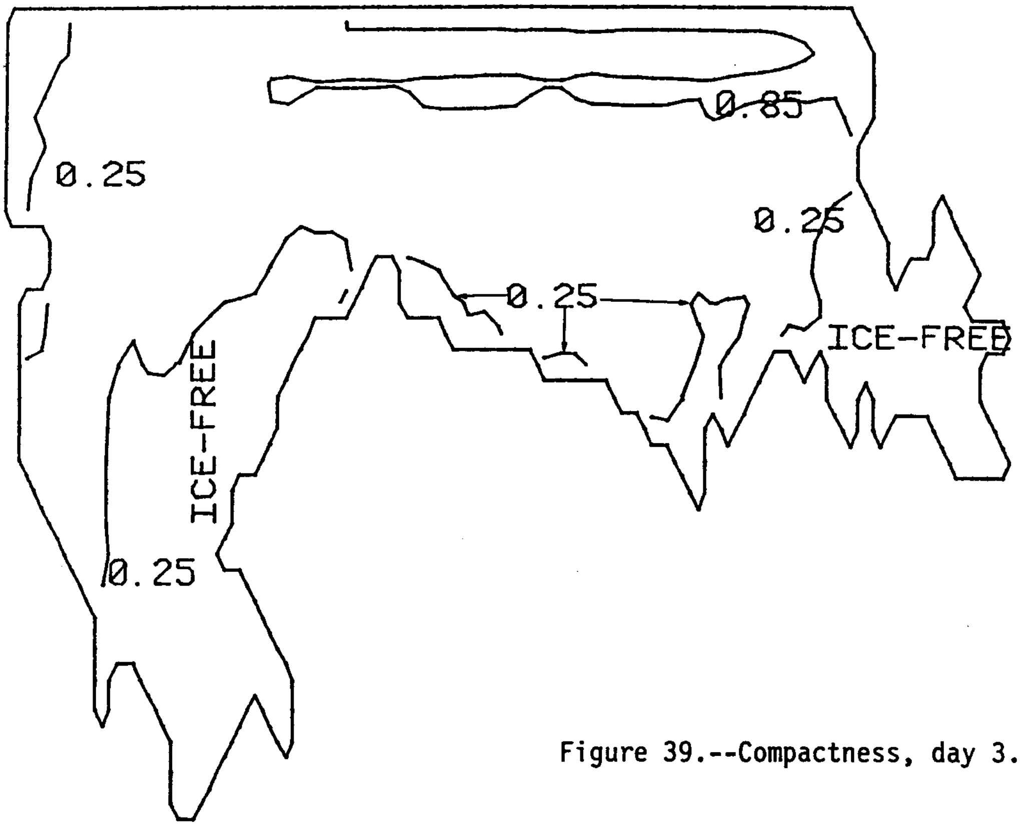

Figure 39.--Compactness, day 3.

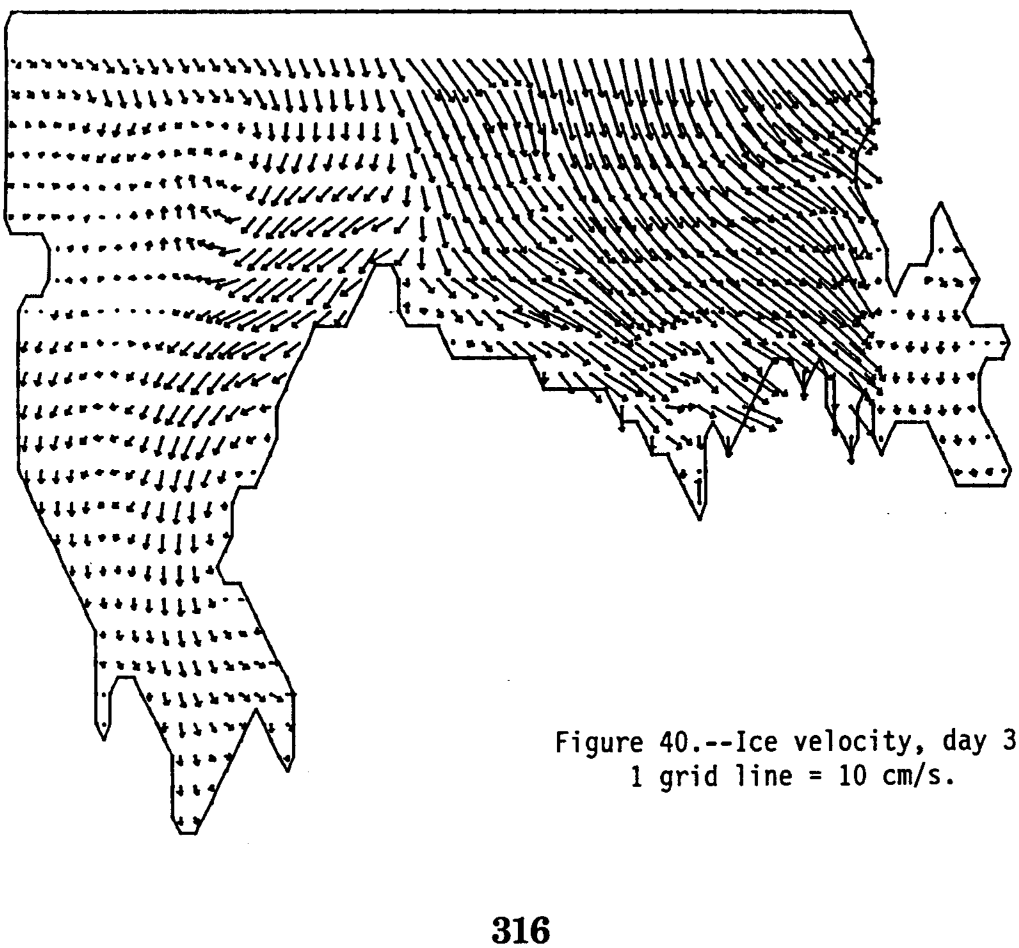

Figure 40.--Ice velocity, day 3;
1 grid line = 10 cm/s.

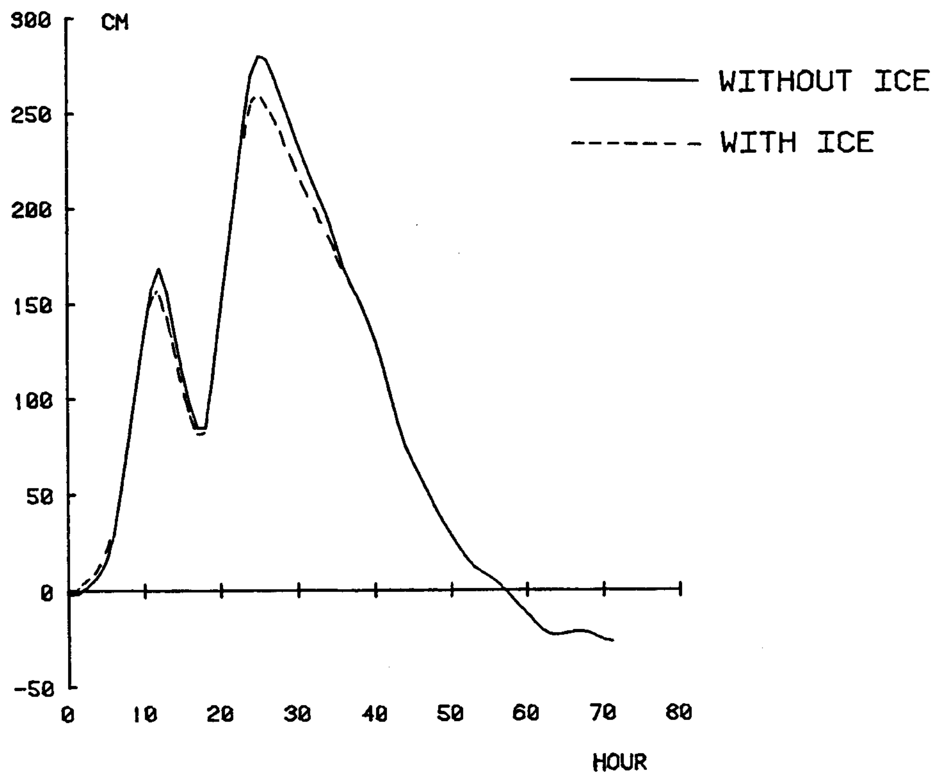

Figure 41.--Sea level variation, Pt. Barrow west.

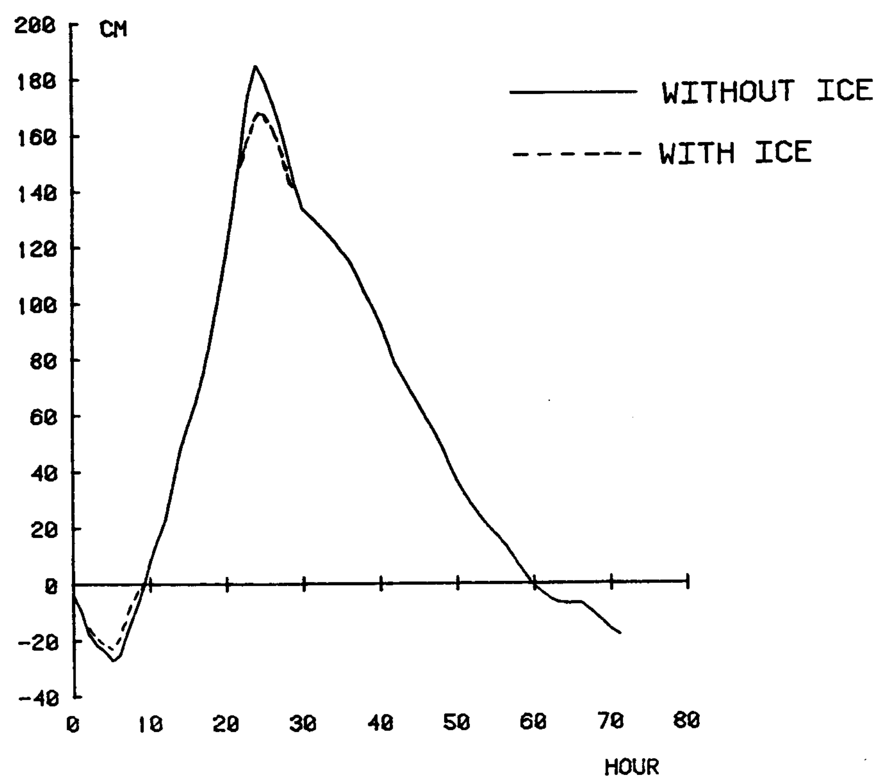

Figure 42.--Sea level variation, Pt. Barrow.

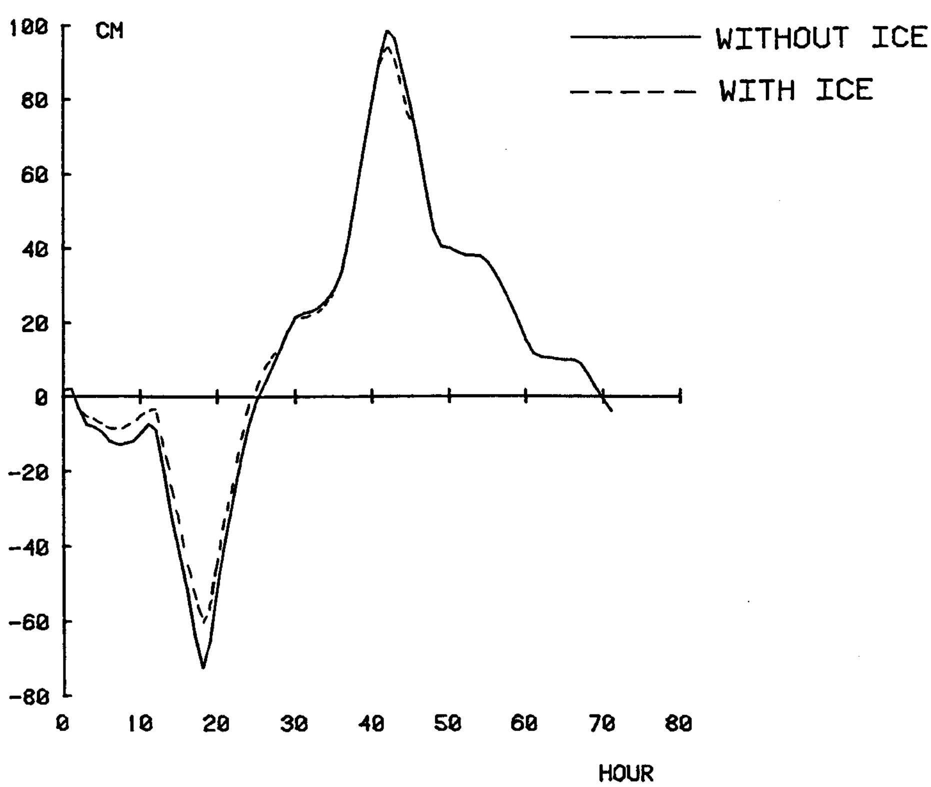

Figure 43.--Sea level variation, Pt. Barrow east.

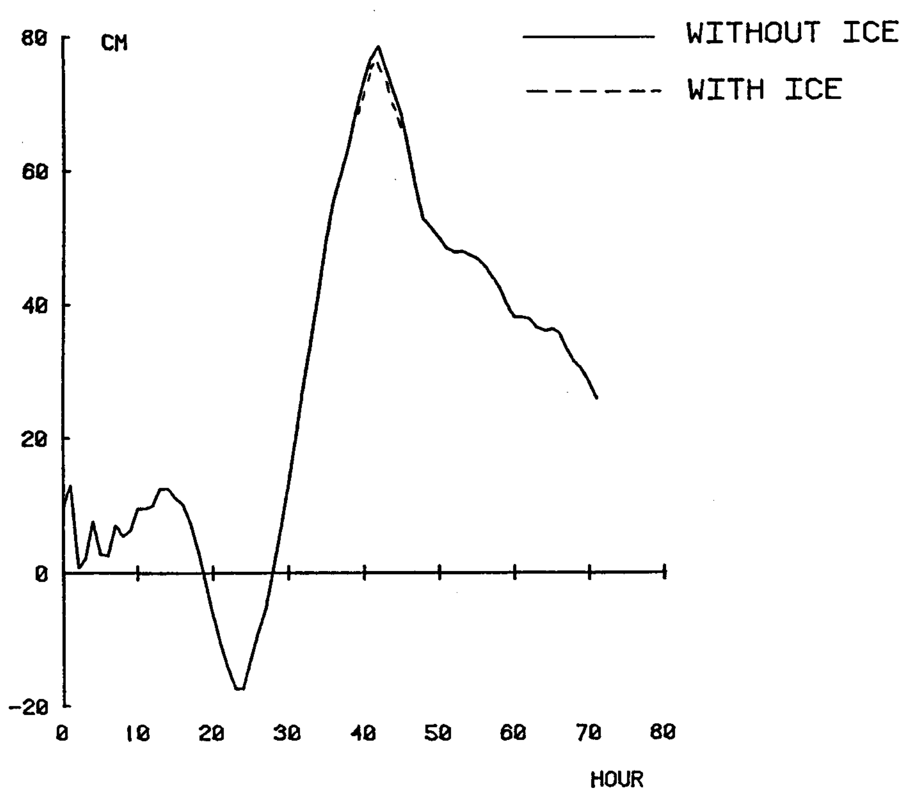

Figure 44.--Sea level variation, Simpson Cove.

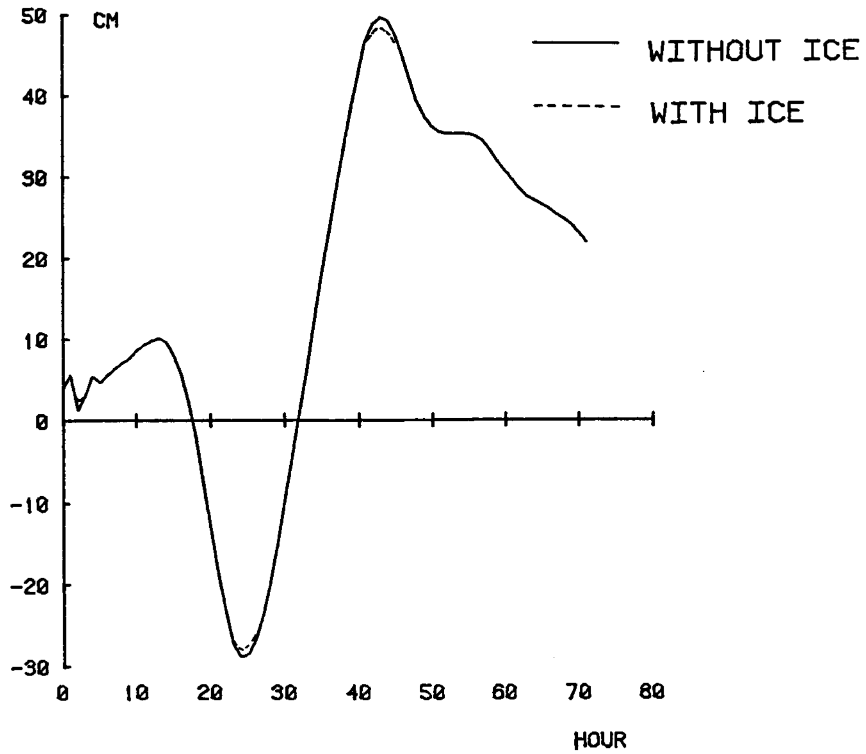

Figure 45.--Sea level variation, Demarcation Bay.

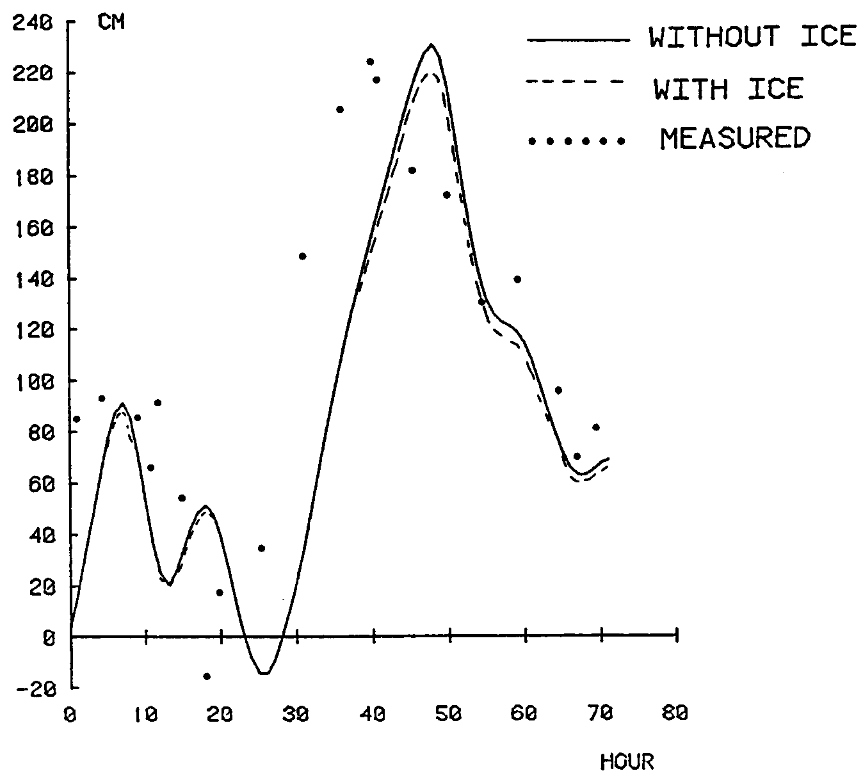

Figure 46.--Sea level variation, Tuktoyaktuk.

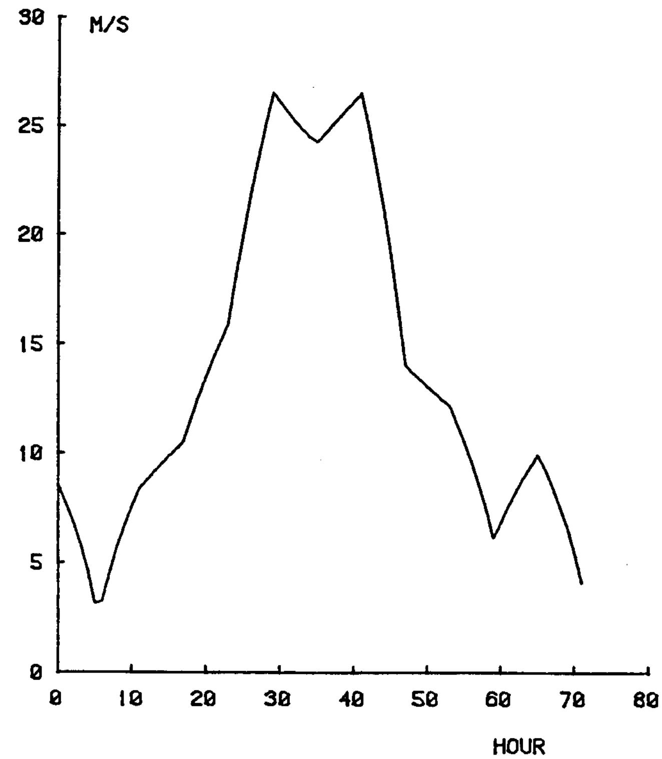

Figure 47.--Wind velocity at 70°30'N, 135°30'W. Speed is linearly interpolated between 6-h intervals.

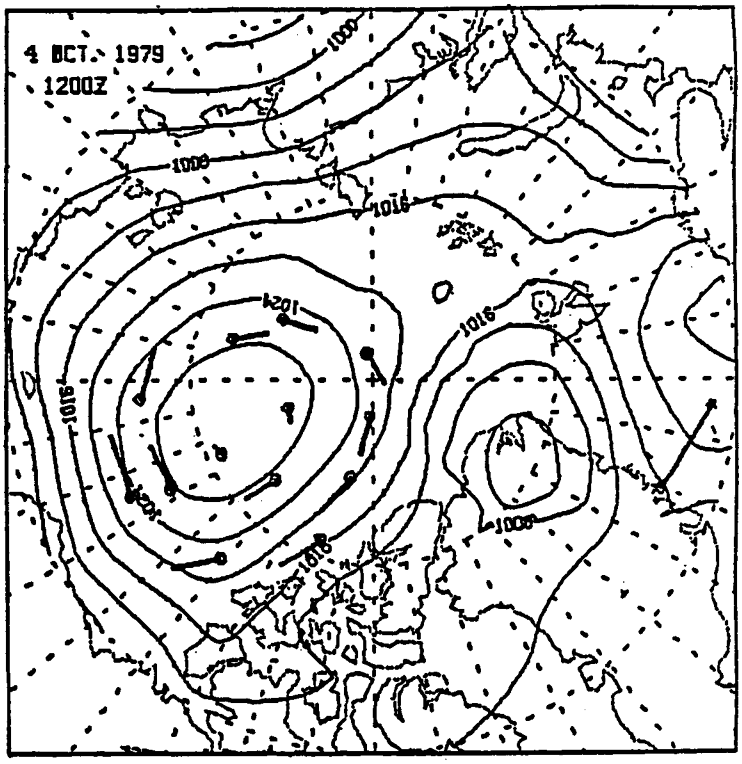

Figure 48.--Weather chart for 4 October 1979, 12Z. Pressure in millibars. Ice motion is described by the vectors originating at the open circles. From Thorndike and Colony (1980).

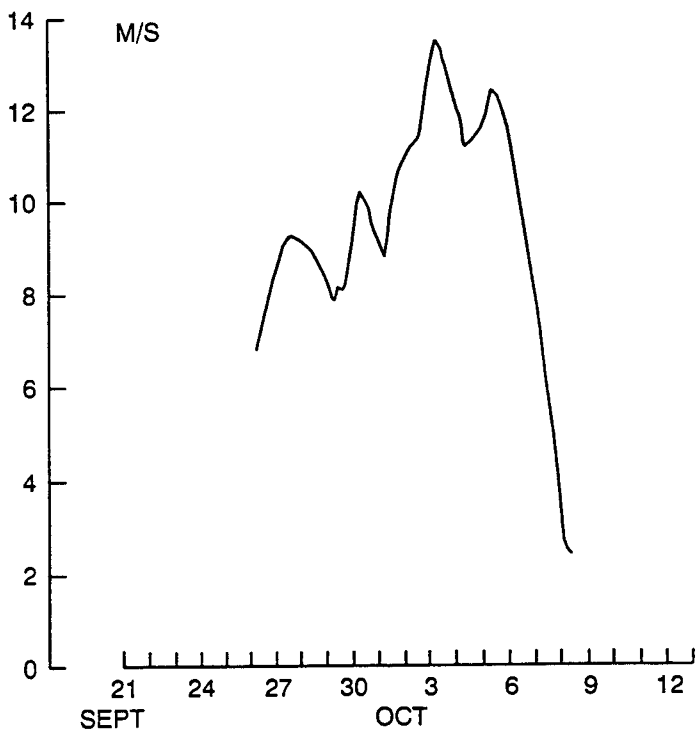

Figure 49.--Wind speed in Harrison Bay (70°30'N, 151°W) during storm from September 26 to October 7, 1979.

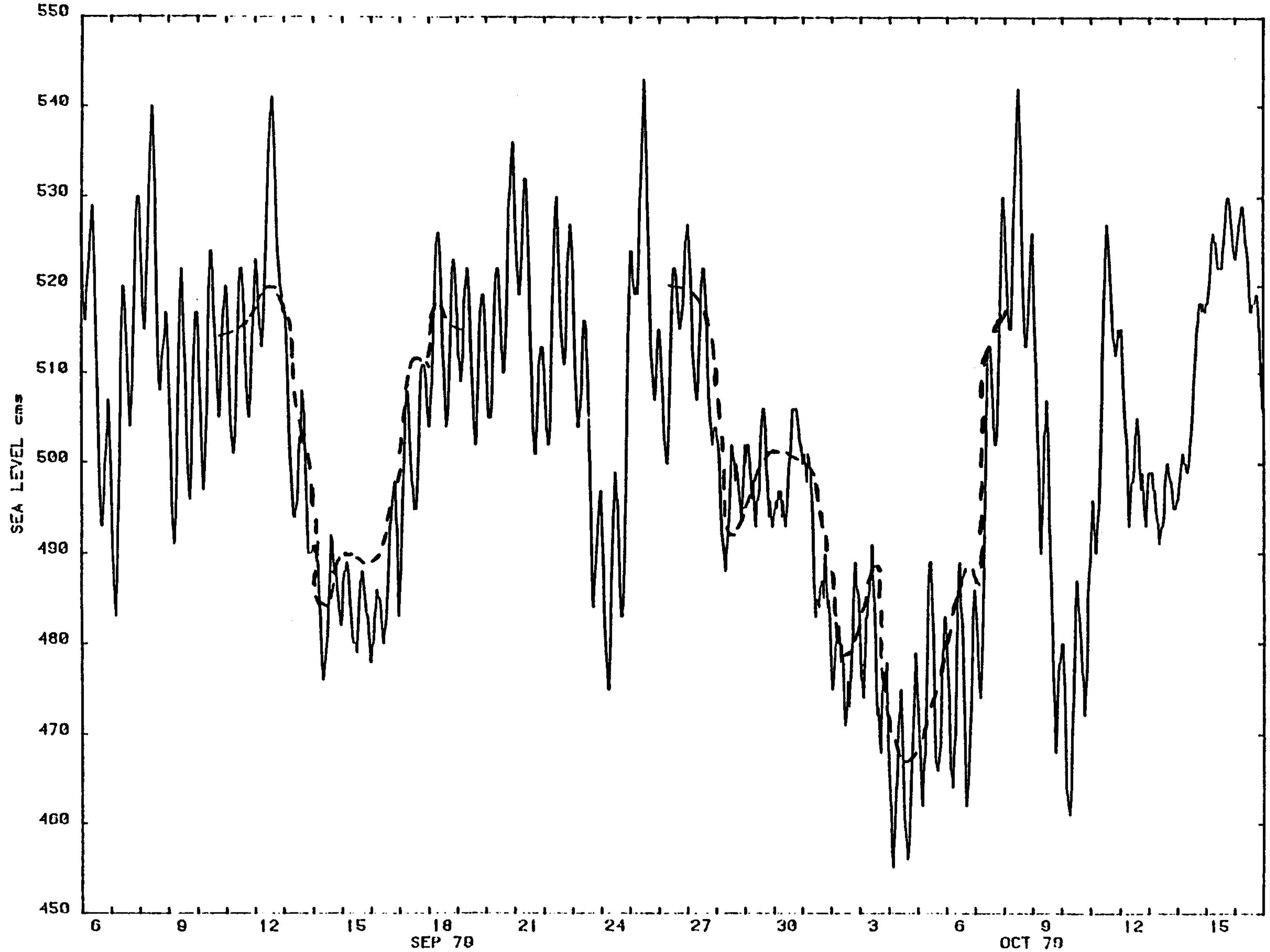

Figure 50.--Sea level in Harrison Bay. Solid line represents measured sea level, dashed line represents computed level.

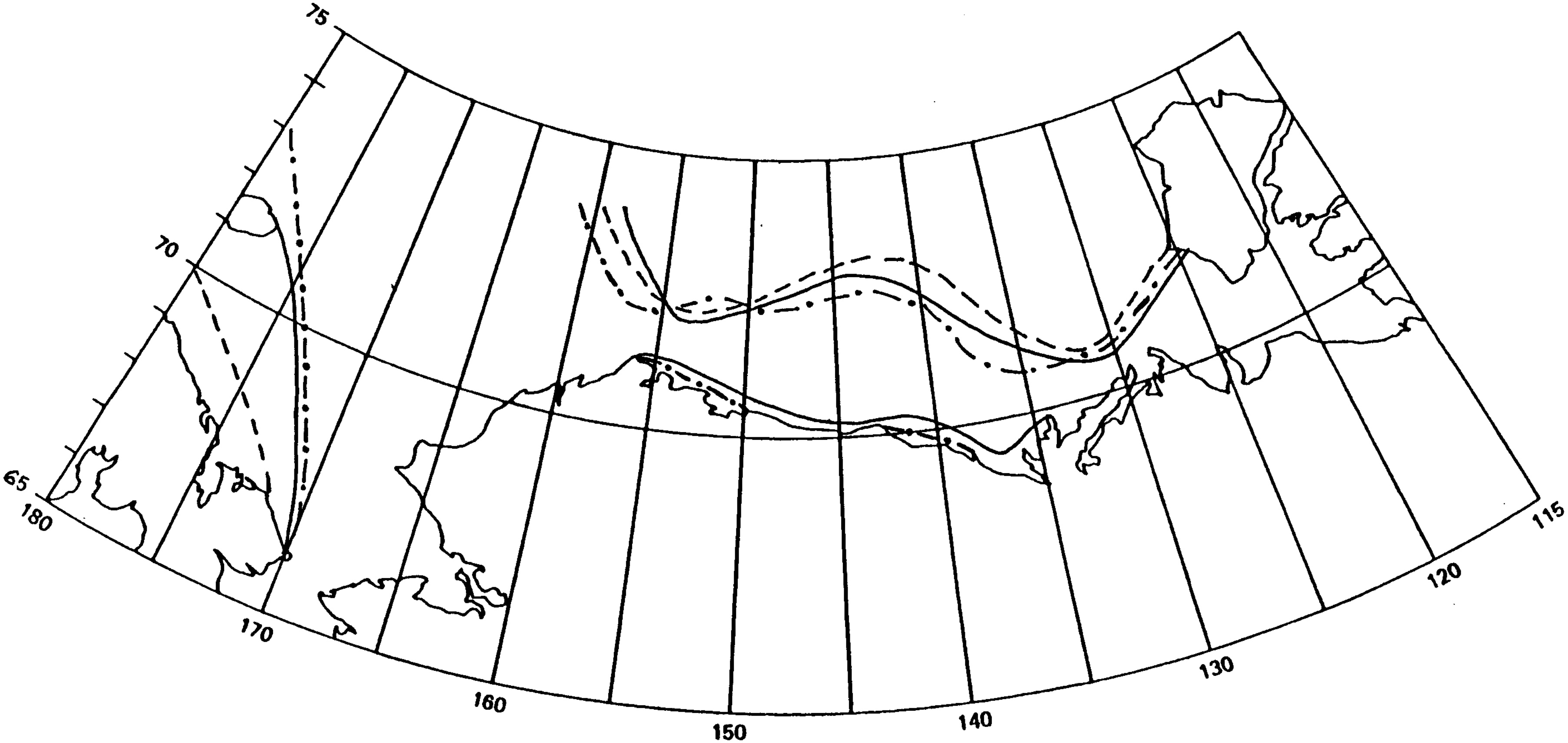

Figure 51.--Ice edge position on September 26 (dashed line) and on October 7 (measured represented by solid line, and computed by dash-dot line).

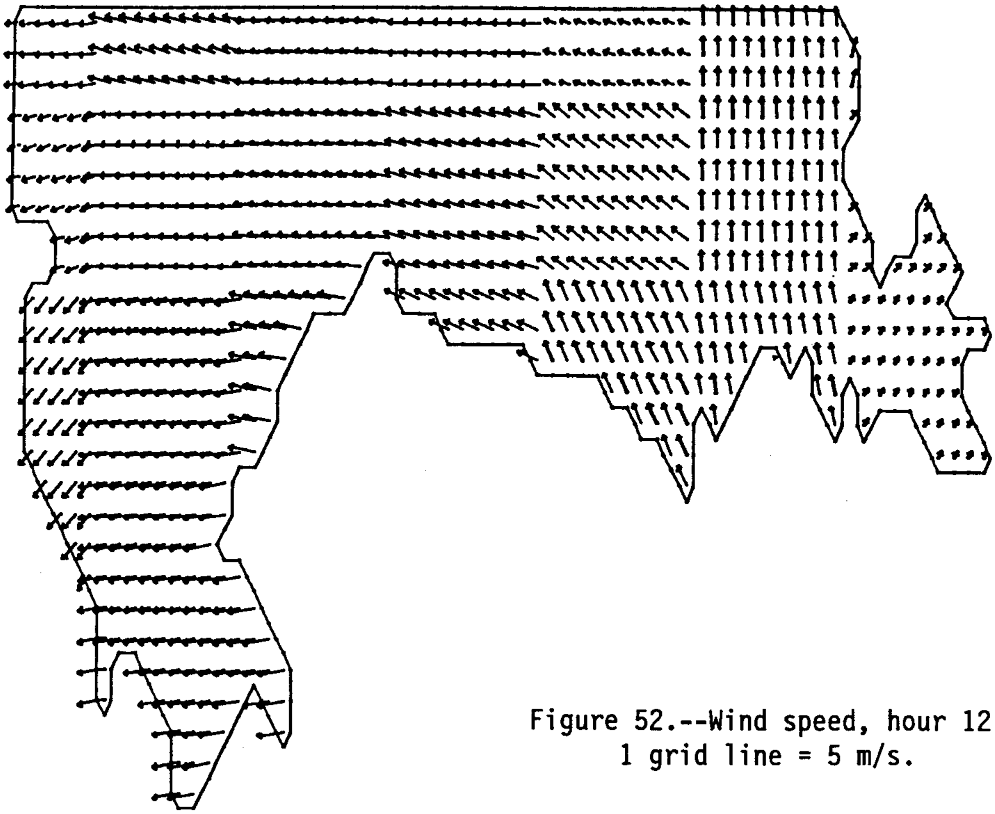

Figure 52.--Wind speed, hour 12;
1 grid line = 5 m/s.

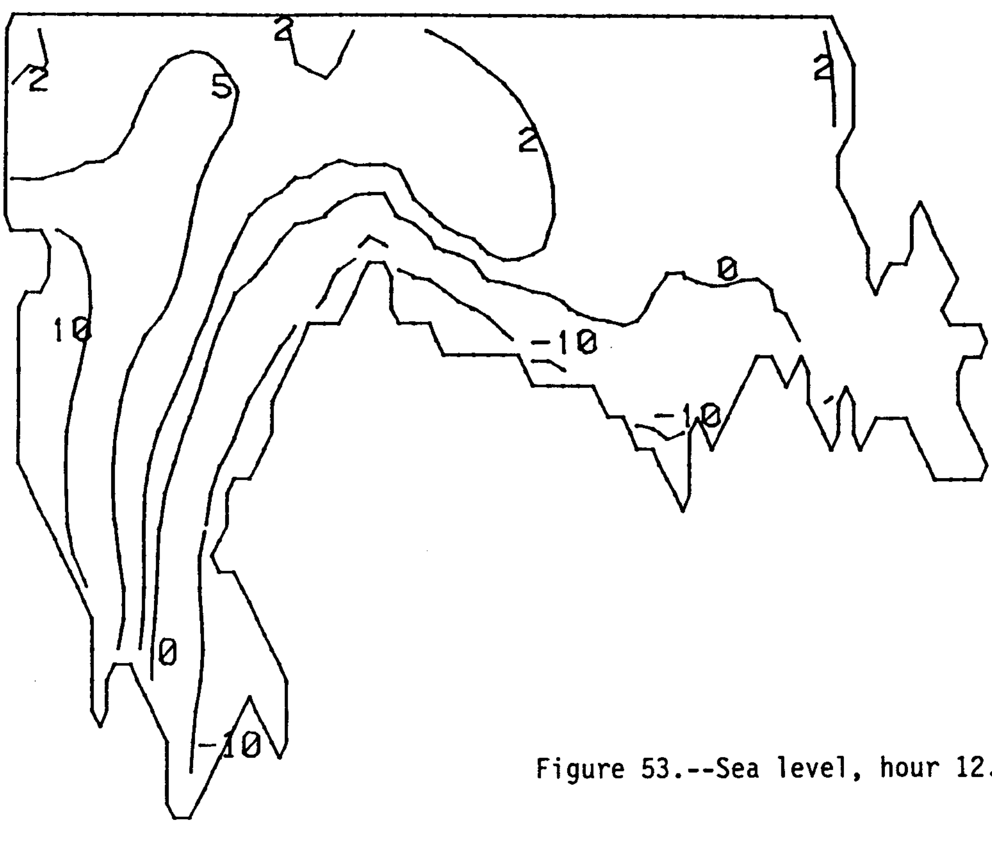

Figure 53.--Sea level, hour 12.

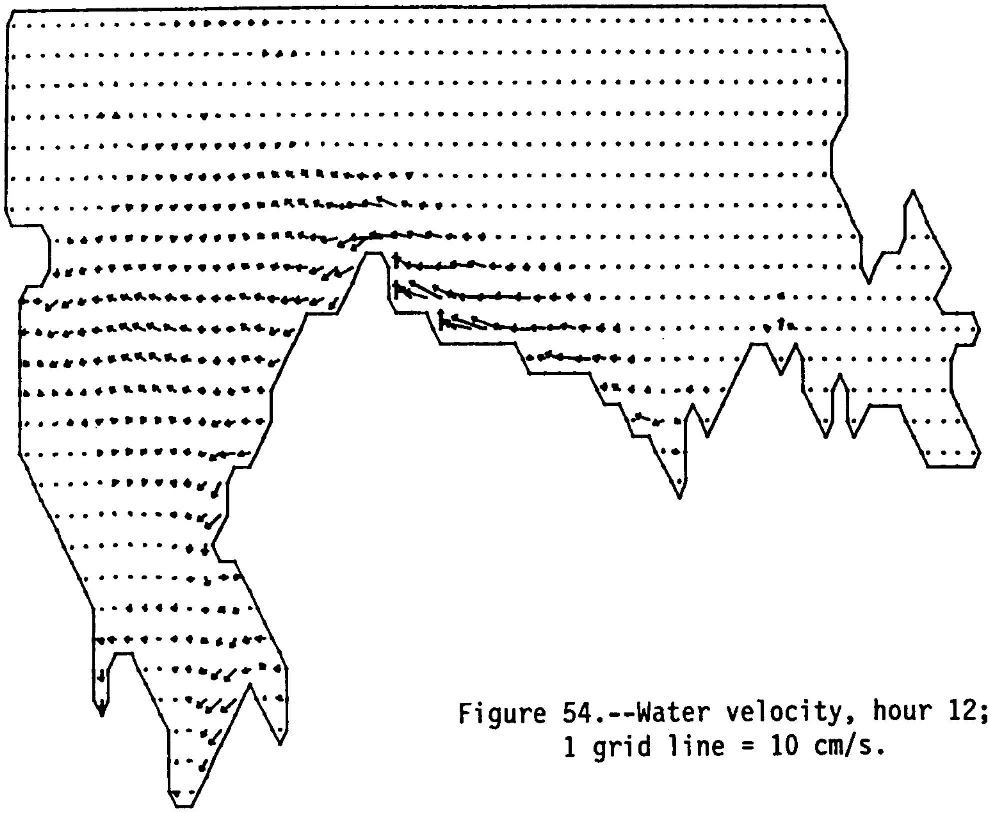

Figure 54.--Water velocity, hour 12;
1 grid line = 10 cm/s.

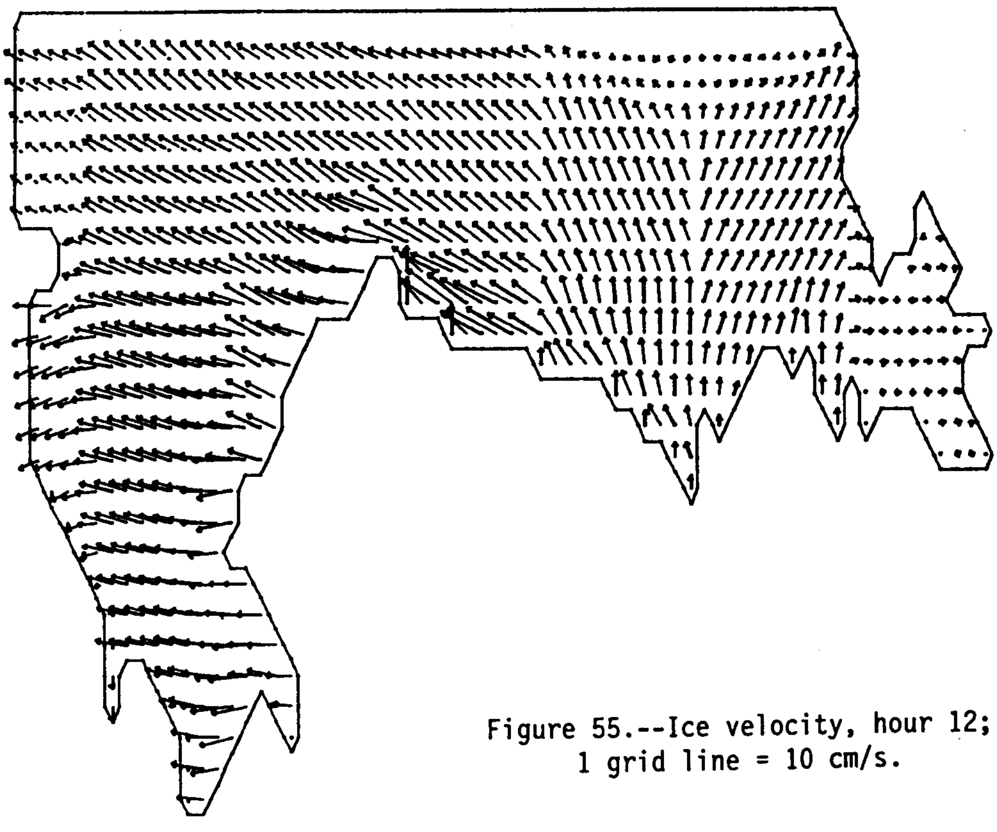

Figure 55.--Ice velocity, hour 12;
1 grid line = 10 cm/s.

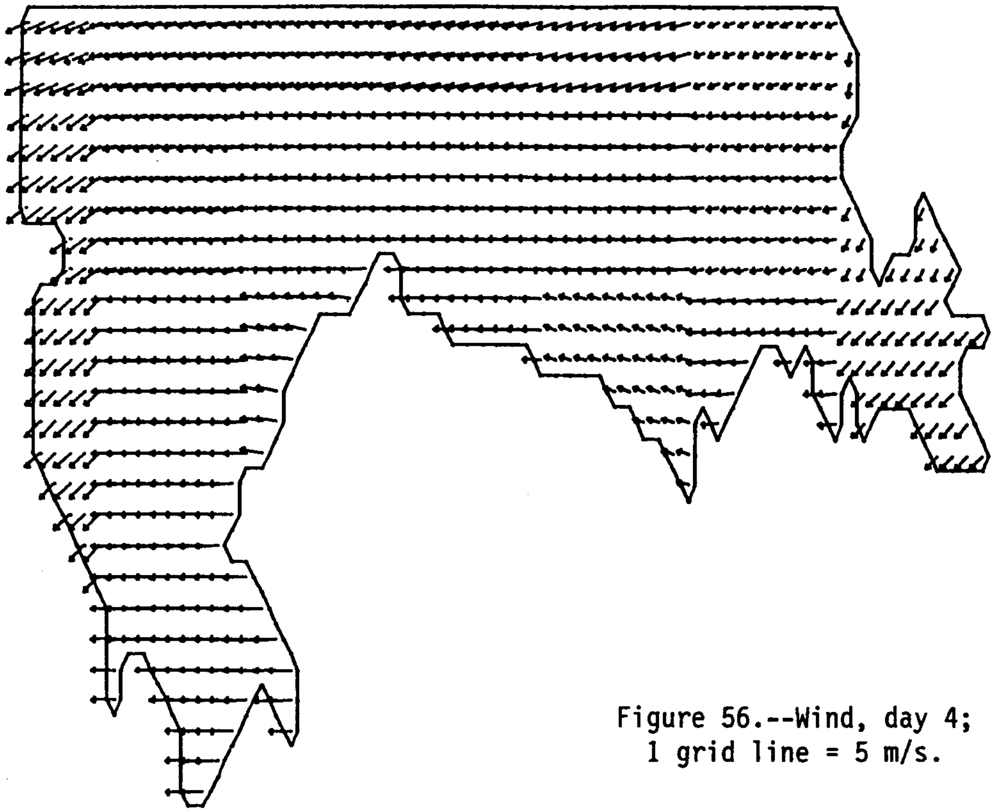

Figure 56.--Wind, day 4;
1 grid line = 5 m/s.

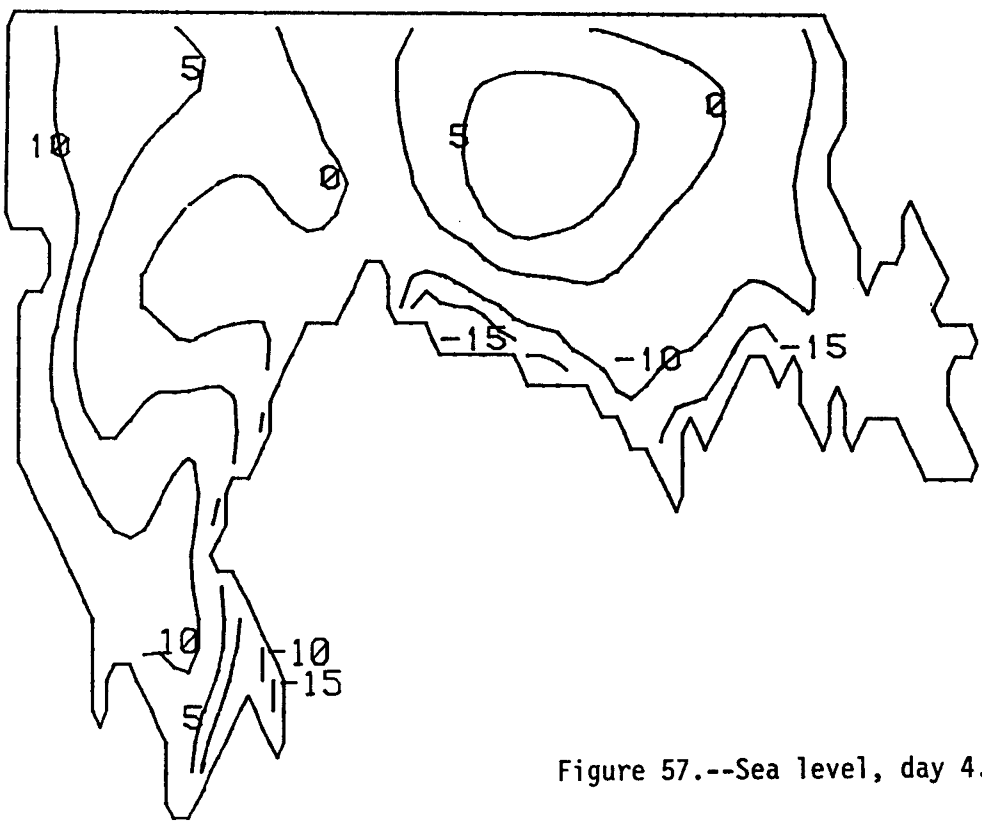

Figure 57.--Sea level, day 4.

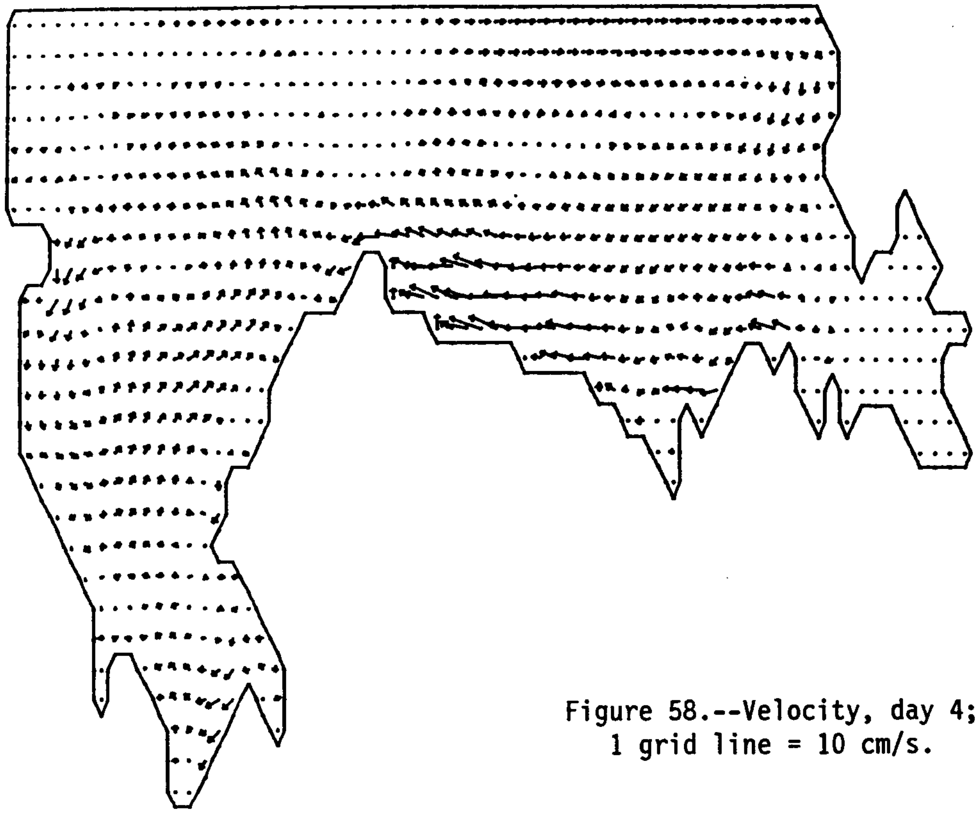

Figure 58.--Velocity, day 4;
1 grid line = 10 cm/s.

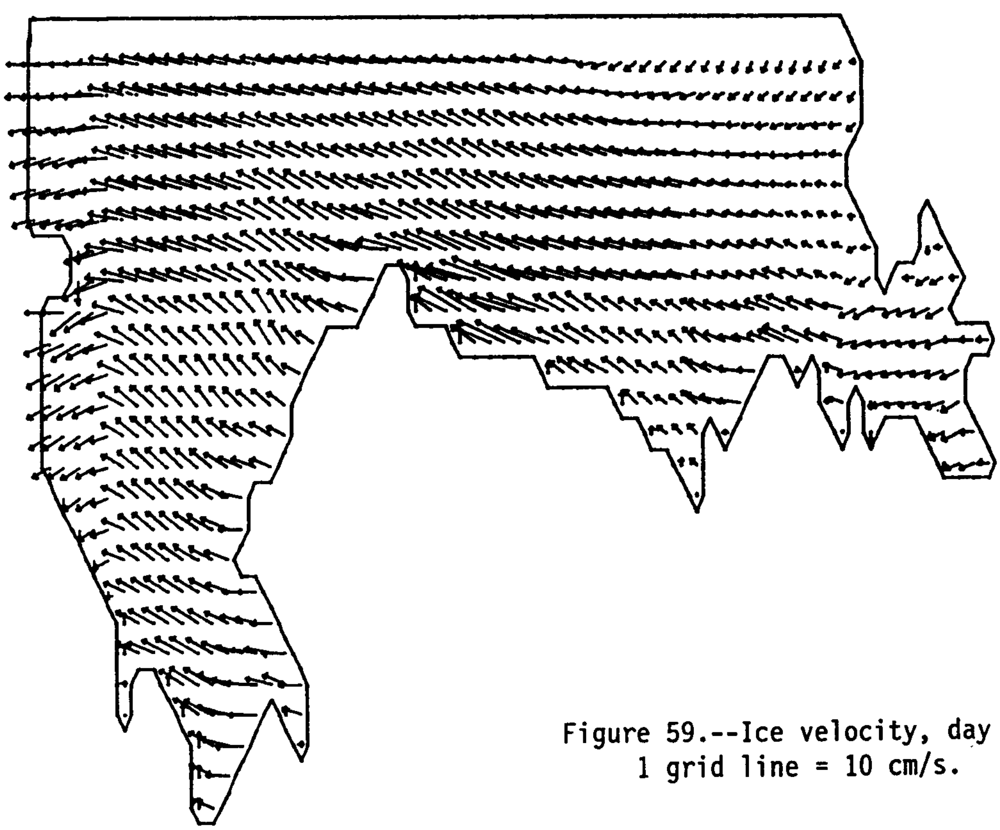

Figure 59.--Ice velocity, day 4;
1 grid line = 10 cm/s.

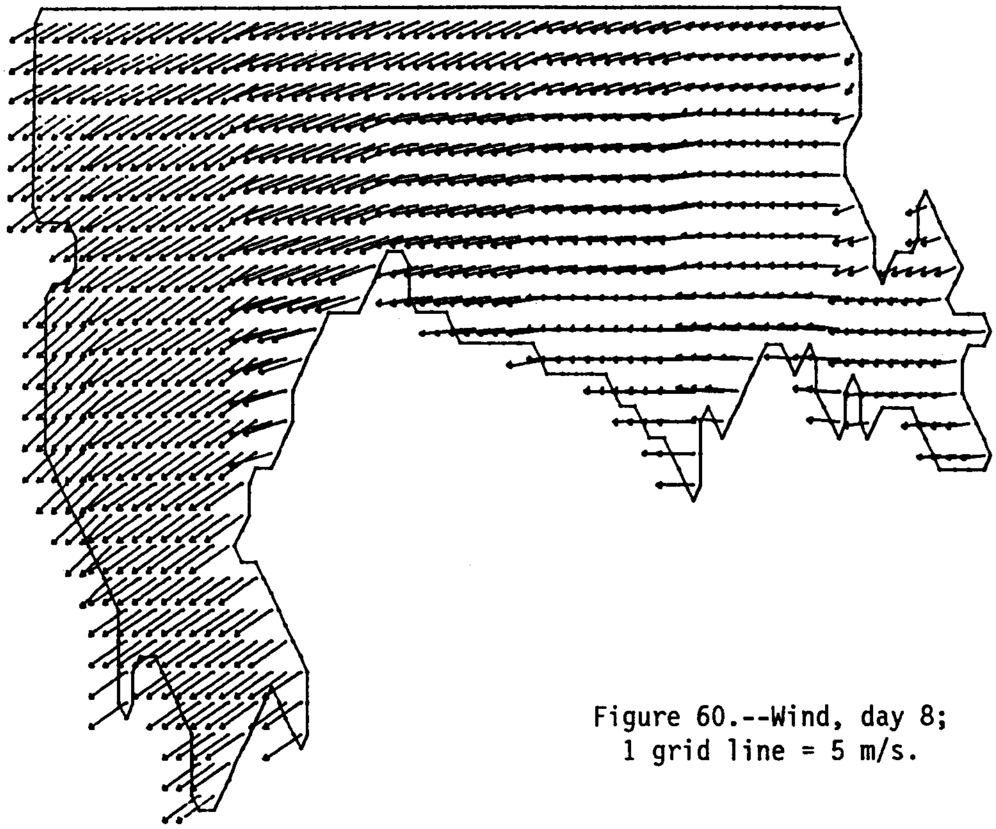

Figure 60.--Wind, day 8;
1 grid line = 5 m/s.

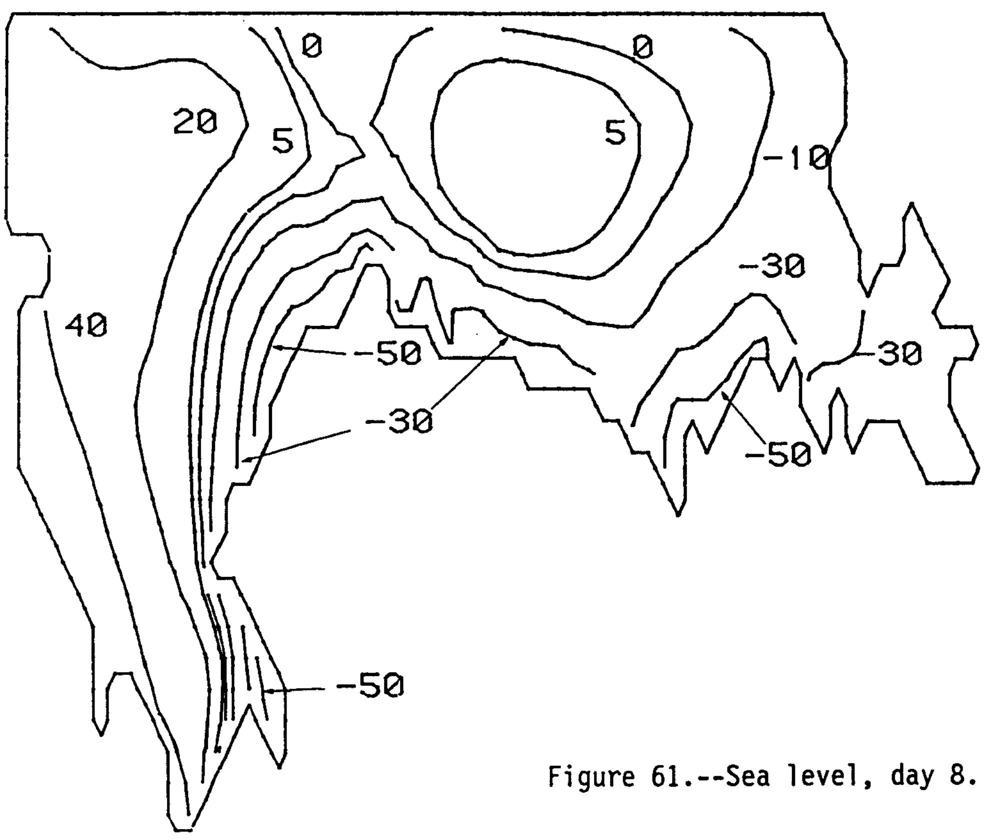

Figure 61.--Sea level, day 8.

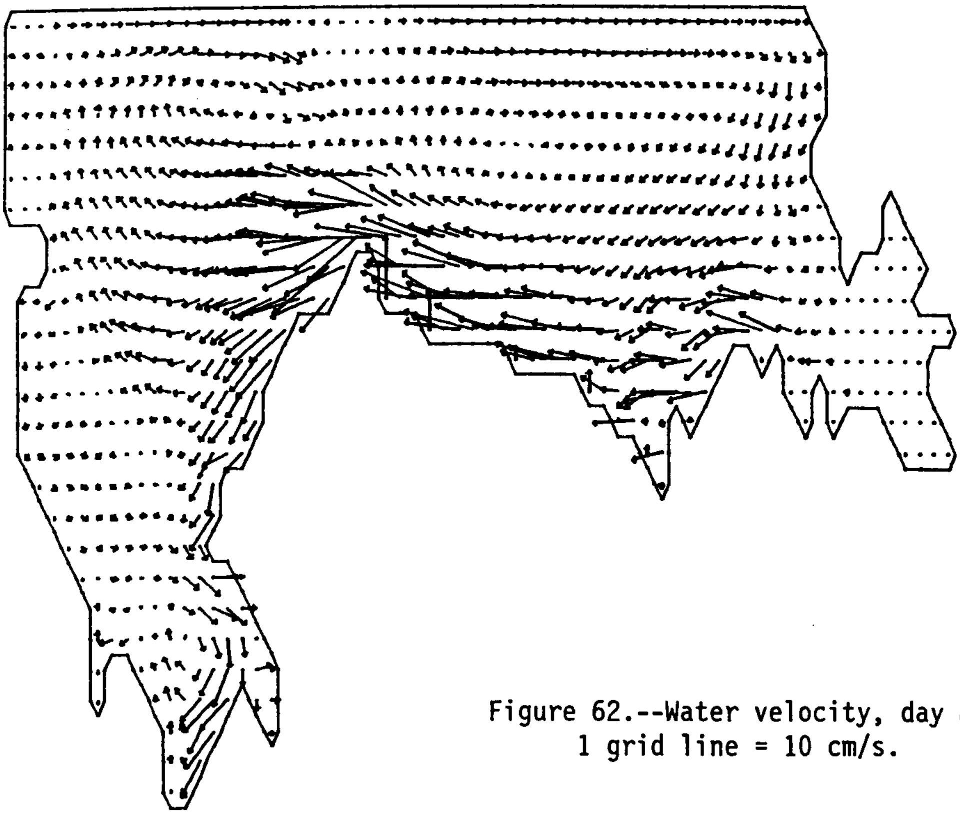

Figure 62.--Water velocity, day 8;
1 grid line = 10 cm/s.

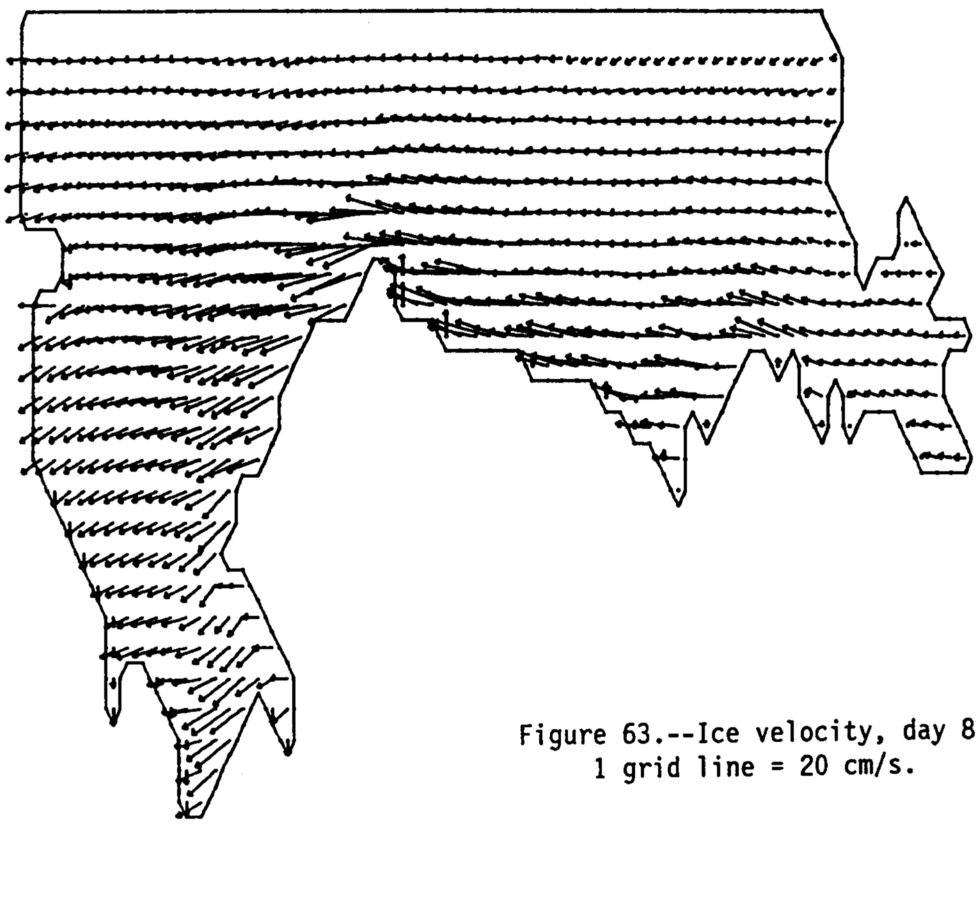

Figure 63.--Ice velocity, day 8;
1 grid line = 20 cm/s.

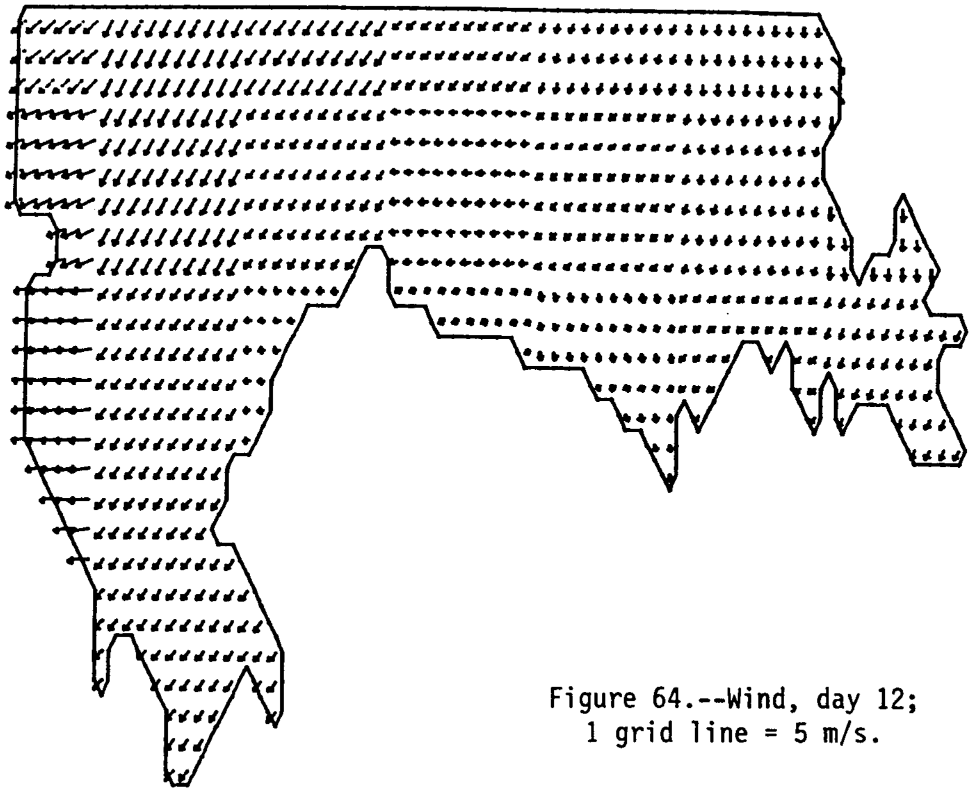

Figure 64.--Wind, day 12;
1 grid line = 5 m/s.

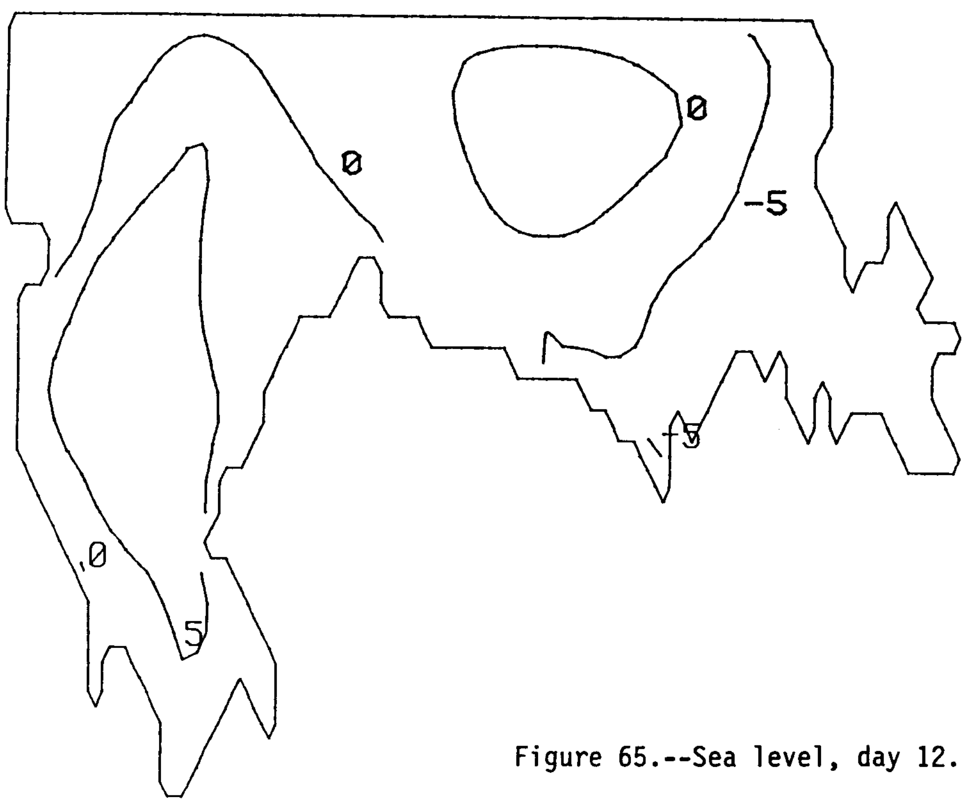

Figure 65.--Sea level, day 12.

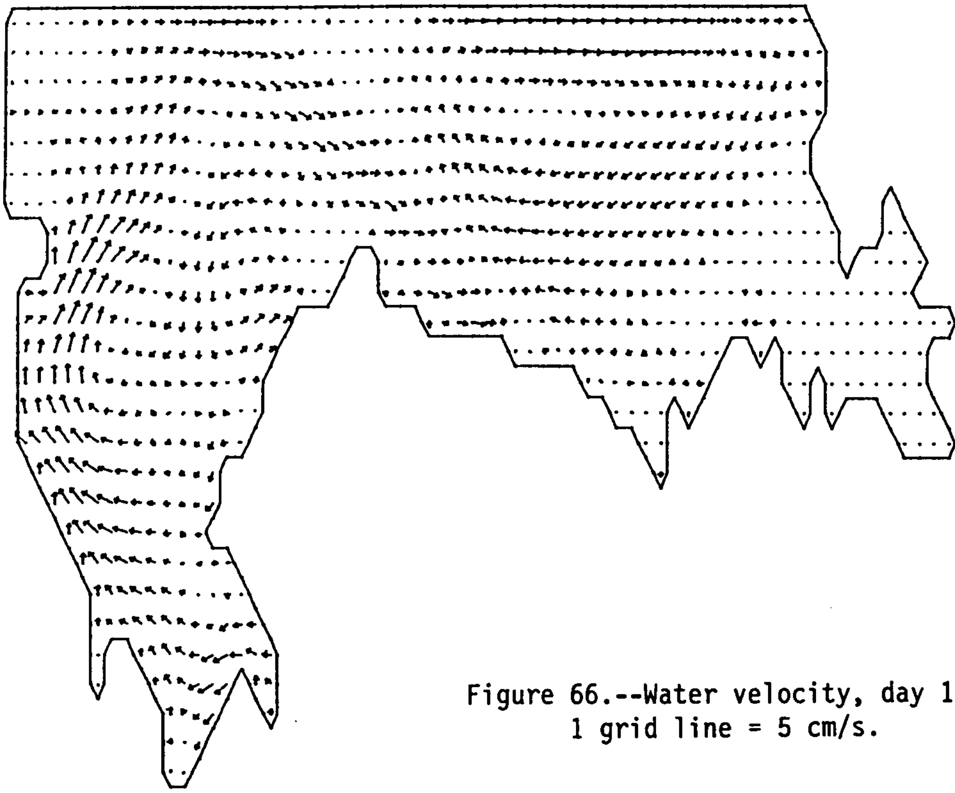

Figure 66.--Water velocity, day 12;
1 grid line = 5 cm/s.

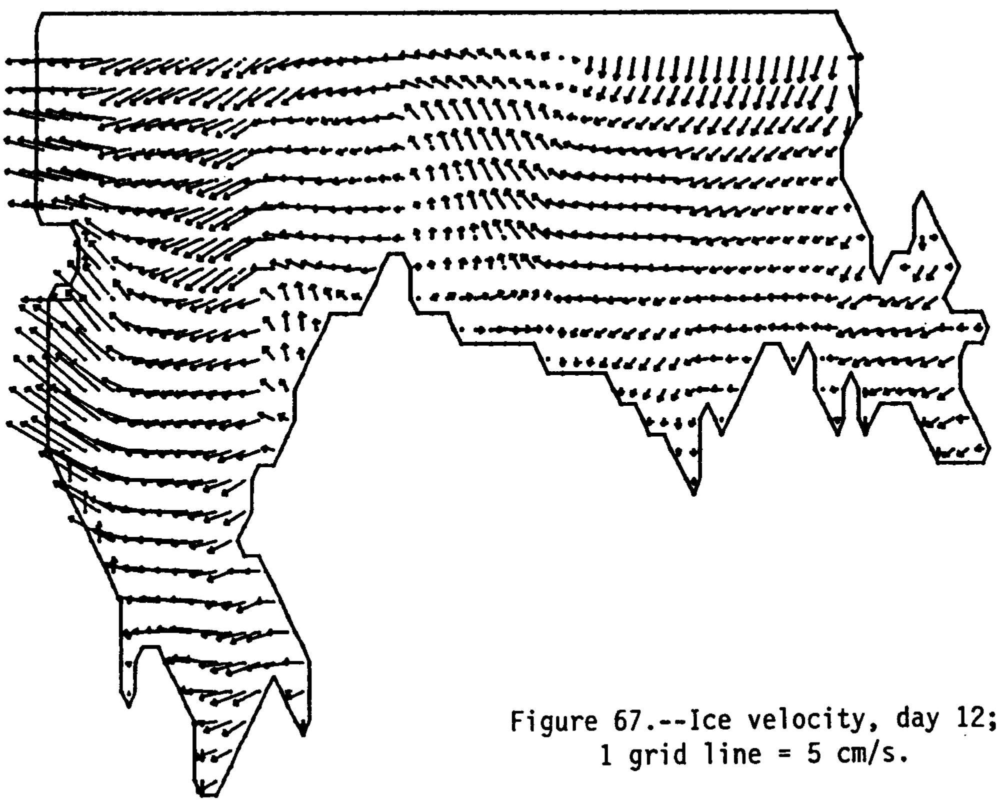

Figure 67.--Ice velocity, day 12;
1 grid line = 5 cm/s.

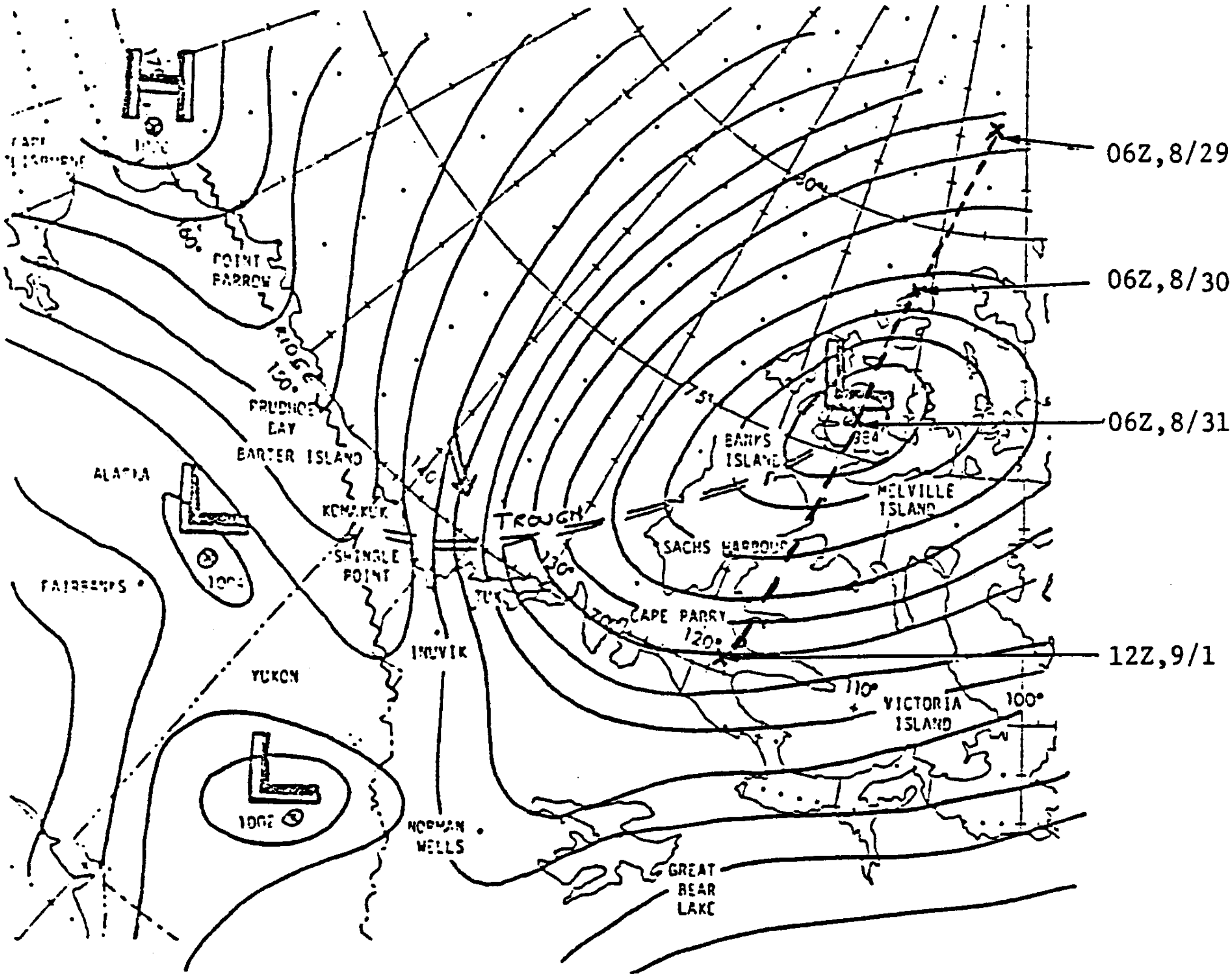

Figure 68.--Surface weather chart for 31 August 1981, 06Z. Pressure in millibars. Dashed line represents the track of the low. From Beaufort Weather and Ice Office 1981 Report.

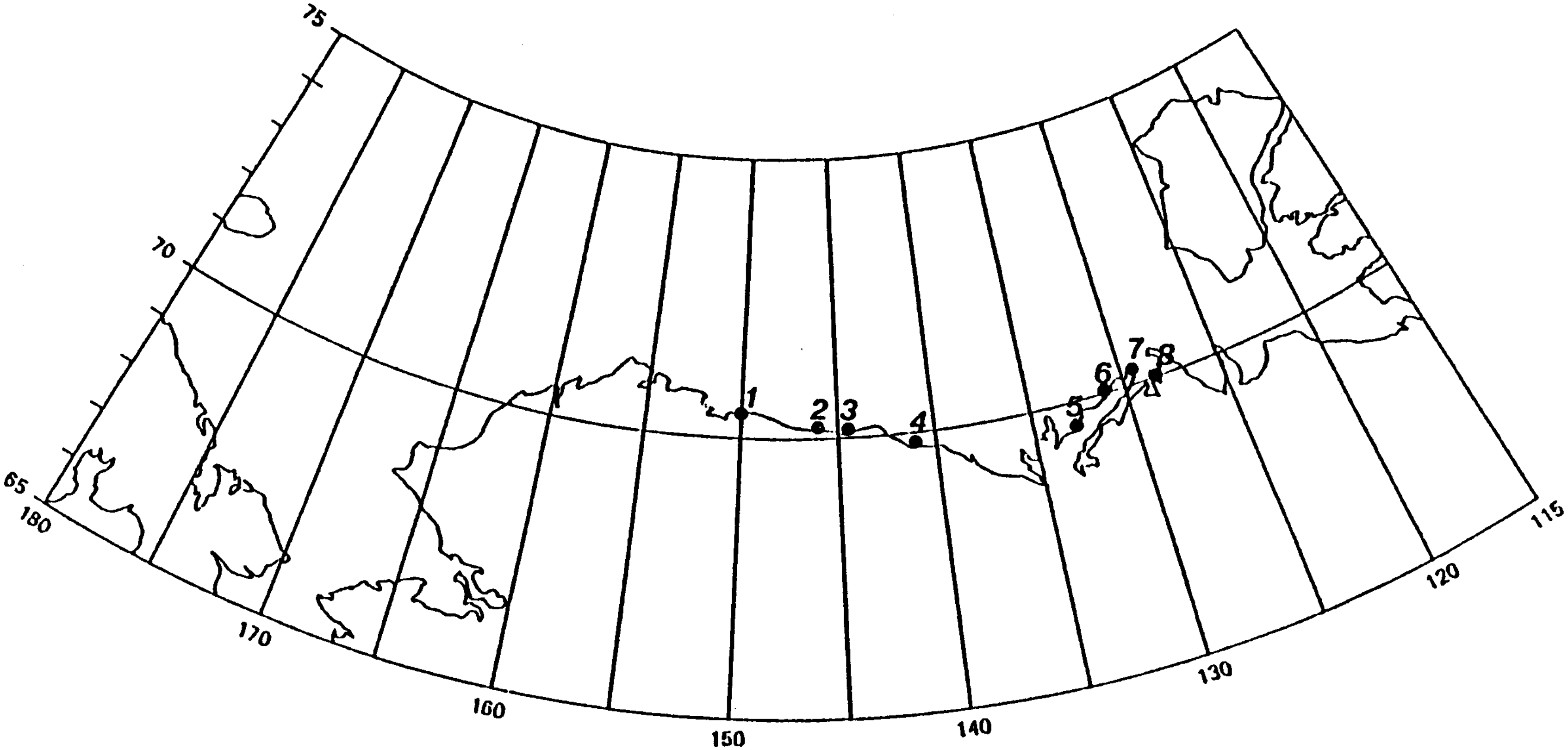

Figure 69.--Positions of the tide gauges deployed along the coast of the Beaufort Sea in August and October 1981: 1, Oliktok; 2, Flaxman Island; 3, Simpson Cove; 4, Demarcation Bay; 5, Tuktoyaktuk; 6, Atkinson Point; 7, Cape Dalhousie; and 8, Baillie Island.

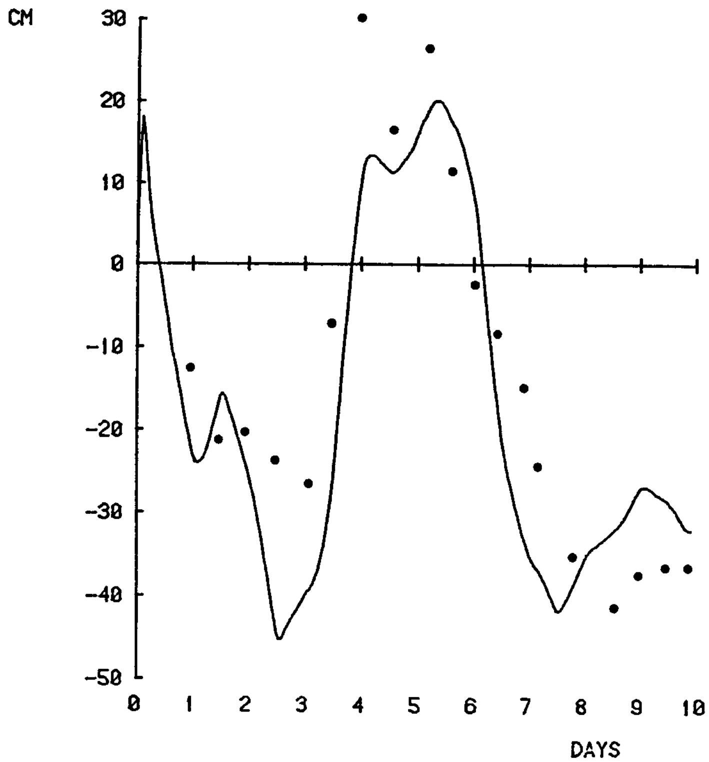

Figure 70.--Sea level variation, Oliktok.

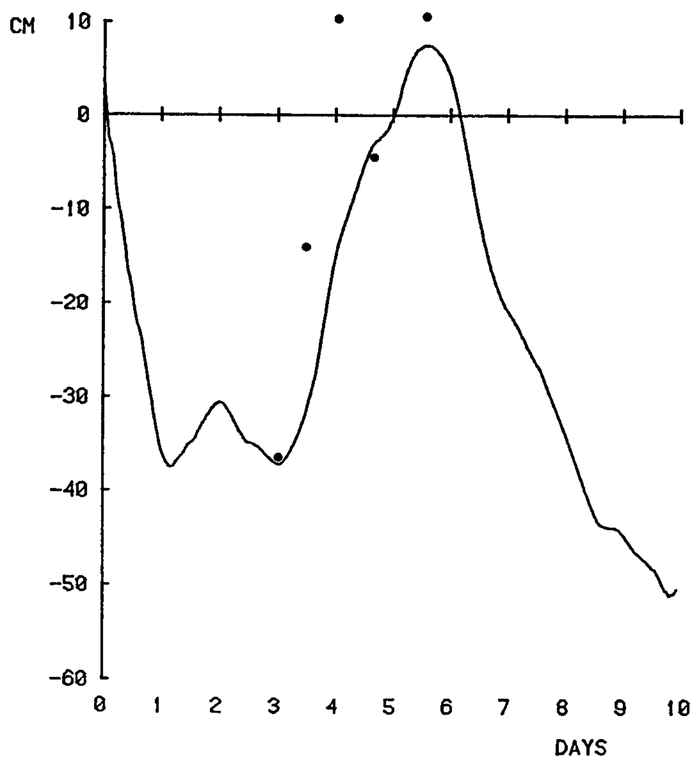

Figure 71.--Sea level variation, Flaxman Island.

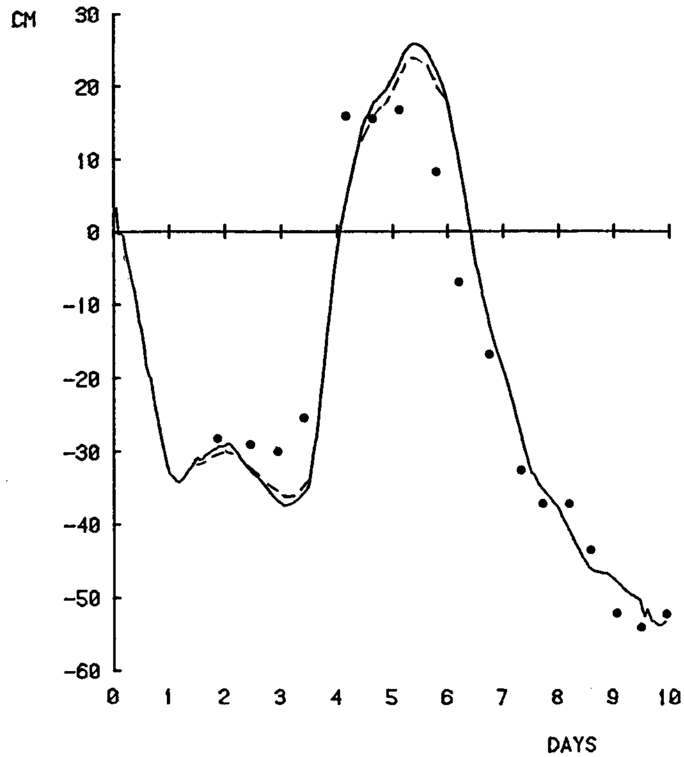

Figure 72.--Sea level variation, Simpson Cove.

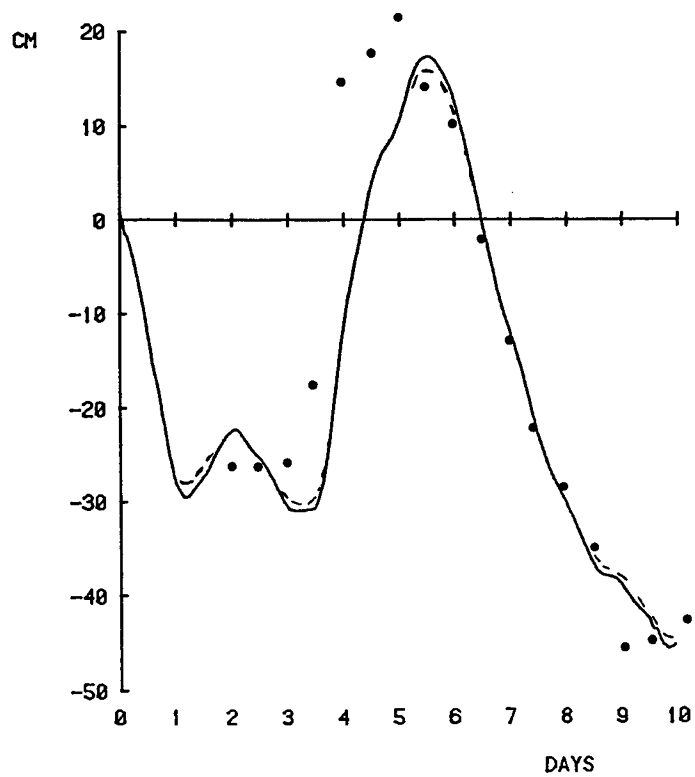

Figure 73.--Sea level variation, Demarcation Bay.

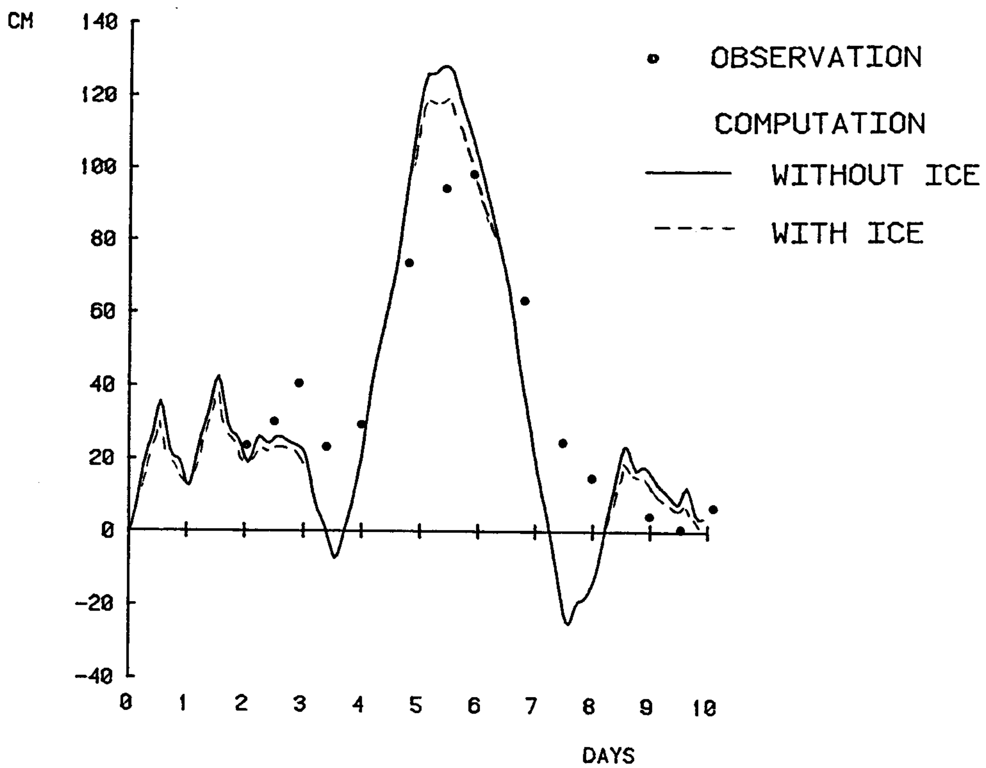

Figure 74.--Sea level variation, Tuktoyaktuk.

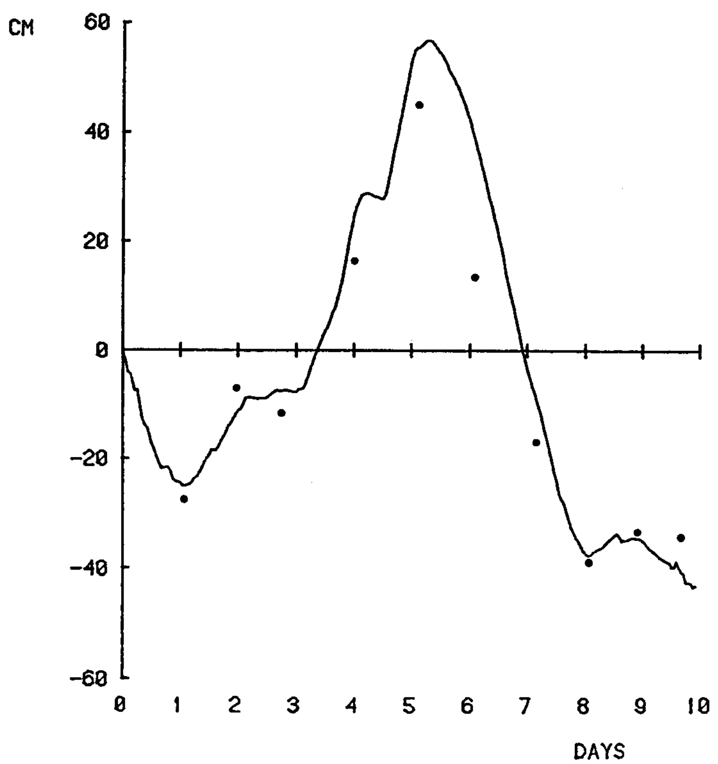

Figure 75.--Sea level variation, Atkinson Point.

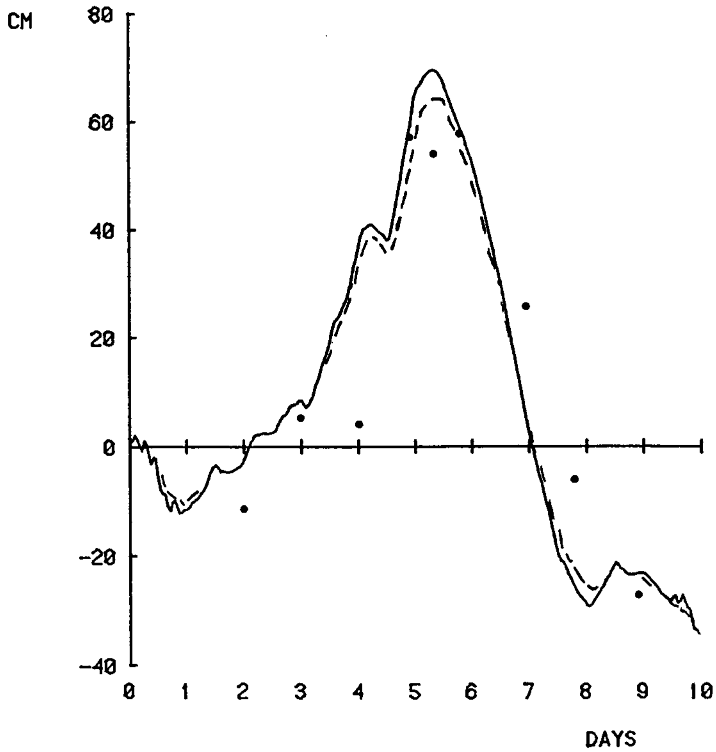

Figure 76.--Sea level variation, Cape Dalhousie.

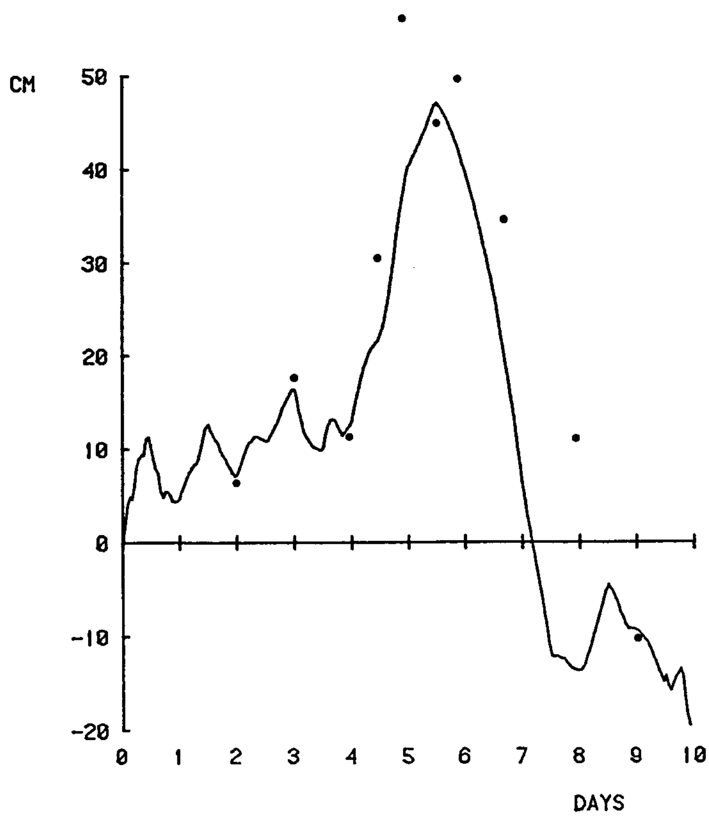

Figure 77.--Sea level variation, Baillie Island.

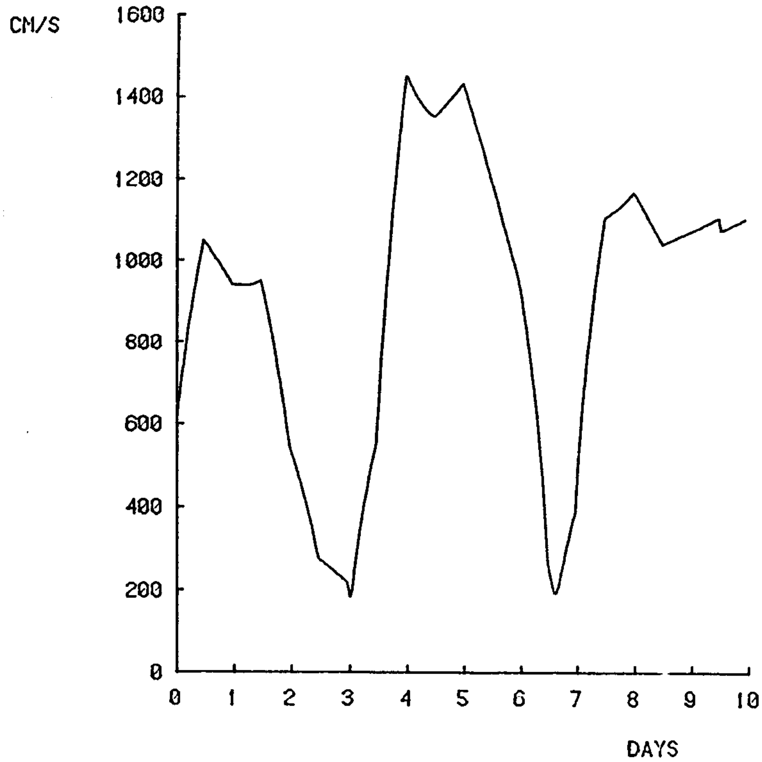

Figure 78.--Wind speed at 70°30'N, 135°30'W.

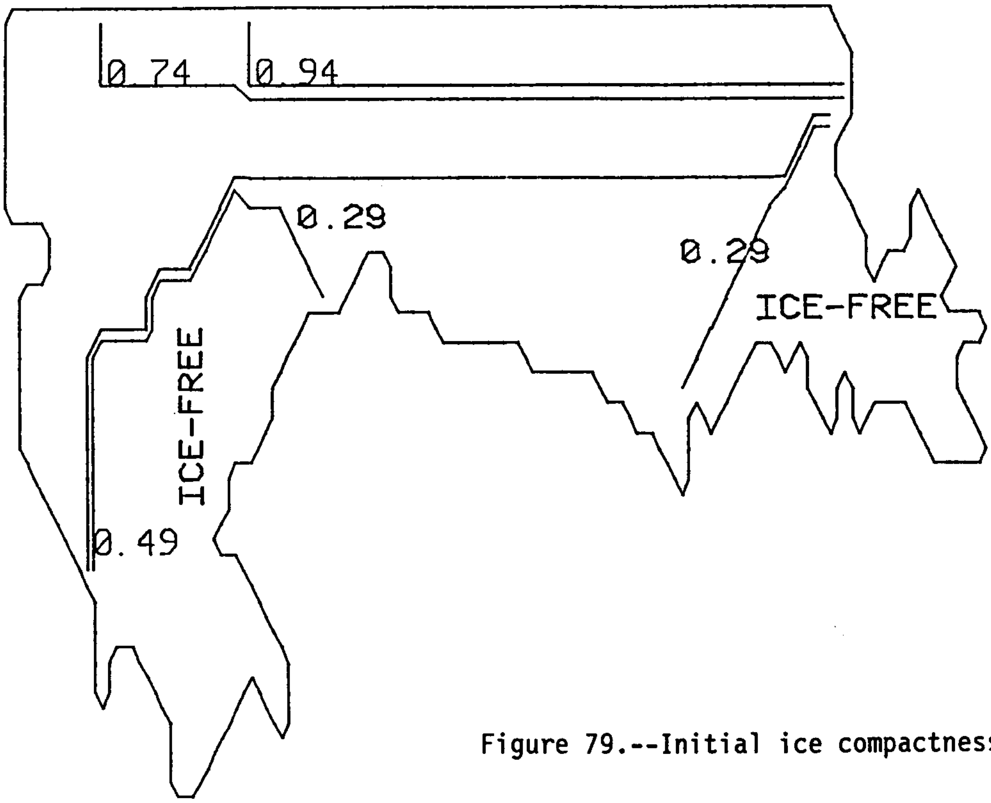

Figure 79.--Initial ice compactness.

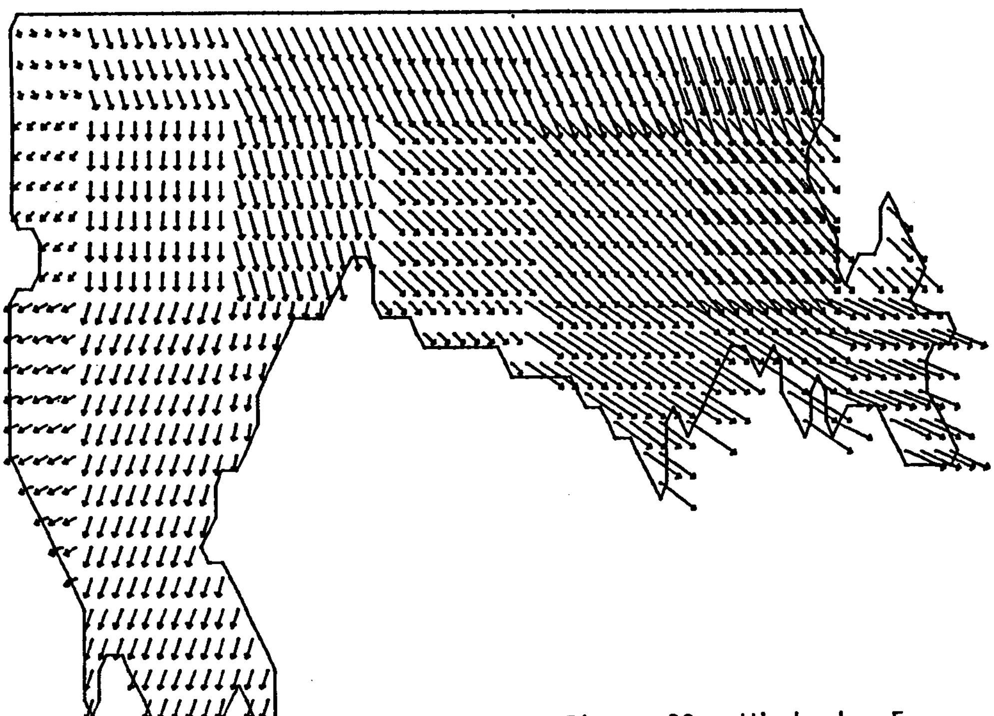

Figure 80.--Wind, day 5;
1 grid line = 5 m/s.

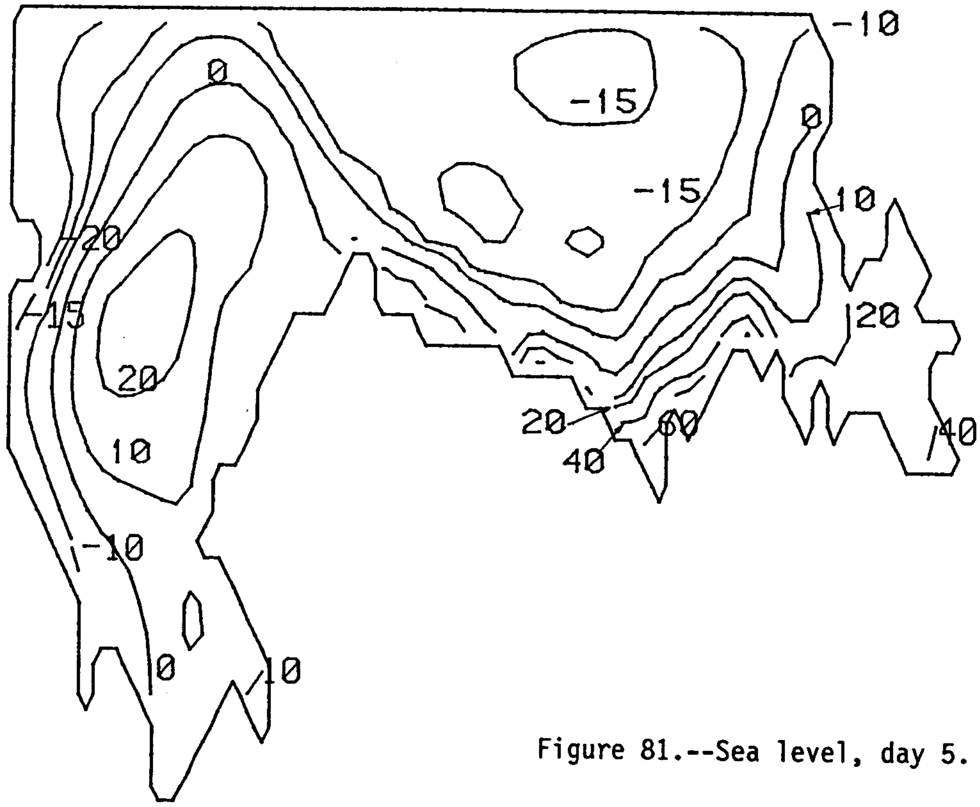

Figure 81.--Sea level, day 5.

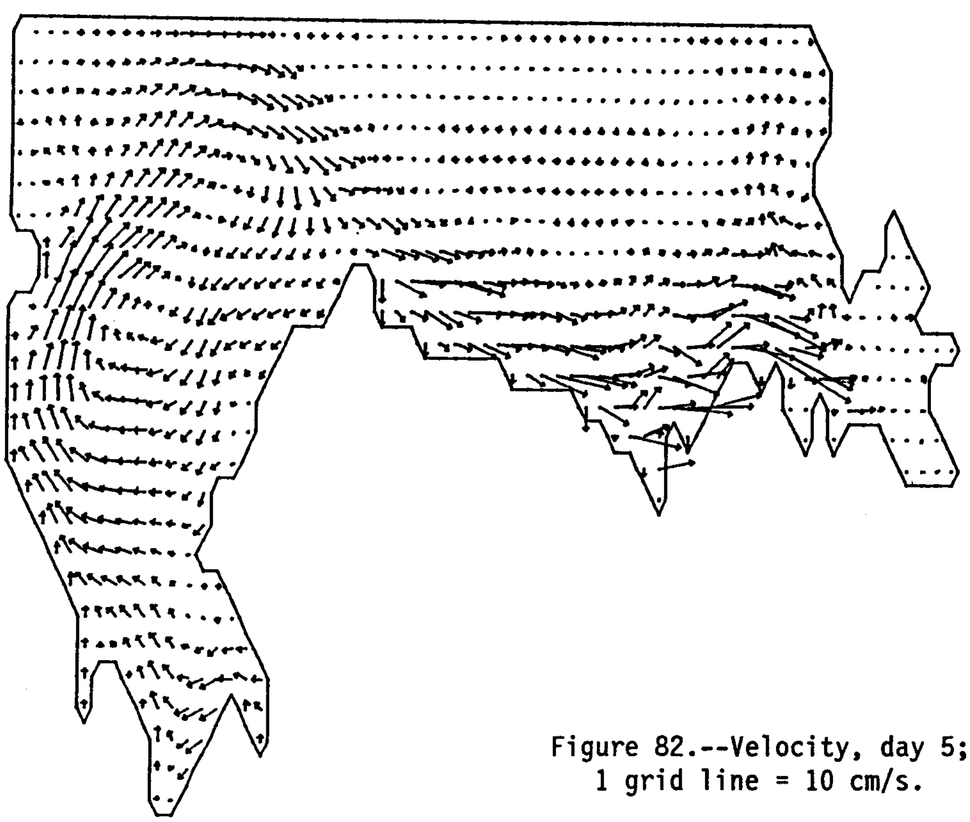

Figure 82.--Velocity, day 5;
1 grid line = 10 cm/s.

NUMERICAL MODELING OF STORM SURGES IN NORTON SOUND

by

Zygmunt Kowalik and Walter R. Johnson

Institute of Marine Science
University of Alaska
Fairbanks, Alaska 99701

Final Report
Outer Continental Shelf Environmental Assessment Program
Research Unit 627

July 1985

ACKNOWLEDGMENTS

We are grateful for the sea level data supplied to us by Drs. H. Mofjeld and J. Schumacher of NOAA/PMEL; J. Oswald of ITECH; and R. Mitchel, D. Bain, and S. Hamrick of the State of Alaska, Department of Natural Resources. We are indebted to Dr. W. Stringer for preparing charts of the ice distribution and discussion of essential features of ice motion in the Bering Sea and Norton Sound. This is the final report of OCSEAP Research Unit 627, Contract Number NA-84-ABC-00225.

ABSTRACT

Storm surges and associated water and ice motion are important considerations in offshore exploration for petroleum on the continental shelf. The shore of the Bering Sea in the Norton Sound region is generally of low relief, so coastal plains can be inundated by surge and waves. Knowledge of sea level variations along the Alaska coast is scant. Tide gauges have been operated in this region only at irregular intervals, and the present set of data is too small to estimate a statistically valid distribution of sea level variations. The goal of this project was to develop methods of predicting storm surges based on the equations of motion and continuity.

Specific problems of storm-surge modeling in the polar seas were analyzed. Vertically integrated equations of motion and continuity were applied to the prediction of storm-surge waves in both ice-free and ice-covered seas. The interactions of atmosphere, ice, and water were expressed by normal and tangential stresses. A numerical grid was established over the Bering Sea and Norton Sound and three storm-surges were simulated and briefly described. The Norton Sound area was investigated using an additional smaller scale model. Comparison of the measured and computed sea level and observed and computed ice velocities proves that the model is suitable to reproduce both water and ice motion.

TABLE OF CONTENTS

1. INTRODUCTION

The Bering Sea has one of the largest continental shelves in the world. Along this shelf during late summer and fall low pressure systems generate storm surge waves. Two regions of the Bering Sea are obvious candidates for large sea level variations, i.e., Bristol Bay and Norton Sound. Shallow Norton Sound, with an average depth of about 20 m, leads to strong amplification of the storm wave, especially in conjunction with west and southwest winds.

The knowledge of sea level changes caused by storm surges is quite modest in Norton Sound mainly due to the absence of any permanent tide gauges in this area. The frequency of major storms, when compared to the other regions of the Bering Sea, is rather low. Late summer and fall storms, if they generate south, southwest or northwest winds, can cause extensive flooding to the coastal areas of low relief surrounding Norton Sound. The main storm track during summer and fall is toward the north and northeast [*Brower et al.*, 1977]. Storm surges of as much as 4 m have occurred in this area and the most recent storm of such intensity was in November 1974 [*Fathauer*, 1978]. The most severe flooding occurred at Nome, where the damage sustained was estimated at $12 million. The low pressure system moved from the Aleutians to the Bering Sea. Winds as high as 75 knots were recorded. The extent of flooding were tracked by USGS through an observation of the driftwood and debris line after the storm [*Sallenger*, 1983]. This storm has been used as the wind forcing for one of the model cases (Section 4.4). Surges of 1 to 2 m regularly flood the Norton Sound area and cause serious problems to the coastal communities [*Wise et al.*, 1981]. Until now tide gauges were installed in this region only for short periods of time. Sea level data were recorded in Norton Sound during a sediment transport study in summer and fall 1977 [*Cacchione and Drake*, 1979]. The Yukon River discharges about 60 million tons of suspended matter per year into the Bering Sea [*Drake et al.*, 1980]. The fall storm surges are responsible for much of the transport and resuspension of the sediments derived from the Yukon.

In 1978 a set of sea level data was gathered over the shelf by *Schumacher and Tripp* [1979]. An extensive observational study of tides and tidal currents in the northeastern Bering Sea from November 1981 until August 1982 was conducted by NOAA/PMEL [*Mofjeld*, 1984]. At the same time, sea level was recorded at a nearshore station in Stebbins (R. Mitchel, personal comm.) — an area where fast ice usually occurs in winter. During 1982 ice drift motion was also studied from several ARGOS drifting ice platforms [*Reynolds and Pease*, 1984]. This set of diverse data gave a good opportunity to test our model, especially the influence of nearshore fast ice on the storm surge wave propagation.

Wise et al. [1981] compiled all available data on the storm surges and were able to identify 13 floodings at Nome and 10 at Unalakleet. Although the present set of data is too small to estimate a statistically valid distribution of the sea level variations, the statistics developed by *Wise et al.* [1981] may serve as a first approach to the prediction of the surge range.

The lack of knowledge on the sea level distribution can be modified by applying numerical modeling. Numerical models are useful because they provide a possibility to study the time-dependent distribution of sea level and vertically averaged current. *Leendertse and Liu* [1981] developed a three-dimensional model of Norton Sound to study the density and tide-driven motion. We have applied a model to study storm surge in the Norton Sound area based on a model previously tested in the Beaufort and Chukchi Seas [*Kowalik and Matthews*, 1982; *Kowalik*, 1984]. To drive the storm surge model, suitable wind data are required; we used the surface pressure charts to compute the geostrophic and surface winds. First, geostrophic wind was computed from the atmospheric pressure, then the "true" wind was computed by application of empirical coefficients [*Albright*, 1980; *Walter and Overland*, 1984].

In the polar regions, ice cover impedes the transfer of momentum from the atmosphere to the ocean thus influencing the spatial and temporal distribution of the storm surges [*Henry*, 1974]. Therefore, while developing a storm surge model for the Beaufort and Chukchi Seas, a scheme to include ice cover was developed. Various constitutive laws to describe sea ice, proposed by *Coon et al.* [1974] and *Hibler* [1979], contain both mechanical and thermal properties of ice. A storm surge is a phenomenon of short duration. In such cases thermal properties of ice growth and decay can be neglected and only ice mechanics needs to be considered. Therefore, for storm surge modeling, a simpler constitutive law has been implemented, as proposed by *Doronin* [1970]. Ice motion in Norton Sound has been studied by *Stringer and Henzler* [1981]. Direct comparison of the ice motion observed through the satellite imagery with the ice movement computed by the model seems to be the best approach to validate this segment of the model. Unfortunately, the acquisition of the cloud-free images during storms has a rather small probability.

Air-ice interaction has been studied both from ice floe stations and aircraft. *Macklin* [1983] reported a wind drag coefficient over ice of

3.1×10^{-3}. Measurements by *Walter and Overland* [1984] gave a similar value for the drag coefficient. These values are among the largest for the polar seas [*Leavitt*, 1980].

The steady-state slab models of the wind-driven ice drift developed for the Bering Sea shelf by *Pease and Overland* [1984] and *Overland et al.* [1984] show a very good correlation with the observed ice motion. Through the application of these models it has been established that the influence of the bathymetry on the wind-drift of ice in shallow seas is constrained to water depth less than 30 m.

Storm surges occur together with astronomical tides and therefore it is essential to understand the tide distribution. The tide distribution in the Norton Sound is known approximately through the observations and numerical modeling [*Pearson et al.*, 1981; *Mofjeld*, 1984]. A tidal range of the order of 1 m to 1.5 m can be expected. The semidiurnal (M_2) component has an amphidromic point in the Norton Sound, therefore the diurnal components dominate tidal regime.

2. FORMULATION OF BASIC EQUATIONS

The basis for calculations is the vertically integrated equations of water motion and continuity, written in the Cartesian coordinate system $\{x_i\}$, with x_1 directed to the east and x_2 directed to the north:

$$\frac{\partial u_i}{\partial t} + \varepsilon_{ij} u_j + \frac{\partial}{\partial x_j}(u_i u_j) = - g \frac{\partial \zeta}{\partial x_i} - \frac{1}{\rho_w} \frac{\partial P_a}{\partial x_i} + \frac{(1-c)\tau_i^a}{H\rho_w} + \frac{c\tau_i^w}{H\rho_w} - \frac{\tau_i^b}{\rho_w H} + A \frac{\partial^2 u_i}{\partial x_j^2} \tag{1}$$

$$\frac{\partial \zeta}{\partial t} + \frac{\partial (H u_i)}{\partial x_i} = 0 \tag{2}$$

The ice motion induced by wind is studied through the following equations of motion [*Rothrock*, 1975];

$$m \frac{\partial v_i}{\partial t} + m \frac{\partial}{\partial x_j}(v_i v_j) + m\, \varepsilon_{ij} v_j = - mg \frac{\partial \zeta}{\partial x_i} - hc \frac{\partial Pa}{\partial x_i} + c\,(\tilde{\tau}_i^a - \tau_i^w) + F_i \tag{3}$$

Rate of change of the ice mass (m) over a specific area is equal to the net influx of mass to that area plus all sources and sinks (ϕ) [*Rothrock*, 1970]. The equation of continuity for the ice mass consistent with the above considerations is;

$$\frac{\partial m}{\partial t} + \frac{\partial (m v_i)}{\partial x_i} = \phi$$

In the above equations the following notation is used;

- i,j - indices ($i,j = 1,2$) where 1 stands for east coordinate, and 2 for north coordinate;
- t - time;
- u_i - components of the water velocity vector;
- v_i - components of the ice velocity vector;
- τ_i^a - components of the wind stress vector over the sea;

$\tilde{\tau}_i^a$ - components of the wind stress vector over the ice;

τ_i^w - components of the water stress;

τ_i^b - components of the bottom stress;

F_i - components of the force due to internal ice stress;

P_a - atmospheric pressure;

ε_{ij} - Coriolis tensor;

ζ - variation of the sea level or the ice around the undisturbed level;

c - ice compactness; $0 \leqslant c \leqslant 1$;

H - water depth;

ρ_w - water density;

A - lateral eddy viscosity, usually will be taken as 5×10^8 cm^2/s;

m - ice concentration or mass per unit area;

h - ice thickness;

g - gravity acceleration.

Einstein's summation convention is applied throughout all indexed expressions. The variables and coefficients in the equations are expressed in CGS units.

Assuming that the ice is not spread evenly over the whole sea surface, the mass of ice can be expressed through the ice compactness (c), ice thickness (h), and ice density (ρ);

$$m = \rho hc \tag{5}$$

A storm surge is a phenomenon of a relatively short duration, therefore thermodynamic sources and sinks linked to ϕ in equation (4) can be neglected. The equation of mass balance can be divided into two separate equations, i.e., a continuity equation for the ice compactness and an equation of thickness balance;

$$\frac{\partial c}{\partial t} + \frac{\partial (v_i c)}{\partial x_i} = 0 \tag{6}$$

$$\frac{\partial h}{\partial t} + v_i \frac{\partial h}{\partial x_i} = 0 \tag{7}$$

Both equations (4) and (6) are applied along with equations (1) through (3) to obtain the ice mass and the ice compactness distributions. It is reasonable to assume that when the ice is not packed closely ($c<1$) the ice thickness is not changed due to the ice motion. If, on the other hand due to internal ice stress, the ice compactness will grow beyond $c=1$, the excess of compactness will lead to a change of the ice thickness. In such a case the new ice thickness distribution is computed through equation (5).

To derive a solution to equations (1) through (6), suitable boundary and initial conditions must be stated. Among all possible sets of the boundary conditions, the one chosen should lead to a unique solution to the above system of equations. Such a set of conditions is still undefined for the ice-ocean interaction, therefore we shall assume (since the ice flow equations are analogous to the water flow equations) that the specification of the normal and tangential velocities along the boundaries is sufficient to derive the unique solution [*Marchuk et al.*, 1972]. Usually on the open boundaries (i.e., water boundaries) the storm surge velocity distribution is unknown. To overcome this hindrance the conditions on the open boundary are specified for the sea level and instead of a parabolic problem, a new problem is formulated in which the horizontal exchange of momentum is neglected. This simplified problem is solved along the open boundary to define velocity distribution. Having defined the velocity at the boundary, the solution of the complete system of equations is sought.

3. NUMERICAL MODELING: AREA, GRID, BOUNDARY CONDITIONS AND NUMERICAL SOLUTION

The main modeling effort is confined to Norton Sound (Fig. 1). The Norton Sound model has three open boundaries (broken lines); in the Bering Strait, between Siberia and St. Lawrence Island, and between St. Lawrence Island and Alaska. The grid intervals of the numerical lattice are 1/6 of a degree of latitude and 1/2 degree of longitude. To check the validity of the model with the open boundaries we also compute the storm surges throughout the Bering Sea area with a larger numerical grid spacing of 0.5 degree of latitude and 1.5 degree of longitude (Fig. 1). The application of the radiation condition by *Reid and Bodine* [1968] and the modified versions by *Camerlengo and O'Brien* [1980], and *Raymond and Kuo* [1984] lead to a distorted sea level distribution in Norton Sound. Such behavior of the solution may be related to the depth distribution since the average depth of Norton Sound is about 20 m and the open boundaries of the numerical model were located at the 30- to 50-m depth.

Normally, in a storm surge computation, the radiating boundary is situated beyond the shelf break (and/or far away from the region of interest) and the comparison of calculated and measured sea level in the shelf zone is quite satisfactory. The radiation condition is applied to waves generated inside the domain of integration. In those instances when only certain portions of the shelf are considered, waves generated outside the domain may influence the solution. Therefore, to solve the equations of water motion and continuity in Norton Sound, first, the solution for the entire Bering Sea is calculated. Then the distribution of velocity and sea level at the open boundary of the refined model is defined by linear interpolation from the results of those calculations.

Numerical solutions to equations (1)-(6) were obtained by applying an explicit-in-time and staggered-in-space numerical scheme proposed by *Hansen* [1962]. Internal ice stresses (F_i) in the equations of motion are expressed by a linear viscous model

$$F_i = \eta \frac{\partial^2 v_i}{\partial x_j \partial x_j} \quad m \tag{8}$$

with the magnitude of kinematic viscosity coefficient ranging from $5 \cdot 10^8$ cm^2/s to $5 \cdot 10^{12}$ cm^2/s. For large viscosity coefficient the explicit scheme is unstable [*Kowalik*, 1981]. Therefore, to model fast ice (which is parameterized by a large value of viscosity coefficient), a modified scheme of numerical computation, unconditionally stable in time, has been introduced. We shall explain the approach only for the one component of equation (3). The time variations of the E-W component of ice velocity caused by internal stresses are expressed by

$$\frac{\partial v}{\partial t} = \eta \left(\frac{\partial^2 v}{\partial x_1^2} + \frac{\partial^2 v}{\partial x_2^2} \right) \tag{9}$$

(where v_1 is changed to v).

To integrate numerically the above equation, the time step T and space lattice with step h is introduced. Independent variables t, x_1, and x_2 are expressed as t = KT, x_1 = Lh, x_2 = Mh, and the numerical form of (a)

$$\begin{aligned} \frac{v_{L,M}^{K+1} - v_{L,M}^{K}}{T} = {} & \frac{\eta}{h} \left(\frac{v_{L+1,M}^{K} - v_{L,M}^{K}}{h} - \frac{v_{L,M}^{K+1} - v_{L-1,M}^{K+1}}{h} \right) \\ & + \frac{\eta}{h} \left(\frac{v_{L,M+1}^{K} - v_{L,M}^{K}}{h} - \frac{v_{L,M}^{K+1} - v_{L,M-1}^{K+1}}{h} \right) \end{aligned} \tag{10}$$

is the advancing solution in time from $t = KT$ to $t = (K+1)T$. This numerical scheme is unconditionally stable for any (positive) η. The actual computation is explicit although the values $v_{L-1,M}^{K+1}$ and $v_{L,M-1}^{K+1}$ seem to be unknown. The process of computation usually takes place along increasing values of indices L and M, thus when the solution is sought at the point (L,M) the new values of variable v are already known at the points (L,M-1) and (L-1,M).

To advance the solution in time, the following explicit formula is used:

$$v_{L,M}^{K+1} = \left\{\frac{\eta T}{h^2}\left[v_{L+1,M}^{K} + v_{L-1,M}^{K+1} + v_{L,M+1}^{K} + v_{L,M-1}^{K+1} - 2v_{L,M}^{K}\right] + v_{L,M}^{K}\right\} \Big/ \left(1 + \frac{2\eta T}{h^2}\right) . \tag{11}$$

The method presented above is closely related to the angle derivative method [*Roache*, 1972].

The influence of fast ice on the storm wave is studied through a linear viscous model of the ice internal stress. The difference between the pack ice and fast ice will be expressed through the different values of the viscosity coefficient η.

Through a comparison of the ice drift motion of the ARGOS stations set on the pack ice and the drift computed by the model, we found that for a compactness of 0.7 to 0.8 the viscosity coefficient (η) ranged from $5 \cdot 10^8$ cm^2/s to $5 \cdot 10^9$ cm^2/s.

To define the ice friction coefficient suitable for the storm surge propagation in the fast ice, the magnitude of the coefficient which will cause the ice velocity to be nearly zero must be determined. A series of experiments was carried out with the whole area of Norton Sound covered by fast ice ($c = 1$) and applying a friction coefficient from the range $1 \text{ cm}^2/\text{s}$ to $5 \times 10^{12} \text{ cm}^2/\text{s}$. Friction through the viscous stresses suppresses the ice motion and when the ice friction coefficient attains $10^{12} \text{ cm}^2/\text{s}$, the ice motion is stopped (Fig. 2). Because water motion depends on the energy transfer from the atmosphere to the water through the ice cover, the high values of ice friction coefficient and ice compactness $c = 1$, lead to suppression of the water motion as well. The motion decreased faster at the nearshore location (Stebbins) than in the open sea region (NC17) probably due to the higher bottom friction. Fast ice never covered the whole Norton Sound area but only a narrow nearshore band, therefore the damping of the surge wave under the pack ice was only partial.

In the process of computation, instabilities are generated because of the explicit numerical formulas for the stress between ice and water. This occurs only if the velocity of ice or water attains large values. Considering the time variations of the ice velocity caused by the stress alone

$$\frac{\partial v}{\partial t} = -Rv \tag{12}$$

one can write an explicit numerical scheme

$$\frac{v^{K+1}_{L,M} - v^{K}_{L,M}}{T} = -Rv^{K}_{L,M} \tag{13}$$

which is stable when time step $T < \frac{2}{R}$.

Since R is proportional to an absolute value of ice velocity, for the larger values of velocity, the time step limit may become very short. The application of a fully implicit scheme,

$$\frac{v_{L,M}^{K+1} - v_{L,M}^{K}}{T} = -Rv_{L,M}^{K+1} \tag{14}$$

establishes a stable numerical computation.

To find a unique solution to the set of equations (1)-(6), the boundary conditions both for the water and ice have to be specified. The boundary conditions for the equations of water motion are specified either by the radiation condition or by linear approximation of the velocities and sea level from the large scale grid model located at the boundary of the refined grid model. The boundary conditions for the ice motion are neither understood nor readily available. For the equations of ice motion we found that the best results are derived by assuming a continuity of velocity along the normal to the open boundary. In the first series of experiments, the equation of ice transport (5) was solved with known compactness along the open boundaries. An ice distribution closer to the observed one has been obtained by applying an advection equation.

$$\frac{\partial c}{\partial t} + v\frac{\partial c}{\partial x} = 0 \tag{15}$$

along the direction (x) normal to the open boundary. Assuming the point at the boundary has coordinates L,M, the numerical form for (15)

$$\frac{C_{L,M}^{K+1} - C_{L,M}^{K}}{T} + \frac{(v + |v|)}{2}\frac{\left(C_{L,M}^{K} - C_{L-1,M}^{K}\right)}{h} + \frac{(v - |v|)}{2}\frac{\left(C_{o}^{K} - C_{L,M}^{K}\right)}{h} = 0 \tag{16}$$

will set compactness at the boundary as a function of velocity direction. The positive v is directed out of the integration domain. C_o^K is the ice compactness outside of the domain boundary and is assumed to be known from observation; it is advected into the domain by condition (16) if the velocity across the boundary has a negative sign.

We are not able to measure the same storm surge in the summer and winter, but this is possible for the astronomical tide wave. The sea level recorded at Stebbins in February-March 1982 under the fast ice (Fig. 3a) and in August 1982 (Fig. 3b) displays a clear difference in the tide amplitude. The harmonic analysis (Table 1) shows that the amplitudes of the main constituents, K_1, O_1, M_2, increase from winter (H_w) to summer (H_s) by about 40%. We therefore expect an inhibitory effect on the storm surge by fast ice as well. In addition, fast ice may produce a shift in the time of arrival of the surge wave.

Results from model calculations with and without ice are given in the storm descriptions in the following section. The presence of ice does modifies the sea level distribution over time to a varying extent. The sea level is most greatly affected in the fast ice zone, and some grid points under pack ice not near the boundary do not show large differences.

4. STORM SURGES IN THE BERING SEA AND NORTON SOUND

The Bering Sea has one of the largest continental shelves in the world. The late summer and fall storms move from the south and southeast, therefore there is sufficient fetch to generate strong variations in the sea level. The late summer storms are often caused by the low pressure centers which, in the northeastern Bering Sea, generate positive sea level changes. During the winter, the weather over the Bering Sea depends on the east Siberian high pressure system. The northeasterly winds generate negative sea levels in the Norton Sound area and the ice movement from the northeastern Bering Sea towards the south [*Muench and Ahlnas*, 1976]. Because of geographical location, two shelf regions are candidates for the

Table 1. Amplitude (H) and phase (G) of the principal tidal constituents at Stebbins, Alaska.

Constituent	Frequency CPD	Summer Amplitude (H_s) cm	Summer Phase (G_s) degree	Winter Amplitude (H_w) cm	Winter Phase (G_w) degree	H_w/H_s
Q_1	0.89324	5.01	34.8	2.91	359.4	0.58
O_1	0.92954	25.81	61.9	14.98	30.1	0.58
M_1	0.96645	1.83	89.1	1.06	61.0	0.58
P_1	0.99726	15.69	112.2	10.28	87.3	0.65
K_1	1.00274	47.41	116.3	31.07	91.9	0.65
J_1	1.03903	2.04	143.3	1.18	122.6	0.58
$2N_2$	1.85969	0.96	109.6	0.92	27.0	0.96
μ_2	1.86455	1.15	117.7	1.11	35.7	0.96
N_2	1.89598	7.21	170.3	6.91	91.3	0.96
ν_2	1.90084	1.40	178.5	1.34	100.0	0.96
M_2	1.93227	19.46	231.1	13.40	155.6	0.69
L_2	1.96857	0.54	288.4	0.38	176.8	0.70
T_2	1.99726	0.28	333.7	0.10	193.6	0.36
S_2	2.00000	4.70	338.0	1.76	195.2	0.37
K_2	2.00548	1.28	346.6	0.48	198.4	0.37

extreme sea level changes — Bristol Bay and Norton Sound. Norton Sound is situated in the northeastern region of the Bering Sea as a relatively shallow embayment of about 200 km in length. Large portions of Norton Sound have a depth less than 10 m and the average depth is about 20 m [*Muench et al.*, 1981]. During the storm dominated season from August to November, an average of 2 to 4 low pressure systems with wind velocity ranging from 15 to 25 m/s may hit the Norton Sound area. The Norton Sound shore is generally of low relief, therefore during storms, the coastal plains can be inundated by the surge or wind waves superimposed on the surge wave. There is only limited knowledge of the sea level changes along the Bering Sea coast due to the lack of permanent tide gauges. An insufficient number of observations is the main reason that the surge height computed through a statistical method, developed for Alaska shores by *Wise et al.* [1981], has to be taken as an approximate value. We have reproduced three storm surges; two are from the winter 1982 when various oceanographic and atmospheric measurements were underway by NOAA/PMEL over the northeastern shelf of the Bering Sea [*Reynolds and Pease*, 1984; *Mofjeld*, 1984]. After the model had been tested against sea level data both in the pack ice and the fast ice area, the largest recently recorded storm surge in the Bering Sea, which occurred in November 1974, was reproduced. The model has been applied to study the water motion and sea level variation as well as the ice motion and distribution. The model is able to reproduce the essential features of ice motion and distribution; i.e., polynya region at the leeward shore of St. Lawrence Island, the ice edge motions caused by the wind, and the relatively fast transport of ice from the Bering Strait region to the southeastern shelf by the so-called "race track" [*Ray and Dupré*, 1981; *Shapiro and Burns*, 1975; *Thor and Nelson*, 1979].

4.1 *Propagation of the Surge Wave in the Ice-Covered Bering Sea*

To test the model against measurements, we have simulated two storms. The first storm was driven by a high pressure system with the center situated over East Siberia during February 12-19, 1982 which caused a negative surge in the Norton Sound area. The second storm occurred from March 7-11, 1982, with a low pressure traveling from the central Bering Sea towards the northeastern Bering Sea. The southwesterly winds generated a positive surge of about 1 to 2 m in Norton Sound. The Bering Sea, during February and March 1982, was partly covered by ice with typical distribution from the Navy-NOAA Joint Ice Center, Naval Polar Oceanography Center redrawn as compactness in Figure 4. We shall use two measuring stations where the sea level was recorded during the storm surge passage. One point, located at $\phi = 62°53'$N, $\lambda = 167°04'$W, a bottom pressure gauge (designated NC17) was situated under the pack-ice [*Mofjeld*, 1984]. The second point was located close to Stebbins, Alaska ($\phi = 63°30'$N, $\lambda = 162°20'$W) and the measurements were taken under the fast ice (personal comm. John Oswald). The fast ice usually covers the southern part of Norton Sound (Fig. 4), therefore the measurements at Stebbins should provide the opportunity to study the influence of fast ice on propagation of the long wave.

4.2 *Storm Surge of February 1982*

The meteorological observations at the time of the storm are described by *Reynolds and Pease* [1984]. The storm surge of February 12-19 was induced by the high pressure system with the center located over eastern Siberia (Fig. 5). Northeasterly winds up to 20 m/s caused a negative surge over the northeastern shelf and a positive level at the southeast end of the Bering Sea. The numerical model reproduces a 7-day period from 00Z, 12 February to 00Z, 19 February. The surface wind used to drive the model was calculated over the entire Bering Sea every 6 hour from the surface pressure maps. The wind was linearly interpolated for the shorter time steps of the numerical computations; 6 minutes for the Norton Sound model and 2 minutes for the Bering Sea model. The wind charts every 24 h for the entire period of storm are plotted in Figures 6 to 12. The wind directions during the computation were fairly steady. One horizontal grid distance in the above figures is scaled to a wind speed of 10 m/s. Quasi-steady north-northeast winds generate the wind-driven current mainly along the Bering Shelf (Figs. 13-19). The southward and southwestward flow along the eastern part of the shelf after about 2-3 days is compensated by northward and northeastward flow in Anadyr Bay and Anadyr Strait. Currents in Anadyr Bay flow in the opposite direction to the wind, therefore, such flow is due to the sea level distribution. Indeed, calculations of the wind-driven motion for the constant wind in the Bering Sea showed that the model steady state is achieved after about 2 days.

The southward and southwestward flow along the eastern Bering Shelf follow the bottom and coastal contours. In the shallow embayments like Norton Sound, the flow is directed to the east along the northern shore and to the west along the southern shore. In Figures 13 to 19 one horizontal grid distance of numerical lattice is scaled to 10 cm/s of velocity. The sea level charts are plotted every 24 hours in Figures 20 to 26. Along the northeastern shelf the strongest changes occurred, and on February 16 and 17 the negative level reached about 1 m in Norton Bay.

The ice motion (Figs. 27 to 29) is much more strongly coupled to the wind magnitude and direction than the water motion. Ice velocity as high as 1 m/s occurred within the shelf (the horizontal grid-distance in Figures 27, 28 and 29 is scaled to 10 cm/s). The north and northeast winds pushed the ice from north to south with especially high velocity between St. Lawrence Island and Norton Sound; the area which is known from satellite and aircraft observation as a "race track".

Ice concentration (or ice compactness) is plotted after 24 hours from the onset of the computation (Fig. 30); after 120 hours, at the maximum of sea level change (Fig. 31), and at the end of the storm — 00Z Feb 19 (hour 168) (Fig. 32). Comparison of observed ice edge location before the storm and the observed and computed ice edge location after the storm show that the model is able to predict the correct direction of the ice edge motion (Fig. 31).

To study both the ice and water motion in Norton Sound, a fine grid model of three times shorter space grid has been applied (Fig. 1). Open boundary conditions for the model were defined by linear interpolation of velocity and sea level from the large scale Bering Sea model. Smaller grid step allowed for better resolution of the bottom and coastal topography which in turn leads to better reproduction of the local surge variations. The charts of currents over the northeastern shelf throughout the entire storm are given in Figures 33 to 39. Two regions of different dynamics can be singled out from the figures: high velocity area extended throughout the entire domain from Bering Strait to the southern boundary; and Norton Sound — an area of small and variable velocities. Sea level maps are shown in Figures 40 to 46, with the lowest level of about -150 cm occurring in Norton Bay. In the vicinity of St. Lawrence Island, the level throughout the entire storm was close to zero. The sea level contours and the current direction tend to be parallel.

The space-time variations of the ice compactness are plotted in Figures 47 to 49. Except for the southern nearshore region of Norton Sound and Norton Bay area where fast ice ($c = 0.99$) was set as a permanent feature, the initial ice compactness was set constant everywhere ($c = 0.7$) (Fig. 47). At the northern boundary (Bering Strait) the compactness was assumed to be constant and equal to 0.9. At both the eastern and southern boundaries, the ice compactness also remained constant during computation at 0.7. The boundary ice compactness altered the distribution of ice inside the domain of integration through the advective boundary condition (16). The northeast wind is dominant during the winter, therefore, it also sets a dominant ice pattern, i.e., areas of low compactness along the north shore of the Norton Bay and a band of high compactness ($c = 0.85$) southward from the Bering Strait (Fig. 48). The influence of St. Lawrence Island on the ice distribution is also eminent; at the windward side of the island the high compactness was produced — a feature often corroborated by observations [*McNutt*, 1981]. Resultant ice distribution is closely related to the ice velocity (Figs. 50-52). Three general modes of ice motion, inferred by *Stringer and Henzler* [1981] through the observation in Norton Sound, can also be seen in the computational results i.e., outbound ice motion, inbound ice motion and gyre. In all figures an abrupt change in the ice movement between Norton Sound and the open Bering Sea is very apparent.

In February, 1982 PMEL deployed within the Norton Sound ice drift stations, therefore we have attempted a comparison for a period of three days (February 14-17, Julian day 45-48) of observed (continuous line) and calculated (dashed line) ice floe tracks. Figure 53 depicts the results for Station 2322B and Figure 54 for Station 2321B.

Three different temporal variations of the sea level at the time of the February storm surges in Stebbins are plotted in Figure 55. Observed changes are given by a continuous line, the computed level by the storm surge model without ice cover by a dotted line, and the computed level with pack and fast ice by a dashed line. Stebbins observations were located under the fast ice, therefore the calculated sea level with fast ice show essential differences from the ice free computations. The sea level changes at NC17 during the storm surge were calculated with the pack ice cover only, and they do not show any difference from the ice free computations (Fig. 56). The time dependent sea level changes have been plotted in a few locations along the Bering Sea coast (Figs. 57-60).

4.3 *Storm Surge of March 1982*

Although the dominant wind pattern over the Bering Sea is related to a high pressure system, the northwesterly flow is often reversed by low pressure systems. A storm surge due to a low pressure occurred on 8 and 9 March, 1982; the model computation spans the period 18Z, March 7 to 18Z, March 10.

At the time of the storm, a few tide gauges were deployed in the Bering Sea and ice motion was monitored by ice drift stations [*Reynolds and Pease*, 1984]. Again, to compare the measured and computed sea level changes, we shall use data from Stebbins and NC17. The low pressure system comprises two or three low pressure centers which were situated over the central and eastern Bering Sea (Fig. 61). The low pressure system displayed a slow motion towards the northeast, therefore, during the first part of the storm, southwesterly winds (Fig. 62) generated a positive surge in Norton Sound. Later, when the low pressure center was located over Alaska, the northeasterly and northwesterly winds (Figs. 63 and 64) caused a negative surge in Norton Sound.

The horizontal grid distance in Figures 62 to 64 has been scaled to 5 m/s of wind velocity. Both sea level (Figs. 65 to 67) and currents (Figs. 68 to 70), computed from the large scale model, follow the wind pattern. Storm activity, i.e., large changes of velocity and sea level are located along shallow northern and eastern regions of the Bering Sea. Although high ice velocity was observed (Figs. 71 to 73), the ice concentration after 3 days of storm remained close to the initial distribution since the winds reversed.

The model of the Norton Sound region repeats the results derived from the Bering Sea model but the picture is more detailed. Based on the fine grid model, the ice and water interaction are shown at the time of the highest sea level occurrence; about 36 hours from onset of storm, i.e., at 18Z, March 7. The sea level increases from zero at St. Lawrence Island to above 1 m at Norton Bay area (Fig. 74). The water motion indicates that the velocity is parallel to the sea level isolines (Fig. 75).

Initial ice distribution has been taken to be the same as in Figure 47, thus, except for the southern shore of Norton Sound and the Norton Bay area where the fast ice is located, the ice compactness over the entire region is constant and set at 0.7. The southwesterly wind produced along the northern and northeastern shores an area of high ice compactness ($c = 0.85$). Close to St. Lawrence Island the ice compactness has been diminished to $c = 0.55$ (Fig. 76). The regions of the fast ice stayed uniform during the entire computation since the ice velocity was negligible in these regions. The ice velocity pattern (Fig. 77) essentially follows the wind distribution.

Again, due to the flow constraints, the high velocity region is generated between St. Lawrence Island and Alaska. In this case, ice is transported into the Chukchi Sea.

To study the influence of ice cover on the storm surge propagation, the computations were performed with the ice cover and with an ice-free sea surface. The results of the computations along with the recorded sea level in Stebbins and at point NC17 are plotted in Figures 78 and 79. Somewhat better agreement with the observed sea level variations was achieved for this case than for the February case. Between Julian day 66 and 69, we have attempted a comparison of the ice floe tracks recorded by drifting station and calculated from the ice velocity. Due to the variable and slow motion around day 69, the comparison given in Figures 80 and 81 has been possible only for the period of two days, between days 66.5 and 68.5.

4.4 *Storm Surge of November 1974*

This storm surge was caused by a low pressure system traveling from the Aleutian Islands to the Bering Strait. Winds of 25 m/s to 35 m/s were recorded [*Fathauer*, 1978]. Along the shores of Norton Sound combined storm surge and wind waves reached as high as 5 m [*Sallenger*, 1983]. On November 11, 12 and 13 coastal communities from Bristol Bay to Kotzebue Sound were severely flooded and damaged. After the storm, observations of a debris line along the Norton Sound shore by *Sallenger* [1983] showed that at all but a few locations only one debris line was found. This would indicate that the storm surge of November 1974 was the strongest in recent history, since it had incorporated older debris lines and pushed them higher. The numerical calculation spans the period from 00Z, November 10 to 00Z, November 14. The largest flooding indicated by the model calculation occurred between day 2 and day 3 from the onset of computations, i.e. between November 12 and 13. To describe the weather pattern during the storm, the pressure distribution at 18Z, November 12 is plotted in Figure 82. The charts of wind distribution as calculated from the surface pressure are given in Figures 83 to 86. South and southwesterly winds in the range 20 to 40 m/s generated conspicuous set up (Figs. 87-90). Even in the large scale model, sea level on day 3 (Nov 13) in Norton Bay reached about 3 m. Currents as large as 1 m/s pushed the water toward the Bering Strait (Figs. 91 to 94). The surge wave did not interact with ice cover because apart from fresh ice in Norton Sound, the entire Bering Sea was ice-free. The boundary data from the large-scale model and the wind served to drive the fine-scale model. The results show how shallow water bodies such as Norton Sound enhance the surge wave. At the peak of the storm the wave reached about 5 m in Norton Bay (Fig. 95). Storm surge related currents are transporting water towards the Chukchi Sea (Fig. 96). Temporal variations of the sea level calculated for several locations along the shore show that entire coast from south (Stebbins) to north (Diomedes) was severely flooded with set up higher than 2.5 m (Figs. 97-100). In certain locations, like Nome, flooding occurred several times. Although no tide gauge observations are available to compare against computation, the magnitude of surge derived from the model compares well with debris line observation and flood reports from Nome [*Wise et al.*, 1981].

5. CONCLUSIONS

Results from the storm surge computations show the relationships of the sea level and currents. In addition, the inclusion of fast ice in the model can produce some measurable differences in the results. The Bering Sea model reproduces several observed features of the ice distribution as well as predict the sea level changes. The polynya south of St. Lawrence Island, the movement of the ice edge and the movement of the ice in the "race-track" region are good examples. The Bering Sea model is adequate to determine the boundary conditions for the Norton Sound region model. The Norton Sound model required the specification of velocity and sea level at the open boundaries. When the model was run with only radiation conditions on those boundaries, the model did not reproduce the observed variations in sea level, due to the lack of interaction with the larger domain. The fact that the regional Norton Sound model had the boundaries in relatively shallow water appears to be the source of this difficulty. If the radiation boundary conditions can be applied in deep water, the model is less sensitive to the alongshore regions. With the boundaries specified by the Bering model, the Norton Sound model made possible a more detailed examination of the surge within the sound, particularly in the regions of small scale bathymetry near Stebbins and in Norton Bay.

REFERENCES

Albright, M., Geostrophic wind calculations for AIDJEX, *Sea Ice Processes and Models*, edited by R. S. Pritchard, pp. 402-409, Univ. of Washington Press, Seattle and London, 1980.

Brower Jr., W. A., H. W. Searby, J. L. Wise, H. F Diaz and A. S. Prechtel, Climatic atlas of the outer continental shelf waters and coastal regions of Alaska. Arctic Environmental Information and Data Center, Anchorage, Alaska, 443 pp., 1977.

Cacchione, D. A. and D. E. Drake, Sediment transport in Norton Sound, Alaska. *Open-file Rep. 79-1555, USGS* Menlo Park, California, 88 pp., 1979.

Camerlengo, A. L. and J. J. O'Brien, Open boundary conditions in rotating fluids, *J. Comp. Physics, 35*, 12-35, 1980.

Coon, M. D., G. A. Maykut, R. S. Pritchard, D. A. Rothrock and A. S. Thorndike, Modeling the pack ice as an elastic-plastic material, *AIDJEX Bulletin, 24*, 1-105, 1974.

Doronin, Y. P., On the method to calculate compactness and drift of ice, Trudy Arctic-Antarctic Institute, Leningrad, T., *291*, 5-17, 1970.

Drake, D. E., D. A. Cacchione, R. D. Muench and C. H. Nelson, Sediment transport in Norton Sound, Alaska, *Marine Geology, 36*, 97-126, 1980.

Fathauer, T. F., A forecast procedure for coastal floods in Alaska, *NOAA Tech. Memo, NWS AR-23*, 27 pp., 1978.

Hansen, W., Hydrodynamical methods applied to the oceanographical problems. Proc. Symp. Math.-Hydrodyn. Meth. Phys. Oceanography. Mitt. Inst. Meeresh., Univ. Hamburg, *1*, 25-34, 1962.

Henry, R. F., Storm surges in the southern Beaufort Sea, *Inter. Rept.*, Beaufort Sea Project. Institute of Ocean Sciences, Patricia Bay, Sidney, B.C., Canada, 41 pp., 1974.

Hibler, W. D., Modelling pack ice as a viscous-plastic continuum, *J. Phys. Oceanogr.*, *9*, 815-846, 1979.

Kowalik, Z., A study of the M_2 tide in the ice-covered Arctic Ocean. Modeling, identification, control, *Norwegian Research Bull.*, *2*(4), 201-223, 1981.

Kowalik, Z., Storm surges in the Beaufort and Chukchi Seas, *J. Geophys. Res.*, *89*(C11), 10,570-10,578, 1984.

Kowalik, Z. and J. B. Matthews, The M_2 tide in the Beaufort and Chukchi Seas, *J. Phys. Oceanogr.*, *12*(7), 743-746, 1982.

Leavitt, E., Surface-based air stress measurements made during AIDJEX, in *Sea Ice Processes and Models*, edited by R. S. Pritchard, pp. 419-329, Univ. of Washington Press, Seattle, 1980.

Leendertse, J. J. and S. K. Liu, Modeling of tides and circulations of the Bering Sea, Environmental Assessment of the Alaska Continental Shelf Annual Rept. of P.I. V. 5: Transport, NOAA, pp. 87-108, 1981.

Macklin, S. A., Wind drag coefficient over first-year sea ice in the Bering Sea, *J. Geophys. Res.*, *88*(C5), 2845-2852, 1983.

Marchuk, G., R. Gordev, B. Kagan and V. Rivkind, Numerical method to solve tidal dynamics equation and result of its testing, 78 pp., Report Comput. Centre, Novosibirsk, U.S.S.R., 1972.

McNutt, L. S., Remote sensing analysis of ice growth and distribution in the eastern Bering Sea, in *The Eastern Bering Sea Shelf: Oceanography and Resources*, edited by D. W. Hood and A. Calder, pp. 141-165, Univ. of Washington Press, Seattle, 1981.

Mofjeld, H. O., Recent observations of tides and tidal currents from the northeastern Bering Sea shelf, *NOAA Tech. Mem. ERL PMEL-57*, 36 pp., PMEL, Seattle, 1984.

Muench, R. D. and K. Ahlnas, Ice movement and distribution in the Bering Sea from March to June 1974, *J. Geophys. Res.*, *81*(24), 4467-4476, 1976.

Muench, R. D., R. B. Tripp and J. D. Cline, Circulation and hydrography of Norton Sound, in *The Eastern Bering Sea Shelf: Oceanography and Resources*, edited by D. W. Hood and A. Calder, pp. 77-93, Univ. of Washington Press, Seattle, 1981.

Overland, J. E., H. O. Mofjeld and C. H. Pease, Wind-driven ice motion in a shallow sea, *J. Geophys. Res.*, *89*(C4), 6525-6531, 1984.

Pearson, C. A., H. O. Mofjeld and R. B. Tripp, Tides of the eastern Bering Sea shelf, in *The Eastern Bering Sea Shelf: Oceanography and Resources*, edited by D. W. Hood and A. Calder, pp. 111-130, Univ. of Washington Press, Seattle, 1981.

Pease, C. H. and J. E. Overland, An atmospherically driven sea-ice drift model for the Bering Sea, *Annals of Glaciology*, *5*, 111-114, 1984.

Ray, V. M. and W. R. Dupré, The ice-dominated regimen of Norton Sound and adjacent areas of the Bering Sea, in *The Eastern Bering Sea Shelf: Oceanography and Resources*, edited by D. W. Hood and A. Calder, pp. 263-278, U.S. GPO and Univ. of Washington Press, Seattle, 1981.

Raymond, W. H. and H. L. Kuo, A radiation boundary condition for multi-dimensional flow, *Quart. J. R. Met. Soc.*, *110*, 535-551, 1984.

Reid, R. O. and B. R. Bodine, Numerical model for storm surges in Galveston Bay, *J. Waterway and Harbour Div.*, *94*(WWI), 33-57, 1968.

Reynolds, M. and C. H. Pease, Drift characteristics of northeastern Bering Sea ice during 1982, *NOAA Tech. Mem. ERL PMEL-55*, 135 pp., PMEL, Seattle, 1984.

Roache, P. J., *Computational Fluid Dynamics*, 446 pp., Hermosa Pub., Albuquerque, 1972.

Rothrock, D. A., The kinematics and mechanical behaviour of pack ice: the state of subject, *AIDJEX Bull.*, *2*, 1-10, 1970.

Rothrock, D. A., The mechanical behavior of pack ice. *Annual Rev. of Earth and Planetary Sciences*, *3*, 317-342, 1975.

Sallenger, A. J., Jr., Measurements of debris-line elevations and beach profiles following a major storm: Northern Bering Sea coast of Alaska. *Open-file Rep. 83-394, USGS*, Menlo Park, California, 1983.

Schumacher, J. D. and R. B. Tripp, Response of northeast Bering Sea shelf waters to storms, *EOS*, *60*(46), 1979.

Shapiro, L. H. and J. J. Burns, Satellite observations of sea ice movement in the Bering Strait region, in *Climate of the Arctic*, edited by G. Weller and S. Bowling, pp. 379-386, Geophysical Institute, University of Alaska, Fairbanks, 1975.

Stringer, W. J. and R. D. Henzler, Ice deplacement vectors measured in Norton Sound and the adjacent Bering Sea, 1973-1979, *Rep. for NOAA-OCSEAP*, 37 pp., 1981.

Thor, D. R. and C. H. Nelson, A summary of interacting, surficial geologic processes and potential geological hazards in the Norton Sound Basin, northern Bering Sea. Proc. 11th Ann. offshore Tech. Conf. OTC paper 3400:377-365, 1979.

Walter, B. A. and J. E. Overland, Air-ice drag coefficients for first-year sea ice derived from aircraft measurements, *J. Geophys. Res.*, *89*(C3), 3550-3560, 1984.

Wise, J. L., A. L. Comiskey and D. Becker, Jr., Storm surge climatology and forecasting in Alaska. Arctic Envir. Inform. and Data Center. Univ. Alaska, Anchorage, 26 pp., 1981.

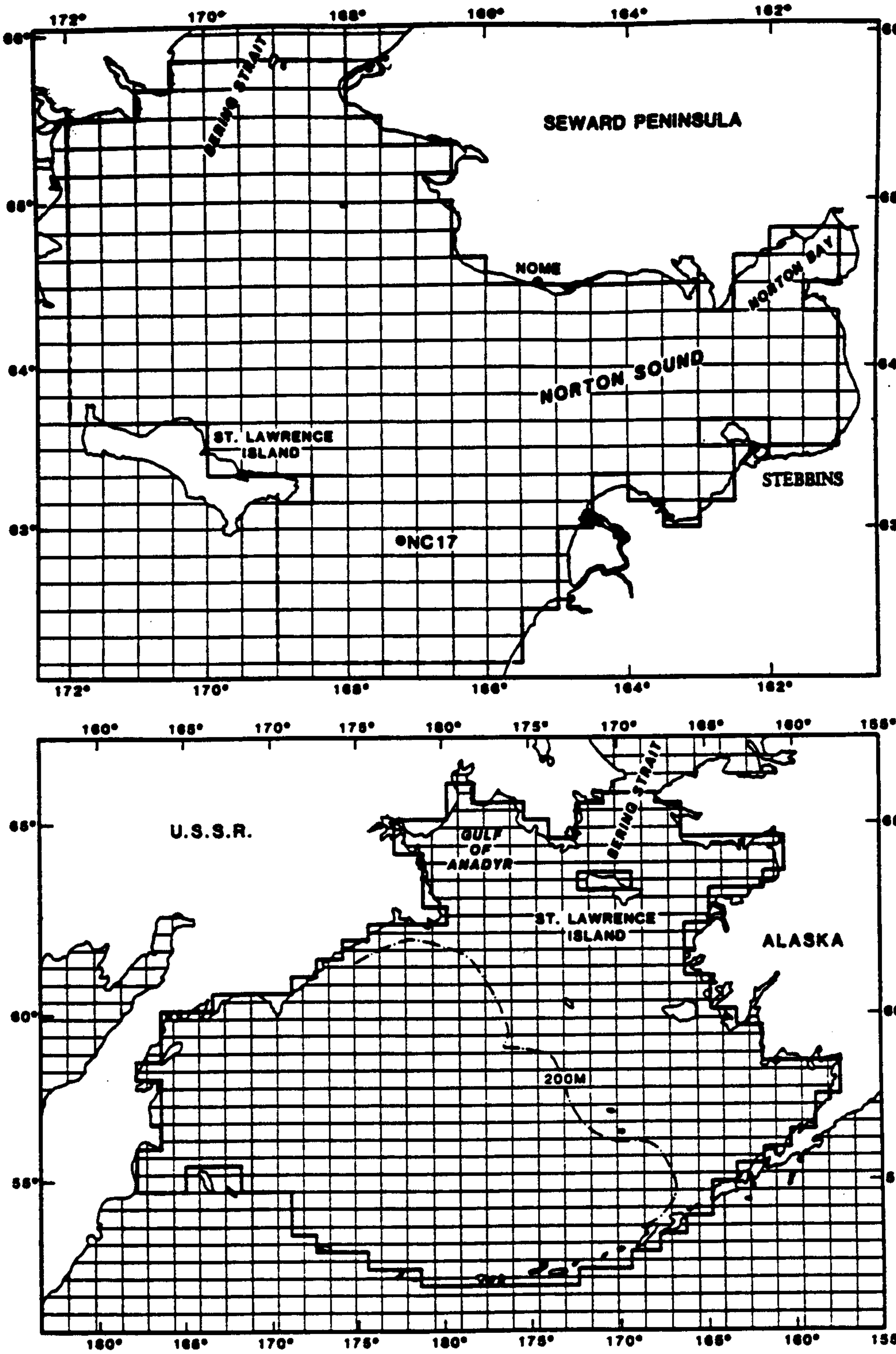

Figure 1.--Model regions: upper panel shows grid used for detailed Norton Sound model, lower panel shows grid used for Bering Sea model.

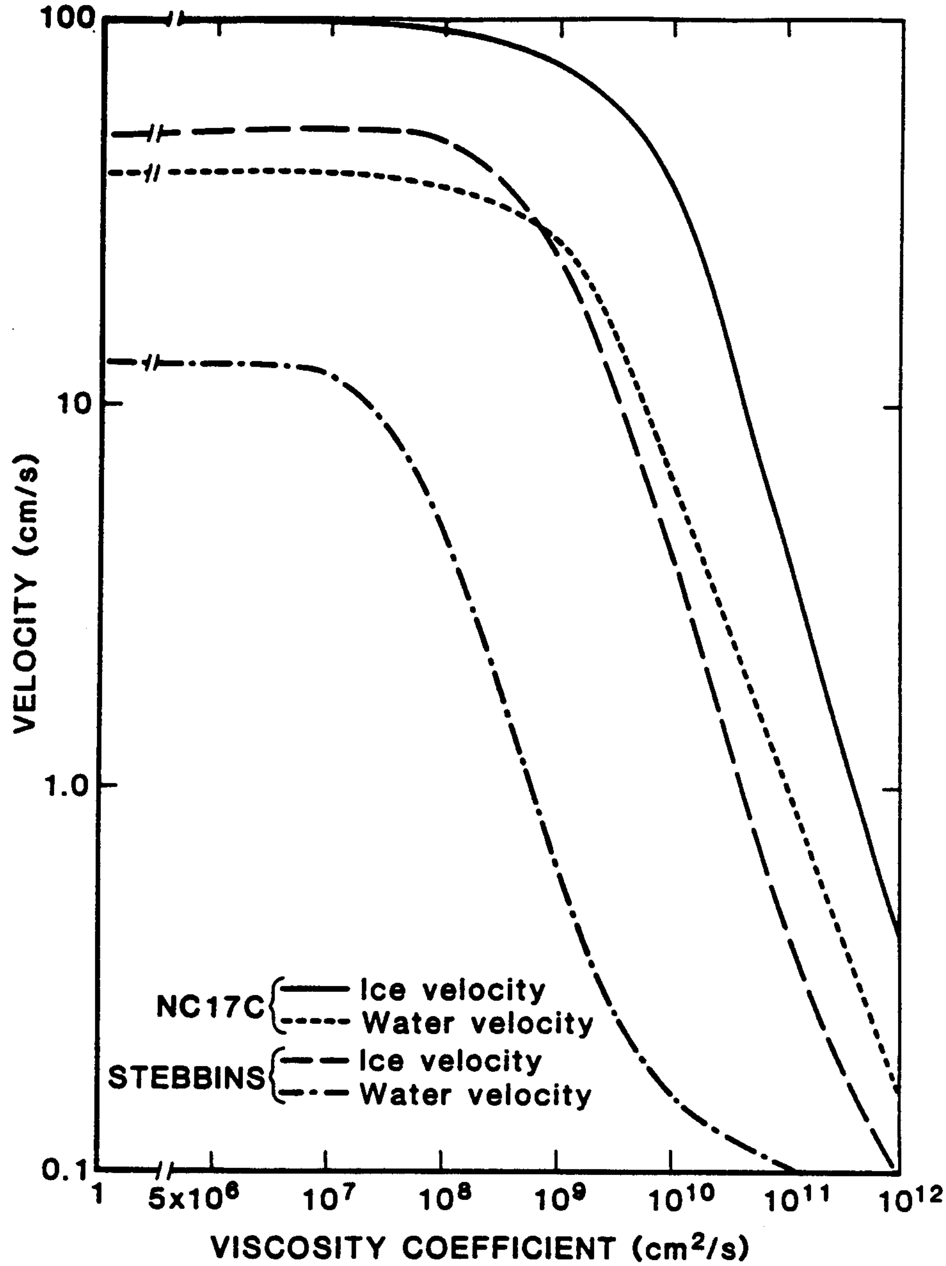

Figure 2.--Water and ice velocity as a function of the viscosity coefficient of the ice. The domain is covered by ice with 0.99 compactness.

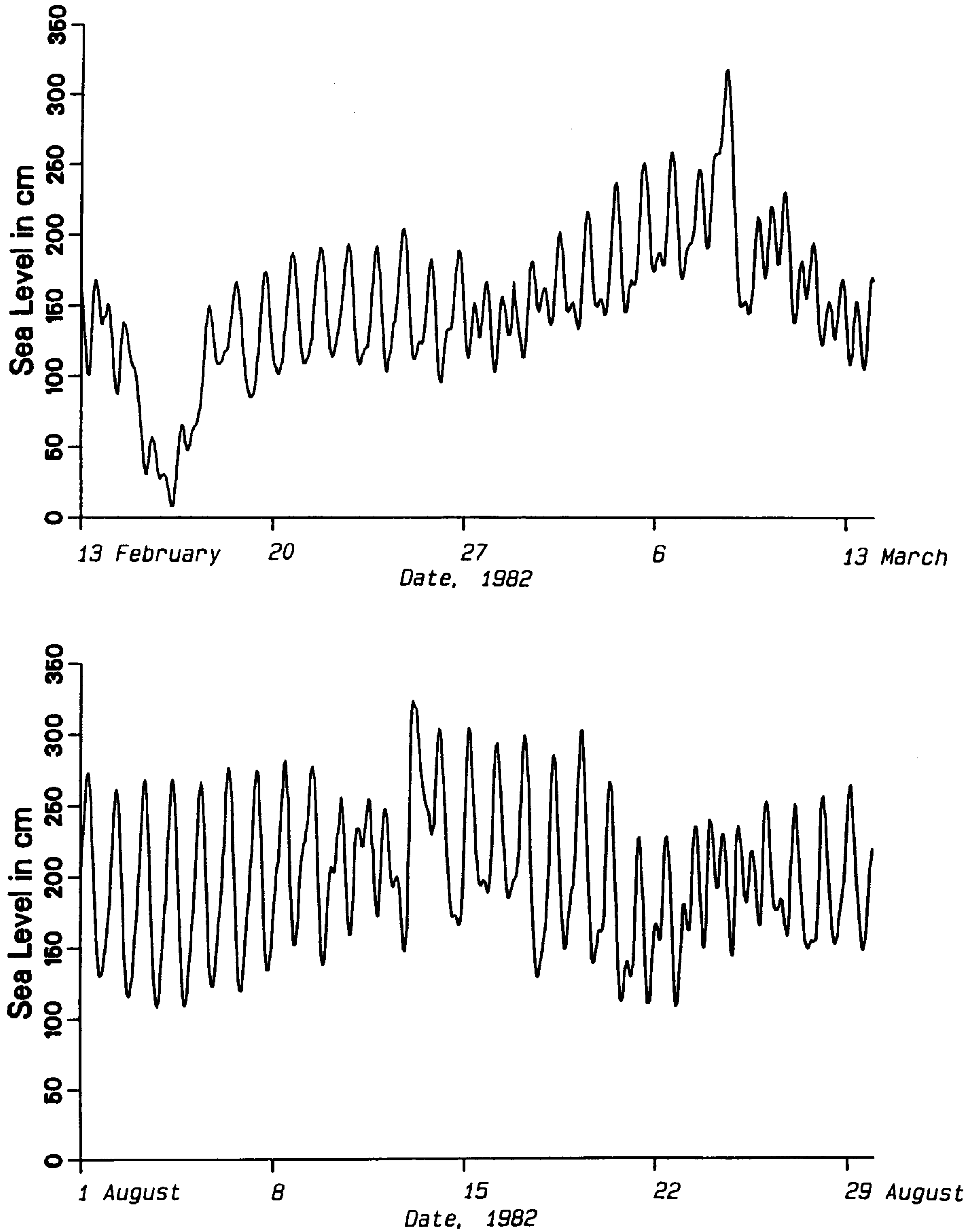

Figure 3.--Time series of sea level measurements from Stebbins, Alaska, February-March (upper chart) and August (lower chart) 1982.

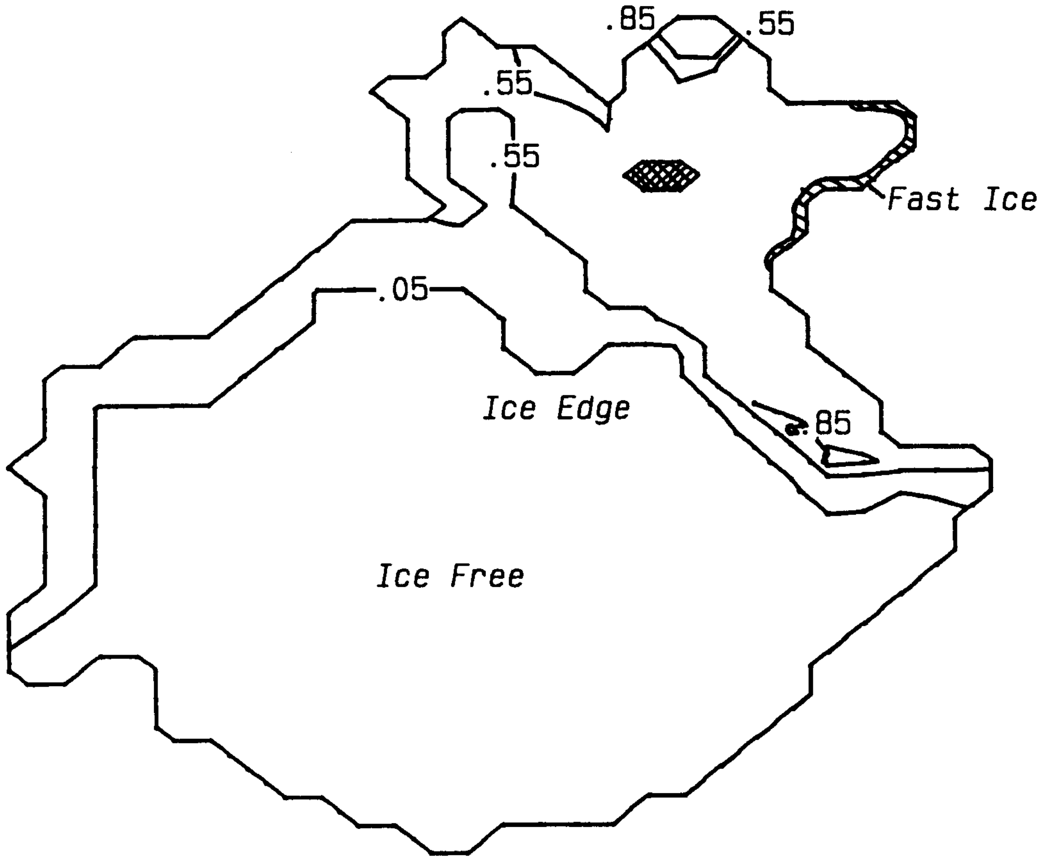

Figure 4.--Ice compactness in the Bering Sea, case 1, day 1 (13 February 1982).

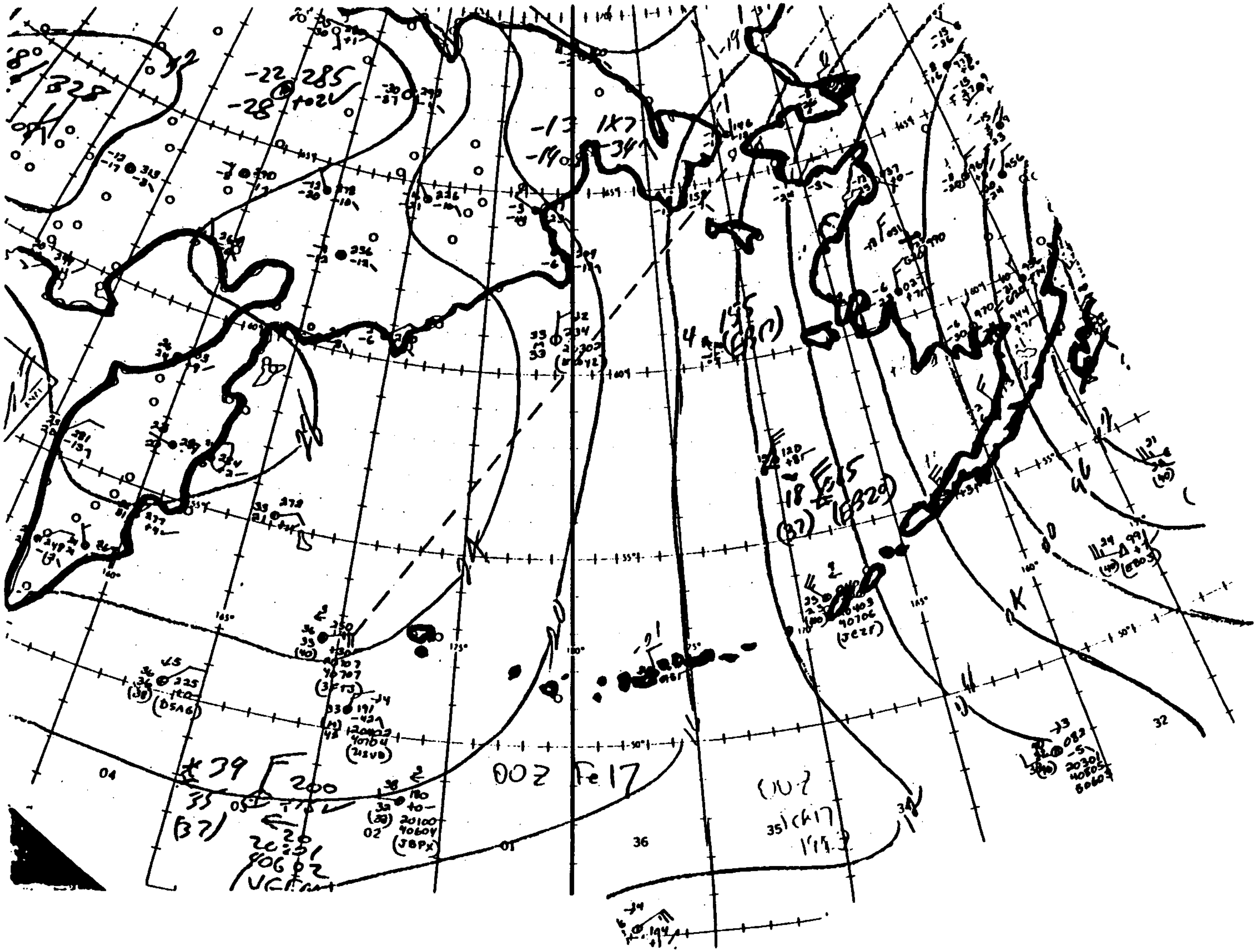

Figure 5.--Surface weather chart for 00Z, 17 February 1982. Pressure in millibars.

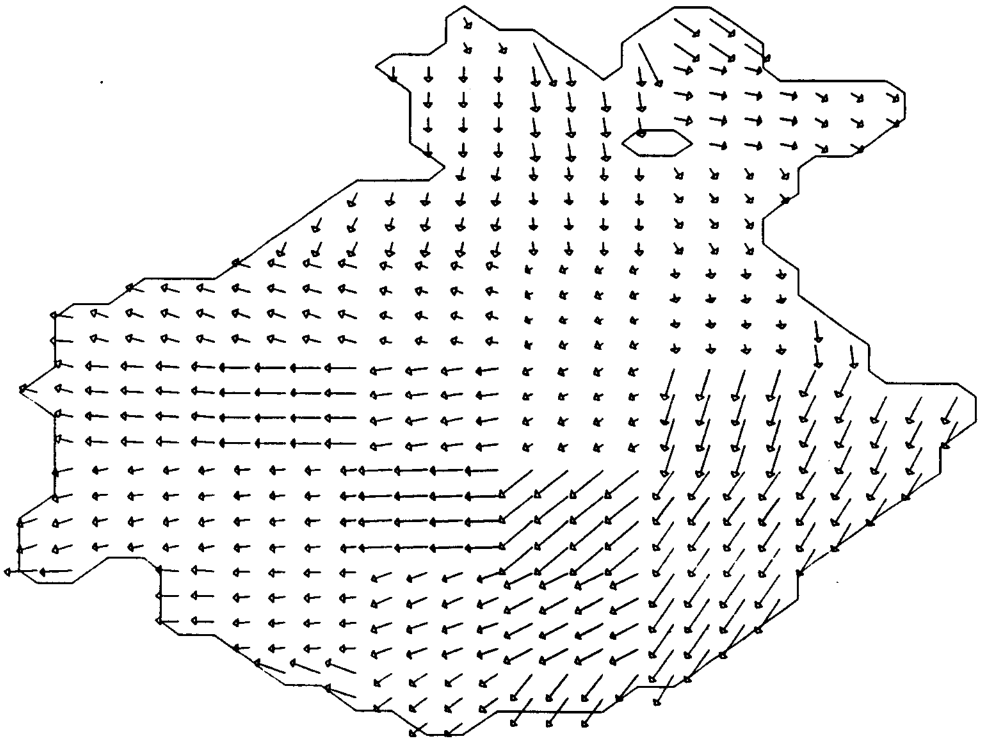

Figure 6.--Wind, Bering Sea, case 1, day 1
(00Z, 13 Feb. 1982); 1 horizontal grid line = 10 m/s.

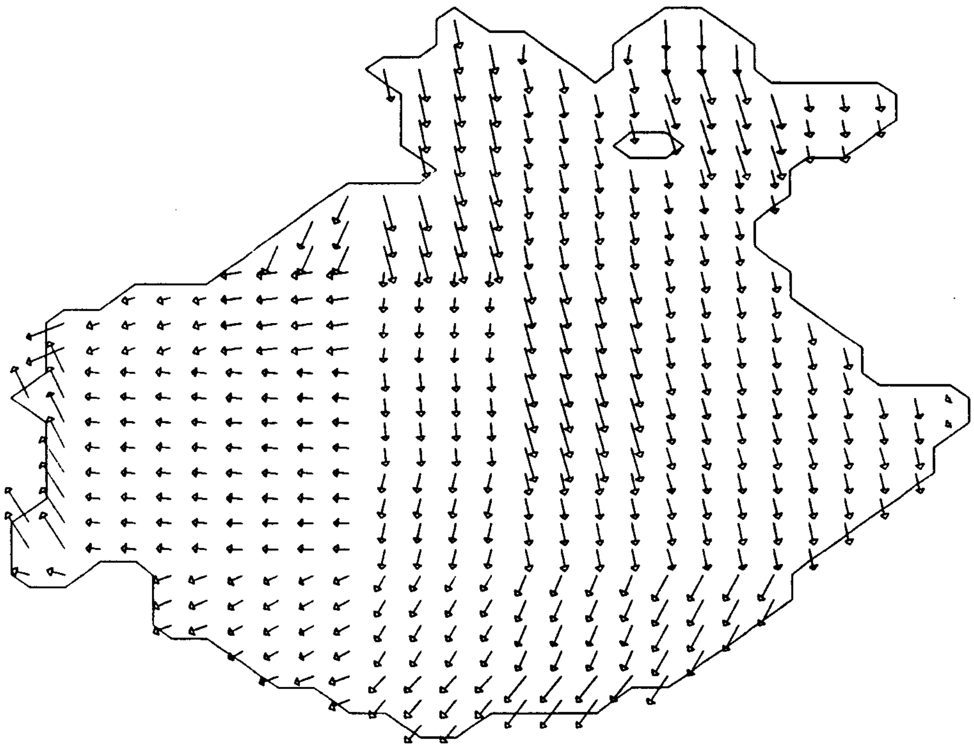

Figure 7.--Wind, Bering Sea, case 1, day 2
(00Z, 14 Feb. 1982); 1 grid line = 10 m/s.

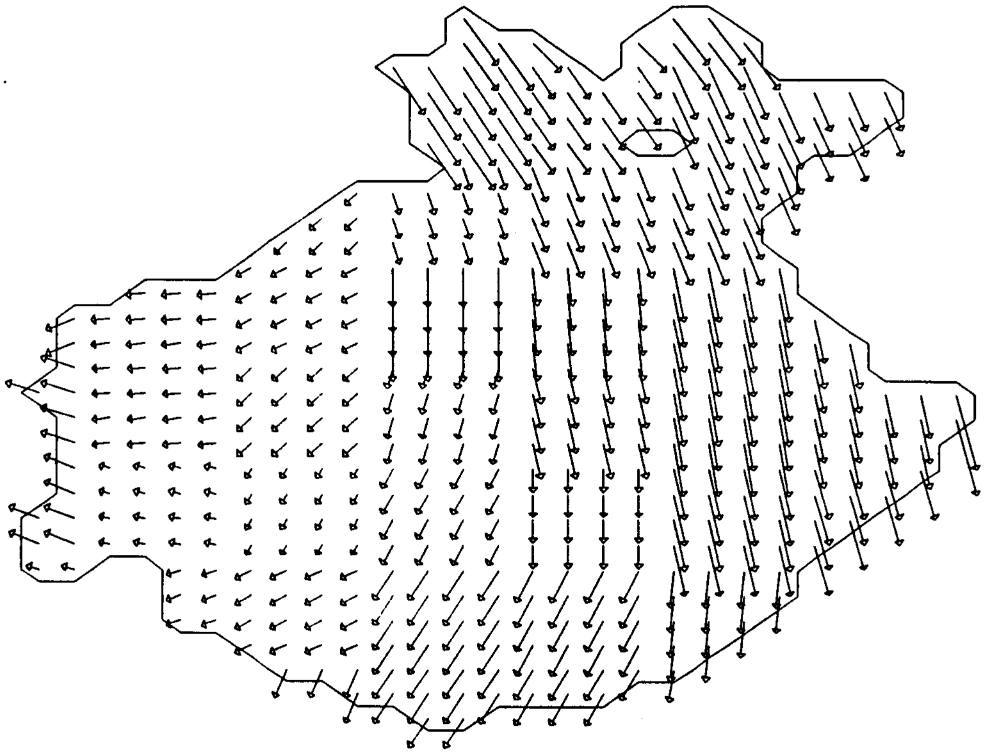

Figure 8.--Wind, Bering Sea, case 1, day 3
(00Z, 15 Feb. 1982); 1 grid line = 10 m/s.

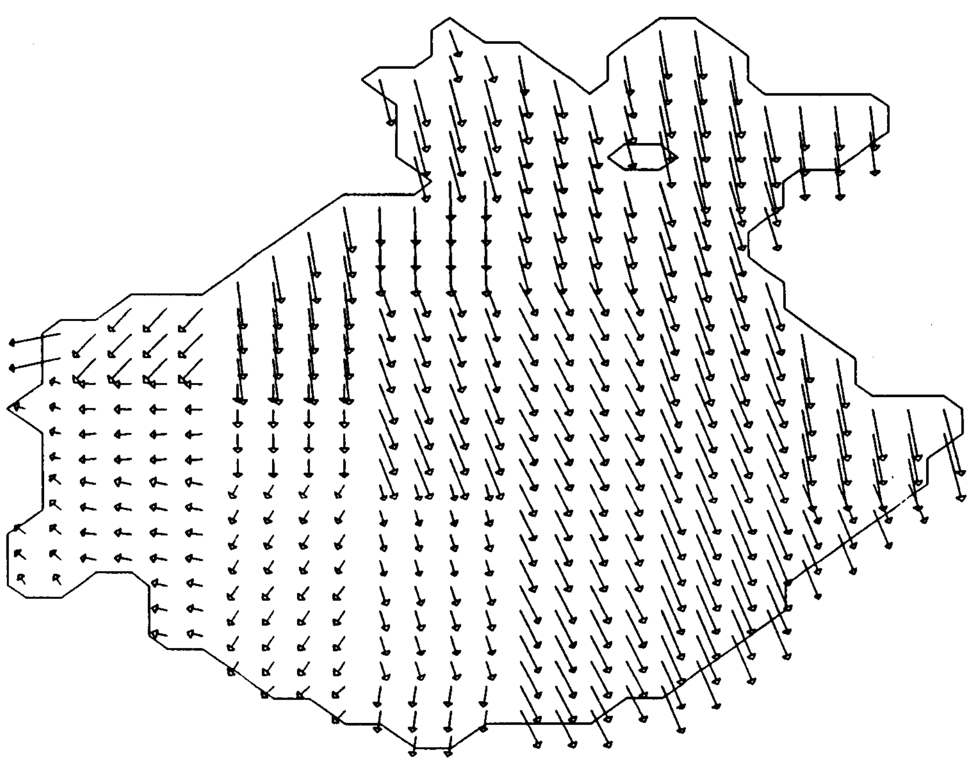

Figure 9.--Wind, Bering Sea, case 1, day 4
(00Z, 16 Feb. 1982); 1 grid line = 10/m/s.

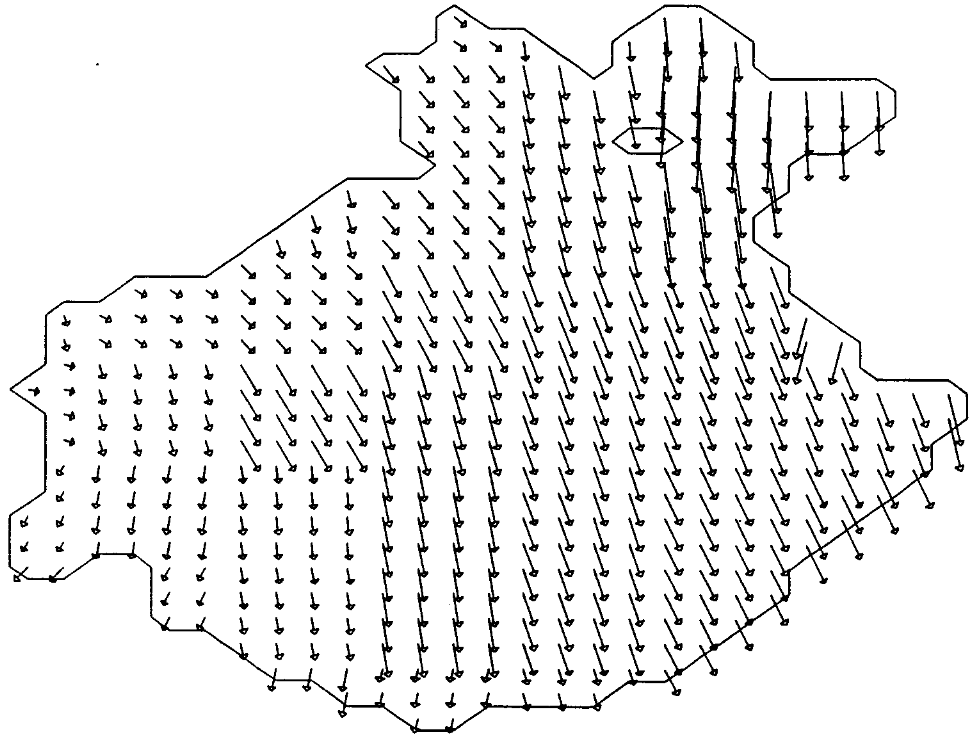

Figure 10.--Wind, Bering Sea, case 1, day 5 (00Z, 17 Feb. 1982); 1 grid line = 10 m/s.

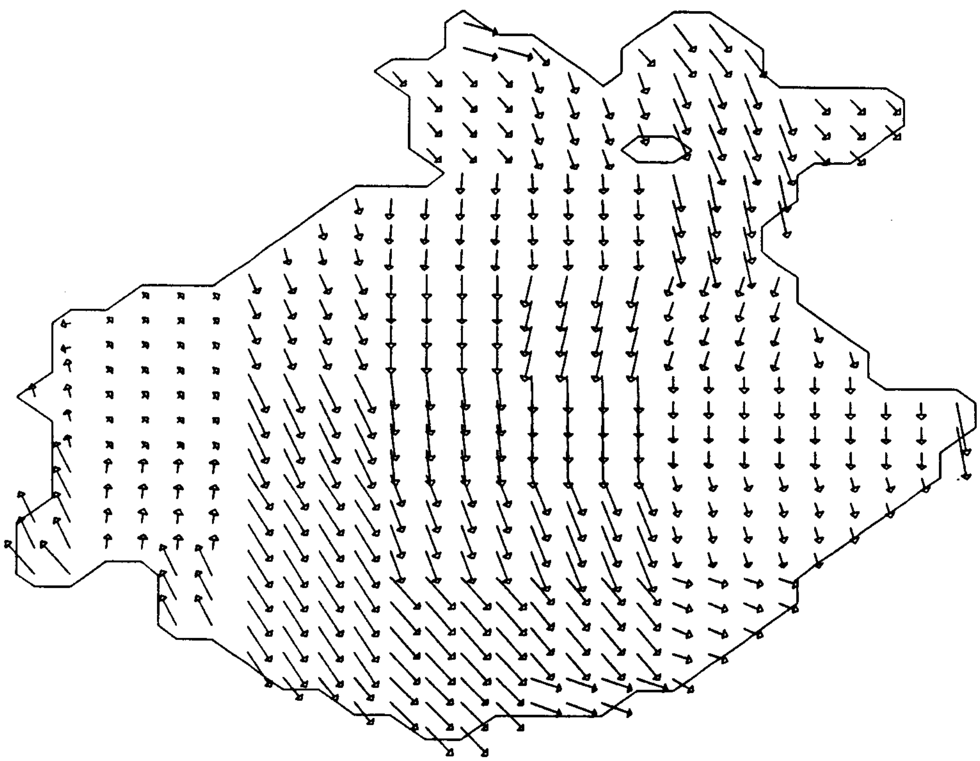

Figure 11.--Wind, Bering Sea, case 1, day 6 (00Z, 18 Feb. 1982); 1 grid line = 10 m/s.

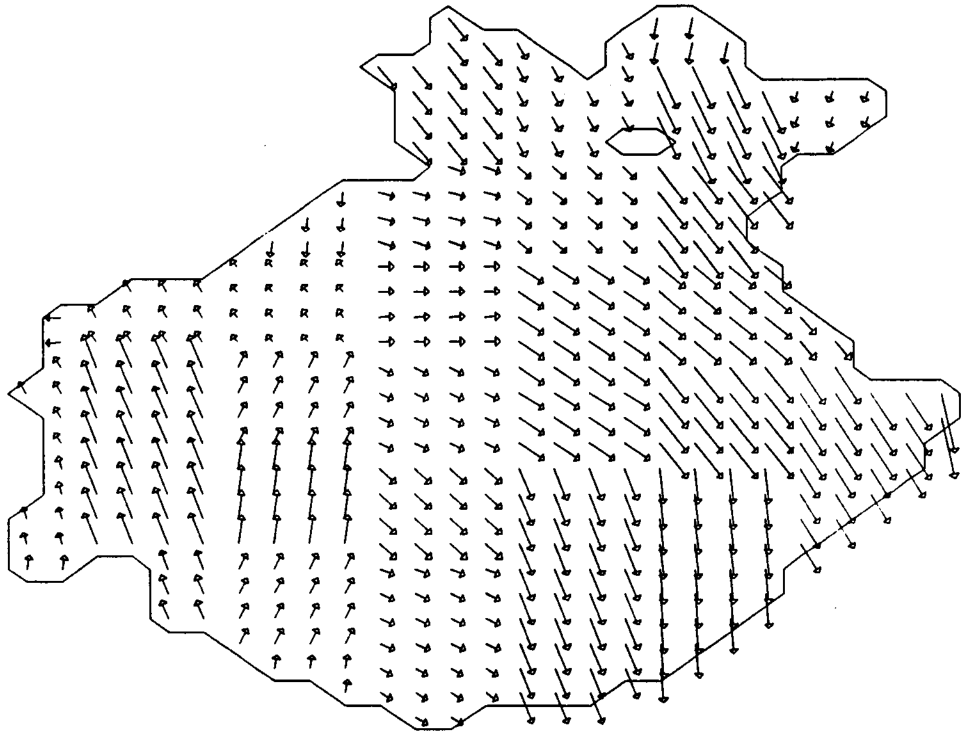

Figure 12.--Wind, Bering Sea, case 1, day 7 (00Z, 19 Feb. 1982); 1 grid line = 10 m/s.

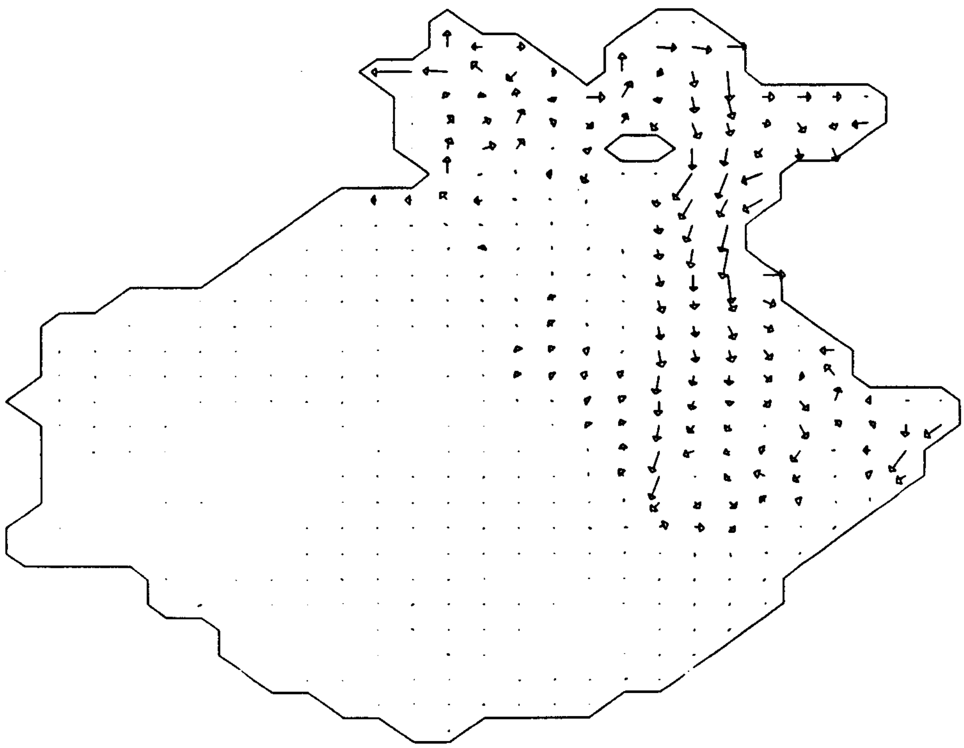

Figure 13.--Velocity, Bering Sea, case 1, day 1 (00Z, 13 Feb. 1982); 1 grid line = 10 cm/s.

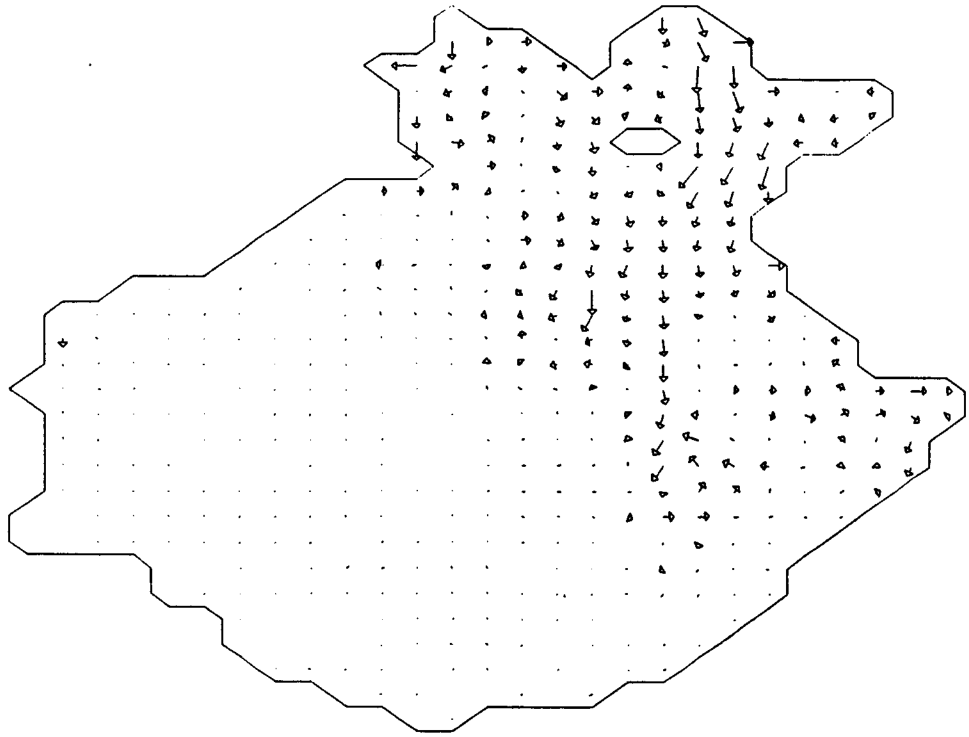

Figure 14.--Velocity, Bering Sea, case 1, day 2 (00Z, 14 Feb. 1982); 1 grid line = 10 cm/s.

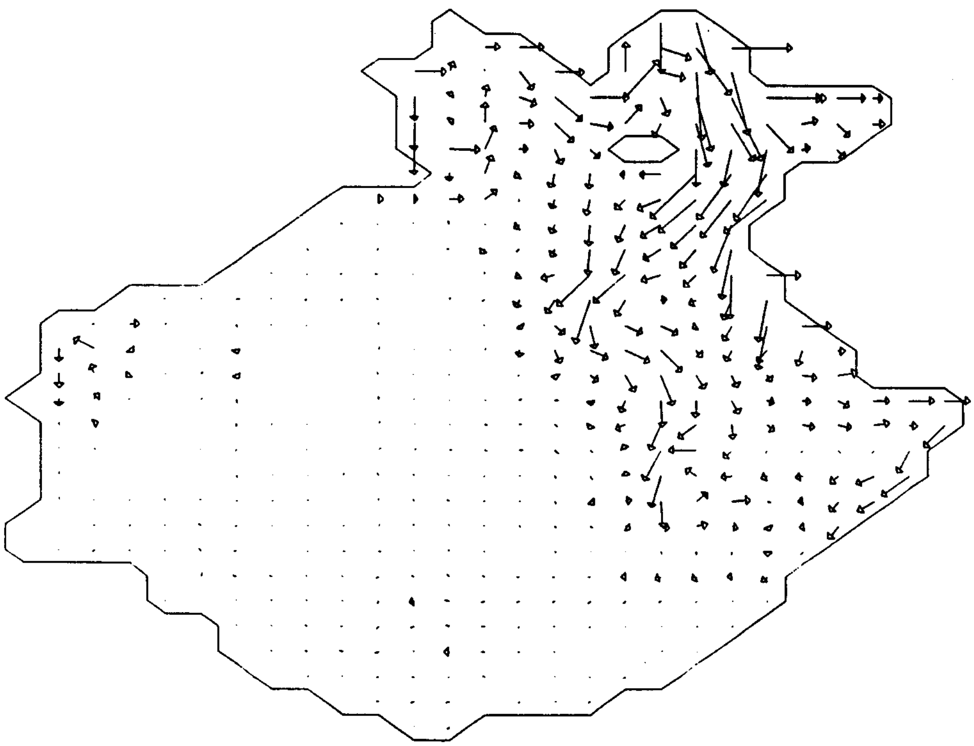

Figure 15.--Velocity, Bering Sea, case 1, day 3 (00Z, 15 Feb. 1982); 1 grid line = 10 cm/s.

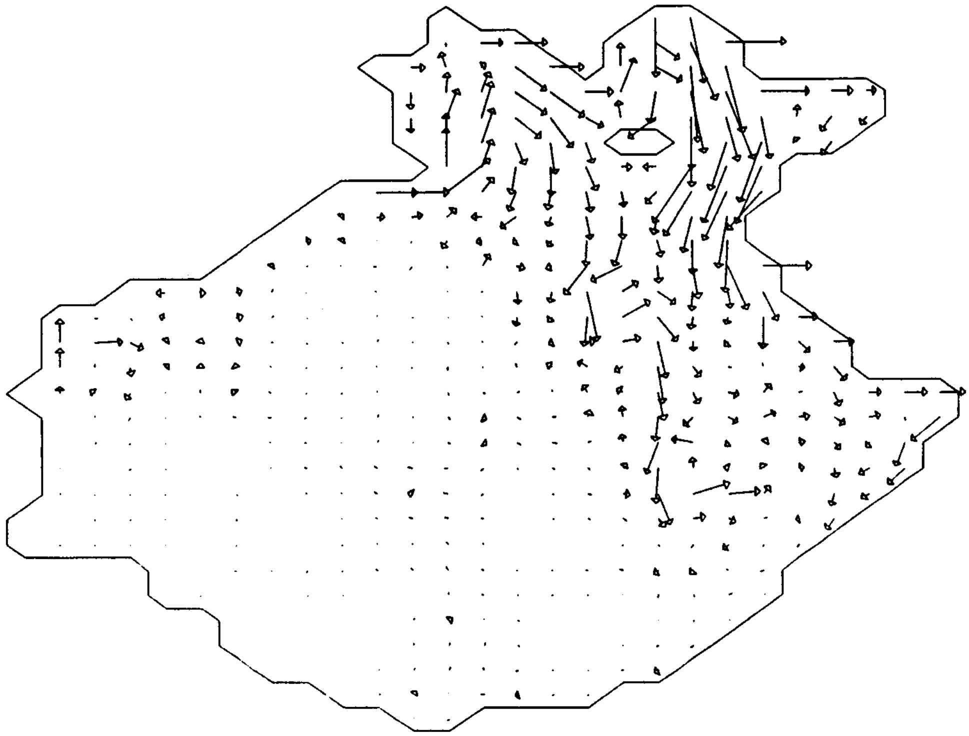

Figure 16.--Velocity, Bering Sea, case 1, day 4 (00Z, 16 Feb. 1982); 1 grid line = 10 cm/s.

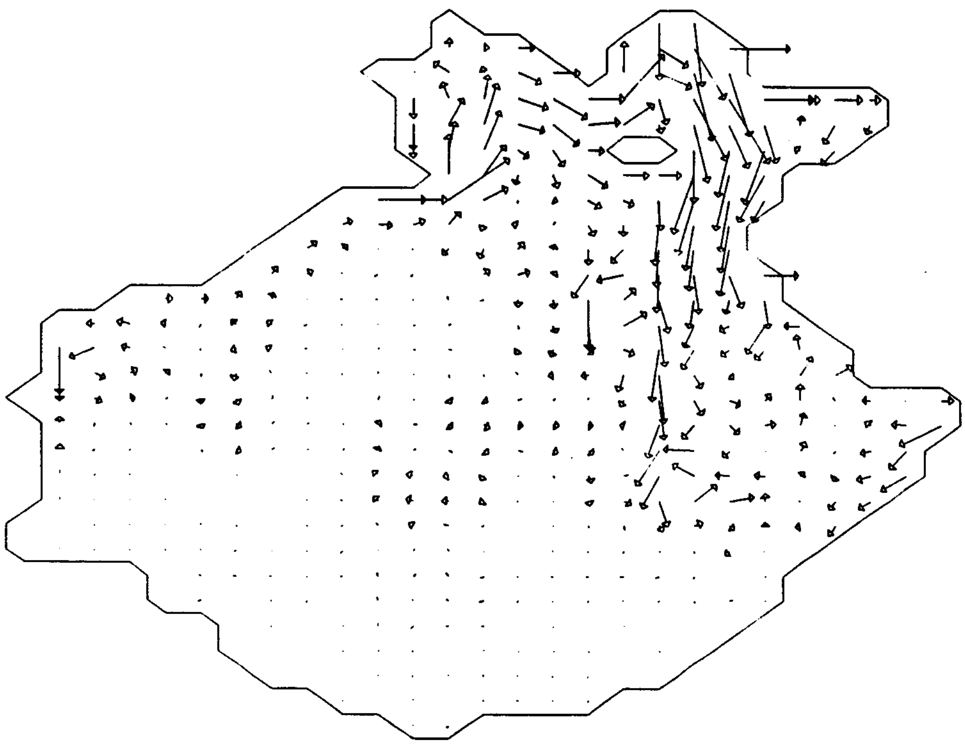

Figure 17.--Velocity, Bering Sea, case 1, day 5 (00Z, 17 Feb. 1982); 1 grid line = 10 cm/s.

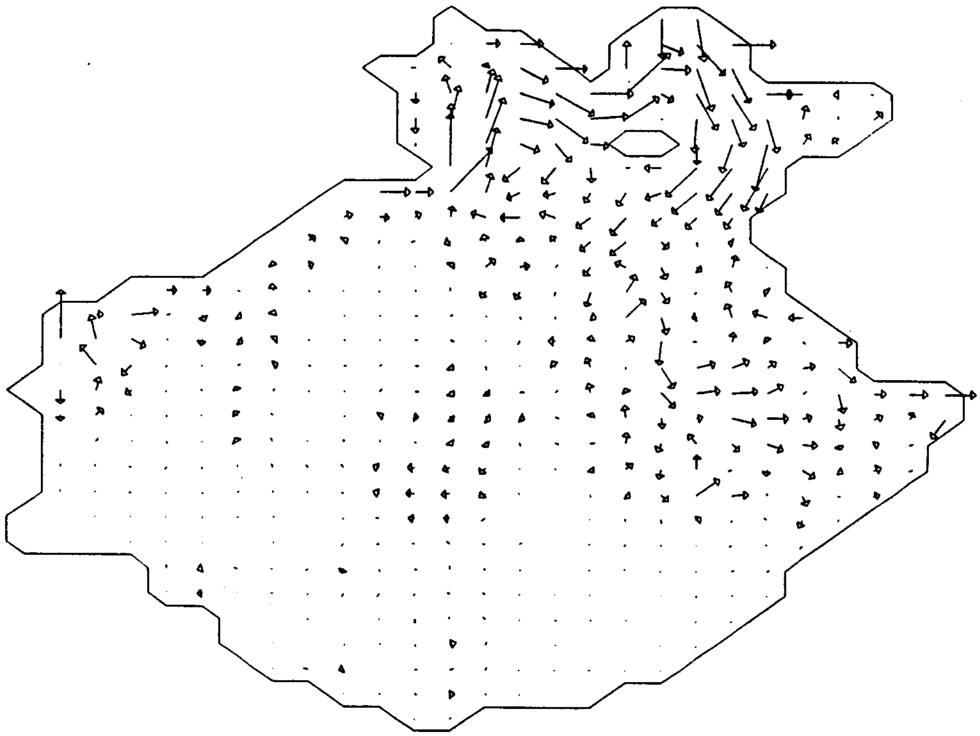

Figure 18.--Velocity, Bering Sea, case 1, day 6 (00Z, 18 Feb. 1982); 1 grid line = 10 cm/s.

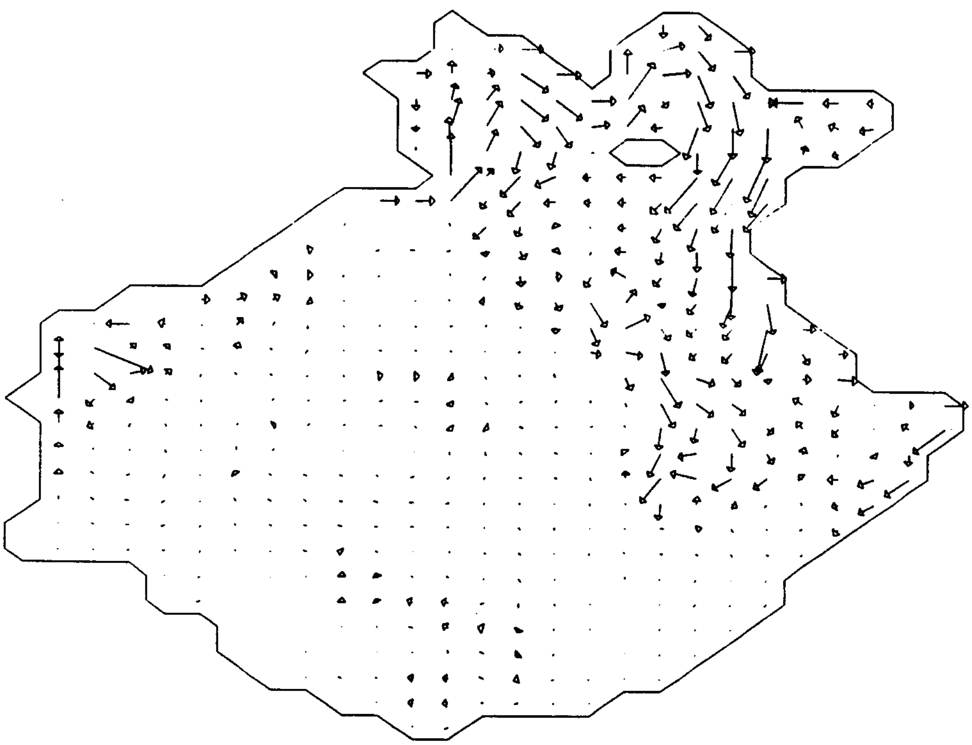

Figure 19.--Velocity, Bering Sea, case 1, day 7 (00Z, 19 Feb. 1982); 1 grid line = 10 cm/s.

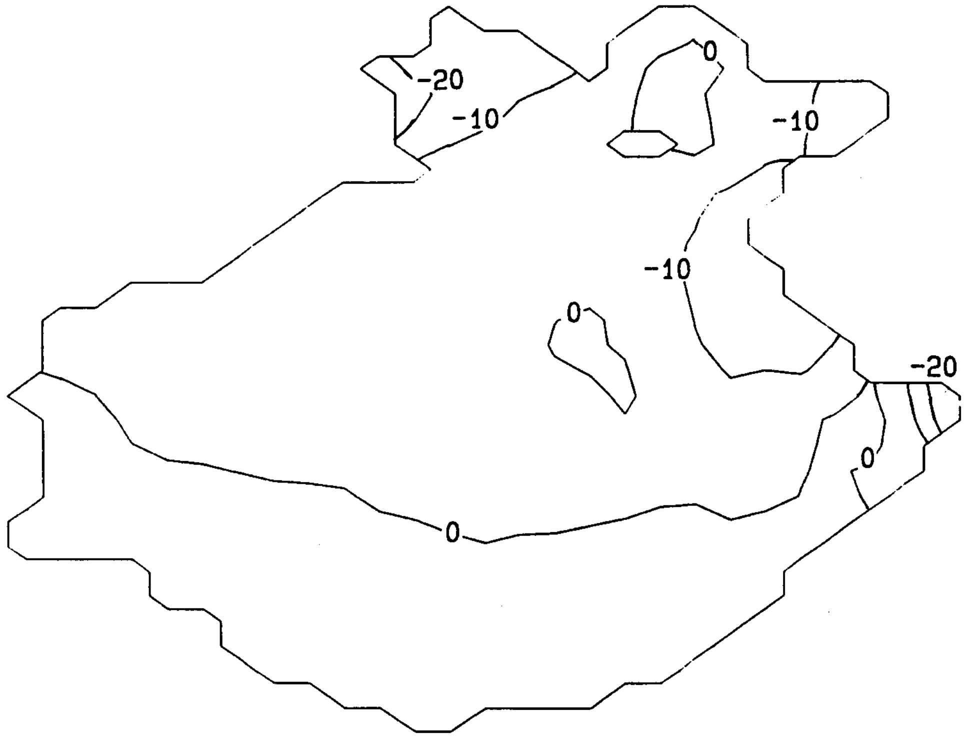

Figure 20.--Sea level, Bering Sea, case 1, day 1
(00Z, 13 Feb. 1982), in centimeters.

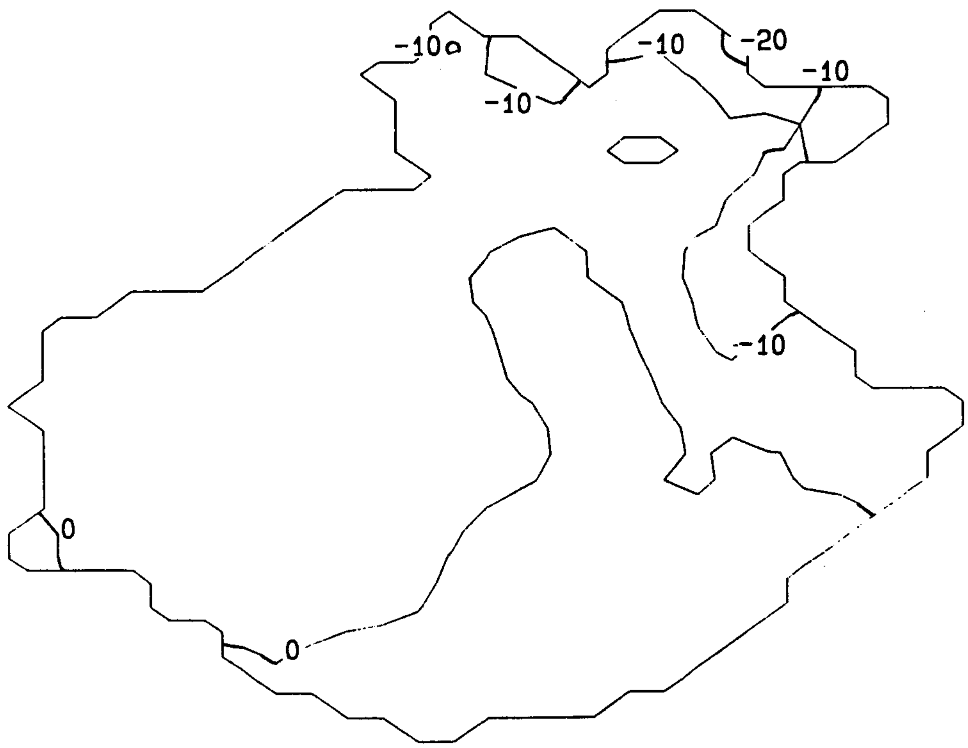

Figure 21.--Sea level, Bering Sea, case 1, day 2
(00Z, 14 Feb. 1982), in centimeters.

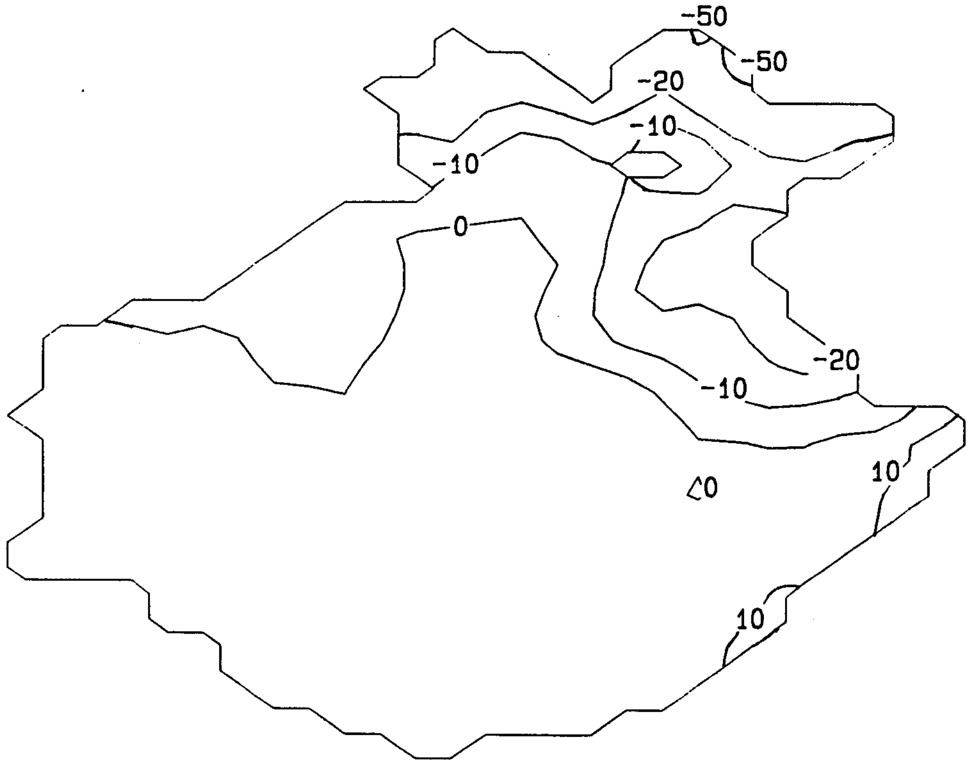

Figure 22.--Sea level, Bering Sea, case 1, day 3 (00Z, 15 Feb. 1982), in centimeters.

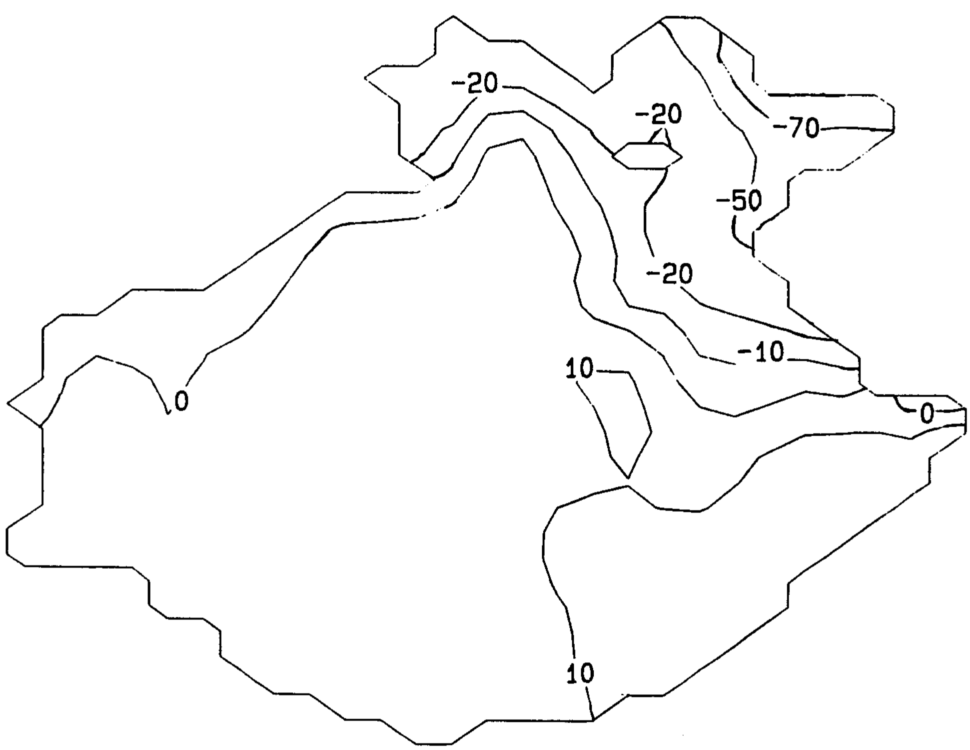

Figure 23.--Sea level, Bering Sea, case 1, day 4 (00Z, 16 Feb. 1982), in centimeters.

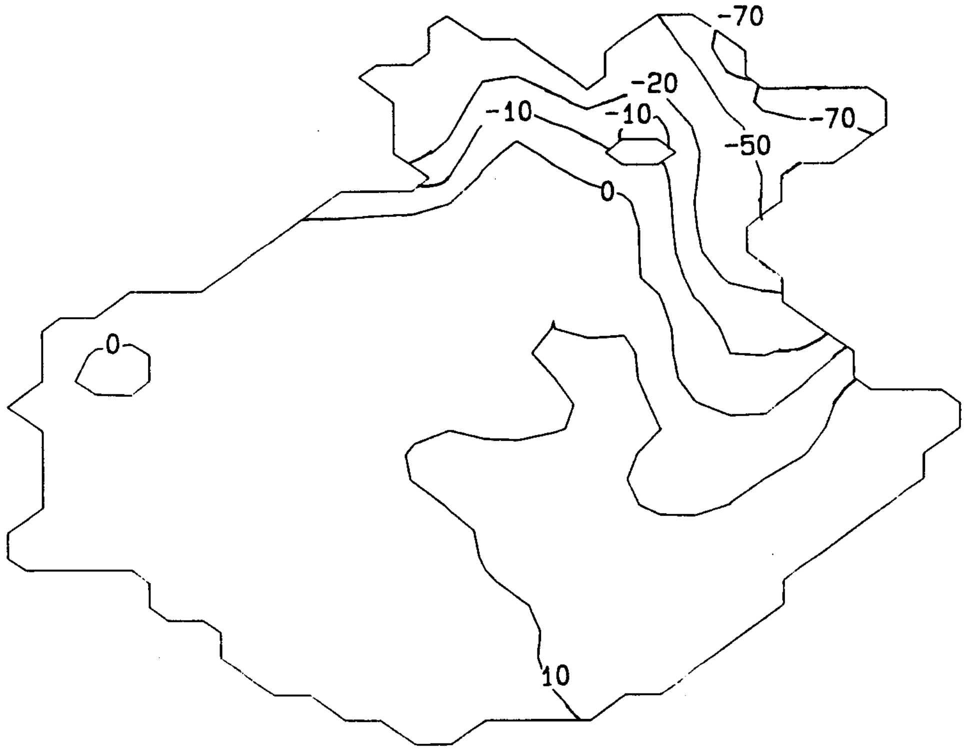

Figure 24.--Sea level, Bering Sea, case 1, day 5 (00Z, 17 Feb. 1982), in centimeters.

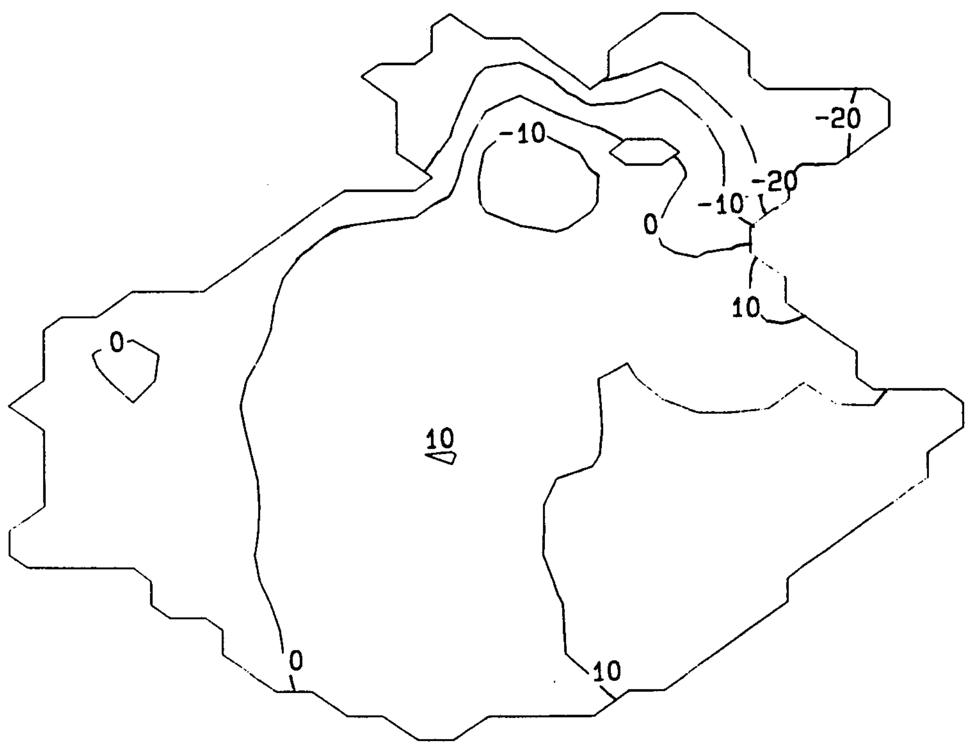

Figure 25.--Sea level, Bering Sea, case 1, day 6 (00Z, 18 Feb. 1982), in centimeters.

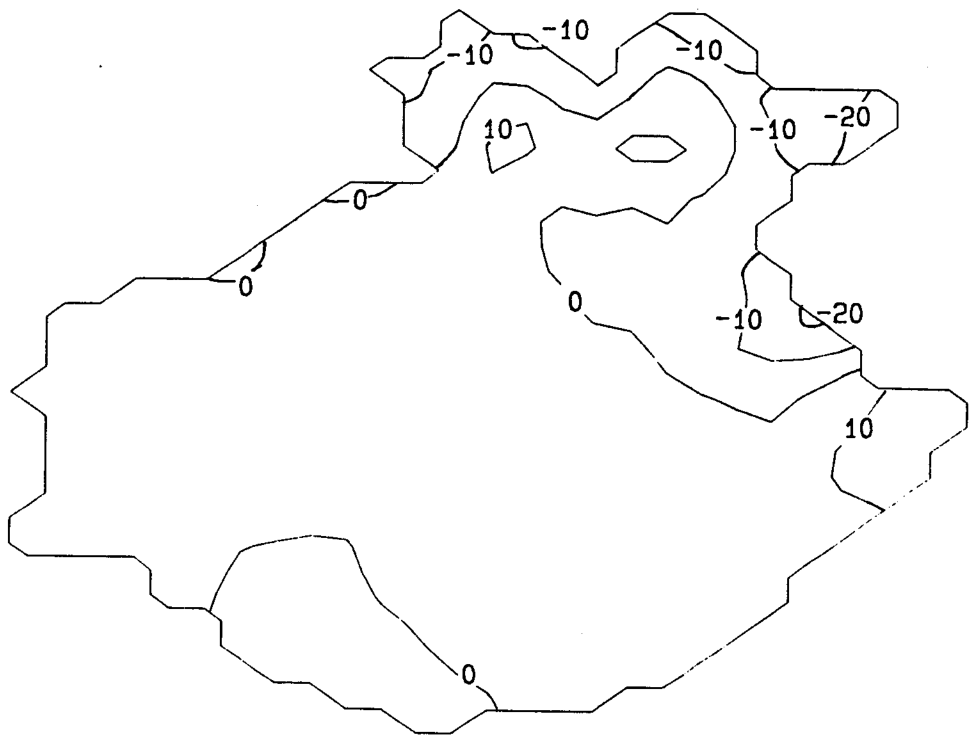

Figure 26.--Sea level, Bering Sea, case 1, day 7 (00Z, 19 Feb. 1982), in centimeters.

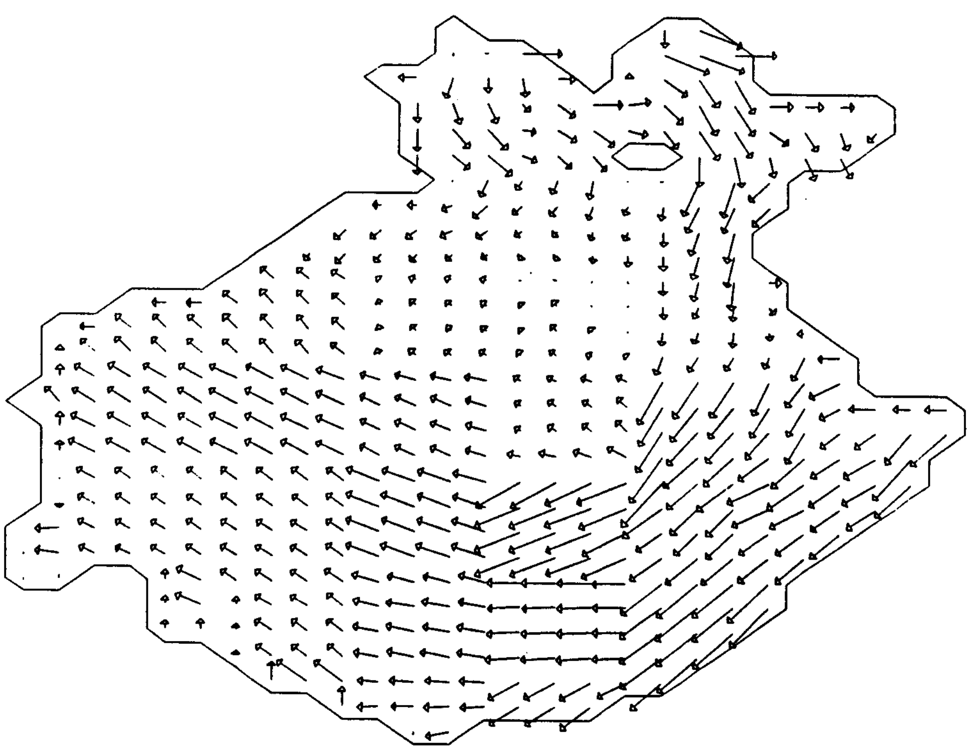

Figure 27.--Ice velocity, Bering Sea, case 1, day 1 (00Z, 13 Feb. 1982); 1 grid line = 10 cm/s.

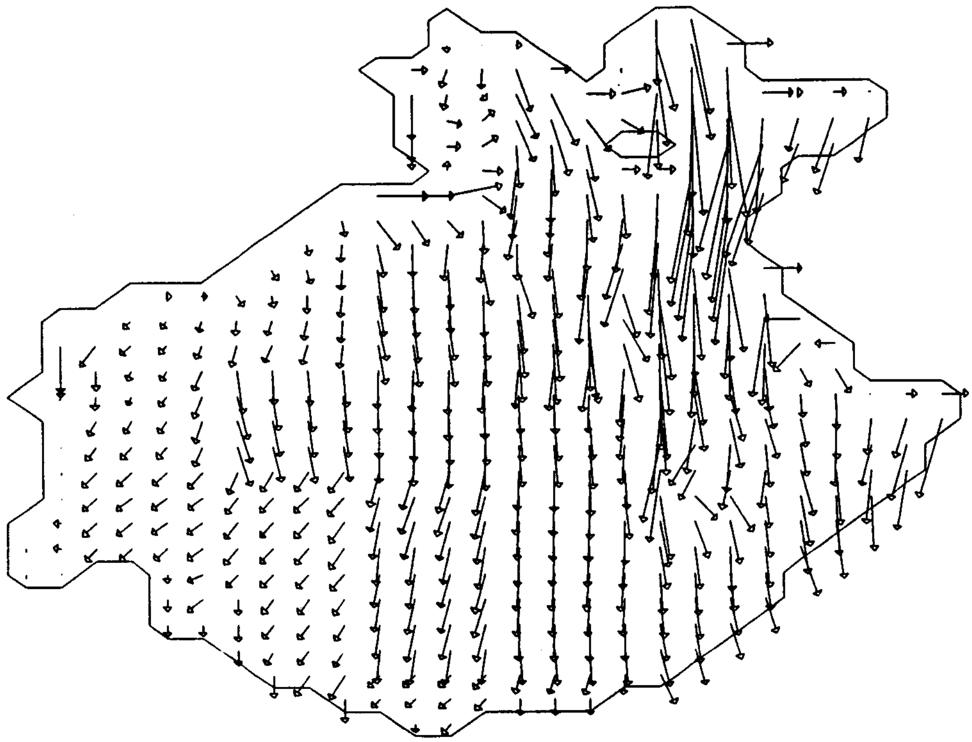

Figure 28.--Ice velocity, Bering Sea, case 1, day 5 (00Z, 17 Feb. 1982); 1 grid line = 10 cm/s.

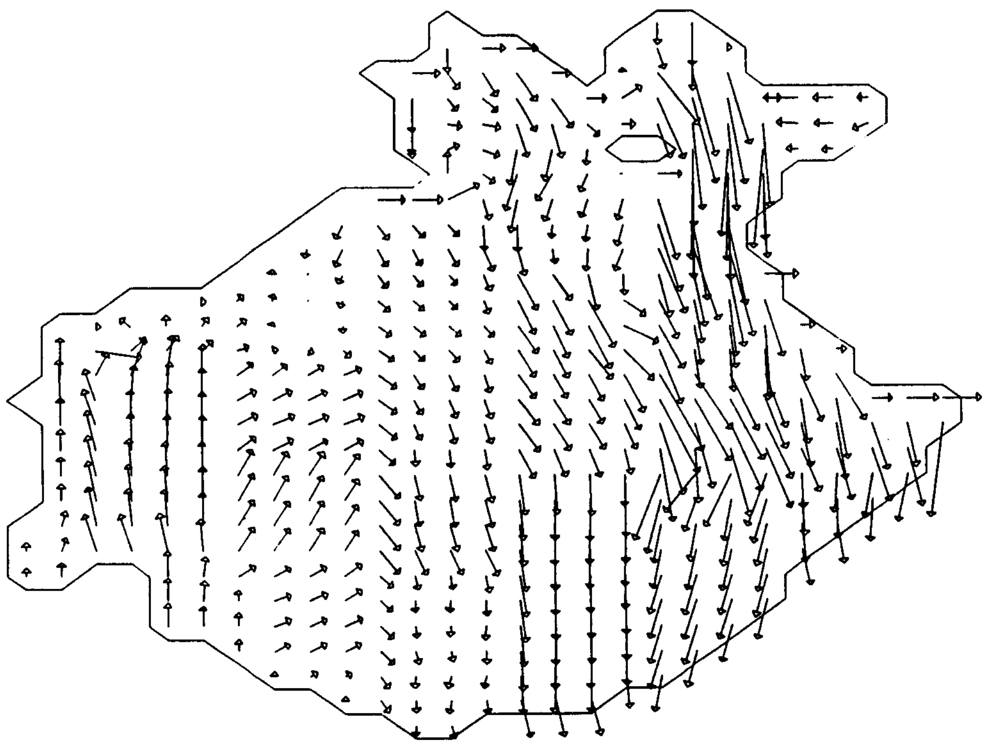

Figure 29.--Ice velocity, Bering Sea, case 1, day 7 (00Z, 19 Feb. 1982); 1 grid line = 10 cm/s.

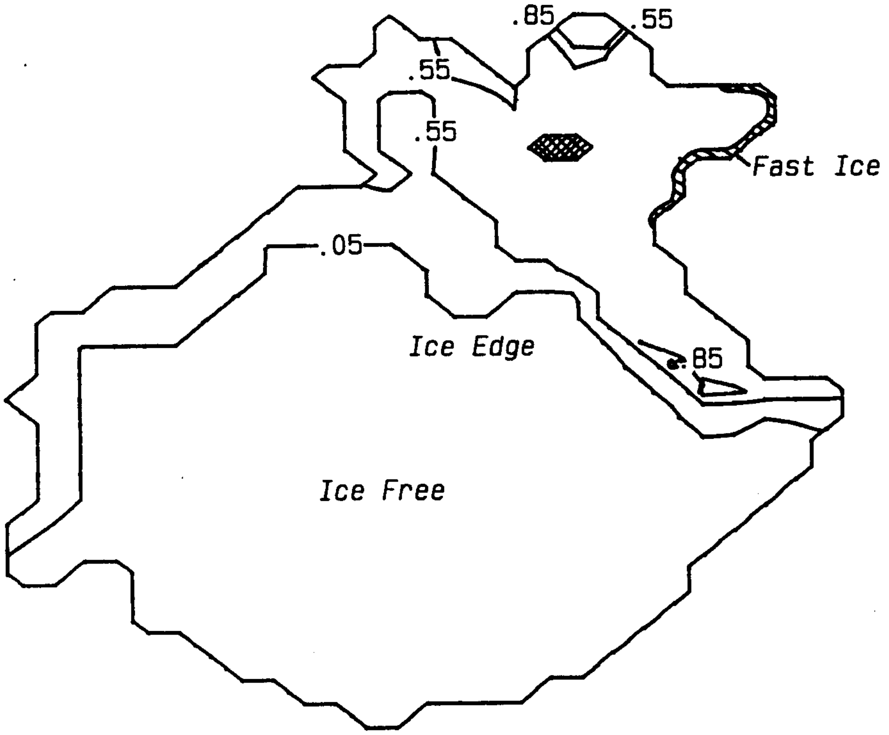

Figure 30.--Ice compactness, Bering Sea, case 1, day 1 (00Z, 13 Feb. 1982).

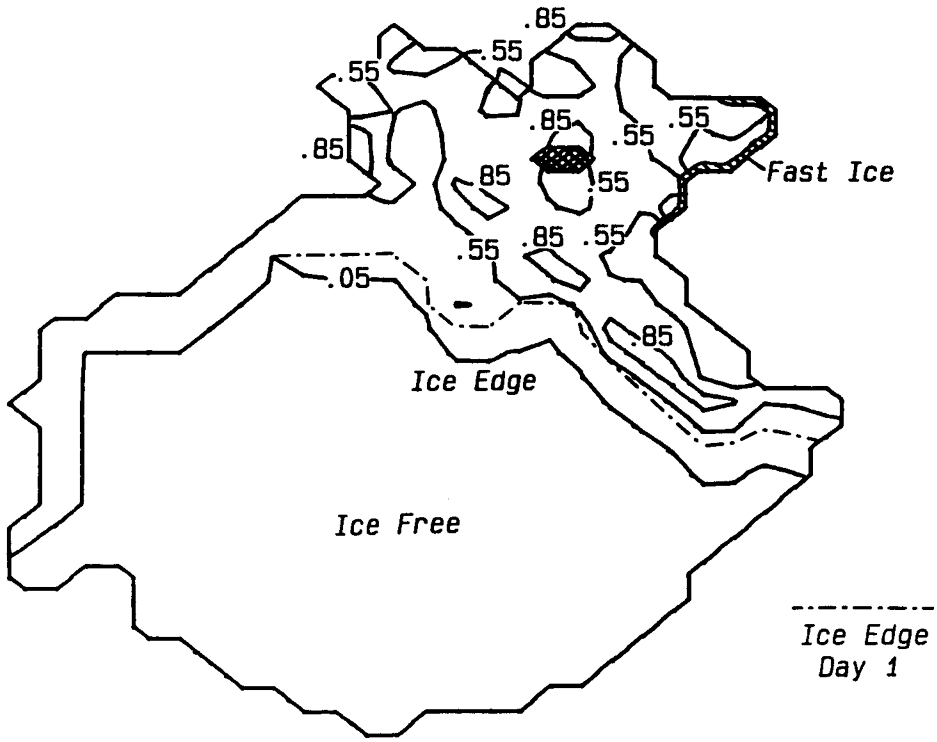

Figure 31.--Ice compactness, Bering Sea, case 1, day 5 (00Z, 17 Feb. 1982).

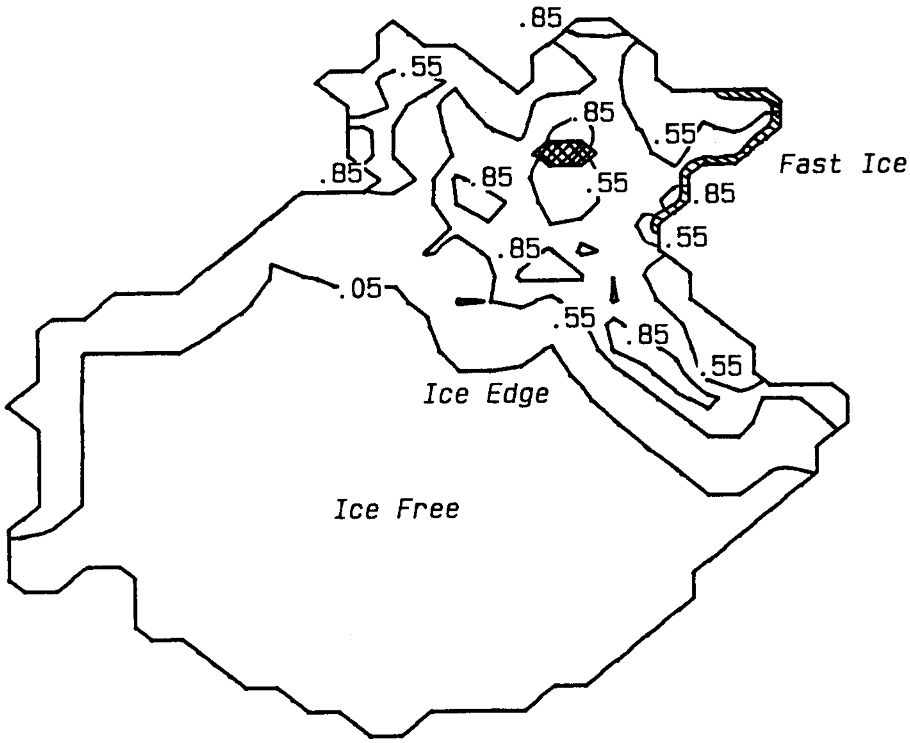

Figure 32.--Ice compactness, Bering Sea, case 1, day 7 (00Z, 19 Feb. 1982).

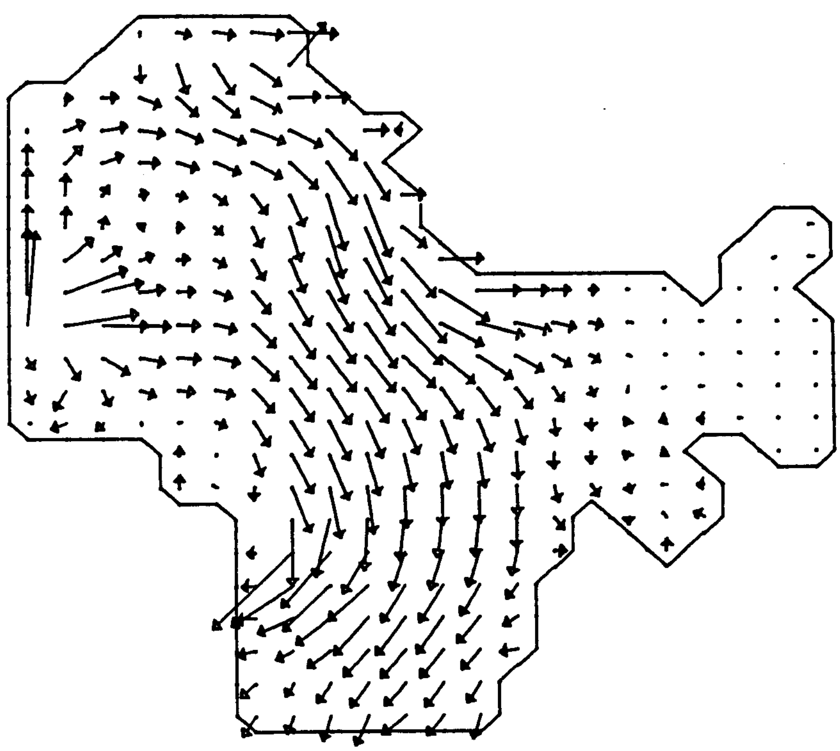

Figure 33.--Velocity, Norton Sound, case 1, day 1 (00Z, 13 Feb. 1982); 1 horizontal grid line = 10 cm/s.

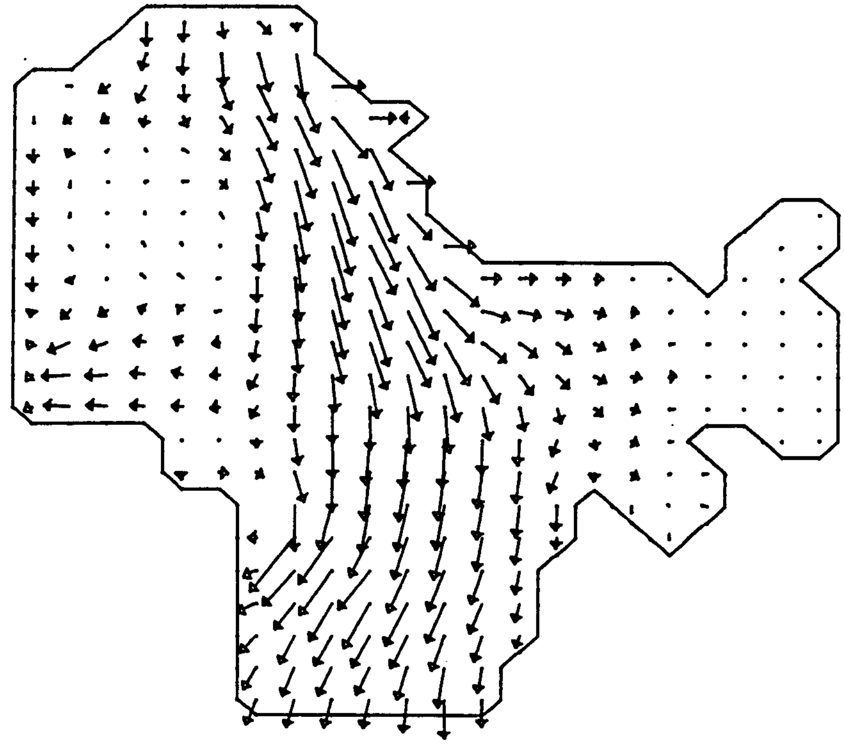

Figure 34.--Velocity, Norton Sound, case 1, day 2 (00Z, 14 Feb. 1982); 1 grid line = 10 cm/s.

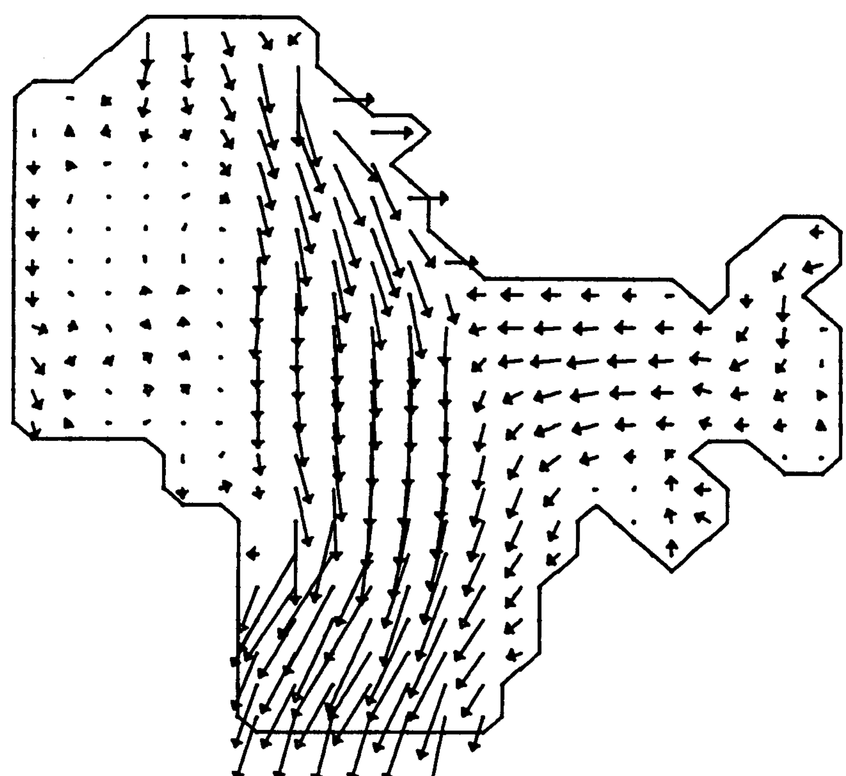

Figure 35.--Velocity, Norton Sound, case 1, day 3 (00Z, 15 Feb. 1982); 1 grid line = 20 cm/s.

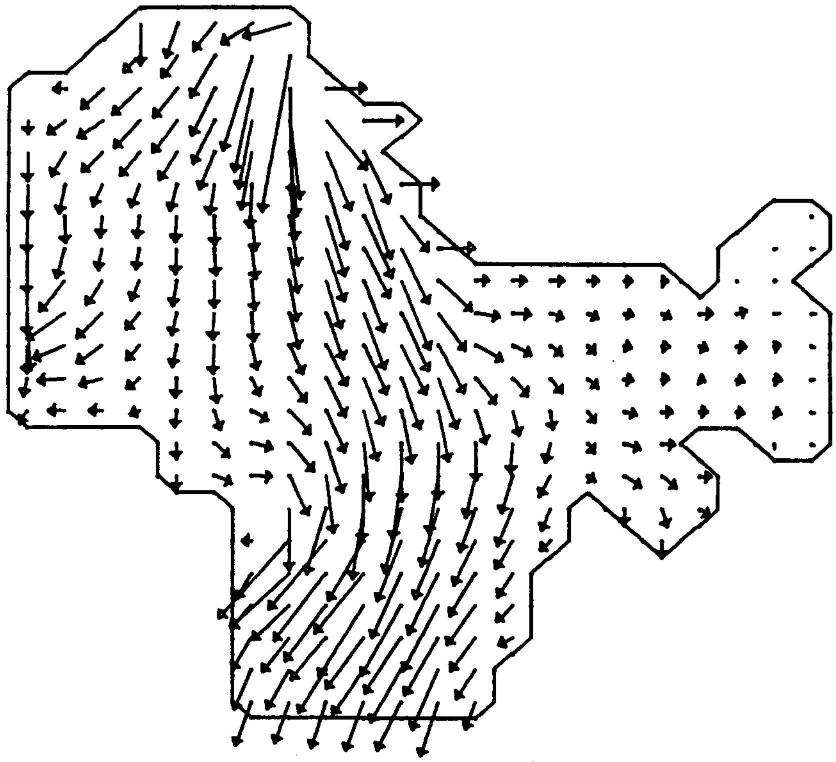

Figure 36.--Velocity, Norton Sound, case 1, day 4 (00Z, 16 Feb. 1982); 1 grid line = 20 cm/s.

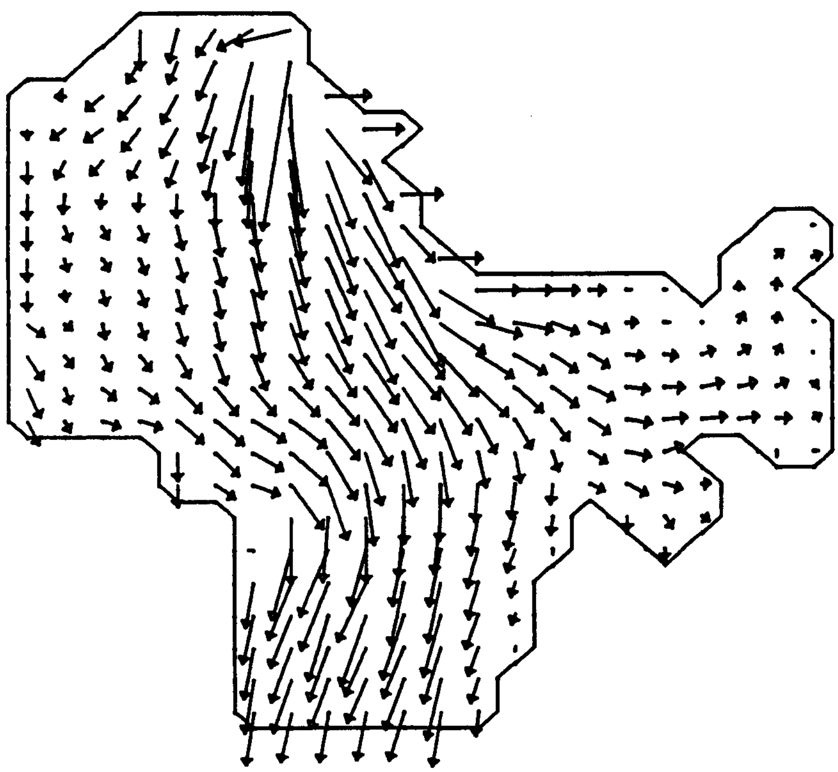

Figure 37.--Velocity, Norton Sound, case 1, day 5 (00Z, 17 Feb. 1982); 1 grid line = 20 cm/s.

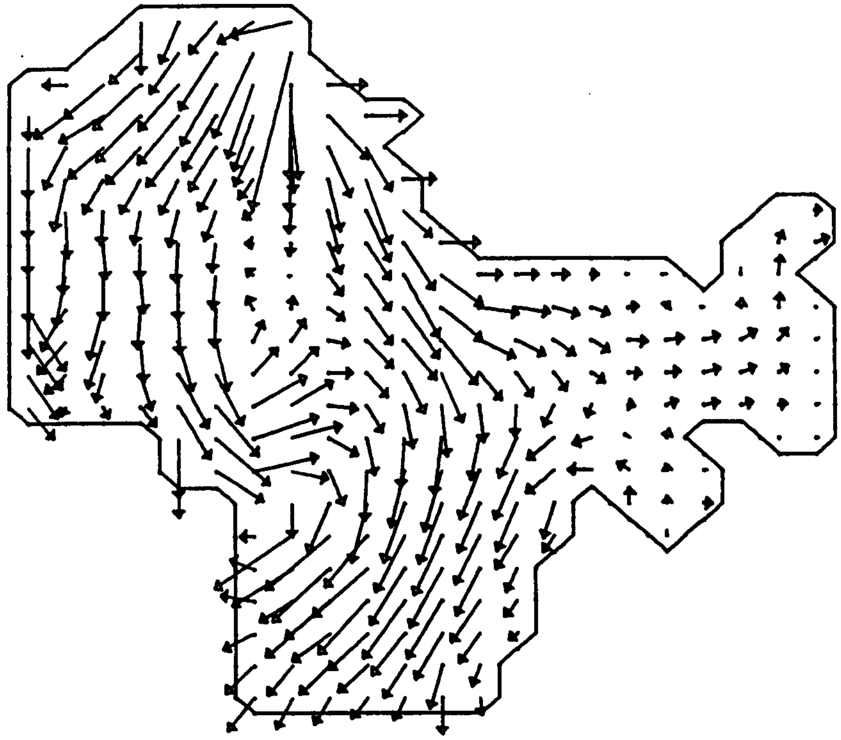

Figure 38.--Velocity, Norton Sound, case 1, day 6 (00Z, 18 February 1982); 1 grid line = 10 cm/s.

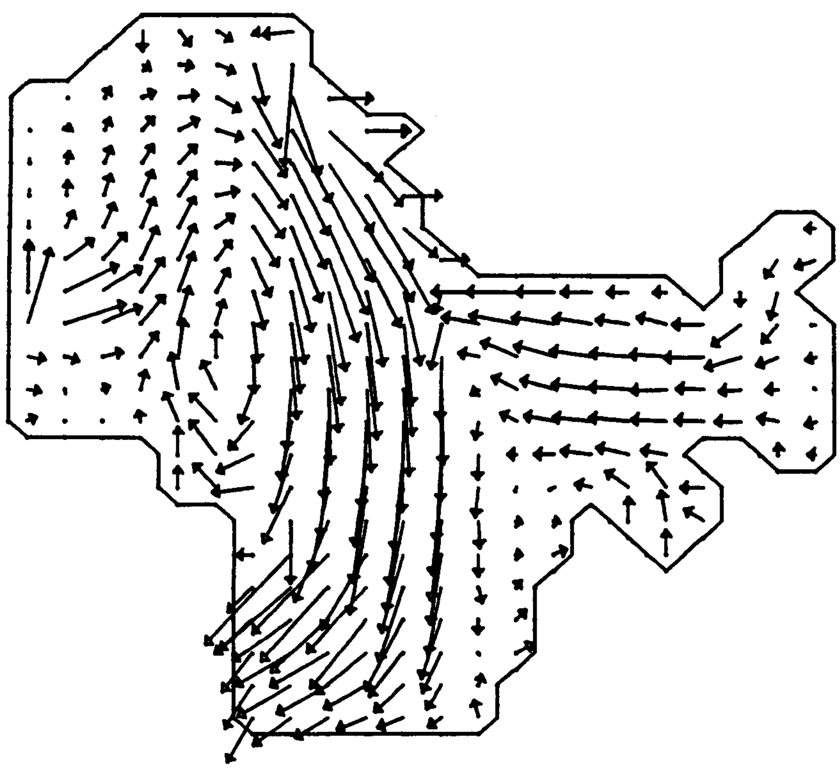

Figure 39.--Velocity, Norton Sound, case 1, day 7 (00Z, 19 Feb. 1982); 1 grid line = 10 cm/s.

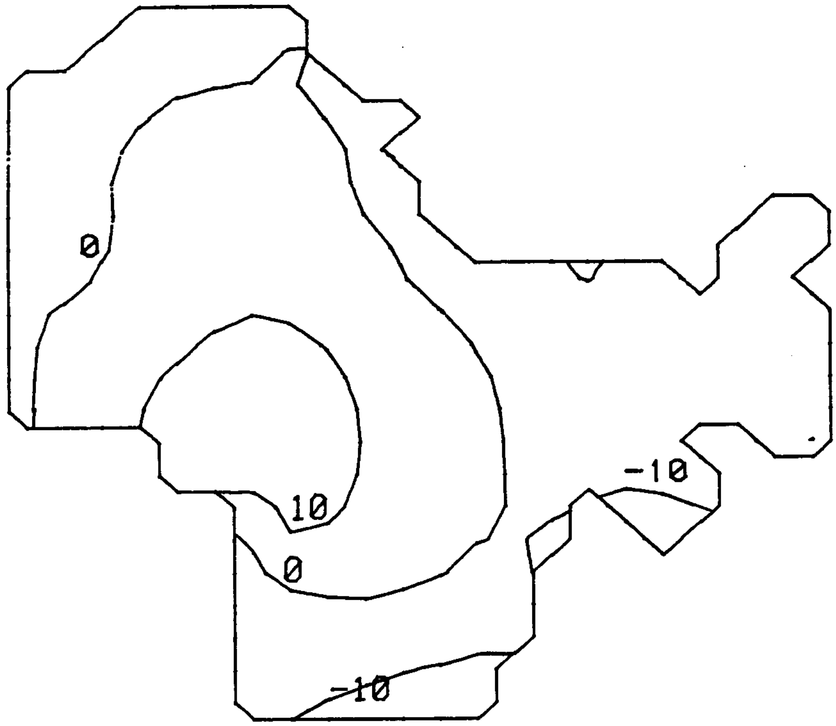

Figure 40.--Sea level, Norton Sound, case 1, day 1 (00Z, 13 Feb. 1982), in centimeters.

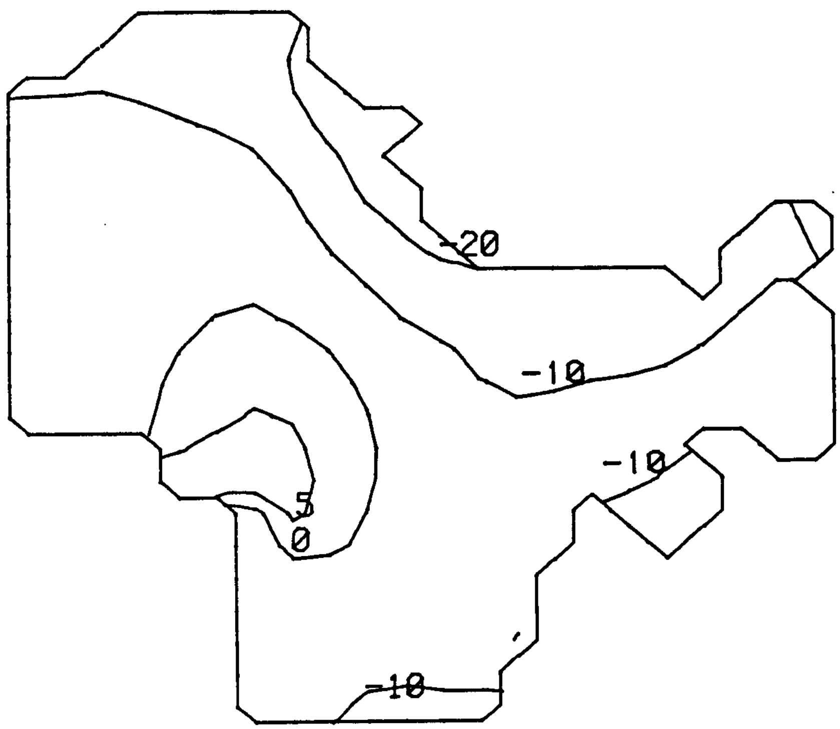

Figure 41.--Sea level, Norton Sound, case 1, day 2 (00Z, 14 Feb. 1982), in centimeters.

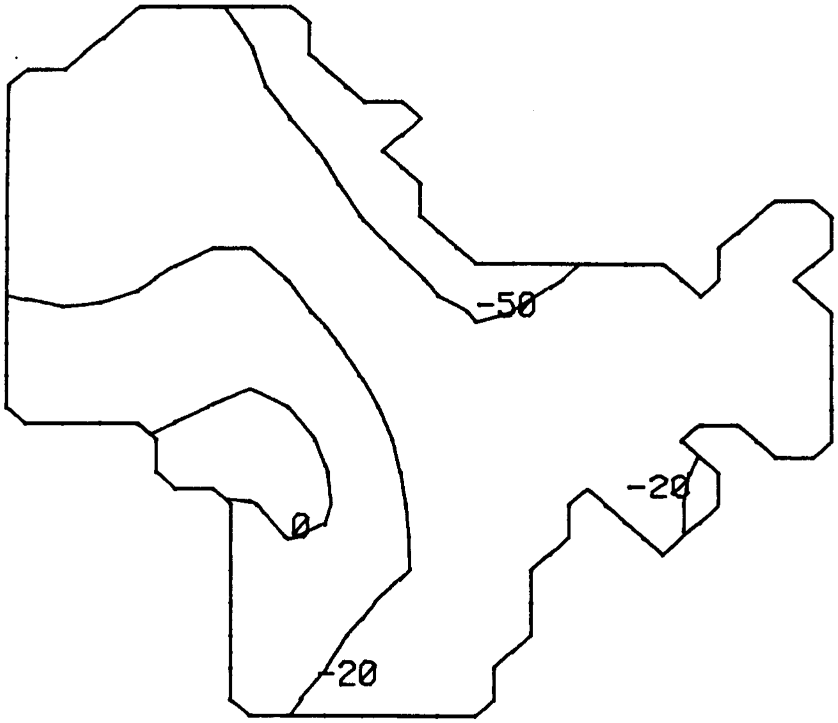

Figure 42.--Sea level, Norton Sound, case 1, day 3 (00Z, 15 Feb. 1982), in centimeters.

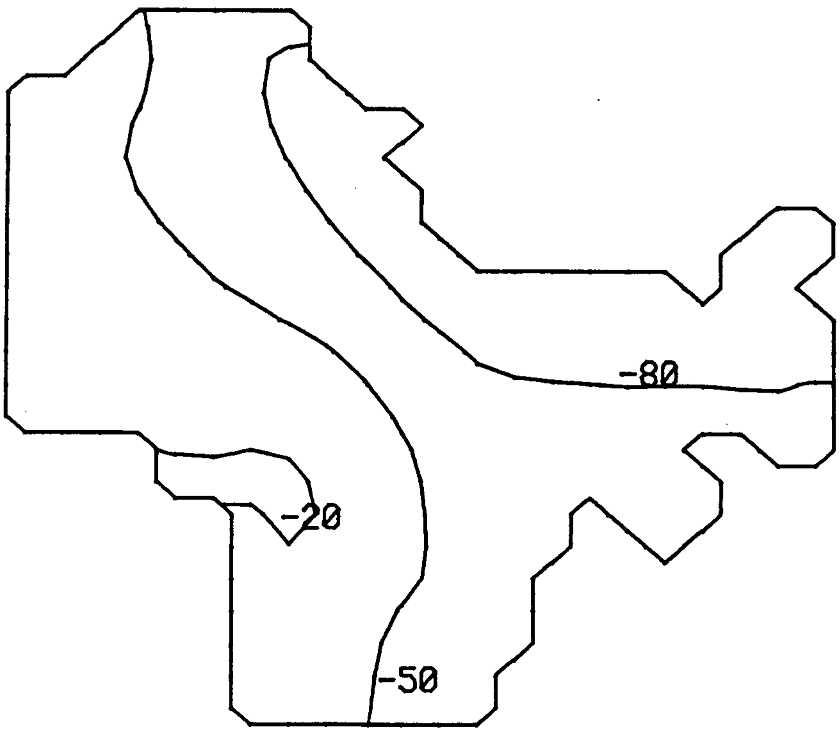

Figure 43.--Sea level, Norton Sound, case 1, day 4 (00Z, 16 Feb. 1982), in centimeters.

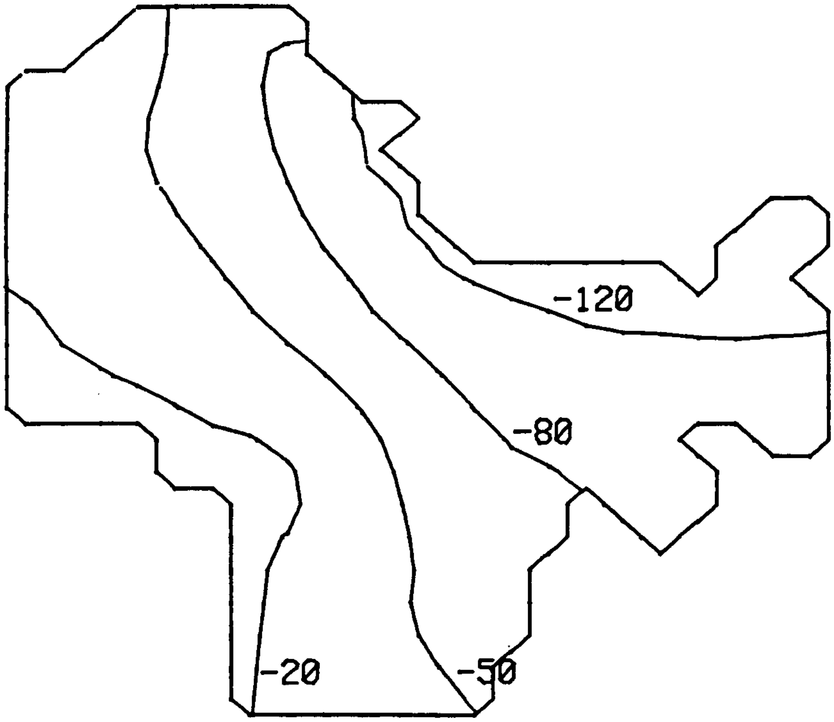

Figure 44.--Sea level, Norton Sound, case 1, day 5 (00Z, 17 Feb. 1982), in centimeters.

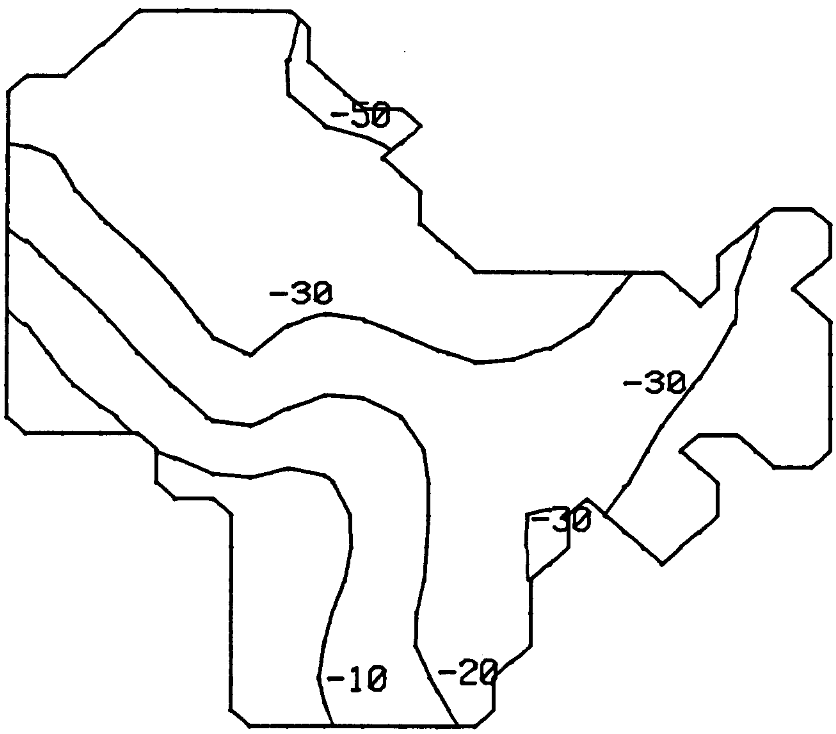

Figure 45.--Sea level, Norton Sound, case 1, day 6 (00Z, 18 Feb. 1982), in centimeters.

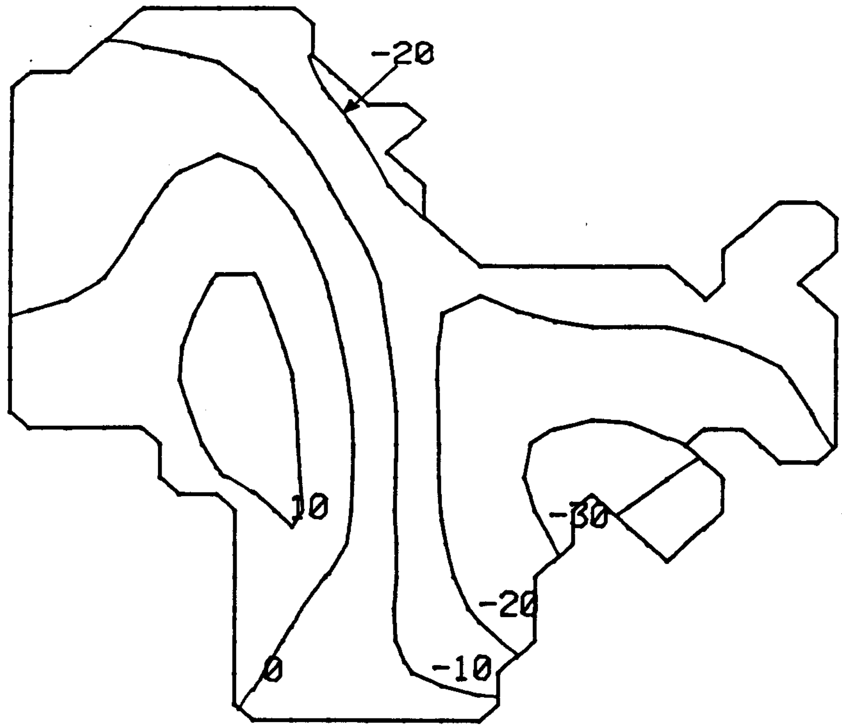

Figure 46.--Sea level, Norton Sound, case 1, day 7 (00Z, 19 Feb. 1982), in centimeters.

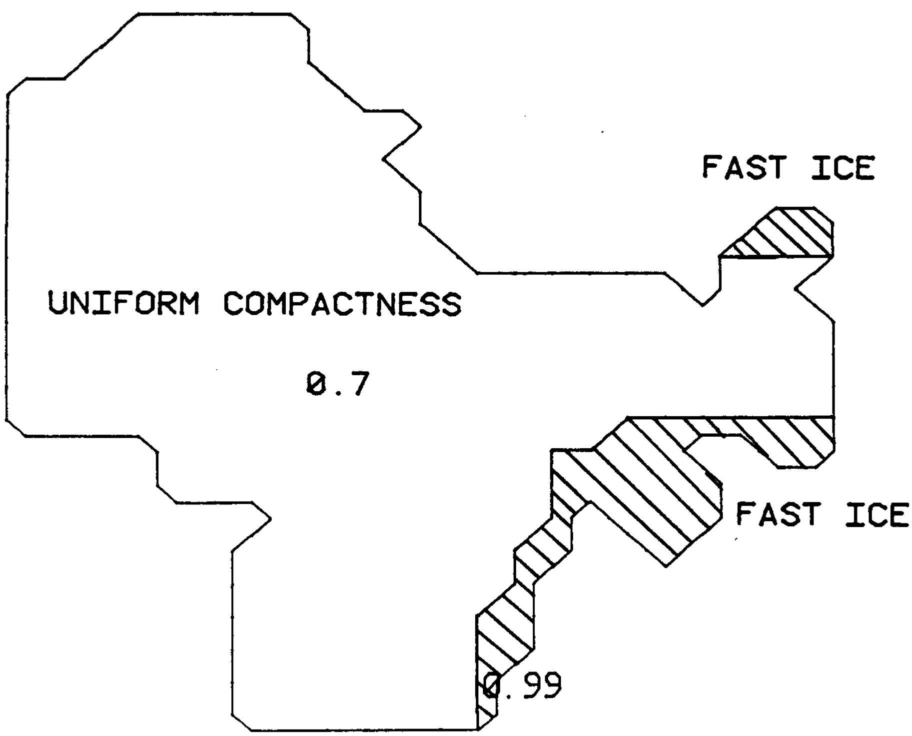

Figure 47.--Ice compactness, Norton Sound, case 1, day 1 (00Z, 13 Feb. 1982).

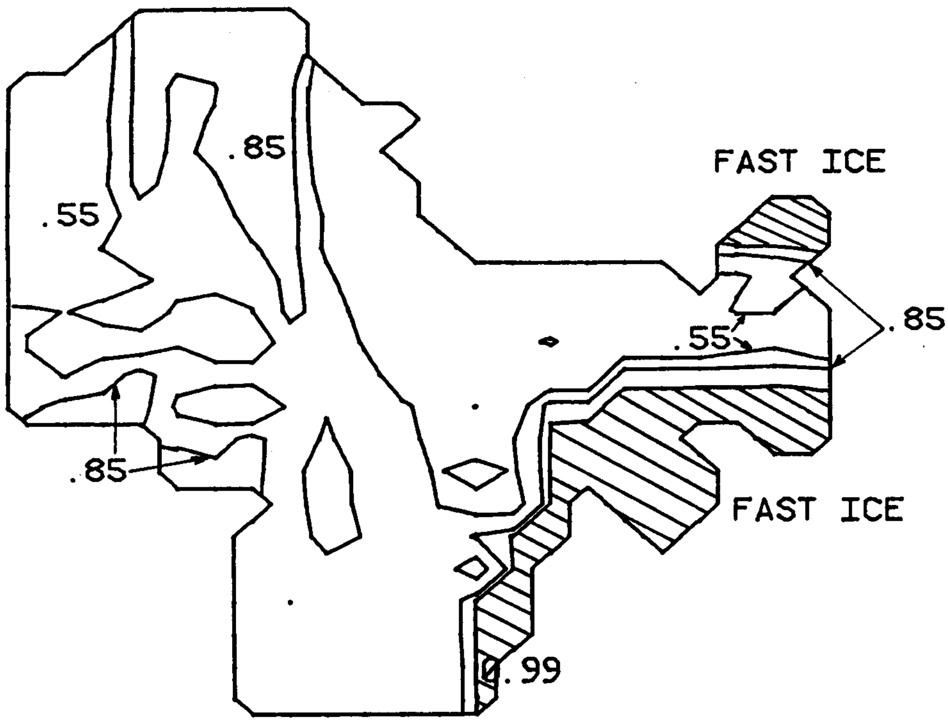

Figure 48.--Ice compactness, Norton Sound, case 1, day 5 (00Z, 17 Feb. 1982).

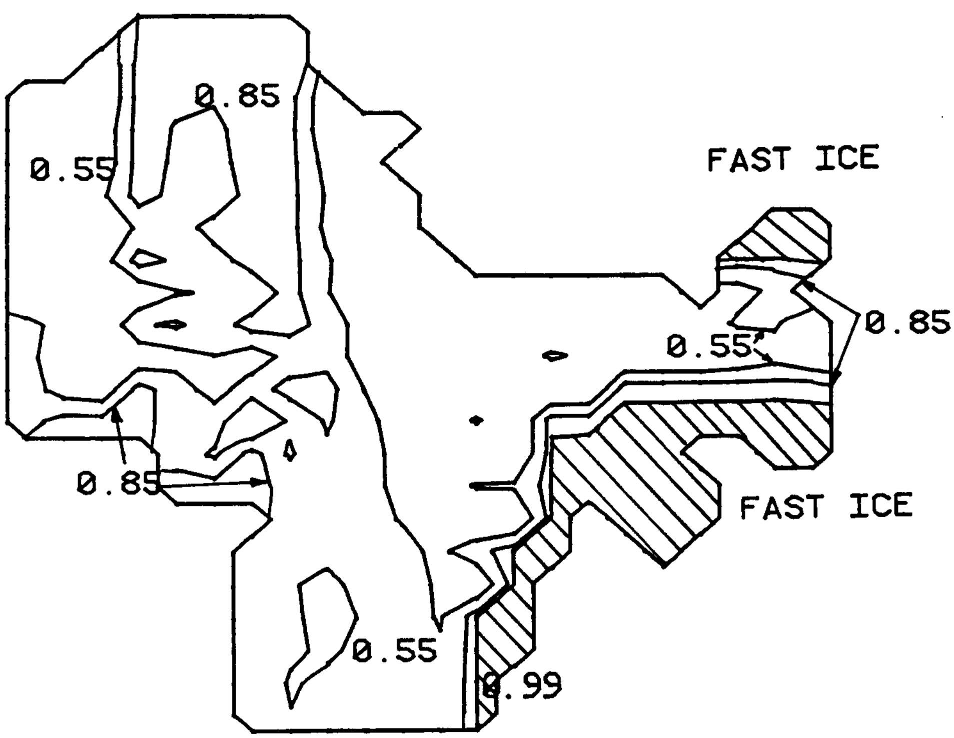

Figure 49.--Ice compactness, Norton Sound, case 1, day 7 (00Z, 19 Feb. 1982).

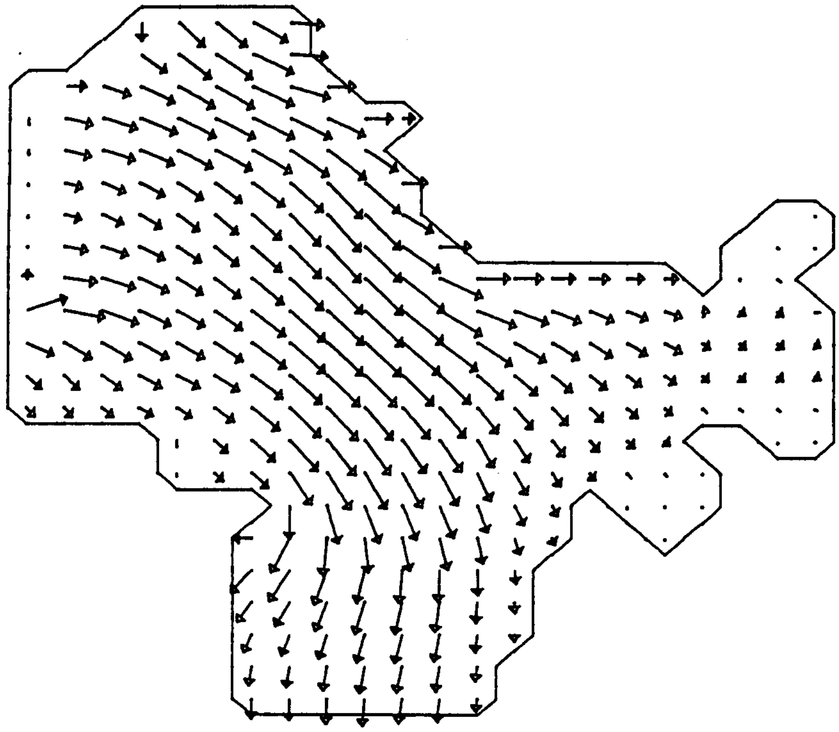

Figure 50.--Ice velocity, Norton Sound, case 1, day 1 (00Z, 13 Feb. 1982); 1 grid line = 20 cm/s.

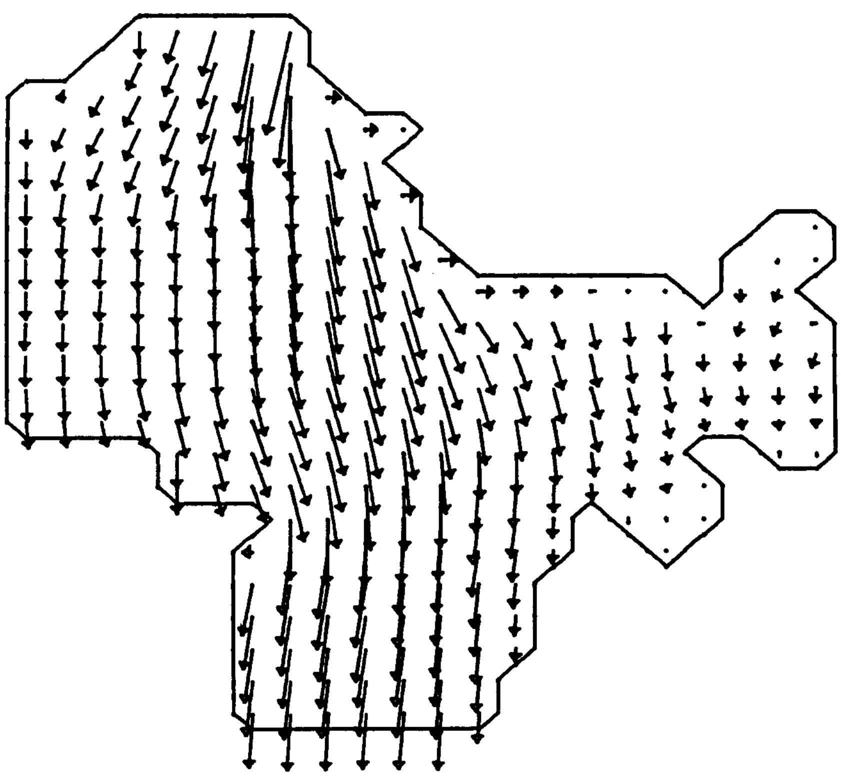

Figure 51.--Ice velocity, Norton Sound, case 1, day 5 (00Z, 17 Feb. 1982); 1 grid line = 40 cm/s.

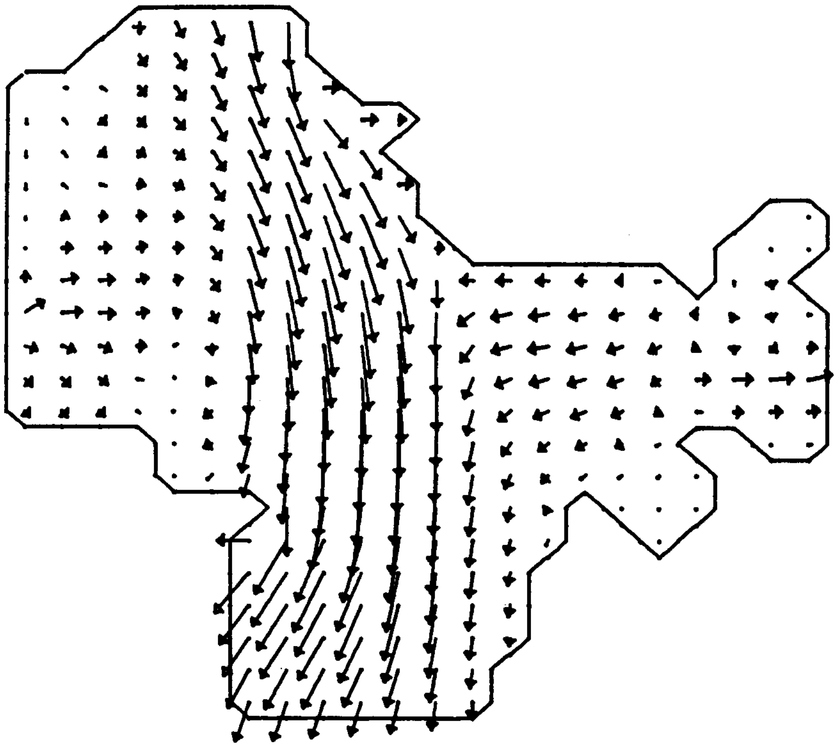

Figure 52.--Ice velocity, Norton Sound, case 1, day 7 (00Z, 19 Feb. 1982); 1 grid line = 20 cm/s.

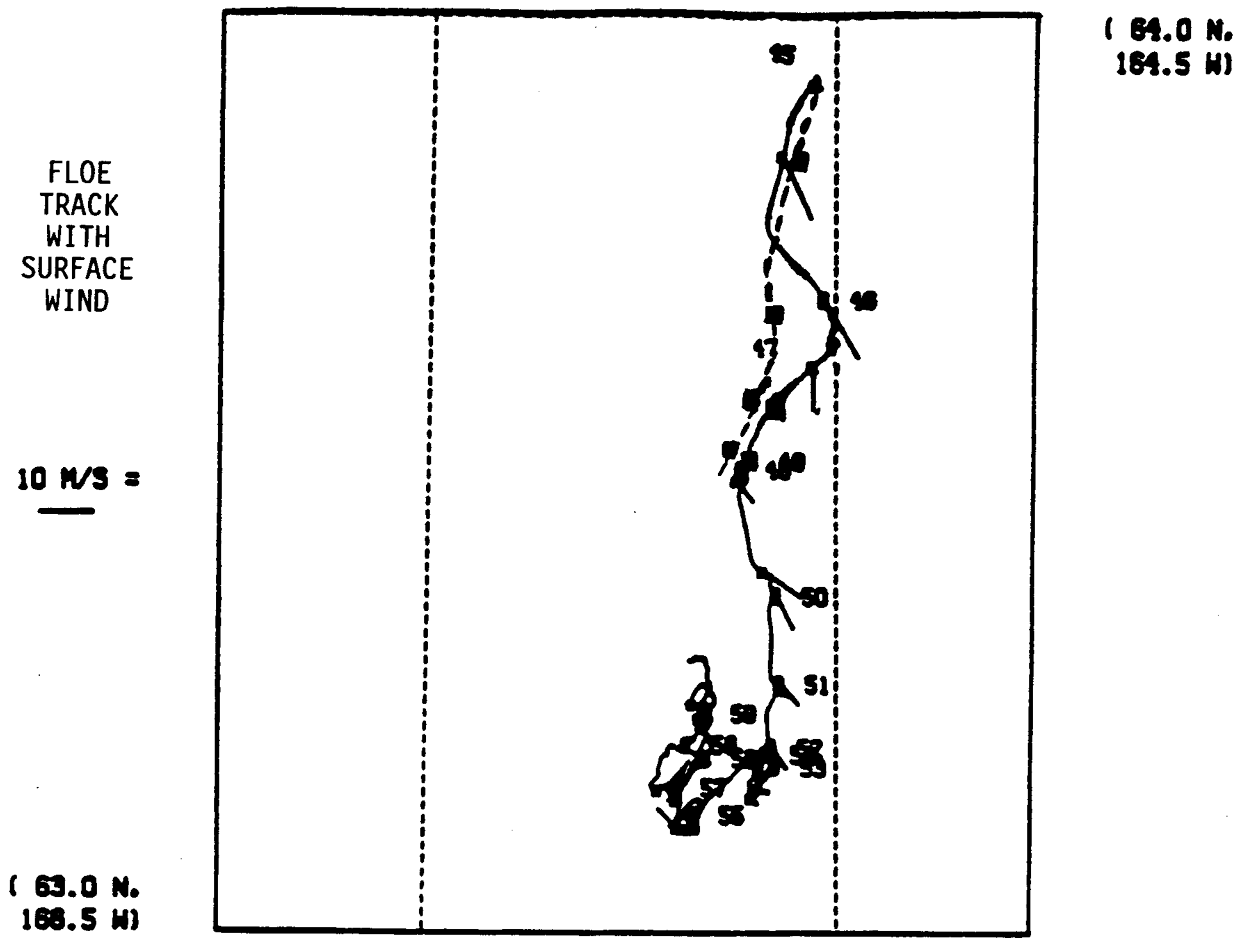

Figure 53.--Ice drift floe track, case 1, 14-28 February 1982 (JD 45-59). Measured by Reynolds and Pease (1984). Floe station 2322B = continuous line; calculated from model = broken line.

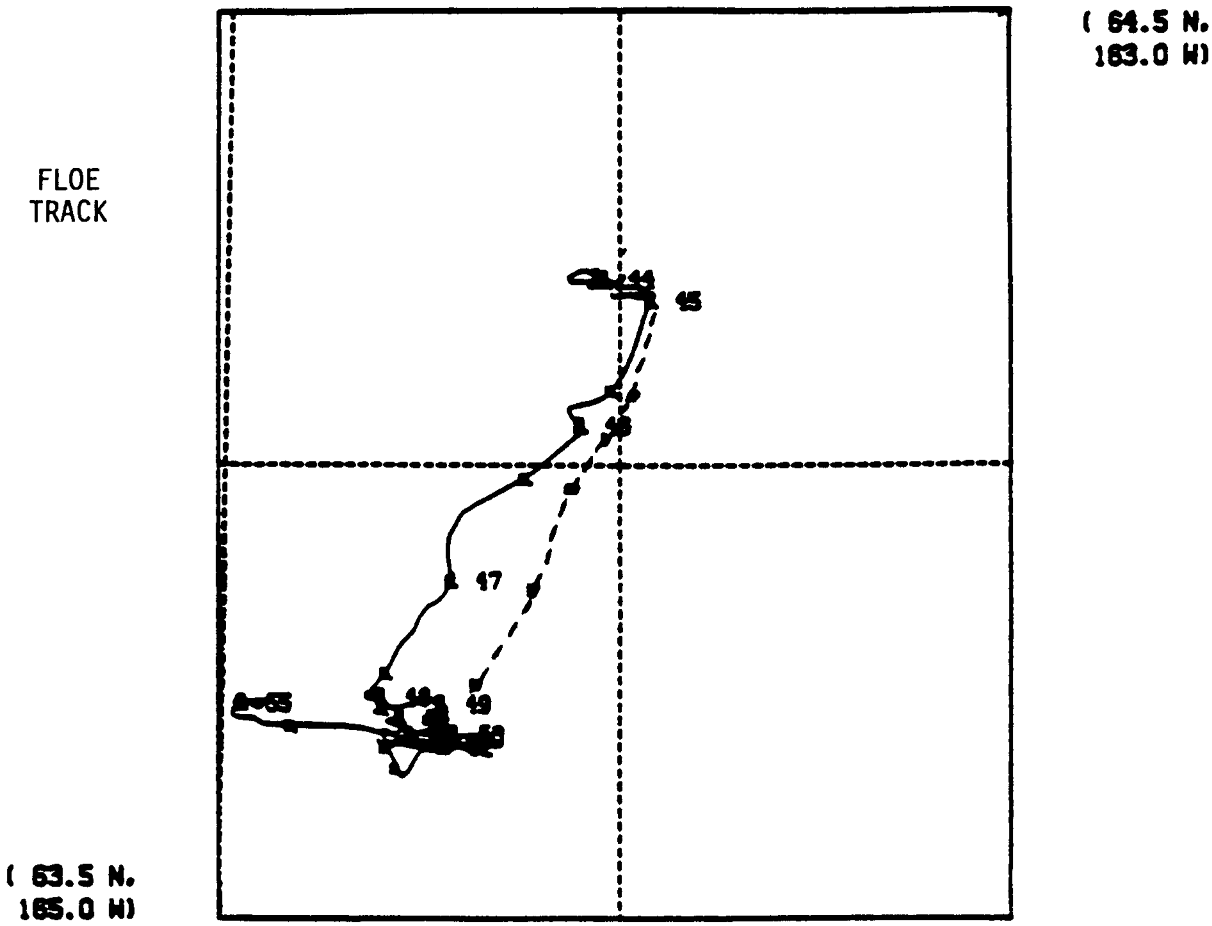

Figure 54.--Ice drift floe track, case 1, 13-28 February 1982 (JD 44-59). Measured by Reynolds and Pease (1984). Floe station 2321B = continuous line; calculated from model = broken line.

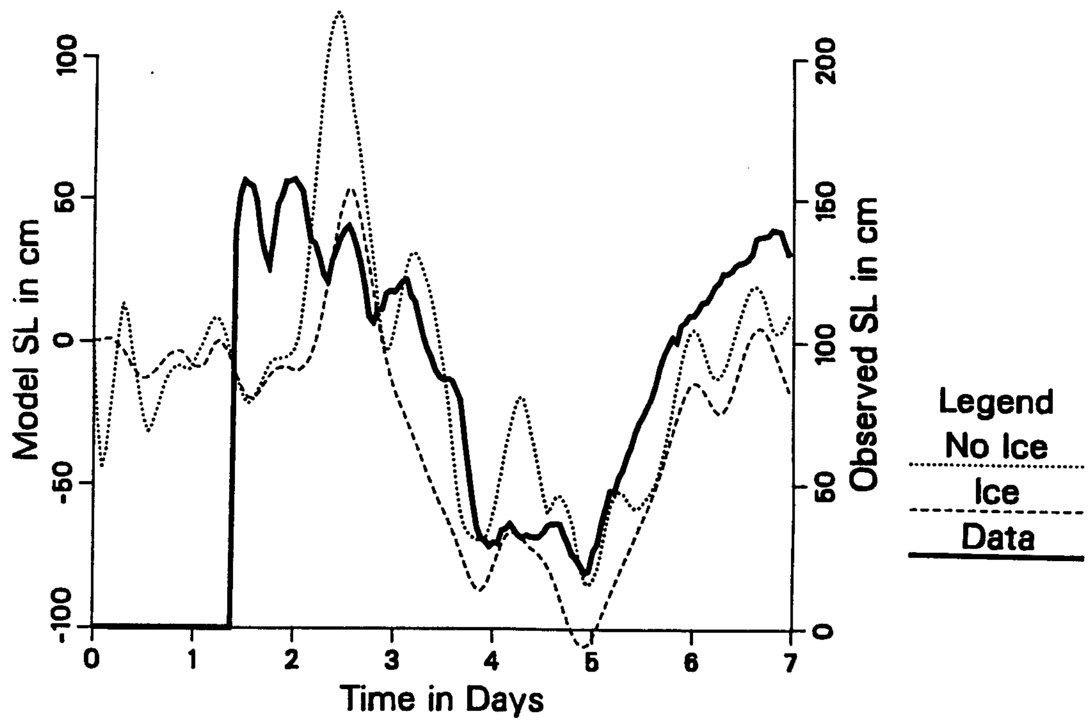

Figure 55.--Model comparison to observed sea level at Stebbins, Alaska, case 1, February 1982.

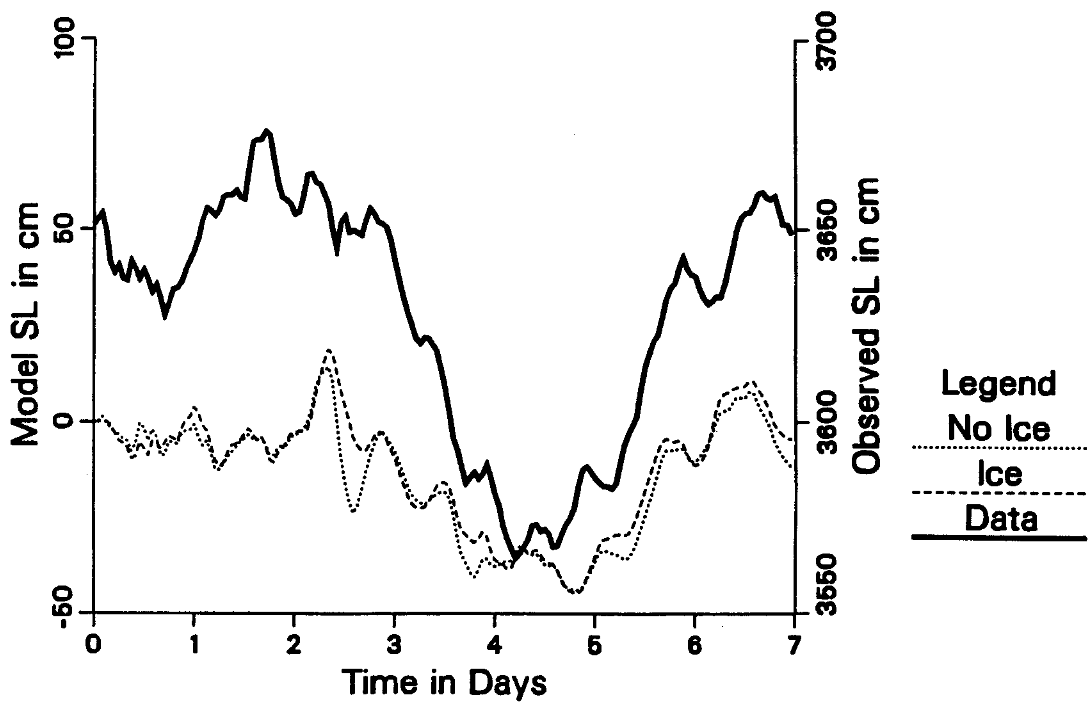

Figure 56.--Model comparison to observed sea level at point NC17, case 1, February 1982.

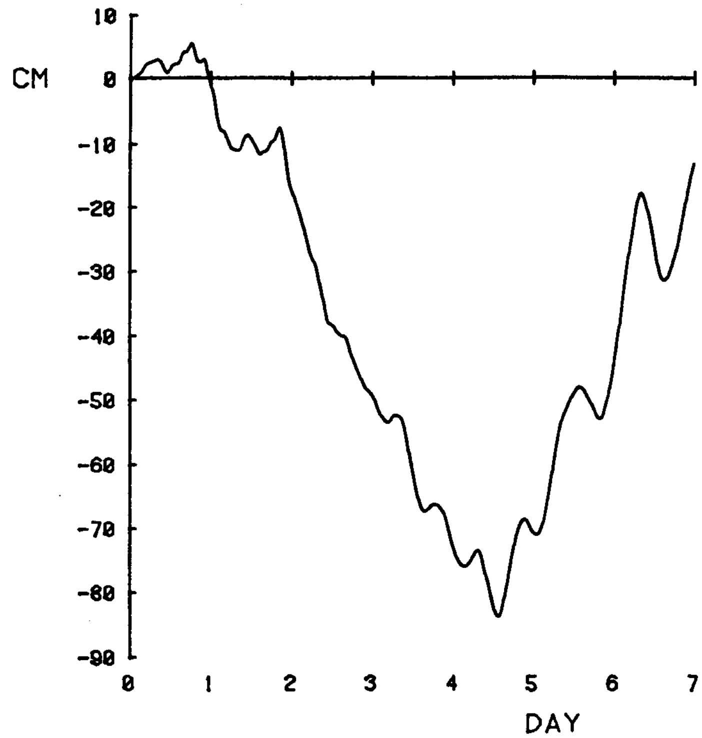

Figure 57.--Computed sea level, Diomedes, case 1.

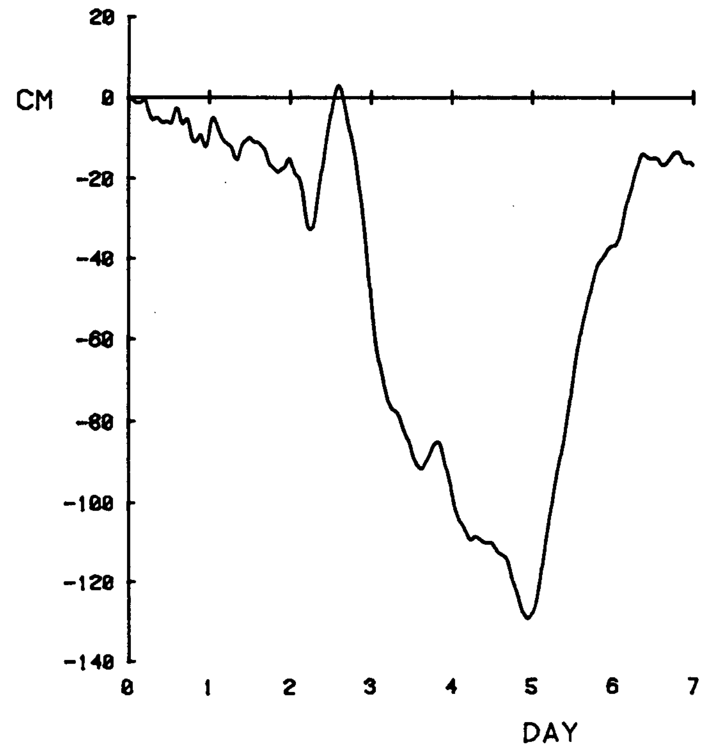

Figure 58.--Computed sea level, Nome, case 1.

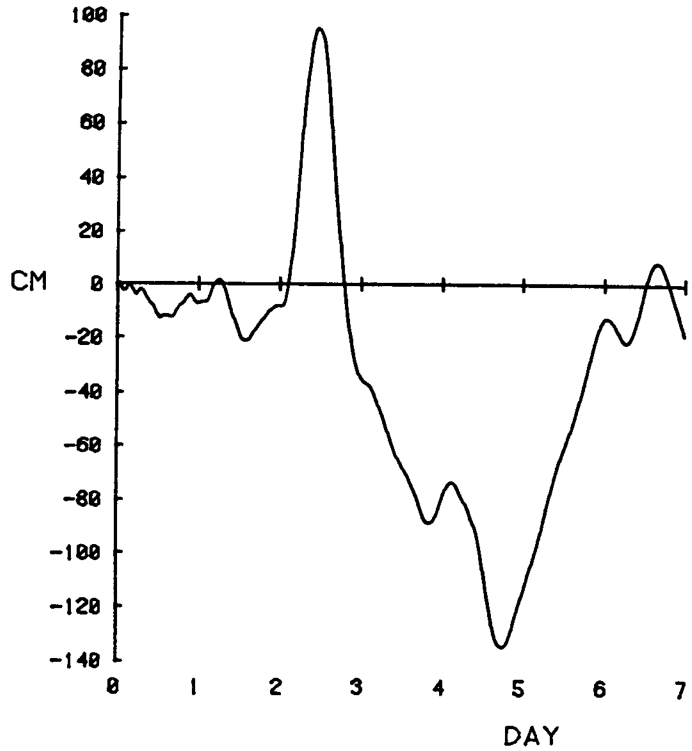

Figure 59.--Computed sea level, Unalakleet, case 1.

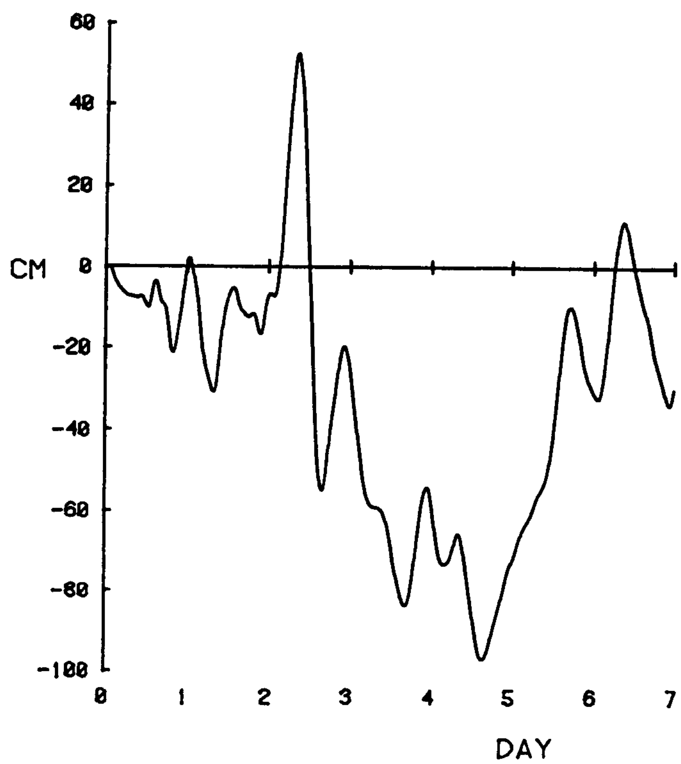

Figure 60.--Computed sea level, Yukon River outflow, case 1.

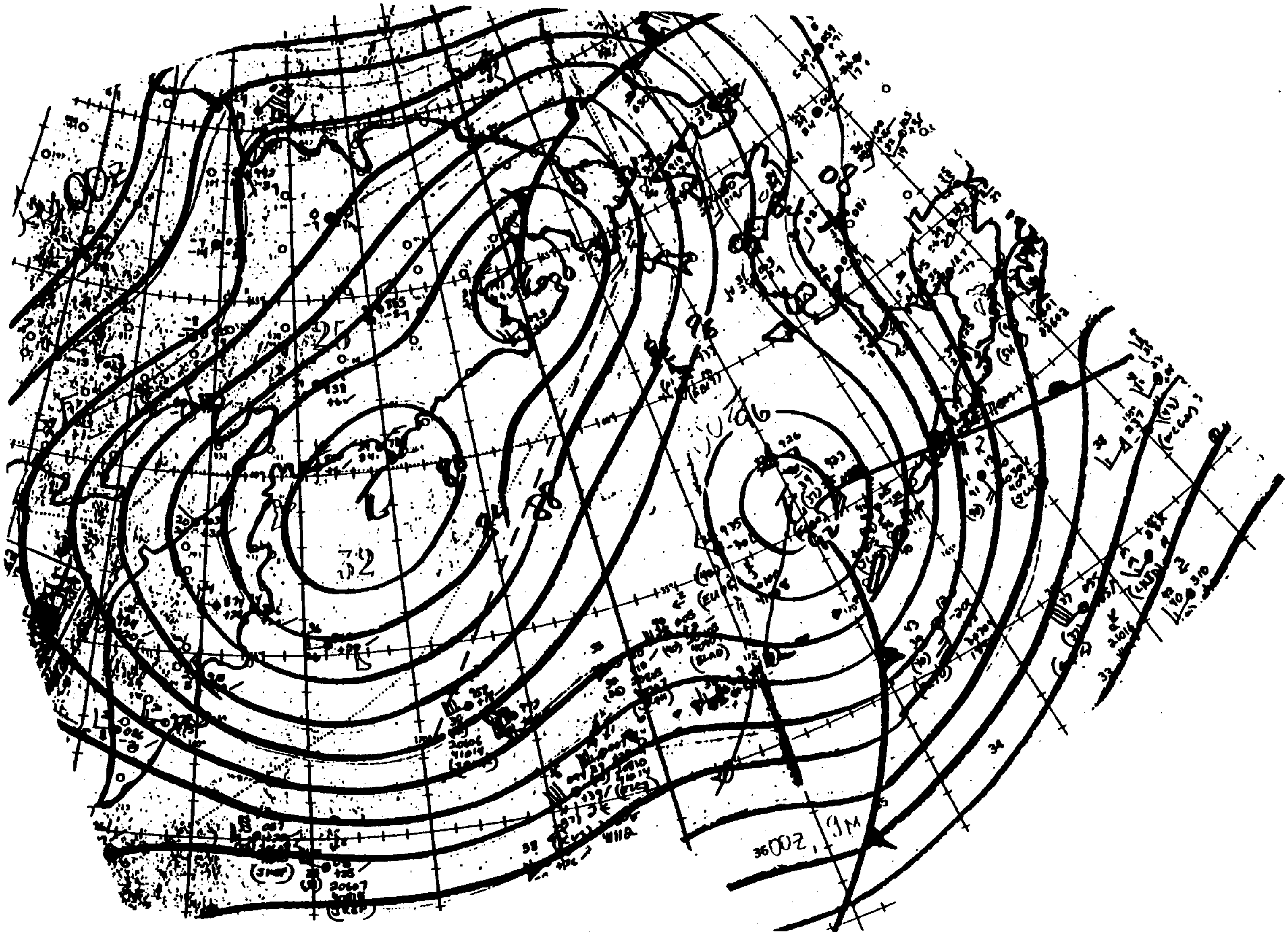

Figure 61.--Surface weather chart for 00Z, 9 March 1982. Pressure in millibars.

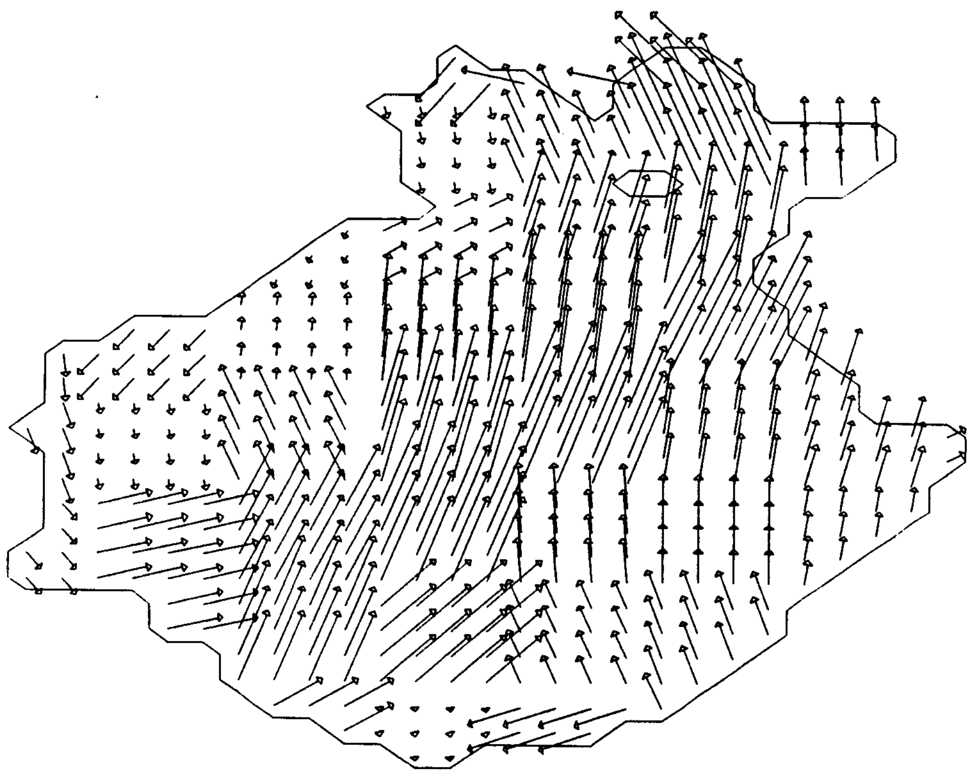

Figure 62.--Wind, Bering Sea, case 2, day 1 (18Z, 8 Mar. 1982); 1 horizontal grid length = 5 m/s.

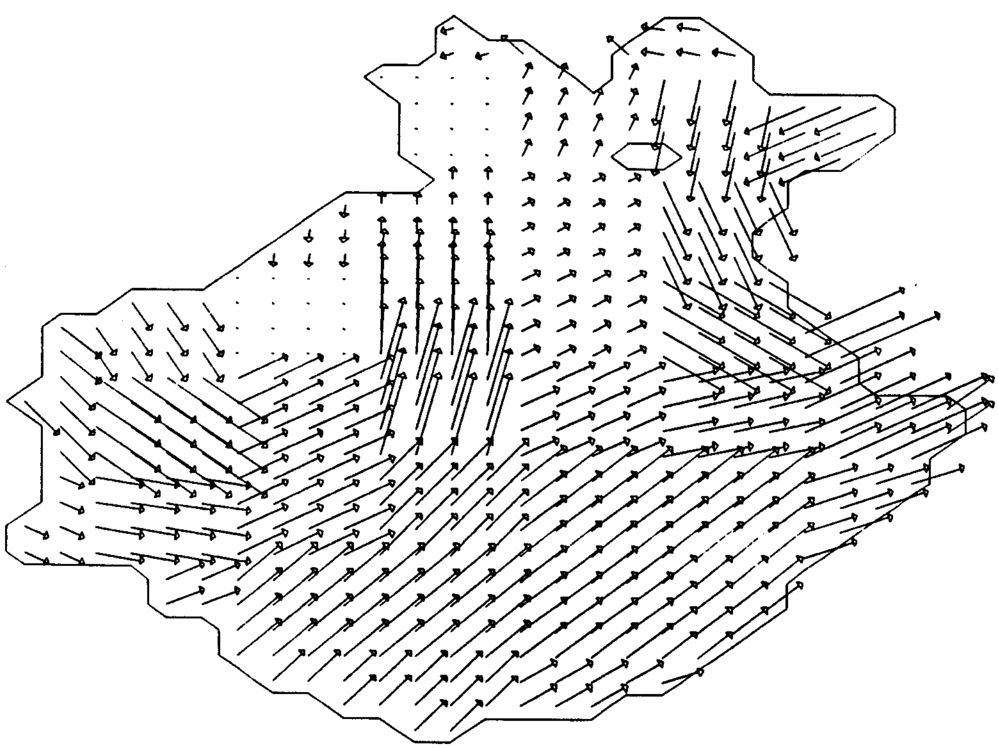

Figure 63.--Wind, Bering Sea, case 2, day 2 (18Z, 9 Mar. 1982); 1 grid length = 5 m/s.

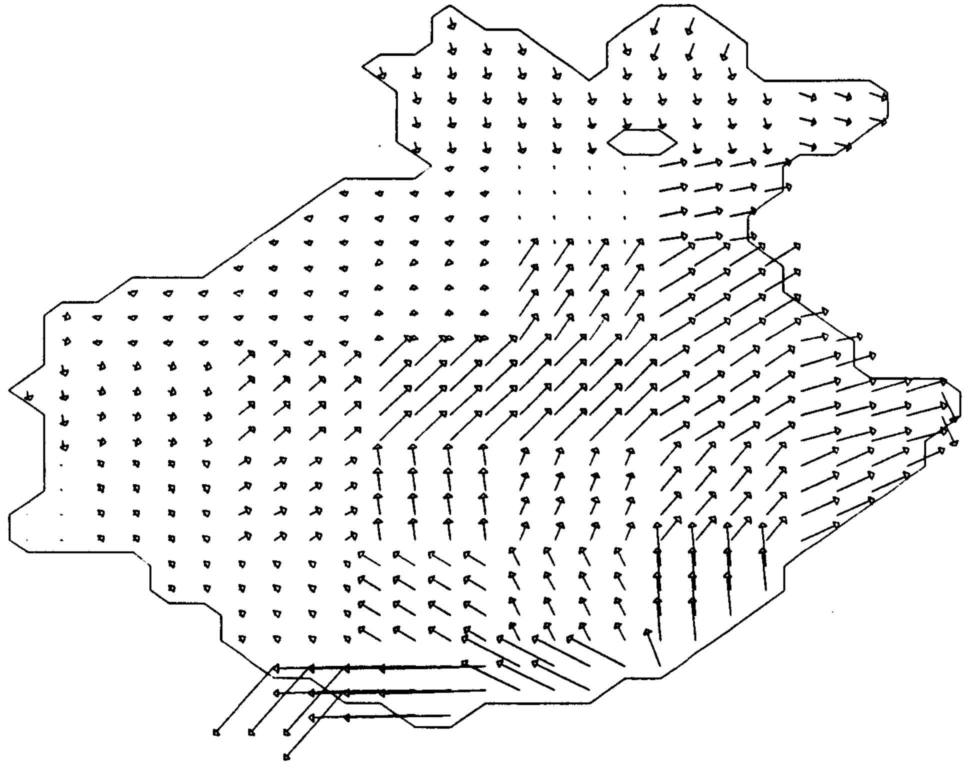

Figure 64.--Wind, Bering Sea, case 2, day 3 (18Z, 10 Mar. 1982); 1 grid length = 5 m/s.

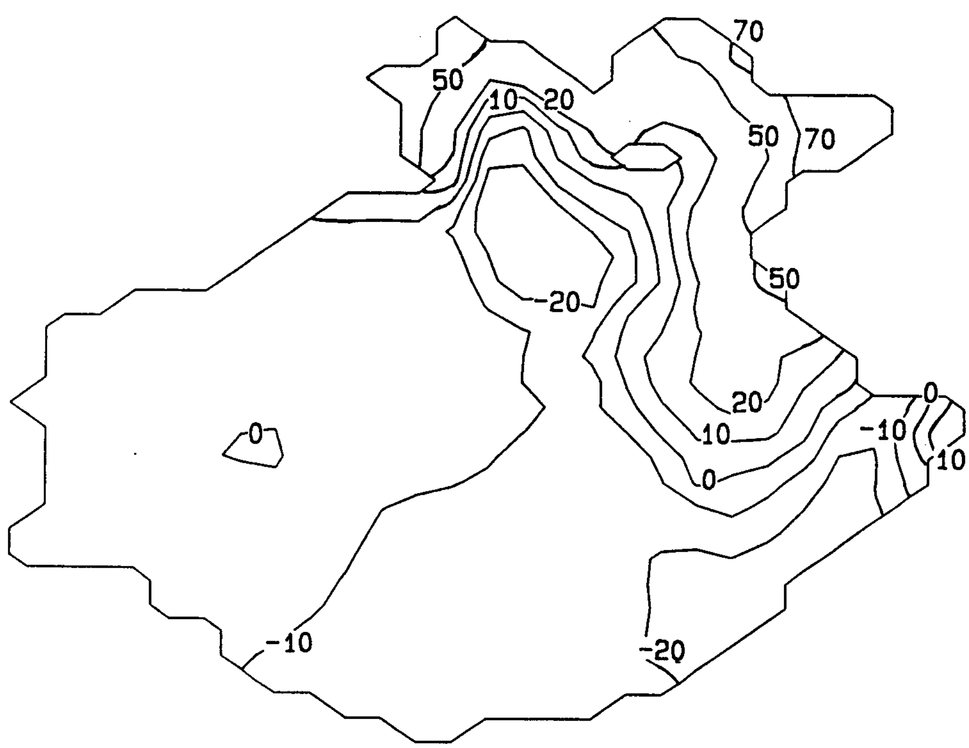

Figure 65.--Sea level, Bering Sea, case 2, day 1 (18Z, 8 Mar. 1982), in centimeters.

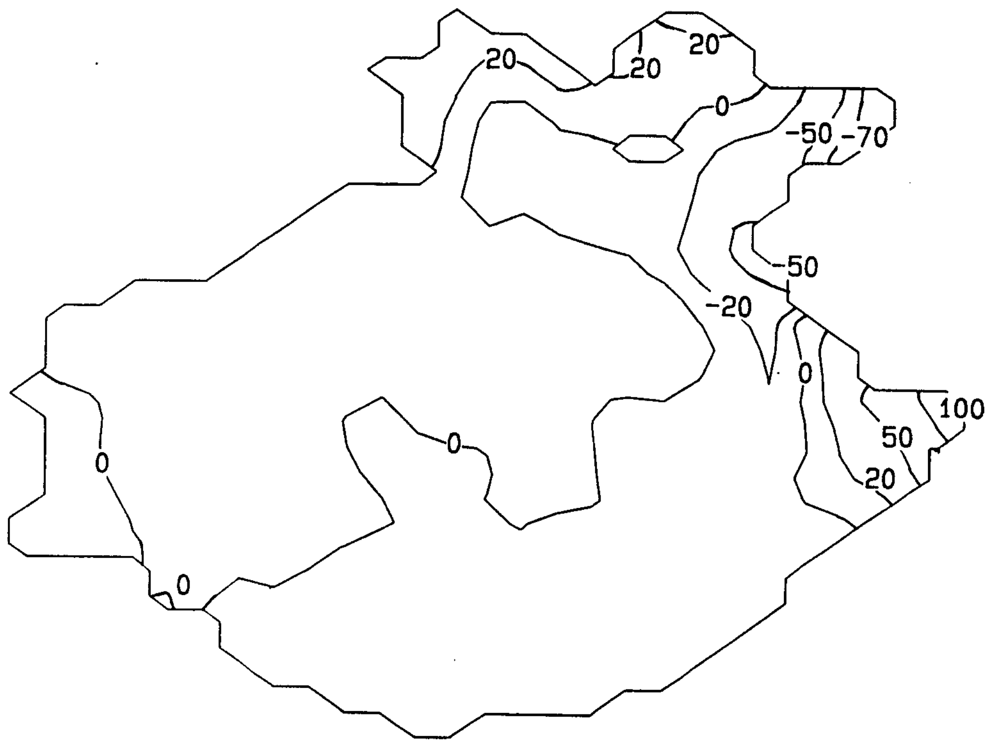

Figure 66.--Sea level, Bering Sea, case 2, day 2 (18Z, 9 Mar. 1982), in centimeters.

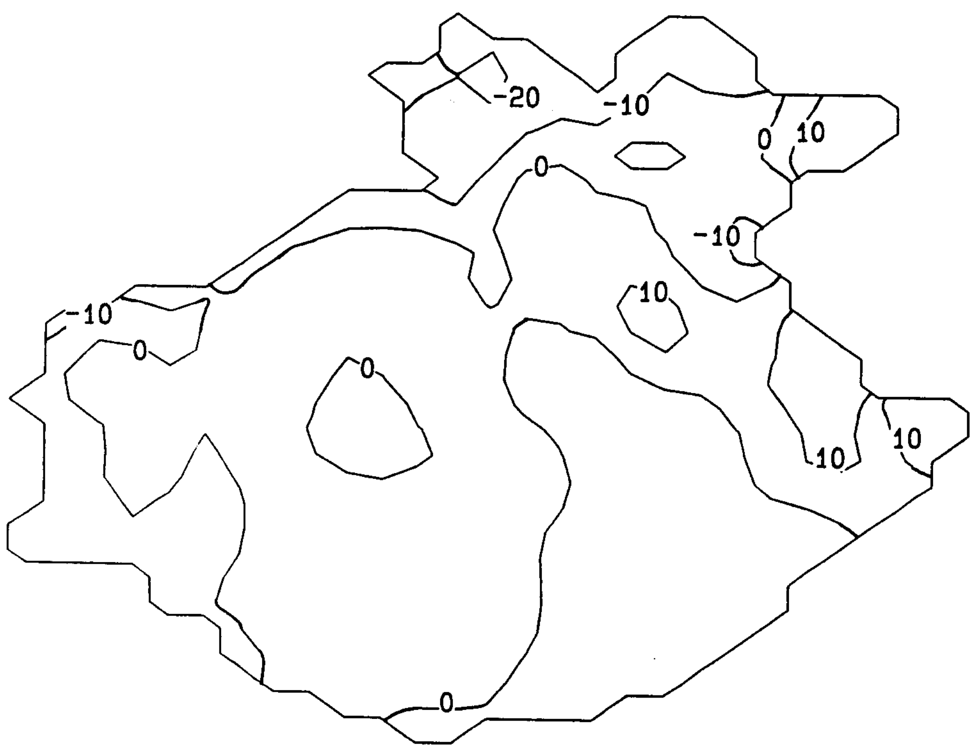

Figure 67.--Sea level, Bering Sea, case 2, day 3 (18Z, 10 Mar. 1982), in centimeters.

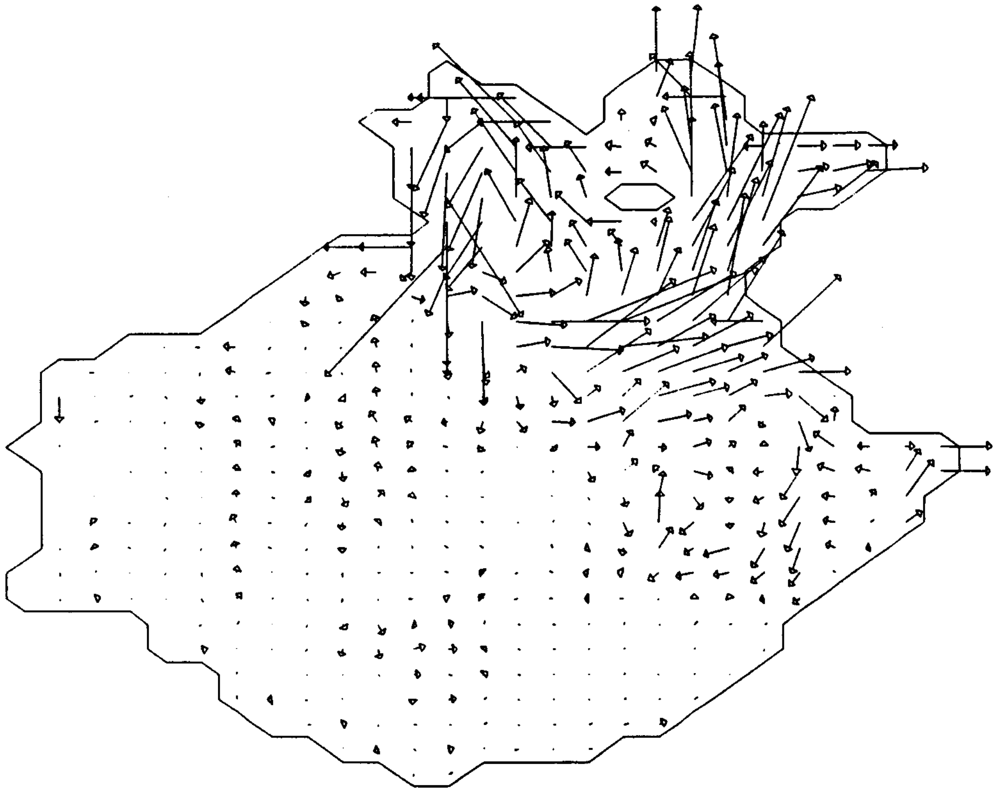

Figure 68.--Velocity, Bering Sea, case 2, day 1 (18Z, 8 Mar. 1982); 1 grid length = 10 cm/s.

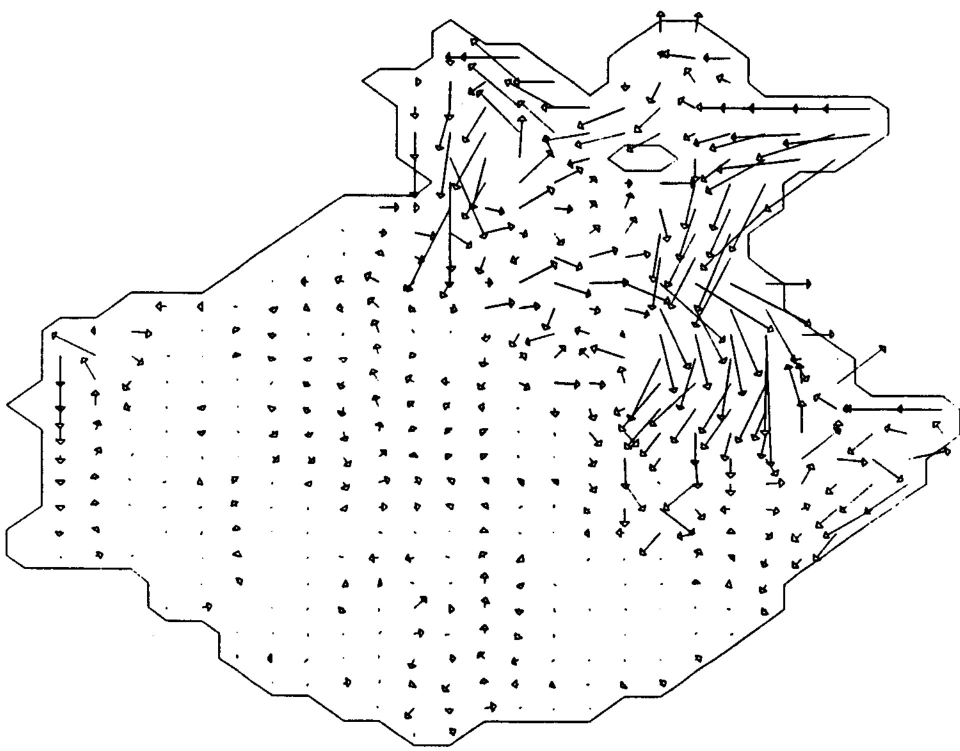

Figure 69.--Velocity, Bering Sea, case 2, day 2 (18Z, 9 Mar. 1982); 1 grid length = 10 cm/s.

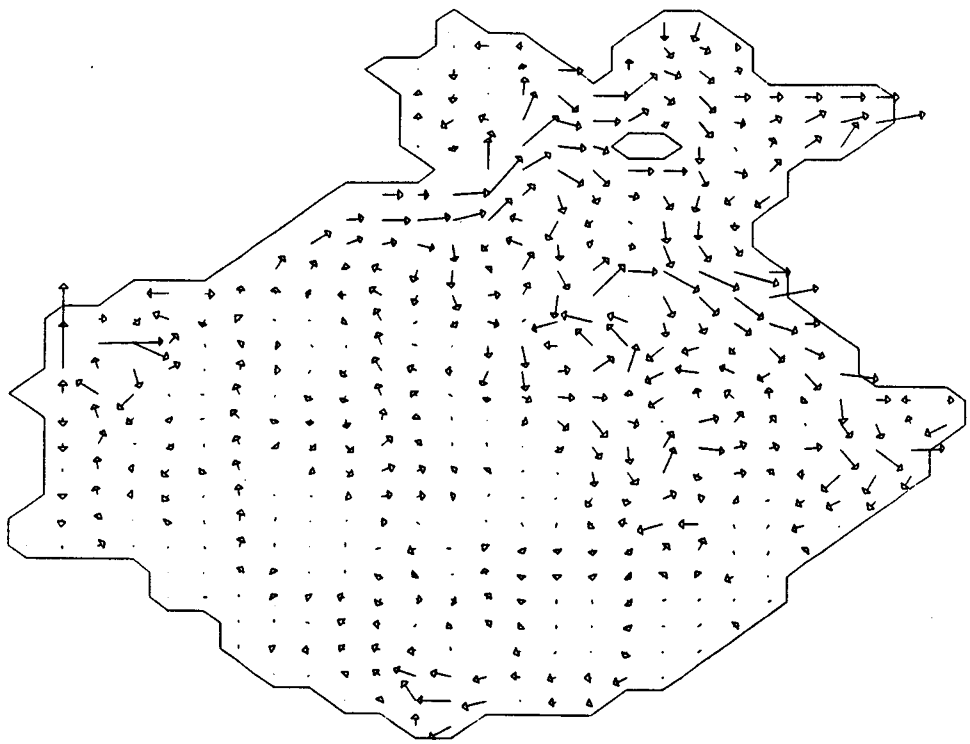

Figure 70.--Velocity, Bering Sea, case 2, day 2 (18Z, 10 Mar. 1982); 1 grid length = 10 cm/s.

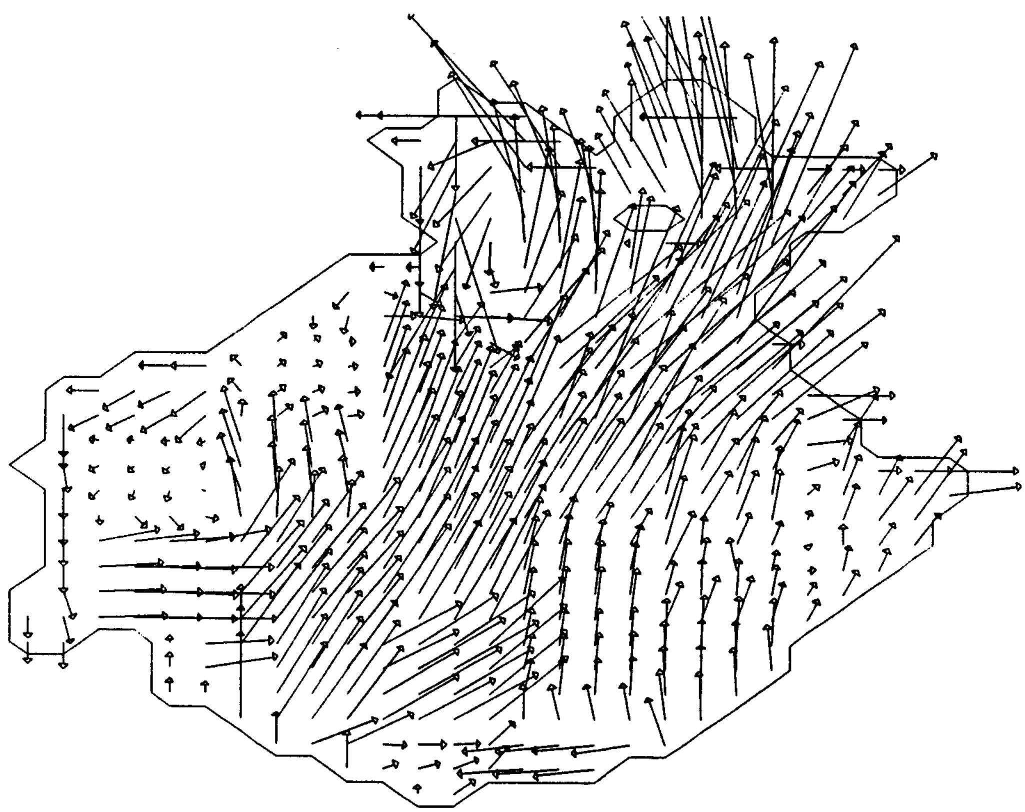

Figure 71.--Ice velocity, Bering Sea, case 2, day 1 (18Z, 6 Mar. 1982); 1 grid length = 10 cm/s.

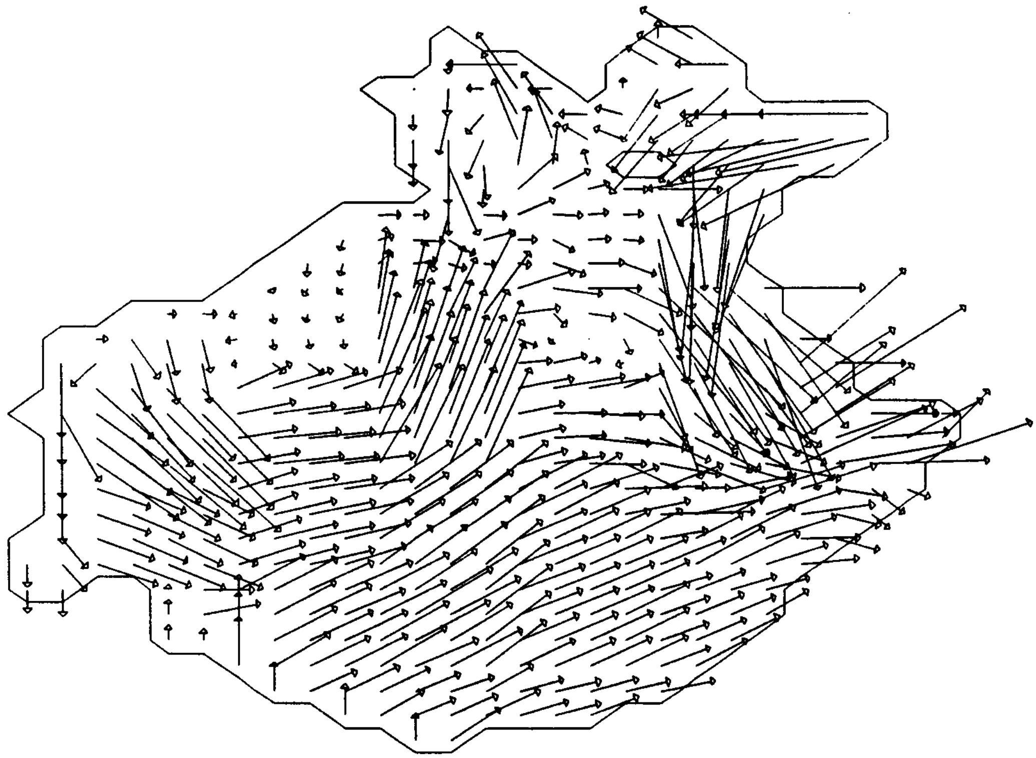

Figure 72.--Ice velocity, Bering Sea, case 2, day 2 (18Z, 9 Mar. 1982); 1 grid length = 10 cm/s.

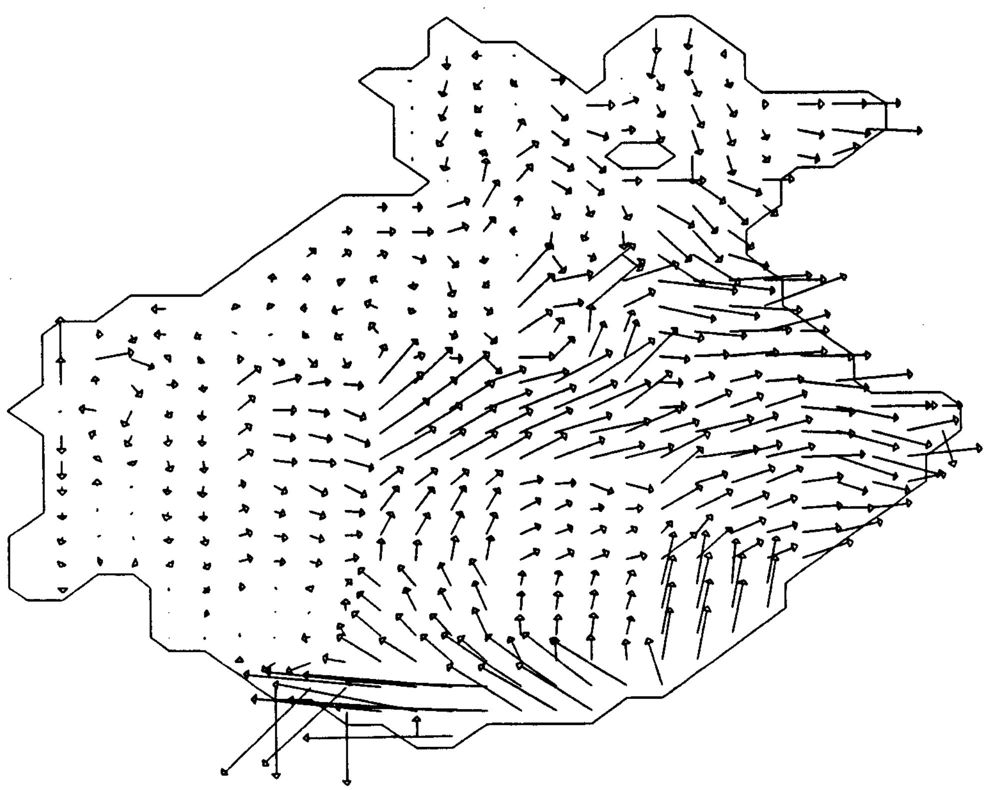

Figure 73.--Ice velocity, Bering Sea, case 2, day 3 (18Z, 10 Mar. 1982); 1 grid length = 10 cm/s.

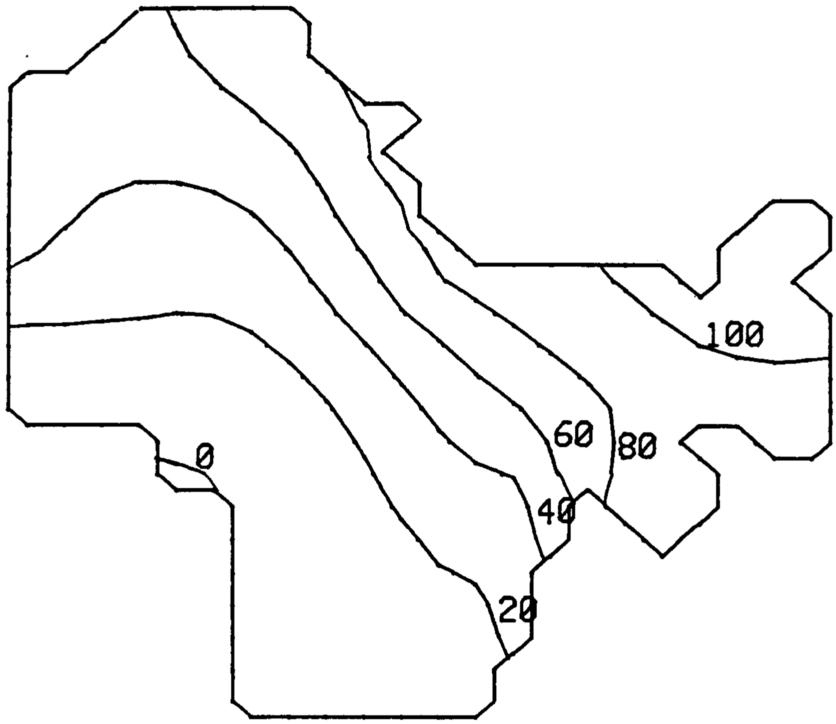

Figure 74.--Sea level, Norton Sound, case 2, day 1.5 (06Z, 9 Mar. 1982), in centimeters.

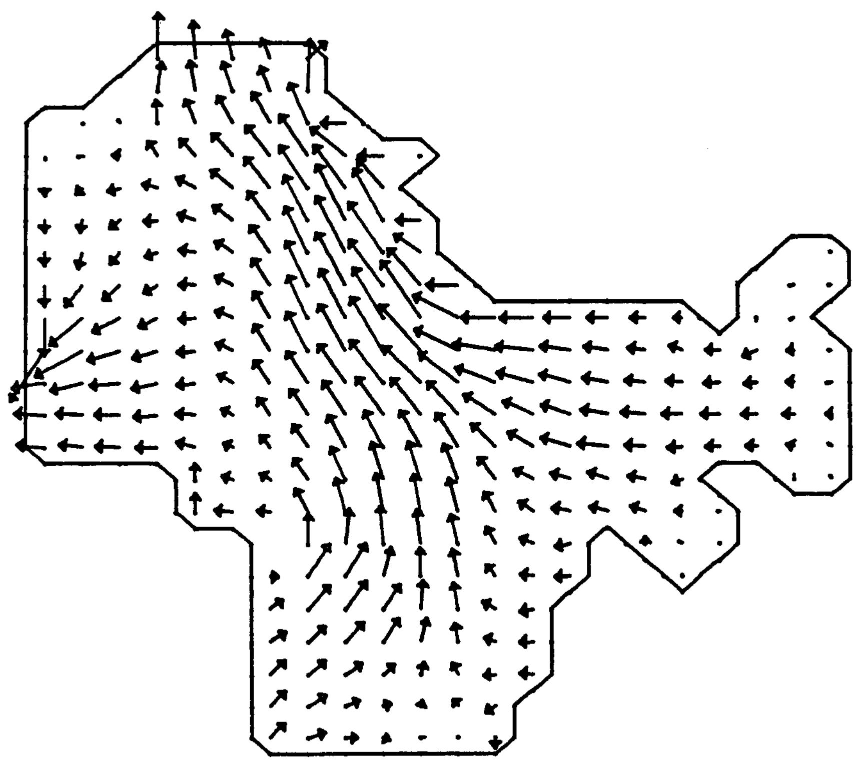

Figure 75.--Velocity, Norton Sound, case 2, day 1.5 (06Z, 9 Mar. 1982); 1 horizontal grid length = 20 cm/s.

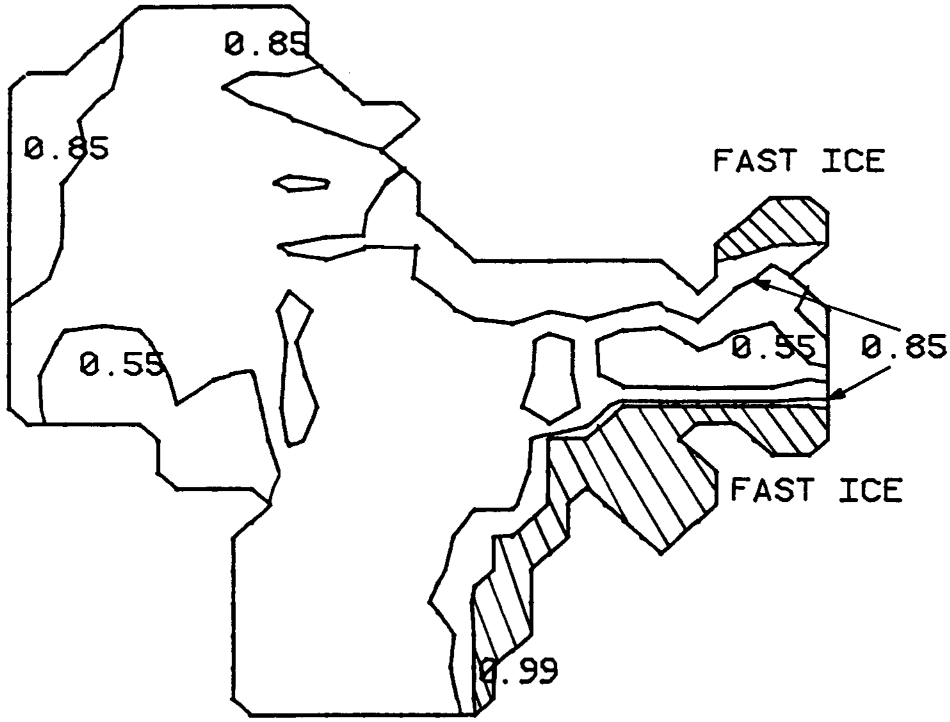

Figure 76.--Ice compactness, Norton Sound, case 2, day 1.5 (06Z, 9 Mar. 1982).

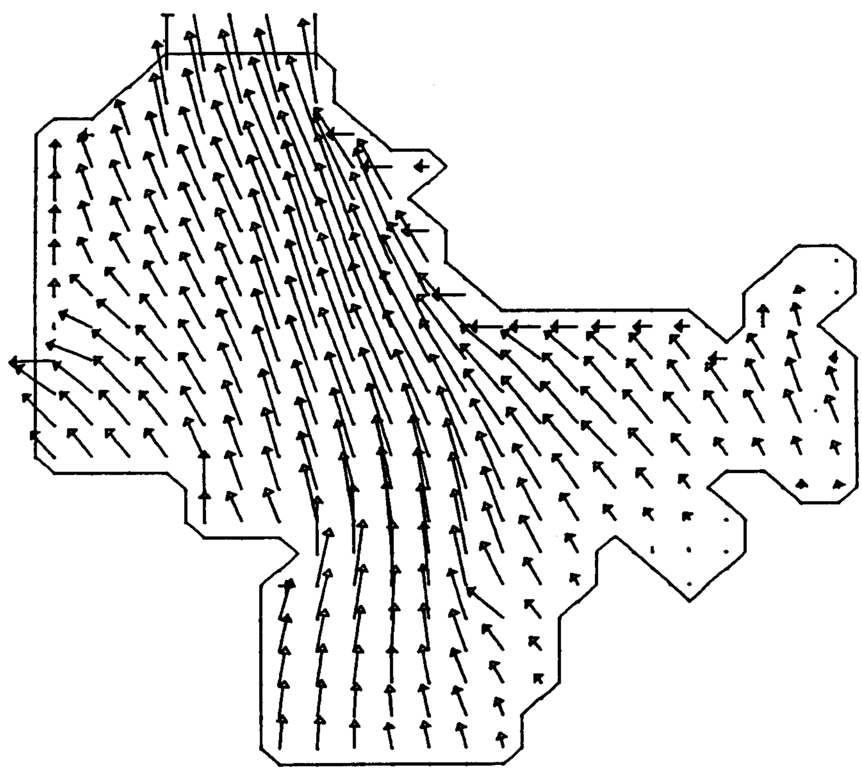

Figure 77.--Ice velocity, Norton Sound, case 2, day 1.5 (06Z, 9 Mar. 1982); 1 grid length = 20 cm/s.

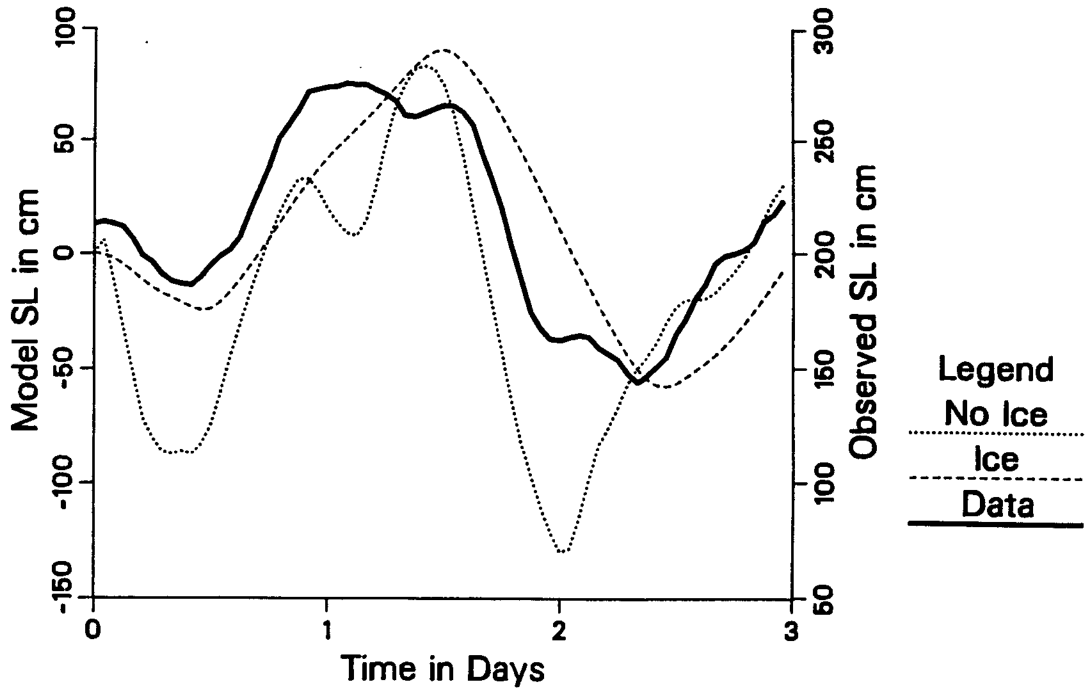

Figure 78.--Model comparison to observed sea level at Stebbins, Alaska, case 2, March 1982.

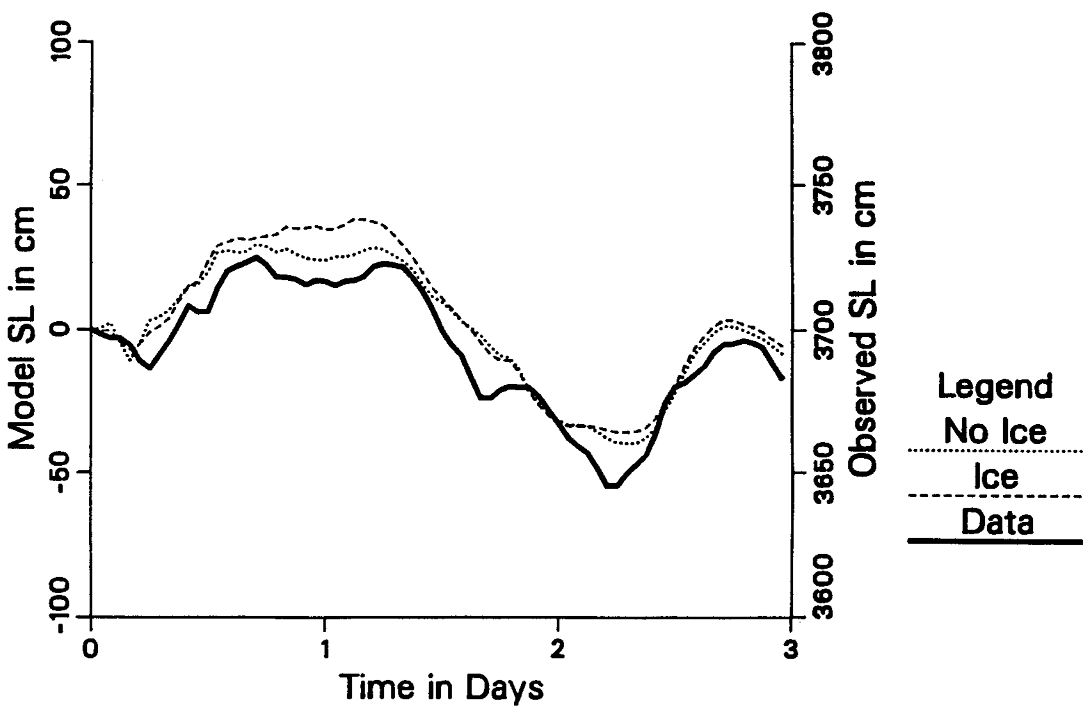

Figure 79.--Model comparison to observed sea level at point NC17, case 2, March 1982.

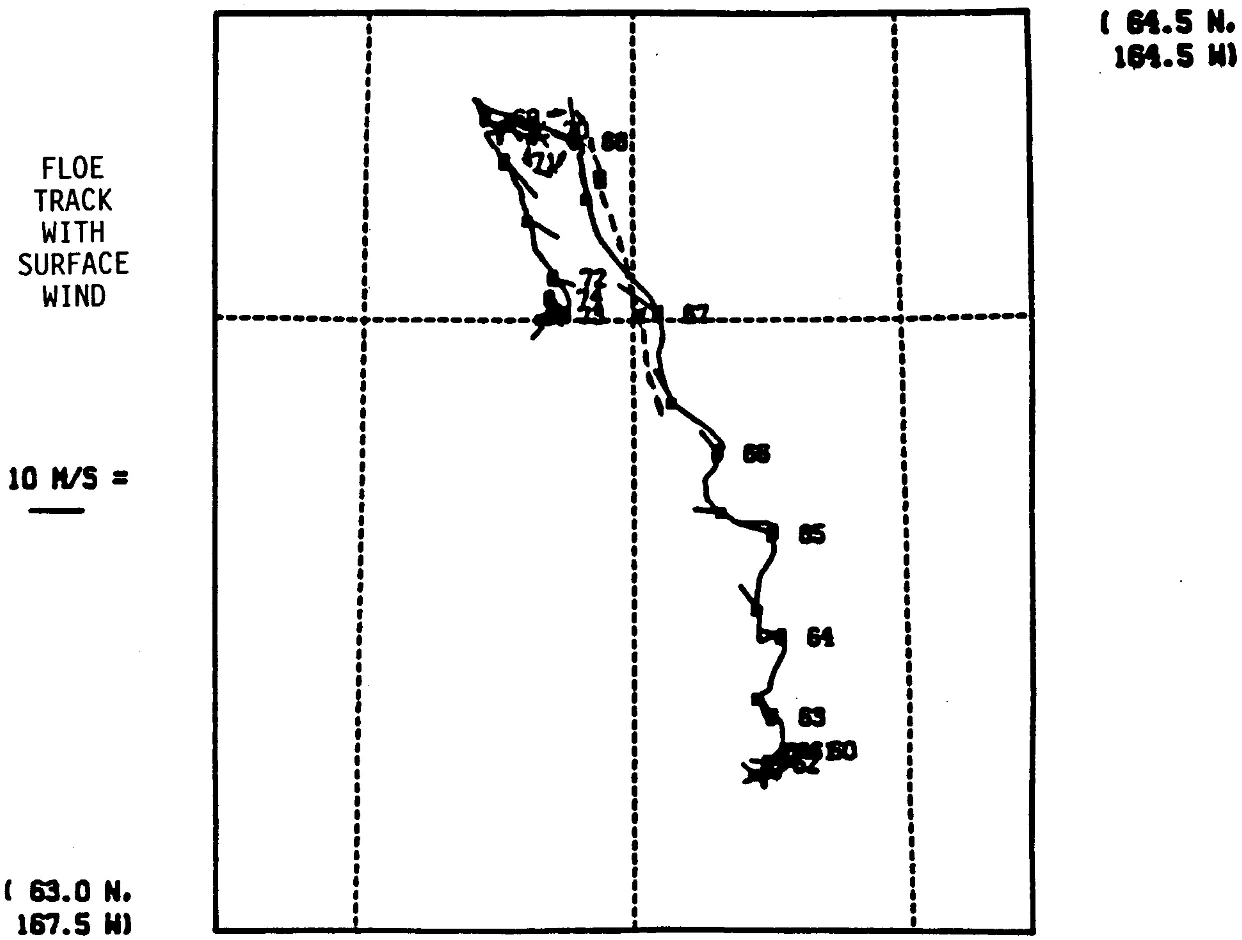

Figure 80.--Ice drift floe track, 1-15 March 1982 (JD 60-74). Measured by Reynolds and Pease (1984). Floe station 2322B = continuous line; calculated from model = broken line.

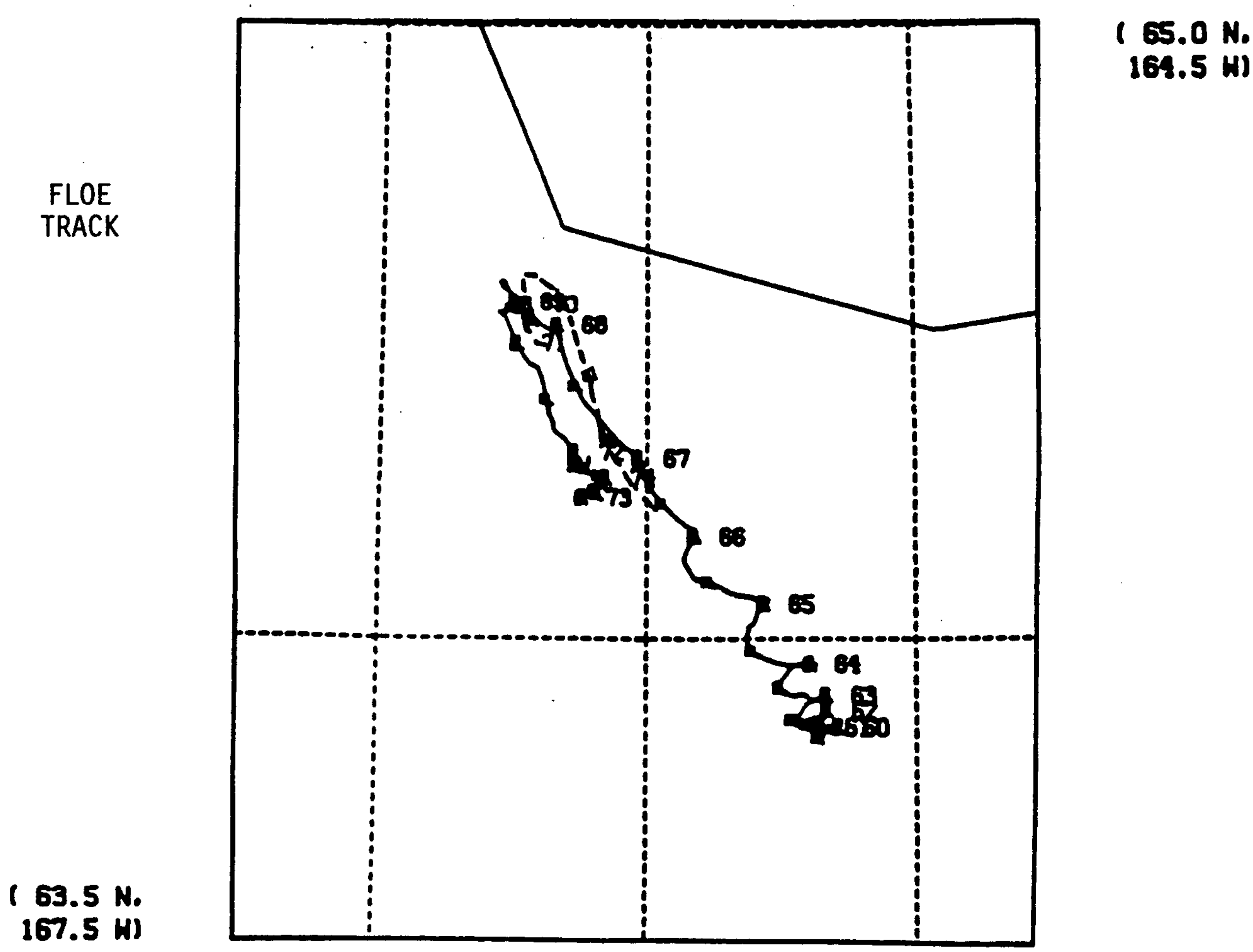

Figure 81.--Ice drift floe track, 1-15 March 1982 (JD 60-74). Measured by Reynolds and Pease (1984). Floe station 2321B = continuous line; calculated from model = broken line.

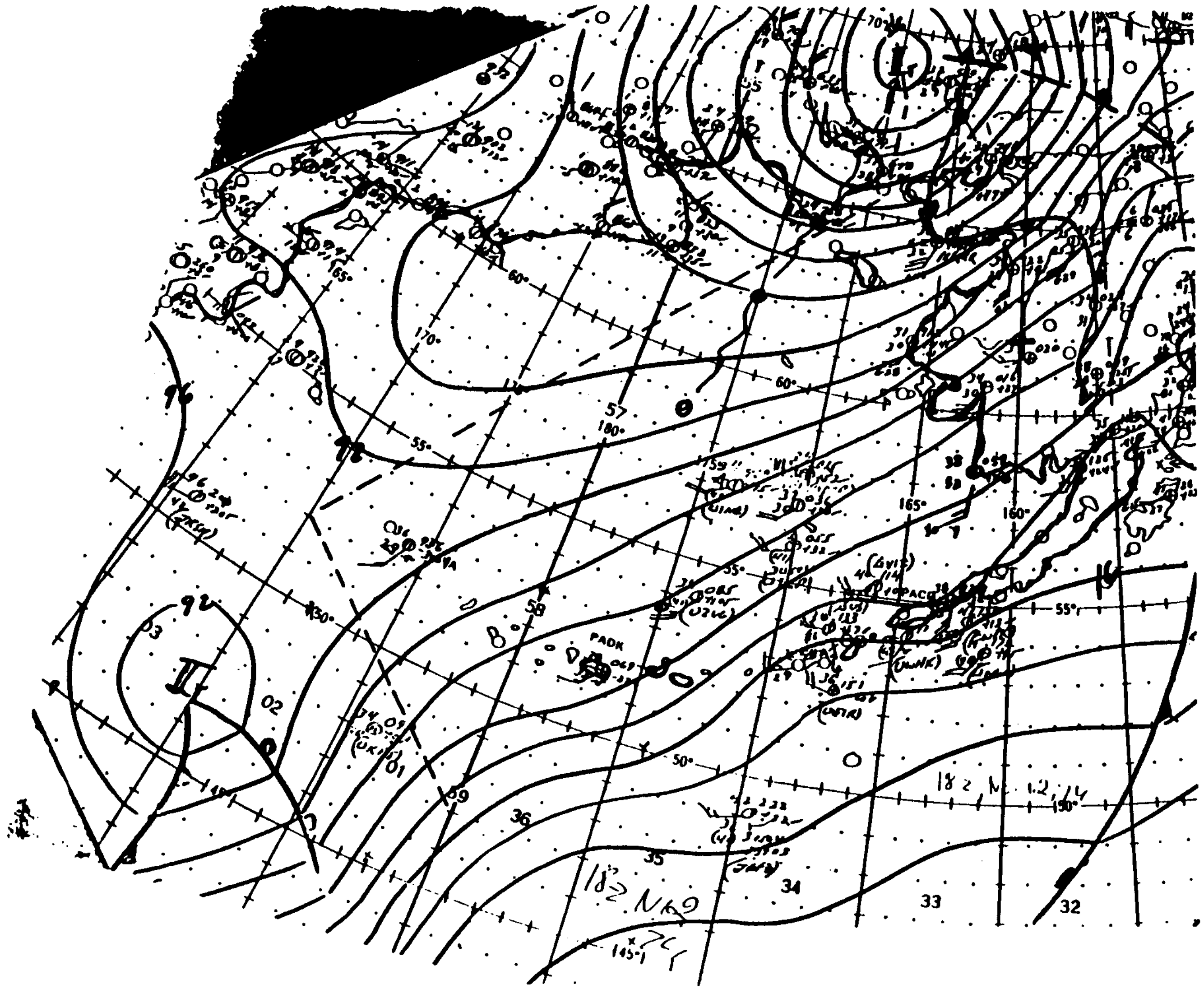

Figure 82.--Surface weather chart for 18Z, 12 November 1974. Pressure in millibars.

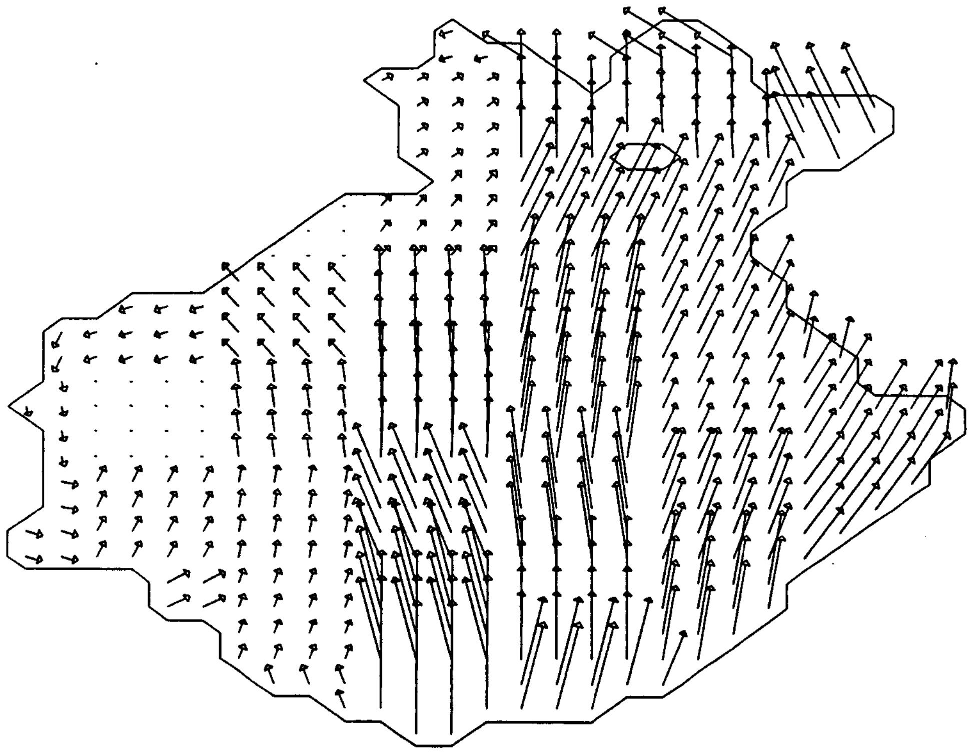

Figure 83.--Wind, Bering Sea, case 3, day 1
(00Z, 11 Nov. 1974); 1 horizontal grid length = 10 m/s.

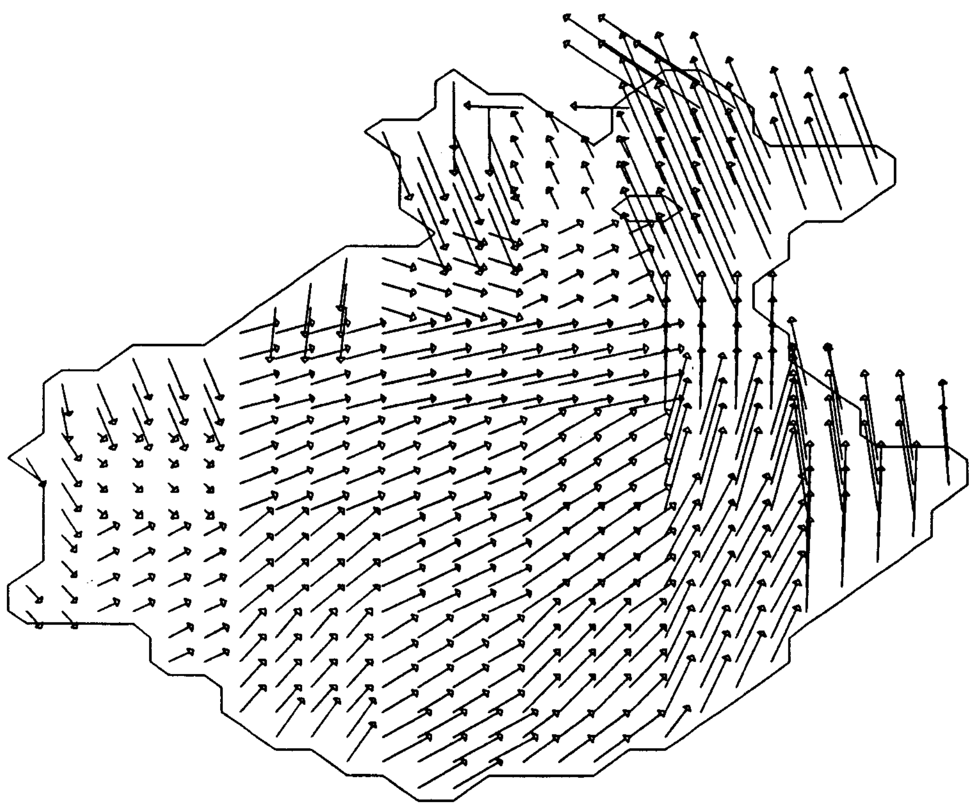

Figure 84.--Wind, Bering Sea, case 3, day 2
(00Z, 12 Nov. 1974); 1 grid length = 10 m/s.

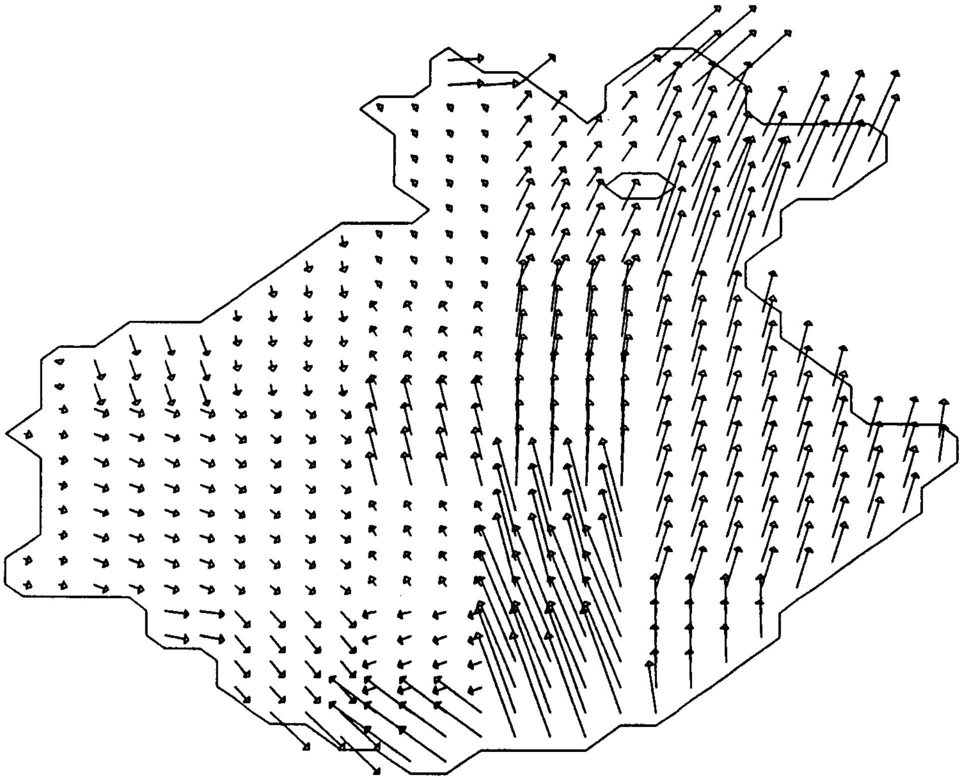

Figure 85.--Wind, Bering Sea, case 3, day 3 (00Z, 13 Nov. 1974); 1 grid length = 10 m/s.

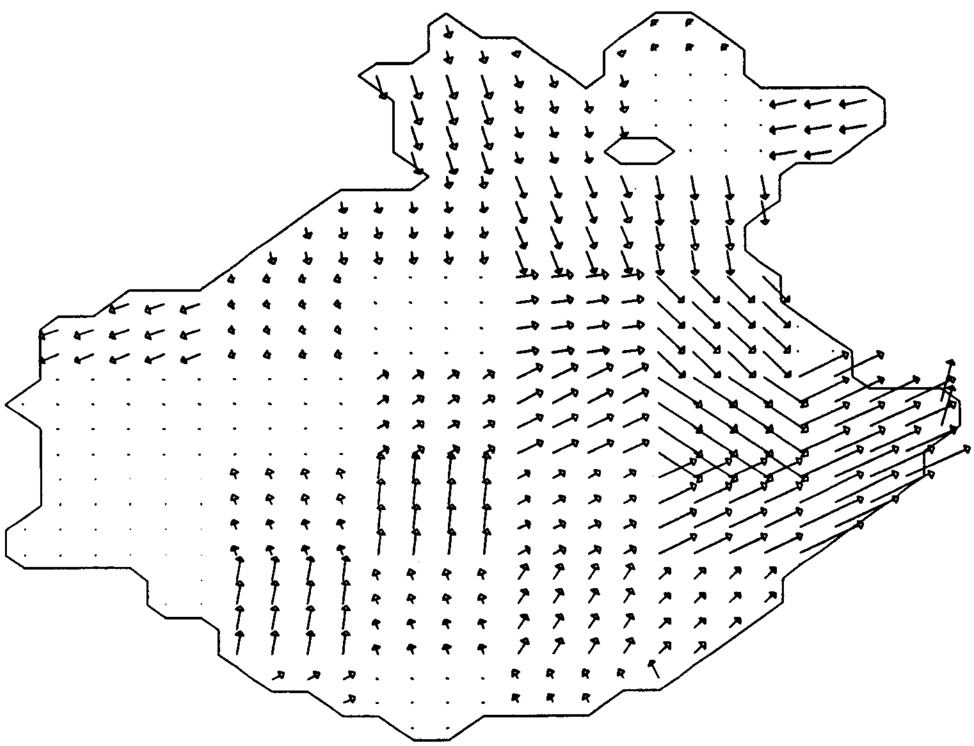

Figure 86.--Wind, Bering Sea, case 3, day 4 (00Z, 14 Nov. 1974); 1 grid length = 10 m/s.

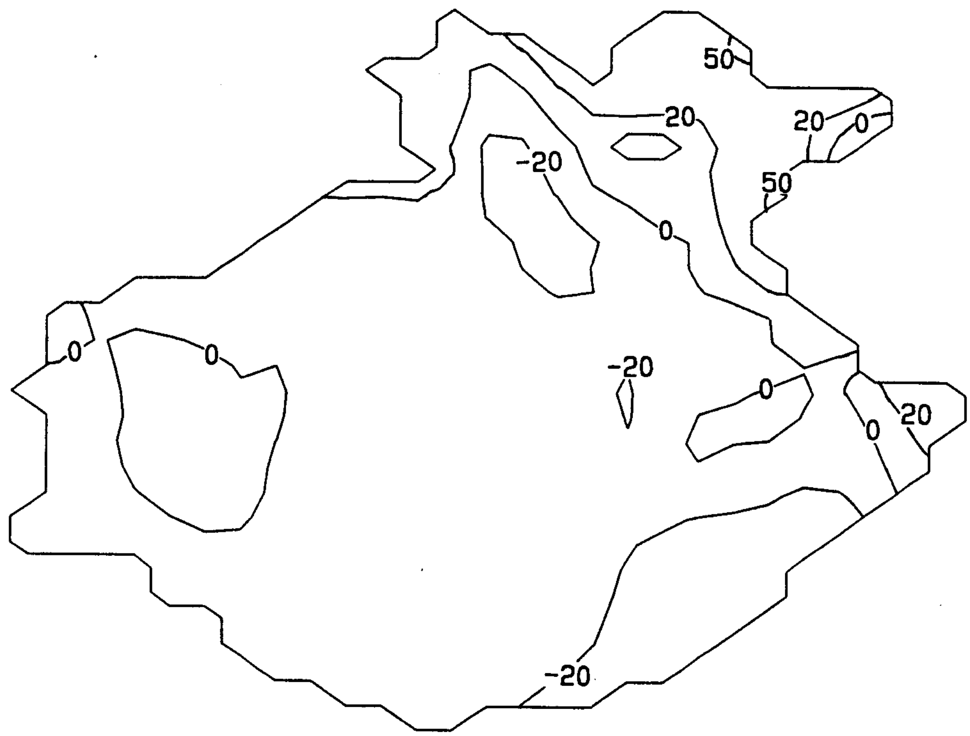

Figure 87.--Sea level, Bering Sea, case 3, day 1 (00Z, 11 Nov. 1974), in centimeters.

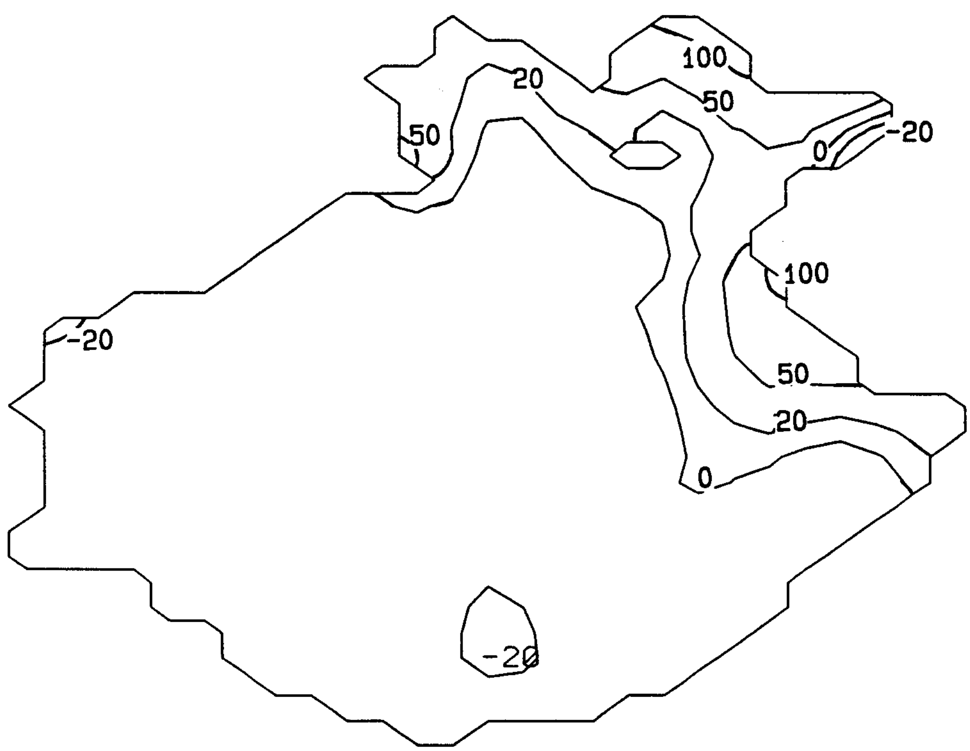

Figure 88.--Sea level, Bering Sea, case 3, day 2 (00Z, 12 Nov. 1974), in centimeters.

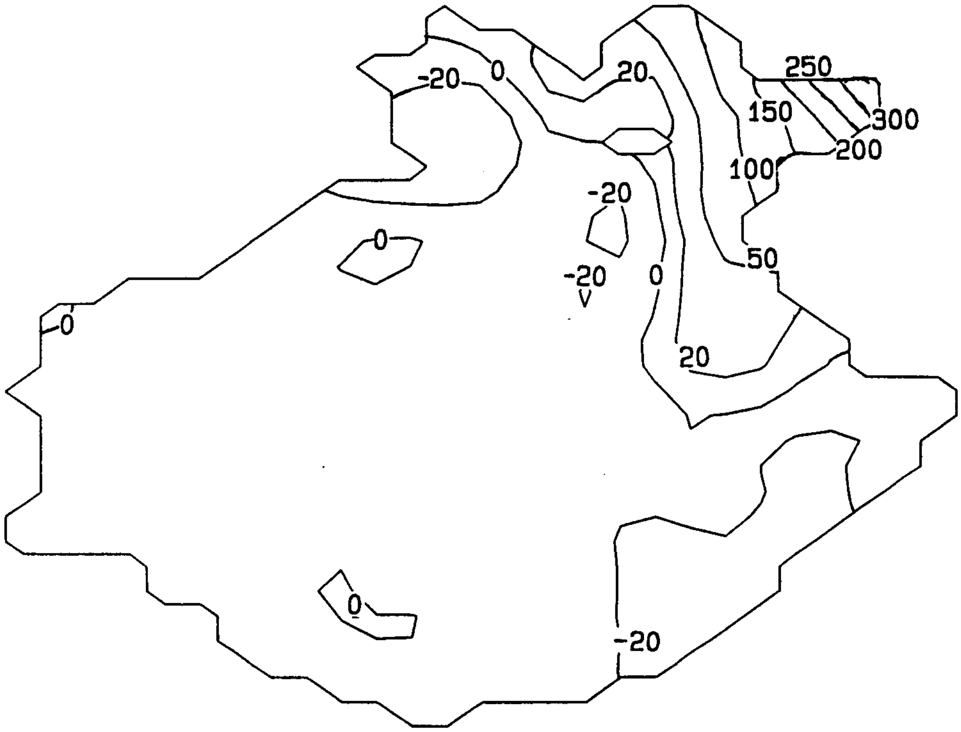

Figure 89.--Sea level, Bering Sea, case 3, day 3 (00Z, 13 Nov. 1974), in centimeters.

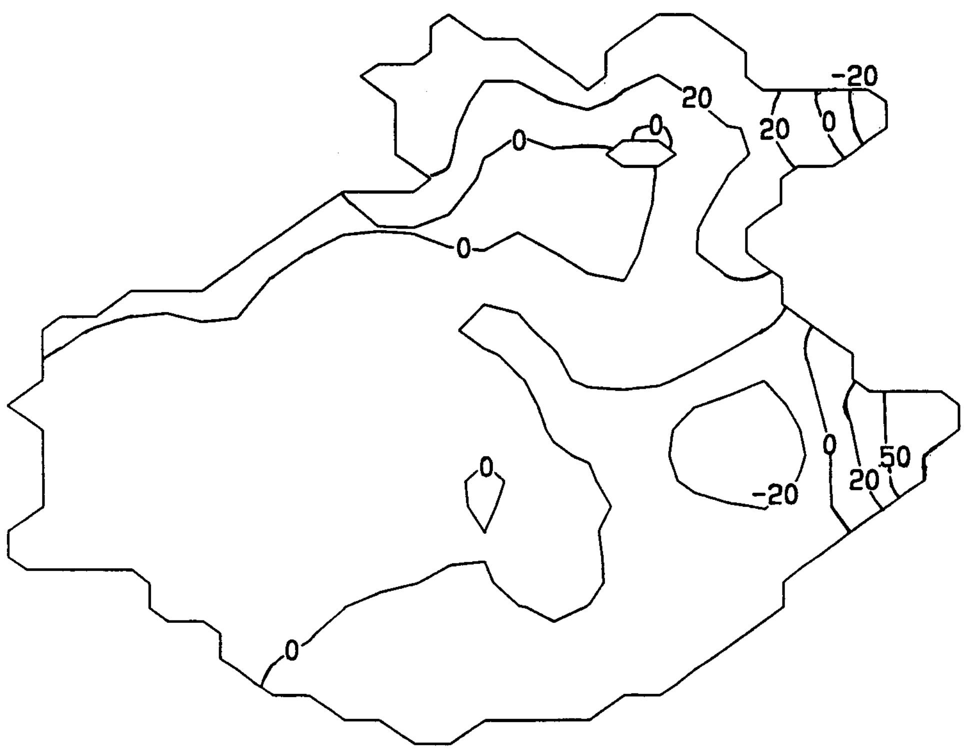

Figure 90.--Sea level, Bering Sea, case 3, day 4 (00Z, 14 Nov. 1974), in centimeters.

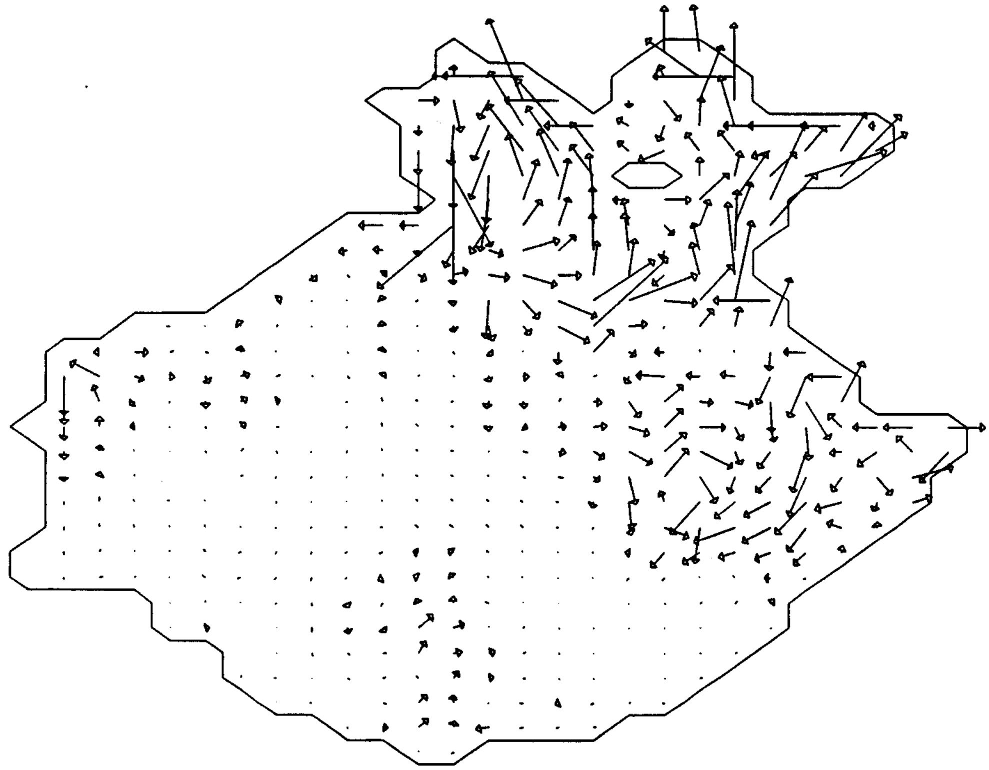

Figure 91.--Velocity, Bering Sea, case 3, day 1 (00Z, 11 Nov. 1974); 1 grid length = 10 cm/s.

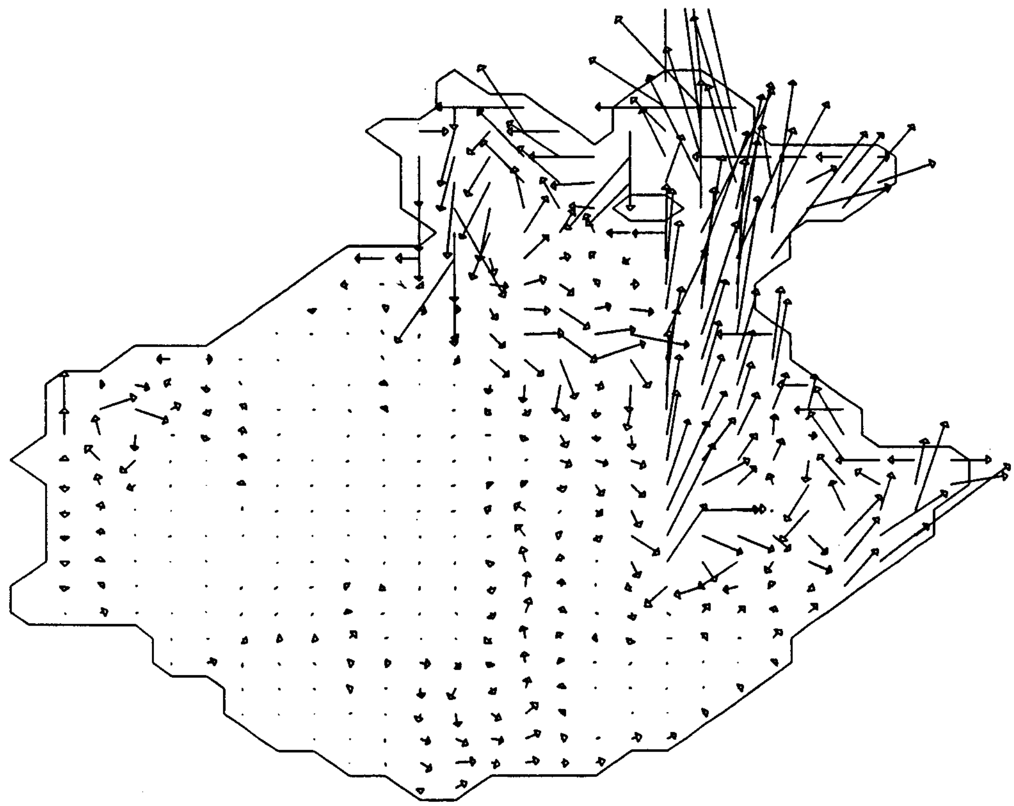

Figure 92.--Velocity, Bering Sea, case 3, day 2 (00Z, 12 Nov. 1974); 1 grid length = 10 cm/s.

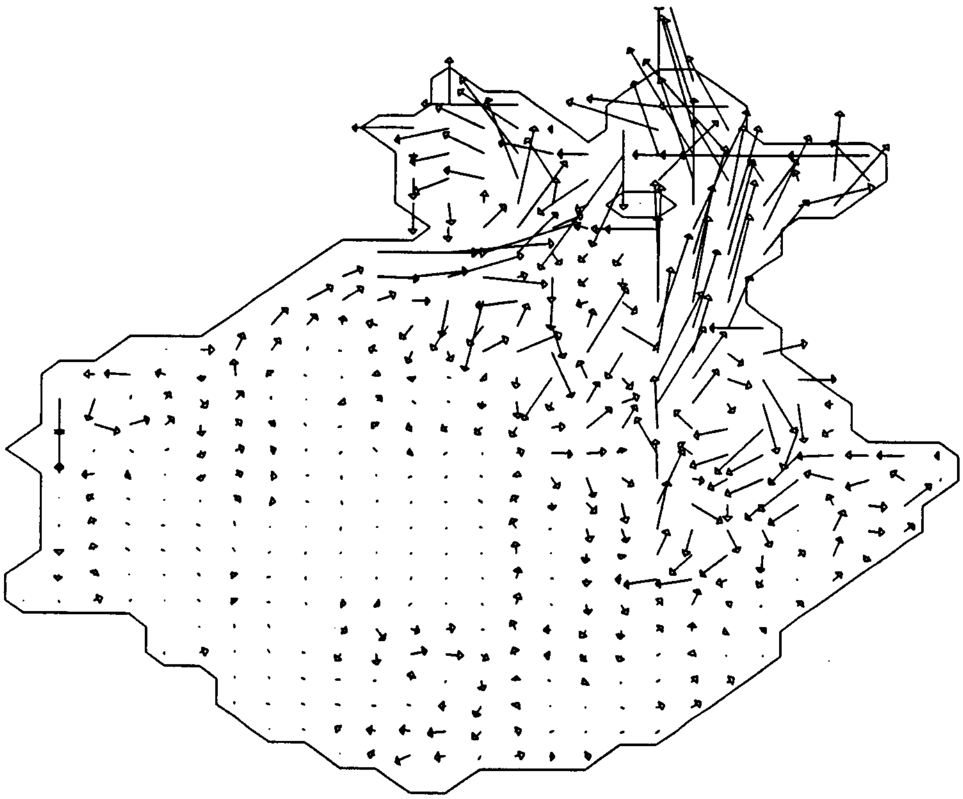

Figure 93.--Velocity, Bering Sea, case 3, day 3 (00Z, 13 Nov. 1974); 1 grid length = 10 cm/s.

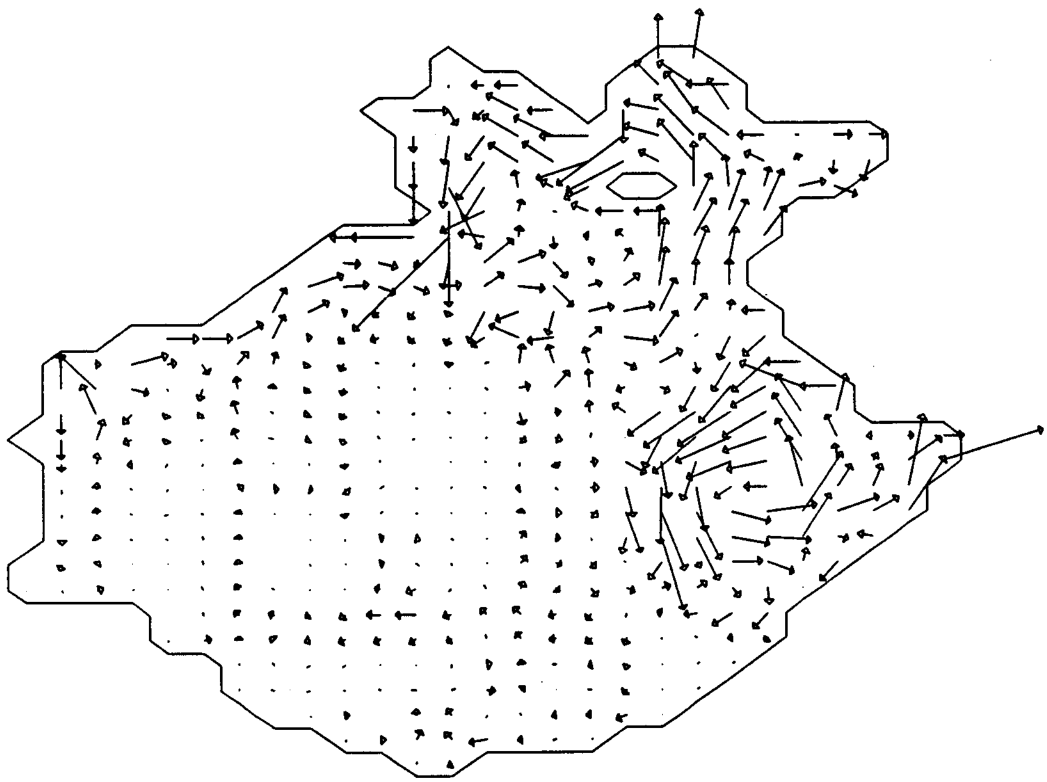

Figure 94.--Velocity, Bering Sea, case 3, day 4 (00Z, 14 Nov. 1974); 1 grid length = 10 cm/s.

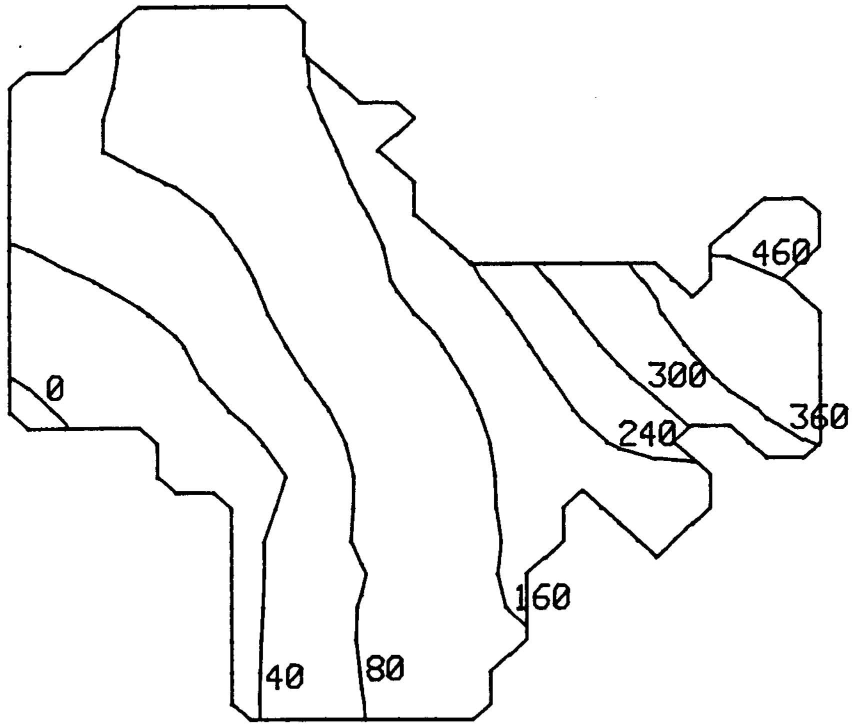

Figure 95.--Sea level, Norton Sound, case 3, day 3
(00Z, 13 Nov. 1974), in centimeters.

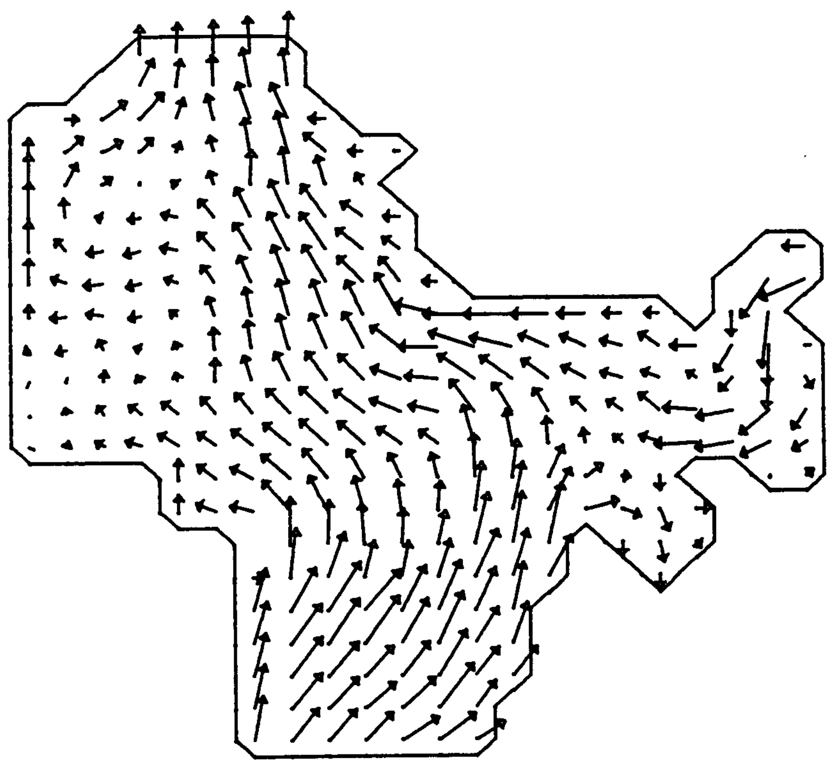

Figure 96.--Velocity, Norton Sound, case 3, day 3
(00Z, 13 Nov. 1974); 1 horizontal grid length = 40 cm/s.

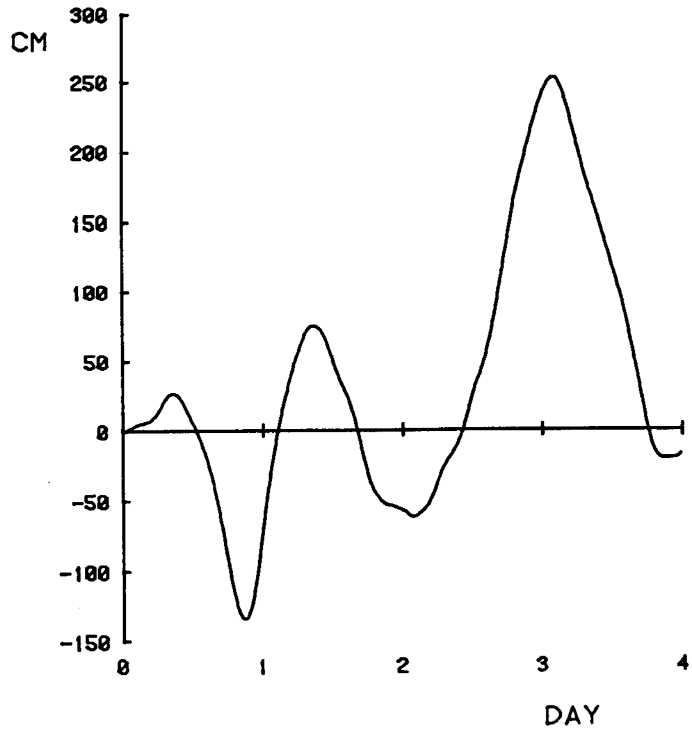

Figure 97.--Computed sea level, Stebbins, case 3.

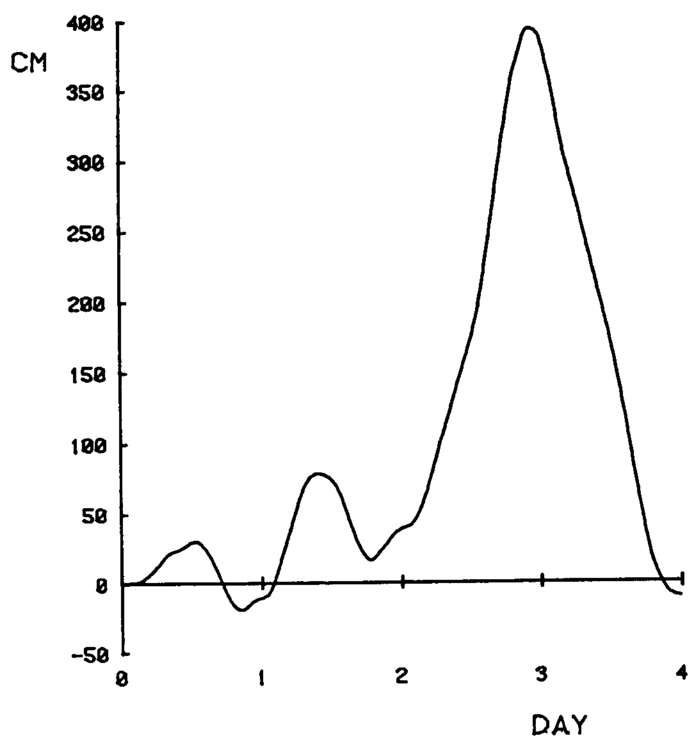

Figure 98.--Computed sea level, Unalakleet, case 3.

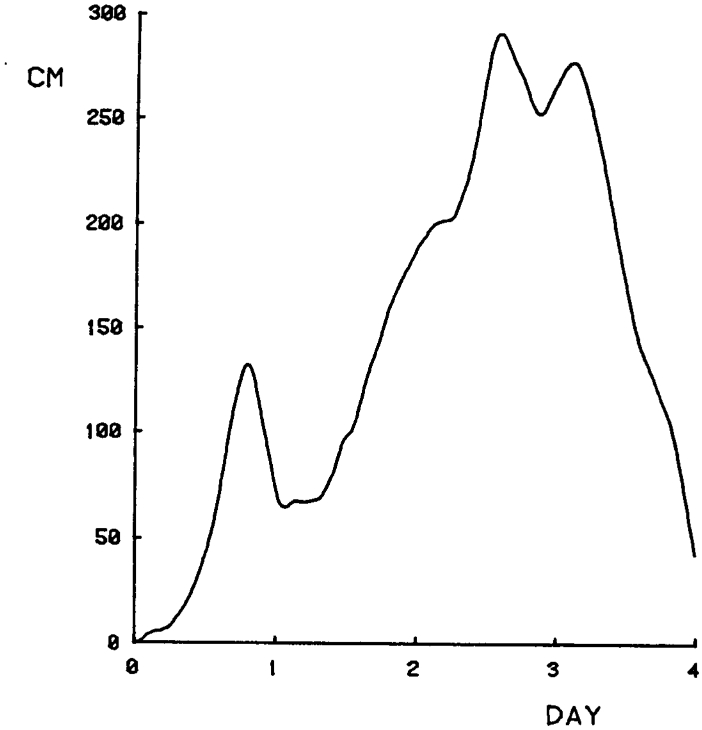

Figure 99.--Computed sea level, Nome, case 3.

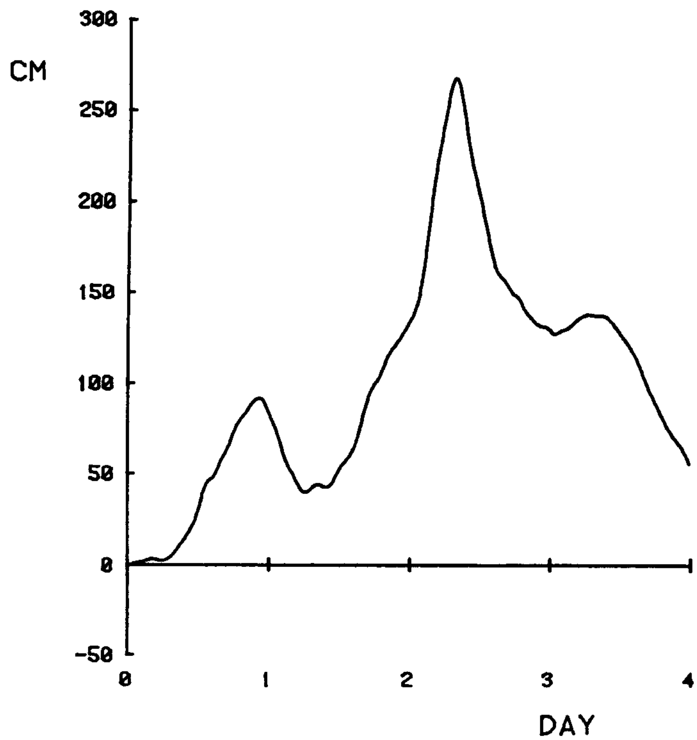

Figure 100.--Computed sea level, Diomedes, case 3.

YUKON DELTA OCEANOGRAPHY AND METEOROLOGY

by

Thomas L. Kozo

VANTUNA Research Group
Occidental College
Los Angeles, California

Final Report
Outer Continental Shelf Environmental Assessment Program
Research Unit 519

1983

TABLE OF CONTENTS

ESTUARINE MIXING PROCESSES

The Yukon River discharges 1,000,000 f^3s^{-1} of fresh water during its peak flow in late spring through 12 active delta distributaries (Dupré, 1977) and a number of sloughs shown as unconnected streams in Fig. 1. The sloughs between the north fork (A) and the middle fork (C) are shown to be disconnected by late July in Fig. 2. The mouths of each distributary and slough (during peak flow periods especially) behave as estuaries since they connect to the open sea and sea water is measurably diluted by freshwater derived from land drainage (Jones and Kirchoff, 1978). Excluding the ice dominated season (Fig. 3), the mouths of main distributaries are river controlled estuaries by late May of each year with circulation and stratification patterns primarily determined by the rate at which river water is being added at their heads. Seasonal variations in response to their runoff cycles can be observed; and from early August to early November (Fig. 3) these main distributary estuaries are controlled by a combination of storm tides, astromonical tides and river runoff. Slough mouths, however, undergo a transition from river control in May to tide control in late summer. Evidence for these transitions (Jones and Kirchhoff, 1978) is the relatively clear waters off the sloughs in August (Fig. 4) indicating little upstream input of sediment-laden fresh water and lack of connection to the major distributaries. Opaque sediment-laden water was seen off Apoon (A), Kawanak (C) and Kwikluak (B) mouths (Fig. 1), which are the end points of the major distributaries.

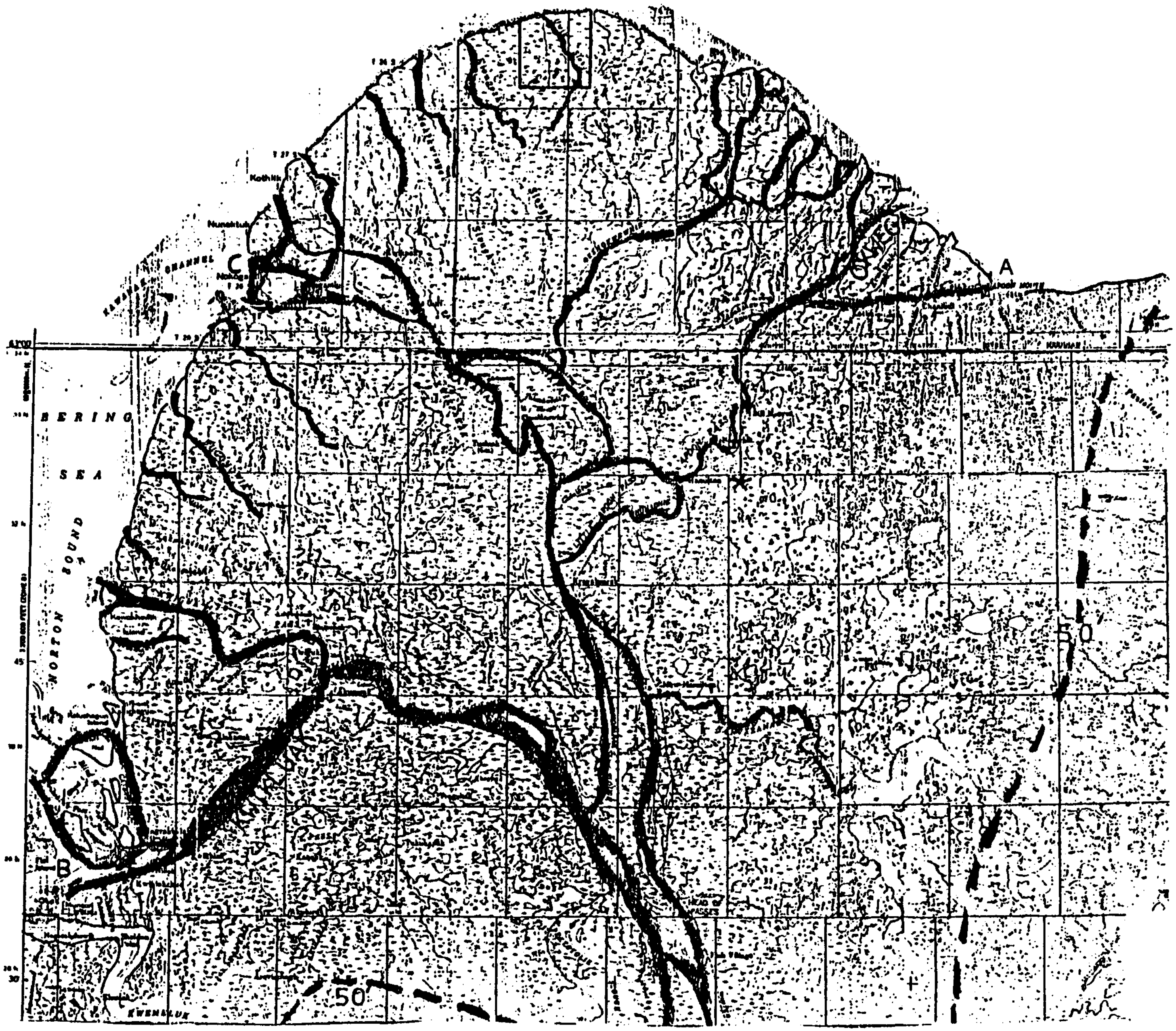

Figure 1. Yukon River distributaries and sloughs with approximate 50' elevation contour.

YUKON RIVER DELTA PHOTOGRAPHED IN SUMMER (July 22, 1975).
(Delta area from Stuart Island to South Mouth of Yukon River.)

Figure 2. Source: Landsat photograph No. E2181-21360-7 Stringer, OCSEAP R.U. #267.

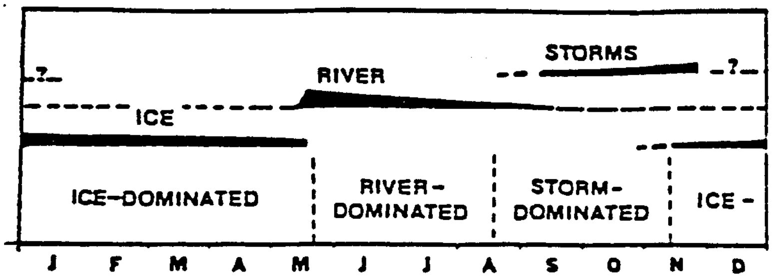

Figure 3. Seasonal variability of coastal processes in the Yukon Delta region of Norton Sound (from Dupré and Thompson, 1979).

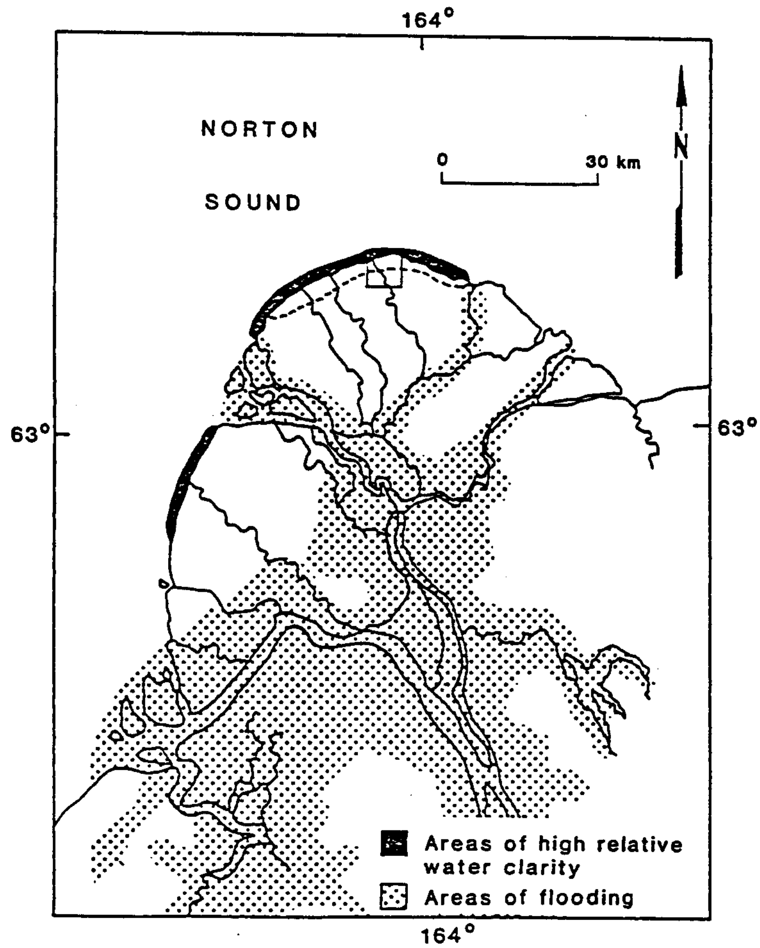

Figure 4. The Yukon Delta showing interdistributary clear waters and extent of storm surge flooding (Jones and Kirchhoff, 1978).

A. Sloughs

Using limited data (Jones and Kirchhoff, 1978) an attempt to predict the upstream extent of oceanic salt intrusions in sloughs has been made. The mouth of Uwik slough (enclosed in rectangle, top of Fig. 1) had a salinity of 4 $^{o}/_{oo}$, and 12 km inland, it showed "barely a trace" of salt at high tide. Its depth ranged from 3 m at the mouth to .38 m at its head (more than 24 km inland). The tidal range is ~ 1 m and of the mixed (mainly diurnal) type (NOS chart, 16240 Rev. May 1982, and Defant, 1960). Silvester (1974) has devised a mathematical technique to estimate tidally driven salt intrusion distances upstream as follows (see Fig. 5):

$$D \equiv \text{Eddy Diffusion Coefficient} = (x'V_r/2)/\ln(\bar{s}/s_o) \qquad (1)$$

Where $V_r \equiv$ mean river velocity

$s_o \equiv$ salinity of source (coastal water)

$\bar{s} \equiv$ salinity of river mouth during low water slack

$x' \equiv$ distance offshore of source salinity at low tide (its most seaward position)

$$x' = \frac{T\sqrt{gd}}{2\pi}\,[1 - \cos(2\pi t/T] \qquad (2)$$

Where $T \equiv$ period of tide ~ (86,4000 seconds for diurnal period)

$g \equiv$ acceleration of gravity = 9.8 ms^{-2}

$t \equiv$ time of tidal cycle in seconds

$d \equiv$ depth of river or slough

$L_{lws} \equiv$ length of intrusion of water with salinity s' at low water slack tide (lws)

$$L_{lws} \equiv x' \ (K\sqrt{D/V_r x'} - 1) \tag{3}$$

Note: $K = 3$ for $\frac{s^1}{s_o} = .01$ (1 % of source)

At high water slack tide (hws) the bulk of water of given salt concentration is forced upstream a length L_{hws} by the amount of tidal excursion (H). According to Ippen (1966):

$$L_{hws} - L_{lws} = \left(\frac{T\sqrt{gd}}{2\pi} - L_{lws}\right) (1 - \exp[-H/d])$$

Note: This equation does not include frictional effects and assumes $H/d < 1$.

Since V_r has not been measured, we make assumptions that the slough is connected to the distributaries in August to arrive at an upper bound value. The Yukon River flow in August is ~ 400,000 f^3s^{-1} (Carlson, 1977). Dividing this flow rate by 2 allows for shunting (electrical analog) water to the south mouth (A) and the middle (C) and north (A) mouths combined (Fig. 1). Dividing the resultant half flow rate by 3 allows for shunting water to the 3 main distributaries between the north and middle mouths. If the four sloughs to the northwest of the Okshokwewhik distributary are connected to it and it branches off to feed 5 minor distributaries to the northeast (Fig. 1) we must divide its flow rate by (4 · 2)8. This gives an approximate river flow rate for Uwik Slough (rectangle, Fig. 1) of 8333 f^3s^{-1} or 236.1 m^3s^{-1}. An idealized rectangular river of 250 m · 3m cross section (N.O.S. chart, 16240, and Jones and Kirchoff, 1978) would have a river current (V_r) of ~ .3 ms^{-1} (computed from flow rate divided by cross section). If we assume that the salinity of $4°/_{oo}$ is reduced to $2°/_{oo}$ during low water slack at the Uwik Slough mouth and it goes back up to $4°/_{oo}$ 1 hour later, equation (2) can be written:

$$x' = \frac{86400\sqrt{9.8 \cdot 3}}{2\pi}(1-\cos[360 \cdot 1/24])$$

$$x' = 2.535 \cdot 10^3\text{m seaward of the mouth}$$

From equation (1)

$$D = \frac{-.3}{2}(2535)/\ln(.5)$$

Where $V_r = -.3$ (due to negative direction, Fig. 5)
$D = 548.6\ m^2s^{-1}$

Inserting these results into (3) and solving for the distance where the salinity is $.01\ s_o$

$$L_{lws} = 2535(3\sqrt{548.6/.3(23535)}-1)$$

$$= 3.924 \cdot 10^3\text{m at low water slack}$$
(min distance upstream)

Using equation (4)

$$L_{hws}-L_{lws} = (74560-3924)[1-\exp(-1/3)]$$

$$= 20.023 \cdot 10^3\ \text{m}$$

or $L_{hws} = 23.947 \cdot 10^3$ m inshore from the mouth for a salinity of $\frac{s_o}{100}$ or .04%

Since a salinity of $.04°/_{oo}$ can be considered "barely a trace" (Jones and Kirchoff, 1978) and the calculated ~ 24 km distance inshore doesn't include frictional effects and actual depth changes, it is apparent that Silvester's techniques (above) can be used for modelling salinity intrusion distances in sloughs.

B. Major Distributaries

The first major distributary, Okwega Pass (counter clockwise from A, Fig. 1), has its bottom depths recorded (N.O.S. Chart, 16240, rev. May 1982) and averages at least 6 m depth from its mouth to Hamilton (* on Fig. 1). At Hamilton, a distance of ~ 50 km, saline water has been found underlying the surface freshwater (Norton Sound, E.I.S., 1982) as in Part A above, the August total Yukon flow rate of 400,000 f^3s^{-1} is divided in 2 at the first major bifurcation. The next 3 major shunts divide it by 3. Finally the Apoon mouth distributary and the Okwega Pass distributary act to divide the flow by at least 2. Therefore 400,000/12 yields a flow rate of 33333 f^3s^{-1} or 945 m^3s^{-1} at the mouth of Okwega Pass. An idealized rectangular river of $1.5 \cdot 10^3$ m $\cdot$ 6 m (N.O.S. Chart 16240) cross section results in an estimated river current (V_r) of $[945/(1.5 \cdot 10^3 \cdot 6)] \sim .1\ ms^{-1}$.

If we again assume that a recorded salinity of 4°/₀₀ is reduced to 2°/₀₀ during low water slack at the river mouth, and it takes 3 hours to get back to 4°/₀₀ after low water slack (more than 3 times the volume in Part A) Equation (2) can be used as:

$$x' = \frac{86400\sqrt{9.8 \cdot 6}}{2\pi} (1-\cos[360 \cdot 3/24])$$

$$x' = 30.833 \cdot 10^3 \text{ m seaward of the mouth}$$

From equation (1) (V_r expressed as a (-) velocity, Fig. 5)

$$D = \left(\frac{-.1}{2}\right) (30833)/\ln .5 = 2227.7\ m^2s^{-1}$$

Inserting these results into (3) and solving for the distance where the salinity is .01 s_o

$$L_{lws} = 30883\ (3\sqrt{2227.7/.1(30883)}-1)$$

$$= 47.805 \cdot 10^3 \text{ m at low water slack}$$

Using equation (4)

$$L_{hws} - L_{lws} = (105444\text{-}47805.2)\ (1\text{-}\exp[-1/6])$$

$$= 8.849 \cdot 10^3 \text{ m}$$

or $L_{lws} = 56.653 \cdot 10^3$ m inshore from the mouth ($s_o/100 = .04$ °/$_{oo}$)

It must be noted that any initial salinity s_o can be used. Again, these simple approximations effectively model the salinity intrusion distance upstream.

The Okwega Pass estuary can become predominantly tidally driven by late August. For a tidal range (H) of 1 m, a depth (d) of 6 m and a diffusion coefficient of 2227.7 m^2s^{-1} (above), pollutant concentrations after tidal cycles can be estimated (Silvester, 1974):

$$U \equiv \text{mean tidal current} = \frac{(Hg^{\frac{1}{2}})}{2d^{\frac{1}{2}}}\ \frac{2}{\pi} \tag{5}$$

$$U \equiv \frac{1(9.8)^{\frac{1}{2}}}{(6)^{\frac{1}{2}}\pi} = .41\ ms^{-1} (4 \times \text{the estimated river current from above})$$

$$C \equiv \text{concentration} = \frac{M}{\rho A(4\pi Dt)^{\frac{1}{2}}}\ \exp[-(x\text{-}ut)^2/4Dt]$$

Where $M \equiv$ pollutant mass

$A \equiv$ cross section

$e \equiv$ density of water (ambient fluid)

$t \equiv$ time

Assuming that at the river mouth ($x = 0$), the concentration of pollutant is well mixed after two tidal cycles (water soluble fraction of an oil spill for example) and is measured, then the concentration one week after the spill can be estimated.

at 2T (tidal cycles)

$$C_1 = \frac{M}{\rho A(4\pi D \cdot 2T)^{\frac{1}{2}}} \{\exp[-(0-.41 \cdot 2T)^2/(4D\cdot 2T)]\}$$

at 7T (one week for diurnal tide)

$$C_2 = \frac{M}{\rho A(4\pi D \cdot 7\ T)^{\frac{1}{2}}} \{\exp[-[0-.41 \cdot 7T)^2/(4D.7T)]\}$$

$$\text{or } C_2/C_1 = \frac{1}{(7/2)^{\frac{1}{2}}} \exp\{[(.41)^2/4D][T(-7+2)]\}$$

inserting $D = 2227.7\ m^2s^{-1}$ and $T = 86400s$

$C_2/C_1 = .00015$ or .015% of the well mixed original concentration.

Assuming that the parameters have been selected properly, a week's time would disperse most pollutants. However, toxicity levels for specific pollutants are not estimated here.

C. Significant Information Needs

Investigators will need to determine the missing parameters indicated in Parts A and B above. These are:

1) Salinities of the distributary and slough mouths at both high and low water slack
2) Salinities of the distributary and slough interiors at both high and low water slack
3) The time for the salinity to reach the high water slack value after low water slack
4) River currents and depths (survey data)
5) Accurate tidal excursions
6) The time of the year when sloughs are effectively disconnected from main distributaries

EFFECTS OF STORMS, WAVES, AND CURRENTS

Though storms may hit the delta in any season, there is an actual storm dominated season existing from August to November (Fig. 3). During this period frequent high speed southwesterly winds with longer fetch distances result in high wave energy particularly on the western side of the delta. In addition, due to wave refraction, wave energy is concentrated by delta formations (Bascom, 1964). This combination of high wave energy and rapidly decreasing sediment discharge from the Yukon causes significant coastal erosion (Dupré and Thompson, 1979).

Though long time series of surface wind data have not been collected in the Yukon Delta area, Kozo (1984) has shown that wind data from Alaskan surface wind stations (Fig. 6) separated by distances less than 200 km

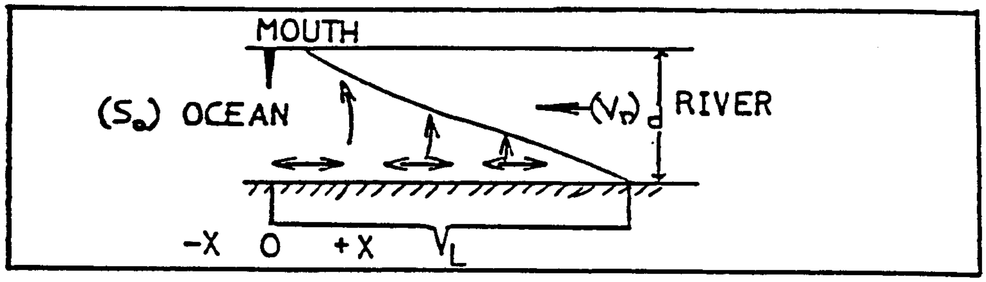

Figure 5. Sketch of interaction of ocean waters and river waters at an estuary mouth under tidally induced mixing $V_r \equiv$ river current, $s_0 \sim$ Salinity at high water slack at mouth of estuary.

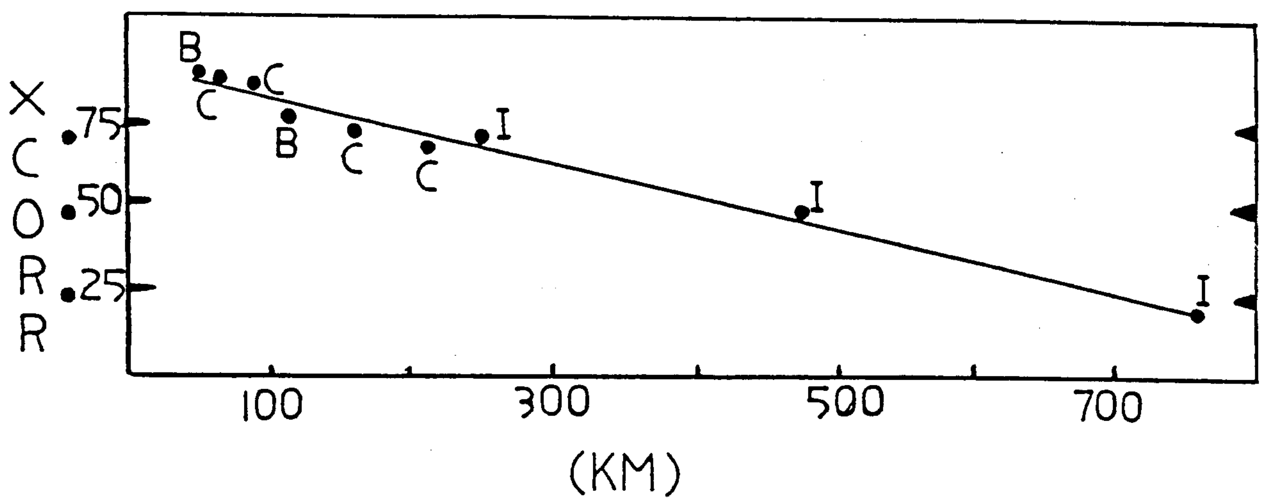

Figure 6. Wind velocity cross correlation values for land wind stations versus distance (km) of separation. B ≡ Beaufort coast, C ≡ Chukchi coast, I ≡ Islands in Bering Sea.

have cross correlation values of .75 at 0 lag time. This criterion is met by both Unalakleet (~ 170 km from the Yukon Delta) and Cape Romanzof (~ 125 km from the Yukon Delta). They both have orographic wind channeling in the winter months under stable atmospheric conditions but in the summer months when atmospheric stability approaches neutral and synoptic wind conditions promote southwesterly flow, they definitely represent Yukon Delta wind conditions.

A closer examination of the synoptic and mesoscale meteorology shows that the average large scale wind vector switches from the northeast in winter to the southwest for the open water periods of July and August (Brower *et al.*, 1977). This accomplishes two things since the current flow also has the same general direction (Fig. 7). The first, is that surface contaminants southwest of the Yukon Delta can be pushed by the wind and currents toward shore. At the same time, surface contaminants in the Lease Sale 57 area (Fig. 7, near shaded area in Norton Sound) will be pushed away from the Yukon Delta most likely impacting on the coast to the east of Nome (**, Fig. 7, Samuels and Lanfear, 1981) or moving to the northwest out of Norton Sound under winds and prevailing currents combined. The second, is that the average summer wind field promotes a downwelling and shoreward transport of outershelf water and with concomitant increase in the water level at the coast. This increased water level allows waves which are focused by the delta to push contaminants further inshore.

Summer mesoscale winds, in particular sea breezes, can dominate the local meteorology 25% of the time and reach speeds up to 15 ms^{-1}

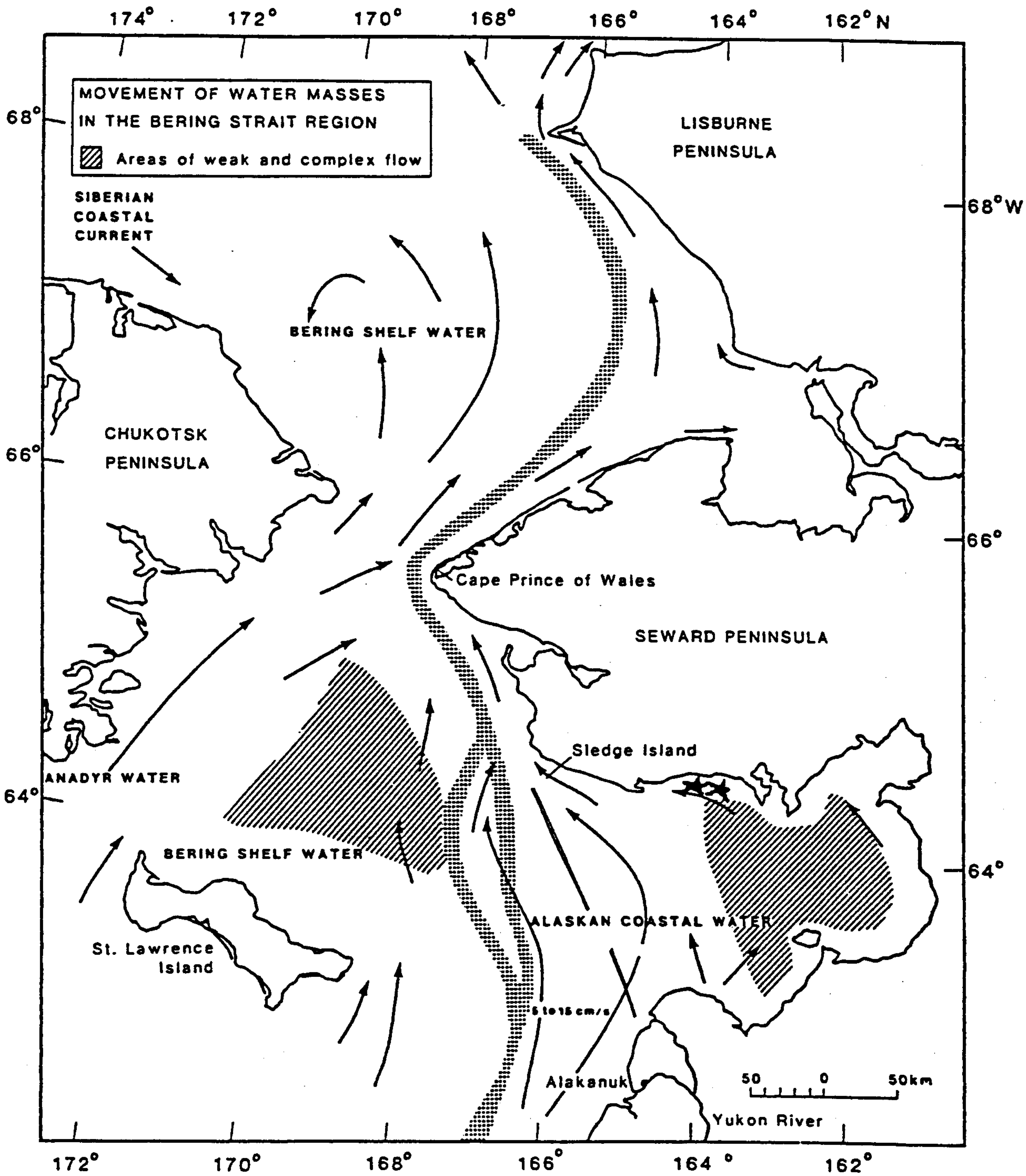

Figure 7. Movement of water masses in the Bering Strait region (Drury *et al.*, 1981).

(Zimmerman, 1982). They also promote a shoreward transport of surface contaminants in a 20 km zone (Fig. 8) seaward of the coast (Kozo, 1982). The convex curvature of the Yukon Delta (opposite to that of a bay) also promotes focusing of thermally driven wind systems (as well as ocean waves, see above) which tend to blow perpendicular to coastlines (McPherson, 1970).

A. Storm Surges

Rises in water level due to strong winds (setup) are of major concern. Abnormal setup in nearshore regions will not only flood low-lying terrain, but provide a base on which high waves can attack the upper part of a beach and penetrate farther inland (U.S. Army Shore Protection Manual, 1977). Accretion and erosion of beach materials, cutting of new inlets through barrier beaches and shoaling of navigational channels can occur.

The Bering Sea has an average of 3.5 cyclonic events in the 15-20 ms^{-1} range (David Liu, Rand Corporation, pers. comm.). Given the average wind direction, the probability of oceanic and atmospheric events occurring in tandem, and the Yukon Delta geomorphology, it has a high vulnerability to storm surge events. Figure 9 shows the coastline of Alaska divided into 25 coastal sectors (Wise *et al.*, 1981). Sector 10 has limited data to compute surge height-frequency interval curves. Data from Figure 6, however, indicate that the interval curve (Fig. 10) for sector 9 can be applied since wind frequencies are proportional to storm surge heights. It should also be noted that the large percentage of

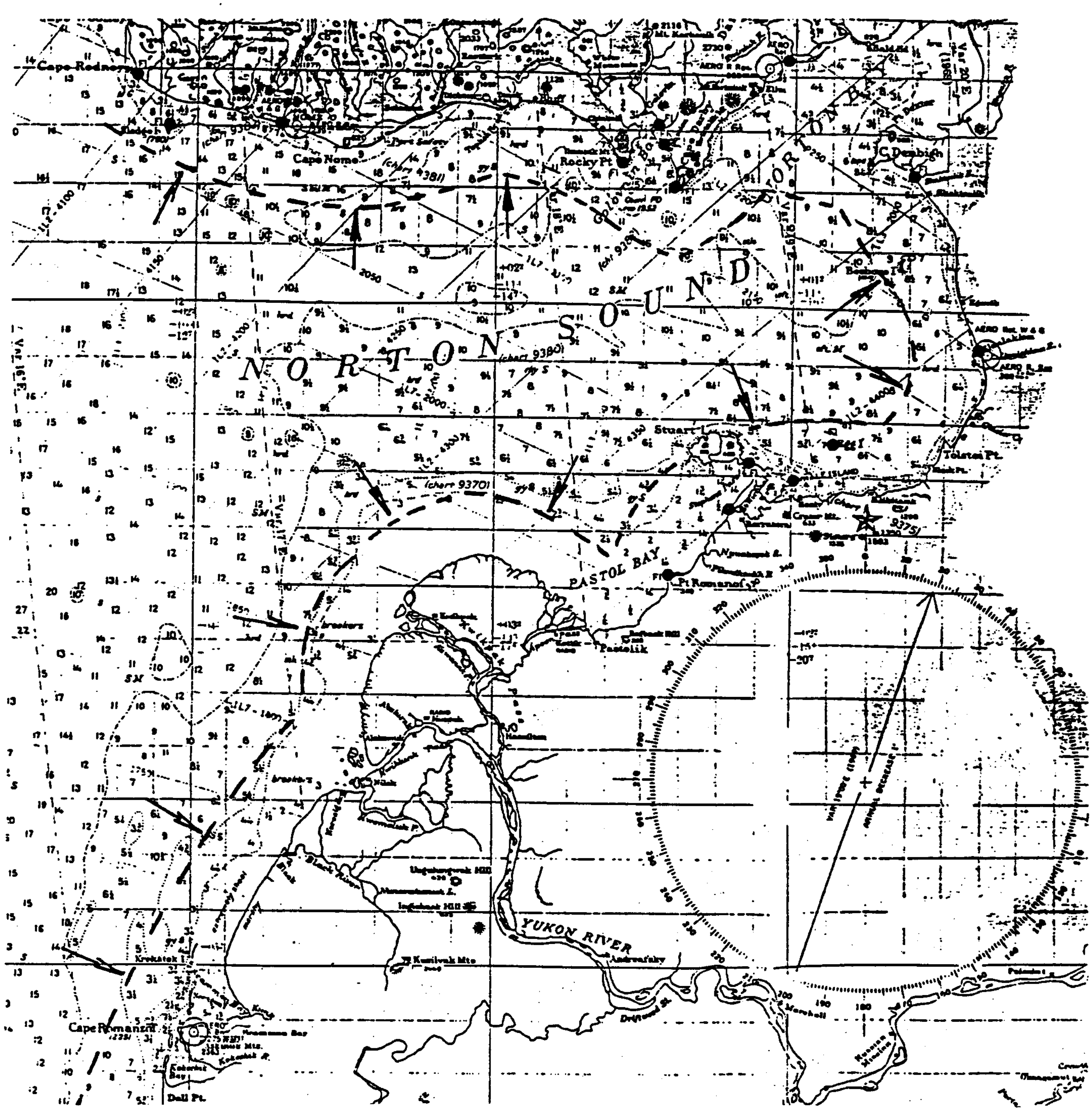

Figure 8. Local winds perpendicular to the shoreline caused by thermal contrast in a 20-km nearshore zone (dashed line). These will dominate when large-scale winds are less than 5 knots (2.5 m/s). Soundings are in fathoms (Coast and Geodetic Survey, 9302, 1968).

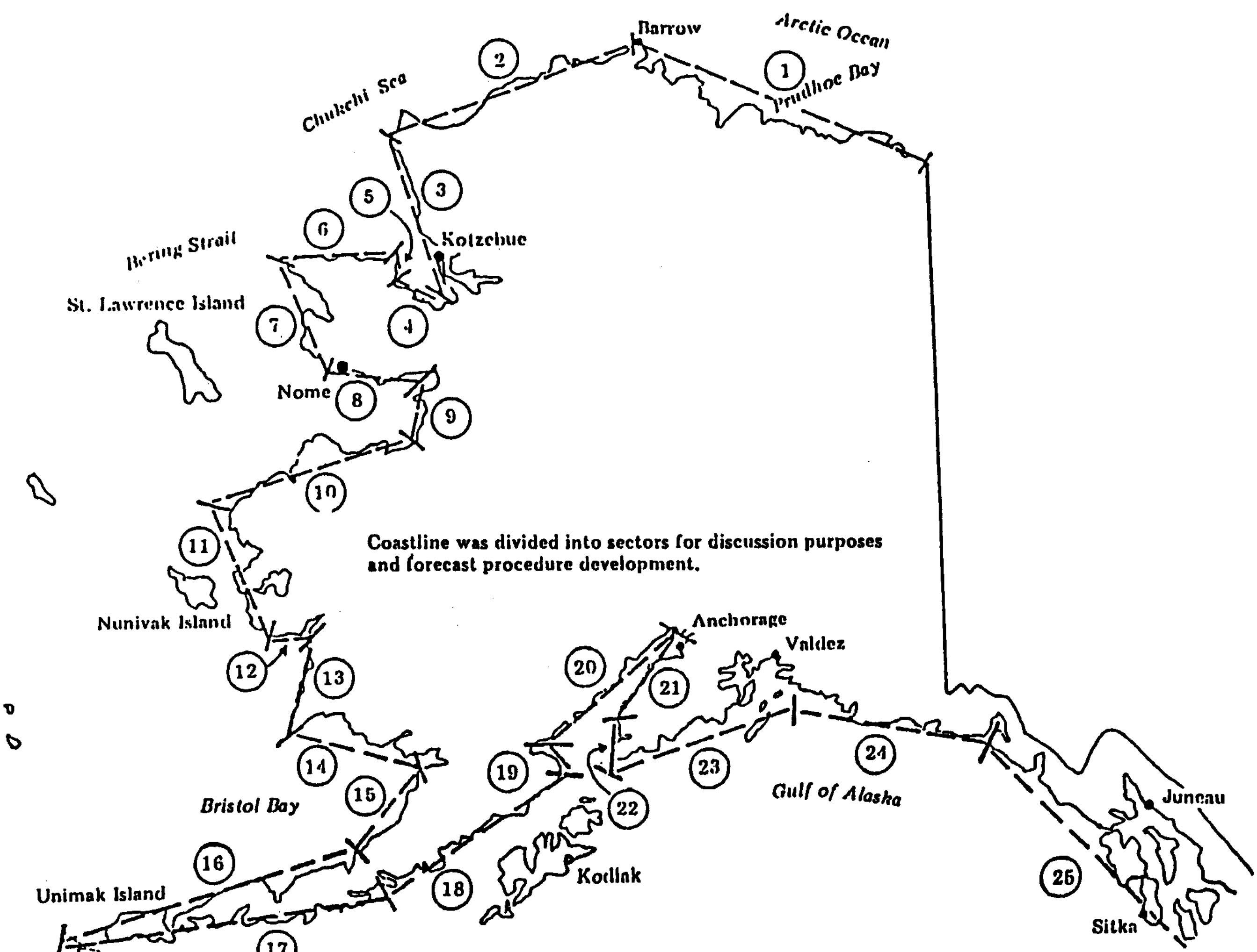

Figure 9. Coastal sectors (Wise *et al.*, 1981).

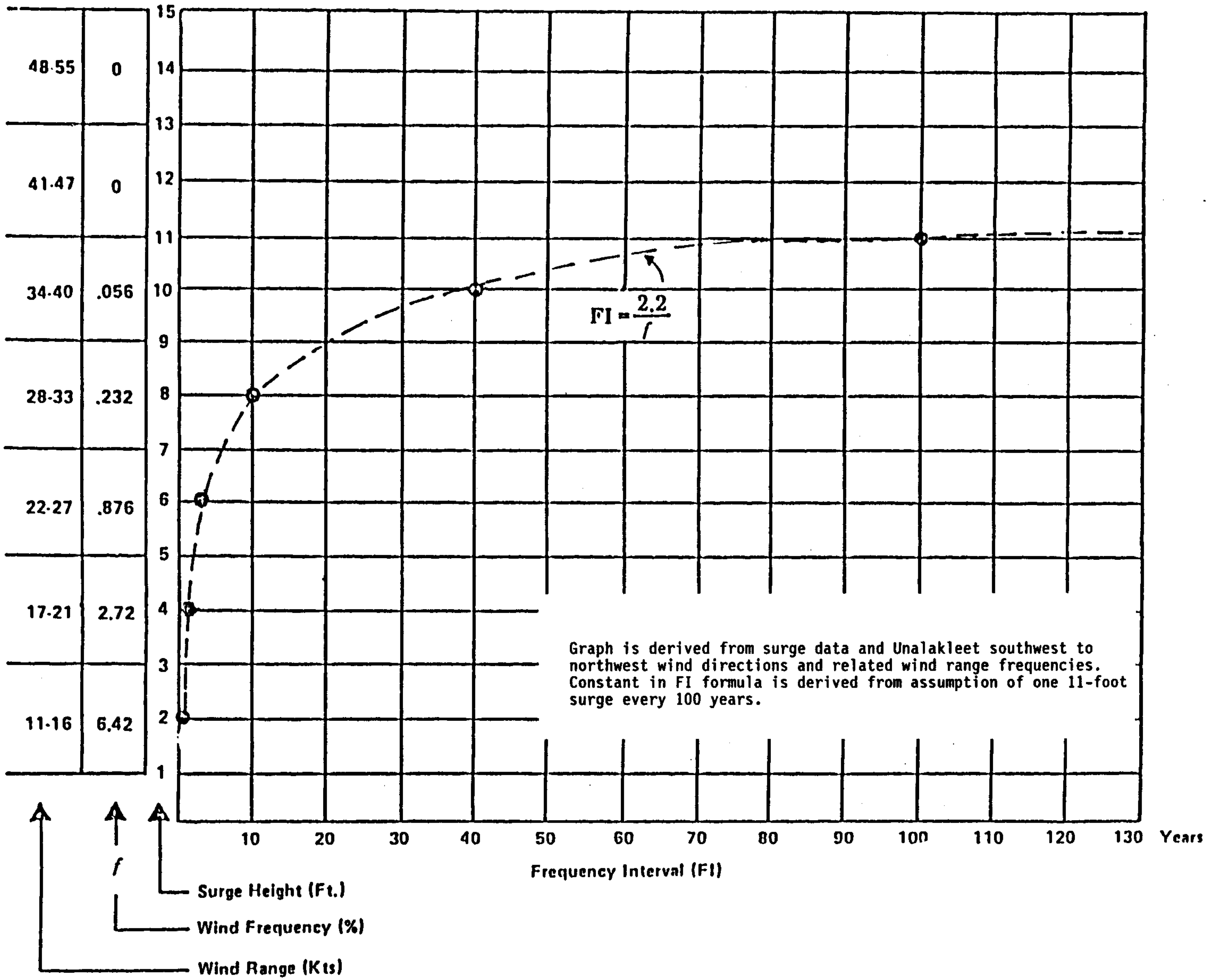

Figure 10. Surge height-frequency interval curve, Sector 9 (Wise *et al.*, 1981).

atypical easterly orographic winds at Unalakleet in winter months are not included in Figure 10 since only winds from the southwest to northwest quadrant are used to construct the curve (favorable fetch directions, Wise *et al.*, 1981).

The proportionality equation is (Wise *et. al.*, 1981):

$$FI = \frac{K}{f}$$

Where FI ≡ frequency interval

f ≡ wind frequencies for a given wind speed class and set of directions

K ≡ constant of proportionality for a given area such as sector 9

A typical storm surge forecast for August can be made using data from storm case histories (Wise *et al.*, 1981) and duration tables (Brower *et al.*, 1977). Assume a cyclonic gale force wind of 35 knots (17.5 ms^{-1}) from the southwest. The preliminary surge height from Figure 10 is 9 ft (20-year return period). Duration tables (Brower *et al.*, 1977) show that at least 5% of the August wind events greater than 20 knots last 12 hours. The preliminary surge height must be reduced by 10% to 8.1 for a 12-hour duration (see Appendix A, Part II C). Typical low pressure centers are 970 mb from storm case histories. Appendix A, Part II E, states that the surge height should be raised 1 ft. for every 30 mb increment below 1004 mb. Therefore the surge height must be raised 1.1' to 9.2'. It will be assumed that high water (astronomical tide) is coincident with the surge so no further corrections are made. This sea level rise (2.8 m) is consistent with actual reports in the area (Zimmerman, 1982).

B. Waves

The above wind speeds and direction, with unlimited fetch for the above duration produce significant wave heights (deep water) of 24 ft (Pierson *et al.*, 1971) as seen on co-cumulative spectra charts for wind speeds as a function of duration. This wave height in shallow water for a 10 sec. period converts to a wave of 30 ft. or 9.1 m (Table C1, U.S. Army Shore Protection Manual, Vol. III, 1977). The surge height in A, above, coupled to the shallow water significant wave height totalling 39.2 ft. or 11.9 m shows that 40 km inland penetration in the delta (Zimmerman, 1982) is very possible since the 50' contour is ~ 100 km inland (Fig. 1 and U.S. Geological Survey charts for Kwigak and St. Michael, Alaska, 1952).

C. Significant Information Needs

Investigators will need to determine missing data histories as indicated in Parts A and B above. These are:

1. Surface winds at the south, middle and north distributary mouths coincident in time with Unalakleet surface wind measurements. Note: This will accomplish two things: first, the applicability of Unalakleet winds to the Delta area (there may still be orographic effects at Unalakleet in the summer); second, wind focusing of the mesoscale sea breeze can be measured at the three mouths.
2. Meteorological and astronomical tides should be measured at the 3 major mouths.

3. Synoptic weather charts should be examined during the experimental season and back in history as a hindcast procedure. In particuluar the chronologies of previous storm surges recorded in Wise *et al.* (1981) should be compared to weather charts.

4. Currents and wave lengths should be measured at appropriate coastal locations.

SEA ICE

The sea and river ice dominated season in the Yukon Delta extends from mid-November to mid-May (Fig. 3). It is easily seen as the season of greatest length, but it is also the season where movement of pollutants is most restricted. Positively bouyant oil spills occurring under an ice canopy require current speeds in excess of 20 cm s^{-1} to move against the opposing friction of the ice skeletal layer and in a week's time can become incorporated into the skeletal layer through the winter freezing process. The Norton Sound is well within the 75% probability of sea ice cover from December 1 until May 15 (Figs. 11 and 12) and is considered as an ice factory supplying up to ten times its area of ice to the Bering Sea (Thomas and Pritchard, 1981). As ice leaves the Sound, it moves either north, following the generally northward moving currents (Fig. 7), or south under the influence of northerly winds. These southward periods could become relevant to Yukon Delta operations.

Though sea ice in Norton Sound is mainly first year (less than 1 m thick), large ice rubble field features have been seen indicating total ridge thicknessess of 24 m caused by ice pile-up (Thomas and Pritchard,

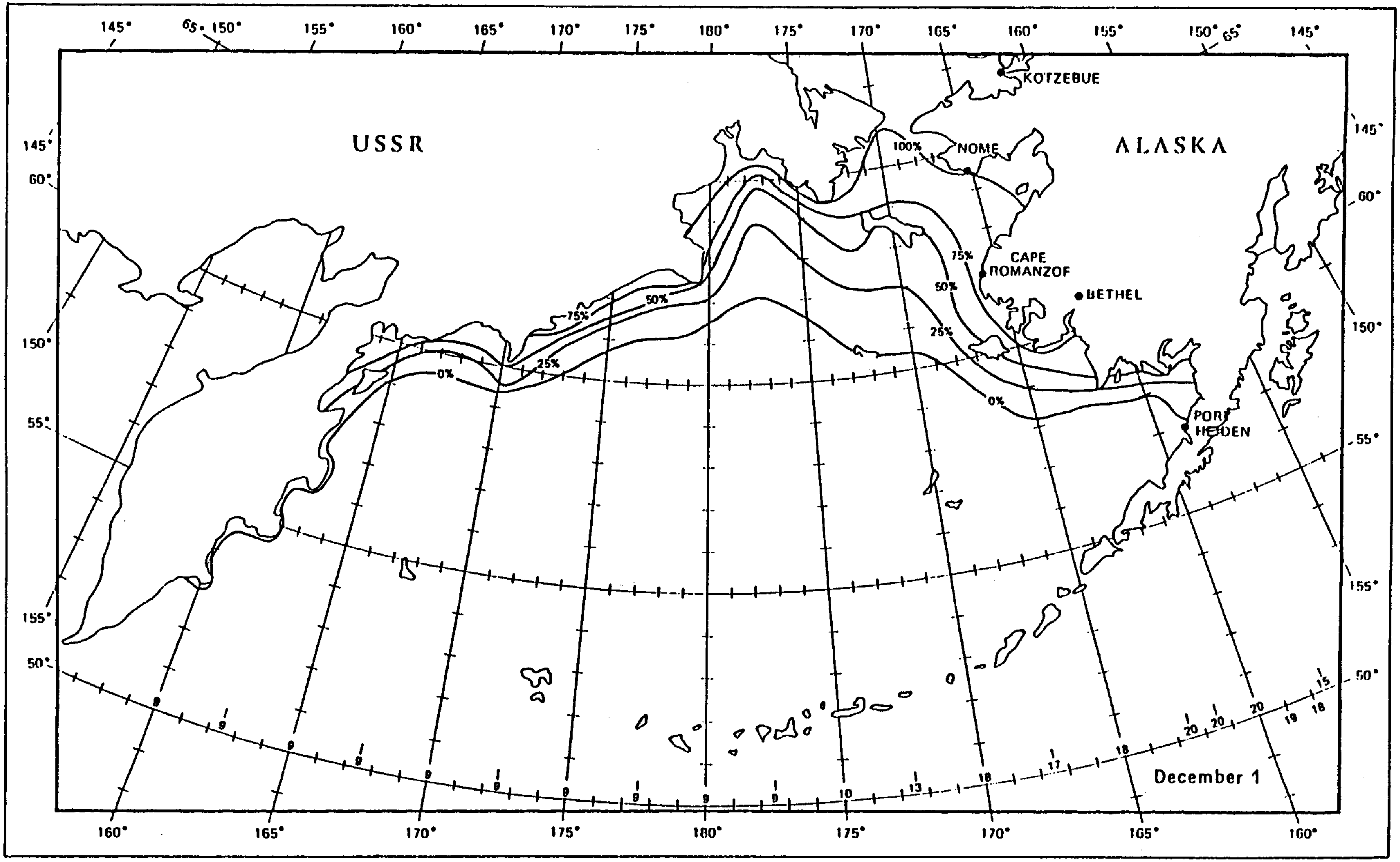

Figure 11. Empirical probabilities of the ice limit for December 1 (Webster, 1981).

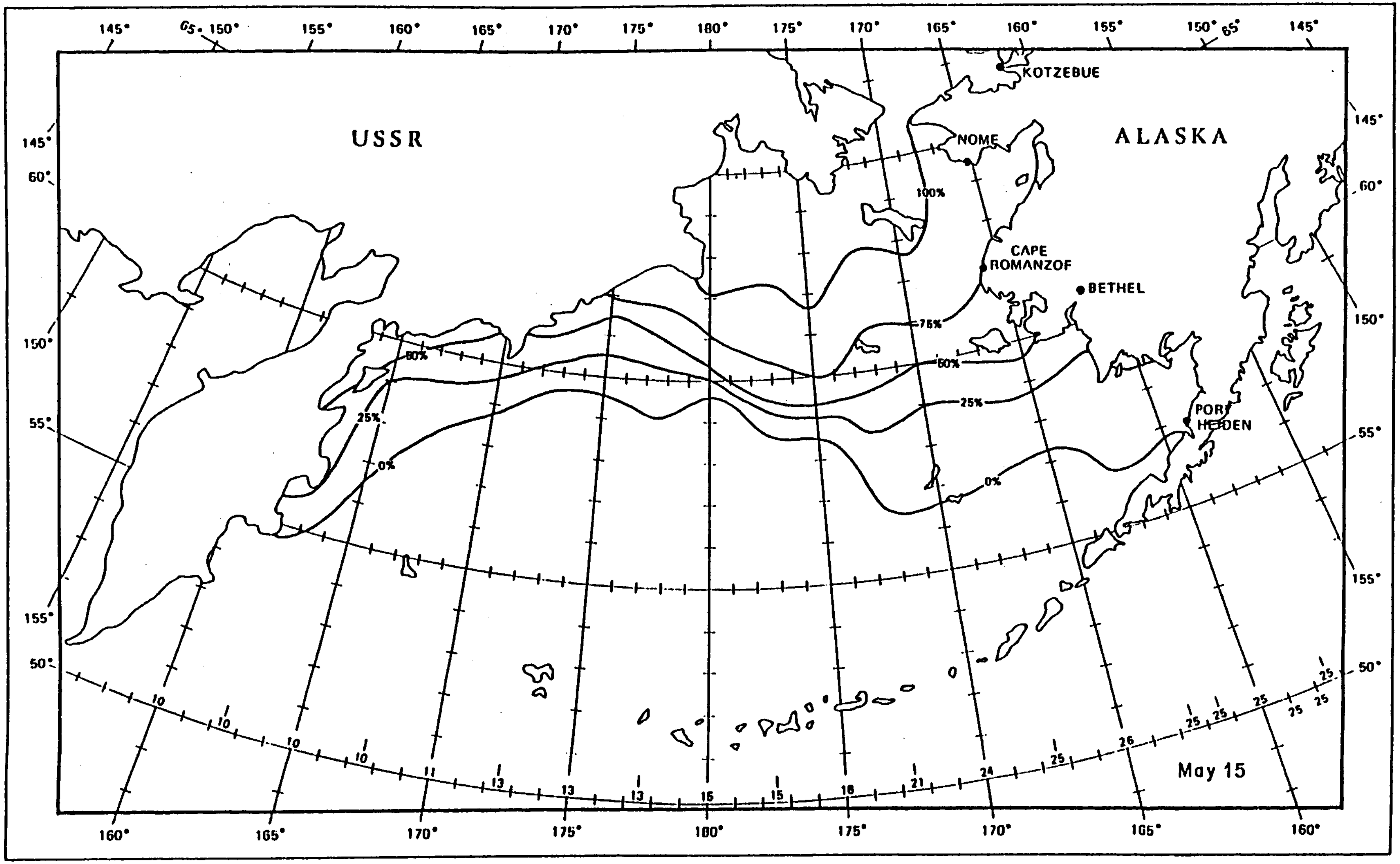

Figure 12. Empirical probabilities of the ice limit for May 17 (Webster, 1981).

1981). The largest concentration of these piles are in shoal areas off the Yukon Delta. Periodic strong winds can move these rubble piles seaward and they can represent extreme ice hazards to transiting ice breakers which ordinarily cannot crash through ice greater than 4 m thick. Also, if they impinge on drilling structures, the structure will be destroyed. Another source of ice thicker than 1 m is Arctic pack ice (2 to 3 m thick) moving through the Bering Strait from the Chukchi Sea after "breakout" periods caused by northerly winds and/or current reversals.

There is a major zone west of the Yukon Delta in water depths of 3 to 14 m characterized by periods of ice deformation and accretion during westerly winds and by periods of offshore ice movement and large polynya development during easterly winds (Dupré, 1980). This area is significant because it is offshore of the south and middle Yukon Delta mouths which have sub-ice channels connected to the polynya area. These channels are considered active during the ice season, from recent observations (Dupre, 1980) of suspended sediments.

A. Sub-ice Channels

The sub-ice channels are extensions of the major distributary channels (Dupré, 1980) and are most common on the western margin of the Delta. Significant amounts of suspended sediments have been measured beneath the ice canopy in the channels in winter (Dupré, 1980). The channel geometry is $\sim 1.5 \cdot 10^3$ m wide by $\sim$ 10 m deep and they can extend up to 20 km beyond the shoreline. The flow rate for the Yukon in mid winter is approximately 40,000 f^3s^{-1} or

10% of the August rate (Carlson, 1977). The method of dividing the flow rate by the number of distributaries used in part I (B) above gives a hypothetical distributary current of .02 ms^{-1} (2 cms^{-1}) moving at a depth below the river ice and running into a sub-ice channel. The tidal current can now be estimated in a subsurface channel under a 1 meter tidal excursion. Though the underice channel to the sea is topped by a sea ice lid, a tidal excursion of 1 m can produce a pressure difference which will force sea water and sediment into the channel and shoreward. The situation is approximated as a classical Poiseville flow in a pipe driven by a pressure differential. The equation (6) (Lamb, 1945) is:

$$U = \frac{\Delta\rho}{4\rho D l}(a^2-r^2) \equiv \text{velocity in the channel} \tag{6}$$

Where $\Delta\rho \equiv$ the pressure differential caused by the tidal excursion (H)

$\Delta\rho \equiv \rho g H$, ρ = density of sea water

$D \equiv$ turbulent diffusion coefficient

$l \equiv$ length of the channel (sub-ice) (taken here as ~ 10km from N.O.S. chart 16240)

$a \equiv$ radius of an equivalent pipe that approximates the channel (since $[1.5 \cdot 10^3$ m $\cdot$ 10 m$] = 1.5 \cdot 10^4$ m letting $\pi a^2 = 1.5 \cdot 10^4$ m gives $a = 69$ m for an equivalent pipe radius)

$r \equiv$ radial length from the center of the pipe ($r = 0$) to the side ($r = a$)

$g \equiv$ acceleration of gravity

Using the above information and substituting into (6) we have:

$$U = \frac{9.8 \cdot 1 \cdot (69)^2}{4 \cdot D \cdot 10^4} \quad \text{(at } r = 0 \text{ center of channel)}$$

D is calculated from the method in Part I using equations (1) and (2) and the .02 ms^{-1} river current estimated above. The time for the salinity offshore at the ice-channel mouth to reach the salinity at high water slack was chosen as ~ ½ hour (less than any other season due to limited volume output). This gives a diffusion coefficient (D) equal to 16.8 m^2s^{-1}, which can be used above to give a U = .07 ms^{-1} within the subice channels. U which depends on D is very speculative but while not moving oil under an ice canopy (less than 20 cms^{-1}) it could move water soluble fractions and some sediment types. Kuenen (1950) shows that a .07ms^{-1} current will transport particles up to .9 mm in diameter which includes muds and fine sand. The motion would be shoreward at high tides and offshore at low tides.

B. Breakup and Freezeup

The breakup period which terminates the ice dominated season signals the beginning period when ice floes containing oil are highly mobile being subject to both winds and currents. Ice in the shore fast ice zone ablates and can also move. River flooding causes freshwater to overflow the shore fast ice areas. A concomitant change in albedo causes increased radiational ablation which together with the above-mentioned mechanical ablation speeds the near shore ice destruction. River sediment can deposit on the ice itself and float beyond the inner shelf. The breakup sequence has a short time scale but it is perhaps the most dynamic part of the year since storm and river influence can also play a role.

The freezeup period is also dynamic since late fall storms may fracture new thin ice and move it out of the area, leading to new manufacture of ice with later small scale winds blowing offshore due to to land breeze effects. Thermohaline ocean circulation will be at its peak nearshore, leading to small scale circulation cells perpendicular to the shelf. The flow will be offshore at depth and onshore under the ice (Kozo, 1983). These density driven flows will be augmented in subice channels which have greater bottom slopes.

C. Significant Information Needs

The freezeup and breakup periods usually have the least amount of available data, both before a study has begun and after several years of study. Since they are so dynamic, they are the most hazardous to men and equipment. Specific needs are:

1. Synoptic atmospheric pressure chart studies during ice "breakout" events (may move ice from the Chukchi to the Bering and possibly toward the Yukon Delta) both as an ongoing program and as post analysis combined with satellite imagery.
2. Current, salinity, and temperature measurements in the sub-ice channels and delta front during the winter months to determine diffusion coefficients and flow directions of sediment.
3. Monitoring the frequency of occurrence of the West Yukon Delta Polynya and thermohaline circulation associated with it.
4. Dumping tracers into the sub-ice channels in winter and monitoring the nearshore distributary bottoms to detect movement of "pollutants" under tidal oscillations.

5. Monitoring currents and sediment transport on top of and below the ice canopy during breakup.

6. Fall freezeup: monitoring currents in existing sub-ice channels before the ice canopy thickens to check for accelerated thermohaline movement due to the greater bottom slopes.

REFERENCES

Bascom, W., 1964: Waves and Beaches, Anchor Books, 267 pp.

Brower, W. A., H. F. Diaz, A. S. Prechtel, H. W. Searby and J. L. Wise, 1977: Climatic Atlas of the Outer Continental Shelf Waters and Coastal Regions of Alaska. NOAA, NCC, EDS, Asheville, 409 pp.

Carlson, R. F., 1977: Effects of seasonality and variability of streamflow on Nearshore Coastal Areas. NOAA/OCSEAP Res. Unit 111, 174 pp.

Defant, A., 1960: Physical Oceanography, Vol. II, Pergamon Press, 598 pp.

Drury, W. H., C. Ramsdell, J. B. French, Jr., 1981: Ecological studies in the Bering Strait region. Environmental assessment of the Alaskan continental shelf. NOAA/OCSEAP Final Rpt. Bio. Studies 11:175-487.

Dupré, W. R., 1977: Yukon Delta Coastal Processess Study Annual Report, NOAA, R.U. 208, 44 pp.

Dupré, W. R., 1980: Final Rpt. Part A, Yukon Delta Coastal Processes Study, NOAA Res. Unit 208, 1980, 79 pp.

Dupré, W. R. and R. Thompson, 1979: The Yukon Delta: A model for Deltaic Sedimentation in an ice-dominated environment, Offshore Technology Conference Paper #3434, 9 pp.

Ippen A. T., 1966: Estuary and Coastline Hydrodynamics, McGraw-Hill, 744 pp.

Jones, R. D. and M. Kirchhoff, 1978: Avian Habitats of the Yukon Delta, U.S. Fish and Wildlife Service, Anchorage, Alaska, 33 pp.

Kozo, T. L., 1982: An observational study of sea breezes along the Alaskan Beaufort Sea Coast: Part I. J. App. Meteor., 12, 891-905.

Kozo, T. L., 1983: Initial model results for arctic mixed layer circulation under a refreezing lead. J. Geo. Res., 88, 2926-2934.

Kozo, T. L., 1984: Alaskan Arctic Mesoscale Meteorology, Final Rpt., MMS, NOS. Contract 03-5-022-67.

Kuenen, P. H., 1950: Marine Geology, John Wiley and Sons, Inc., New York 568 pp.

Lamb, H., 1945: Hydrodynamics, Sixth edition, Dover Publications, New York, 738 pp.

McPherson, R. D., 1970: A numerical study of the effect of a coastal irregularity on the sea breeze, J. App. Meteor., 9, 767-777.

Norton Sound, E.I.S., 1982: Final Environmental Impact Statement, OCS Proposed Oil & Gas Lease Sale 57, BLM, Dept. of Interior, 330 pp.

Pierson, W. J., G. Neumann, and R. W. James, 1971: Practical Methods for Observing and Forecasting Ocean Waves, U.S. Naval Oceanographic Office Pub. #603, 283 pp.

Samuels, W. B. and K. J. Lanfear, 1981: An oilspill risk analysis for the Norton Sound, Alaska, (Proposed sale 57) outer continental shelf lease area, USGS, open-file report #81-320, 43 pp.

Silvester, R., 1974: Coastal Engineering, II, sedimentation, estuaries, tides, effluents, and modelling, Elsevier Scientific Publishing Co, 338pp.

Thomas, D. R. and R. S. Pritchard, 1981: Norton sound and Bering Sea Ice Motion: 1981, Flow Research Rpt #209, Kent, Washington, 37 pp.

U.S. Army Shore Protection Manual Vol. III, 1977: U.S. Army Coastal Engineering Research Center U.S. Govt. Printing Office, Washington, D.C., 144 pp.

Webster, B. D., 1981: A climatology of the ice extent in the Bering Sea, NOAA Tech. Memo., NWS AR-33, Anchorage, Alaska, 38 pp.

Wise, J. L., A. L. Comiskey, and R. Becker, 1981: Storm surge climatology and forecasting in Alaska, Alaska Council on Science and Technology, Alaskan Natural Hazards Research, 45 pp.

Zimmerman, S. T., 1982. The Norton Sound Environment and Possible Consequences of Planned Oil and Gas Development: Proceedings of a Synthesis Meeting: Anchorage, Alaska, October 28-30, 1980. BLM, NOAA, 55 pp.

APPENDIX A

Forecast Procedures (Wise *et al.*, 1981)

I. DEFINITIONS

A. Surge

The height of the ocean's surface above forecast (tidal) levels.

B. Favorable Relative Fetch Wind Direction

Assume the coastal configuration to be straight line segments as shown on Figure 9. When facing seaward the *relative* wind direction is measured *clockwise* from the coast. Thus the coast to the left is 0°; seaward +090°; to the right 180°. If to the left and offshore, it has negative values. Favorable relative wind directions are:

Sector	Favorable Direction
1	-020 to 090
2	-020 to 090
3	080 to 140
4	010 to 050
5	-050 to -010
6	040 to 090
7	020 to 090
8	120 to 190
9	030 to 100
10	-020 to 080
11	-020 to 120
12	050 to 150
13	-020 to 090
14	070 to 120
15	010 to 090
16	-020 to 090

In an idealized model the most favorable directions are from -020 to 090 but topography working in conjunction with gravity acting on anomalous sea surface slopes creates surges (generally of lesser magnitude) in areas wherein the wind is not blowing from an idealized "favorable" direction. The favorable directions *shown above* are those relative directions where the wind creates an anomalous sea height somewhere nearby that, in turn, affects the sector of interest.

C. <u>Fetch</u>

An area in which wind direction and speed are reasonably constant and do not vary past the following units:

1) The wind direction or orientation of the isobars does not change direction at a rate greater than 15° per 180 nmi and the total change does not exceed 30°.

2) The wind speed does not vary more than 20 percent from the average wind speed in the area of the direction fetch being considered. Example: average wind is 40; acceptable range is 32 to 48.

D. <u>Fetch Duration</u>

The number of hours a coastal area is subjected to fetch winds.

E. <u>Lowest Pressure</u>

The lowest pressure coincident with fetch induced surge.

F. <u>Sea Ice Coverage</u> (minimum expected during storm).

Percent of sea ice coverage in tenths.

G. <u>Sea Ice Character</u>

Primary concern is thinness and weakness. Thin or unconsolidated ice can be destroyed by storm action.

H. <u>Boundary Layer Stability</u>

The difference between the sea and air temperatures. The boundary layer temperature difference should be used when estimating the fetch wind speed. The following guidelines are suggested:

Correction to Geostrophic Wind for the Sea-Air Temperature Difference

$T_s - T_a$	Percent of geostrophic winds used
0 or negative	60
0 to 10	65
10 to 20	75
20 or above	90

II. PROCEDURE

A. <u>Determine</u>

1. Fetch wind (speed, and direction). Consider boundary layer conditions. If direction is favorable continue with determination of:

   a. fetch duration

   b. ice cover

   c. lowest pressure

   d. tidal variation if over 1 foot

B. <u>Preliminary Surge Height</u>

Using wind speed, read correlated surge height from appropriate coordinate tables (Fig. 10).

C. Duration Adjusted Surge Height--if fetch duration is less than:

1. 3 hours reduce surge by 60 percent
2. 6 hours reduce surge by 40 percent
3. 9 hours reduce surge by 20 percent
4. 12 hours reduce surge by 10 percent
5. 12+ hours no reduction

D. Ice Cover Adjusted Surge Height--if ice cover is less than:

1. 1.5 tenths no reduction
2. 3.0 tenths reduce surge by 20 percent (cumulative to above)
3. 5.0 tenths reduce surge by 50 percent (cumulative)
4. 10.0 tenths reduce surge by 75 percent (cululative)
5. Surges to 3 feet with 10 tenths ice cover have been reported with ice to 3 feet thick between October and January. Also, consider sea ice character. Thin ice, weak, ice, or unconsolidated ice can be effectively destroyed during storm conditions--particularly in the northern Bering Sea, with subsequent surges to 9 feet.

E. Pressure Adjusted Surge Height

Raise the surge height one foot for every 30 mb pressure increment below 1004 mb.

F. Tidal Adjusted Surge Height

Check tidal tables or other sources. If peak of surge is reasonably coincident with normal high water, make no correction. If surge misses normal high water, subtract as appropriate from surge height.

SUPERSTRUCTURE ICING AND WAVE HINDCAST STATISTICS IN THE NAVARIN AND ST. GEORGE BASIN AREAS

by

Thomas L. Kozo

VANTUNA Research Group
Occidental College
Los Angeles, California

Final Report
Outer Continental Shelf Environmental Assessment Program
Research Unit 519

1983

TABLE OF CONTENTS

SUPERSTRUCTURE ICING

A. INTRODUCTION

Icing is mainly a function of the amount of water which remains liquid after striking a ship's or fixed platform's surface and the elapsed time before this water freezes. There are two types of ice accumulation, rime ice and glaze ice. Rime is rough, milky, opaque ice with minimal adhesion and is formed when small, super-cooled drops of water freeze on contact with a surface. It does not spread and can form at any temperature in the icing range. Glaze is formed on slow freezing of large super-cooled drops. It can spread over a larger surface and is harder to remove than rime icing (the preceeding paragraph has been paraphrased from Berry et al., 1975).

Ice accretion depends on many factors. Meteorology and sea conditions are paramount (see below). However, vessel size, navigational peculiarities, structural design, kinematic and thermodynamic interaction at the surface of a design member and water droplets (stagnation zones on a surface, Ackley and Templeton, 1979) also become critical.

B. EFFECTS ON SHIPS

Ships such as fishing trawlers, smaller merchant ships, and Coast Guard Cutters are most vulnerable to icing due to less freeboard and the increased amount of travel time through an area experiencing icing conditions. It should be noted that the right combination of events can produce icing on large vessels also. Icing on a vessel increases its weight, changes its trim, elevates its center of gravity, decreases its metacentric height and increases its sail area and heeling moment leading to extreme handling difficulties (Berry et al. 1975).

C. ICING ON OFFSHORE STATIONARY PLATFORMS

As on ships, a coating of ice on external surfaces can elevate the platform's center of gravity. In addition, the ice will usually form in stagnation zones on the windward side (Ackley and Templeton, 1979) causing an imbalanced weight distribution on a platform. Vertical and horizontal members of offshore structures are designed to meet oscillatory stresses due to wave action. The forces on the structure are made up of hydrodynamic drag and inertial (mass) components. Icing changes the physical characteristics of structure members, such as diameter, surface roughness, mass and flexural response (Ippen 1966). Therefore, a fixed structure's ability to withstand a design wave is questionable after and during an extreme ice accumulation.

Depending on freezing rates, the ice forming on structures due to sea spray will generally have a salt content much less than the sea salinity and may even approach 0 ‰ salinity. The maximum pressure produced by water freezing in a confined space is 30,000 lb in^{-2}. This stress on a structure or ship occurring during a freezing sea spray condition can drastically weaken support members.

D. METEOROLOGY AND SEA CONDITIONS (the following Parts 1-4 have been paraphrased from Berry et al. 1975).

1. Freezing Rain and Snow

Freezing rain itself seldom reaches large enough accumulations to be the sole source of danger to a ship. However, combined with freezing salt spray (see below) it becomes dangerous since, as freshwater, it freezes faster than salt water and can act as a nucleus for faster ice accumulation from salt spray. Snow is not considered a threat due to inherent lack of adhesion.

2. Arctic Sea-smoke

Arctic sea-smoke forms when extremely cold air flows over much warmer water. The water vapor that results from the ensuing evaporation condenses immediately in the cold air and super-cooled droplets become visible as rising columns of "steam". Weight of ice deposited is only a problem if the condition exists for a long time since it is a low wind phenomenon.

3. "Sea Ice"

Water taken over the side of the ship will not freeze readily unless trapped by ice chocked rails and ports. This is considered a minimal hazard.

4. Freezing Spray

The Figs. 1-17 below have been developed mainly for freezing spray conditions. This is the most common and dangerous form of icing, resulting in glaze ice characterized by high density and great adhesion power. This type of icing is a function of several simultaneously occurring variables:

a. Air Temperature

The critical range for this study (Bering Sea Area) is from 0°F to 32°F (-18°C to 0°C). At temperatures below 0°F the water striking the structure will usually be in the form of non-adhering small dry ice crystals (Berry et al., 1975).

b. Wind

Sea spray generation depends on the wave height and period of waves. Waves in turn depend on the duration of the wind and fetch. Generally, the higher the wind speed for the above temperature range, the greater the ice accumulation. The range of wind speeds covered in this study are from 25 knots (12.5 ms^{-1}) to 60 knots (30 ms^{-1}). Data indicate that wind speeds below 25 knots do not produce icing, while wind speeds in excess of 60 knots are rare. Wu (1982) mentions that a wind speed of 12.5 ms^{-1} is considered the incipient velocity for entrainment of water particles in air (without need of waves).

c. Effect of the Ice Pack

When the ice pack concentration reaches 50% areal coverage, superstructure icing is thought to be minimal since wave formation is reduced and freezing spray is eliminated.

d. Sea Temperature

The criticial range of sea surface temperatures are 28° F (-2.2° C) to 48° F (8.9° C). Seawater of normal salinities is generally frozen below 28° F. The upper value of 48° F is not an impediment to freezing since sea spray can be cooled rapidly when air temperatures are below 28° F.

A dangerous layer of ice accumulation occurs at 3.9 in (10 cm, Berry et al., 1975). Of the five icing categories used in this study, extreme icing would produce this thickness in nine hours, heavy icing would produce this thickness in 16 hours, and light icing would produce this thickness in two days.

E. ICING MAPS

To construct the icing contours for Figs. 1-17, a combination of data sources were used. The 50% probability of 50% sea ice areal coverage position was taken from Webster (1981) for the middle of each month shown. The positions of the 50% probability of 50% sea ice areal coverage and the 50% probability of any sea ice diverge only in the Spring (May on). The minimum and maximum positions of the 50% sea ice concentration edge which were used to construct the extreme icing condition maps (below) have also been taken from Webster (1981).

Average and extreme contours of sea surface and air temperatures for map construction came from Brower et al. (1977).

The wind speed data for the Navarin Basin came from a combination of new data (Kozo, 1983) and Marine Areas A and B data (Brower et al. 1977) on its eastern boundary. Wind speed data for St. George Basin came from Marine Areas B, C and nearby land stations (Brower *et al.* 1977). There is no evidence of any area in the Bering having monthly mean winds of 25 knots (12.5 ms^{-1}). Therefore mean wind contours were not useful in constructing icing maps. However, David Liu of Rand Corporation has stated that the Bering Sea has an average of 3.5 cyclonic events per month (pers. comm. 1982). The World Meterological

Organization (W.M.O.) lists 28 knots (14 ms^{-1}) as the onset of dangerous wind speeds (gale level winds) and 50 knots (25 ms^{-1}) as the onset of real storm level winds. Hence, these levels were used as the critical winds for mean and extreme icing. Table 1 (a. and b.) has been constructed to show the % time of occurrence of gale and storm level winds during possible icing months. Table 1a. is for the Navarin Basin (10 months of icing) and Table 1b. is for St. George Basin (9 months of icing). In addition the % of air temperatures below 0° F (18° C), which generally preclude superstructure icing, are shown. It must be noted that while the percentages are low for the total time of occurrence of these wind speeds, the probability of these speeds existing in each month is 100% and the duration of these speeds are sufficient to produce severe icing provided the other environmental conditions are met. Therefore, fixed structures which remain in place in one locaton over many months will be more susceptible to icing than vessels which may move in and out of a given area.

A new nomogram for superstructure icing has been used which replaces that of Brower et al. (1977). The nomogram takes into account the lower wet and dry bulb temperatures, the lower relative humidity, and the higher freezing rates found in the Bering Sea and North Pacific (Wise and Comiskey, 1980).

Five rates of ice accumulation are used in icing maps (Figs. 1-17) constructed for this study.

1. Mean Maps

Mean monthly 50% ice coverage positions, sea surface temperatures and air temperatures were examined under 28 knot wind speed conditions. The Wise and Comiskey Nomogram (Eastern Bering Sea and Gulf of Alaska, 1980) was used to arrive at the icing rates.

a. Navarin Basin

Superstructure icing can be seen to exist at various levels for the months of October through April (Figs. 2, 4, 6, 8, 10, 12, and 14). Mean conditions and 28 knot winds did not produce icing in the Navarin for the months of May through September. From December through April (Figs. 6, 8, 10, 12, and 14), moderate icing conditions can exist for a long enough time period (see Table 1a) to easily reach the dangerous 10 cm accumulation mentioned above. Also a 10 knot increase in wind speed will normally change the icing category from moderate to heavy if the other parameters stay constant. By April under mean ice conditions (Fig. 14) over 50% of the Navarin Basin is covered with sea ice and therefore superstructure icing is eliminated north of the ice edge.

b. St. George Basin

Superstructure icing exists at certain levels from December through April (Figs. 6, 8, 10, 12 and 14). Mean conditions and 28 knot winds should not produce icing in St. George Basin from May through November. February (Fig. 10) is the only month capable of producing moderate icing conditions of sufficient duration (see Table 1b) to reach the 10 cm dangerous accumulation stage. Sea ice covers a small percentage of St. George Basin under mean conditions; therefore, superstructure icing is a distinct possibility for most of the Basin from December through April.

2. Extreme Maps

a. Navarin Basin

Storm level winds (50 knots) and appropriate combinations of air temperatures, sea surface temperatures and sea ice edge conditions will produce icing in ten months from September through June (Figs. 1, 3, 5, 7, 9, 11, 13, 15, 16 and 17). It must be remembered that when ice edge positions are used (mean, minimum or maximum) the corresponding sea surface temperatures "adjust" to the edge position with the lowest sea temperatures adjacent to the ice. However, even on light sea ice years (minimal sea ice extent, higher than average sea surface temperature) a sudden cold front with high winds can move into the Bering Sea and produce severe icing. Atmospheric conditions will generally change on a shorter time scale than the oceanic conditions and appear to be the most important variable in superstructure icing. Figures 1, 3, 5, 7, 9, and 11 representing the months of September through February respectively show that the most extreme icing possible for 50 knot winds results under conditions of minimum air and ocean temperatures and maximum extent of 50%

of sea ice coverage. This occurs because the maximum 50% sea ice coverage is associated with low ocean temperatures over most of the Navarin Basin area, even though the sea ice edge position does not reach the basin as in September and October.

Figures 13, 15, and 16, representing the months of March, April, and May, depict conditions of 50 knot winds, minimum air temperatures, and minimum extent of 50% sea ice with ocean temperatures corresponding to the sea ice position. In these months the maximum 50% ice edge position covered too much of the Basin for extensive spray-induced icing to occur. Instead, the minimum ice edge position led to the necessary sea surface temperatures and wave action to produce the most severe conditions over most of the Navarin Basin.

In June, the maximum ice edge was too far south for minimum June air temperature to cause icing. The minimum ice edge for June was so far north that sea surface temperatures in the Navarin Basin precluded icing even under 50 knot winds. Hence, 50 knot winds at the mean 50% areal coverage ice edge position with corresponding water temperatures and minimum air temperatures produced June icing for the Navarin (Fig 17).

b. St. George Basin

Extreme conditions (outlined above) will produce icing from October through June (Figs. 3, 5, 7, 9, 11, 13, 15, 16, 17). Figures 3, 5, 7, 9, and 11 representing the months of October through February respectively show that the most extreme icing possible for 50 knot winds results under conditions of minimum air and ocean temperatures and maximum extent of 50% sea ice coverage. Again, this occurs because the maximum of 50% sea ice coverage is associated with lower ocean temperatures over most of the St. George Basin area, even though the sea ice edge position does not reach the basin.

Figures 13, 15, and 16 represent the months of March, April, and May, respectively. They depict conditions of 50 knot winds, minimum air temperatures, and minimum extent of 50% sea ice with ocean temperature corresponding to the sea ice position. Again, the minimum ice edge position led to the necessary sea surface temperatures and wave action to produce the most severe conditions over the St. George Basin.

Fifty knot winds at the mean 50% areal coverage ice edge position with corresponding water temperatures and minimum air temperatures produced June icing for St. George Basin (Fig. 17).

Real icing conditions will fall somewhere between the conditions shown on the extreme and mean maps (Figs. 1-17). It should again be mentioned that the thermal inertia of the oceans makes atmospheric changes the most dangerous variables in the icing puzzle. Table 1 shows that 50 knot winds may exist for 1% of a month's time or approximately 7 hours. Seven consecutive hours of extreme icing will approach the critical accretion of 10 cm (3.9 in.) and be very dangerous.

F. FURTHER STUDY

A data gathering program should be initiated in the Navarin and St. George Basins. Among the parameters measured during icing events should be salinity of adhering ice, materials with or without coatings adhered to, percentage due to sea spray, ship size, ship speed, types of waves, directionality and thickness of ice.

WAVE HINDCAST STATISTICS

A. INTRODUCTION

The environmental conditions characterized by the wave field in the Navarin and St. George Basins (areas outlined by thin black lines east of 180° and northwest of the Aleutian Islands respectively, Fig. 1) were determined by a deep water wind wave hindcast scheme. The calculated deep water wave heights and periods were based on the assumption of uniform steady wind conditions along each wind direction. The fetch simulated for the establishement of wave statistics was chosen as the largest fetch across the basin along the direction of the wave hindcast. In months when the fetch was ice limited it corresponded to the 50% probability of the 50% ice edge position as shown in Figs. 4, 6, 8, 10, 12, 14, 18, and 19. In the Navarin Basin, the wind statistics derived by Kozo (1983) were adopted, adjusted for the desired directional distribution function, and used for the calculation of deep water wave statistics. Similarly, wind statistics from St. Paul (Pribilof Islands) Marine Area B, and Marine Area C (Brower *et al.* 1977) were used for the derivation of St. George Basin deep water wave statistics.

B. DEEP WATER WAVE HINDCAST THEORY

Hasselmann's parametric wind-wave model (Hasselman, 1976) was adopted for the hindcast of the deep water wave. The fundamental concept of Hasselmann's one parameter model is based on the premise that the response of the wave field to the wind input can be described by two processes which occur at different rates: 1) the rapid adjustment of the spectrum to a universal shape and an energy level such that the input by the wind in the dominant region of the spectrum is balanced by the nonlinear transfer and possibly dissipation, and 2) the slower migration of the peak toward lower frequency due to the nonlinear energy transfer across the peak. This concept has been verified by JONSWAP'S field results (Hasselmann et al., 1973) and also by Wu's laboratory results (Wu et al., 1979). The one parameter model is limited to growing seas and cannot be extended into the swell range. The governing equation is:

$$\frac{1}{f_o}\frac{\partial f_o}{\partial \tau} + P_o \frac{\partial f_o}{\partial \eta} = -N_o f_o^{7/3} \cdot + \frac{1}{u}\left(\frac{\partial u}{\partial \tau} + \frac{\partial u}{\partial \eta}\right)$$

Where, $P_o = 0.95$

$N_o = 5.5 \times 10^{-4}$

$\frac{\partial}{\partial \tau} = \frac{u}{g}\frac{\partial}{\partial t}, \quad \frac{\partial}{\partial \eta} = \frac{u}{g}\vec{V}_m \cdot \bar{\nabla}, \quad |\vec{V}_m| = \frac{\alpha g}{4\pi f_m}$

$f_o = Uf_m/g$, $\quad q = 0.85$ for $\cos^2\theta$ spreading factor

U is wind speed, g is gravitional acceleration,

f_m is peak wave frequency.

For a uniform wind field, the governing equation for predicting a local peak frequency can be simplified as:

$$\frac{\partial f_m}{\partial t} = -5.5 \times 10^{-4} \cdot \left(\frac{g}{U}\right)^{-4/3} \cdot f_m^{10/3}$$

The analytical solution of the above equation in terms of the normalized peak wave period, T_p and normalized significant wave height, H_s can be expressed as follows:

For

$$X \leq 3.5 \times 10^3 \cdot$$

$$H_s = 1.53 \times 10^{-3} X^{0.5}$$

$$T_p = 0.341 \hat{X}^{0.3}$$

otherwise

$$H_s = 0.283 \tanh (0.0125 X^{0.42})$$

$$T_p = 7.54 \tanh (0.077 X^{0.25})$$

Where $X = gX/U^2$, $H_s = g_s/U^2$, $T_p = gT_p/U$. The results calculated by the above equations compare quite well with experimental observations made in other parts of the world over many years.

C. Results and Conclusions

1. <u>Navarin Basin</u>

The calculated results of wave statistics are in Table 2 (a and b) through 13 (a and b) for the Navarin Basin. Both significant wave height (Hs) and peak wave period (Tp) are presented in frequency of occurrence and total percentage. The significant wave height is the average height of the 1/3 highest waves. The height of the 5% highest waves is 1.73 Hs. (Pierson et al., 1971). This value will be representative of individual wave height observations such as the 51 foot seas (15.5 m) reported (Petroleum Information, 1983) for the Navarin in October, 1983. For example, October in Table 10 shows a maximum Hs of 10 m. Therefore, 1.73 Hs yields 17.3 m, putting the 51 foot waves within the predicted envelope. The hindcasted maximum significant wave height and peak wave period are 13 m and 16 seconds for the Navarin Basin. These extreme events occurred in the months of February and November. During the months of ice coverage influence (November through June) most of the events occurred concurrently with the wind from the directions of north, northeast and east. The majority of wave heights ranged from 1 to 5 m and wave period ranged from 6 to 10 seconds. During the months from July to October (no ice coverage effect), both wind and waves had less directionality. The majority of significant wave heights ranged from 1 to 3 m and peak wave periods ranged from 4 to 8 seconds.

2. St. George Basin

The calculated results of wave statistics are in Table 14 (a. and b.) through 25 (a. and b.) for the St. George Basin. Both significant wave height and peak wave period are presented in percentages. The hindcasted maximum significant wave height and peak wave period are 16 m and 18 seconds, respectively. These extreme events occurred in the months of February and November (also see Navarin Basin above). During the months of possible ice cover influence on fetch (November through May) most of the events occurred concurrently with wind directions from north, northeast and east. The majority of wave heights ranged from 1 to 5 m and wave periods ranged from 6 to 10 seconds. During the months from July to October (no ice coverage effect) both wind and waves had less directionality. The majority of significant wave heights ranged from 1 to 3 m and peak wave periods ranged from 4 to 8 seconds. The computed statistics for St. George Basin and the Navarin Basin were very similar. However, the position of the sea ice cover in the Bering Sea will always result in a greater fetch distance for St. George Basin simulations. Therefore, under conditions of similar duration the seas will be more fully developed in the southernmost basin. In addition, the tables will show that greater significant wave heights (from specified directions) do not always produce greater peak wave periods. Again, fetch is a controlling factor.

D. FURTHER STUDY

A more detailed raw data analysis is strongly recommended and required for the establishment of design wave criteria related to Artic region oil and gas development activity. In particular, wind time series records of at least five years duration in each month should be studied.

REFERENCES

Ackley, S. F. and M. K. Templeton, 1979: Computer modeling of atmospheric ice accretion, CRREL Rpt. #79-4. Hanover, New Hampshire, 36 pp.

Berry, M.O., P. M. Dutchak, M. E. Lalonde, J. A. W. McCulloch and I. Savdie, 1975: Weather, waves and icing in the Beaufort Sea, Technical Rpt. #21. Meteorological Applications Branch, Atmospheric Environment Service, Ottawa, Ontario. 57 pp.

Brower, W. A., H. F. Diaz, A. S. Prechtel, H. W. Searby and J. L. Wise, 1977: Climatic Atlas of the Outer Continental Shelf Waters and Coastal Regions of Alaska. Volume II Bering Sea, NOAA, NCC, EDS. Asheville, North Carolina. 409 pp.

Hasselmann, K., 1976: A parametric wave prediction model. J. Phys. Ocean. 6, 200-228.

Hasselman, K., T. P. Barnett, E. Bouws, and H. Carlson, 1973: Measurements of wind-wave growth and swell decay during the Joint North Sea Wave Project, Deutches Hydrographisches Institut, Hamburg, 20 pp.

Ippen, A. T., 1966: Estuary and Coastline Hydrodynamics. McGraw-Hill, New York, 744 pp.

Kozo, T. L., 1983: Navarin Basin Mesometeorology. Annual Rpt., MMS, NOS, NOAA, contract #03-5-022-6, R.U. 519, Juneau, Alaska, 43 pp.

Kozo, T. L., 1984: Alaskan Arctic Mesoscale Meteorology. Annual Rpt., MMS, NOS, contract #03-5-022-67, R.U. 519, Juneau Alaska, in press.

Petroleum Information, 1983: Alaska Rpt., vol. 29, #41. P.I. Corp., Anchorage, Alaska, Section 1, 2 pp.

Pierson, W. J., G. Neumann, and R. W. James, 1971: Observing and forecasting ocean waves, H.O. Pub. #603, U. S. Naval Oceanographic Office, Washington D. C, 284 pp.

Shore Protection Manual, 1977: Volume II. U. S. Army Coastal Engineering Research Center. Dept. of Army, Fort Belvoir, Virginia, 535 pp.

Webster, B. D., 1981: A climatology of the ice extent in the Bering Sea, NOAA Technical memo, NWS AR-33, Anchorage, Alaska, 38 pp.

Wise, J. L. and A. L. Comiskey, 1980: Superstructure icing in Alaskan Waters, NOAA Special Rpt. Pacific Marine Evironmental Laboratory, Seattle, Washington, 30 pp.

Wu, H. Y., E. Y. Hsu, and R. L. Street, 1979: Experimental study of non-linear wave-wave interaction and white cap dissipation of wind-generated waves, J. of Dynamics of Atmospheres and Oceans, 3, 55-78.

Wu, J., 1982: Sea Spray: A further look, J. Geoph. Res., 87, 8905-8912.

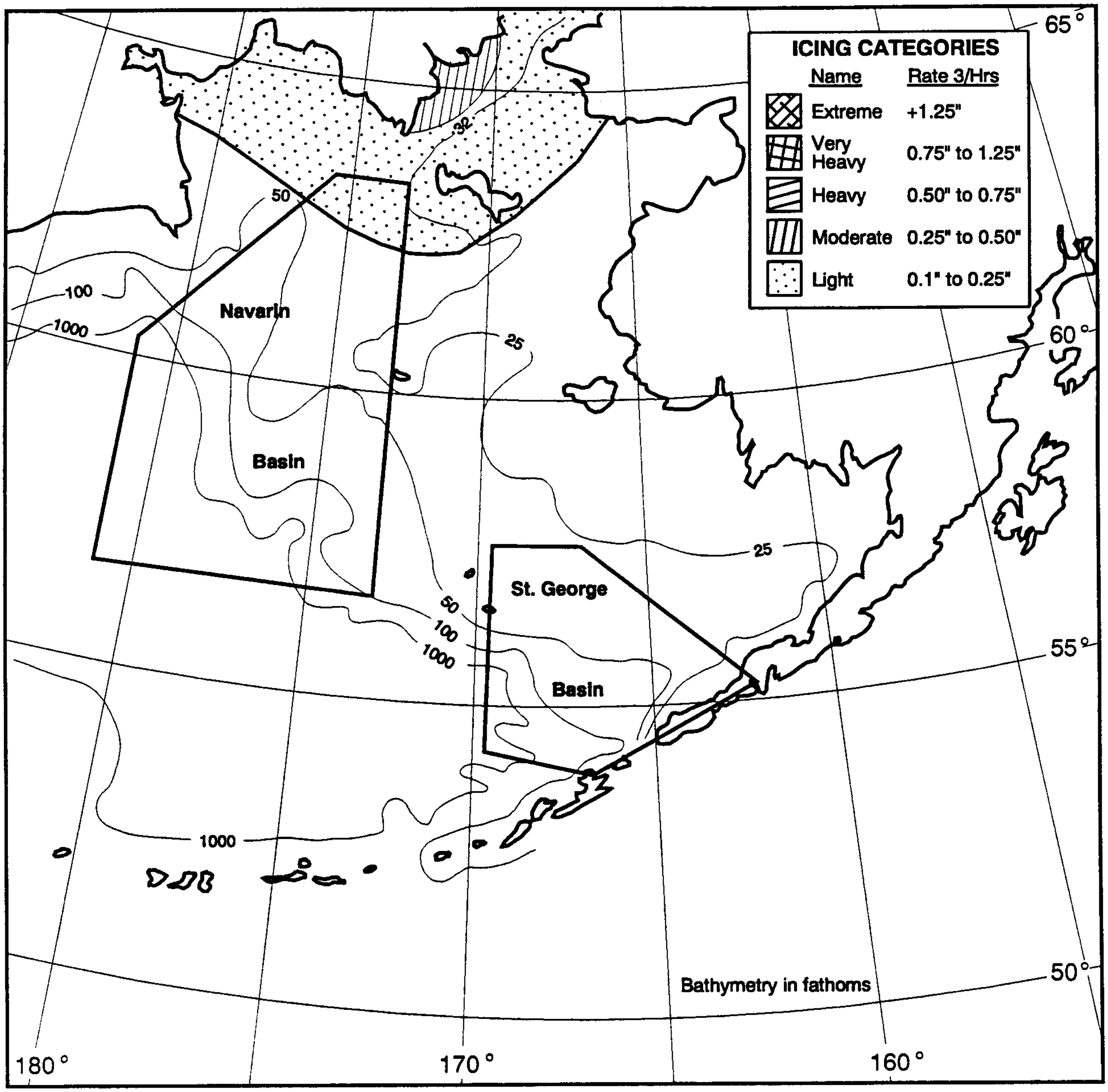

Figure 1.--September extreme conditions: produced by minimum recorded air and ocean temperatures (some ice in Bering Strait). A 50 knot (25 m/s) wind speed (storm level) is imposed. (Adapted from VANTUNA Research Group, Kozo, 1984.)

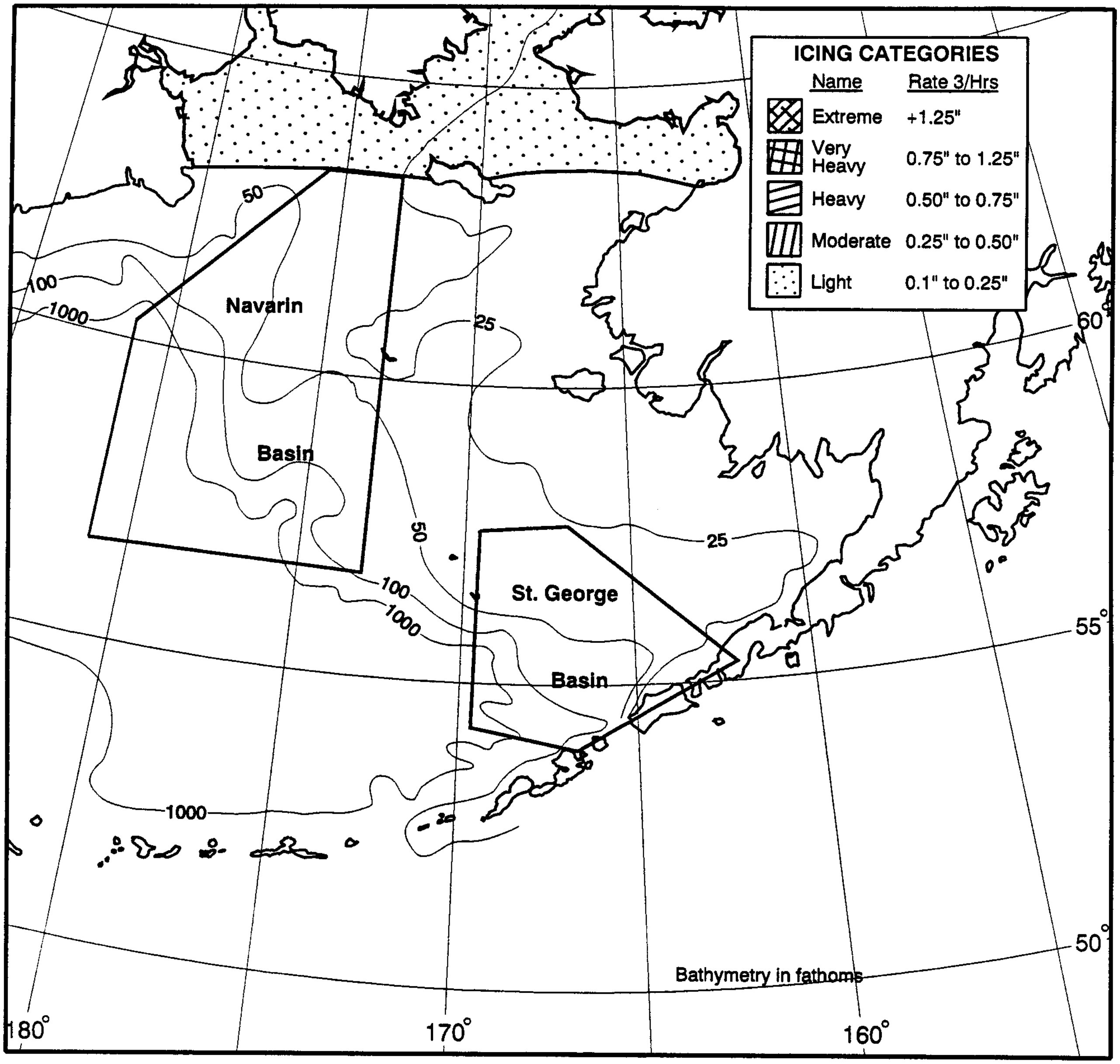

Figure 2.--October mean conditions: No ice in Bering Sea, mean air temperature, and mean ocean surface temperature. A 28 knot (14 m/s) wind speed (gale level) is imposed. (Adapted from VANTUNA Research Group, Kozo, 1984.)

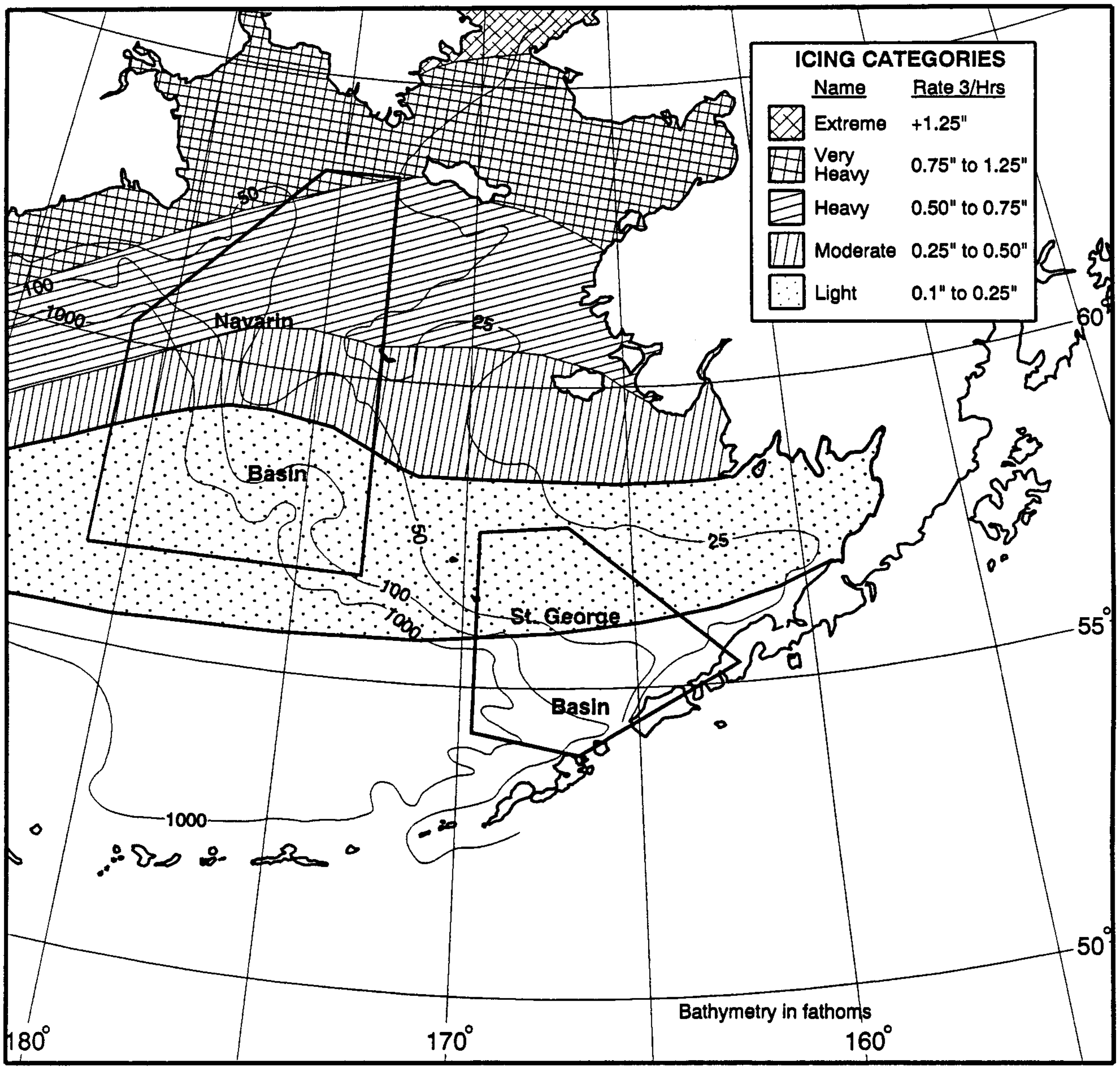

Figure 3.--October extreme conditions: produced by minimum recorded air and ocean surface temperatures. Maximum extent of 50% ice coverage does not reach the Navarin Basin area. It occurs in the Gulf of Anadyr and Norton Sound only. A 50 knot (25 m/s) wind speed (storm level) is imposed. (Adapted from VANTUNA Research Group, Kozo, 1984.)

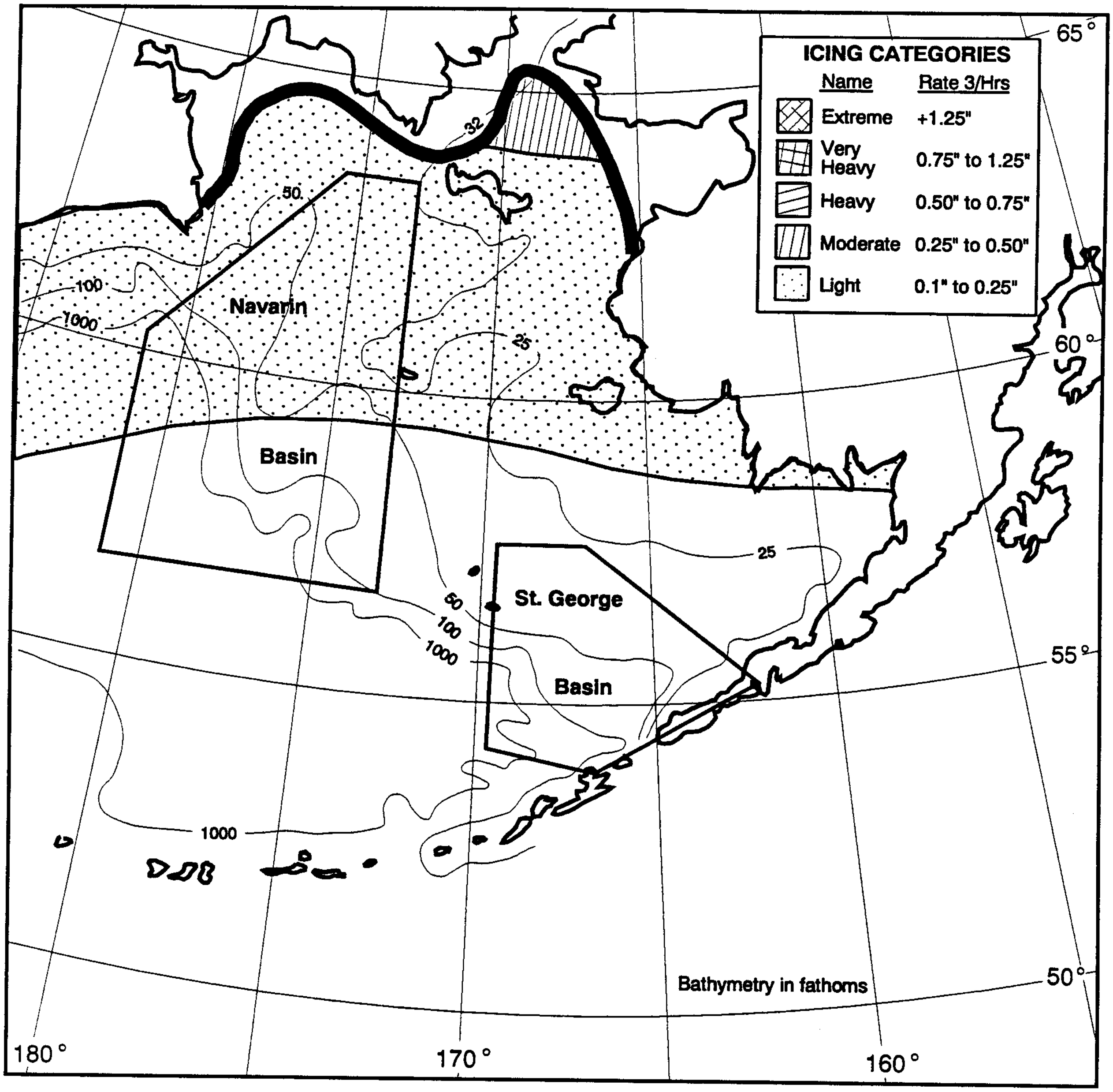

Figure 4.--November mean conditions: 50% probability of 50% ice coverage (heavy line), mean air temperature, and ocean surface temperature corresponding to ice coverage. A 28 knot (14 m/s) wind speed (gale level) is imposed. (Adapted from VANTUNA Research Group, Kozo, 1984.)

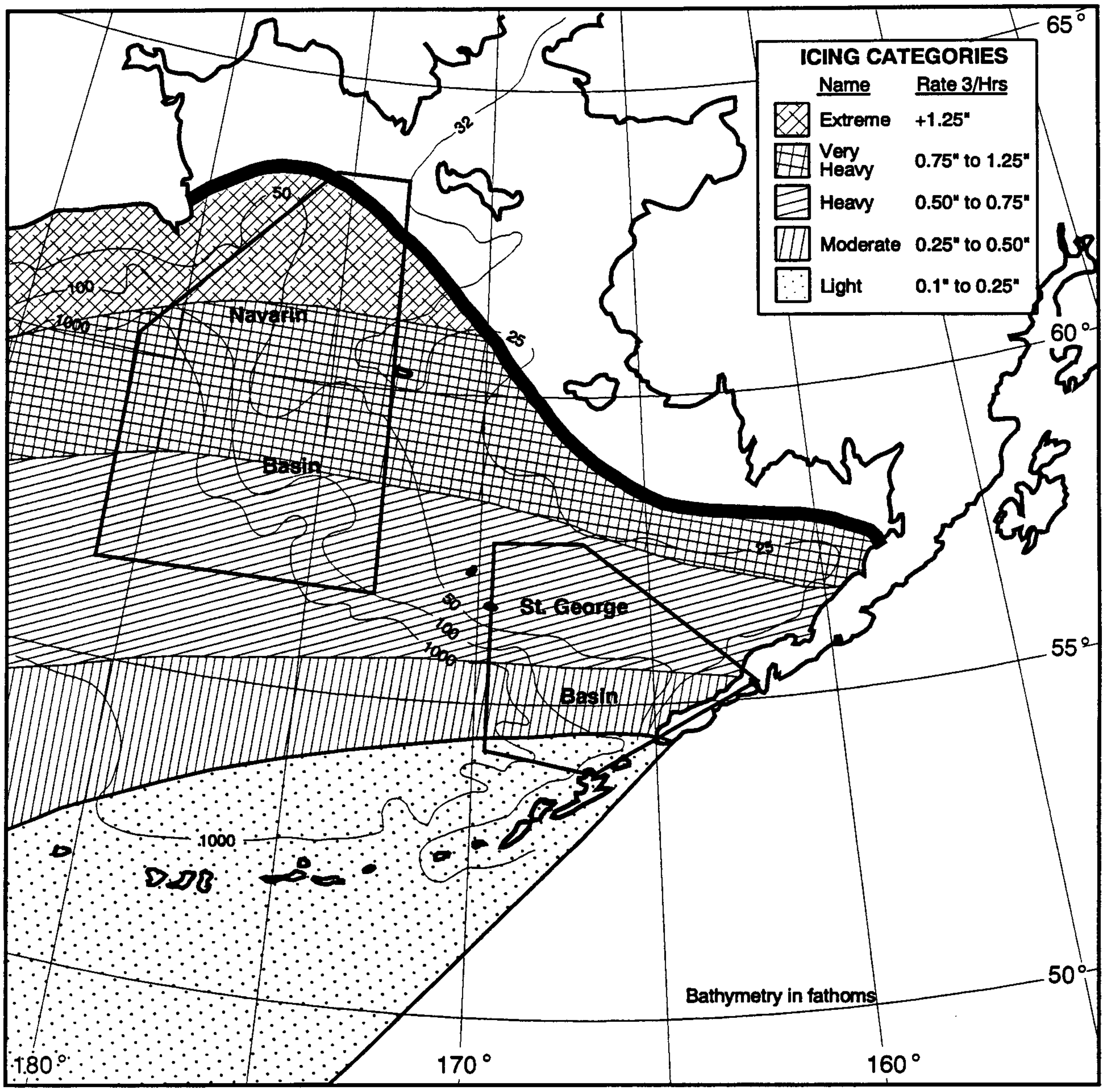

Figure 5.--November extreme conditions: produced by maximum extent of 50% ice coverage (heavy line), minimum recorded air temperatures, and ocean surface temperatures corresponding to ice coverage. A 50 knot (25 m/s) wind speed (storm level) is imposed. (Adapted from VANTUNA Research Group, Kozo, 1984.)

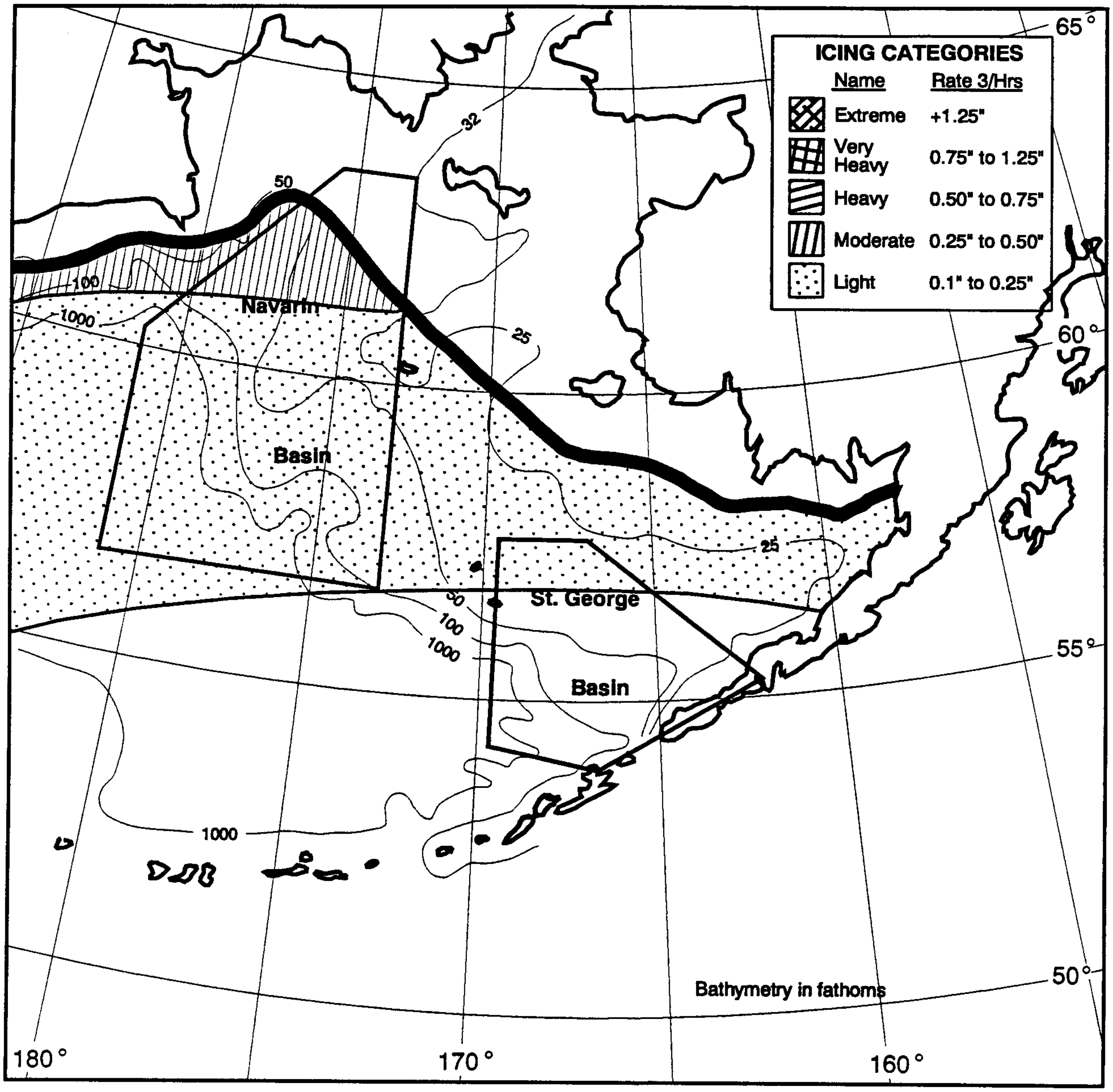

Figure 6.--December mean conditions: 50% probability of 50% ice coverage (heavy line), mean air temperature, and ocean surface temperature corresponding to ice coverage. A 28 knot (14 m/s) wind speed (gale level) is imposed. (Adapted from VANTUNA Research Group, Kozo, 1984.)

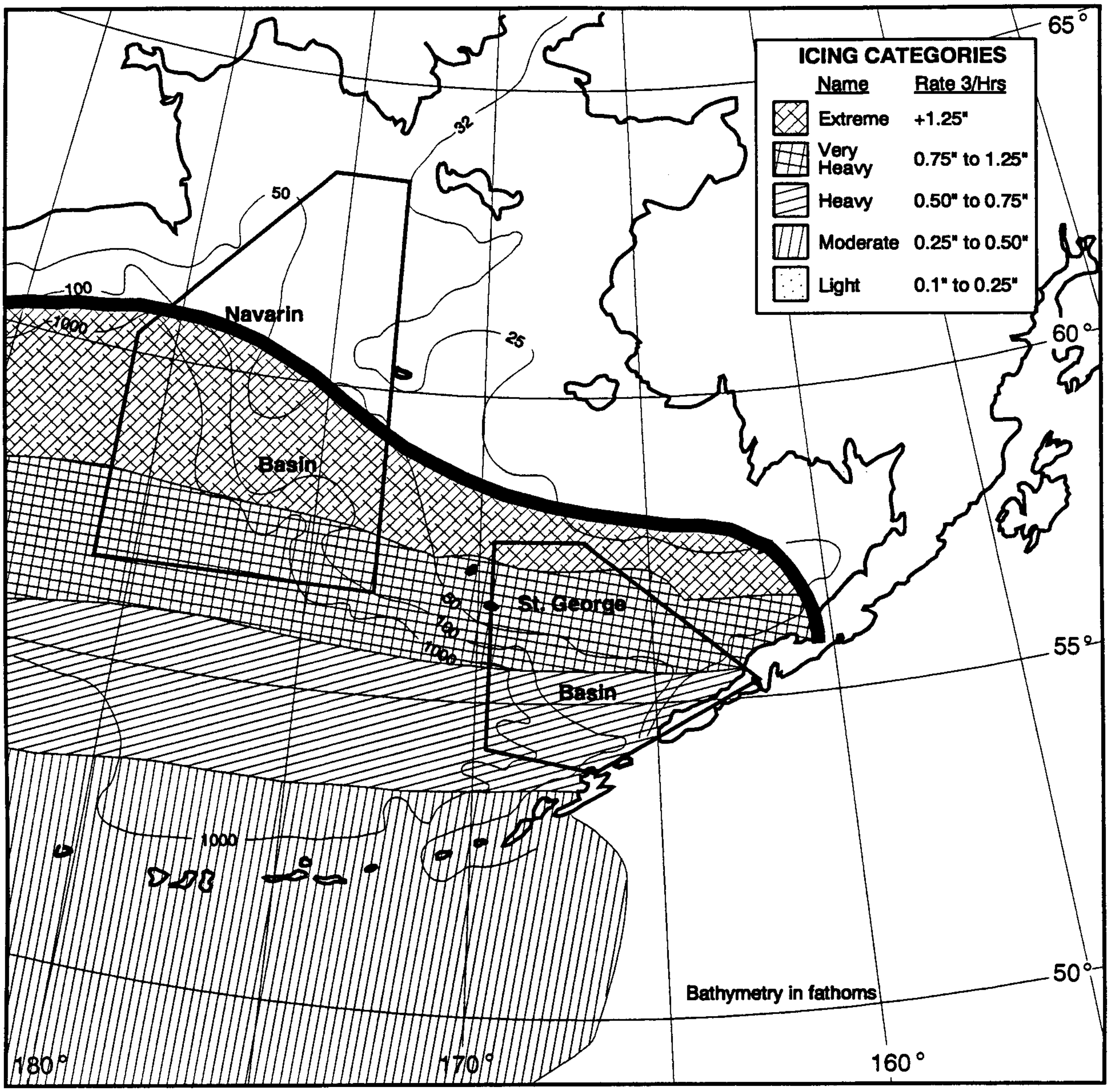

Figure 7.--December extreme conditions: produced by maximum extent of 50% ice coverage (heavy line), minimum recorded air temperatures, and ocean surface temperatures corresponding to ice coverage. A 50 knot (25 m/s) wind speed (storm level) is imposed. (Adapted from VANTUNA Research Group, Kozo, 1984.)

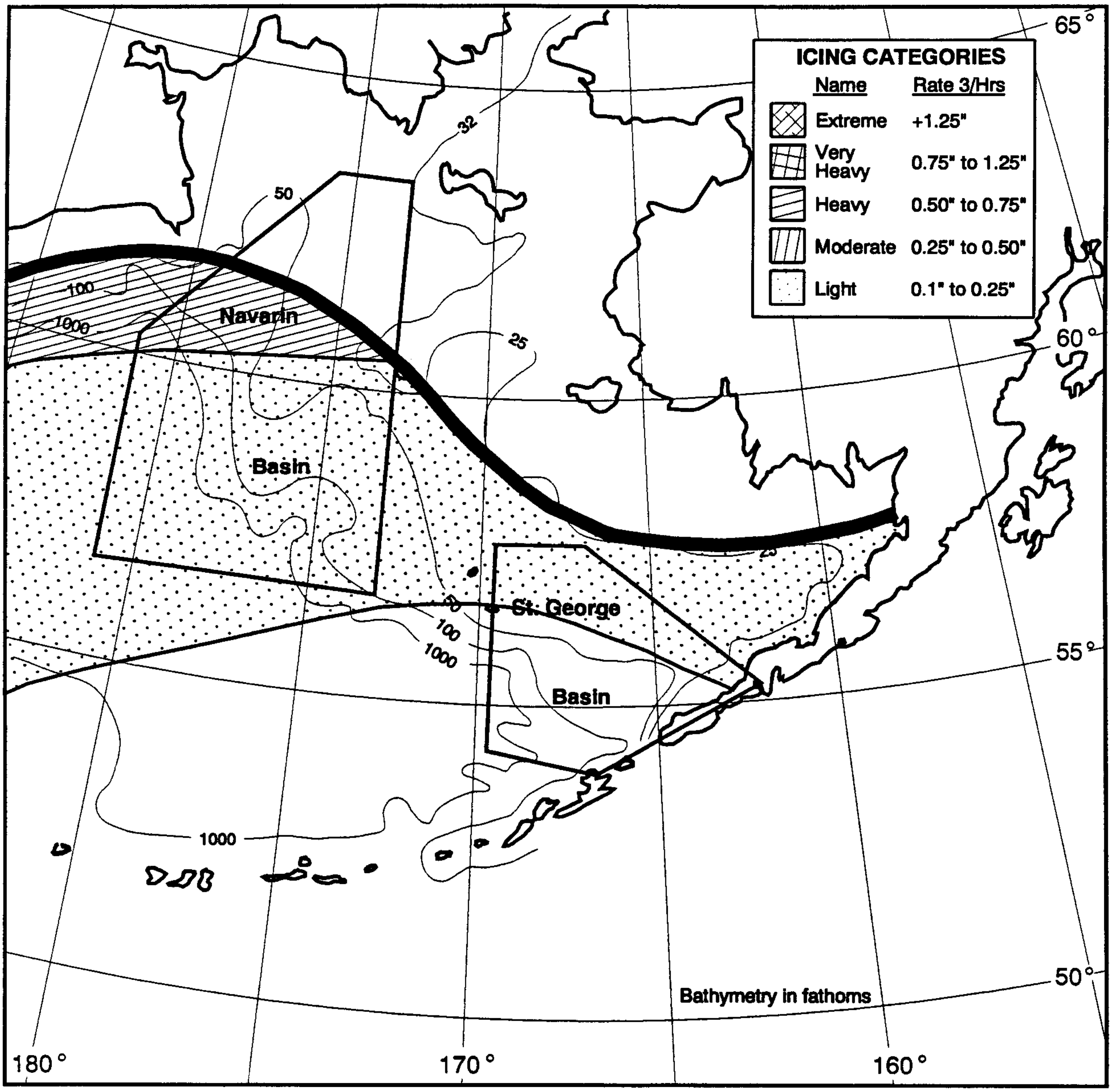

Figure 8.--January mean conditions: 50% probability of 50% ice coverage (heavy line), mean air temperature, and ocean surface temperature corresponding to ice coverage. A 28 knot (14 m/s) wind speed (gale level) is imposed. (Adapted from VANTUNA Research Group, Kozo, 1984.)

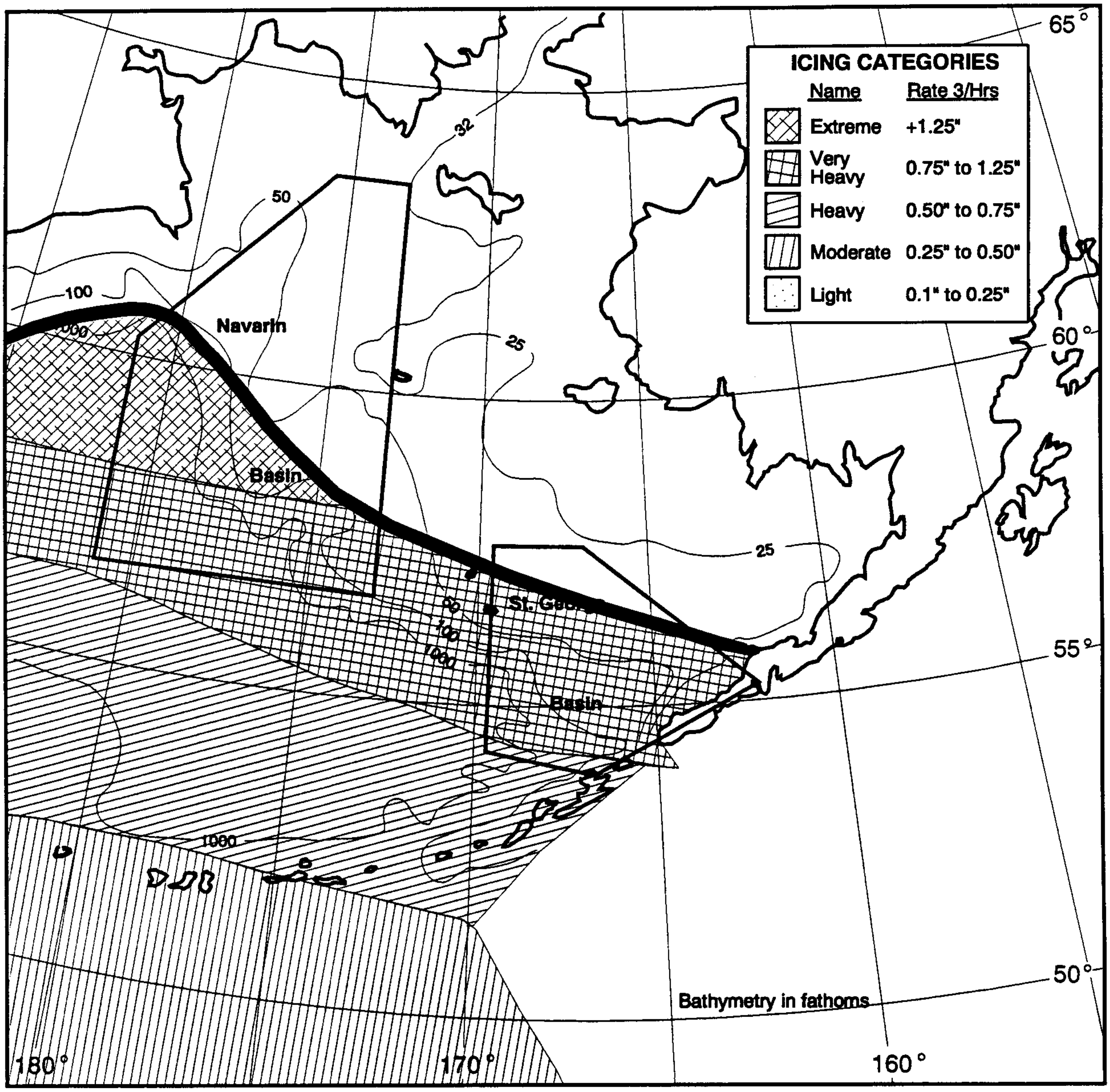

Figure 9.--January extreme conditions: produced by maximum extent of 50% ice coverage (heavy line), minimum recorded air temperatures, and ocean surface temperatures corresponding to ice coverage. A 50 knot (25 m/s) wind speed (storm level) is imposed. (Adapted from VANTUNA Research Group, Kozo, 1984.)

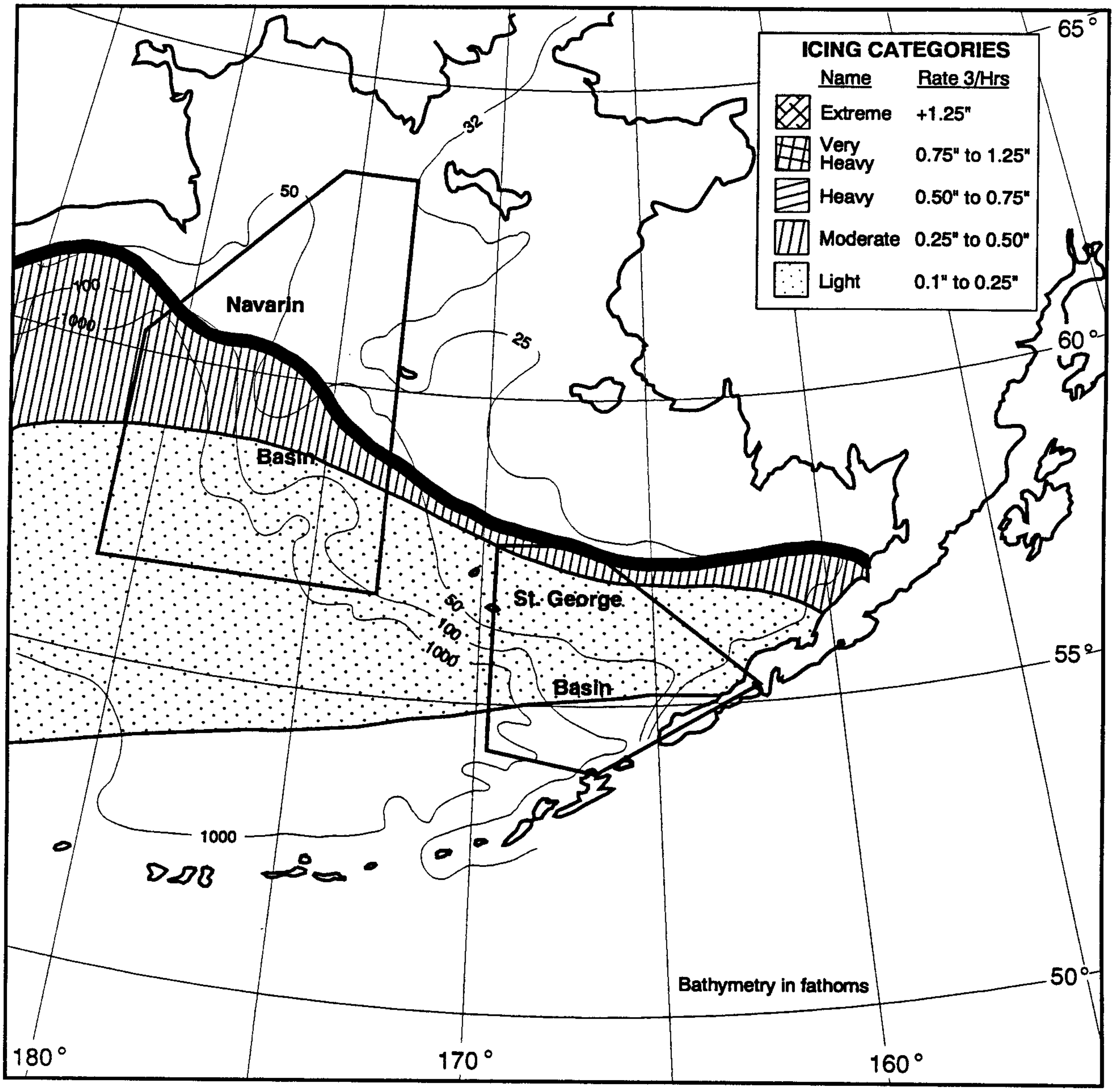

Figure 10.--February mean conditions: 50% probability of 50% ice coverage (heavy line), mean air temperature, and ocean surface temperature corresponding to ice coverage. A 28 knot (14 m/s) wind speed (gale level) is imposed. (Adapted from VANTUNA Research Group, Kozo, 1984.)

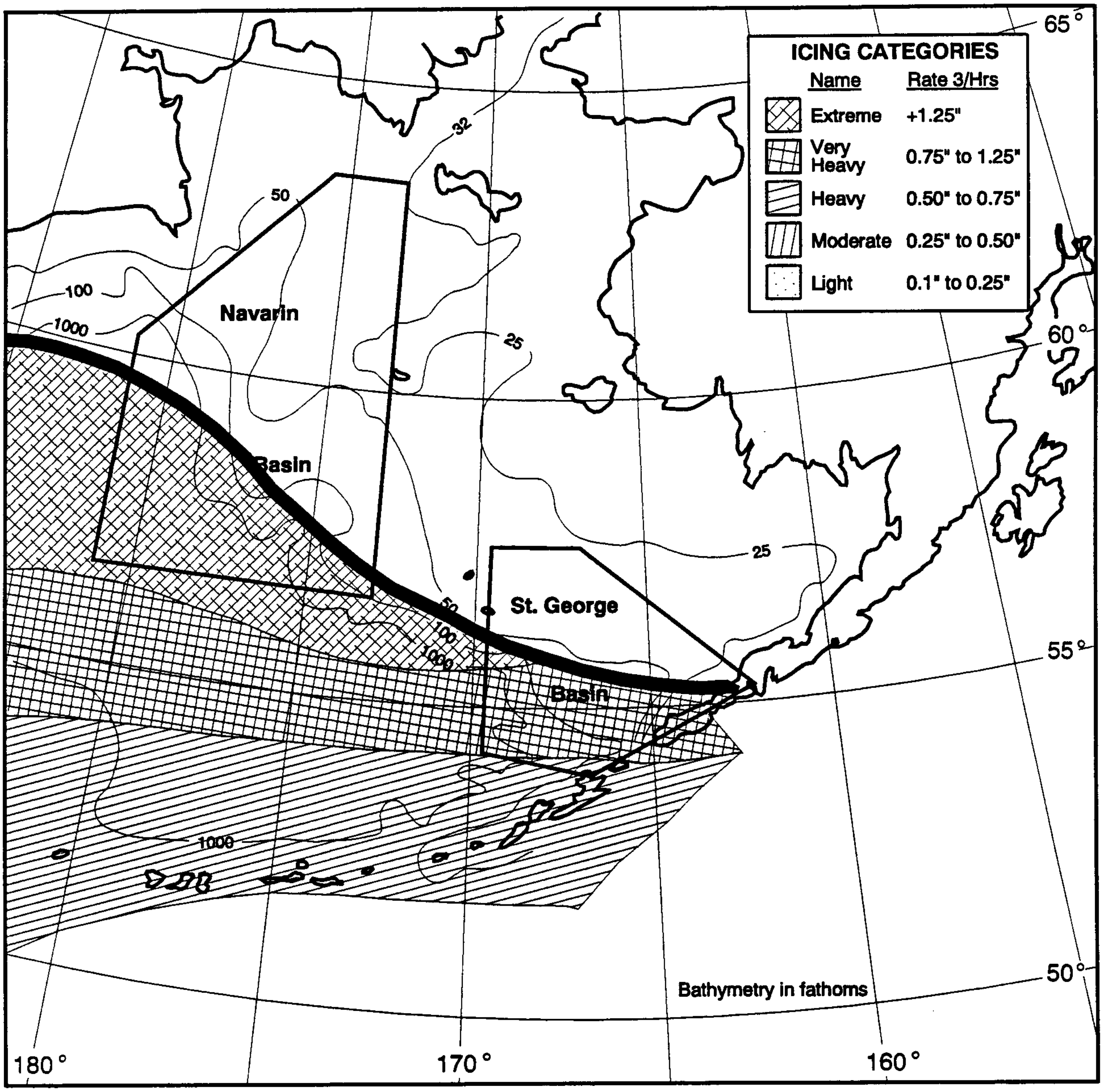

Figure 11.--February extreme conditions: produced by maximum extent of 50% ice coverage (heavy line), minimum recorded air temperatures, and ocean surface temperatures corresponding to ice coverage. A 50 knot (25 m/s) wind speed (storm level) is imposed. (Adapted from VANTUNA Research Group, Kozo, 1984.)

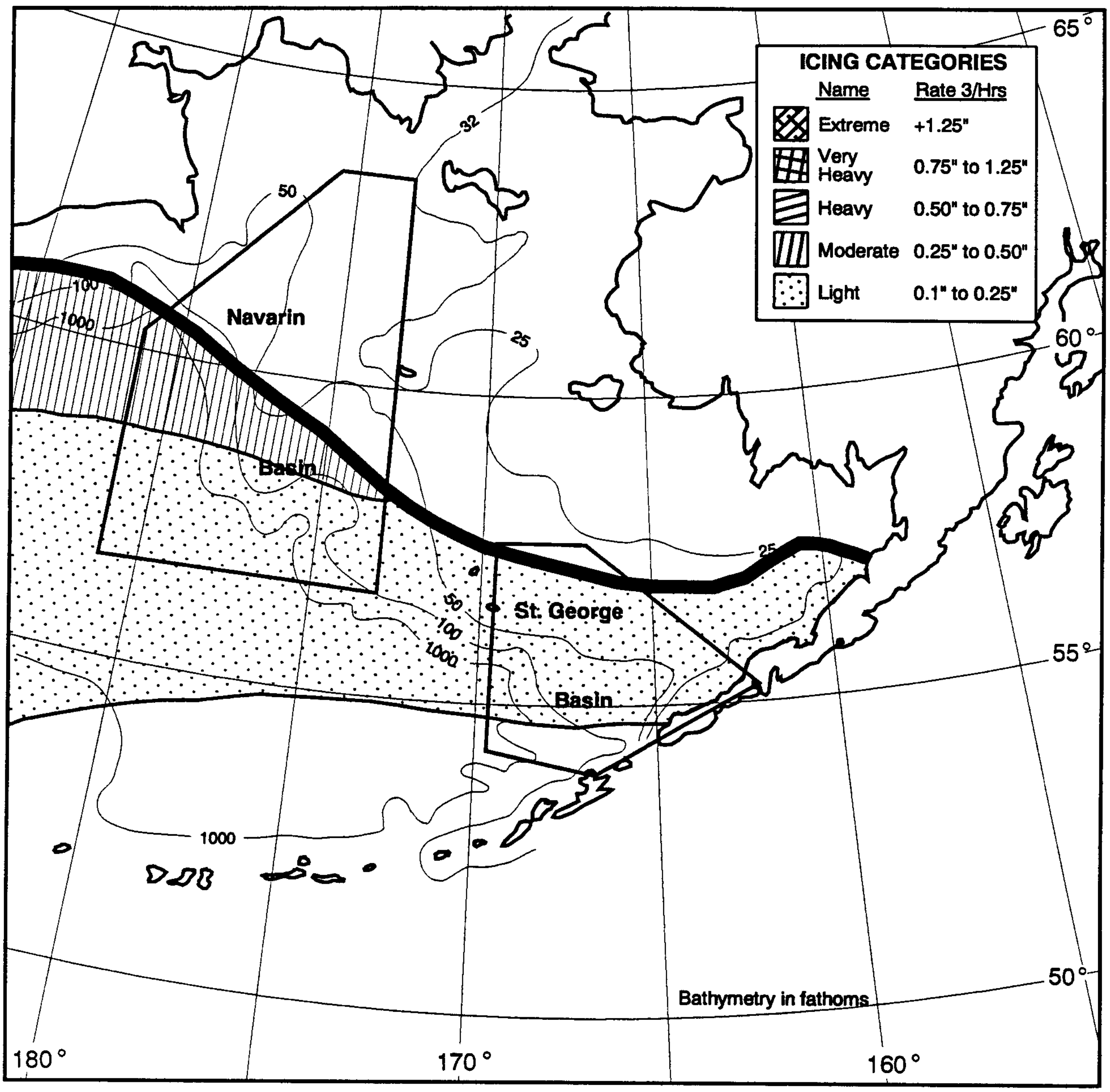

Figure 12.--March mean conditions: 50% probability of 50% ice coverage (heavy line), mean air temperature, and ocean surface temperature corresponding to ice coverage. A 28 knot (14 m/s) wind speed (gale level) is imposed. (Adapted from VANTUNA Research Group, Kozo, 1984.)

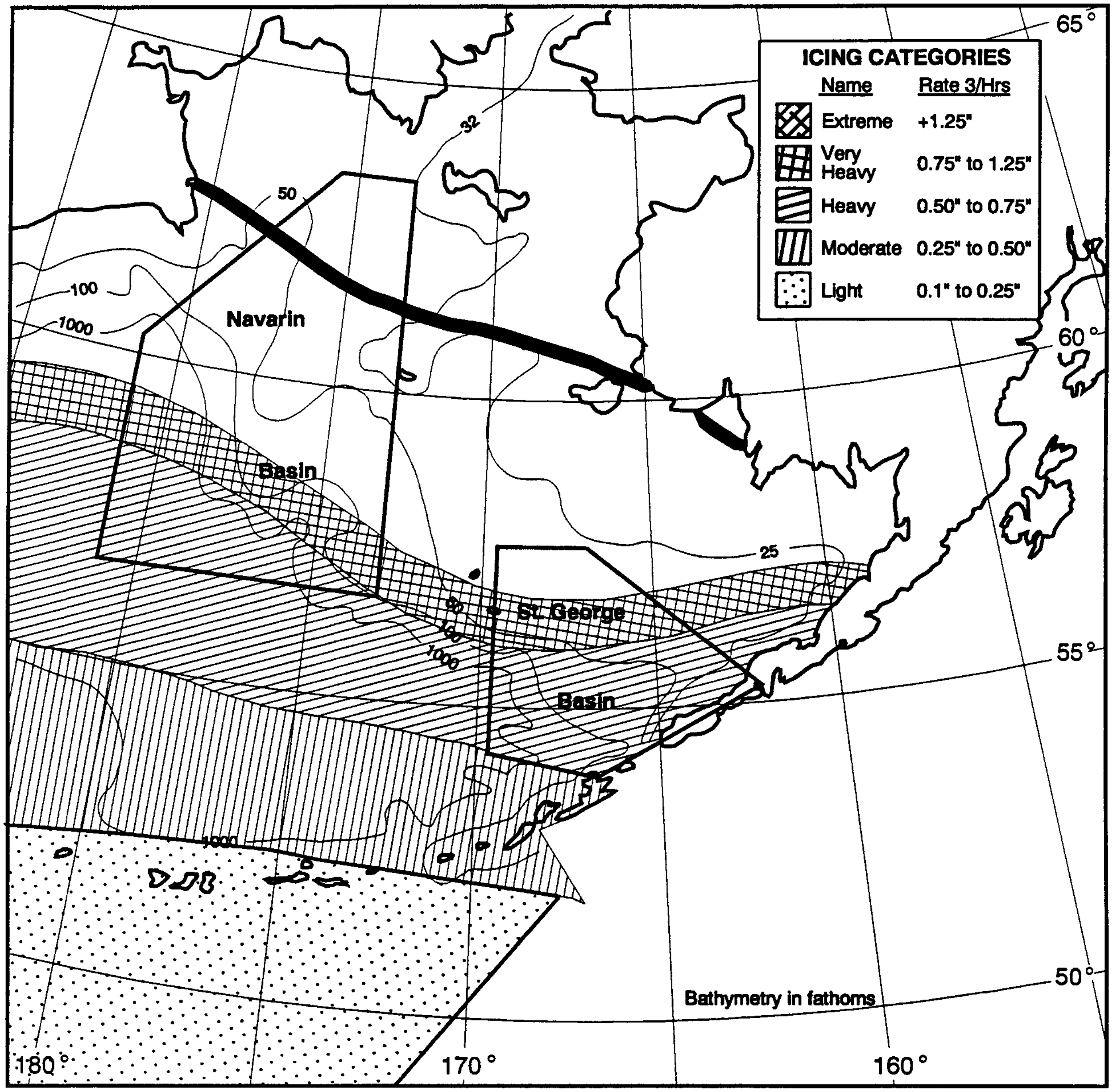

Figure 13.--March extreme conditions: produced by minimum extent of 50% ice coverage (heavy line), minimum recorded air temperatures, and ocean surface temperatures corresponding to ice coverage. A 50 knot (25 m/s) wind speed (storm level) is imposed. (Adapted from VANTUNA Research Group, Kozo, 1984.)

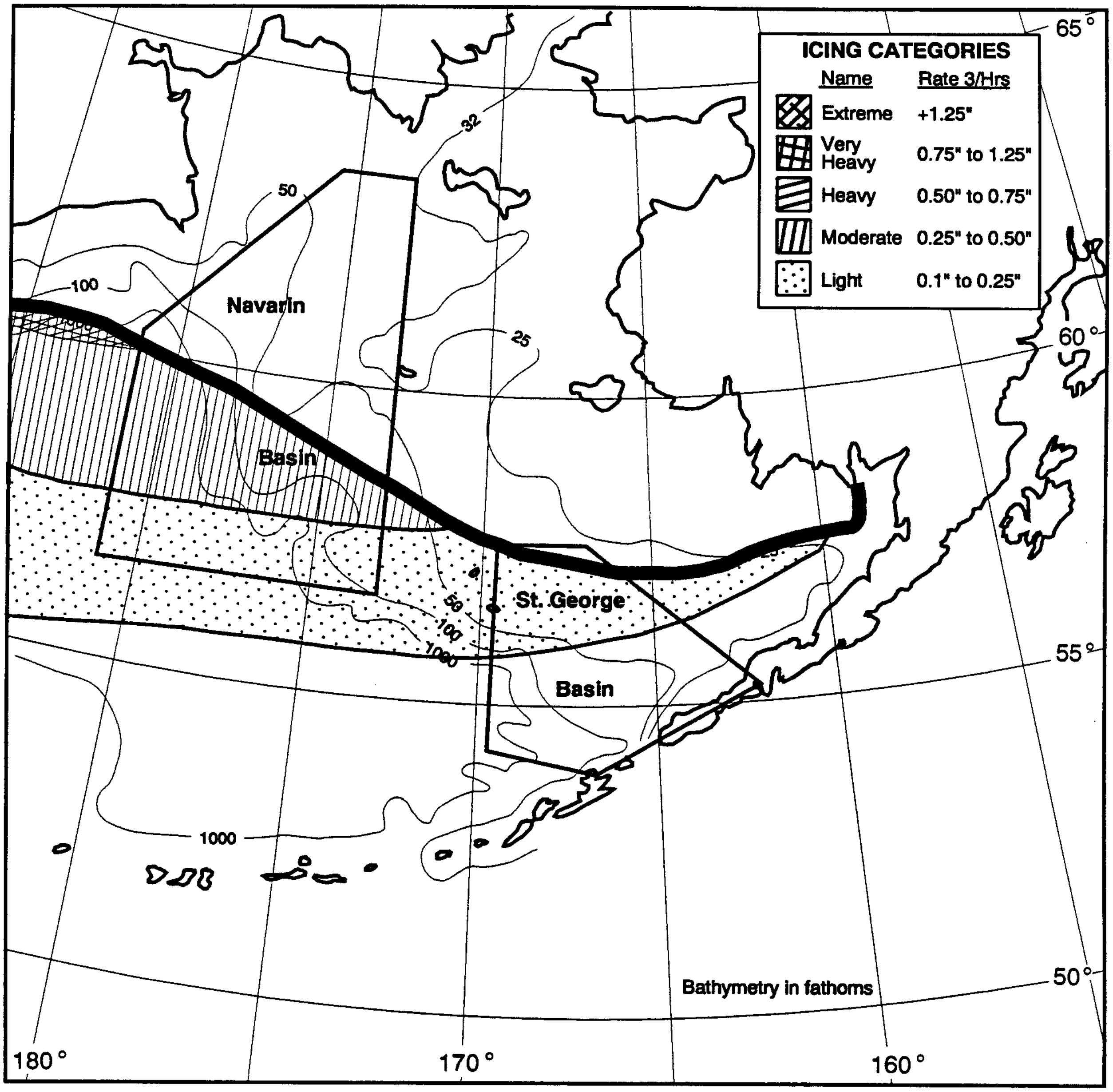

Figure 14.--April mean conditions: 50% probability of 50% ice coverage (heavy line), mean air temperature, and ocean surface temperature corresponding to ice coverage. A 28 knot (14 m/s) wind speed (gale level) is imposed. (Adapted from VANTUNA Research Group, Kozo, 1984.)

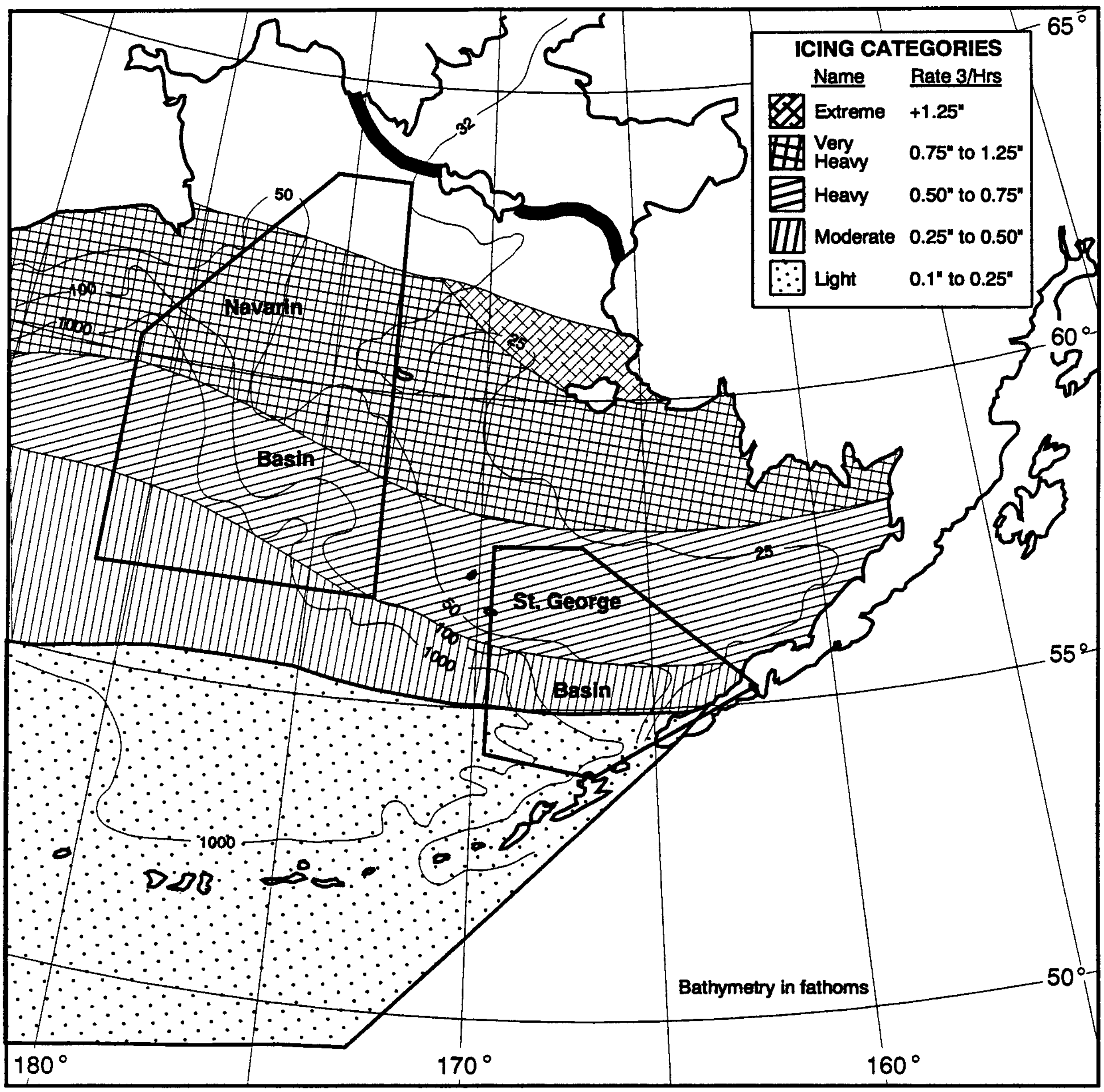

Figure 15.--April extreme conditions: produced by minimum extent of 50% ice coverage (heavy line), minimum recorded air temperatures, and ocean surface temperatures corresponding to ice coverage. A 50 knot (25 m/s) wind speed (storm level) is imposed. (Adapted from VANTUNA Research Group, Kozo, 1984.)

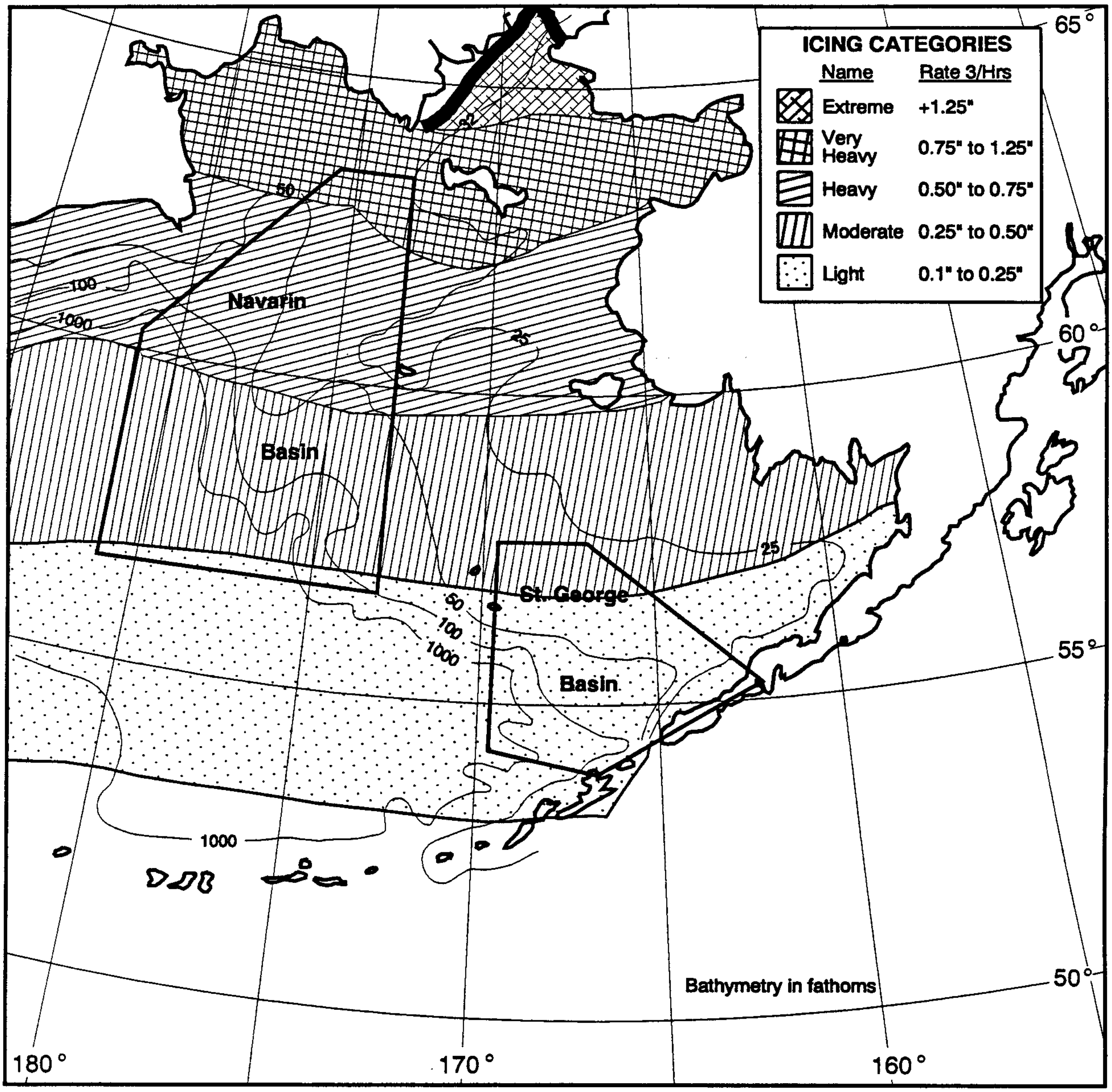

Figure 16.--May extreme conditions: produced by minimum extent of 50% ice coverage (heavy line), minimum recorded air temperatures, and ocean surface temperatures corresponding to ice coverage. A 50 knot (25 m/s) wind speed (storm level) is imposed. (Adapted from VANTUNA Research Group, Kozo, 1984.)

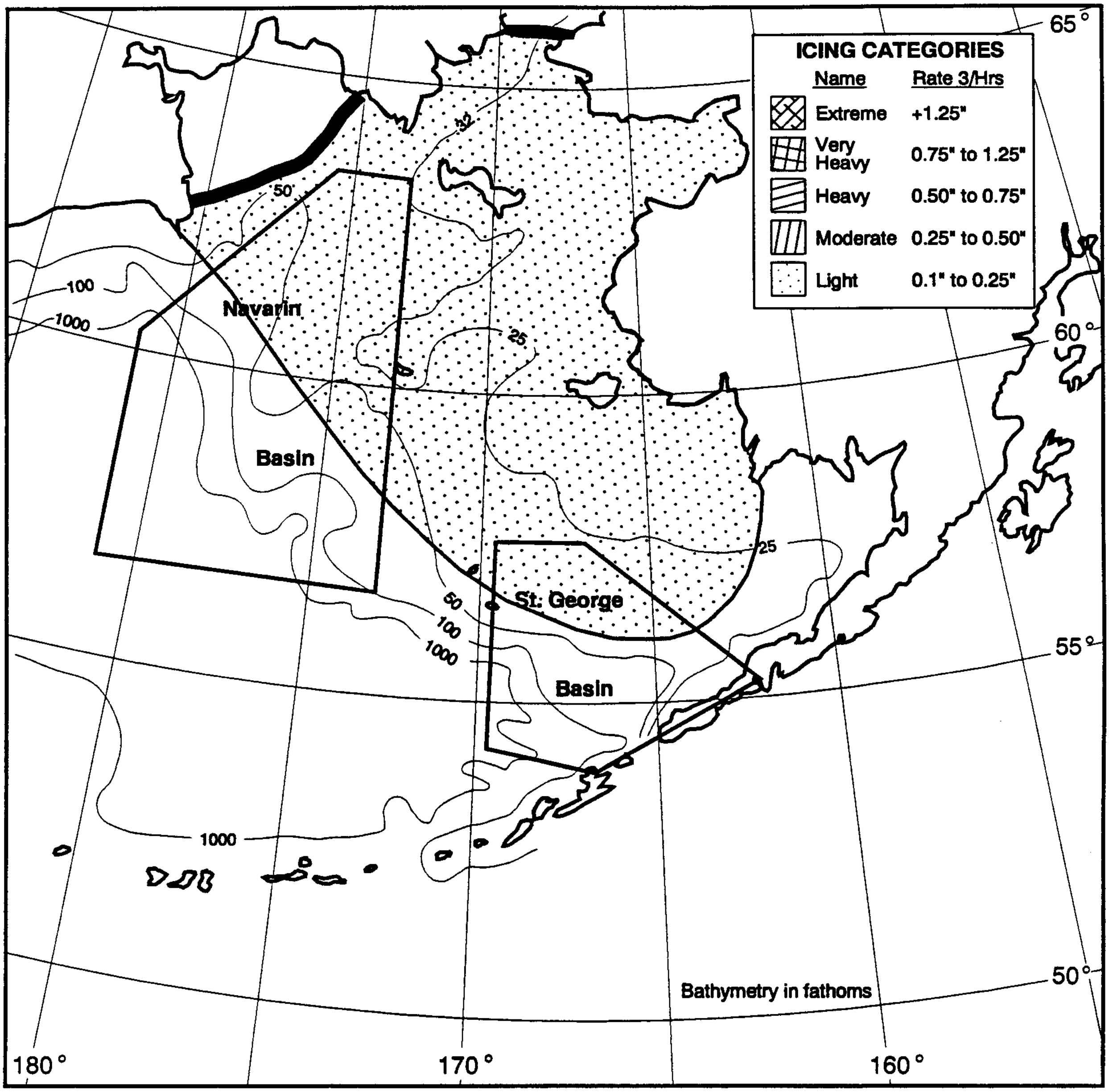

Figure 17.--June extreme conditions: produced by mean extent of 50% ice coverage (heavy line), minimum recorded air temperatures, and ocean surface temperatures corresponding to ice coverage. A 50 knot (25 m/s) wind speed (storm level) is imposed. (Adapted from VANTUNA Research Group, Kozo, 1984.)

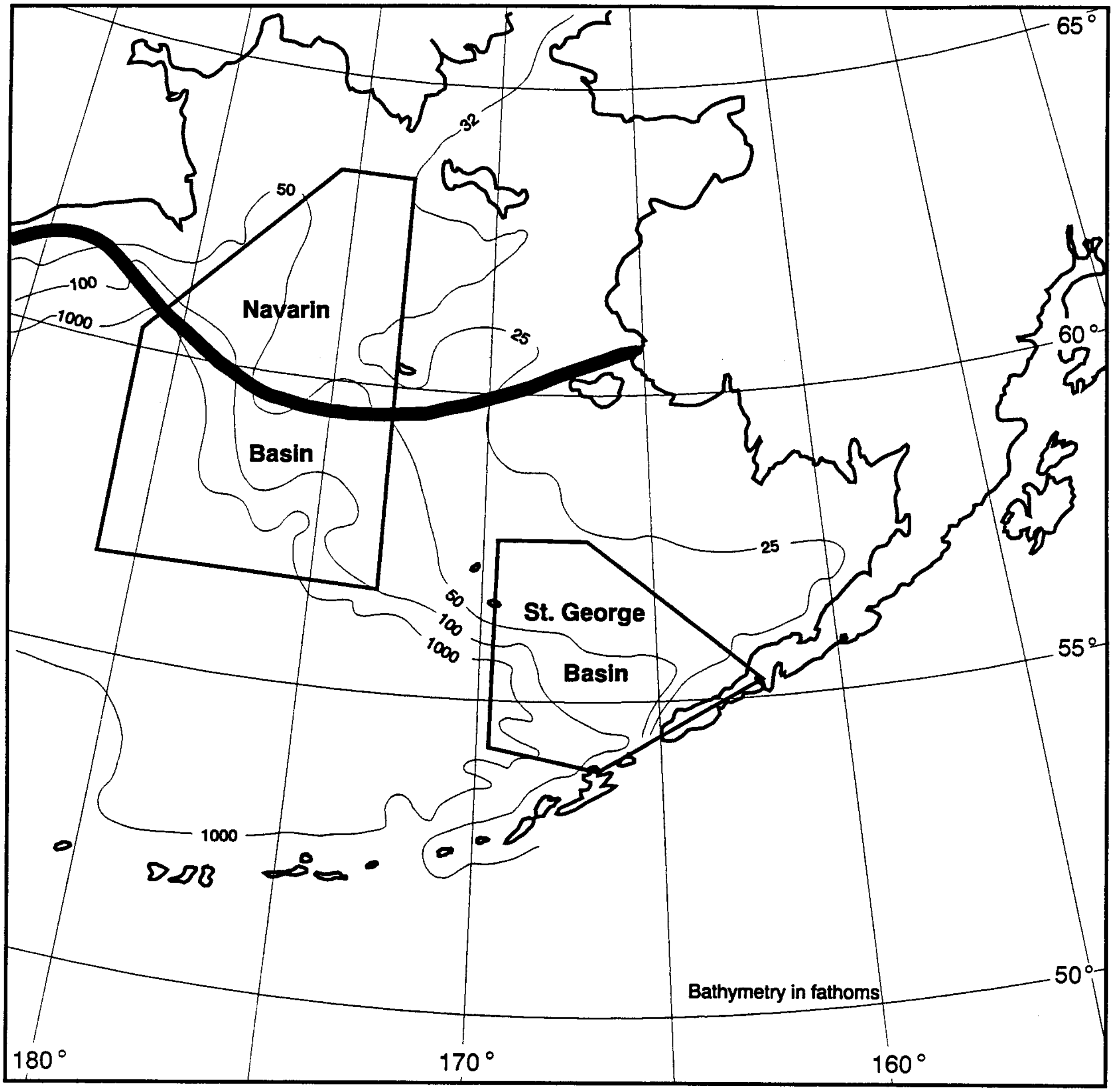

Figure 18.--50% probability of 50% ice coverage (heavy line) for May.

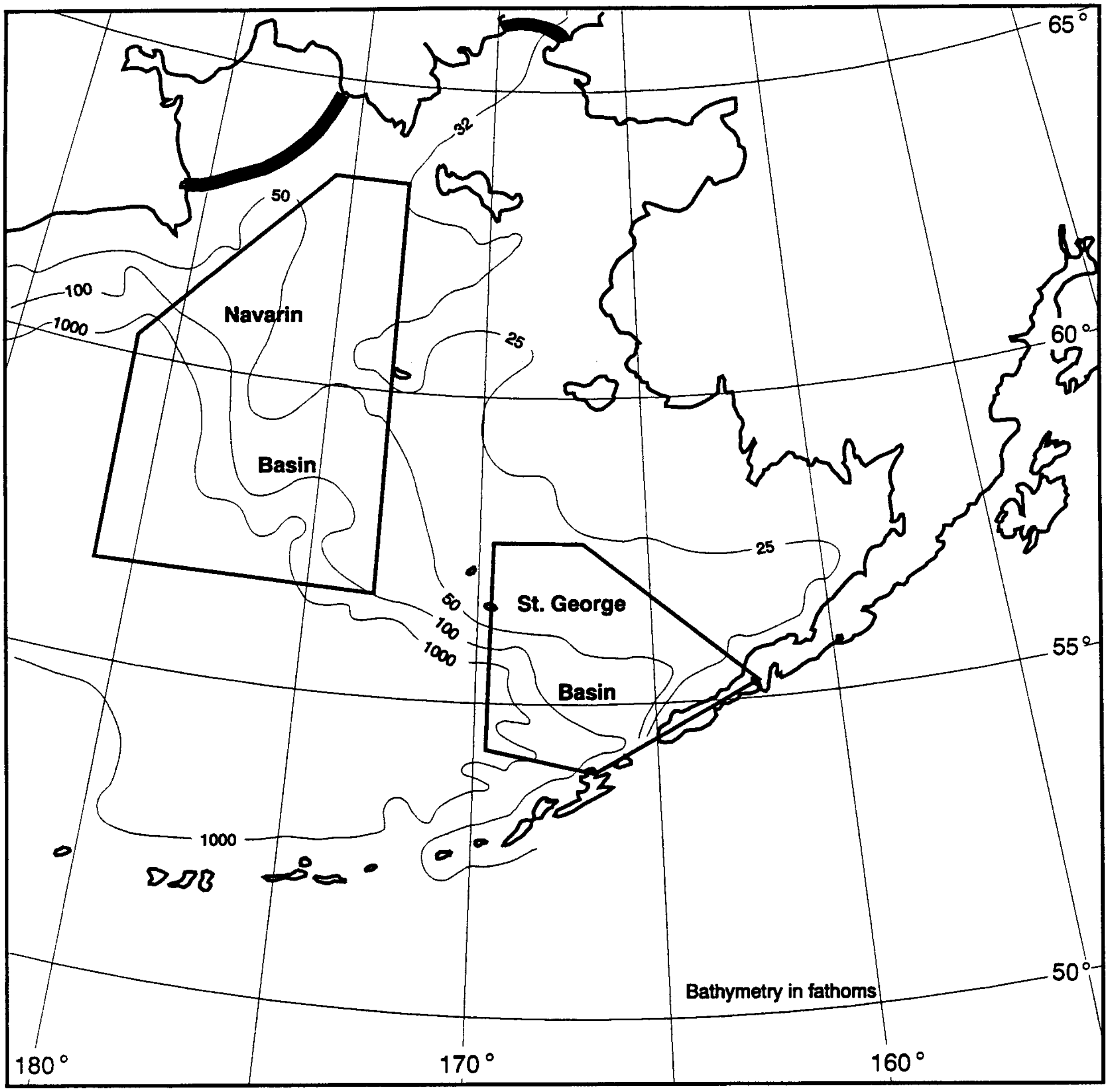

Figure 19.--50% probability of 50% ice coverage (heavy line) for June.

Table 1a. Navarin Basin Area.

Months	% Winds >28 kn ($14\ ms^{-1}$) *W.M.O. Gale	% Winds >50 kn ($25\ ms^{-1}$) *W.M.O. Storm	% air temperature <0° F (18° C)
September	7.0	<1	0.0
October	15.0	1	0.0
November	18.0	1	0.0
December	13.0	<1	0.0
January	17.0	1	0.0
February	20.0	1	2.5
March	7.3	<1	4.0
April	5.3	<1	0.0
May	3.5	<<1	0.0
June	2.0	0.0	0.0

Table 1b. St. George Basin Area.

Months	% Winds >28 kn ($14\ ms^{-1}$) *W.M.O. Gale	% Winds >50 kn ($25\ ms^{-1}$) *W.M.O. Storm	% air temperature <0° F (18° C)
October	20.0	<1	0.0
November	23.5	1	0.0
December	16.5	<1	0.0
January	16.5	<1	1.0
February	18.5	1	1.5
March	12.0	<1	1.0
April	11.5	<<1	0.0
May	5.0	<<1	0.0
June	2.5	0.0	0.0

*W.M.O. ≡ World Meteorological Organization.

Hs (m)	1	2	3	4	5	6	7	8	9	10	11	12	13	TOTAL	%
N	43	18	25	17	33	9	7	5	3	1	1			162	22.4
NE	51	34	45	35	38	23	17	10	7	2				262	36.3
E	29	23	24	15	15	0	7	5	3	0	1			122	16.9
SE	34	11	13	7	2	0	4	0	2					73	10.1
S	27	5	8	2	2	2	0	2	1					49	6.8
SW	9	2	2	0	1									14	1.9
W	7	2	2	2	0	5								18	2.5
NW	19	1	2											22	3.1
TOTAL	219	96	121	78	91	39	35	22	16	3	2			722	
%	30.3	13.3	16.8	10.8	12.6	5.4	4.9	3.1	2.2	.4	.3				

Table 2a. The predicted frequency of significant wave heights (Hs) in meters for waves coming from 8 specified directions in January. These data were derived from 3 hourly wind velocity measurements (Kozo, 1983).

Tp(S)	2	4	6	8	10	12	14	16	TOTAL	%
N	13	13	35	42	42	15	2		162	22.4
NE	4	15	66	80	61	36			262	36.3
E	6	9	37	24	30	12	4		122	16.9
SE	11	13	21	20	2	6			73	10.1
S	8	10	14	10	4	3			49	6.8
SW	3	6	0	4	1				14	1.9
W	2	3	4	2	7				18	2.5
NW	2	11	7	2					22	3.1
TOTAL	49	80	184	184	147	72	6		722	
%	6.8	11.1	25.5	25.5	20.4	10.0	.8			

Table 2b. The predicted frequency of peak wave periods (Tp) in seconds for waves coming from 8 specified directions in January. These data were derived from 3 hourly wind velocity measurements (Kozo, 1983).

Hs (m)	1	2	3	4	5	6	7	8	9	10	11	12	13	TOTAL	%
N	38	19	20	69	19	19	8	6	5	1				204	35.7
NE	23	6	18	25	37	19	7	5	0	1				141	24.7
E	34	9	5	2	1	0	0	1	2	2	0	0	2	58	10.2
SE	22	12	6	4	3	0	5	5						57	10.0
S	15	7	4	4	1									31	5.4
SW	15	1	3											19	3.3
W	17	4	2											23	4.0
NW	23	7	4	3	1									38	6.7
TOTAL	187	65	62	107	62	38	20	17	7	4	0	0	2	571	
%	32.8	11.4	10.9	18.7	10.9	6.7	3.5	3.9	.4	.4	.4	0	.4		

Table 3a. The predicted frequency of significant wave heights (Hs) in meters for waves coming from 8 specified directions in February. These data were derived from 3 hourly wind velocity measurements (Kozo, 1983).

Tp(S)	2	4	6	8	10	12	14	16	TOTAL	%
N	6	16	35	89	38	19	1		204	35.7
NE	4	9	16	43	56	12	1		144	24.7
E	5	16	22	5	3	1	4	2	58	10.2
SE	6	8	20	10	3	10			57	10.0
S	3	4	15	8	1				31	5.4
SW	5	4	6	4					19	3.3
W	5	4	12	2					23	4.0
NW	6	8	16	7	1				38	6.7
TOTAL	40	69	142	168	102	42	6	2	571	
%	7.0	12.1	24.9	29.4	17.9	7.4	1.1	.4		

Table 3b. The predicted frequency of peak wave periods (Tp) in seconds for waves coming from 8 specified directions in February. These data were derived from 3 hourly wind velocity measurements (Kozo, 1983).

Hs (m)	1	2	3	4	5	6	7	8	9	10	11	12	13	TOTAL	%
N	72	35	36	50	8	5	2	2	1					211	33.0
NE	30	14	19	35	8	4	1	2						113	17.7
E	25	7	6	4	6	0	1	1	2					52	8.1
SE	16	9	5	5	4	0	3							42	6.6
S	21	5	7	5	3	2	1							44	6.9
SW	28	11	9	0	2	1	0	0	0	1				52	8.1
W	22	9	3	1	0	2	1	0	1					39	6.1
NW	34	21	14	9	8	1								87	13.6
TOTAL	248	111	99	109	39	15	9	5	4	1				640	
%	38.8	17.3	15.5	17.	6.1	2.3	1.4	.8	.6	.2					

Table 4a. The predicted frequency of significant wave heights (Hs) in meters for waves coming from 8 specified directions in March. These data were derived from 3 hourly wind velocity measurements (Kozo, 1983).

Tp(S)	2	4	6	8	10	12	14	16	TOTAL	%
N	11	19	77	86	13	5			211	33.0
NE	3	10	31	54	12	3			113	17.7
E	4	7	21	6	10	2	2		52	8.1
SE	3	4	18	10	4	3			42	6.6
S	6	3	17	12	5	1			44	6.9
SW	6	15	7	20	2	1	1		52	8.1
W	3	8	20	3	3	2			39	6.1
NW	4	12	39	23	9				87	13.6
TOTAL	40	78	230	214	58	17	3		640	
%	6.3	12.2	35.9	33.4	9.1	2.7	1.3			

Table 4b. The predicted frequency of peak wave periods (Tp) in seconds for waves coming from 8 specified directions in March. These data were derived from 3 hourly wind velocity measurements (Kozo, 1983).

Hs (m)	1	2	3	4	5	6	7	8	9	10	11	12	13	TOTAL	%
N	37	20	33	5	2									97	20.9
NE	37	22	40	8	3	3	1							114	24.5
E	10	7	12	9	4									42	9.0
SE	32	10	3	2	3									50	10.8
S	27	3	2	1										33	7.1
SW	21	3	0	0	1									25	5.4
W	48	8	2											58	12.5
NW	35	4	6	1										46	9.9
TOTAL	247	77	98	26	13	3	1							465	
%	53.1	16.7	21.1	5.6	2.8	.7	.2								

Table 5a. The predicted frequency of significant wave heights (Hs) in meters for waves coming from 8 specified directions in April. These data were derived from 3 hourly wind velocity measurements (Kozo, 1983).

Tp(S)	2	4	6	8	10	12	14	16	TOTAL	%
N	9	13	35	38	2				97	20.9
NE	3	11	45	48	7				114	24.5
E	0	6	11	12	13				42	9.0
SE	5	11	26	5	3				50	10.8
S	6	10	14	3					33	7.1
SW	3	7	11	3	1				25	5.4
W	5	22	29	2					58	12.5
NW	5	17	17	7					46	9.9
TOTAL	36	97	188	118	26				465	
%	7.7	20.9	40.4	25.4	5.6					

Table 5b. The predicted frequency of peak wave periods (Tp) in seconds for waves coming from 8 specified directions in April. These data were derived from 3 hourly wind velocity measurements (Kozo, 1983).

Hs (m)	1	2	3	4	5	6	7	8	9	10	11	12	13	TOTAL	%
N	61	18	14	16	1	1								111	22.8
NE	60	17	21	12	8	3								121	24.9
E	22	15	6	3	3	0	2							51	10.5
SE	27	4	0	1										32	6.6
S	36	6	7	1										50	10.3
SW	43	6	1	0	0	1								51	10.5
W	22	5												27	5.6
NW	35	7	1											43	8.9
TOTAL	306	78	50	33	12	5	2							486	
%	63.0	16.1	10.3	6.8	2.5	1.0	.4								

Table 6a. The predicted frequency of significant wave heights (Hs) in meters for waves coming from 8 specified directions in May. These data were derived from 3 hourly wind velocity measurements (Kozo, 1983).

Tp (S)	2	4	6	8	10	12	14	16	TOTAL	%
N	6	23	50	30	2				111	22.8
NE	4	19	54	33	11				121	24.9
E	6	6	25	6	6	2			51	10.5
SE	10	9	12	1					32	6.6
S	14	13	15	8					50	10.3
SW	8	21	14	7	0	1			51	10.5
W	3	10	14						27	5.6
NW	6	16	20	1					43	8.9
TOTAL	57	117	204	86	19	3			486	
%	11.7	24.1	42.	17.7	3.9	.6				

Table 6b. The predicted frequency of peak wave periods (Tp) in seconds for waves coming from 8 specified directions in May. These data were derived from 3 hourly wind velocity measurements (Kozo, 1983).

Hs (m)	1	2	3	4	5	6	7	8	9	10	11	12	13	TOTAL	%
N	45	16	13	5	1	1								81	18.2
NE	28	13	14	10	1									66	14.8
E	10													10	2.3
SE	34													34	7.6
S	36	1	1											38	8.5
SW	67	2												69	15.5
W	56	22	3	2	0	1	1							85	19.1
NW	42	12	5	2	1									62	13.9
TOTAL	318	66	36	19	3	2	1							445	
%	71.5	14.8	8.1	4.3	.7	.5	.2								

Table 7a. The predicted frequency of significant wave heights (Hs) in meters for waves coming from 8 specified directions in June. These data were derived from 3 hourly wind velocity measurements (Kozo, 1983).

Tp(S)	2	4	6	8	10	12	14	16	TOTAL	%
N	12	18	31	18	2				81	18.2
NE	7	9	25	14	11				66	14.8
E	3	5	2						10	2.3
SE	13	17	4						34	7.6
S	9	20	8	1					38	8.5
SW	17	33	17	2					69	15.5
W	14	13	51	3	3	1			85	19.1
NW	13	17	24	7	1				62	13.9
TOTAL	88	132	162	45	17	1			445	
%	19.8	29.7	36.4	10.1	3.8	.2				

Table 7b. The predicted frequency of peak wave periods (Tp) in seconds for waves coming from 8 specified directions in June. These data were derived from 3 hourly wind velocity measurements (Kozo, 1983).

Hs (m)	1	2	3	4	5	6	7	8	9	10	11	12	13	TOTAL	%
N	34	12	10	4	8	2								70	9.8
NE	32	13	10	2	6	0	2							65	9.1
E	42	5	2											49	6.9
SE	83	5	2	4										94	13.2
S	112	5	1											118	16.6
SW	118	5	2											125	17.5
W	104	11	5	1	0	1								122	17.1
NW	52	10	7	1										70	9.8
TOTAL	577	66	39	12	14	3	2							713	
%	80.9	9.3	5.5	1.7	2.0	.4	.3								

Table 8a. The predicted frequency of significant wave heights (Hs) in meters for waves coming from 8 specified directions in July. These data were derived from 3 hourly wind velocity measurements (Kozo, 1983).

Tp(S)	2	4	6	8	10	12	14	16	TOTAL	%
N	7	12	27	14	10				70	9.8
NE	8	10	27	10	8	2			65	9.1
E	4	14	29	2					49	6.9
SE	27	41	20	6					94	13.2
S	42	58	17	1					118	16.6
SW	41	56	21	7					125	17.5
W	14	49	52	5	2				122	17.1
NW	7	24	31	8					70	9.8
TOTAL	150	264	224	53	20	2			713	
%	21.0	37.	31.4	7.4	2.8	.3				

Table 8b. The predicted frequency of peak wave periods (Tp) in seconds for waves coming from 8 specified directions in July. These data were derived from 3 hourly wind velocity measurements (Kozo, 1983).

Hs (m)	1	2	3	4	5	6	7	8	9	10	11	12	13	TOTAL	%
N	121	44	19	17	5	1								207	17.1
NE	109	28	25	10	4	0	1							177	14.6
E	72	27	24	12	1	0	2							138	11.4
SE	107	17	18	10	3	0	1							156	12.9
S	106	18	6	4	4									138	11.4
SW	104	18	13	0	2	1								138	11.4
W	100	26	20	1	0	1								148	12.2
NW	85	17	5	1	1									109	9.0
TOTAL	804	195	130	55	20	3	4							1211	
%	66.4	16.1	10.7	4.5	1.7	.3	.3								

Table 9a. The predicted frequency of significant wave heights (Hs) in meters for waves coming from 8 specified directions in August. These data were derived from 3 hourly wind velocity measurements (Kozo, 1983).

Tp(S)	2	4	6	8	10	12	14	16	TOTAL	%
N	12	46	107	36	6				207	17.1
NE	12	57	68	25	14	1			177	14.6
E	10	25	64	24	13	2			138	11.4
SE	30	48	46	28	3	1			156	12.9
S	29	49	46	10	4				138	11.4
SW	22	44	38	31	2	1			138	11.4
W	18	38	70	20	2				148	12.2
NW	14	39	49	6	1				109	9.0
TOTAL	147	346	488	180	45	5			1211	
%	12.1	28.6	40.3	14.9	3.7	.4				

Table 9b. The predicted frequency of peak wave periods (Tp) in seconds for waves coming from 8 specified directions in August. These data were derived from 3 hourly wind velocity measurements (Kozo, 1983).

Hs (m)	1	2	3	4	5	6	7	8	9	10	11	12	13	TOTAL	%
N	102	46	40	11	6	2								207	21.8
NE	63	20	15	4	1	0	3							106	11.2
E	57	8	5	2	4	0	3	2						81	8.5
SE	47	10	5	3										65	6.8
S	51	15	9	3	2									80	8.4
SW	79	23	14	0	3	1								120	12.6
W	100	25	11	2	0	2								140	14.7
NW	98	31	16	7										152	16.0
TOTAL	597	178	115	32	16	5	6	2						951	
%	62.8	18.7	12.1	3.4	1.7	.5	.6	.2							

Table 10a. The predicted frequency of significant wave heights (Hs) in meters for waves coming from 8 specified directions in September. These data were derived from 3 hourly wind velocity measurements (Kozo, 1983).

Tp (S)	2	4	6	8	10	12	14	16	TOTAL	%
N	12	40	96	51	8				207	21.8
NE	7	21	55	15	5	3			106	11.2
E	7	23	35	5	6	5			81	8.5
SE	12	19	26	8					65	6.8
S	12	21	33	12	2				80	8.4
SW	19	31	29	37	3	1			120	12.6
W	19	40	66	11	4				140	14.7
NW	13	48	68	23					152	16.0
TOTAL	101	243	408	162	28	9			951	
%	10.6	25.6	42.9	17.0	2.9	1.0				

Table 10b. The predicted frequency of peak wave periods (Tp) in seconds for waves coming from 8 specified directions in September. These data were derived from 3 hourly wind velocity measurements (Kozo, 1983).

Hs (m)	1	2	3	4	5	6	7	8	9	10	11	12	13	TOTAL	%
N	58	28	23	11	8	8	3	0	7					146	31.4
NE	34	14	10	4	3									65	14.0
E	26	7	10	8	3	0	0	4	3					61	13.1
SE	18	6	6	4	2	0								36	7.7
S	7	2	3	3	1	0	2							18	3.9
SW	8	6	8	0	4	1	0	1						28	6.0
W	12	11	9	0	2	2	0	2	0	1				39	8.4
NW	37	20	8	2	1	2	1	1						72	15.5
TOTAL	200	94	77	32	24	13	6	8	10	1				465	
%	43.	20.2	16.6	6.9	5.2	2.8	1.3	1.7	2.2	.2					

Table 11a. The predicted frequency of significant wave heights (Hs) in meters for waves coming from 8 specified directions in October. These data were derived from 3 hourly wind velocity measurements (Kozo, 1983).

Tp (S)	2	4	6	8	10	12	14	16	TOTAL	%
N	8	26	52	34	16	10			146	31.4
NE	6	13	29	10	7				65	14.0
E	7	7	19	10	11	4	3		61	13.1
SE	4	4	16	10	2				36	7.7
S	2	3	4	6	1	2			18	3.9
SW	1	5	2	14	4	2			28	6.0
W	3	4	5	11	11	4	1		39	8.4
NW	3	14	40	10	3	2			72	15.5
TOTAL	34	76	167	105	55	24	4		465	
%	7.3	16.3	35.9	22.6	11.8	5.2	.9			

Table 11b. The predicted frequency of peak wave periods (Tp) in seconds for waves coming from 8 specified directions in October. These data were derived from 3 hourly wind velocity measurements (Kozo, 1983).

Hs (m)	1	2	3	4	5	6	7	8	9	10	11	12	13	TOTAL	%
N	83	41	59	33	10	4	1							231	32.4
NE	29	25	28	16	15	25	0	14	7	3	1			163	22.9
E	16	9	21	17	16	0	14	8	4	0	2	1	1	109	15.3
SE	9	7	9	6	4	0	3	1						39	5.5
S	17	9	9	2	1									38	5.3
SW	10	4	1											15	2.1
W	23	6	2											31	4.4
NW	69	8	8	1										86	12.1
TOTAL	256	109	137	75	46	29	18	23	11	3	3	1	1	712	
%	36.	15.3	19.2	10.5	6.5	4.1	2.5	3.2	1.5	.4	.4	.1	.1		

Table 12a. The predicted frequency of significant wave heights (Hs) in meters for waves coming from 8 specified directions in November. These data were derived from 3 hourly wind velocity measurements (Kozo, 1983).

Tp(S)	2	4	6	8	10	12	14	16	TOTAL	%
N	15	18	91	92	14	1			231	32.4
NE	1	6	47	44	40	21	4		163	22.9
E	1	4	20	21	33	22	7	1	109	15.3
SE	1	2	13	15	4	4			39	5.5
S	0	6	20	11	1				38	5.3
SW	1	7	2	5					15	2.1
W	1	9	19	2					31	4.4
NW	22	29	26	9	0				86	12.1
TOTAL	42	81	238	199	92	48	11	1	712	
%	5.9	11.4	33.4	28.	12.9	6.7	1.5	.1		

Table 12b. The predicted frequency of peak wave periods (Tp) in seconds for waves coming from 8 specified directions in November. These data were derived from 3 hourly wind velocity measurements (Kozo, 1983).

Hs (m)	1	2	3	4	5	6	7	8	9	10	11	12	13	TOTAL	%
N	64	44	23	23	4	6	2	1	0	1				168	23.1
NE	71	39	34	26	13	12	14	1	2					212	29.2
E	37	11	9	7	11	0	10	12	7	0	5	3		112	15.4
SE	9	9	10	3	8	0	4	5	2					50	6.9
S	14	11	7	11	11	0	3	0	1					58	8.0
SW	17	5	6	0	7	5	0	2						42	5.8
W	20	9	8	5	0	6	2							50	6.9
NW	29	4	1	1										35	4.8
TOTAL	261	132	98	76	54	29	35	21	12	1	5	3		727	
%	35.9	18.2	13.5	10.5	7.4	4.0	4.8	2.9	1.7	.1	.7	.4			

Table 13a. The predicted frequency of significant wave heights (Hs) in meters for waves coming from 8 specified directions in December. These data were derived from 3 hourly wind velocity measurements (Kozo, 1983).

Tp(S)	2	4	6	8	10	12	14	16	TOTAL	%
N	14	14	80	46	10	3	1		168	23.1
NE	7	22	81	60	25	17			212	29.2
E	5	6	37	9	18	22	15		112	15.4
SE	1	3	14	13	8	11			50	6.9
S	2	4	19	18	11	4			58	8.0
SW	2	9	6	11	7	7			42	5.8
W	5	6	18	8	11	2			50	6.9
NW	9	10	14	2					35	4.8
TOTAL	45	74	269	167	90	66	16		727	
%	6.2	10.2	37.	23.	12.4	9.1	2.2			

Table 13b. The predicted frequency of peak wave periods (Tp) in seconds for waves coming from 8 specified directions in December. These data were derived from 3 hourly wind velocity measurements (Kozo, 1983).

Hs (m)	1	2	3	4	5	6	7	8	9	10	11	12	13	TOTAL %
N	3	4	4	0	4	1	0	1	0	+	+			17
NE	3	5	0	3	4	0	2	0	1	0	+	+		18
E	2	4	0	4	4	2	0	1	0	+				17
SE	3	4	3	0	3	2	0	+	+	+				15
S	2	3	2	0	2	1	0	+	0	+	+			10
SW	1	0	2	2	2	0	1	0	+	0	0	+		8
W	2	0	1	1	0	1	0	0	1	0	0	+		6
NW	3	0	2	2	0	1	+	0	0	+	0	+		8
CALM	2													2
TOTAL%	20	20	14	12	19	8	3	2	2	+	+	+		

Table 14a. The predicted frequency of significant wave heights (Hs) in meters for waves coming from 8 specified directions in January. These data were derived from wind velocity measurements (Brower *et al.*, 1977).

Tp(S)	2	4	6	8	10	12	14	16	TOTAL %
N	+	3	4	4	5	1	+	+	17
NE	+	1	7	3	4	3	+	+	18
E	+	+	6	4	6	1	+		17
SE	+	3	4	3	5	+	+		15
S	+	2	3	2	3	+	+	+	10
SW	+	+	1	4	2	1	+		8
W	+	1	1	1	1	2	+		6
NW	+	1	2	4	1	+	+		8
CALM	2								2
TOTAL%	2	11	28	25	27	8	+	+	

Table 14b. The predicted frequency of peak wave periods (Tp) in seconds for waves coming from 8 specified directions in January. These data were derived from wind velocity measurements (Brower *et al.*, 1977).

Hs (m)	1	2	3	4	5	6	7	8	9	10	11	12	13	14	15	16	TOTAL%
N	4	5	5	0	5	3	0	1	+	+							23
NE	3	5	0	5	5	0	3	0	1	0	+	+					22
E	3	3	0	3	2	2	0	1	0	+	+						14
SE	1	4	2	0	2	1	0	+	+								10
S	1	3	2	0	2	1	0	+	0	+	+						9
SW	1	0	2	2	1	0	1	0	+	0	0	+					7
W	2	0	1	1	0	1	0	0	1	0	0	+	0	0	+	+	6
NW	3	0	2	1	1	0	1	0	0	+	0	+					8
CALM	1																1
TOTAL%	19	20	14	12	18	8	5	2	2	+	+	+	0	0	+	+	

Table 15a. The predicted frequency of significant wave heights (Hs) in meters for waves coming from 8 specified directions in February. These data were derived from wind velocity measurements (Brower *et al.*, 1977).

Tp (S)	2	4	6	8	10	12	14	16	18	TOTAL%
N	+	4	5	5	8	1	+			23
NE	+	1	7	5	5	4	+	+		22
E	+	1	5	3	4	1	+	+		14
SE	+	1	4	2	3	+				10
S	+	1	3	2	3	+	+	+		9
SW	+	+	1	4	1	1	+			7
W	+	1	1	1	1	2	+	+	+	6
NW	+	1	2	3	1	1	+			8
CALM	1									1
TOTAL%	1	10	28	25	26	10	+	+	+	

Table 15b. The predicted frequency of peak wave periods (Tp) in seconds for waves coming from 8 specified directions in February. These data were derived from wind velocity measurements (Brower *et al.*, 1977).

Hs (m)	1	2	3	4	5	6	7	8	9	10	11	12	13	14	15	16	TOTAL%
N	4	5	4	0	3	2	1	0	+	+							19
NE	3	5	0	3	3	0	2	0	1	0	+	+					17
E	3	4	0	4	3	2	0	1	0	+							17
SE	4	3	2	0	1	1	0	+	+	+							11
S	3	3	2	0	2	1	0	+	0	0	+						11
SW	2	0	2	2	1	0	+	0	+	0	0	+					7
W	2	0	2	1	0	1	0	0	+	0	0	+	0	0	+	+	6
NW	4	0	3	3	2	0	1	0	0	+							13
CALM	2																2
TOTAL%	28	20	15	13	15	7	4	1	1	+	+	+	0	0	+	+	

Table 16a. The predicted frequency of significant wave heights (Hs) in meters for waves coming from 8 specified directions in March. These data were derived from wind velocity measurements (Brower *et al.*, 1977).

Tp(S)	2	4	6	8	10	12	14	16	18	TOTAL%
N	+	4	5	4	5	1	+			19
NE	+	1	7	3	3	3	+	+		17
E	+	1	6	4	5	1	+			17
SE	+	4	3	2	2	+	+			11
S	+	3	3	2	3	+	0	+		11
SW	+	1	1	4	1	+	+			7
W	+	1	1	2	1	1	+	+	+	6
NW	+	1	3	6	2	1	+			13
CALM	2									2
TOTAL%	2	16	29	27	22	7	+	+	+	

Table 16b. The predicted frequency of peak wave periods (Tp) in seconds for waves coming from 8 specified directions in March. These data were derived from wind velocity measurements (Brower *et al.*, 1977).

Hs (m)	1	2	3	4	5	6	7	8	9	10	11	12	13	14	15	16	TOTAL %
N	4	6	4	0	3	2	0	1									20
NE	2	3	0	3	1	0	1	0	+	0	+						10
E	3	3	2	0	2	1	0	+	0	+							11
SE	3	3	2	0	1	1	0	+	0	+							10
S	3	3	3	0	2	1	0	+	0	+	+						12
SW	3	0	3	2	1	0	+	0	+								9
W	3	0	3	2	0	1	0	0	+	0	0	+	0	0	+		9
NW	4	0	5	4	3	0	1	0	0	+							17
CALM	2																2
TOTAL%	27	18	22	11	13	6	2	1	+	+	+	+	0	0	+		

Table 17a. The predicted frequency of significant wave heights (Hs) in meters for waves coming from 8 specified directions in April. These data were derived from wind velocity measurements (Brower *et al.*, 1977).

Tp (S)	2	4	6	8	10	12	14	16	TOTAL %
N	+	4	6	4	5	1			20
NE	+	+	5	3	1	1	+		10
E	+	3	3	2	3	+	+		11
SE	+	3	3	2	2	+	+		10
S	+	3	3	3	3	+	+	+	12
SW	+	1	2	5	1	+			9
W	+	1	2	3	2	1	+	+	9
NW	+	1	3	9	3	1	+		17
CALM	2								2
TOTAL%	2	16	27	31	20	4	+	+	

Table 17b. The predicted frequency of peak wave periods (Tp) in seconds for waves coming from 8 specified directions in April. These data were derived from wind velocity measurements (Brower *et al.*, 1977).

Hs (m)	1	2	3	4	5	6	7	8	9	10	11	12	13	TOTAL %
N	4	7	0	4	3	0	1	0	+					19
NE	2	0	4	3	2	0	+							11
E	4	5	0	2	1	+	0	+						12
SE	4	4	2	0	1	+	0	+						11
S	5	5	2	0	1	+	0	+						13
SW	3	0	3	2	1	0	+	0	+					9
W	3	0	3	1	0	+	0	0	+	0	0	+		7
NW	4	0	5	3	0	2	0	+	0	+				14
CALM	1													1
TOTAL%	30	21	19	15	9	2	1	+	+	+	0	+		

Table 18a. The predicted frequency of significant wave heights (Hs) in meters for waves coming from 8 specified directions in May. These data were derived from wind velocity measurements (Brower *et al.*, 1977).

Tp(S)	2	4	6	8	10	12	14	16	TOTAL %
N	+	1	10	4	3	1			19
NE	+	+	6	3	2	+			11
E	+	1	8	2	1	+			12
SE	+	4	4	2	1	+			11
S	+	5	5	2	1	+			13
SW	+	1	2	5	1	+			9
W	+	1	2	3	1	+	+		7
NW	+	1	3	8	2	+	+		14
CALM	1								1
TOTAL%	1	14	40	29	12	1	+		

Table 18b. The predicted frequency of peak wave periods (Tp) in seconds for waves coming from 8 specified directions in May. These data were derived from wind velocity measurements (Brower *et al.*, 1977).

Hs (m)	1	2	3	4	5	6	7	8	9	10	11	12	13	TOTAL %
N	6	0	6	3	0	1	0	+						16
NE	4	0	5	2	1	0	+							12
E	4	4	0	2	1	+								11
SE	5	4	1	0	+	+	0	+						10
S	7	5	1	0	+	+								13
SW	4	0	4	1	+									9
W	4	0	3	1	0	+	0	0	+	0	0	+		8
NW	6	0	3	1	0	+	0	+						10
CALM	1													1
TOTAL%	41	13	23	10	2	1	+	+	+	0	0	+		

Table 19a. The predicted frequency of significant wave heights (Hs) in meters for waves coming from 8 specified directions in June. These data were derived from wind velocity measurements (Brower *et al.*, 1977).

Tp(S)	2	4	6	8	10	12	14	16	TOTAL %
N	+	2	4	9	1	+			16
NE	+	1	8	2	1	+			12
E	+	1	7	2	1				11
SE	+	5	4	1	+	+			10
S	+	7	5	1	+				13
SW	+	1	3	5	+				9
W	+	1	3	3	+	+	+		8
NW	+	2	4	3	1	+	+		10
CALM	1								1
TOTAL%	1	20	38	26	5	+	+		

Table 19b. The predicted frequency of peak wave periods (Tp) in seconds for waves coming from 8 specified directions in June. These data were derived from wind velocity measurements (Brower *et al.*, 1977).

Hs (m)	1	2	3	4	5	6	7	8	9	10	11	12	13	TOTAL %
N	4	0	3	1	0	+								8
NE	4	0	3	1	+									8
E	5	4	0	1	+									10
SE	7	5	1	0	+									13
S	10	6	1	0	1	+								18
SW	7	0	6	2	+	0	+							15
W	5	0	5	2	0	+	0	0	+					12
NW	5	0	5	2	0	+								12
CALM	2													2
TOTAL%	51	15	24	9	1	+	+	0	+					

Table 20a. The predicted frequency of significant wave heights (Hs) in meters for waves coming from 8 specified directions in July. These data were derived from wind velocity measurements (Brower *et al.*, 1977).

Tp (S)	2	4	6	8	10	12	14	16	TOTAL %
N	+	1	3	4	+				8
NE	+	1	6	1	+				8
E	+	1	8	1	+				10
SE	+	7	5	1	+				13
S	+	10	6	1	1				18
SW	+	2	5	8	+	+			15
W	+	1	4	5	2	+			12
NW	+	1	4	7	+				12
CALM	2								2
TOTAL%	2	24	41	28	3	+			

Table 20b. The predicted frequency of peak wave periods (Tp) in seconds for waves coming from 8 specified directions in July. These data were derived from wind velocity measurements (Brower *et al.*, 1977).

Hs (m)	1	2	3	4	5	6	7	8	9	10	11	12	13	TOTAL %
N	4	0	4	2	0	1	0	+						11
NE	1	0	2	1	+	0	+							4
E	2	2	0	1	+	+	0	+						5
SE	4	4	1	0	1	+	0	+						10
S	8	7	2	0	1	+	0	+						18
SW	7	0	7	3	1	0	+	0	+					18
W	6	0	5	2	0	1	0	0	+					14
NW	6	0	6	2	0	1	0	+						15
CALM	1													1
TOTAL%	41	13	27	11	3	3	+	+	+					

Table 21a. The predicted frequency of significant wave heights (Hs) in meters for waves coming from 8 specified directions in August. These data were derived from wind velocity measurements (Brower *et al.*, 1977).

Tp(S)	2	4	6	8	10	12	14	16	TOTAL %
N	+	1	3	6	1	+			11
NE	+	+	3	1	+	+			4
E	+	+	4	1	+	+			5
SE	+	4	4	1	1	+			10
S	+	8	7	2	1	+			18
SW	+	2	5	10	1	+			18
W	+	2	4	5	2	1			14
NW	+	1	5	8	1	+			15
CALM	1								1
TOTAL%	1	18	35	34	7	1			

Table 21b. The predicted frequency of peak wave periods (Tp) in seconds for waves coming from 8 specified directions in August. These data were derived from wind velocity measurements (Brower *et al.*, 1977).

Hs (m)	1	2	3	4	5	6	7	8	9	10	11	12	13	TOTAL %
N	4	0	6	4	0	2	0	1	+	0	+			17
NE	3	0	4	2	1	0	+	+	0	+				10
E	3	3	0	2	1	+	0	+						9
SE	3	3	2	0	1	+	0	+	+					9
S	4	4	2	0	1	+	0	+	+					11
SW	3	0	3	2	1	0	+	0	+					9
W	5	0	3	2	0	1	0	0	+					11
NW	8	0	7	4	0	2	0	+	0	+				21
CALM	1													1
TOTAL%	35	10	27	16	5	5	+	1	+	+	+			

Table 22a. The predicted frequency of significant wave heights (Hs) in meters for waves coming from 8 specified directions in September. These data were derived from wind velocity measurements (Brower *et al.*, 1977).

Tp (S)	2	4	6	8	10	12	14	16	18	TOTAL %
N	+	1	3	10	2	1	+	0	+	17
NE	+	1	6	2	1	+	+	+		10
E	+	1	5	2	1	+				9
SE	+	3	3	2	1	+				9
S	+	4	4	2	1	+	+			11
SW	+	1	2	5	1	+	+			9
W	+	2	3	3	2	1				11
NW	+	2	6	11	2	+	+			21
CALM	1									1
TOTAL%	1	15	32	37	11	2	+	+	+	

Table 22b. The predicted frequency of peak wave periods (Tp) in seconds for waves coming from 8 specified directions in September. These data were derived from wind velocity measurements (Brower *et al.*, 1977).

Hs (m)	1	2	3	4	5	6	7	8	9	10	11	12	13	TOTAL %
N	4	0	5	4	0	4	0	1	+	+				18
NE	2	0	2	2	2	0	1	+	0	+	+			9
E	1	1	0	1	1	1	0	+	0	+				5
SE	1	1	2	0	1	1	0	+	+					6
S	2	3	3	0	2	1	0	+	+					11
SW	3	0	4	3	2	0	1	0	+	+	+			13
W	4	0	4	3	0	2	0	0	1	0	0	+	+	14
NW	7	0	7	5	0	3	0	1	0	+	+	+		23
CALM	2													2
TOTAL%	25	5	27	18	8	12	2	2	1	+	+	+	+	

Table 23a. The predicted frequency of significant wave heights (Hs) in meters for waves coming from 8 specified directions in October. These data were derived from wind velocity measurements (Brower *et al.*, 1977).

Tp(S)	2	4	6	8	10	12	14	16	18	TOTAL%
N	+	1	3	9	4	1	+	+		18
NE	+	1	3	2	2	1	+	+		9
E	0	+	2	1	2	+	0	+		5
SE	+	1	1	2	2	+				6
S	+	2	3	3	3	+	+			11
SW	+	1	2	7	2	1	+	+		13
W	+	1	3	4	3	3	+	+		14
NW	+	2	5	12	3	1	+	+	+	23
CALM	2									2
TOTAL%	2	9	22	40	21	7	+	+	+	

Table 23b. The predicted frequency of peak wave periods (Tp) in seconds for waves coming from 8 specified directions in October. These data were derived from wind velocity measurements (Brower *et al.*, 1977).

Hs (m)	1	2	3	4	5	6	7	8	9	10	11	12	13	14	15	16	TOTAL%
N	3	0	3	3	0	3	0	2	0	+	0	+	+				14
NE	2	0	3	2	2	0	1	+	0	+	+						10
E	1	3	0	3	2	1	0	+	0	+							10
SE	1	2	2	0	2	1	0	1	+	+							9
S	1	3	3	0	3	1	0	+	+	+							11
SW	2	0	3	4	3	0	1	0	+	+	+						13
W	3	0	3	2	0	1	0	0	+	0	0	+	+	+			9
NW	4	0	4	4	0	3	0	1	0	+	+	+					16
CALM	1																1
TOTAL%	21	8	21	18	12	10	2	4	+	+	+	+	+	+			

Table 24a. The predicted frequency of significant wave heights (Hs) in meters for waves coming from 8 specified directions in November. These data were derived from wind velocity measurements (Brower *et al.*, 1977).

Tp(S)	2	4	6	8	10	12	14	16	18	TOTAL%
N	+	1	2	6	3	2	+	+		14
NE	+	1	4	2	2	1	+	+		10
E	+	+	4	3	3	+	+			10
SE	+	1	2	2	3	1	+			9
S	+	1	3	3	4	+	+	+		11
SW	+	+	2	7	3	1	+	+		13
W	+	1	2	3	2	1	+	+	+	9
NW	+	1	3	8	3	1	+	+	+	16
CALM	1									1
TOTAL%	1	6	22	34	23	7	+	+	+	

Table 24b. The predicted frequency of peak wave periods (Tp) in seconds for waves coming from 8 specified directions in November. These data were derived from wind velocity measurements (Brower *et al.*, 1977).

Hs (m)	1	2	3	4	5	6	7	8	9	10	11	12	13	TOTAL %
N	4	5	0	4	3	0	2	1	0	+				19
NE	3	4	0	4	4	0	2	0	1	0	+	+	+	18
E	1	3	0	2	3	2	0	1	0	+	+			12
SE	2	3	2	0	2	1	0	+	+	+				10
S	1	2	3	0	2	1	0	+	+					9
SW	1	0	2	2	1	0	1	0	+	+				7
W	2	0	1	1	0	1	0	0	1	0	0	+	+	6
NW	4	0	4	2	0	2	0	1	0	+	0	+		13
CALM	1													1
TOTAL%	23	17	12	15	15	7	5	3	2	+	+	+	+	

Table 25a. The predicted frequency of significant wave heights (Hs) in meters for waves coming from 8 specified directions in December. These data were derived from wind velocity measurements (Brower *et al.*, 1977).

Tp(S)	2	4	6	8	10	12	14	16	18	TOTAL%
N	+	1	8	4	5	1	+			19
NE	+	1	6	4	4	3	+	+		18
E	+	+	4	2	5	1	+	+		12
SE	+	2	3	2	3	+	+			10
S	+	1	2	3	3	+	+			9
SW	+	+	1	4	1	1	+			7
W	+	1	1	1	1	2	+	+		6
NW	+	1	3	6	2	1	+			13
CALM	1									1
TOTAL%	1	7	28	26	24	9	+	+		

Table 25b. The predicted frequency of peak wave periods (Tp) in seconds for waves coming from 8 specified directions in December. These data were derived from wind velocity measurements (Brower *et al.*, 1977).

U.S. DEPARTMENT OF COMMERCE
NATIONAL OCEANIC AND ATMOSPHERIC ADMINISTRATION
NATIONAL OCEAN SERVICE
Arctic Environmental Assessment Center
Grace Hall, Suite 300
4230 University Drive
Anchorage, Alaska 99508

UNIV OF ALASKA/INFO SERVICES
ARCTIC ENV INFO AND DATA CTR
707 A STREET
ANCHORAGE, AK 99501